

For Reference

NOT TO BE TAKEN FROM THIS ROOM

For Reference

NOT TO BE TAKEN FROM THIS ROOM

Ex LIBRIS
UNIVERSITATIS
ALBERTAENSIS





Digitized by the Internet Archive
in 2019 with funding from
University of Alberta Libraries

<https://archive.org/details/Ellis1964>

Thesis
1964 (F)
#5D

THE UNIVERSITY OF ALBERTA

ANALYSIS OF NATURAL ULTRA LOW FREQUENCY
ELECTROMAGNETIC FIELDS

by

ROBERT MALCOLM ELLIS

A THESIS

SUBMITTED TO THE FACULTY OF GRADUATE STUDIES
IN PARTIAL FULFILMENT OF THE REQUIREMENTS FOR THE DEGREE
OF DOCTOR OF PHILOSOPHY

DEPARTMENT OF PHYSICS

EDMONTON, ALBERTA

AUGUST, 1964

UNIVERSITY OF ALBERTA

FACULTY OF GRADUATE STUDIES

This thesis is an investigation of the earth's natural electromagnetic field in the frequency range .001 to 5 cps. Its application to determine the conductivity of the earth at depth, and a study of geophysical techniques as a means of analysis.

The undersigned certify that they have read, and recommend to the Faculty of Graduate Studies for acceptance, a thesis entitled ANALYSIS OF NATURAL ULTRA LOW FREQUENCY ELECTROMAGNETIC FIELDS, submitted by Robert Malcolm Ellis, in partial fulfilment of the requirements for the degree Doctor of Philosophy.

ABSTRACT

This thesis is an investigation of the earth's natural electromagnetic field in the frequency range .001 to 5 cps, its application to determine the conductivity of the earth at depth, and a study of spectral techniques as a method of analysis.

Magnetotelluric results from central Alberta give crustal resistivities of about 1000 ohm-m with no indication of a major decrease in resistivity at the Mohorovicic discontinuity (or at shallower depths). In southern Alberta the crustal resistivities are also found to be about 1000 ohm-m to a depth of 35 km where there is a decrease to 30 ohm-m.

Data from a single station near Montreal Lake in central Saskatchewan have been interpreted as indicating that the station is on the conductive (60 ohm-m) side of a vertical fault striking NNE and extending to a depth of 10 to 25 km. The resistivity contrast across the fault may be of the order of 100/1. The basement is more conductive than either surface layer.

A study of the large vertical magnetic field at Montreal Lake indicates that sources are important for individual pulsations. However, averaged over long sections of record, the geologic effects may predominate.

For Montreal Lake records with $K_p = 3+$ or less, the energy falls off quite rapidly up to 0.14 cps and then decreases very slowly over the frequency range to 5 cps. The spectra with larger K_p decrease much less rapidly to about 0.75 cps but to a lower energy level.

Digital spectral analysis was found to be a satisfactory quantitative tool. Prewhitening is effective in improving estimates but trend removal must be used with caution. Daniell estimates are more satisfactory than hanning as all the estimates are positive and the coherencies are more meaningful in the case of noisy records.

Coherency was found to be only a rough measure of the quality of the data as even for very large values ($> .99$), the orthogonal electric-magnetic ratios are not necessarily smooth.

ACKNOWLEDGEMENTS

I wish to express my sincere thanks to Professor K. Vozoff for his help, ideas, and continued optimism throughout the preparation of this thesis.

I am grateful to M. D. Burke who designed, built and operated the field equipment, and performed innumerable tasks necessary for the completion of this thesis.

Professor G. D. Garland, Dr. A. J. Surkan, H. Hasegawa, and C. Quon contributed through their many discussions on magnetotellurics. Mr. Hasegawa's program for the five-layer magnetotelluric case was used to calculate the theoretical curves.

Technical assistance was given by G. T. Sande, Jr., H. McCullough, and K. F. Lam.

The computation was done at the Department of Computing Science, University of Alberta, and the Institute of Computer Science, University of Toronto. The cooperation and assistance of the staff of these centers is gratefully acknowledged.

The author was supported during the preparation of this thesis by the Petroleum Research Fund of the American Chemical Society and the National Research Council.

This project has been sponsored by the Petroleum Research Fund of the American Chemical Society, the National Research Council, the University of Alberta, and the Office of Naval Research.

TABLE OF CONTENTS

	Page
Chapter I. INTRODUCTION	1
Micropulsations and Telluric Currents	1
The Telluric Method	6
The Magnetotelluric Method	6
The Vertical Magnetic Field	12
Objectives of the University of Alberta Group	14
Purpose of this Thesis	15
Chapter II. DETECTION, ANALYSIS, AND PRELIMINARY RESULTS	16
Signal Detection	16
Basic Analysis Techniques	20
Preliminary Results	26
Discussion	33
Chapter III. ANALYSIS OF 1962 DATA	42
Instrumentation	42
Purpose and Location of Field Experiments	43
Analysis Procedures	48
Decimation of Apparent Resistivity Values using Coherency	50
Resistivity Analysis	56
Roughness of Apparent Resistivity Curves	70
Further Analysis of H_z and Source Effects at Montreal Lake	76
K_p - Spectral Relationships	93

Contents	Page
Chapter IV. SUGGESTIONS FOR ANALYSIS PROCEDURES AND FURTHER WORK	98
REFERENCES	102
APPENDICES	A 1
A. Basic Magnetotelluric Theory	A 2
B. Spectral Analysis	A 7
C. Computational Experiments	A 18
D. Plots of Spectral Data	A 56

LIST OF TABLES

	Page
Table 1. Notation for Regular Pulsations	2
Table 2. Notation for Irregular Pulsations	2
Table 3. Station Information	47
Table 4. Tape Information	49
Table 5. Analysis Parameters	40
Table 6. Apparent Resistivity Deviations -- Montreal Lake 2-1 $H_y - E_x$	75
Table C-1.	A 26

LIST OF FIGURES

		Page
Figure	1. Block diagram of magnetotelluric recording system showing one electric and one magnetic system	17
Figure	2. Block diagram of field calibration system	19
Figure	3. Amplitude calibration curves of the 1962 electric and magnetic calibration systems	21
Figure	4. Phase calibration curves of 1962 system	22
Figure	5. Diagrammatic representation of analog-to-digital conversion system	25
Figure	6. Locations of 1961 Alberta field stations with lithology of Precambrian basement as inferred from well samples and gravity anomalies	27
Figure	7. Geological cross-section AB (Figure 6) of Edmonton area with typical well-log resistivities for this region	28
Figure	8. Magnetotelluric apparent resistivity curves -- Cooking Lake, Alberta	30
Figure	9. Magnetotelluric apparent resistivity curves -- Onoway, Alberta	32
Figure	10. Magnetotelluric apparent resistivity curves -- Bon Accord, Alberta	34
Figure	11. Magnetotelluric apparent resistivity curves -- Kavanagh, Alberta	35
Figure	12. Price curves with geologic parameters approximating those of central Alberta	37

Figure	13.	Apparent resistivities computed using 3 different records from Bon Accord	39
Figure	14.	Location of 1962 field stations	44
Figure	15.	Sedimentary resistivities at Montreal Lake based on well-logs from Great Plains Montreal Lake # 2-5	46
Figure	16.	HF spectra with signal and noise of comparable magnitude ($K = 185-205$)	52
Figure	17.	HF spectra with noise present in E_y and not in H_x at $K = 45$, and coherent noise predominating in both at $K = 74, 93, 138, 148$, and $K = 180-220$.	53
Figure	18.	Uncorrected power spectra of Montreal Lake 4-4 using data prewhitened by $z_i = x_i - x_{i-1}$	55
Figure	19.	Averaged H_x-E_y apparent resistivity curve with two-layer theoretical fit	58
Figure	20.	Averaged H_y-E_x apparent resistivity curve with two-layer theoretical fit	59
Figure	21.	Cagniard apparent resistivity -- Montreal Lake 2-2	60
Figure	22.	Cagniard apparent resistivity -- Montreal Lake 4-4	61
Figure	23.	Montreal Lake 4-4 H_y-E_x spectra with coherent noise spikes predominating for $f > 1$ cps	62
Figure	24.	Plot of phase differences -- Montreal Lake	63

Figure	25.	Finite fault considered by d'Erceville and Kunetz	66
Figure	26.	Theoretical curves for fault with conductive basement (\underline{E} perpendicular to strike) with parameters adjusted to fit Montreal Lake data	67
Figure	27.	Apparent resistivity curves - Vulcan 2-4 (H_x-E_y)	69
Figure	28.	Plot of phase differences - Vulcan 2-4	71
Figure	29.	Apparent resistivity and coherency-squared for H_y-E_x and vertical-horizontal power ratio - Montreal Lake 2-1	73
Figure	30.	Apparent resistivity and coherency-squared for H_y-E_x and vertical-horizontal power ratio-Montreal Lake 5	74
Figure	31.	Vertical-horizontal power ratios at Montreal Lake	77
Figure	32.	Vertical-horizontal magnetic power ratios at southern Alberta stations	78
Figure	33.	Plots of orthogonal spectra for Vulcan 2-4 and Montreal Lake 2-2	79
Figure	34.	Illustration of high H_y-H_z coherency compared to H_x-H_z coherency	80
Figure	35.	Coherency-squared for E_x-H_z and H_y-H_z - Montreal Lake 3	81
Figure	36.	Power ratio H_z to H_y for coherency-squared greater than 0.6.	83

Figure 37.	Illustration of increase in H_x-H_z coherency with decrease in H_y-H_z coherency	84
Figure 38.	Power ratio H_z/H_y for coherency-squared less than 0.6	85.
Figure 39.	E_x-H_z and H_y-H_z phase differences at Montreal Lake	86
Figure 40.	Section from Montreal Lake 2 showing three magnetic components	87
Figure 41.	H_y-E_x and H_y-H_z coherency-squared - Montreal Lake 3	91
Figure 42.	Vulcan 2-4 H_x and E_y spectra and coherency	95
Figure 43.	Brooks 2-2 H_x and E_y spectra and coherency	96
Figure 44.	Beiseker 1-2 H_x and E_y spectra and coherency	97
Figure A- 1.	Cagniard two-layer apparent resistivity curves	A 5
Figure A-2.	Master curves of phase differences (ϕ (E-H)) versus period for various resistivity contrasts in a two-layer earth	A 6
Figure B-1.	The lag and spectral window for the hanning estimate	A 11
Figure B-2.	Daniell window for $n/m = 10$	A 13
Figure B-3.	Daniell window for $n/m = 40$	A 14

Figure B-4.	Power transfer function of $z_i = x_i + \lambda x_{i-1}$ for various values of λ (after Munk et al, 1959)	A 17
Figure C-1.	Power spectrum - points 1-1000	A 21
Figure C-2.	Percentage differences from the spectrum of points 1-1000	A 22
Figure C-3.	(Coherency) ² of points 1-1000 with shifted records	A 23
Figure C-4.	Spectra from two independent conversions of the same record	A 25
Figure C-5.	Spectra of a fraction of sinusoid	A 29
Figure C-6.	Effect of trend subtraction on a pulsation spectrum	A 30
Figure C-7.	Effect on E-H coherency of trend subtraction from both	A 31
Figure C-8.	Spectral ratios illustrating effect of trend removal	A 32
Figure C-9.	Illustration of HF spectra without prewhitening	A 35
Figure C-10.	Illustration of HF spectra with prewhitening	A 36
Figure C-11.	Spectral ratios illustrating effect of prewhitening	A 37
Figure C-12.	Daniell and hanning spectra of same digital record	A 39
Figure C-13.	Spectra of computer-generated sinusoid, $f = .081 f_N$	A 43

Figure C-14.	Spectrum of square wave of frequency .0961 cps with coherency and percentage difference between simultaneous conversions	A 45
Figure C-15.	Illustration of HF spectra without prewhitening (CS TUKS)	A 48
Figure C-16.	Illustration of HF spectra with prewhitening (CS TUKS)	A 49
Figure C-17.	Illustration of HF spectra without prewhitening (CROSP2)	A 50
Figure C-18.	Illustration of HF spectra with prewhitening (CROSP2)	A 51
Figure C-19.	Spectral ratios, for comparing CROSP2 with CS TUKS, raw data	A 52
Figure C-20.	Spectral ratios, for comparing CROSP2 with CS TUKS, prewhitened data	A 53
Figure C-21.	Illustration of the unreliability of CS TUKS coherency as a measure of spectral quality	A 54

Chapter 1. INTRODUCTION

This thesis is an investigation of the earth's electromagnetic field in the frequency range .001 to 5 cps (the region of micropulsations and their induced telluric currents) and its application to determine the resistivity of the earth as a function of depth.

Micropulsations and Telluric Currents

Micropulsations are fluctuations in the earth's magnetic field in the frequency range .001 to 10 cps with amplitudes varying from tens of gammas (1 gamma = 10^{-5} oersted) at the low frequencies to .001 gammas at the high frequencies. While interest in this frequency region has blossomed over the past ten years, investigations in most ranges were first reported over twenty-five years ago. Stewart (1861) and Eshenhagen (1897) reported pulsations with 10 to 50 second periods; Ebert (1907) and Sucksdorff (1936) observed oscillations in the 0.1 and 2 to 3 second period ranges respectively; while Rolf (1931) reported the giant pulsations in northern latitudes whose periods exceed 1 minute.

From experimental knowledge it is recognized that micropulsations can be divided into two classes: those of a regular and mainly continuous character and those of an irregular or transient character. The most recent recommendation to the International Association of Geomagnetism

and Aeronomy (Jacobs, Kato, Matsushita, and Troitskaya, 1964) proposes that they be designated Pc and Pi respectively. It is further proposed that they be divided into period ranges based on their physical and morphological properties. Tables 1 and 2 show these classifications.

Table 1

Notation for Regular
Pulsations

Table 2

Notation for Irregular
Pulsations

Notation	Period Range, sec	Notation	Period Range, sec
Pc 1	0.2-5	Pi 1	1-40
Pc 2	5-10	Pi 2	40-150
Pc 3	10-45		
Pc 4	45-150		
Pc 5	150-600		

It should be pointed out that in any such classification the boundary divisions are rather arbitrary. Further, pulsations of different types often occur together. For example, pulsations during a magnetic bay (Pb) can be expressed as

$$Pb = Pi\ 1 + Pi\ 2 + Pc\ 1 \ .$$

Although these classifications are convenient for observatories, the analysis techniques employed in this thesis do not lend themselves to these divisions.

In one of the earliest theoretical papers Störmer (1906) suggested that the charged particles contained in a high speed cloud emitted by the sun are captured by the earth's main magnetic field and spiral about the earth's magnetic line of force. Chapman and Ferraro pointed out that the charges would repel each other and the streams would disperse. Störmer's theory has been revitalized by the work of Bennett and Hulbert (1954) on magnetic focusing. Recently workers have used variations of this model to explain pulsations of type Pc 1. Wentworth and Tepley (1962) have suggested a fast electron bunch model while Heacock (1963) suggests a fast proton bunch model. In both cases the emission frequency is associated with the frequency at which the bunch oscillates between magnetically conjugate mirror points. The conjugate point phase shift should then be close to 0° . Tepley (1964) however reports observations with a phase shift of 180° . Jacobs and Watanabe (1963) proposed that the emission frequency is associated with the resonance frequency of hydromagnetic waves generated in the lower exosphere with the resonance oscillations excited by proton bunches oscillating slowly between magnetically conjugate mirror points. In this case a 180° fine-structure phase shift between conjugate points is predicted. Unfortunately this model predicts that the emission frequency should increase with geomagnetic latitude which conflicts with experimental observation.

Holmberg (1951) proposed that the sources of pulsations are intralayer hydromagnetic oscillations within the E and F layers of the ionosphere. Although this particular trapped mode has been rejected because of the high attenuation of hydromagnetic waves in these regions (Piddington, 1959), hydromagnetic waves continue to form the basis of most theoretical work in this field.

Dungey (1958) considers hydromagnetic waves in the magnetosphere and has concluded that two modes of oscillation are possible, (1) toroidal oscillations with each surface of revolution of a geomagnetic line of force oscillating independently, and (2) poloidal oscillations with the magnetic field oscillating in the meridian plane. He suggests that these disturbances may be excited by the flow of interplanetary gas over the surface of the magnetosphere. Because of the complexity of the equations in spherical coordinates, the coupling terms are usually neglected. In theory, the periods of the fundamental and higher modes may then be calculated and compared with observations. Unfortunately, the Alfvén wave velocity in the exosphere is not yet well enough known to do this with great accuracy.

Watanabe (1961) associates the poloidal oscillations with Pc and the toroidal oscillations with the giant pulsations. He suggests that for non-axisymmetric toroidal oscillations, radial oscillations may be induced which are observed as Pi.

MacDonald (1961) points out that the sharp maximum in the Alfvén wave velocity at an altitude of 3000 km may allow the trapping of energy between this maximum and the F_2 layer of the ionosphere. This allows shorter period oscillations of types Pc 1 and Pc 2.

Jacobs and Watanabe (1962) postulate that the hydromagnetic waves generated in outer space are propagated along the magnetic lines of force towards the polar regions where the lower exosphere acts as an amplifier at selected frequencies. Secondary waves are then emitted from the regions of incidence and propagated to lower latitudes. Their calculations show that periods corresponding to Pc 1 may be amplified by this mechanism. Their suggestion that type Pc 3 might also be explained by this process has been supported by the more detailed calculations of Prince and Bostick (1964).

The electric field amplitudes range from a few tens of mv/km at low frequencies to .001 mv/km at high frequencies. In 1921, Davy postulated the existence of the induced telluric currents. Barlow (1849), however, first obtained convincing evidence that such currents flow in the earth by studying the disturbances created in telegraph lines. He found that these disturbances are most pronounced during periods

of magnetic activity. By the end of the nineteenth century many observatories recorded telluric currents. While the correlation of telluric currents and micropulsations was appreciated, the difficulties of analysis and instrumentation, coupled with a seeming lack of positive results, caused a fluctuation of interest in the subject and consequently in the number of recording stations.

The Telluric Method

The first application of these ULF electromagnetic fields to determine the electrical characteristics of the earth was the telluric method proposed by Schlumberger in 1921. The basis of this technique is that the telluric currents will flow around areas of high resistivity. The quantity measured is the change with time of the average electric field between a pair of grounded electrodes a few hundred feet apart. At a base station two measurements at right angles are made. Simultaneous measurements are made with identical arrangements at various locations in the area of interest. Current patterns may then be mapped and large conductivity contrasts such as highly resistive salt domes located.

The Magnetotelluric Method

The magnetotelluric method uses the horizontal components of both the electric and magnetic fields at the surface of the earth to determine the electrical resistivity

as a function of depth. Tikhonov (1950) suggested the method as a tool for exploration to great depths while almost simultaneously Kato and Kikuchi (1950) showed that measurements made on phase angles between the electric and magnetic fields could be explained on the basis of a two-layered earth. In subsequent papers (Rikitake, 1950; Tikhonov and Lipskaya, 1952; Lipskaya, 1953) the original theory and interpretation was extended. However it was not until Cagniard (1953) published his comprehensive paper on the theory and graphical interpretation techniques that the potential of the magnetotelluric method was realized.

In the basic magnetotelluric theory as proposed by Cagniard, the two fundamental assumptions are that the earth is horizontally layered with each layer being electrically homogeneous and isotropic, and that micro-pulsations are plane electromagnetic waves impinging on the earth. Under these conditions Cagniard showed (see Appendix A) that the resistivity may be found as a function of depth if we know the apparent resistivity

$$\rho_a = 0.2T | \underline{E} |^2 / | \underline{H} |^2$$

as a function of period, where

ρ_a = apparent resistivity (ohm-m),

T = period (sec),

$| E |$ = horizontal electric-field amplitude (mv/km) at period T ,

$| H |$ = horizontal magnetic-field amplitude (γ) at period T .

He also showed that the phase difference between \underline{E} and \underline{H} could be used for interpretation. In this paper Cagniard developed the theory for 1- and 2-layer cases. Berdichevskii (1960) extended the formulas to n-layers while Yungul (1961) has presented 3-layer interpretation curves. Solutions for the effects of a fault on the earth's electromagnetic field have been presented by Neves (1957) and d'Erceville and Kunetz (1962). Rankin (1962) has extended the theory to the case of a dike. These results may also be presented in terms of apparent resistivity. For application of the magnetotelluric theory it is then necessary to find \underline{E} and \underline{H} as a function of period, from which the observed apparent resistivity may be calculated and compared with theoretical models. Neves points out that for two dimensional structures additional information is contained in the phase.

The fundamental advantage of the telluric and magnetotelluric methods over conventional electrical prospecting methods is their depth of penetration. The conventional techniques are limited by the inverse square law for point sources, whereas the penetration of plane electromagnetic waves in a uniform conductor is given by the skin depth

$$p = \frac{1}{2\pi} \sqrt{10 \rho T}$$

where p = penetration (km). For ULF electromagnetic waves and typical resistivities (1 ohm-m to 10^5 ohm-m), the

penetration is many kilometers. A second advantage is that nature provides the signal.

Wait (1954) first investigated the effect of non-plane wave sources on the magnetotelluric theory and found that the correction terms contained second and higher order spatial derivatives. In the case of oscillations of 10 sec period over a homogeneous earth of resistivity 1000 ohm-m, he found that these terms become important if \underline{E} and \underline{H} vary appreciably in a distance of 35 km. He pointed out that if the micropulsation sources were in the lower ionosphere at an altitude of 100 km, corrections would be important for periods greater than 10 sec. On the basis of observational evidence, Cagniard (1954) insisted that the fields are uniform over hundreds of kilometers.

Price (1962) investigated the effect of the source dimension on the intrinsic impedance $|E_x/H_y|$. For a homogeneous earth of conductivity σ , he finds that (MKS units)

$$\frac{E_x}{H_y} = \frac{i\omega}{(v^2 + i\omega\sigma)}$$

where v = separation constant.

He points out that $2\pi/\nu$ can be taken as the linear dimensions of the source field. For $\nu = 0$, the source is infinitely large corresponding to Cagniard's plane wave solution. Wait's result is obtained by taking $\nu^2 \ll \omega\sigma$. To obtain an estimate of the smallest and largest values of ν which can occur he equates $2\pi/\nu$ to the circumference of the earth and to 4 times the height of the ionospheric currents. He concludes that the values of ν of interest will lie in the range $1.57 \times 10^{-4} \text{ km}^{-1}$ to $1.57 \times 10^{-2} \text{ km}^{-1}$. The calculations of Quon (1963) using dipole sources confirms this estimate for the upper limit of ν . Price then considers a two-layer earth with a conductive upper layer and infinitely resistive substratum. In this situation he shows that Wait's estimate of the source effect is too small and that even for sources of global dimensions correction terms may be required at long periods.

Since the publication of Cagniard's classic paper, the results of more than 25 magnetotelluric soundings have appeared in the literature. Because of difficulties in detecting the low amplitude signal at higher frequencies, most investigators have confined themselves to the frequencies below 0.1 cps which correspond to depths where relatively little is known about the resistivity of the earth. Due to the possibility of source effects at these periods and the wide scatter of values obtained in a single experiment, there remains some uncertainty as to the validity of the interpretations.

In addition to the difficulties of signal detection, the problem of quantitatively analyzing the data has been considerable. In almost all cases, workers in this field have used chart recorders. In order to obtain sufficient accuracy at all frequencies, this requires that the response of the detecting system must be closely matched to the character of the signal; otherwise, some part of the spectrum is lost because it is either too large or too small to be read accurately from the chart.

While the technique of picking sinusoidal events from records has been widely used (Scholte and Veldkamp, 1955; Niblett and Sayn-Wittgenstein, 1960; Wiese, 1962), it has not proved very satisfactory. For one thing, the period is never accurately measurable as there is no single period to a discrete event. Secondly, large sections of record must be scanned before observing sinusoids over the complete frequency range. Finally, apparent resistivities calculated using large sinusoids do not yield a smooth curve but exhibit a scatter whose range may be up to a factor of 3. From this, it is questionable whether the Cagniard theory should be applied to single events.

Other groups have digitized the records and found \tilde{E} and \tilde{H} as a function of frequency using mathematical techniques. Garland and Webster (1960) used Fourier analysis.

Cantwell (1960) considered the magnetotelluric field components as samples of stationary stochastic processes and applied the autocorrelation methods of Blackman and Tukey (1958) supplemented by cross-correlation techniques (Robinson, 1954) in order that coherencies between electric and magnetic signals could be found. He assumes low coherencies are caused by high instrumental noise levels. Using only records with high coherence, it was found that comparatively smooth resistivity curves were obtained and estimates from different records were relatively consistent. He also outlines procedures for determining the effects of anisotropy and two-dimensional inhomogeneities in the earth. The Electrical Engineering Research Laboratory at the University of Texas follows similar statistical procedures using analog techniques (Smith, Provazek, and Bostick, 1961). Their use of magnetic tape recording has increased the dynamic range and the elimination of the hand-digitizing procedure has removed one source of noise.

The Vertical Magnetic Field

In Appendix A it has been shown for plane waves incident on a homogeneous half-space that the vertical magnetic field is negligible compared with the horizontal fields and decrease with increasing period. However experimental results show that H_z is sometimes as large as the horizontal field. For this reason workers have investigated H_z from several viewpoints.

Scholte and Veldkamp (1955) theoretically considered reflection of a general electromagnetic field by a sphere. They found H_z to be much larger than predicted by the layered half-space model but still smaller than the observed results. In this case H_z increases with increasing period and the phase shift between E and H_z depends on the form of the field. (For a plane wave impinging on a layered earth the phase difference is 0° .)

The failure to explain the magnitude of H_z using homogeneous or layered earth models has led to investigation of two-dimensional structures and particular source effects. Because of the sharp resistivity contrast, the sea-land interface has attracted the attention of some workers. Rokityanskiĭ (1963) has measured the vertical and horizontal magnetic fields on the landward side at Mirny. He finds that $|Z/H|$ decreases with increasing period for $T > 100$ sec. Using experimental results and the theoretical results of Berdicheskiĭ (1961) and Ponomarev (1960) for the effect of wedges on electromagnetic fields, he has made qualitative plots of the field components near the sea-land boundary. He suggests that H_z should be quite large on the land side but negligible on the ocean side. Weaver (1963) attempts to solve the same problem using a fault of infinite extent. He finds that $|Z/H|$ falls off more rapidly on the seaward side but may be as large as the horizontal fields close to the boundary. His calculations at two periods, $T = 1$ and 10 sec, show $|Z/H|$ to be much larger for the longer period.

Law and Fannin (1961) have considered a line source at ionospheric height over an earth of resistivity 8000 ohm-meters and with a period of 21 sec. The fields have been calculated at the surface of the earth for various distances from the source. It is found that H_z may be as large as 50% of the horizontal field and that the phase between H_z and the electric field remains close to 90° .

Quon (1963) has calculated the fields over a two-layered earth resulting from dipoles at ionospheric heights. He finds that H_z is comparable with the horizontal fields at the longer periods. The phase relationships are rather complicated depending on the type of dipole, distance, and period.

Objectives of the University of Alberta Group

The experimental objectives of the University of Alberta magnetotelluric group have been as follows:

- (1) to develop a mobile recording system capable of detecting micropulsations and telluric currents in the frequency range .001 to 10 cps.
- (2) to develop low noise level analysis techniques,
- (3) to use the system to test Cagniard's theory and study the sources.

Purpose of this Thesis

This investigation is limited to the following problems:

- (1) the development of analysis techniques
- (2) a study of source effects as observed at a single station on the earth's surface
- (3) an interpretation of the field data using the magnetotelluric method.

Chapter II.

DETECTION, ANALYSIS, AND PRELIMINARY RESULTS

Signal Detection

Two perpendicular components each of the electric and magnetic fields are measured at each location. In addition, the vertical H_z component is recorded.

Figure 1 is a schematic representation of one electric and one magnetic detection system. To find E_z , the voltage difference is measured between two copper electrodes approximately 1,000 feet apart. This voltage is fed through a fixed band pass filter to a dc post-amplifier with gains up to 30 db and a high frequency cutoff at 8 cps, and then to the seven-channel FM tape recorder. Normal amplifier settings have been in the range +40 db to +54 db in order to achieve the signal level required by the tape recorder (± 1.5 volts).

The magnetic detectors are induction coils consisting of 15,000 turns of wire wound on a permeable rod core. The coils are 5 feet long and 4 inches in diameter. The submicrovolt signal which emerges from the coil is amplified by a split-beam photocell, feedback amplifier. This signal is further amplified and low-pass filtered before tape recording.

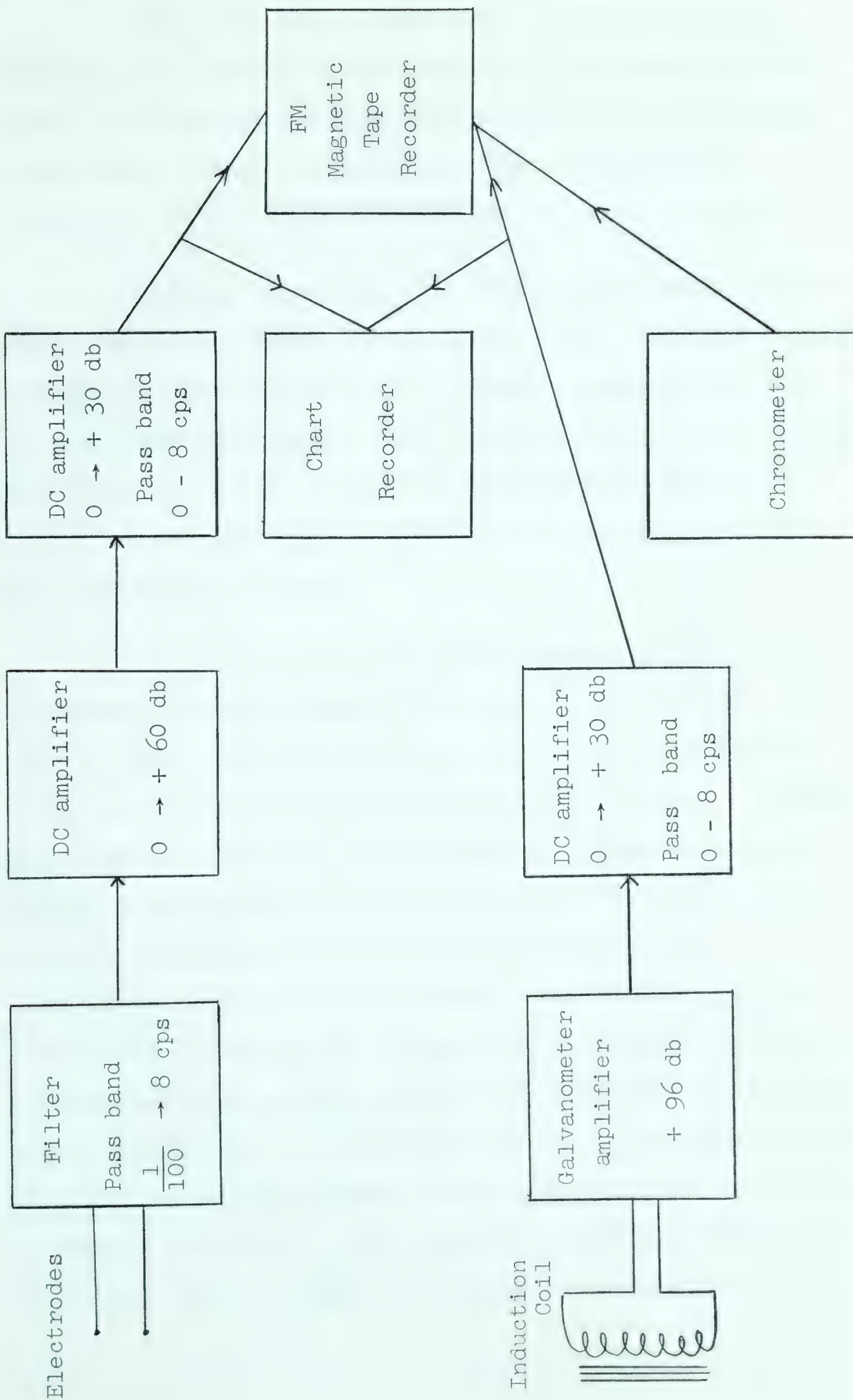


Figure 1. Block diagram of magnetotelluric recording system showing one electric and one magnetic system.

Relative time pulses from a chronometer are recorded on a direct record channel. To obtain absolute time, these pulses are compared with WWV on a high-speed paper monitor when reception permits. This allows comparison of our signal with those at other stations.

During recording, two channels are monitored on a chart recorder. Using this, the amplifier settings may be changed in order that the full dynamic range of the tape is utilized and adjustments made for amplifier drift. If the signal level is too low or the bandwidth too narrow to be useful in calculating an apparent resistivity curve, the tape may then be erased.

Calibration of the entire system at about 10 frequencies in the range of interest is recorded at least once on each tape (4-12 hours). In the earlier systems this was required because of instability in gain. However, gains in the 1962 and 1963 systems were found to be stable within a few percent over an interval of several months. At each calibration frequency, the output of an oscillator (Figure 2) is recorded. At the same time an attenuated output is fed through the 2 electric systems and through solenoids, wound around the detection coils, which are in series with a precision resistor. From the playback of these recordings, phase shifts and amplitude calibration curves in terms of V_{out}/V_{in} for the electric systems and V_{out}/ma_{in} for the magnetic systems are calculated.

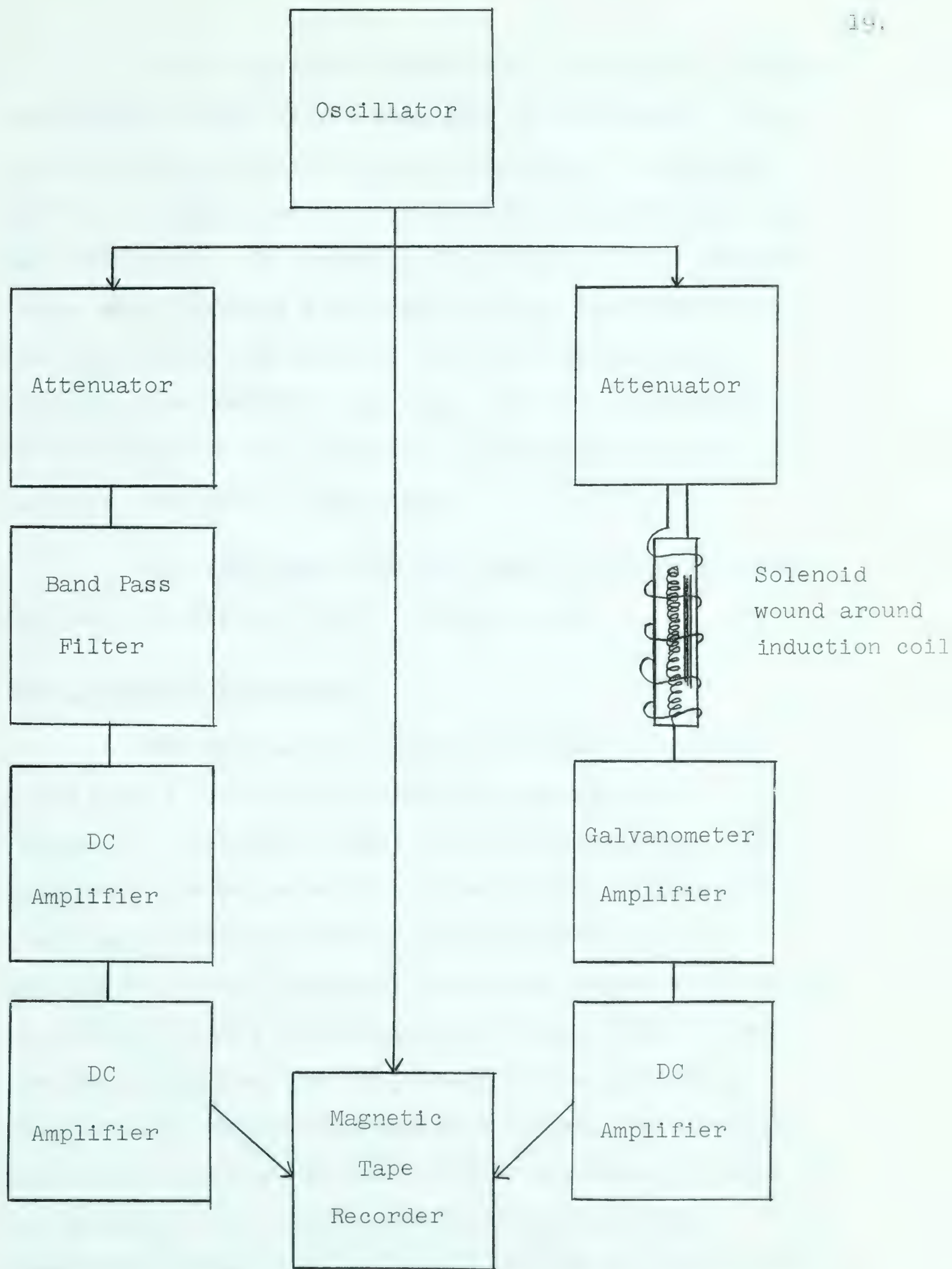


Figure 2. Block diagram of field calibration system.

For an absolute calibration of a magnetic system, the solenoid wound on the coil must be calibrated. This is done by placing the coil at the centre of a solenoid 10 ft. in length, one foot in diameter, and with one turn per centimeter. By comparing the outputs of the magnetic system when currents are passed through the 2 solenoids and calculating the magnetic induction in the large solenoid, the quantity γ_{out}/ma_{in} for the solenoid wound on the induction coil is found. A calibration curve of V_{out}/γ_{in} may then be calculated.

The 1962 amplitude and phase calibration curves are shown in Figure 3 and 4, respectively.

Basic Analysis Techniques

The fundamental analysis problem is to find \underline{E} and \underline{H} as a function of period (or equivalently frequency). Cantwell (1960) and Srivastava et al (1963) considered the recorded data as statistical samples from a stationary random process of infinite duration and applied the "Tukey" spectral techniques (Appendix B) given by Robinson (1954) and Blackman and Tukey (1958). Under the assumption that the stationary random process is Gaussian and the spectrum reasonably flat, the stability associated with each estimate can be expressed in terms of the spread in db of an interval containing, with prescribed probability, the ratio of true smoothed power to estimated smoothed power. For example, the 80 percent

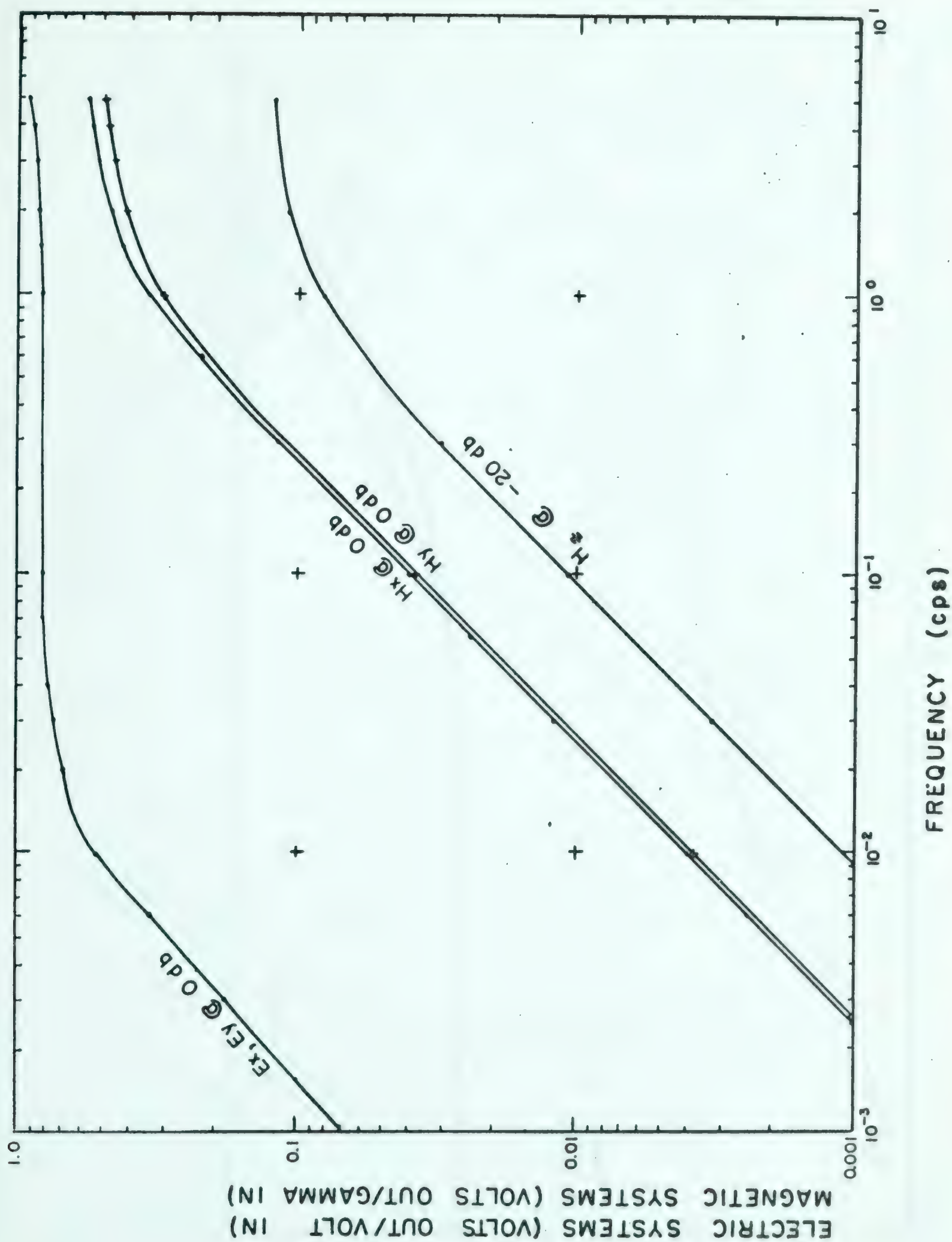


Figure 3. Amplitude calibration curves of the 1962 electric and magnetic systems.

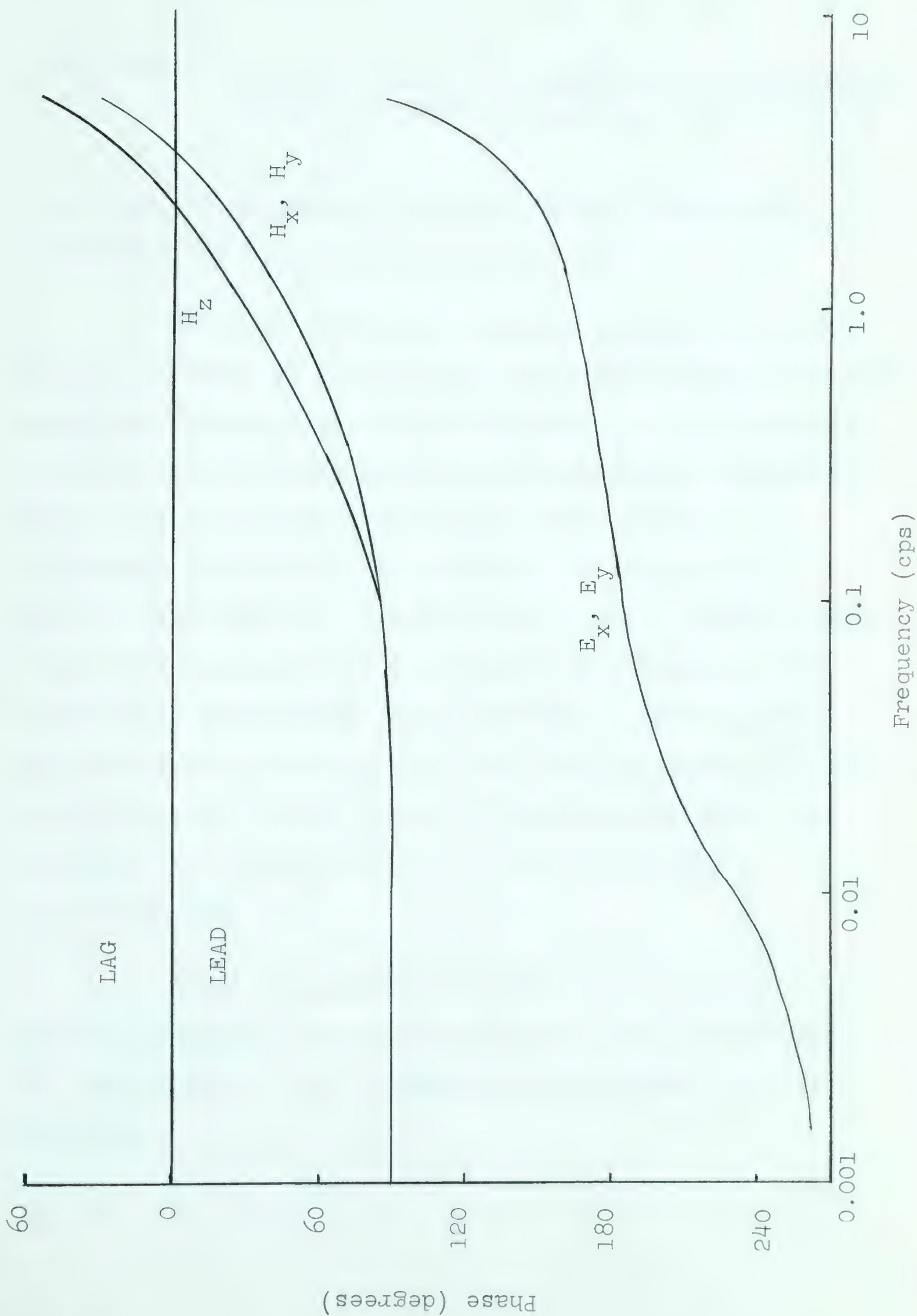


Figure 4. Phase calibration curves of 1962 system.

range in db is given by

$$\left(\begin{array}{c} \text{80\% range} \\ \text{in db} \end{array} \right)^2 = \frac{125}{(\text{no. of records}) \left[\left(\frac{\text{record}}{\text{duration}} \right) (\text{resolution}) - \frac{1}{3} \right] - \frac{1}{3}}$$

From this the duration of record required for a given resolution and accuracy may be calculated.

It is preferable to consider the data as a unique record generated by an aperiodic phenomenon with a continuous spectrum. However, analysis techniques for this case have not been developed and it must be treated using statistical techniques or one of the classical methods where the phenomenon is thought of as periodic. In this thesis, digital Tukey spectral techniques are used. However under these circumstances, the error analysis procedures will have little meaning and questions arise concerning the required size of the ratio of the number of points in the time series (n) to the number of spectral estimates (m). In almost all cases presented in this thesis the ratio $n/m \geq 8$.

Since the spectral analysis is carried out on a digital computer, the analog data must first be converted to digital form. The following analysis procedures are followed:

- (1) The entire magnetic tape is played back onto a 6-channel recorder and long sections of record which contain wide band signal and are free of transients are selected for conversion.
- (2) These sections are converted to digital form by playing the signal from the magnetic tape through a low pass filter (to minimize aliasing problems in spectral calculations) and an analog-to-digital converter driving a high-speed paper-tape punch (Figure 5). During this stage the analog signal is monitored as a check on the analog system and conversion operation.
- (3) To facilitate handling, the paper tape is next converted to cards using at IBM 1620 computer. During this step the paper tape is checked for parity, flagging, record length, and magnitude of successive differences with the invalid numbers being replaced by interpolated values. If the number of errors exceeds approximately 0.2%, the analog to digital conversion is repeated. The data are further edited using the monitor from (2) and a digital plot if necessary.
- (4) The mean and linear trends are then removed and the spectra calculated. The spectra, along with the calibration data, amplifier settings, and electrode spacings are then used to calculate the apparent resistivity as a function of period.
- (5) The apparent resistivity curves are interpreted using theoretical curves.

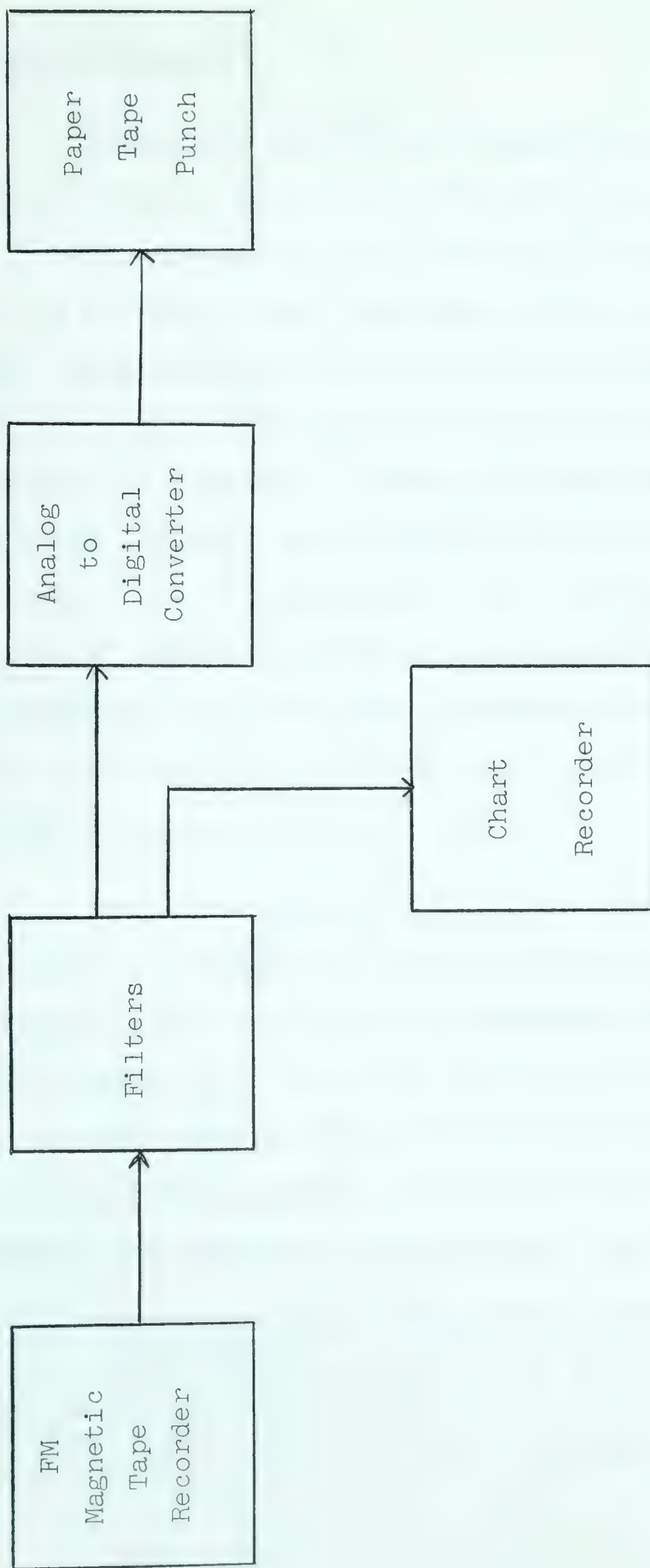


Figure 5. Diagrammatic representation of analog-to-digital conversion system.

Preliminary Results¹

During the 1961 field season, measurements were made at four field stations in the Edmonton area - Cooking Lake, Onoway, Bon Accord, and Kavanagh (Figure 6). This region is a nearly ideal test area for the magnetotelluric method. As shown in Figure 7, it is underlain by a great thickness of flat-lying conductive sediments, beneath which is a resistive basement. There is a vast amount of resistivity log information available, including some from the basement, as well as gravity and aeromagnetic maps of parts of the area. In addition, several crustal thickness determinations have been made by seismic methods within 200 miles of Edmonton (Richards and Walker, 1959; Cumming, Garland, and Vozoff, 1962).

Since the conductivity of the sediments is believed to be independent of horizontal direction, it is expected that the short-period asymptotes of the pair of apparent resistivity curves at one station should be the same. At the longer periods the curves may diverge since aeromagnetics and basement cores show the Precambrian to be grained and variable in composition over short distances

¹ The magnetotelluric data used in this section were originally processed by the author and interpreted by Hasegawa (1962) using regional values for the conductivity of the sediments. After a more detailed well-log analysis, the data were reinterpreted by the author and published as a part of a joint paper by Vozoff, Hasegawa, and Ellis (1963).

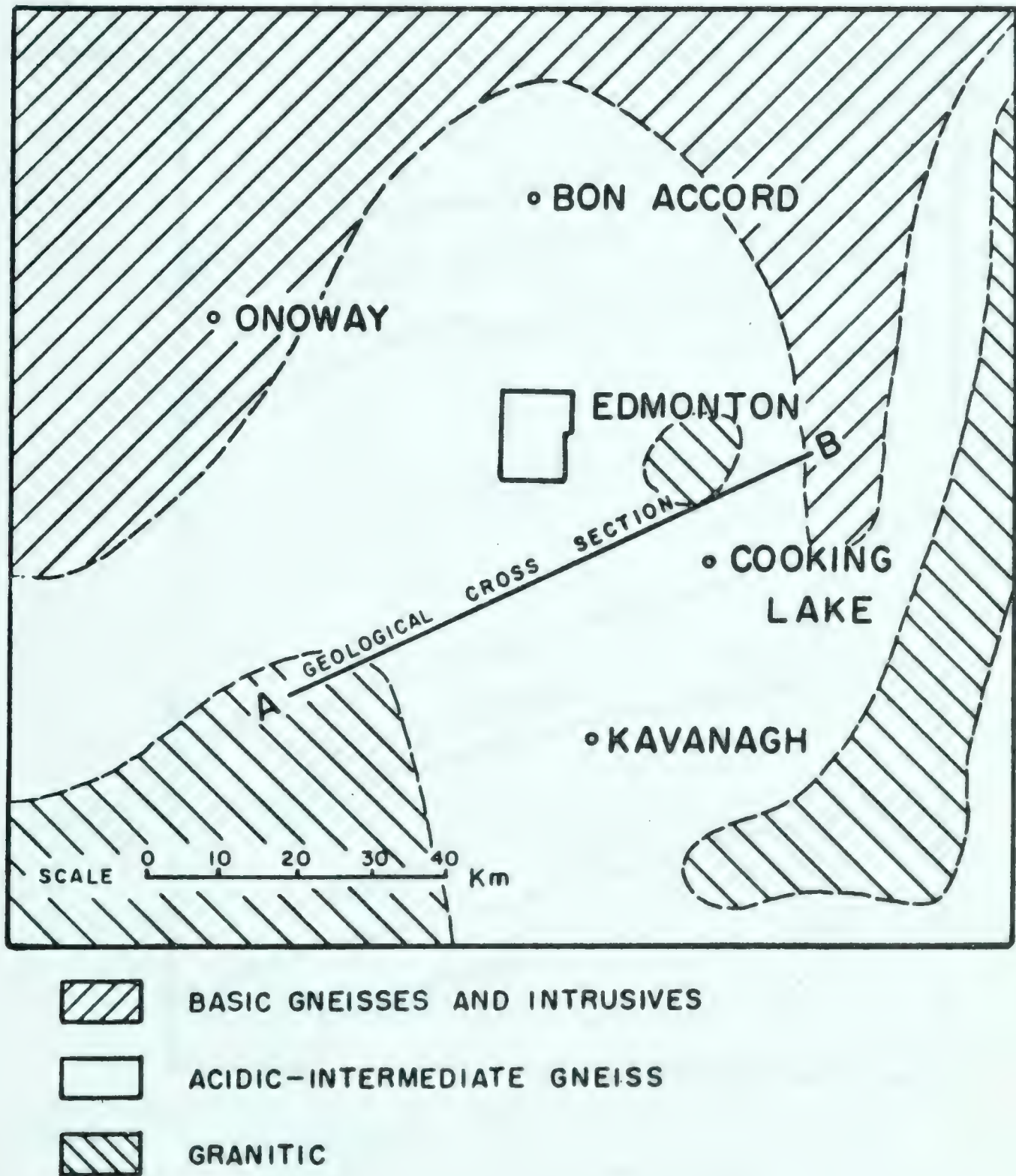


Figure 6. Locations of 1961 Alberta field stations with lithology of Precambrian basement as inferred from well samples and gravity anomalies (after Garland and Burwash, 1959).

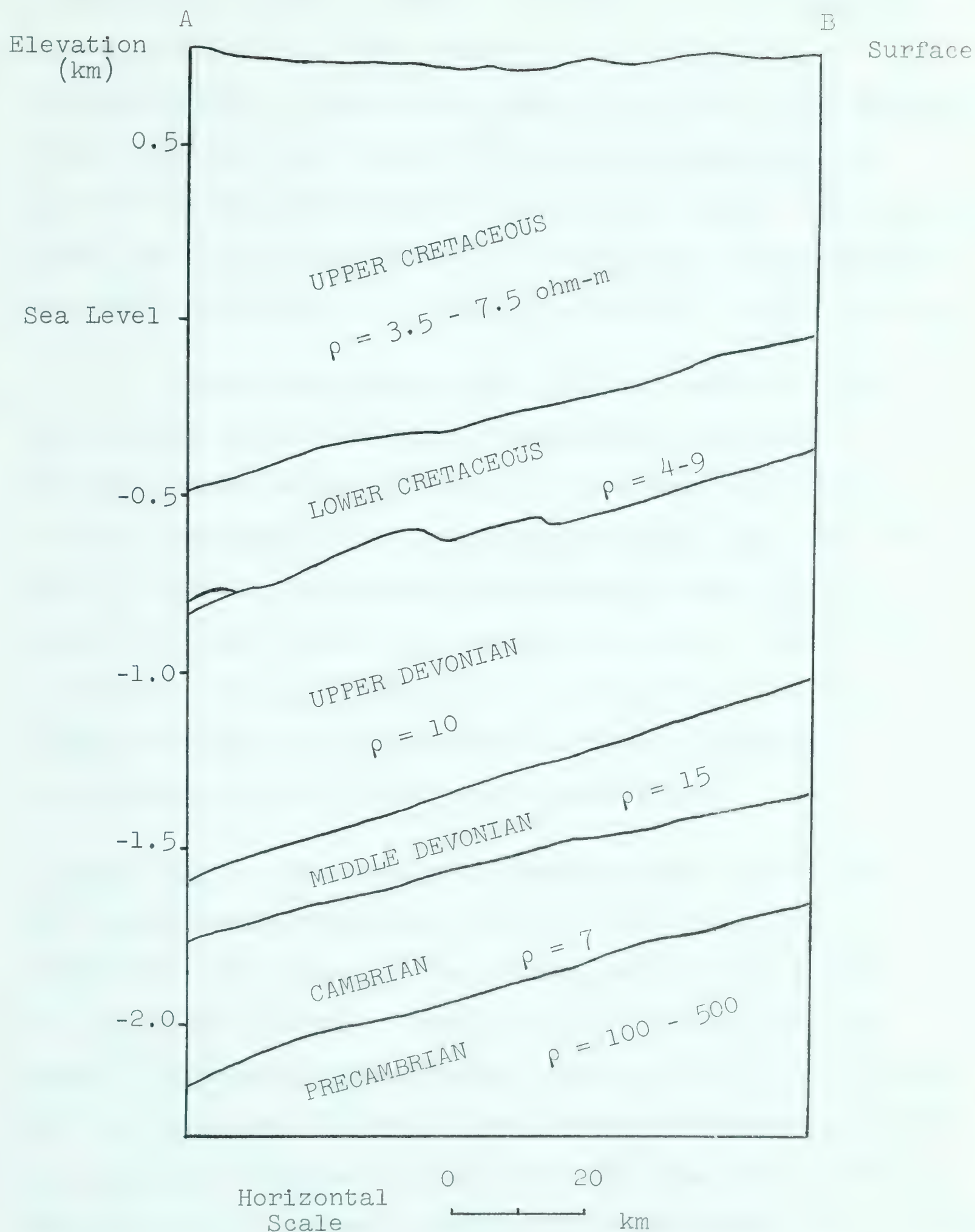


Figure 7. Geological cross-section AB (Figure 6) of Edmonton area (after Alberta Society of Petroleum Geologists regional cross-section GHJ, 1959), with typical well-log resistivities for this region.

(Garland and Burwash, 1959). In addition to this apparent basement anisotropy (due either to anisotropy or to inhomogeneity), a thin, very highly conductive basal sandstone, whose thickness may reflect the basement topography, is present in the eastern portion of the test area. Consequently, there are two regions whose properties might cause measured apparent resistivity to vary with azimuth at longer periods.

Each data channel was digitized separately and autospectra calculated with a program using hanning windows. The computational definitions used were those for the autospectrum in the program CS TUKS (Share No. 574).¹ For interpretation purposes, sedimentary resistivities were calculated using logs from nearby wells. Using these values for the sediments, we then attempted to fit the observed curves with theoretical curves by choosing appropriate values for basement resistivities.

Cooking Lake. - The results at Cooking Lake for the two orthogonal measurements are shown in Figure 8. The observed curves agree at the shorter periods but diverge at the longer periods. This effect can be put into the model by assuming an anisotropic layer exists at the bottom of the sediments (2.5 km). Basal sandstone was encountered in the nearest basement hole, about 10 miles away, where it was 30 m thick and had a resistivity calculated to be 3.5 ohm-m.

¹ Munk, Snodgrass, and Tucker (1959) outlined these computational procedures.

THEORETICAL MODELS

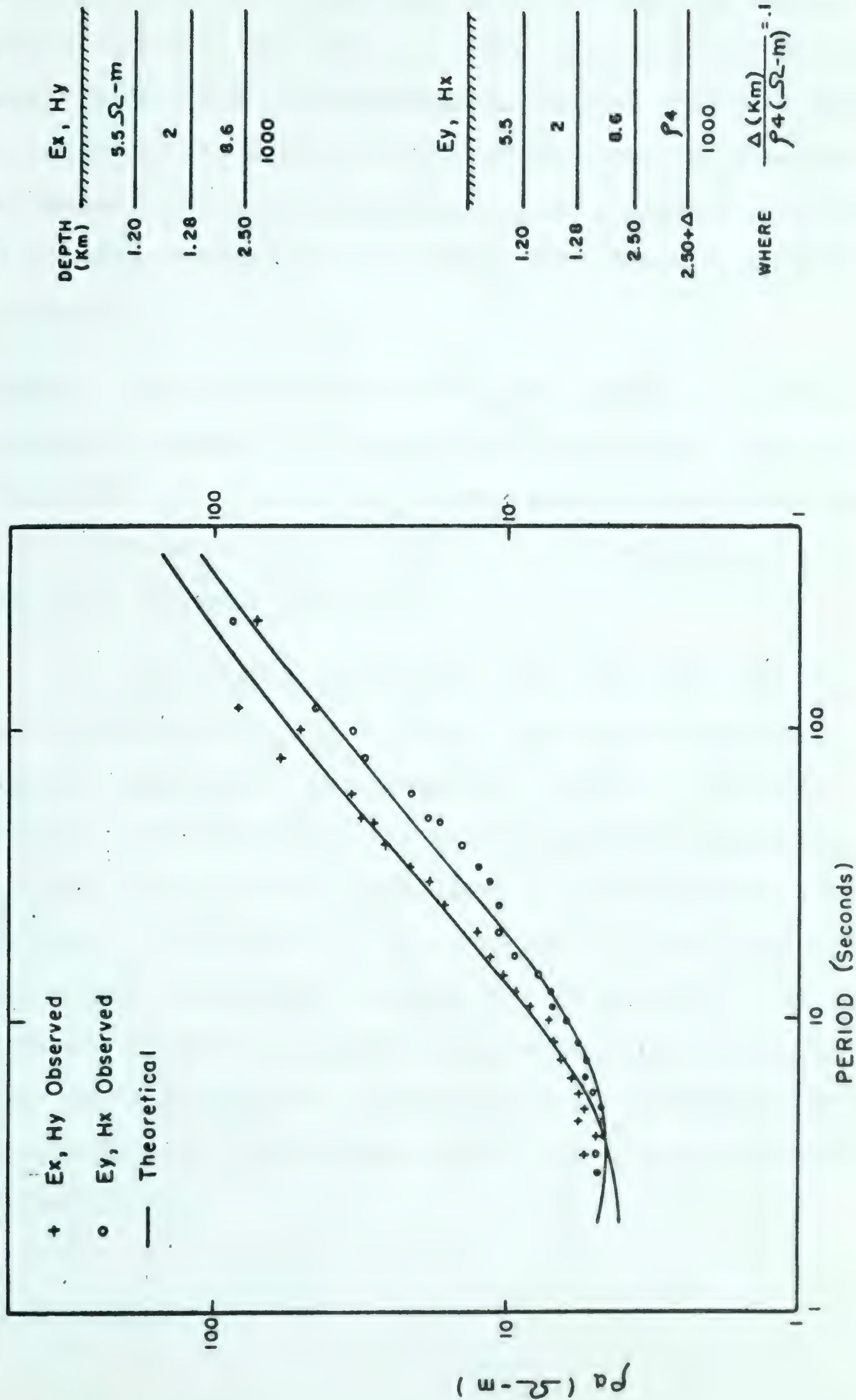


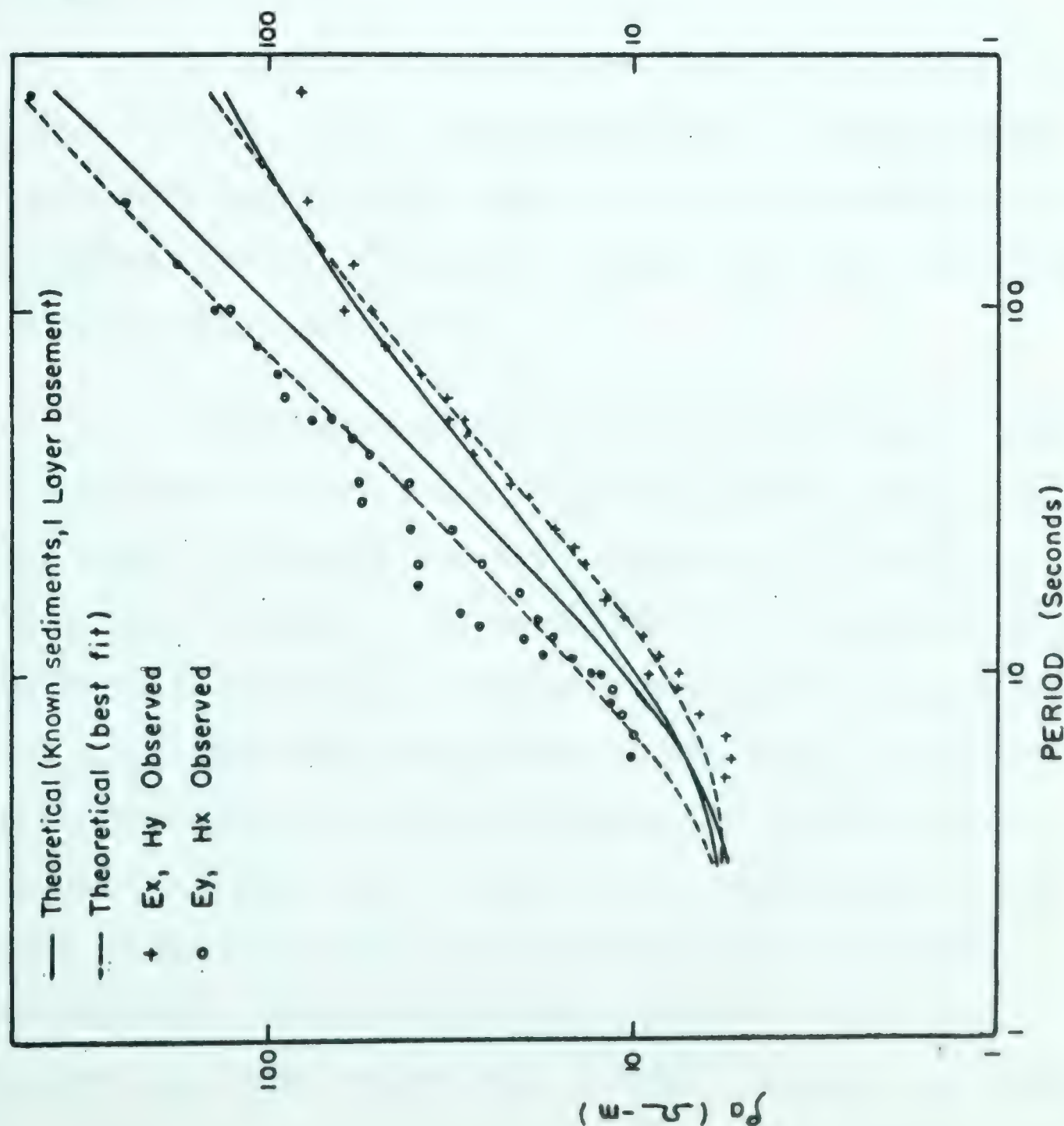
Figure 8. Magnetotelluric apparent resistivity curves - Cooking Lake, Alberta.

This alone is not sufficient to explain the observed effects. We must assume either (a) that near the site its actual resistivity is lower than 3.5 ohm-m (one ohm-m and less is more typical) and its thickness is greater than 30 m in troughs elongated in the E-W direction, or (b) that the observed aeromagnetic "grain" is accompanied by a similar characteristic in basement resistivity. In fact, both factors probably contribute.

Onoway. - For this station it is not possible to obtain agreement between the observed and theoretical models for either the $E_x - H_y$ or $E_y - H_x$ curve using the measured sedimentary resistivities for the 2.7 km of sediments and a one-layer basement (Figure 9).

In a further analysis a good fit was obtained for the observed $E_x - H_y$ curve by inserting a conductive layer at the base of the sediments. Since it is very doubtful that the conductive basal sandstone extends this far west, a conductive upper layer in the Precambrian is required. To fit the $E_y - H_x$ curve the 12 and 5 ohm-m layers must be replaced by a section of 15 ohm-m. An extremely resistive basement is also required, assigning a high degree of apparent anisotropy to the basement. Such anisotropy would undoubtedly affect the shallower apparent resistivities.

THEORETICAL MODELS



KNOWN SEDIMENTS 1 LAYER BASEMENT

DEPTH (Km)	Ex, Hy
1.07	7.4 Ω-m
1.39	4.4
2.43	12
2.70	5
	500

BEST FIT

DEPTH (Km)	Ex, Hy
1.07	7.4 Ω-m
1.39	4.4
2.43	12
2.70	5
2.7 + Δ	ρ5
	1000

Ey, Hx

DEPTH (Km)	Ey, Hx
1.07	7.4
1.39	4.4
2.43	12
2.70	5
	10 ⁶

Ey, Hx

DEPTH (Km)	Ey, Hx
1.07	7.4
1.39	4.4
2.70	15
	10 ⁵

WHERE $\frac{\Delta(Km)}{\rho_5(\Omega-m)} = .03$

Figure 9. Magnetotelluric apparent resistivity curves -
Onoway, Alberta.

Bon Accord. - As no magnetotelluric information was available in the 2 to 10 sec period range (Figure 10), an analysis using detailed well-log information was not carried out. In fitting models to the observed pair of curves it was necessary to use different values for resistivity in the top layer. Aside from this complication, which is discussed below, good fits were obtained using the known basement depth and values for the other parameters comparable to those at Cooking Lake and Onoway.

Kavanagh. - The observed curves at this station (Figure 11) cannot be fitted using reasonable parameters.

Discussion

It should be emphasized that the Cagniard theory does not yield correct interpretations, if resistivities depart from the assumed conditions of homogeneous, isotropic, horizontal layers. However it should still be useful as a semi-quantitative guide.

Interpreted deep resistivities are fairly consistently of the order of 1000 ohm-m -- a value which agrees very well with those of Niblett and Sayn-Wittgenstein (1960) and Srivastava, Douglass, and Ward (1963). By calculating a number of theoretical curves with different basement resistivities and considering the spread of the data, the error in interpreted resistivity is estimated to be ± 250 ohm-m. Calculations show that a decrease in resistivity of one order of magnitude (to 100 ohm-m) at the Mohorovičić discontinuity (40-50 km) is not consistent with the observed apparent resistivity curves. However the curves

THEORETICAL MODELS

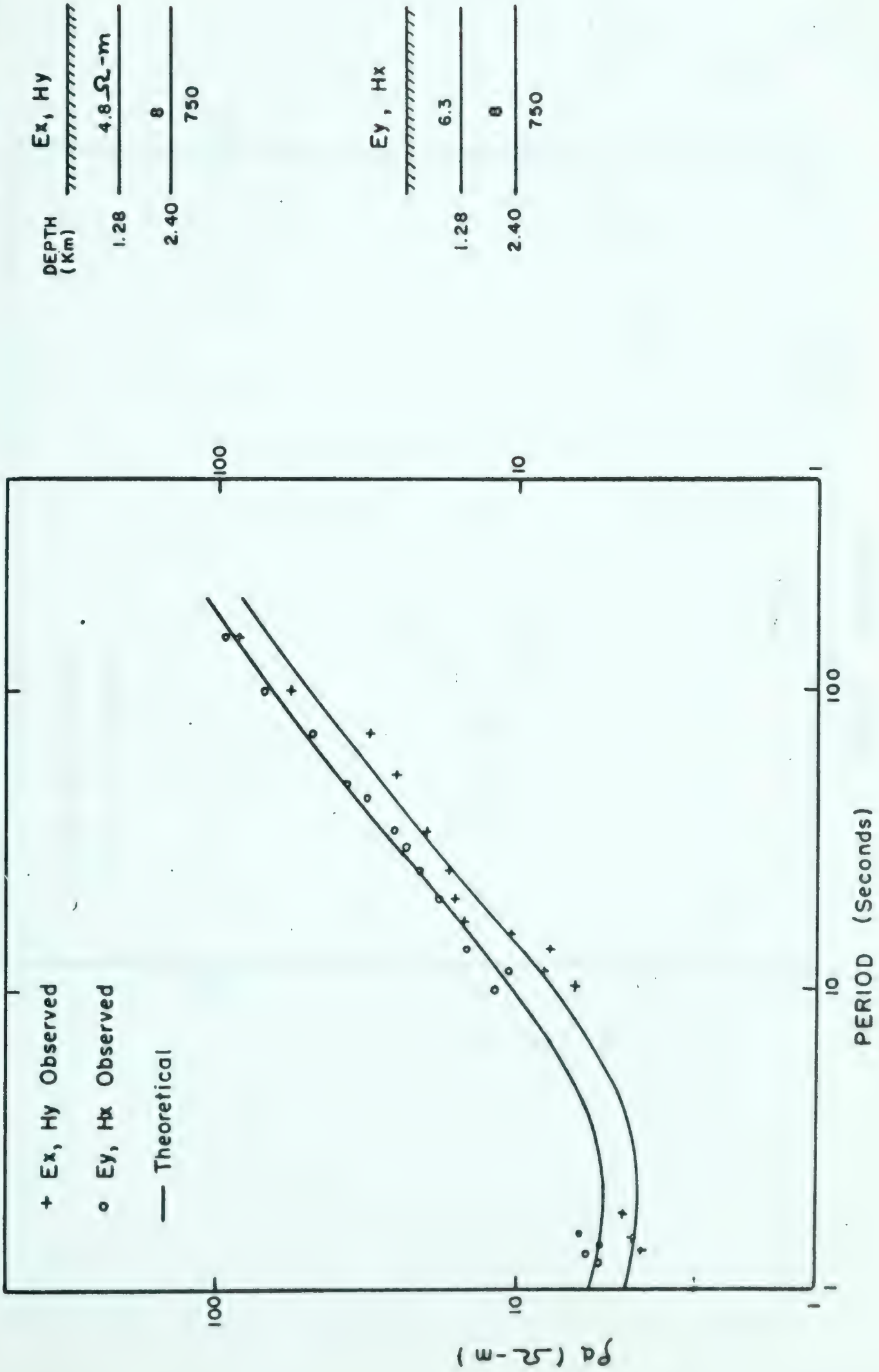


Figure 10. Magnetotelluric apparent resistivity curves - Bon Accord, Alberta.

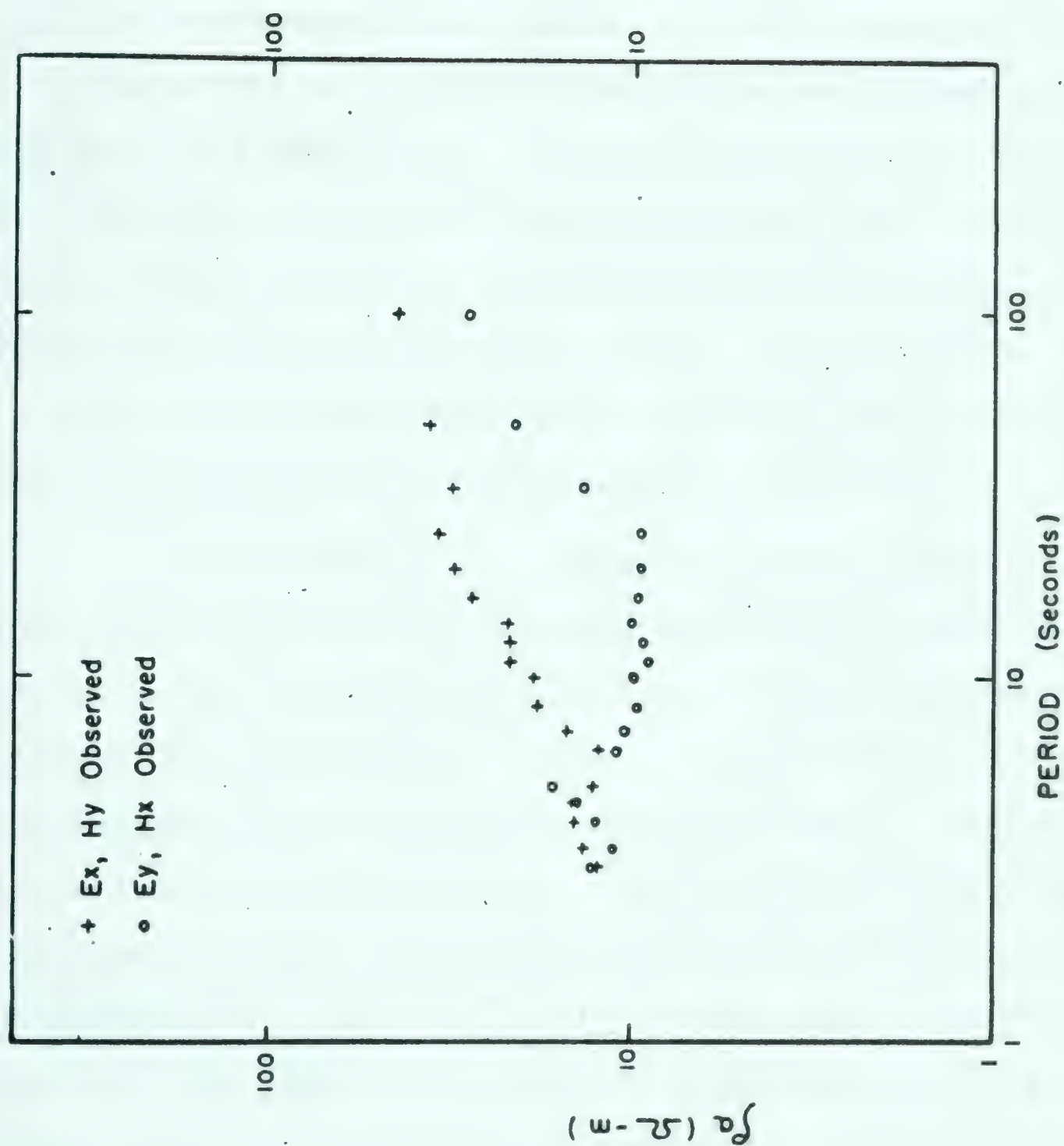


Figure 11. Magnetotelluric apparent resistivity curves - Kavanagh, Alberta.

are insensitive to a resistivity increase at these depths. Earlier results from the southwestern United States (Vozoff, Hasegawa, and Ellis, 1963) indicate an apparent maximum resistivity of about 300 ohm-m at a few tens of kilometers and a rapid decrease beyond that depth. It would seem that the earth at these depths is quite different in central Alberta than in the Basin and Range area. (Seismic velocities in these regions are also quite different (Cumming, Garland, and Vozoff, 1962; Eaton, 1963)). The low resistivities found by Wiese (1962) from European stations and his summary of the results of others confirm our findings that resistivities at deep crustal and upper mantle depths vary considerably from location to location.

As pointed out in Chapter I, Price (1962) showed that for a generalized source apparent resistivity curves can depart markedly from Cagniard's prediction at "long" periods if the resistivity increases with depth. A set of Price curves with the geological parameters approximating those of central Alberta is shown in Figure 12. For the range of periods in the experimental data, it is seen that source effects could only be detected if $v \approx 10^{-2} \text{ km}^{-1}$ which corresponds to very small sources. The situation is further complicated as this effect could also be interpreted as a conductive lower layer. On only two of the curves, E_x-H_y at Cooking Lake and Onoway, is there any evidence of such an apparent decrease in resistivity at the longer periods. Since this evidence is based on a total of only 3 spectral points, and is not supported by the other apparent resistivity curves, it is not thought to be significant.

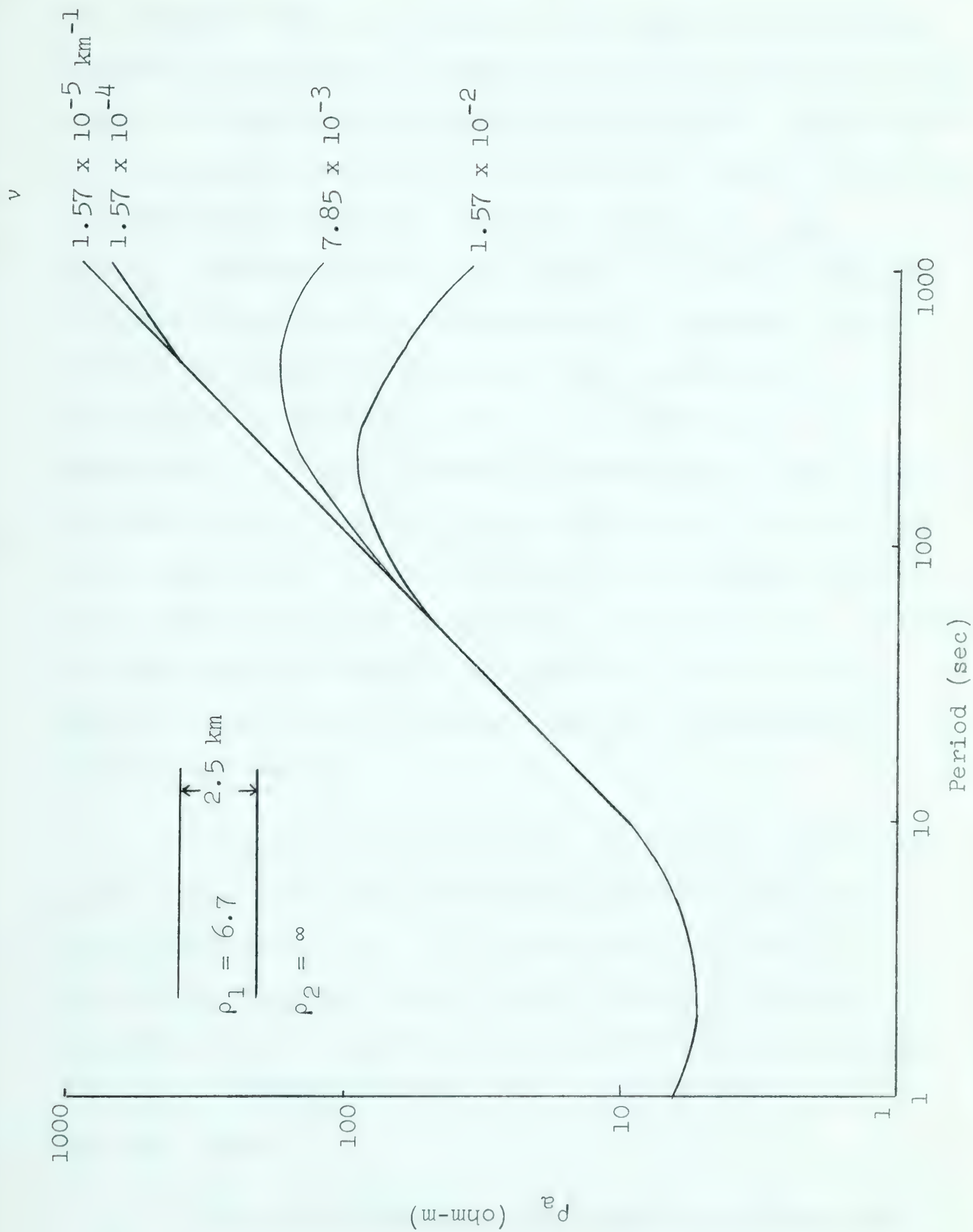


Figure 12. Price curves with geologic parameters approximating those of central Alberta.

In a general way these results seem to verify the Cagniard theory, at least in the range of periods and resistivities involved. However it is clear that the results cannot be completely explained by this theory. At the three stations where interpretation is possible, the $E_x - H_y$ curves are essentially the same. However, the $E_x - H_y$ and $E_y - H_x$ interpretations do not agree. At Cooking Lake this apparent anisotropy can be explained on a geologic basis. However at Onoway and Bon Accord, more difficulty is encountered as anisotropy must be introduced into the sediments. D. Rankin (personal communication) finds similar displacements in apparent resistivity curves obtained from model experiments. He attributes this to boundary effects which would correspond to geologic inhomogeneities. Although this may partially explain the results, it is doubtful whether large enough contrasts exist in the sediments to explain our results.

Figure 13 shows three $E_x - H_y$ apparent resistivity curves which were calculated using different sections of record from Bon Accord. It is impossible to obtain a theoretical Cagniard curve to match the curve obtained from Tape No. 3. Furthermore the differences are so large that it is doubtful whether they can be explained on a geologic basis.

The discrepancies in the results at Onoway and Bon Accord and the rough observed curve at Kavanagh are probably due to a combination of factors.

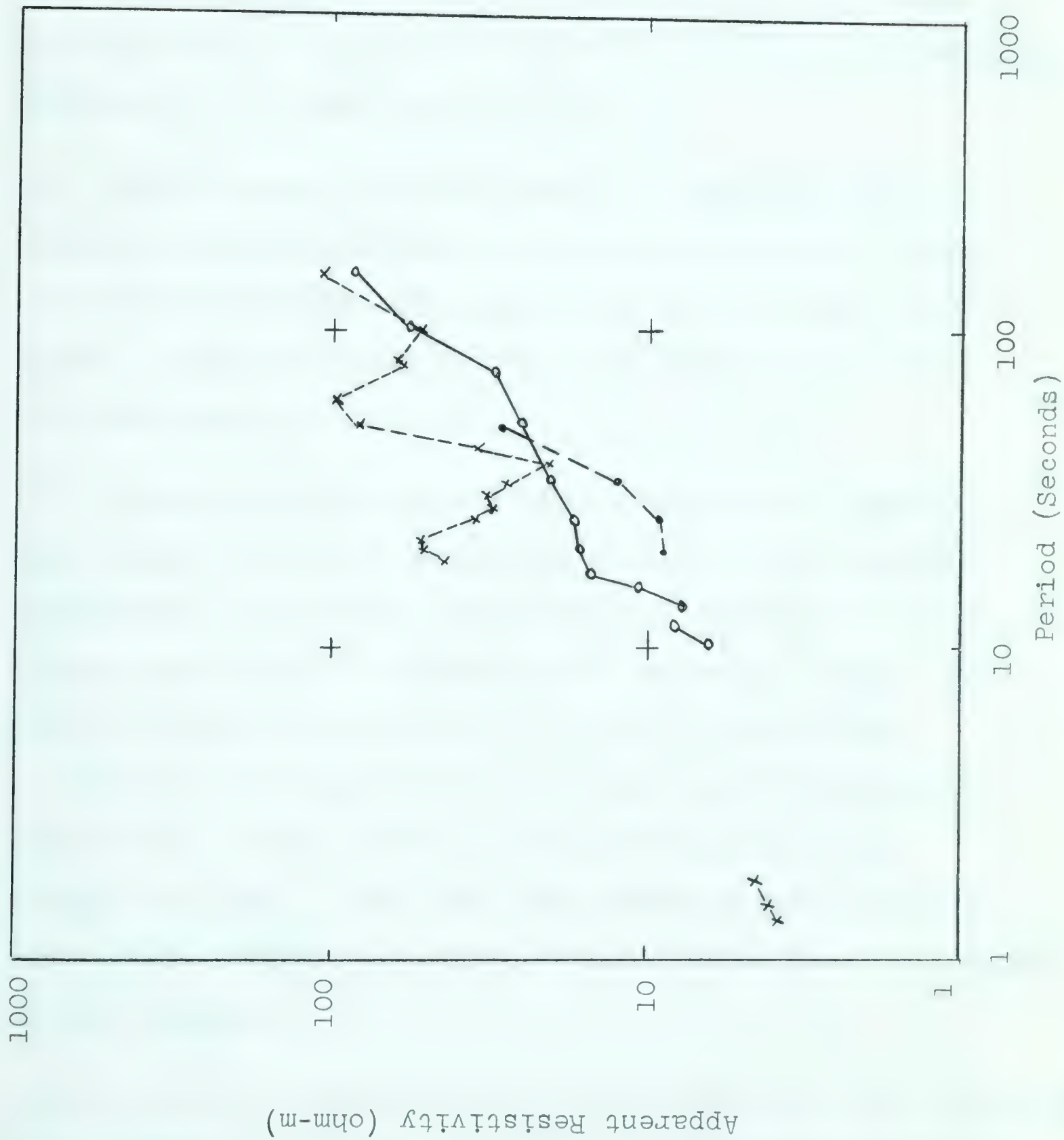


Figure 12. Apparent resistivities computed using 3 different records from Son Accord.

(1) At frequencies above 0.1 cps, the noise level was often high. In some cases this is probably true at lower frequencies. Significantly, our best result (Cooking Lake) comes from the record with the largest signal. For very long periods some results were unreliable due to drift in the magnetic system. It is difficult to say where these problems set in. Where the curves became rough or physically unreasonable the data was rejected.

(2) Using hanning, as with almost all spectral windows, energy estimates on steep slopes are not accurate. Almost invariably magnetotelluric spectra have one or more steep slopes. Again it is difficult to say where on the curve this unreliability sets in.

(3) Finite-sized sources may also influence the results. Quon (1963) shows that under some conditions the apparent resistivity curves which would result if the sources were dipoles might bear no resemblance to Cagniard curves. For example, vertical components of \underline{H} can be appreciable. In reality it is expected that the sources of pulsations observed at a fixed point on the earth's surface will change with time. Thus, the time-averaging power spectrum approach is probably averaging fields from a number of sources at each frequency.

(4) At this time there was also some doubt as to the stability of the detection system. This was checked by frequent calibration at discrete frequencies. However, there is some

difficulty in picking peak-to-peak amplitudes, since, in the magnetic systems, natural signal is always superposed on the calibration signal.

Chapter III

ANALYSIS OF 1962 DATA

Instrumentation

From the results of the 1961 experiments it was clear that improvements were required in the detection system to extend the observable range to both shorter and longer periods. The photocell amplifiers were rebuilt with an improved feedback system which reduced the drift problem at long periods. The use of better dc amplifiers lowered the noise level in the electrics which extended the range of usable frequencies as high as 5 cps. Further, the gains of both the electric and magnetic systems were found to be stable. Thus calibrations were not required as often and periods of low signal level could be selected for this purpose. Amplitude calibration curves were obtained by picking the amplitude of the sinusoids from playbacks of the calibration sections in both analog and digital form except at very long periods where spectral analysis was used because of the poor wave form and low signal-to-noise ratio. Phase calibrations have been obtained by playing back the calibration sections through a phase meter.

Purpose and Location of Field Experiments

With an improved detection system it was desirable to record data for 4 purposes.

- (1) Data recorded at a fixed location at different times were required to test for consistency of apparent resistivity estimates.
- (2) Data from a location with good resistivity control were required to confirm that experimental results could be obtained which are consistent with known geology.
- (3) Data were required to investigate the relationship of H_z to the horizontal magnetic and electric fields.
- (4) Data recorded at a site where the sediments are either very resistive or very thin, would yield resistivities at upper mantle depths provided that crustal resistivities were comparable to those of central Alberta.

As good resistivity control is obtained by using well-logs in thick, conductive sediments, this requirement is incompatible with penetration to upper mantle depths. For this reason, magnetotelluric measurements were made in two areas - at Montreal Lake in central Saskatchewan and at Vulcan, Brooks, and Beiseker in southern Alberta (Figure 14).

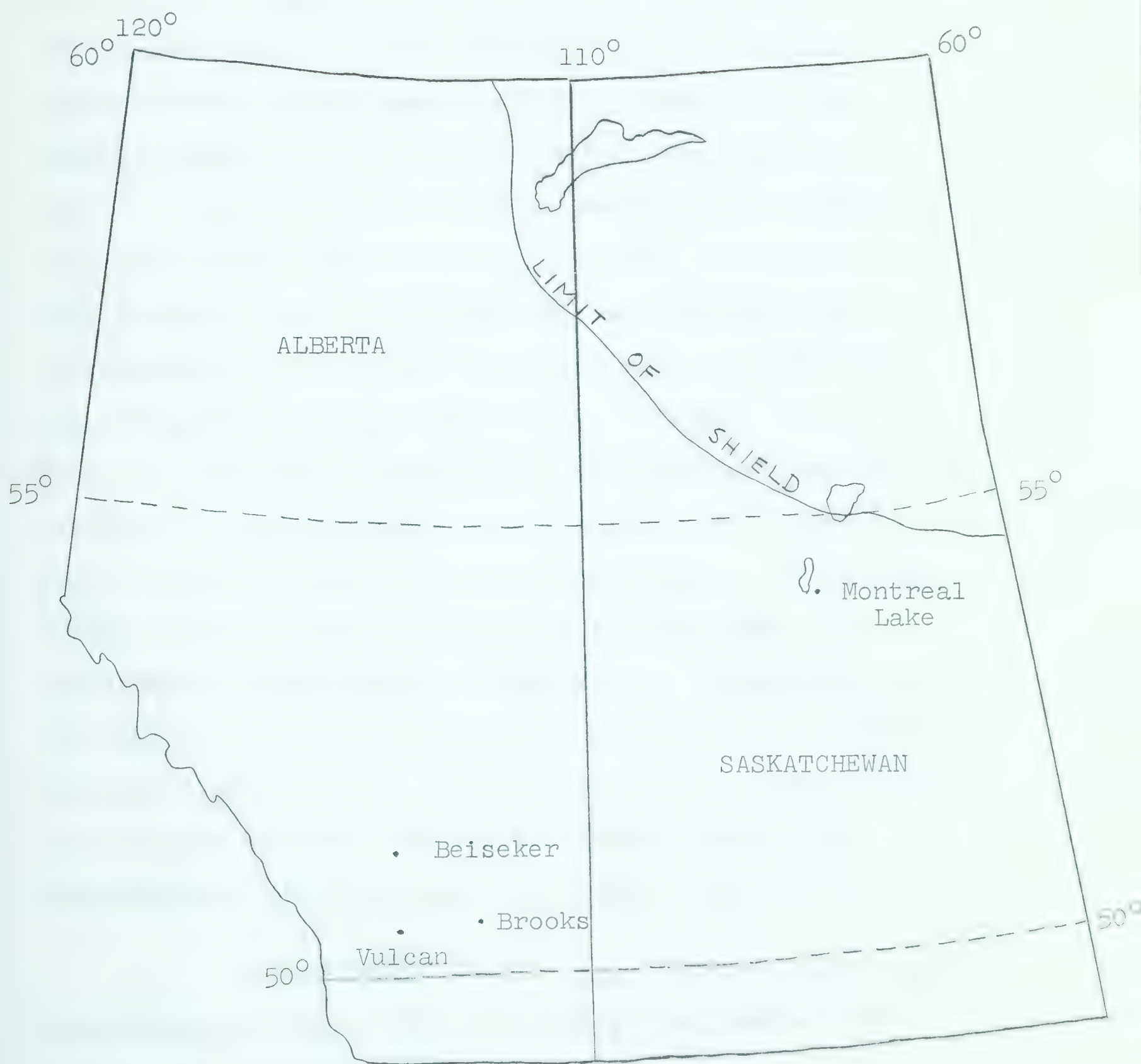


Figure 14. Location of 1962 field stations.

At Montreal Lake the well-logs show that the sediments are thin and resistive (Figure 15). Since the effective resistivity (reciprocal of mean conductivity) is 73 ohm-m, frequencies of almost 100 cps would be required before this thin sedimentary layer would have a marked effect on the magnetotelluric curves. At the nearby basement hole, Great Plains Montreal Lake #2-5, the well-log indicates a basement resistivity of 200 ohm-m, while 13 miles to the northwest at Great Plains McDermott West Montreal Lake #5-22, the resistivity is 80 ohm-m. The basement rock at these locations is mica schist and altered biotite gneiss respectively (Peterman, 1962). No other pertinent geophysical or geological information is available in the immediate area. However the Canadian Shield is exposed 60 miles to the northeast. There, the surface geology shows major trends striking NNE. The aeromagnetics show similar trends which to some extent is a reflection of the presence of pyrrhotite dikes (M. Reford, personal communication). The strike of the gravity trends to the south of this location is between that of the aeromagnetics and true north (Peterman, 1962).

In southern Alberta, the sediments are thick, flat-lying and conductive (Table 3) giving resistivity control at the higher frequencies.

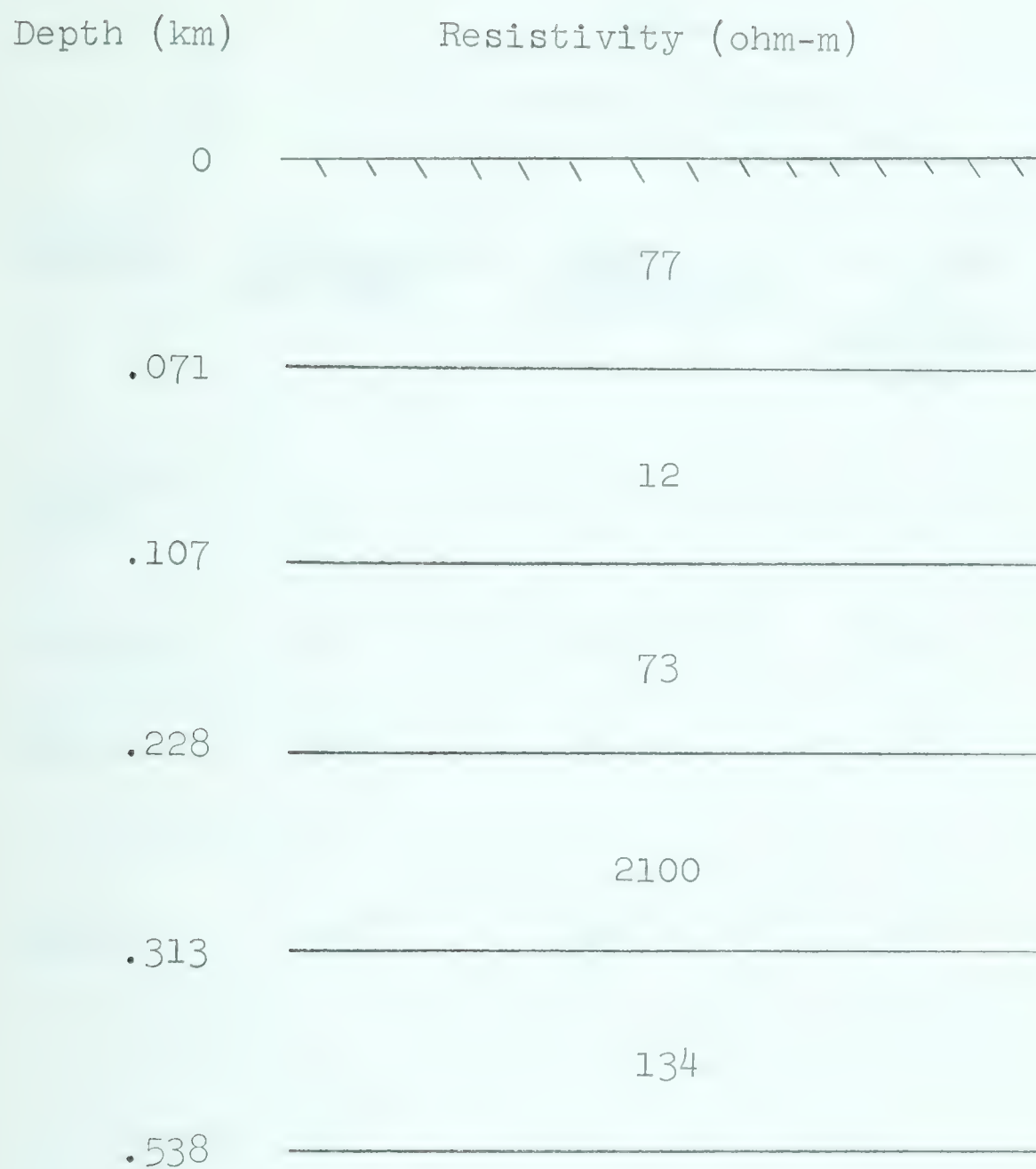


Figure 15. Sedimentary resistivities at Montreal Lake based on well-logs from Great Plains Montreal Lake #2-5.

Table 3
Station Information

<u>Station</u>	<u>Geomagnetic Latitude</u>	<u>Magnetic Declination</u>	<u>Thickness of Sediments (km)</u>	<u>Effective Resistiv- ity of Sediments (ohm-m)</u>	<u>Remarks</u>
Montreal Lake	63°	19° E	.54	73	basement - mica schist
Beiseker	58°	22° E	2.92	8.5	
Vulcan	58°	21° E	3.60	19.5	sediments dip west at 1.5°
Brooks	58°	20° E	1.38	conductive	

At all stations the detection systems were aligned along geomagnetic north-south and east-west directions. Five tapes of data were recorded at the Montreal Lake station during the period August 22-24 from which $12 \frac{1}{2}$ hours were selected for analysis (Table 4). The southern Alberta stations were occupied for shorter periods in early September with a total of 7 hours being digitized. In this thesis the Montreal Lake data are analyzed in some detail with the southern Alberta data (from a simpler geologic situation and lower geomagnetic latitude) being used only for comparison.

Analysis Procedures

Data channels were digitized in pairs with 4 conversions in most cases -- H_x-E_y , H_y-E_x , H_x-H_z , and H_y-H_z . For computational economy each section selected for analysis was digitized at two rates. The entire section was converted at a slow speed for low frequency analysis with subsections being converted at a higher speed for high frequency analysis. During this step, the analog signal was filtered to minimize aliasing problems.

After editing, the autospectra, coherence, and phase angle were calculated at $f = 0, \Delta f, 2\Delta f, \dots, f_{\max}$ where $f_{\max} < f_N$, the Nyquist frequency. CROSP2 (Simpson et al, 1961; Galbraith, 1963) which uses Daniell windows, was used to calculate all spectra with a number also being calculated with CS TUKS for comparison purposes. The conversion and analysis parameters for the two types of conversion are given in Table 5.

Table 4
Tape Information

<u>Tape</u>	<u>Date, 1962</u>	<u>Recording Period (GMT)</u> *	<u>3-hr Range Indices K_p</u> **	<u>Remarks</u>
Montreal Lake 1	Aug 22	2224-2354	5-	
Montreal Lake 2-1	Aug 23	0556-0727	3+ , 3o	
Montreal Lake 2-2	Aug 23	0751-0843	3o	
Montreal Lake 3 (7.55)	Aug 23	1355-1554	3+	
Montreal Lake 3 Marker	Aug 23	1608-1747	3+	
Montreal Lake 4-2	Aug 24	0704-0858	4+	Visible aurora
Montreal Lake 4-4	Aug 24	0929-1132	3+	Visible aurora
Montreal Lake 5	Aug 24	1225-1336	4+	
Beiseker 1-2	Sept 10	0309-0426	4o	
Vulcan 2-4	Sept 12	0947-1146	5o	
Brooks 1	Sept 13	1130-1343	3- , 3+	
Brooks 2-2	Sept 13	1621-1753	4+	

* To obtain local time subtract 6 hours at Montreal Lake and 7 hours at Alberta stations.

** The geomagnetic planetary 3-hr-range indices K_p are after Lincoln (1962, 1963).

Table 5. Analysis Parameters

	Δt (sec)	n	m	f_N (cps)	Δf (cps)	f_{MAX} (cps)
Low frequency	5	≈ 1000	100	0.1	0.001	0.070
High frequency	0.050	4000	500	10	0.02	5

An IBM 836 Document System was then used to plot spectra, coherencies, phase, apparent resistivities and spectral ratios. In this chapter these plots (and others) are used as examples with a larger collection of the machine plots appearing in Appendix D. An explanation of the notation and conventions used in plotting is also contained in this appendix.

These plots have been used as a basis for interpretation of resistivities and vertical magnetic fields in this chapter and for a discussion of the effects of simultaneous conversion, trend removal, prewhitening, and spectral windows in Appendix C.

Decimation of Apparent Resistivity Values using Coherency

Under the assumptions of Cagniard's theory, the orthogonal components of \underline{E} and \underline{H} should be coherent. It has been found (Appendix C) that smooth spectral ratios and therefore smooth apparent resistivities may be found by discarding all points for which coherency-squared is less than 0.9 and the points adjacent to these. In practice it

is found that this is so restrictive that few points are left on some apparent resistivity curves. Since it is preferable to have some estimate of resistivity rather than none at all, points have been used for which coherency-squared is greater than 0.75 or 0.8. This appears to be satisfactory in most cases. Before examining the apparent resistivity curves, the reasons for variation of coherency and some physical implications will be examined.

In practice, "noise" may be introduced by several sources. In any digital record section, noise due to detection systems, recording, and analog-to-digital conversion is always present at some level. At frequencies where the signal predominates the orthogonal electric-magnetic coherency will be high (assuming the Cagniard theory is applicable). On the other hand, if the signal and noise are comparable (in one or both series) or if the noise predominates in one, then the coherency will be low. Figure 16 shows an example of signal and noise of comparable magnitude ($K = 185-205$) while Figure 17 shows a sharp peak in the electric at $K = 45$ with no comparable deviation in the magnetic. If the noise predominates in both channels then the coherency may be large or small depending on whether the noise is common. In our system, coherent noise is introduced at the tape recorder. For this reason it can be detected not only by the change in ratio but by the

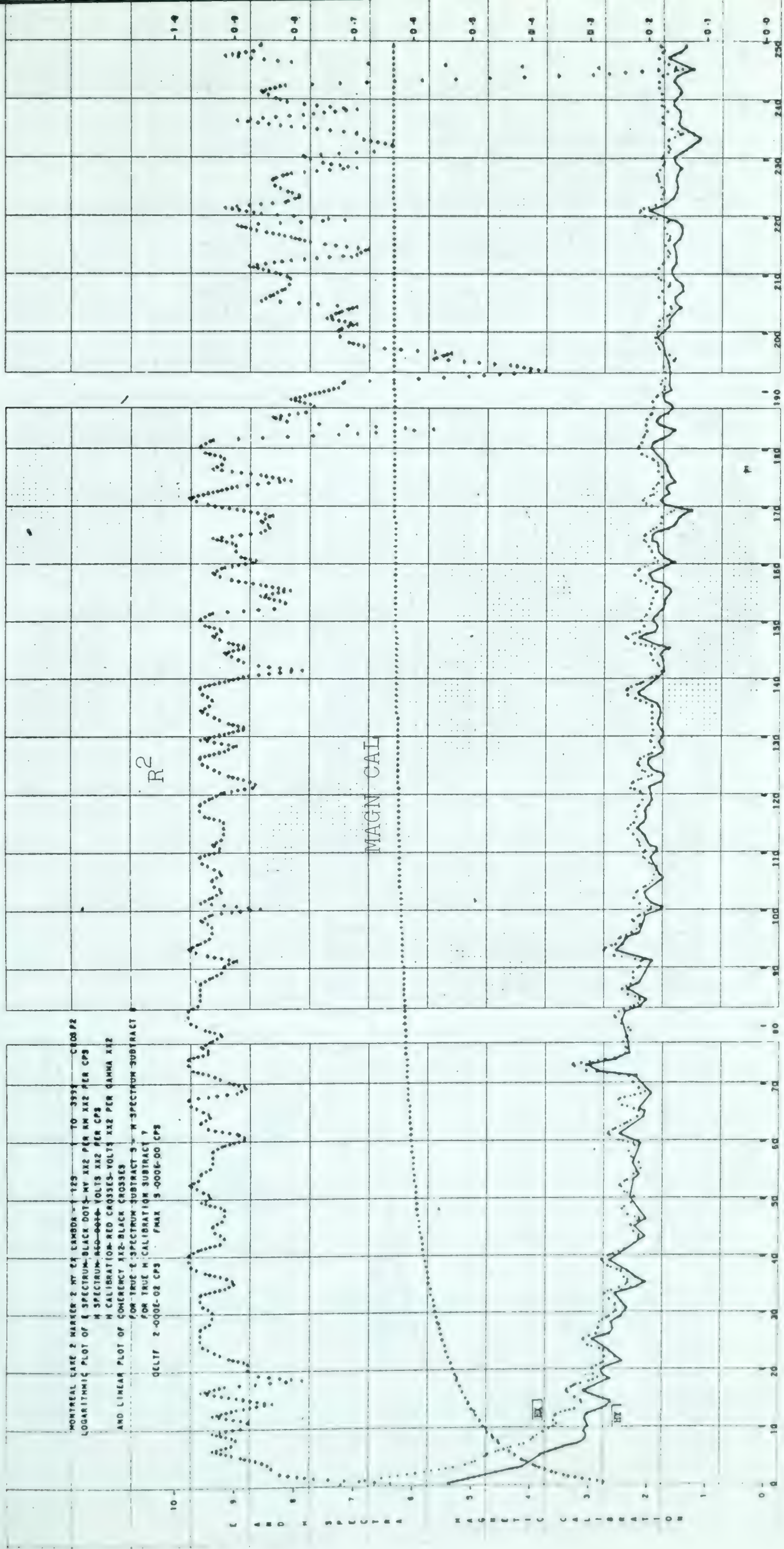


Diagram 43

Figure 16. HF spectra with signal and noise of comparable magnitude ($k = 185 - 205$).



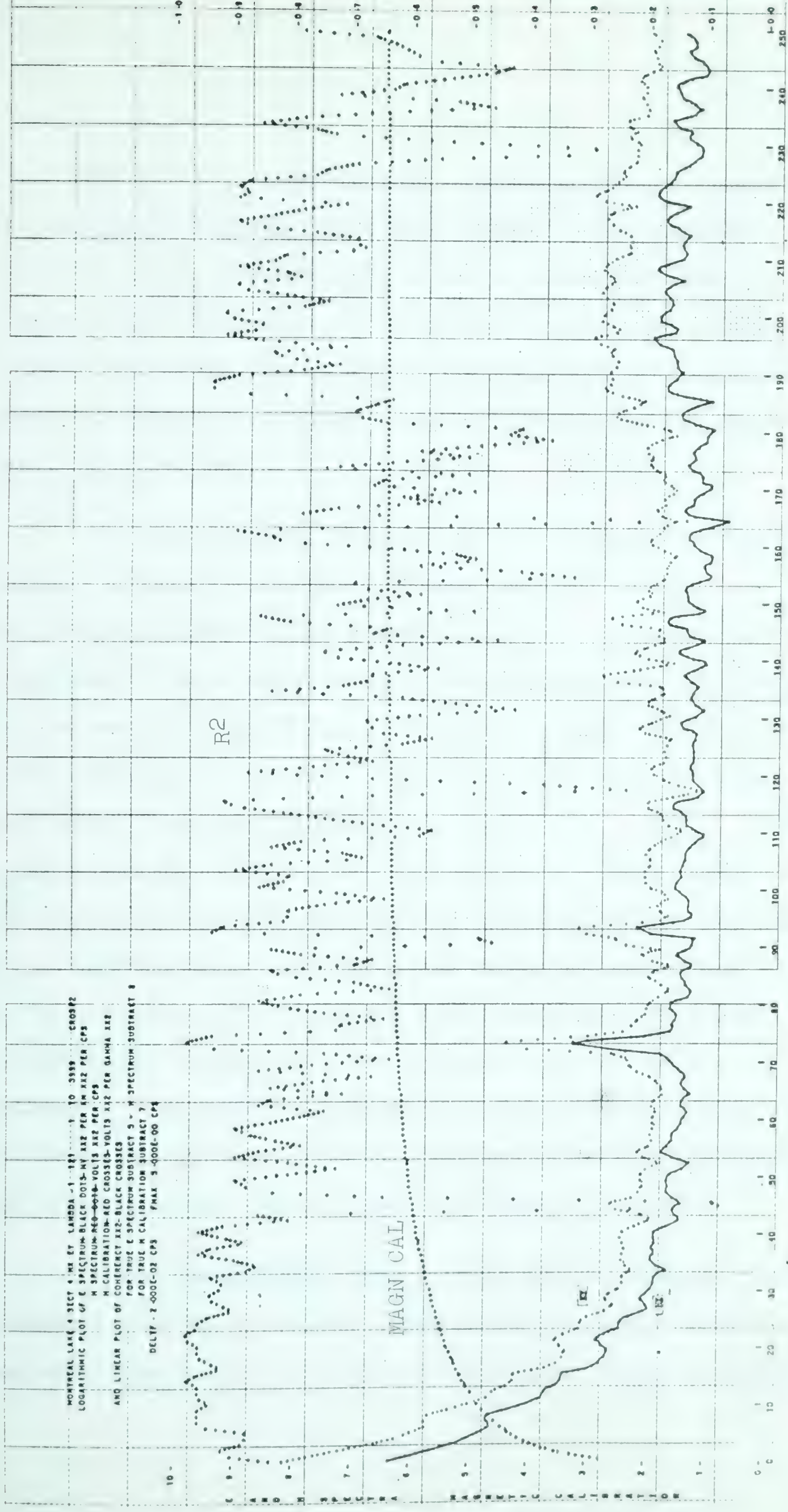


Diagram 79

Figure 17. HF spectra with noise present in E_y and not in H_x at $k = 45$, and coherent noise predominating in both at $k = 74, 93, 138, 148$ and $k = 180 - 220$.

fact that it is in-phase except for the shift introduced by the analog-to-digital conversion system. For Montreal Lake 4-4 H_x-E_y (Figure 17), noise predominates and is coherent for values of K close to 74, 93, 138, 148 and 180 to 120. This has led to a corresponding wide scatter of apparent resistivity values even after decimation on the basis of coherency.

Computational procedures are a second source of noise. Although the simple prewhitening filter $z_i = x_i - x_{i-1}$ has greatly improved the spectral quality and coherency, (Appendix C) some spectra could be improved even further by the use of other filters. Figure 18 shows the uncorrected power spectra for H_y and E_x from Montreal Lake 4-4 using data which have been prewhitened by $z_i = x_i - x_{i-1}$. The spectra are far from flat in this region. Even worse the slopes of the two spectra are quite different and therefore it is expected that the ratio may deviate considerably from its true value. This example also shows that different prewhitening filters may be required for the E and H spectra. For noisy records it has been seen that the value of coherency using the Daniell estimate is more consistent and therefore more useful than the hanning estimate.

In complex geologic situations the simple linear relation between orthogonal components of the electric and magnetic field will no longer hold. Under these circumstances

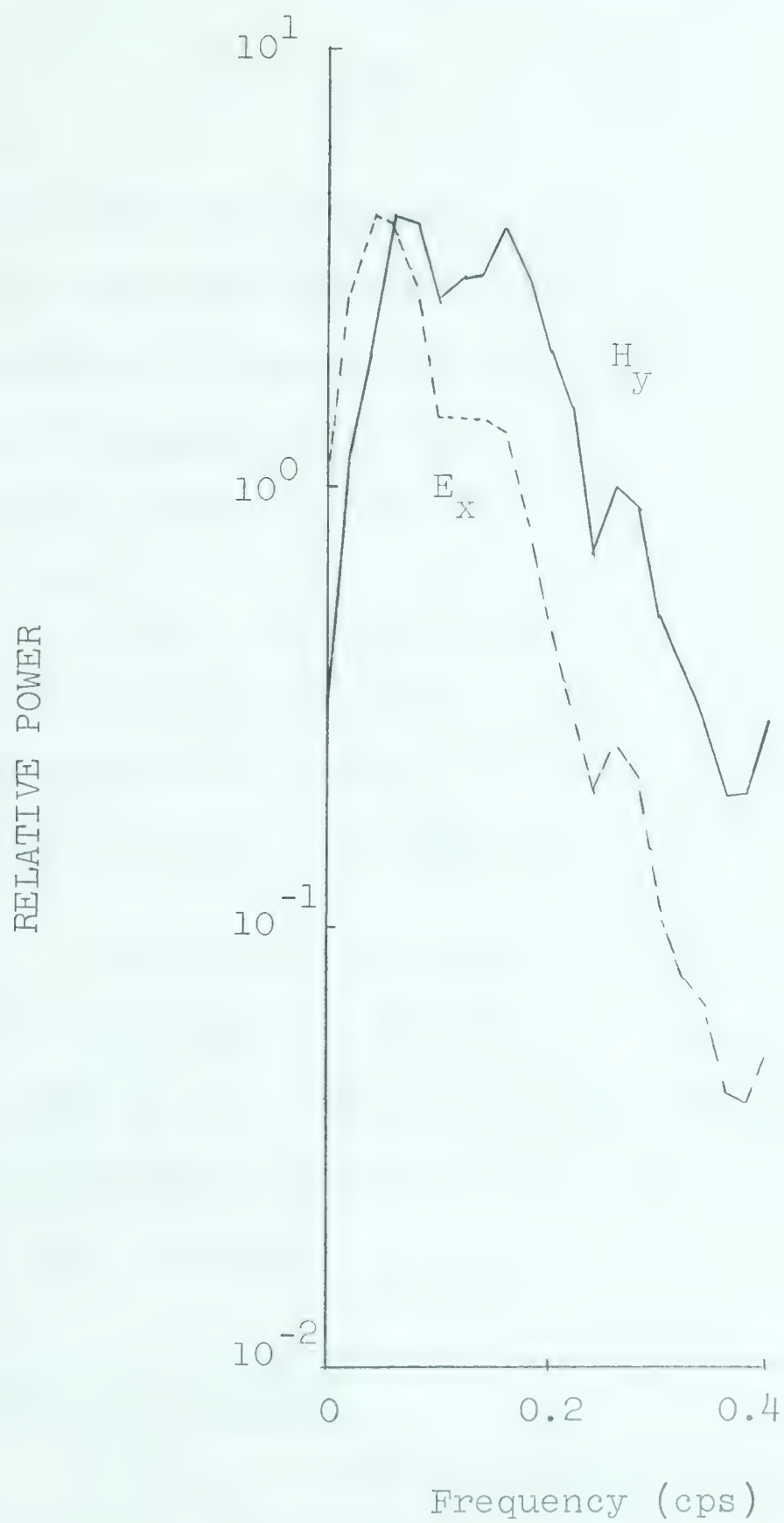


Figure 18. Uncorrected power spectra of Montreal Lake 4-4 using data prewhitened by $z_i = x_i - x_{i-1}$.

the tangential fields will be related by

$$H_i = Y_{ij} E_j \quad i, j = 1, 2$$

In this case the coherency between orthogonal components of the electric and magnetic field may be quite low even in the absence of system and computational noise. This situation should be suspected if low coherencies are obtained when the signal level is high.

Quon (1963) has shown that for dipoles at ionospheric heights, the angle between \underline{E} and \underline{H} at the surface of the earth can deviate considerably from 90° . For multiple sources this again would lead to low coherencies.

From this analysis, it is seen that eliminating data on the basis of coherency does not discard all the data that we would wish and it may discard data from complex geologic situations and complicated source systems which are meaningful.

Resistivity Analysis

In an attempt to obtain the best possible Montreal Lake apparent resistivity curve for each component, the spectral points for which the orthogonal E-H coherency-squared is greater than 0.8 have been averaged at each frequency. In all cases the high frequency data used was

prewhitened using the operator $z_i = x_i - x_{i-1}$. Figures 19 and 20 show the resulting apparent resistivity curves. Since the curves are quite different in the two directions, a layered earth interpretation is not valid. However, to gain a semi-quantitative picture, the curves have been fitted with two-layer theoretical models. The slope in the region 0.2 to 0.4 sec is impossible to fit using a layered earth. No attempt has been made to introduce a trend of this nature in the theoretical curves as it does not appear on the smooth apparent resistivity curves from Montreal Lake 2, (Figure 21) but is introduced by the wide scatter of points from other curves (Figure 22) which are due to coherent noise (Figure 23). It should also be noted that average H_y-E_x apparent resistivity is larger than that of the high energy Montreal Lake 2 spectra (Figure 16) for $T = .4$ to 1.5 sec.

Averaged phase difference curves have also been calculated (Figure 24). A two-layer interpretation of the H_x-E_y curve indicates that the ratio ρ_1/ρ_2 lies between 50 and 100. Using 60 ohm-m as the resistivity of the upper layer, the depth to the interface is found to be 17 km. Although the interpretation of the H_y-E_x curve is very uncertain, the ratio ρ_1/ρ_2 has been calculated to be 2/1 with the boundary at 22 km for a 32 ohm-m surface layer. The H_x-E_y phase interpretation is not consistent with the apparent resistivity curve. However the H_y-E_x interpretations are in good agreement. Such inconsistencies are expected if a layered earth interpretation is applied in an

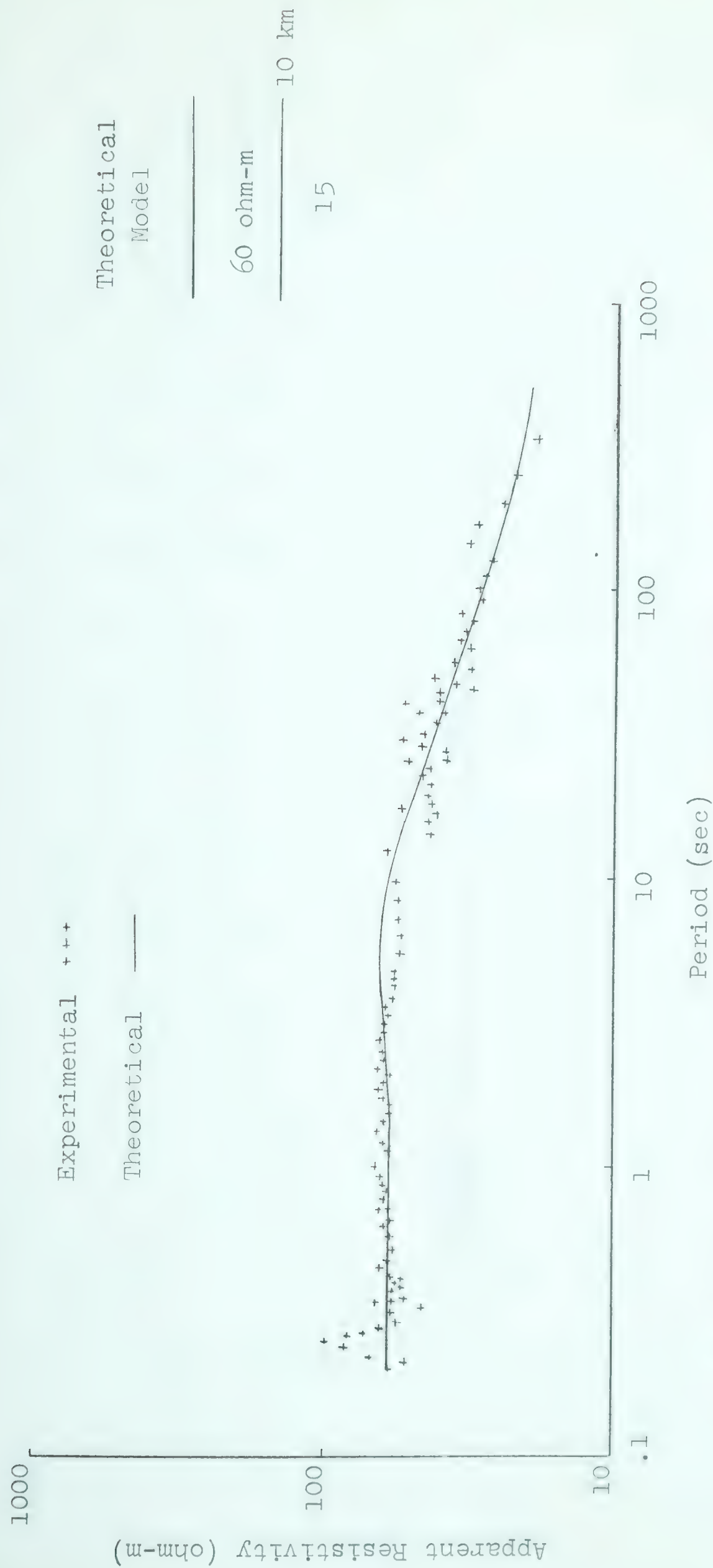


Figure 19. Averaged H_x-E_y apparent resistivity curve with two-layer theoretical fit.

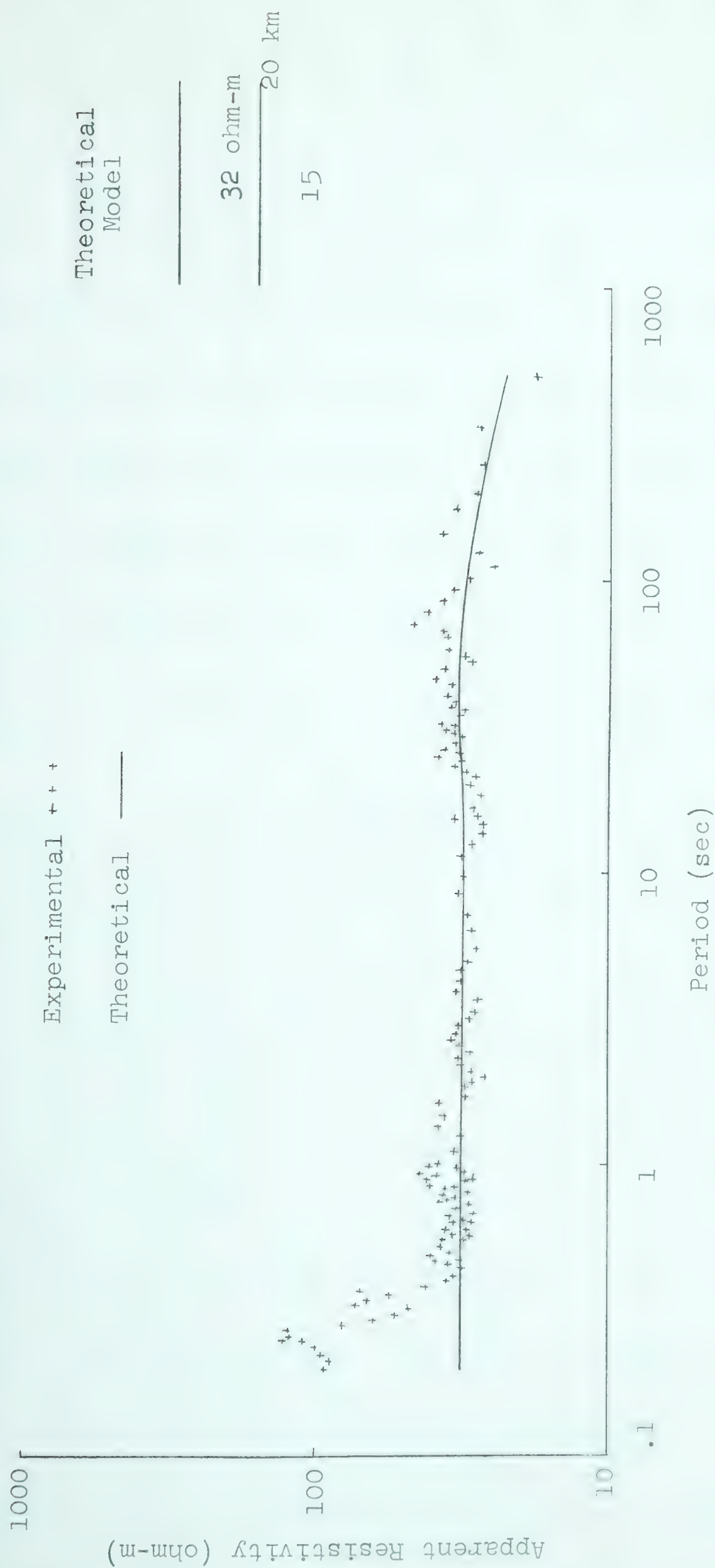


Figure 20. Averaged H_y-E_x apparent resistivity curve with two-layer theoretical fit.

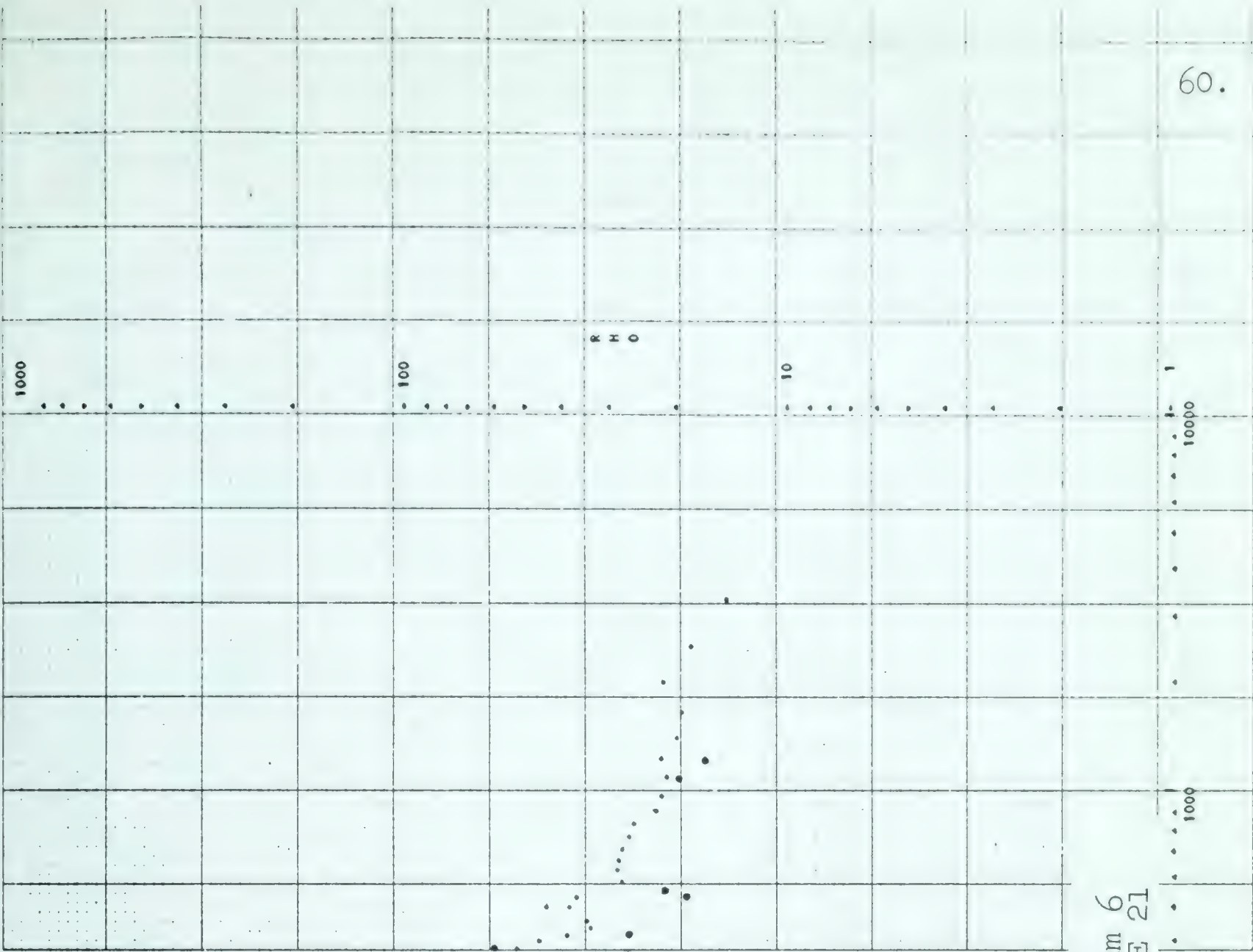
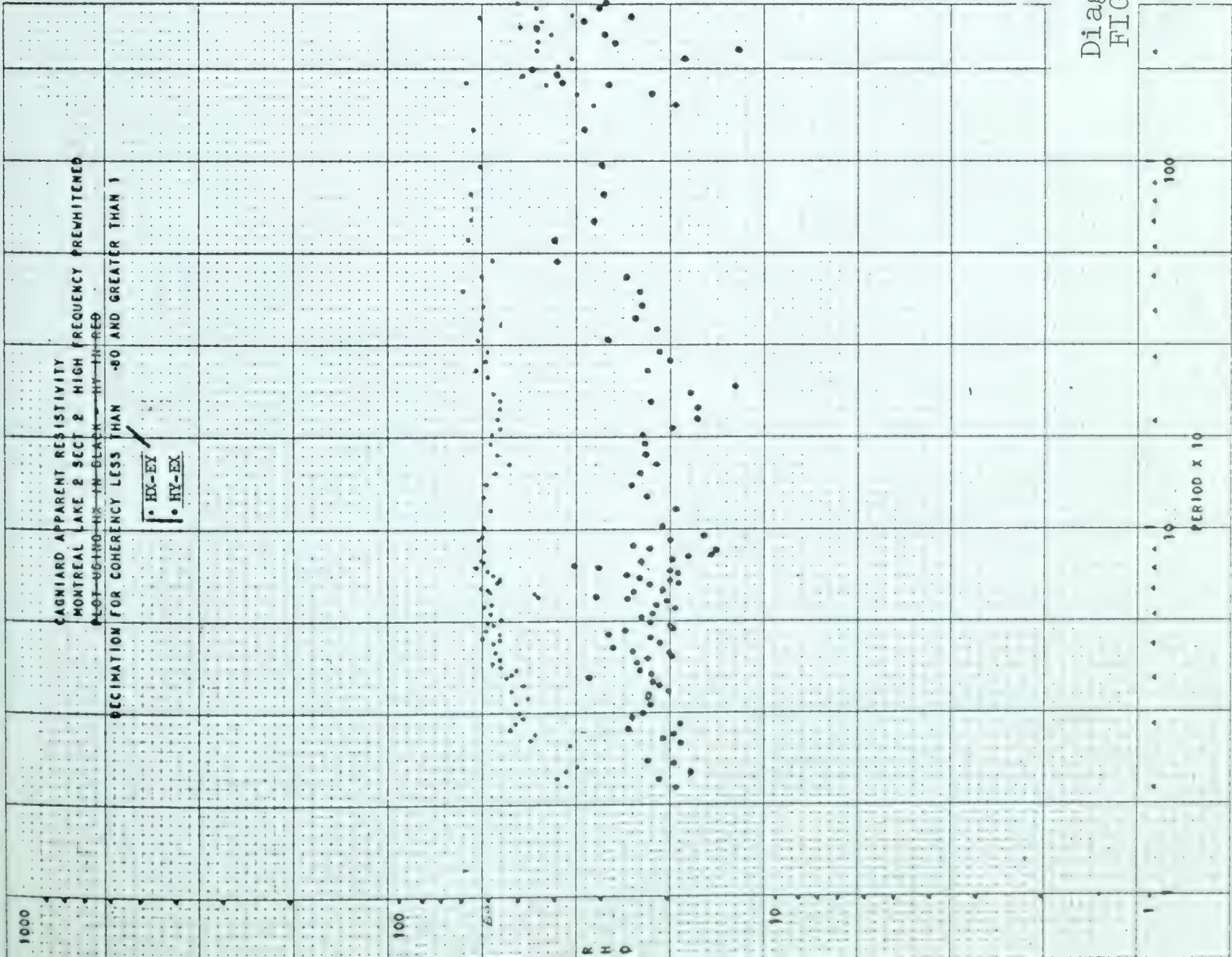


Diagram 6
FIGURE 21

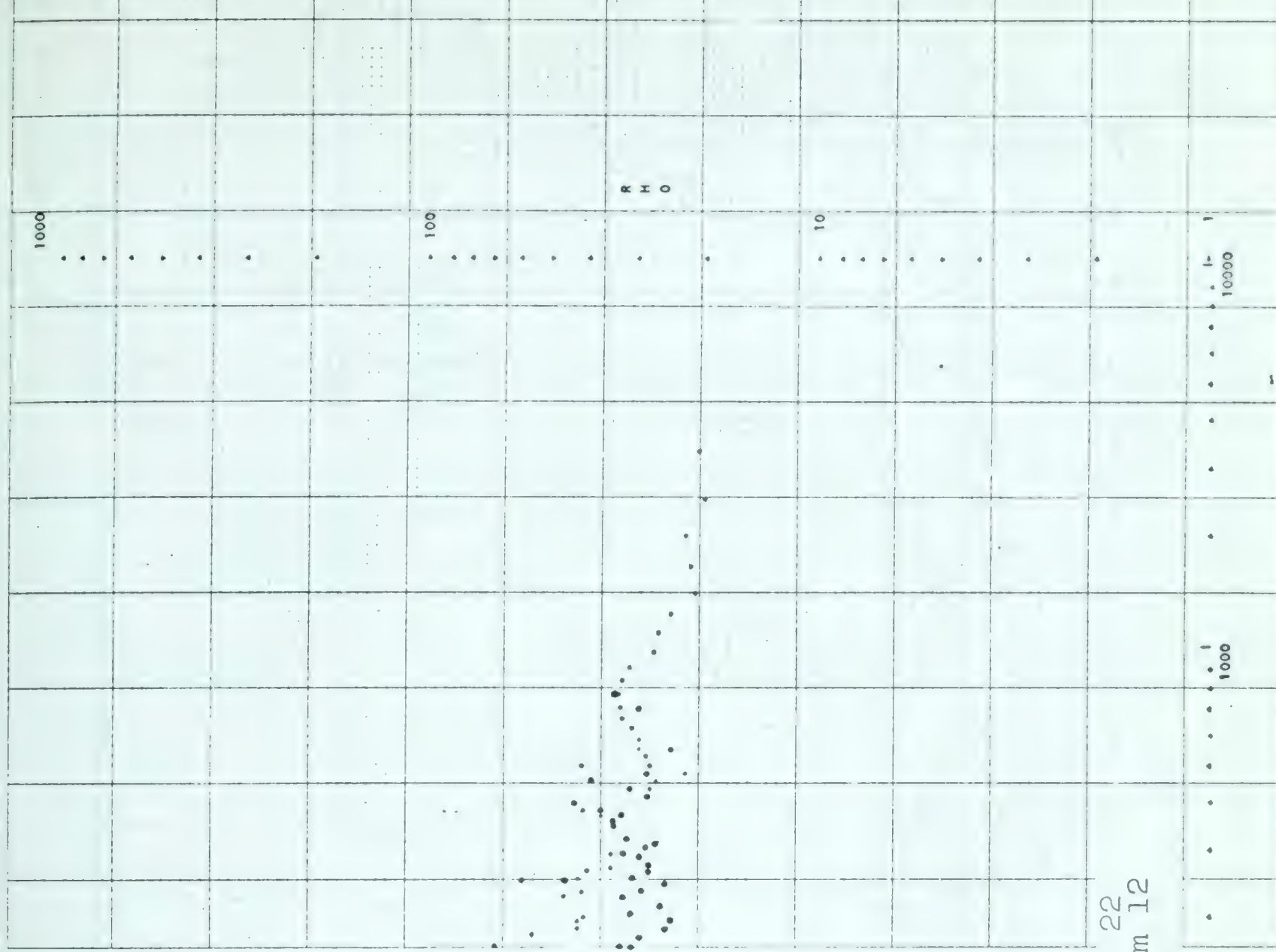
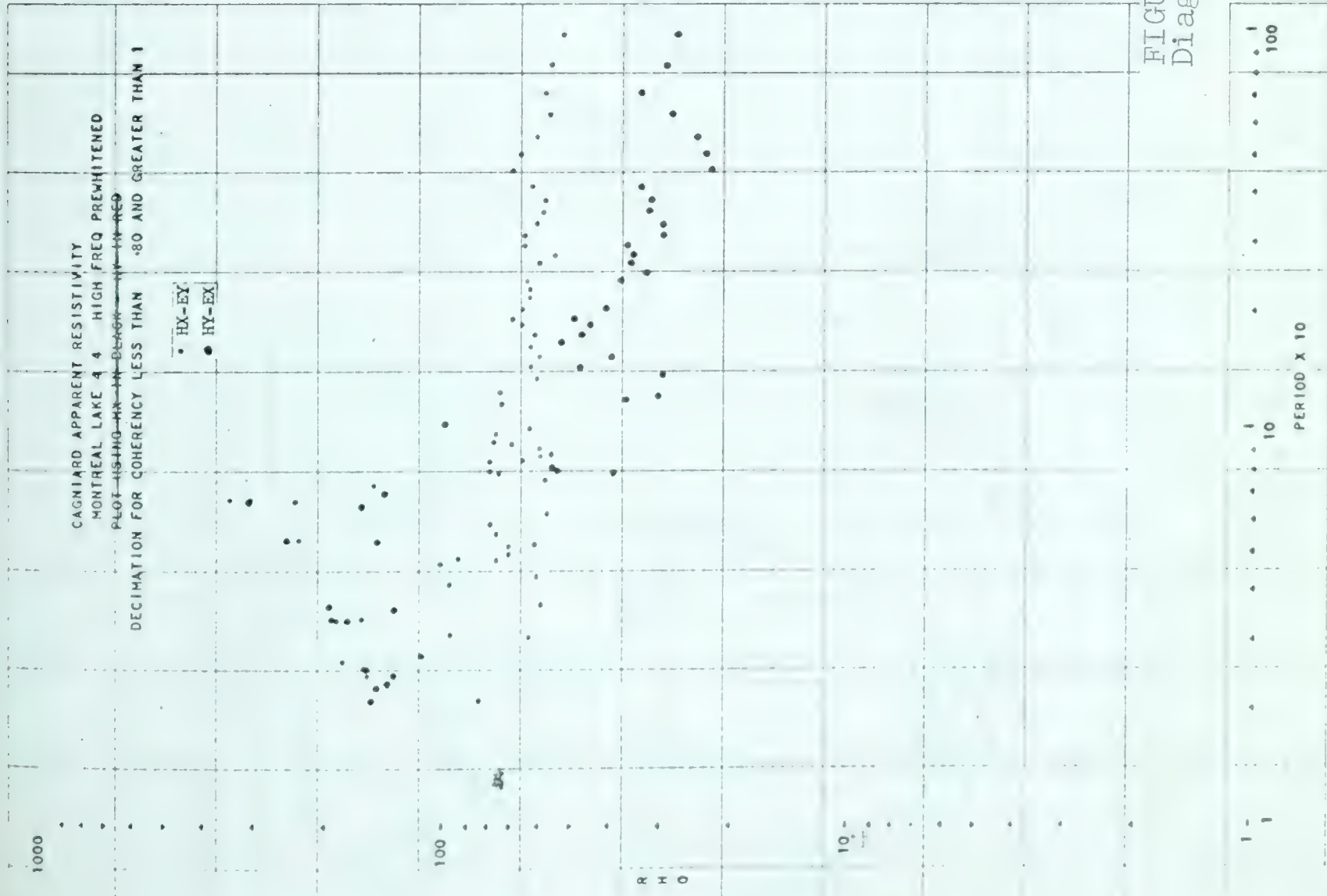


FIGURE 22
Diagram 12

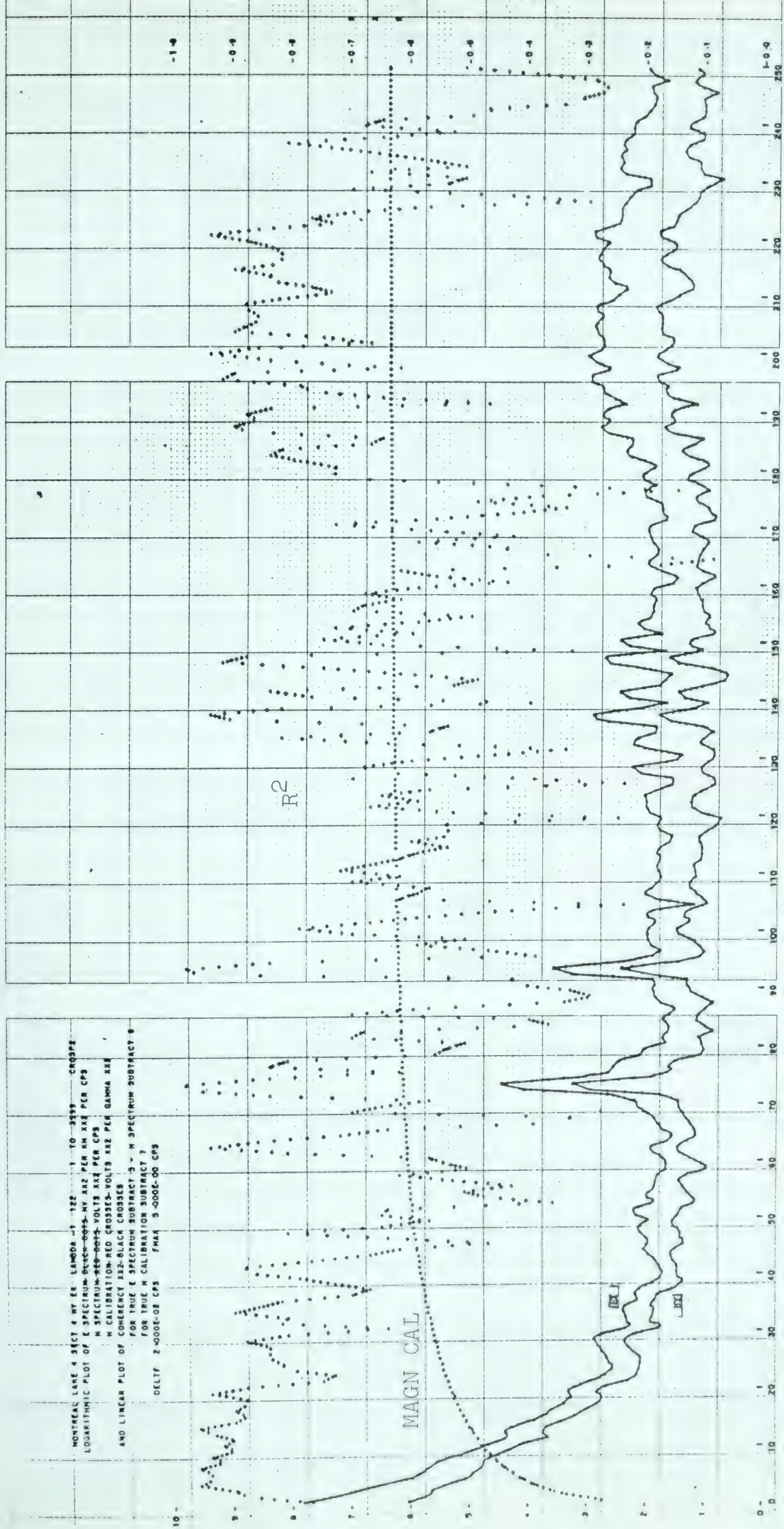


Diagram 80

Figure 23. Montreal Lake 4-4 H_y-E_x spectra with coherent noise spikes predominating for $f > 1$ cps.

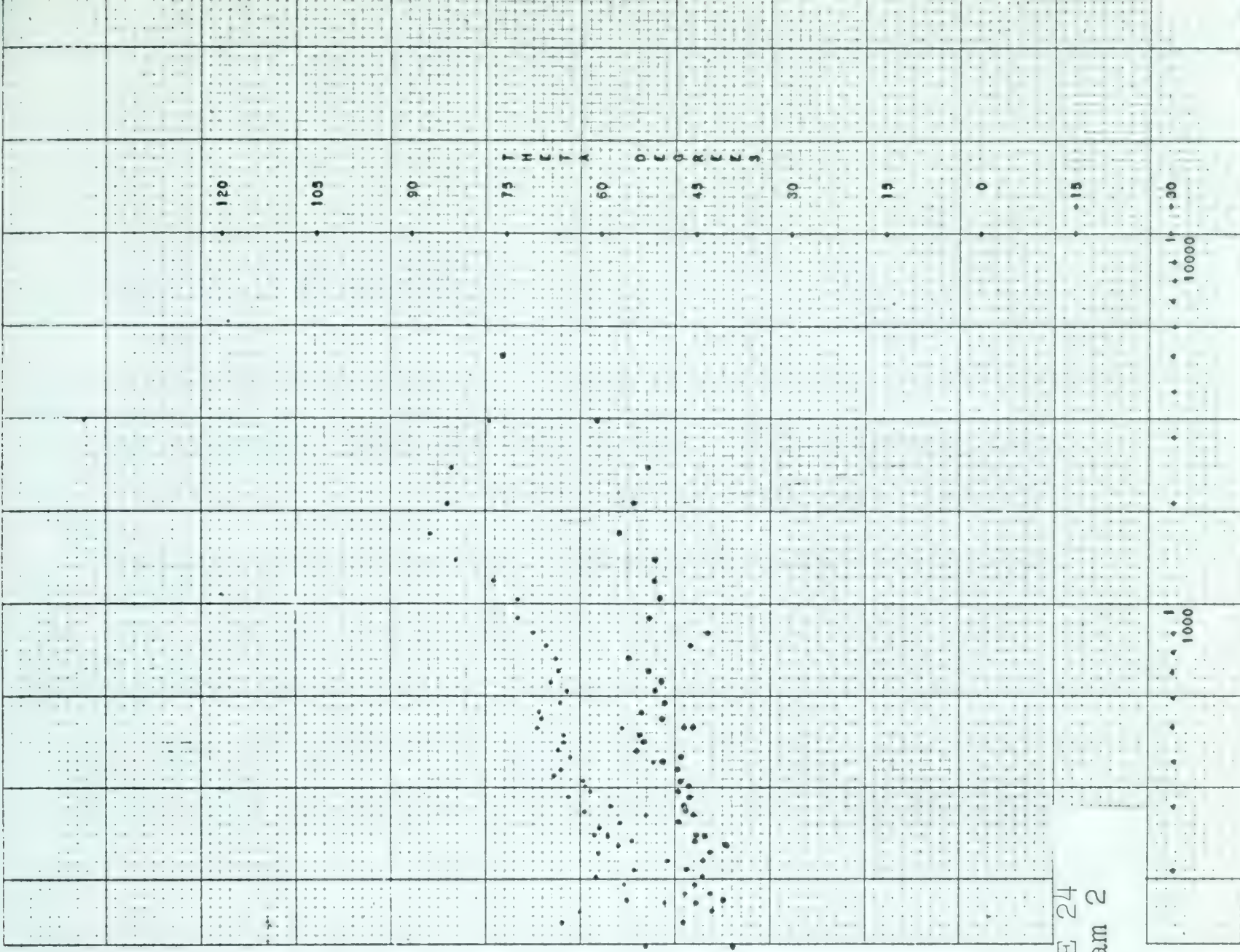
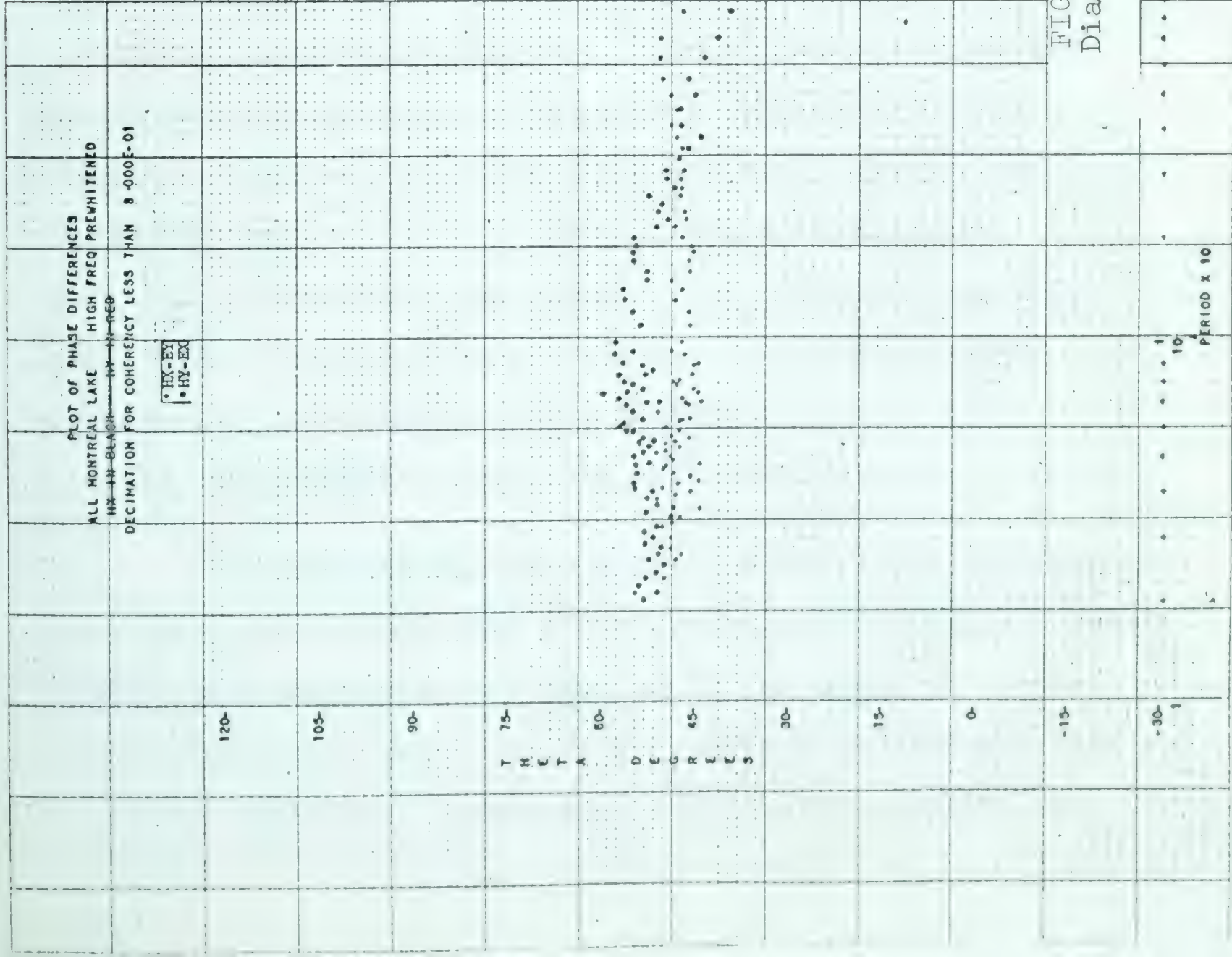


FIGURE 24
Diagram 2

inhomogeneous situation.

The most striking feature of the resistivity interpretation is the apparent geologic anisotropy. Since the magnetic declination at this station is 19° E, the angle between the measuring axes and the regional aeromagnetic trend is less than 20° . If the aeromagnetic "grain" is accompanied by a similar characteristic in crustal resistivity, this apparent anisotropy would be explained. Cantwell (1960) has outlined procedures to determine the major axes and the resistivities along the major axes for an anisotropic earth. In the case of an elliptically polarized wave, this requires that the amplitude and phase relationships between all horizontal components be known. Since these had only been calculated for orthogonal components, the theory using a linearly polarized wave was applied even though the records show that the field is elliptically polarized. This resulted in a meaningless scatter of ρ_a values. The only comforting feature of this experiment was that at high frequencies the rotation angle remained close to 0° . Clearly, too simple a model has been used.

An attempt has been made to explain the experimental data using two-dimensional structures. D'Erceville and Kunetz (1962) have considered the problem of two media in contact along a vertical fault overlying a horizontal basement that is either infinitely conductive, infinitely resistive, or

at infinite depth for the electric field perpendicular to strike (Figure 25). The only promising model is that of a conductive basement with the observing station on the conductive side of the fault ($\rho_3 < \rho_1 < \rho_2$) and the x-direction parallel to strike. Since theoretical data are only available at 3 frequencies and for 2 resistivity contrasts ($\rho_2/\rho_1 = 9$ and $\rho_2/\rho_1 = 100$), only a semi-quantitative fit can be obtained. Theoretical curves for such a fit are shown in Figure 26. In the real situation the resistivity of the basement will be finite which will decrease the thickness of the upper layer and cause a decrease in the phase angle at the longer periods as in the experimental data. No theory is available for the situation with \vec{E} parallel to strike ($H_y - E_x$). However the curves of Neves (1957) for the infinite fault indicate that the change in the phase curves will not be as large nor the changes in the apparent resistivity curves as sharp. This agrees with the observations. A major difficulty may be to find a region on the theoretical curves where the apparent resistivities differ by almost a constant factor over such a wide frequency range. Clearly geographic coverage and more theoretical curves are required before a final interpretation can be made. It may be found that the geology is too complicated to fit with such simple models.

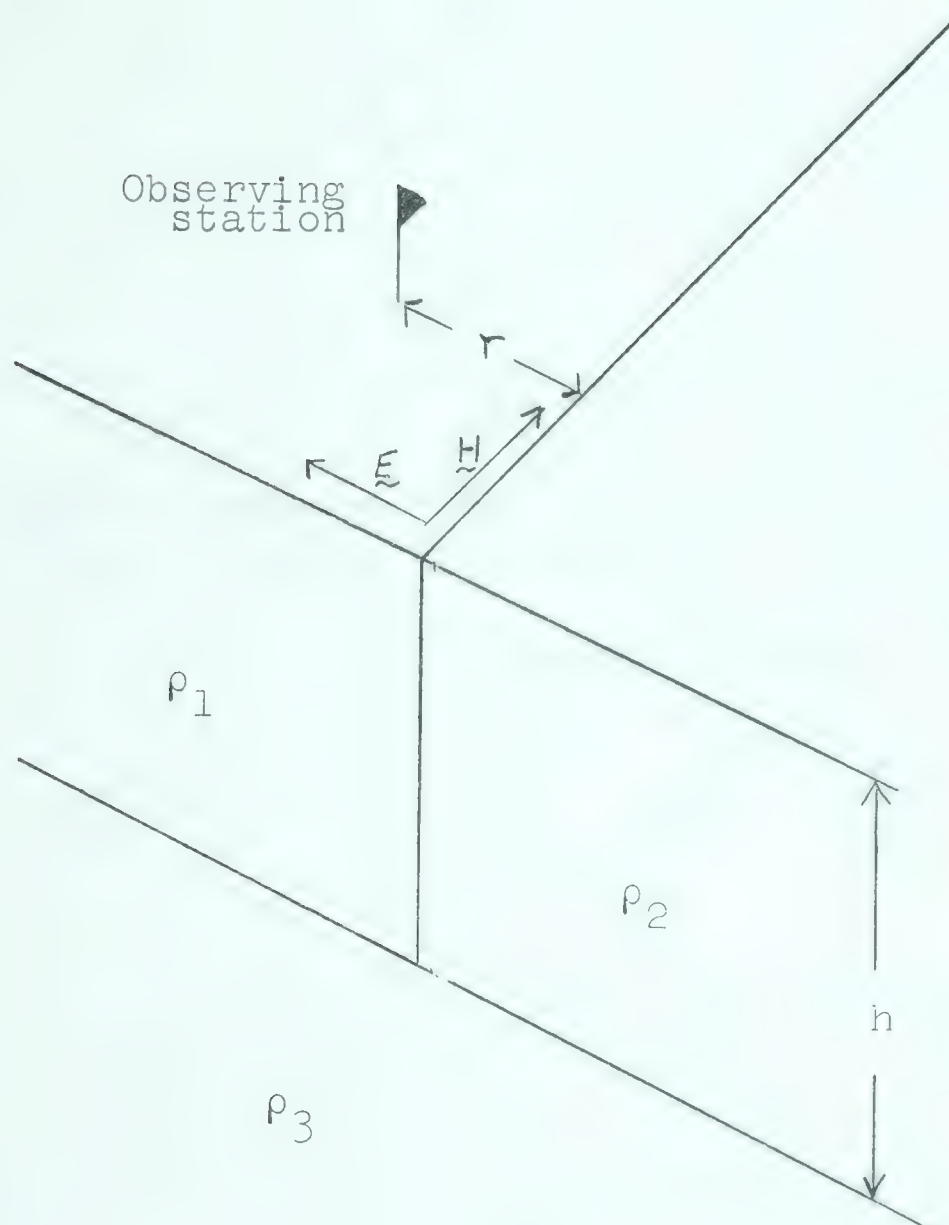


Figure 25. Finite fault considered by d'Erceville and Kunetz (1962).

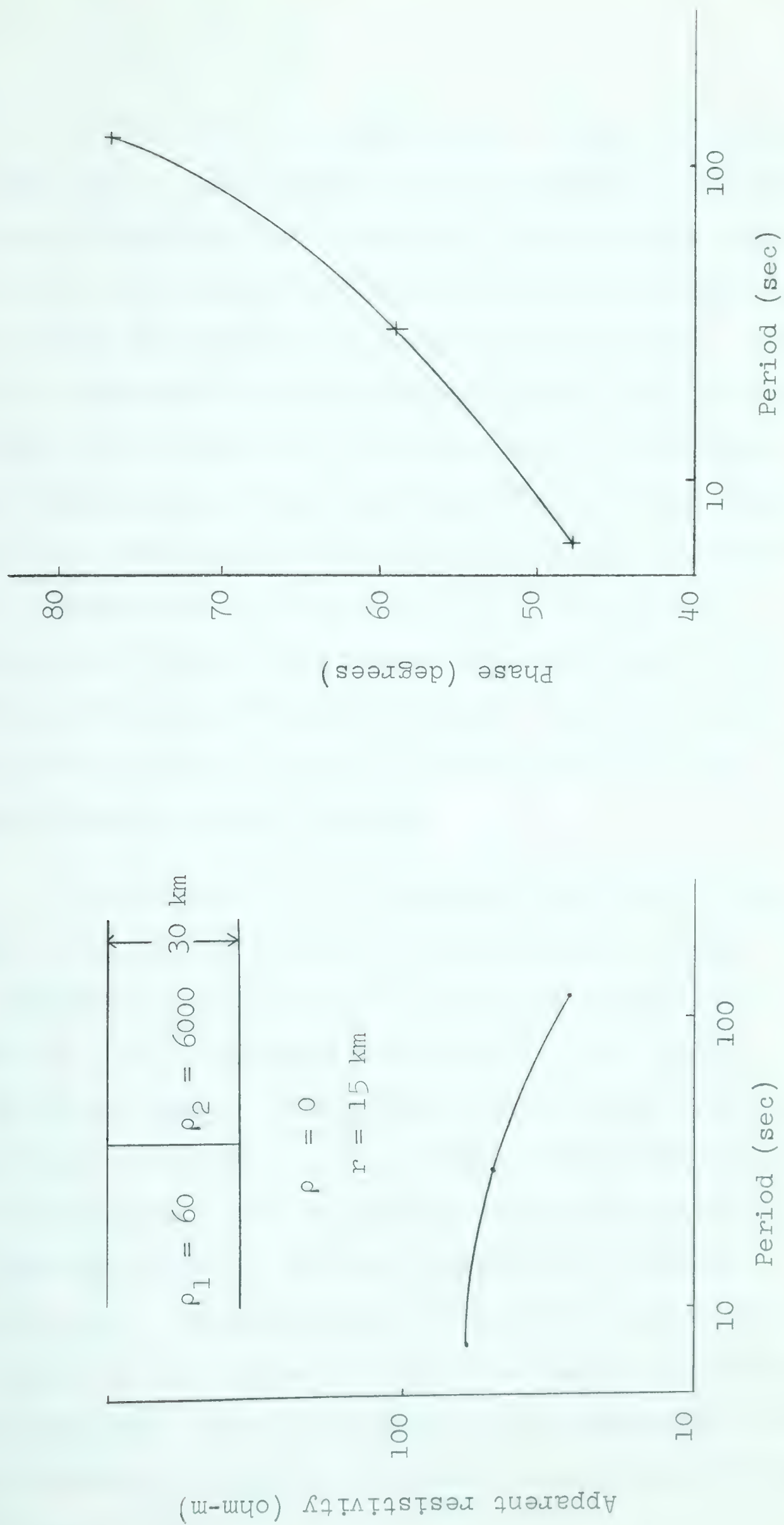


Figure 26. Theoretical curves for fault with conductive basement (E perpendicular to strike) with parameters adjusted to fit Montreal Lake data.

In the above interpretation, source effects have been neglected. Calculations for a homogeneous half-space show that deviations from Cagniard's theory would be unimportant for the conductivities and frequencies under consideration unless the sources are comparable to dipoles. However for this complicated geologic situation and high geomagnetic latitude where sources may be particularly complicated, these effects may play an important role at longer periods. It is hoped that by averaging spectra over all records that these effects might be "smoothed out." Theoretical calculations (Price, 1962; Quon, 1963) show that it is unlikely that the differences at high frequencies could result from sources. Further attention will be given to these problems in later sections.

In contrast to the Montreal Lake results, the Vulcan curves may be fitted by a simple layered model. The experimental and theoretical apparent resistivity curves for H_x-E_y are shown in Figure 27. The H_y-E_x curves are the same. Sedimentary resistivities were calculated using logs from nearby wells. Using these values for the sediments, the theoretical curves were fitted to the observed curves by choosing appropriate basement resistivities. The thickness of the 5 ohm-m layer which was present at the bottom of the holes has been adjusted to give a good fit. This interpretation is basically a three-layer conductive-resistive-conductive situation with boundaries at 3.70 and 35 km.

Theoretical Model	
9.9 ohm-m	1.01 km
15.0	2.31
200.0	3.60
P.C.	5.0
	1000
	30
	3.70
	35

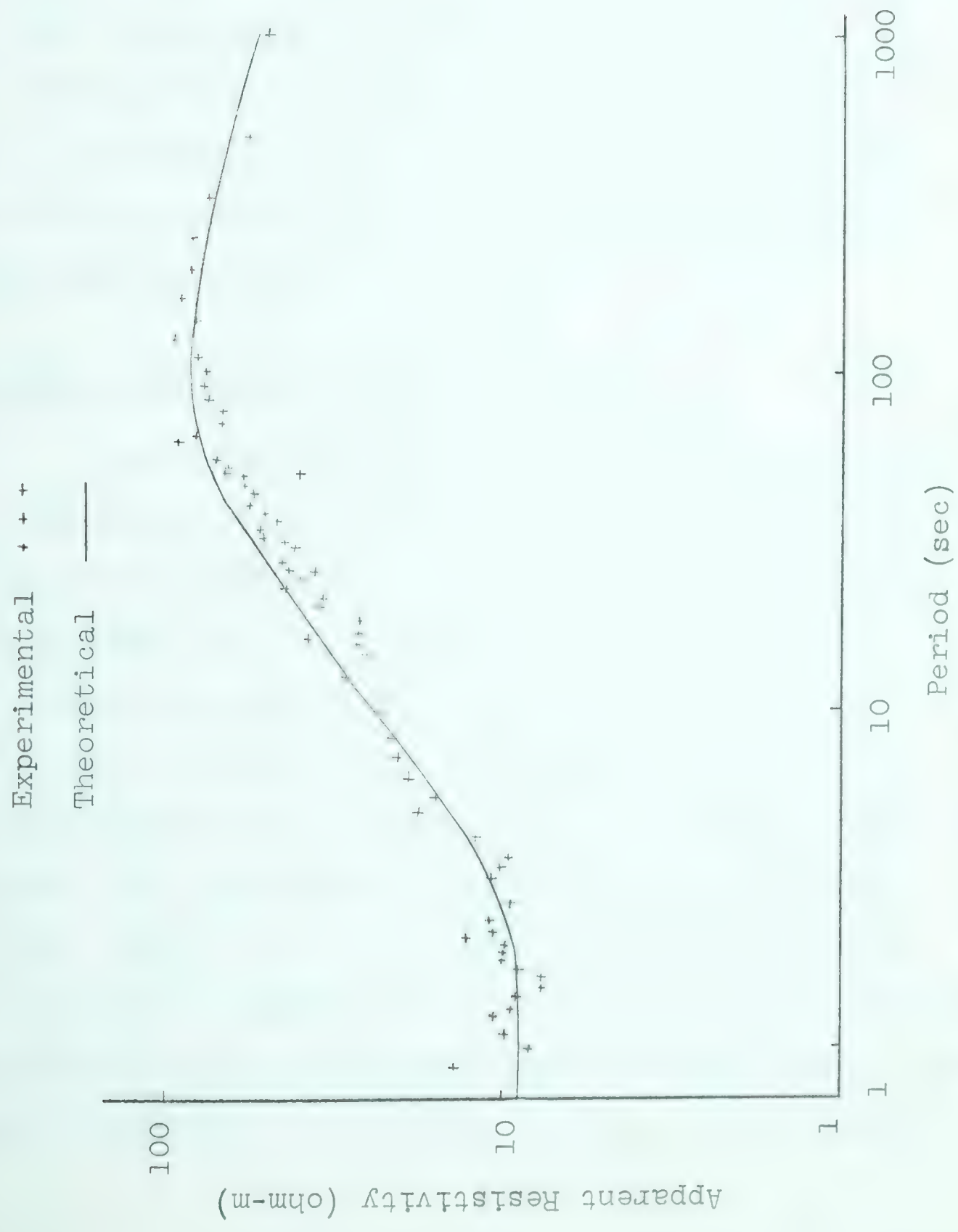


Figure 27. Apparent resistivity curves — Vulcan 2-4 ($H_x - E_y$).

Since only two-layer phase curves are available, a detailed interpretation using phase could not be made. However, the curves (Figure 28) show the essential features of a three-layer conductive-resistive-conductive model. Using a two-layer approximation for the upper layers, it is found that $\rho_2/\rho_1 \approx 50$. For an effective $\rho_1 = 17.7$ ohm-m, then $\rho_2 \approx 885$ ohm-m and $h_1 \approx 3.6$ km which agrees quite well with the apparent resistivity curves. Since the third layer would affect the resistivity ratio, it is expected that ρ_2 is somewhat larger. Using phase little can be said about ρ_3 except that the contrast would not appear to be nearly as large.

Roughness of Apparent Resistivity Curves

Even after decimation on the basis of coherency and elimination of those points where coherent noise sources are important, deviations in the apparent resistivity as large as 100% occur. A second criterion which may be used to eliminate points is the ratio of energy in the vertical and horizontal magnetic components. For plane wave sources and the frequency range of interest, Dosso (1962) has shown for a homogeneous half-space that the maximum value of $|Z/H| \approx .01$. In complex geologic situations $|Z/H|$ may become appreciable. For a vertical fault with a resistivity contrast across the fault of 1000, Weaver (1963) suggests that close to the fault $|Z/H|$ may exceed unity.

Quon (1963) shows that for a horizontal magnetic dipole over a layered earth Z may become larger than H at long periods. In this case the apparent resistivity is much less than the true resistivity. Therefore vertical-horizontal energy ratios which are larger than normal may either indicate a particular polarization of the wave for which the geology causes a large H_z or a source of small dimensions. In both cases deviations from smooth apparent resistivities can be expected.

In a general way it seems possible to explain rough apparent resistivity curves using coherency and vertical-horizontal energy ratios. However, in detail, the problem is more complex. To illustrate this, the apparent resistivity and coherency-squared for one set of orthogonal components and the vertical-horizontal energy ratio have been plotted for two record sections (Figures 29 and 30). In addition a smoothed apparent resistivity curve using all Montreal Lake records of this component has been plotted for comparison.

The characteristics of the Montreal Lake 2-1 H_y-E_x components (Figure 29) are rather typical of the records taken at this location -- the coherency-squared remains between 0.8 and 1.0 except for several frequencies where it drops to smaller values and the vertical energy is 10 to 15 percent of the horizontal except for one or two frequencies

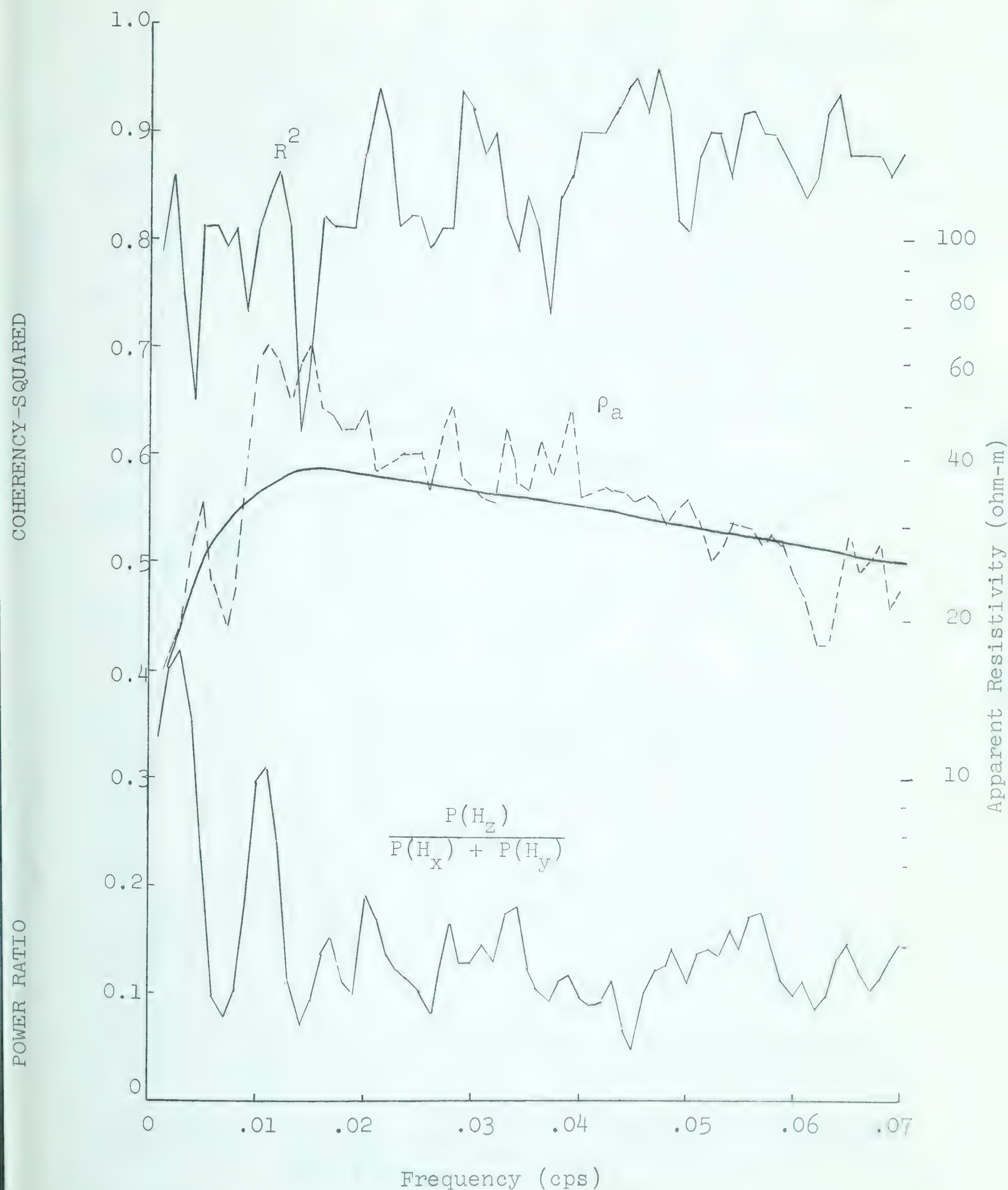


Figure 29. Apparent resistivity and coherency-squared for H_y-E_x and vertical-horizontal power ratio - Montreal Lake 2-1.

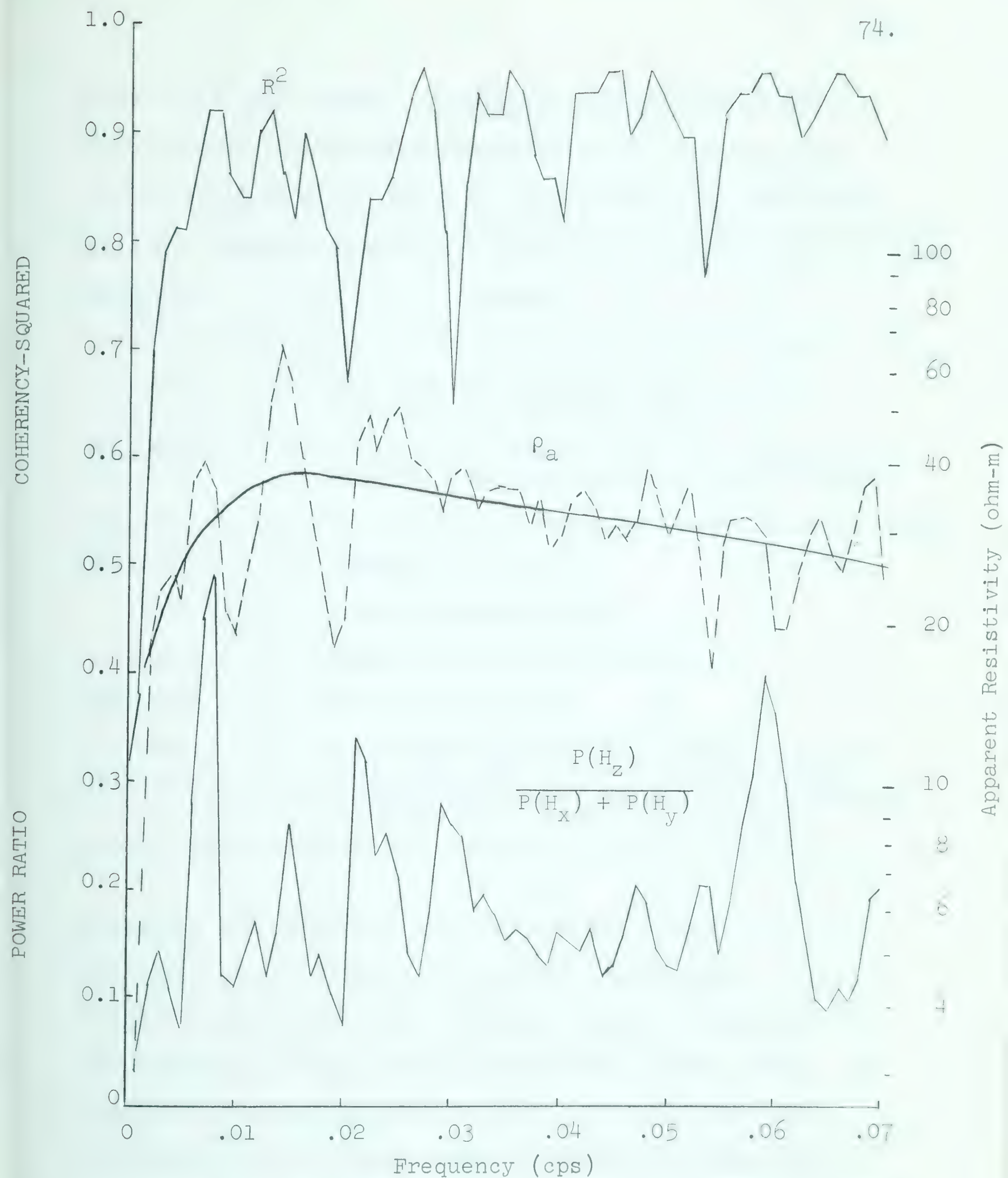


Figure 30. Apparent resistivity and coherency-squared for H_y - E_x and vertical-horizontal power ratio — Montreal^x Lake 5.

where it is much larger. A detailed examination of the deviations of the apparent resistivity from the smoothed mean curve is given in Table 6. It is seen that the maximum

Table 6. Apparent Resistivity Deviations-Montreal Lake 2-1 H_y-E_x

Frequency (cps)	Remarks
.005	The vertical energy is large and at $f = .004$ the coherency is low.
.006-.008	Using the criterion that $R \times R$ should be greater than 0.8, the coherency is marginal
.010-.012	The vertical-horizontal energy ratio is large.
.014-.015	Coherency is low.
.020	Peak in energy ratio.
.028	Small peak in energy ratio.
.033-.034	$R \times R$ is marginal.
.039 .061-.064	No obvious relationship between the large deviation, and either the coherency or vertical-horizontal energy ratio. Coherent noise does not seem to be important.

deviations are sometimes shifted from the minima of $R \times R$ and maxima of the vertical-horizontal energy ratio. Also in the two cases where the deviation cannot be explained by low coherency or high vertical-horizontal energy ratios, the coherency is changing quite rapidly. It would seem that the windows are not sharp enough to handle the spectral changes. However examination of the raw spectra indicates that error from this source should be small. It is also seen that large deviations may occur in regions where the coherency-squared is slightly larger than 0.8. This

confirms the results of Appendix C which indicates that a coherency-squared greater than 0.8 is desirable.

Tape Montreal Lake 5 has very large vertical-horizontal energy ratios (Figure 30). With one exception the apparent resistivity deviations are highly correlated with fluctuations in coherency and the vertical-horizontal energy ratio. At $f = .009$ to $.011$ cps only a small dip in coherency accompanies the low apparent resistivity. Again this coherency-squared is less than 0.9.

Further Analysis of H_z and Source Effects at Montreal Lake

The large vertical-horizontal power ratios of the magnetic field at Montreal Lake (Figure 31) compared to those in southern Alberta (Figure 32) have led to further study of H_z and its relationship to geology and sources. Except where otherwise indicated, the following discussion is limited to the frequency range 0.001 to 0.070 cps.

In interpreting H_z at Montreal Lake, the following experimental evidence is considered.

- (1) The H_x and H_y spectra may be quite different in character at both Montreal Lake and Vulcan (Figure 33).
- (2) The H_y - H_z coherency is quite high. Further, it is generally much larger than the H_x - H_z coherency (Figure 34).
- (3) The E_x - H_z coherency is larger than the H_y - H_z coherency (Figure 35).

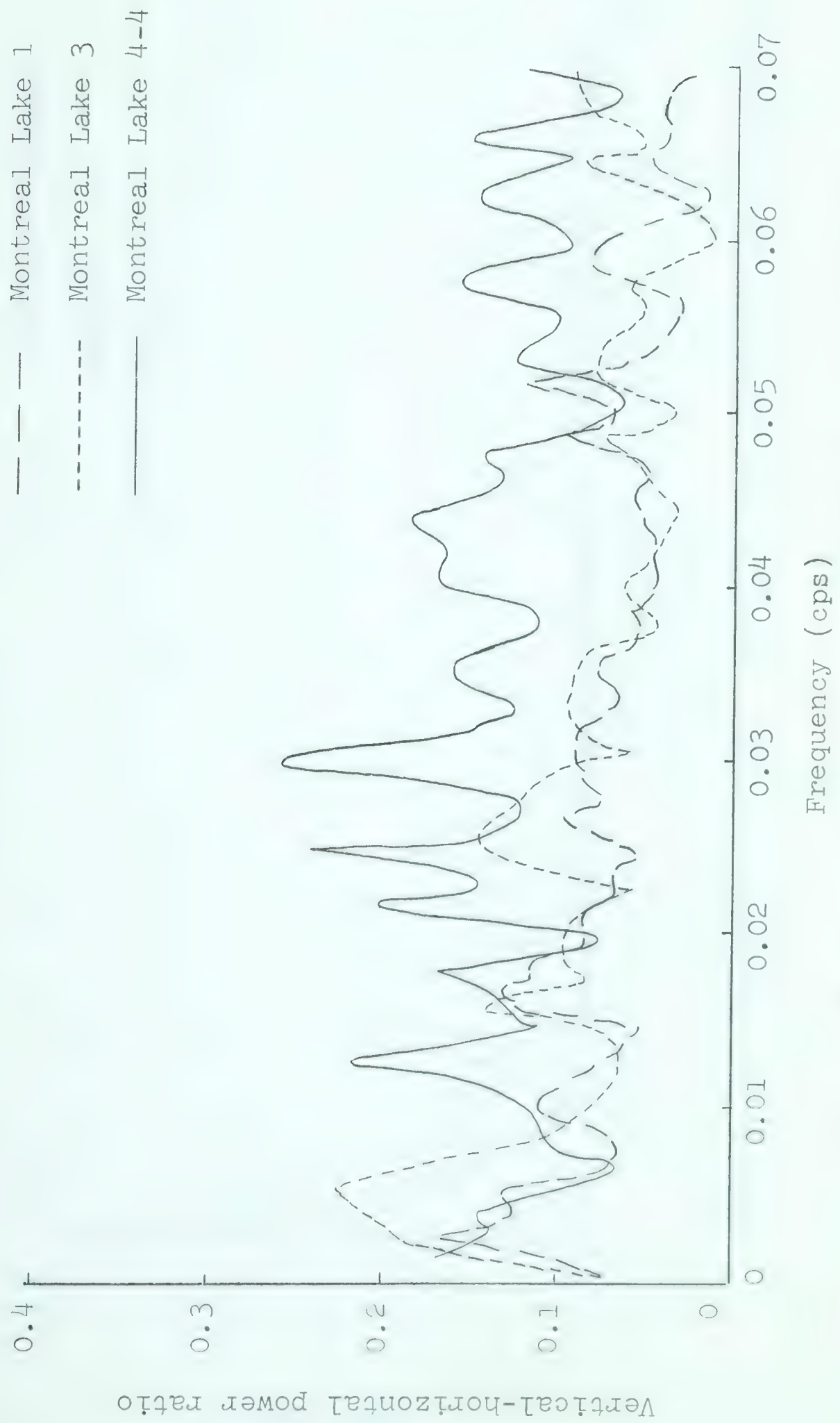


Figure 31. Vertical-horizontal power ratios at Montreal Lake.



Figure 32. Vertical-horizontal magnetic power ratios at southern Alberta stations.

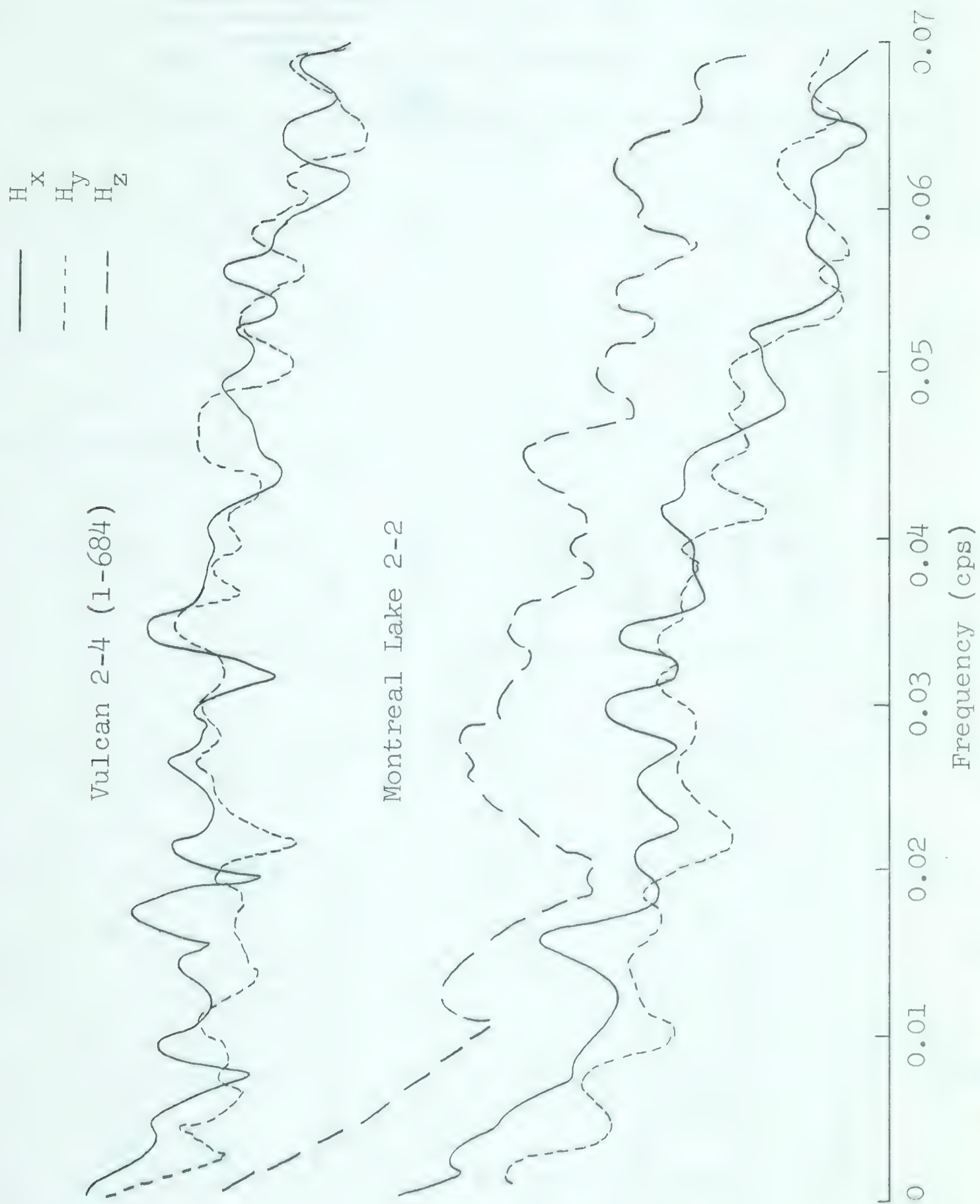


Figure 33. Plots of orthogonal spectra for Vulcan 2-4 and Montreal Lake 2-2.

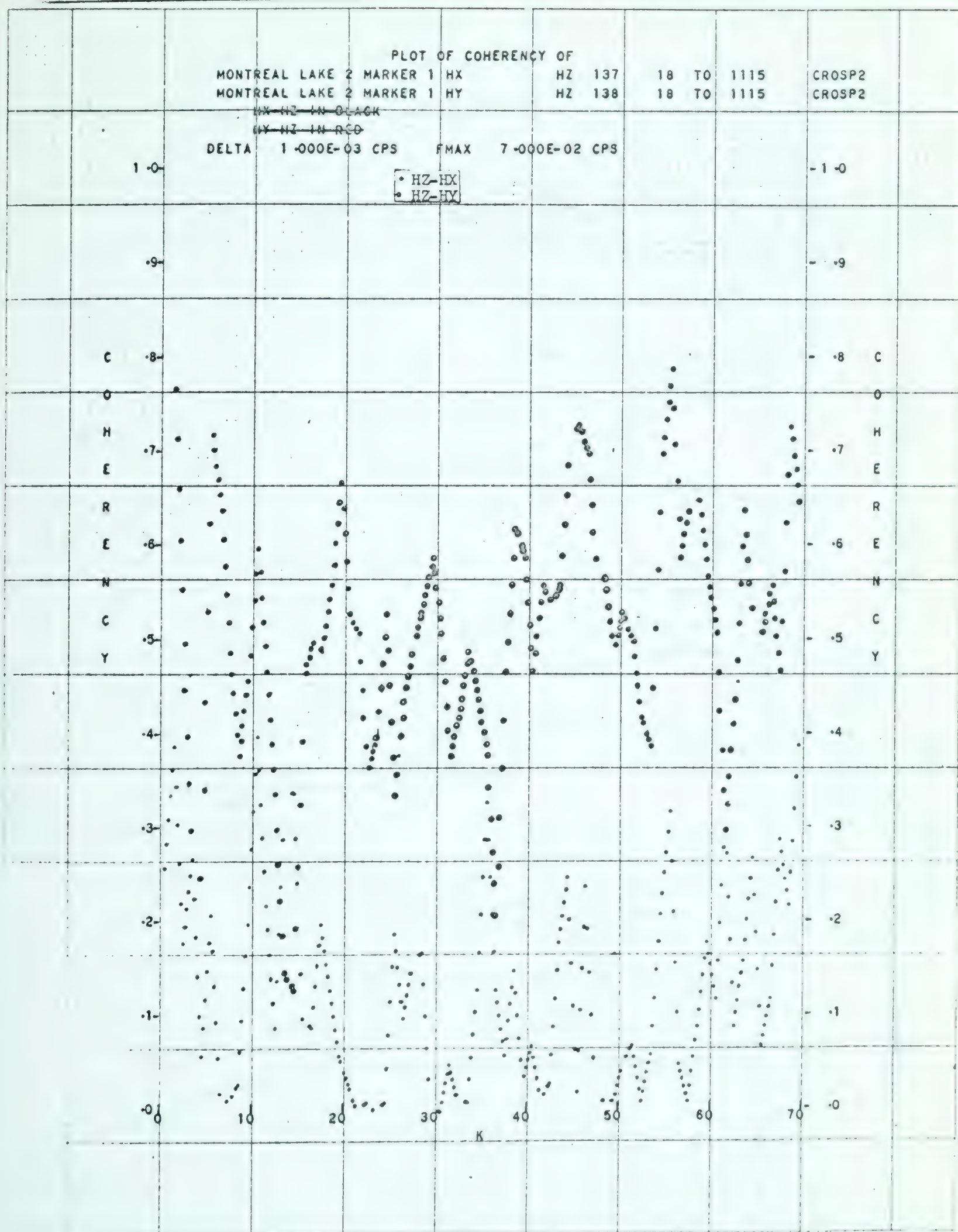


Diagram 33

Figure 34. Illustration of high H_y-H_z coherency compared to H_x-H_z coherency.

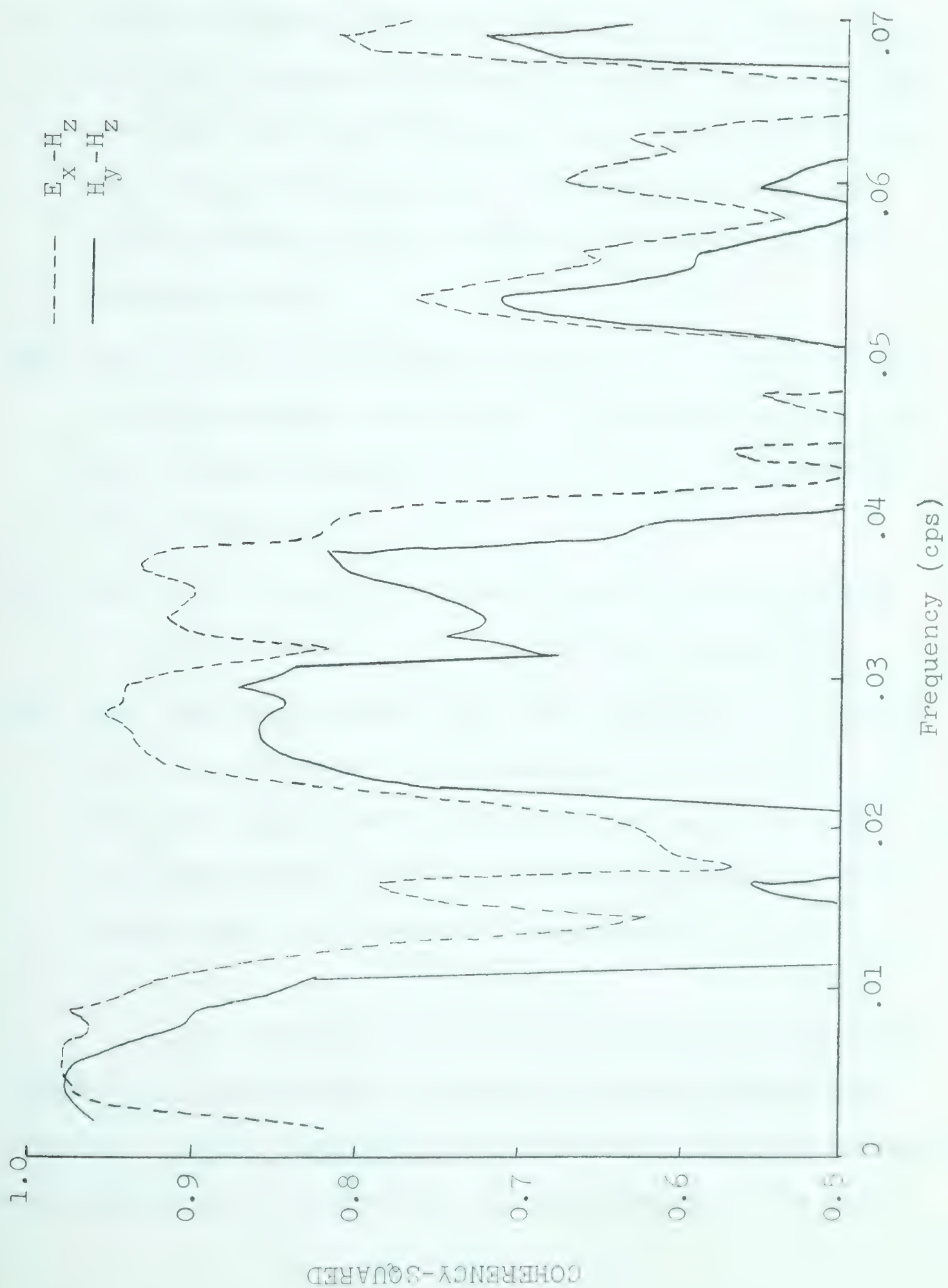


Figure 35. Coherency-squared for E_x-H_z and H_y-H_z ---
Montreal Lake 3.

- (4) The H_y spectrum is flatter than the H_x spectrum. In slope, the H_z spectrum is closest to H_x (Figure 33).
- (5) Figure 36 shows the power ratio H_z/H_y in cases where the H_y - H_z coherency-squared is greater than 0.6. For Montreal Lake 1 and Montreal Lake 3 the plots follow the same general pattern. The Montreal Lake 4-4 ratios decrease with increasing frequency but are somewhat higher.
- (6) Where the H_y - H_z coherency is low, the H_x - H_z coherency often increases (Figure 37). In this situation the H_z/H_y power ratio may fluctuate over a rather wide range (Figure 38).
- (7) Both E_x - H_z and H_y - H_z phases change through 180° in the period range $T = 2$ to 1000 sec (Figure 39).
- (8) For individual events the vertical-horizontal power ratio may be much larger than unity (Figure 40). For the event marked with an arrow, the ratio is 1.8. For the first event in the wave train, H_z is also much larger than the horizontal components.

In a previous section the apparent resistivity curves were interpreted in terms of geology rather than sources. On the basis of the theoretical information available, the data may be interpreted as indicating that the field

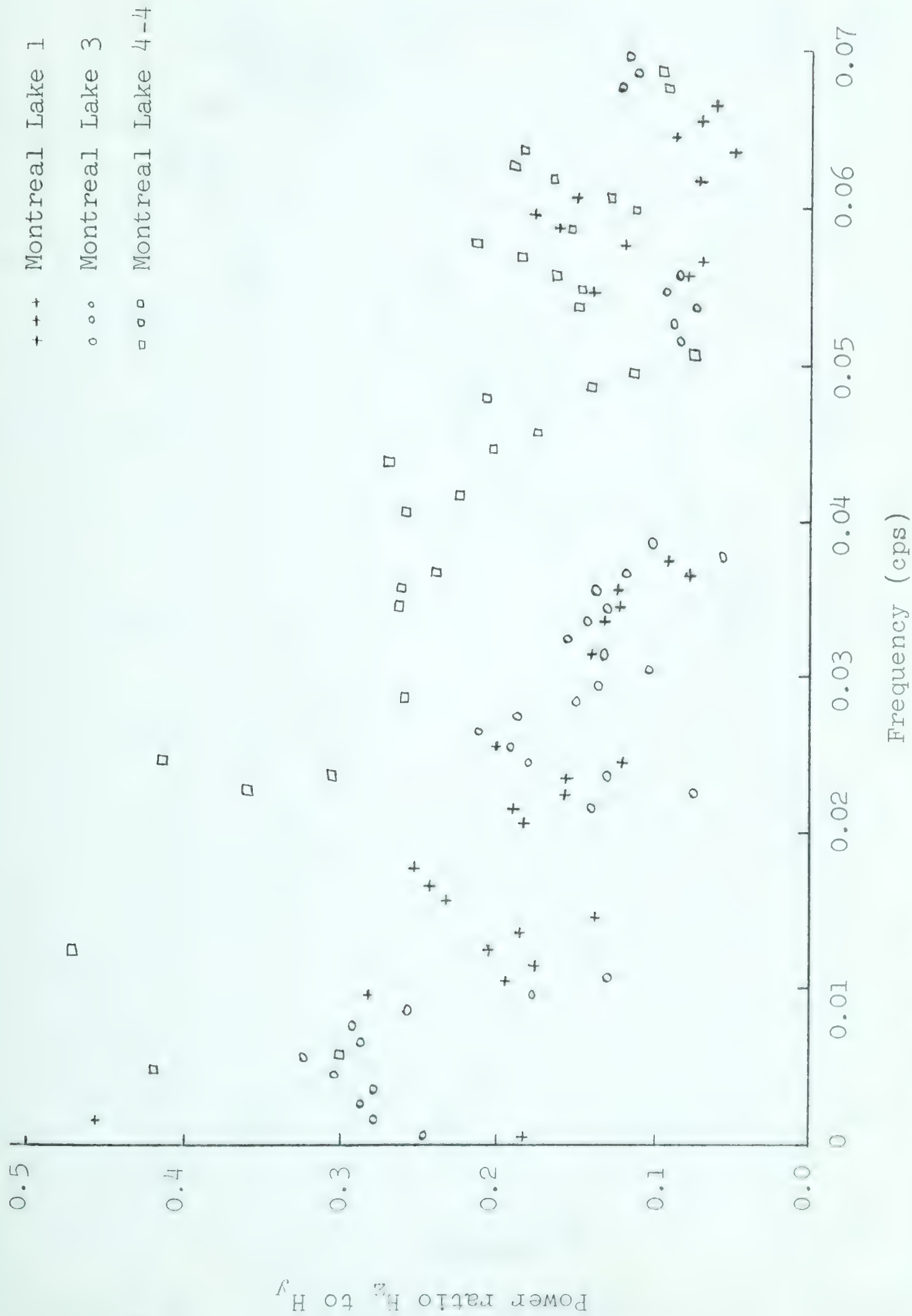


Figure 36. Power ratio H_z to H_y for coherency-squared greater than 0.6 .

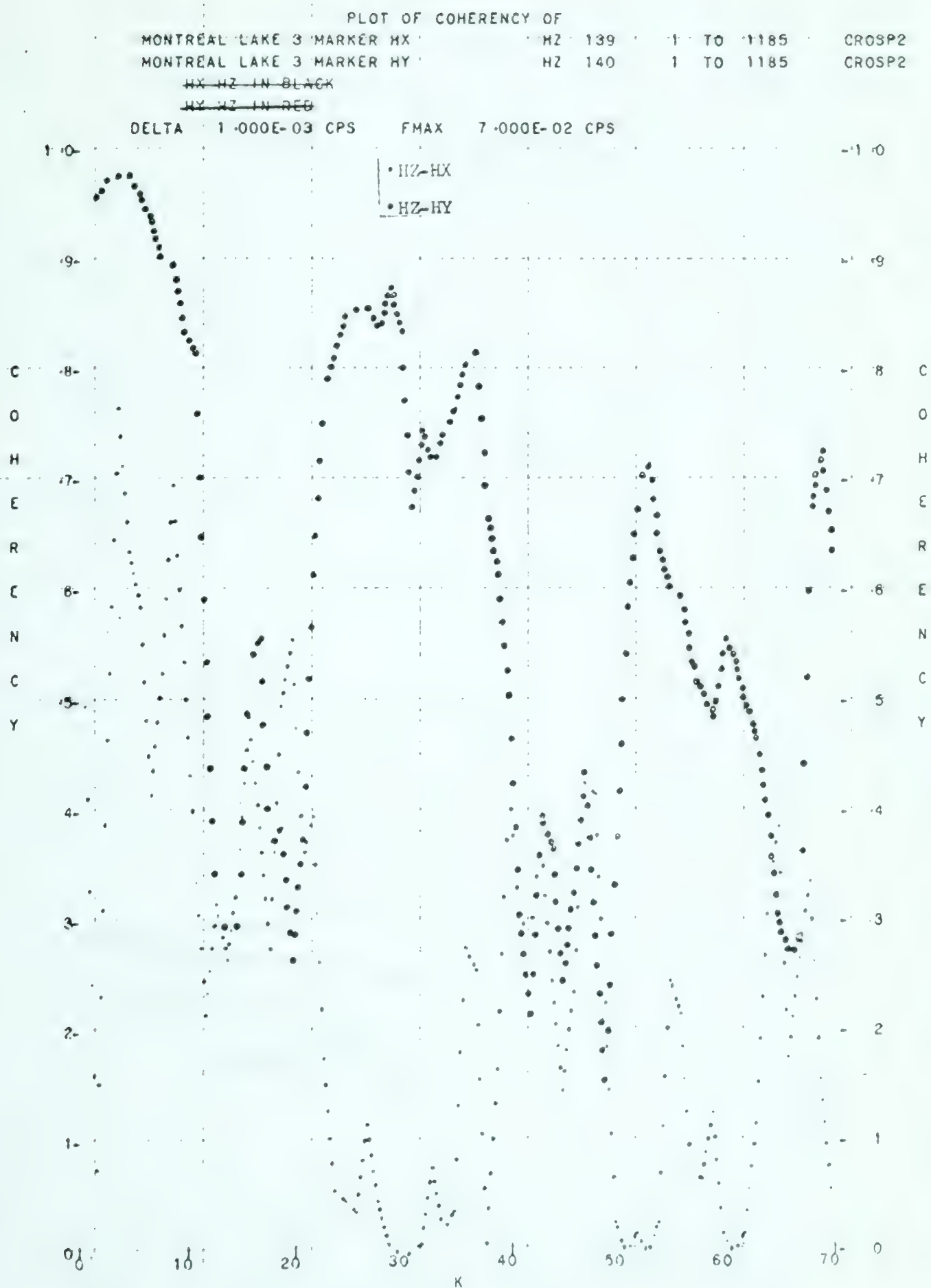


Diagram 55

Figure 37. Illustration of increase in H_X-H_Z coherency with decrease in H_Y-H_Z coherency.

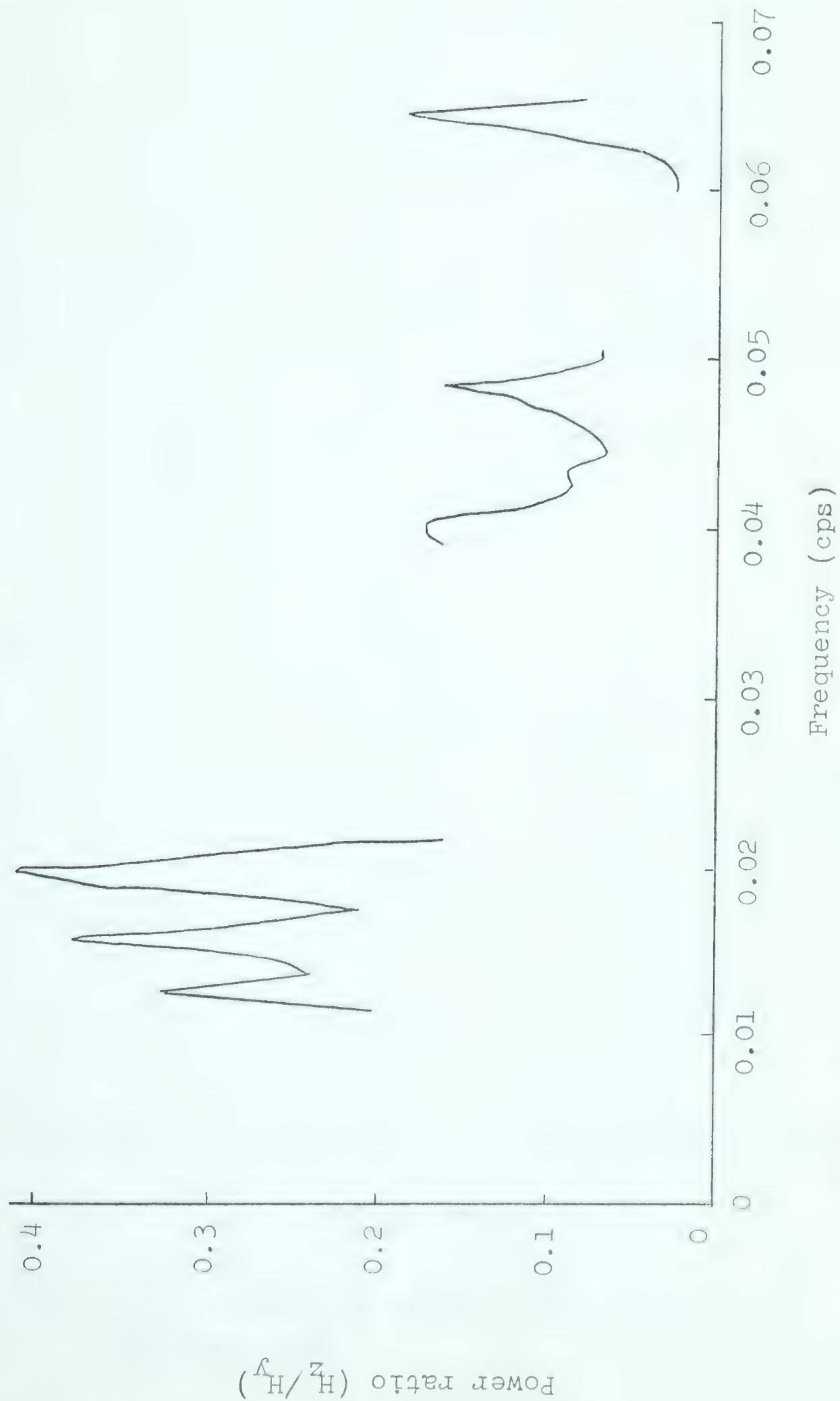


Figure 38. Power ratio H_z/H_y for coherency-squared less than 0.6 .

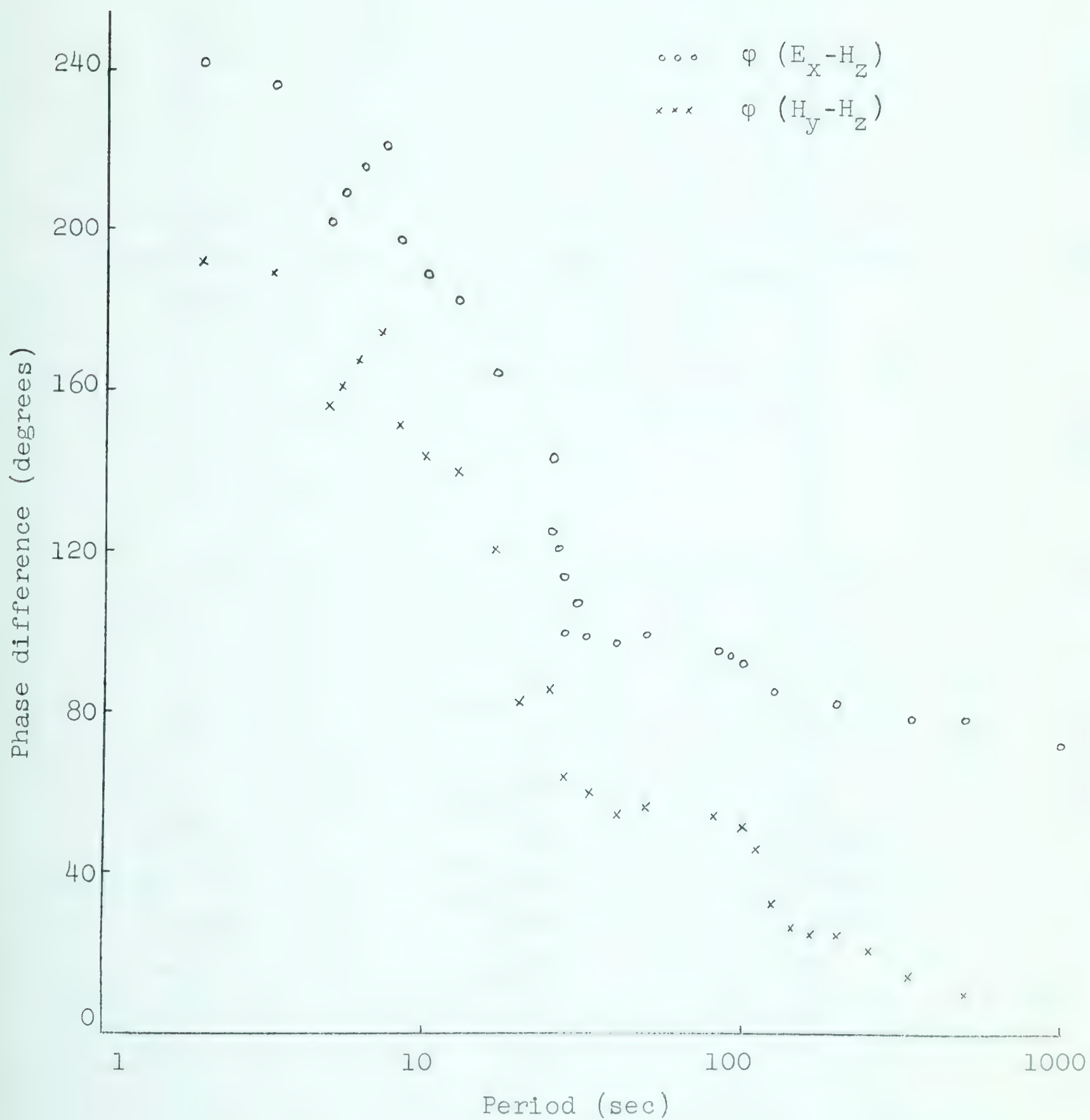


Figure 39. $E_x - H_z$ and $H_y - H_z$ phase differences at Montreal Lake.



Figure 40. Section from Montreal Lake 2 showing three magnetic components. (Scale in gammas for 100 sec period).

station is on the conductive side of a vertical fault striking in the x-direction with a more conductive basement at a depth of 10 to 25 km. A large H_z , associated with the horizontal gradient of current density component parallel to the fault, may be expected. However Rokityanskiĭ (1963) suggests, that in the case of the sea-land boundary, a large H_z should only be observed on the resistive side of the boundary. This does not agree too well with the calculations of Weaver (1963). On the basis of the above observations an attempt is made to gain further understanding of the geologic situation and to determine whether source effects also contribute to H_z .

At Vulcan the orthogonal apparent resistivities are the same and are quite smooth. In this location, it appears that the difference in spectral character is due to directional properties of the source. At Montreal Lake the geology is more complex. Assuming the source can have directional properties similar to those at Vulcan, the differences in spectra are likely due to geology as well as to directional sources.

Since H_z near a two-dimensional structure is due to the horizontal gradient of current density parallel to the structure, and the current density is linearly related to H_z , then a high H_y - H_z coherence is to be expected. Alternatively, if the H_y field were due to a source approximating

a line current in the x-direction, and if H_x were due to a source of somewhat larger dimensions, then a high H_y-H_z coherency compared to the H_x-H_z coherency is to be expected.

The fact that the E_x-H_z coherency is larger than the H_y-H_z coherency shows that H_z is more closely related to the currents than to H_y . This indicates that the differences arise due to differences in current density (geological) rather than to non-plane wave sources. An alternative explanation is that the noise level is higher in the H_y system than it is in the E_x system. However, at higher frequencies, the spectra show that the electric noise level is actually the higher.

Since the spectra of H_x and H_y both have the same slope at the southern Alberta stations, for purposes of discussion it is assumed that they would also have the same slope at Montreal Lake were it not for the more complex geology or a finite-sized source. Although the calculations of Weaver (1963) for \underline{E} tangential to the fault are not in the same frequency range, they indicate that the H_z/H_y ratio should increase with increasing period. Quon (1963) shows that for dipole sources, $|Z/H|$ should increase by almost an order of magnitude between $T = 100$ and 1000 sec. For a rather broad north-south current, this change would be less. In both cases, an increase in H_z will be reflected by a decrease in H_y .

It has been found that the first four observations can be explained on the basis of a two-dimensional structure with strike in the x-direction. In this situation, where the H_y - H_z coherencies are high, the H_z/H_y ratio as a function of frequency should be the same on all records. Looking only at Montreal Lake 1 and Montreal Lake 3 (Figure 36), the data might be interpreted in this way. However the data from Montreal Lake 4-4 show that the relationships are not this simple. The ratios from Montreal Lake 5 are even higher although they again show a decrease with increasing frequency. These observations are probably complicated by the measuring axes being not exactly parallel and perpendicular to strike. Nevertheless, it appears that either inhomogeneities are present for which H_z depends on the directional properties of the source or that H_z changes in time due to a changing source.

In cases where the H_y - H_z coherency is low and thus little relation exists between them, the H_z/H_y ratio should be expected to fluctuate considerably. Decreases in H_y - H_z coherency are sometimes accompanied by smaller decreases in H_y - E_x coherency (Figure 41). This indicates that the signal at this frequency may be rather close to the noise level. What H_z is present may be largely due to inhomogeneities which affect the E_y currents. In this situation, the H_y - H_z coherency will be the most sensitive to decreases in H_y . This would also explain the increase in the H_x - H_z

$H_y - E_x$

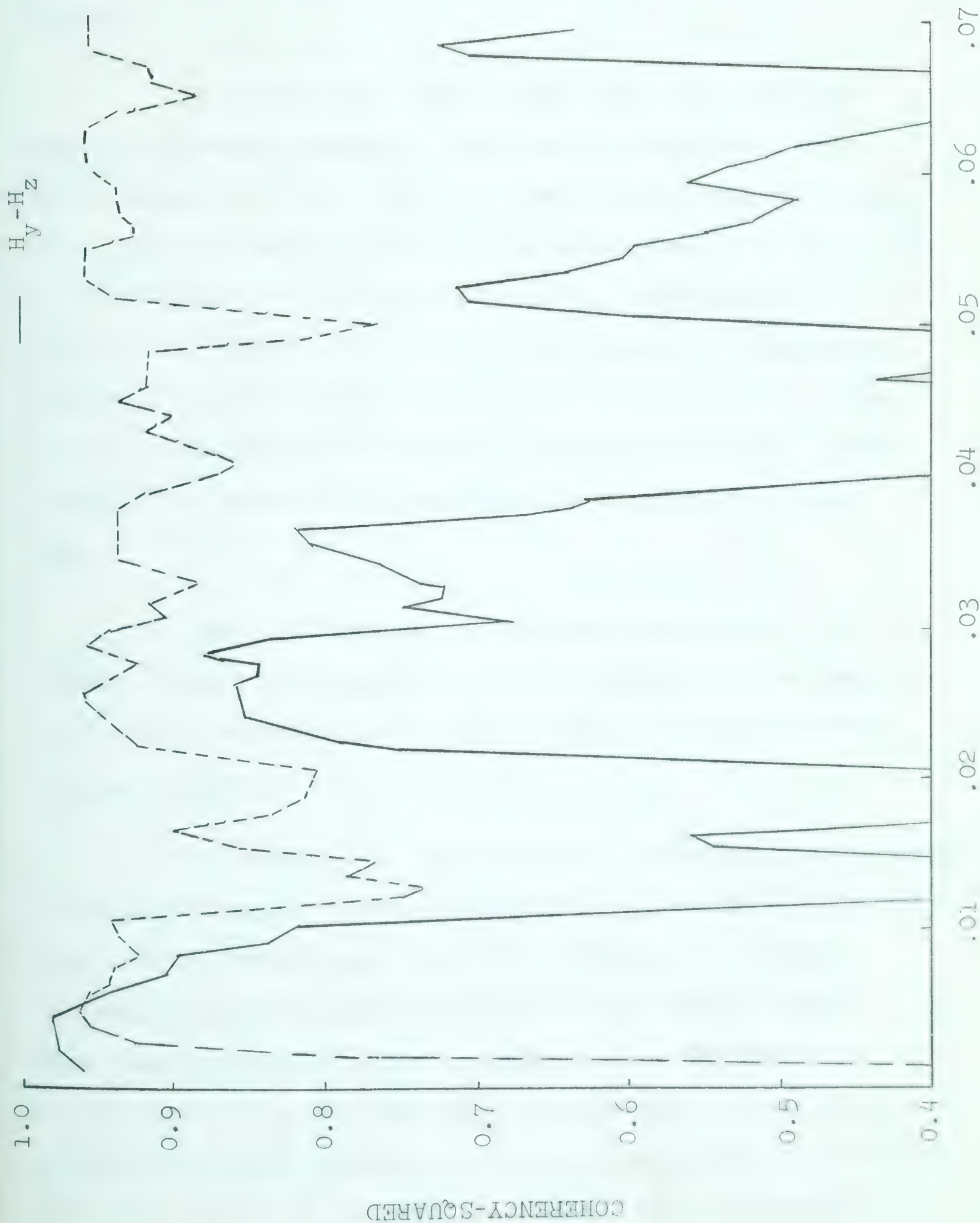


Figure 41. $H_y - E_x$ and $H_y - H_z$ coherency squared - Montreal Lake 3.

coherency. It also appears that this can be explained by an H_x source of small dimensions but larger than the H_y source.

No theoretical results are available for the phase difference between H_z and other components of the electromagnetic field close to a two-dimensional structure. Quon (1963) shows that for a two-layered earth ($\rho_1 = 5$ ohm-m, $\rho_2 = 500$ ohm-m, $h = 5$ km) that $\phi (E-H_z)$ decreases from 226° at $T = 1$ sec to 93° at $T = 1000$ sec for a horizontal dipole. However $\phi (H-H_z)$ only changes through 45° . None of the other dipoles considered provides sufficient phase change. It seems that a geological explanation is most likely.

When the vertical-horizontal power ratios for several events on a record are much larger than the ratio for the entire record, the large ratios for these events are most likely due to sources.

In summary, it seems that all observations involving a length of record can be explained on a geologic basis but that source effects are required to explain the large vertical-horizontal power ratios for individual events. Most observations may also be explained on the basis of sources but it is unlikely that sources can be used to explain the large changes in $\phi (E_x-H_z)$ and $\phi (H_y-H_z)$ or the fact that the E_x-H_z coherency is larger than the H_y-H_z

coherency. It may be that over a length of record, geological effects predominate; but source effects are important for individual events. Clearly, source problems could be better studied in a simpler geologic setting.

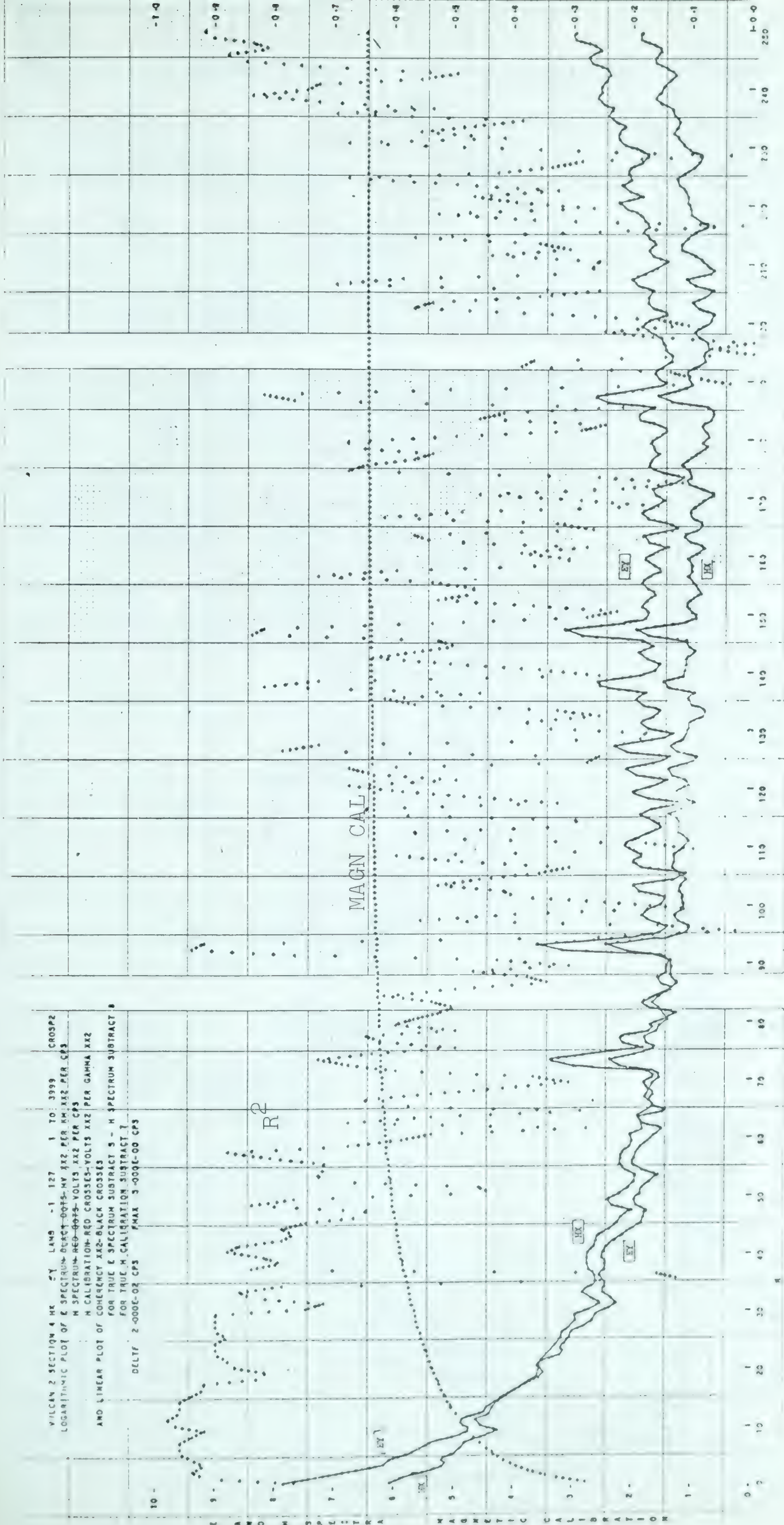
K_p -Spectral Relationships

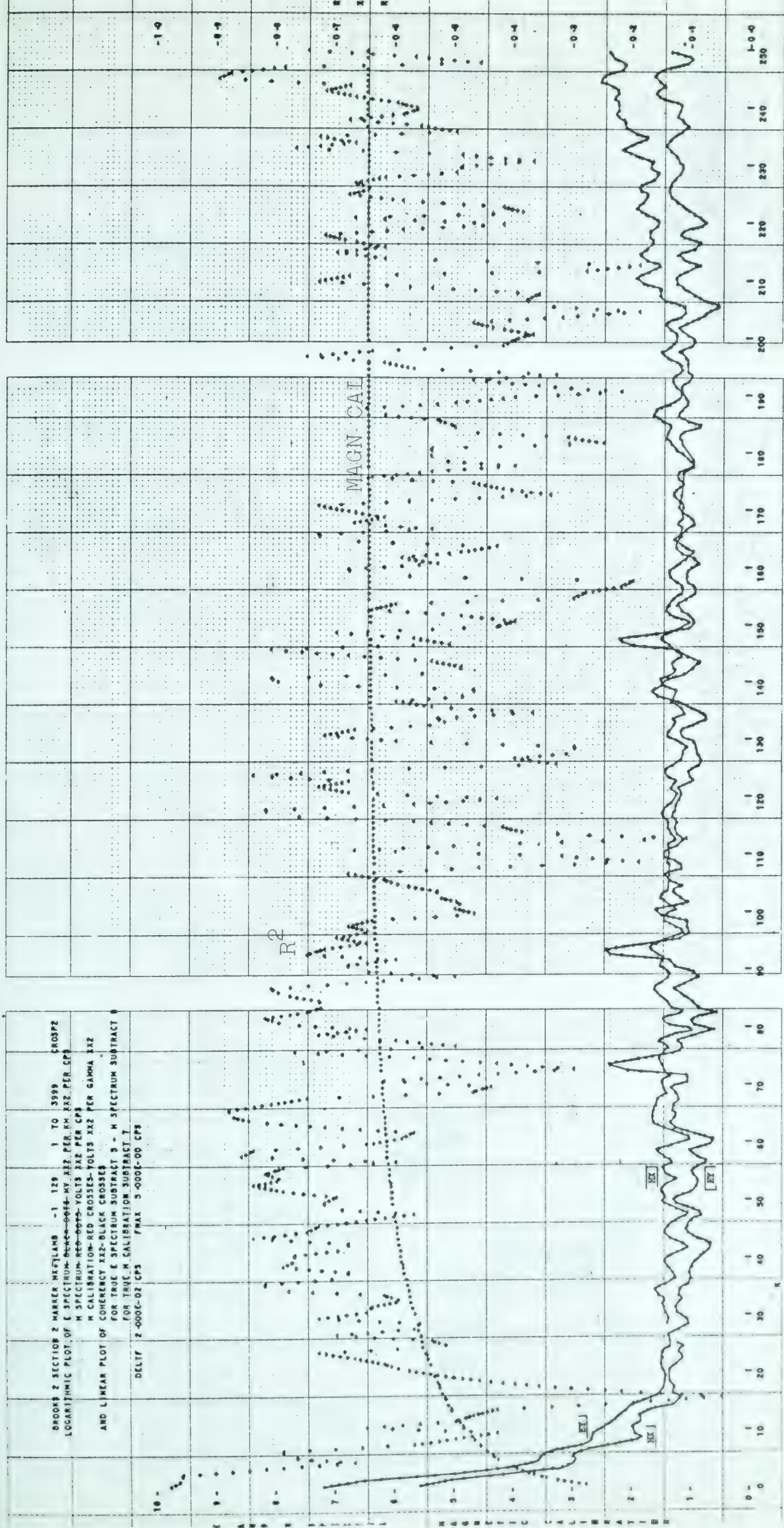
Table 2 shows that the K_p during the recording period at Montreal Lake were of moderate to moderately large values. The Montreal Lake records may be conveniently divided into 2 groups - those for which $K_p = 3+$ or less, those for which $K_p = 4+$. For the records with lower K_p the energy falls off quite rapidly up to $f = 0.14$ cps and then decreases very slowly over the frequency range to 5 cps (Figure 23). The spectra of records with the larger K_p decrease much less rapidly to about 0.75 cps but to a lower energy level (Figure 17). Thus it appears that for large K_p there is a shift of energy to longer periods. The one exception to this picture is Montreal Lake 4-4 ($K_p = 3+$) where the spectra has the appearance of those with high K_p . However for the periods on either side of the recording interval $K_p = 4+$. It should also be remembered that K_p is a world-wide index.

The three high frequency spectra which were calculated for southern Alberta field stations do not show such a simple relationship. Vulcan 2-4 ($K_p = 50$) conforms

to the above analysis by dropping off quite slowly (Figure 42). However the spectra from Brooks 2-2 ($K_p = 4+$) fall off very rapidly (Figure 43) while the spectra for Beiseker 1-2 ($K_p = 40$) are quite different in shape with a broad spectral peak in the 3 to 5 sec period range (Figure 44).

Clearly more data are required to determine whether a relationship between K_p and spectra as indicated by the 8 Montreal Lake records exists. Further, it does not appear that there is any direct relationship between K_p and the total energy in this frequency range.





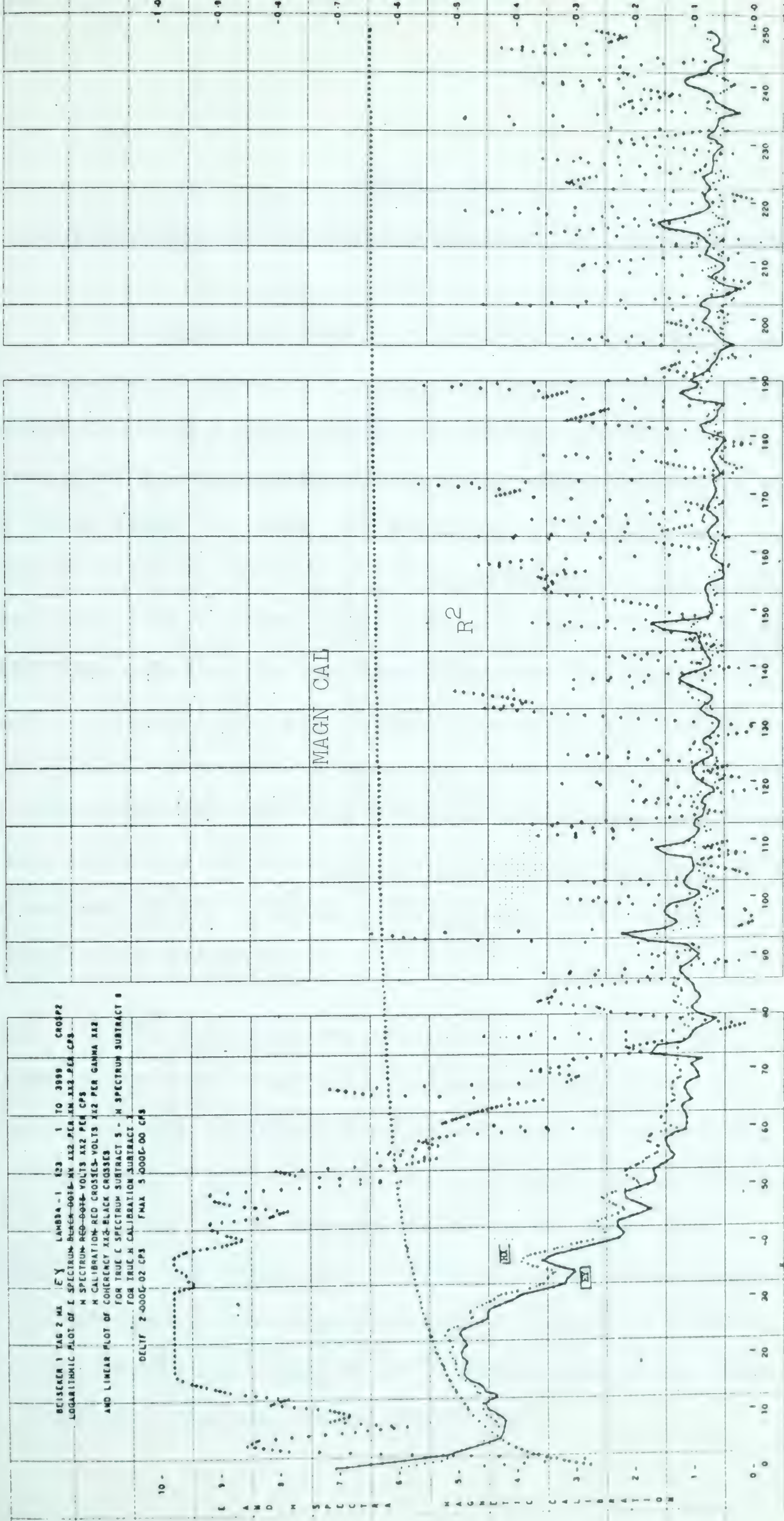


Diagram 97

FIGURE 44.

Chapter IV

SUGGESTIONS FOR ANALYSIS PROCEDURES AND FURTHER WORK

It has been shown that marked improvements can be obtained in spectral quality and apparent resistivity values by using a very simple prewhitening filter. It is clear that in some cases further improvement could be made by using other filters. An ideal way to handle this problem would be to have the analysis program calculate the spectrum using unprewhitened data and fit a filter to this spectrum. It should then prewhiten the time series, calculate its spectrum, and finally calculate the spectrum of the original time series using the power transfer function. In cross-spectral analysis the calculated phase shift will also have to be adjusted by the difference in phase shifts introduced by the filters. With a high speed computer, this procedure is feasible.

The coherency as determined by the Daniell estimate has been found to be more meaningful than that of hanning but the computational noise level is rather high. It is suspected that this is not a property of the Daniell window but due to the approximation techniques used in CROSP2 . If the noise can be reduced, some prewhitening can be avoided. (The speed advantage gained by rounding the data before calculating the correlations is as large as 15 and so this may not be practical).

All data channels should be digitized simultaneously. This would minimize the human errors in the conversion procedure and allow the computation of phase and coherency between all channels with only one conversion per channel. The methods of Cantwell (1960) for analyzing anisotropies and inhomogenieties could then be applied. It would also be preferable to sample all channels at the same instant in order that there should be no phase shift between time series. Rotation of the time series to find the major axes would then be practical. Bostick and Smith (1962) found that this technique yields better results at the Austin station than the procedures suggested by Cantwell (1960).

The trial and error method of fitting Cagniard curves in multilayer cases is time consuming. Moreover one is uncertain whether a better fit could be obtained. An analysis for automatic curve fitting should be made and programmed for the computer. To allow several layers for known resistivities of the sediments and a three-layer basement, a 5- or 6- layer scheme is required.

Effort should be made to extend the present theory for two-dimensional structures to include the case of magnetic polarization and a basement of finite resistivity. More type-curves for the present solutions in terms of apparent resistivities are required, particularly as a

function of frequency. Additional results from model experiments would also be helpful for interpretation.

The Montreal Lake model can only be regarded as a tentative interpretation until geographic coverage is obtained. It will be of interest to determine whether the directional properties are caused by a single large scale discontinuity or by a number of small discontinuities in the direction of the geologic trend. Experience gained in this area where there is some geologic control should be helpful in situations where little geologic or geophysical information is available.

A marked feature of the resistivity interpretations is the variation in crustal resistivity in the 3 areas. In central Alberta the basement resistivity is about 1000 ohm-m with no evidence of a decrease with depth while at Vulcan it is found that the resistivity decreases to about 30 ohm-m at a depth of 35 km. In central Saskatchewan the near surface basement resistivity is in the range 30 to 60 ohm-m with a further decrease in the 10 to 25 km range. Magnetotelluric techniques are now well enough developed that mapping could be carried out to determine whether these changes are associated with discontinuities or are gradual.

In most geologic situations the resolution of the magnetotelluric method is insufficient to give any detail of the sedimentary resistivities since the product of conductivity and thickness of the layers must be large to influence the curves. As a tool for investigation of the upper mantle, two problems arise. With induction coils as magnetic detectors, locations must be found where the effective resistivity of the sediments and crust are high in order that the mantle can be detected with periods of 1000 sec or less. Secondly, source effects may become important at these long periods. The magnetotelluric method is most useful in measuring crustal resistivities. A large scale program which should be considered is the mapping of crustal resistivities over wide areas. This would not only add to our knowledge of the crust, but also determine locations where the mantle can be effectively probed using the magnetotelluric method.

References

- Barlow, W. H., On the spontaneous electric currents observed in the wires of the electric telegraph, Phil. Trans., 139, 61-72, 1849.
- Bennett, W. H., and E. O. Hulbert, Theory of the aurora based on the magnetic self-focusing of solar ion streams, Phys. Rev., 95, 315-319, 1954.
- Berdichevskii^Y, M. N., Electric Prospecting by the Telluric Current Method, Gostoptekhizdot, Moscow, 1960.
- Berdichevskii^Y, M. N., The magnetotelluric field in a horizontally inhomogeneous medium, Applied (Prikl.) Geophysics, No. 31, 1961.
- Blackman, R. B., and J. W. Tukey, The Measurement of Power Spectra, Dover Publications, New York, 1958.
- Bogert, B. P., Hand-digitized seismic data, Vesiac Special Report, Contract SD-78, University of Michigan, 1962.
- Bostick, F. X., Jr., and Smith, H. W., Investigation of large-scale inhomogeneities in the earth by the magnetotelluric method, Proc. IRE, 50, 2339-2346, 1962.
- Bullard, E. C., F. Oglebay, W. H. Munk, and G. Miller, User's Guide to BOMM (Preliminary Version), Cambridge and La Jolla, 1962.
- Cagniard, L., Basic theory of the magnetotelluric method of geophysical prospecting, Geophysics, 18, 605-635, 1953.
- Cagniard, L., Correspondence between J. R. Wait and L. Cagniard, Geophysics, 19, 286-289, 1954.
- Cantwell, T., Detection and analysis of low frequency magnetotelluric signals, Ph. D., thesis, Department of Geology and Geophysics, Massachusetts Institute of Technology, 1960.
- Cumming, G. L., G. D. Garland, and K. Vozoff, Seismological measurements in southern Alberta, 1962, Final Report No. 1 of Vela-Uniform Project 8652, 1962.

- d'Erceville, I., and G. Kunetz, The effect of a fault on the earth's natural electromagnetic field, Geophysics, 27, 651-665, 1962.
- Dosso, H. W., The magnetic field at the surface of a stratified flat conductor in the field of plane waves with applications to geophysics, Can. J. Phys., 40, 1583-1592, 1962.
- Dungey, J. W., Cosmic Electrodynamics, Cambridge University Press, Cambridge, 1958.
- Eaton, J. P., Crustal structure from San Francisco, California, to Eureka, Nevada, from seismic-refraction measurements, J. Geophys. Res., 68, 5789-5806, 1963.
- Ebert, H., Terr. Mag. Atmos. Elect., 12, 1, 1907.
- Eshenhagen, M., On minute, rapid, periodic changes of the earth's magnetism, Terr. Mag. Atmos. Elect., 41, 337-344, 1956.
- Galbraith, J. N., Jr., Computer studies of microseism statistics with applications to prediction and detection, Ph.D. thesis, Department of Geology and Geophysics, Massachusetts Institute of Technology, 1963.
- Garland, G. D., Earth currents, in Methods and Techniques in Geophysics, edited by S. K. Runcorn, Interscience Publishers, New York, 277-307, 1960.
- Garland, G. D., and R. A. Burwash, Geophysical and petrological study of Precambrian of central Alberta, Canada, Bull. Amer. Assoc. Petrol. Geol., 43, 790-806, 1959.
- Garland, G. D., and T. F. Webster, Studies of natural electric and magnetic fields, J. Research NBS, 64D, 405-408, 1960.
- Gratsinskiĭ, V. G., On the spectrum of a segment of a sinusoidal curve, Bull. (Izv.) Acad. Sci., USSR, Geophysics Series, 967-969, 1962, (English edition).
- Hannan, E. J., Time Series Analysis, John Wiley and Sons, Inc., New York, 1960.
- Hasegawa, H., Magnetotelluric studies in central Alberta, M.Sc. thesis, Department of Physics, University of Alberta, 1962.

- Heacock, R. R., Notes on pearl-type micropulsations, J. Geophys. Res., 68, 589-591, 1963.
- Holloway, J. L., Jr., Smoothing and filtering of time series and space fields, in Advances in Geophysics, edited by H. E. Landsberg and J. van Mieghem, Academic Press Inc., New York, 4, 351-389, 1958.
- Holmberg, E. R. R., A discussion of the origin of rapid periodic fluctuations of the geomagnetic field and a new analysis of observational material, Ph. D. thesis, Department of Applied Mathematics, University of London, 1951.
- Jacobs, J. A., Y. Kato, S. Matsushita, and V. A. Troitskaya, Classification of geomagnetic micropulsations, J. Geophys. Res., 69, 180-181, 1964.
- Jacobs, J. A., and T. Watanabe, Propagation of hydromagnetic waves in the lower exosphere and the origin of short period geomagnetic pulsations, J. Atmosph. Phys., 6, 413-429, 1962.
- Jacobs, J. A., and T. Watanabe, Trapped charged particles as the origin of short-period geomagnetic micropulsations, Planetary Space Sci., 11, 869-878, 1963.
- Kato, Y., and T. Kikuchi, On the phase difference of earth currents induced by the changes of the earth's magnetic field, Parts I and II, Science Reports of Tohoku Univ., Series 5, Geophys., 2, 139-145, 1950.
- Law, P. F., and B. M. Fannin, Radiation from a current filament above a homogeneous earth, with application to micropulsations, J. Geophys. Res., 66, 1049-1059, 1961.
- Lincoln, J. V., editor, Geomagnetic and solar data, J. Geophys. Res., 67, 5341-5342, 1962.
- Lincoln, J. V., editor, Geomagnetic and solar data, J. Geophys. Res., 68, 581-585, 1963.
- Lipskaya, N. V., On certain relationships between harmonics of periodic variations of the terrestrial electric and magneto fields, Izv. Akad. Nauk, USSR, Geophysics Series, 41-47, 1953.

- Lipskaya, N. V., N. A. Deniskin, and Y. M. Egorov, Results of electromagnetic soundings in the central region of the Dneiper-Donets depression, Bull. (Izv.) Acad. of Sci., Geophys. Ser., 259-261, 1961, (English Edition).
- MacDonald, G. J. F., Spectrum of hydromagnetic waves in the exosphere, J. Geophys. Res., 66, 3639-3670, 1961.
- Munk, W. H., F. E. Snodgrass, and M. J. Tucker, Spectra of low-frequency ocean waves, Bull. Scripps Institution of Oceanography, 7, 283-362, 1959.
- Neves, A. S., The magnetotelluric method in two dimensional structures, Ph. D. thesis, Department of Geology and Geophysics, Massachusetts Institute of Technology, 1957.
- Niblett, E. R., and C. Sayn-Wittgenstein, Variation of electrical conductivity with depth by the magnetotelluric method, Geophysics, 25, 998-1008, 1960.
- Peterman, Z. E., Precambrian basement of Saskatchewan and Manitoba, Ph. D. thesis, Department of Geology, University of Alberta, 1962.
- Piddington, J., The transmission of geomagnetic disturbance through the atmosphere and interplanetary space, Geophysical J., 2, 173-189, 1959.
- Ponomarev, E. A., On the nature of the shore effect, in Geomagnetic Disturbances, Acad. Sci., USSR Press, 1960.
- Price, A. T., The theory of magnetotelluric methods when the source field is considered, J. Geophys. Res., 67, 1907-1918, 1962.
- Prince, C. E., Jr., and F. X. Bostick, Jr., Ionospheric transmission of transversely propagated plane waves at micropulsation frequencies and theoretical power spectrums, Elec. Eng. Res. Lab., Univ. Texas Rept. 133, 1964.
- Quon, C., Electromagnetic fields of elevated dipoles on a two-layer earth, M. Sc. thesis, Department of Physics, University of Alberta, 1963.

- Rankin, D., The magnetotelluric effect on a dike, Geophysics, 27, 666-676, 1962.
- Richards, T. C., and D. J. Walker, Measurement of the thickness of the earth's crust in the Alberta plains of western Canada, Geophysics, 24, 262-284, 1959.
- Rikitake, T., Electromagnetic induction within the earth and its relation to the electrical state of the earth's interior, Bull. Earthq. Res. Inst. Tokyo, 28, 45-98, 1950.
- Rikitake, T., Changes in earth currents and their relation to the electrical state of the earth's crust, Bull. Earthq. Res. Inst. Tokyo, 29, 270-275, 1951.
- Robinson, E. A., Predictive decomposition of time series with applications to seismic exploration, Ph. D. thesis, Department of Geology and Geophysics, Massachusetts Institute of Technology, 1954.
- Rokityanskiĭ, I. I., The shore effect in variations of the earth's electromagnetic field, Bull. (Izv.) Acad. Sci., USSR, 1101-1105, 1963.
- Rolf, B., Giant pulsations at Abisko, Terr. Mag. Atmos. Elect., 36, 9-14, 1931.
- Scholte, J. G., and J. Veldkamp, Geomagnetic and geoelectric variations, J. Atmosph. Terr. Phys., 6, 33-45, 1955.
- Simpson, S. M., Jr., E. A. Robinson, J. F. Claerbout, J. N. Galbraith, Jr., W. P. Ross, and J. Clark, Time series techniques applied to underground nuclear detection and further digitized seismic data, Scientific Report No. 2 of Contract AF 19(604) 7378 at M.I.T., prepared for Geophysics Research Directorate, Air Force Cambridge Res. Lab., Office of Aerospace Res., USAF, 1961.
- Simpson, S.M., Jr., E. A. Robinson, J.R. Claerbout, J. Clark, J. N. Galbraith, Jr., C. Pan, R. Wiggins, Continued numerical studies on underground nuclear detection and further digitized seismic data, Scientific Report No. 3 of Contract AF 19(604)7378 at M.I.T., prepared for Geophysics Research Directorate, Air Force Cambridge Res. Lab., Office of Aerospace Res., USAF, 1962.

- Smith, H. W., L. D. Provazek, and F. X. Bostick, Jr., Directional properties and phase relations of the magnetotelluric fields at Austin, Texas, J. Geophys. Res., 66, 879-888, 1961.
- Srivastava, S. P., J. L. Douglass, and S. H. Ward, The application of the magnetotelluric and telluric methods in central Alberta, Geophysics, 28, 426-446, 1963.
- Stewart, B., On the great magnetic disturbance of 28 August to 7 September 1859, Phil. Trans. Roy. Soc. (London), 151, 423-430, 1861.
- Störmer, C., Sur les trajectoires périodiques des corpuscles électriques dans l'espace sous l'influence du magnétisme terrestre, avec application aux perturbations magnétiques, Comptes Rendus, 143, 1906.
- Tepley, L., Low-latitude observations of fine-structured hydromagnetic emissions, J. Geophys. Res., 69, 2273-2290, 1964.
- Tikhonov, A. N., Determination of the electrical characteristics of deep layers of the earth's crust, Dok. Akad. Nauk., USSR, 73, 295-297, 1950.
- Tikhonov, A. N., and N. V. Lipskaya, Terrestrial electric field variations, Dok. Akad. Nauk., 87, 547-550, 1952.
- Tikhonov, A. N., and D. N. Shakhshvarov, Concerning the possibility of using the impedance of the earth's natural electromagnetic field for investigating its upper layers, Bull. (Izv.) Acad. Sci., USSR, Geophysics Series, 410-418, 1956.
- Vozoff, K., H. Hasegawa, and R. M. Ellis, Results and limitations of magnetotelluric surveys in simple geologic situations, Geophysics, 28, 778-792, 1963.
- Wait, J. R., On the relation between telluric currents and the earth's magnetic field, Geophysics, 19, 281-285, 1954.

- Watanabe, T., On the origins of geomagnetic pulsations, Science Reports of Tohoku Univ., 13, 127-140, 1961.
- Weaver, J. T., The electromagnetic field within a discontinuous conductor with reference to geomagnetic micropulsations near a coastline, Can. J. Phys., 41, 484-495, 1962.
- Wentworth, R. C., and L. R. Tepley, Hydromagnetic emissions, X-ray bursts, and electron bunches, 2. Theoretical interpretation, J. Geophys. Res., 67, 3335-3343, 1962.
- Wiese, H., Geomagnetische Tiefentellurik, Teil I, Geofisica Pura E Applicata, 51, 59-78, 1962.
- Yungul, S., Magnetotelluric sounding three-layer interpretation curves, Geophysics, 26, 465-473, 1961.

APPENDICES

Appendix A

Basic Magnetotelluric Theory

In this section the basic magnetotelluric equation is developed following the method of Garland (1960). For a more physical development, the reader is referred to the original paper of Cagniard (1953).

In order to develop the basic equation the following assumptions are made:

- (I) Micropulsations are plane electromagnetic waves.
- (II) The angle of incidence is zero.
- (III) The earth is a homogeneous half-space.
- (IV) \vec{E} is entirely in the x-direction, i.e., we have only E_x and H_y components.

For an isotropic medium, the time independent field equation (MKS units) is

$$\nabla^2 \vec{E} + \omega^2 \mu \epsilon \left(1 + \frac{i\sigma}{\omega\epsilon}\right) \vec{E} = 0 \quad (1)$$

In the earth, for the frequencies under consideration

$$\frac{\sigma}{\omega\epsilon} \gg 1$$

Hence (1) may be written

$$\nabla^2 \vec{E} + i\omega\mu\sigma \vec{E} = 0 \quad (2)$$

Under the above assumptions this becomes

$$\frac{\partial^2 E_x}{\partial z^2} + i\omega\mu\sigma E_x = 0 \quad (3)$$

Further

$$\nabla \times \underline{E} = - \frac{\partial \underline{B}}{\partial t}$$

becomes

$$\frac{\partial E_x}{\partial z} = - i\mu\omega H_y \quad (4)$$

The solution of (3) is

$$E_x = Ae^{\sqrt{\frac{\omega\mu\sigma}{2}}(1+i)z} + Be^{-\sqrt{\frac{\omega\mu\sigma}{2}}(1+i)z} \quad (5)$$

Since E_x must remain finite for $z \rightarrow \infty$, $A = 0$.

From (4) and (5)

$$\frac{E_x}{H_y} = \left(\frac{2\pi\rho}{T\mu}\right)^{\frac{1}{2}} e^{i\pi/4} \quad (6)$$

Therefore \underline{E} leads \underline{H} by 45° .

Changing to practical units and setting $\mu = 1$, (6) becomes

$$\rho = .2T |E_x|^2 / |H_y|^2$$

Cantwell (1960) shows that this relation holds for orthogonal components of \underline{E} and \underline{H} in the case of elliptic polarization.

The general propagation constant is

$$k^2 = \omega\mu\sigma i + \omega^2\epsilon\mu$$

In the air

$$\sigma = 0, \quad \text{therefore } k_1^2 = \omega^2 \epsilon \mu.$$

In the earth

$$\omega^2 \epsilon \mu \ll \omega \mu \sigma i, \quad \text{therefore } k_2^2 = \omega \mu \sigma i.$$

For the frequencies and conductivities under consideration, $|k_1^2| \ll |k_2^2|$, hence Snell's Law shows that the angle of refraction is very close to zero regardless of the angle of incidence. Dosso (1962) has calculated the ratio of the amplitude of the vertical to horizontal magnetic field for several stratified conductors with geologic parameters. The largest ratio found was $\approx 1\%$.

In the more general case of a layered earth, the ratio $|\underline{E}/\underline{H}|$ can be found by applying the electromagnetic boundary conditions. In this case the quantity

$$.2T |\underline{E}|^2 / |\underline{H}|^2$$

becomes an apparent resistivity (ρ_a) and the phase difference deviates from 45° . Figures A-1 and A-2 show apparent resistivity and phase curves for a 2-layered earth.

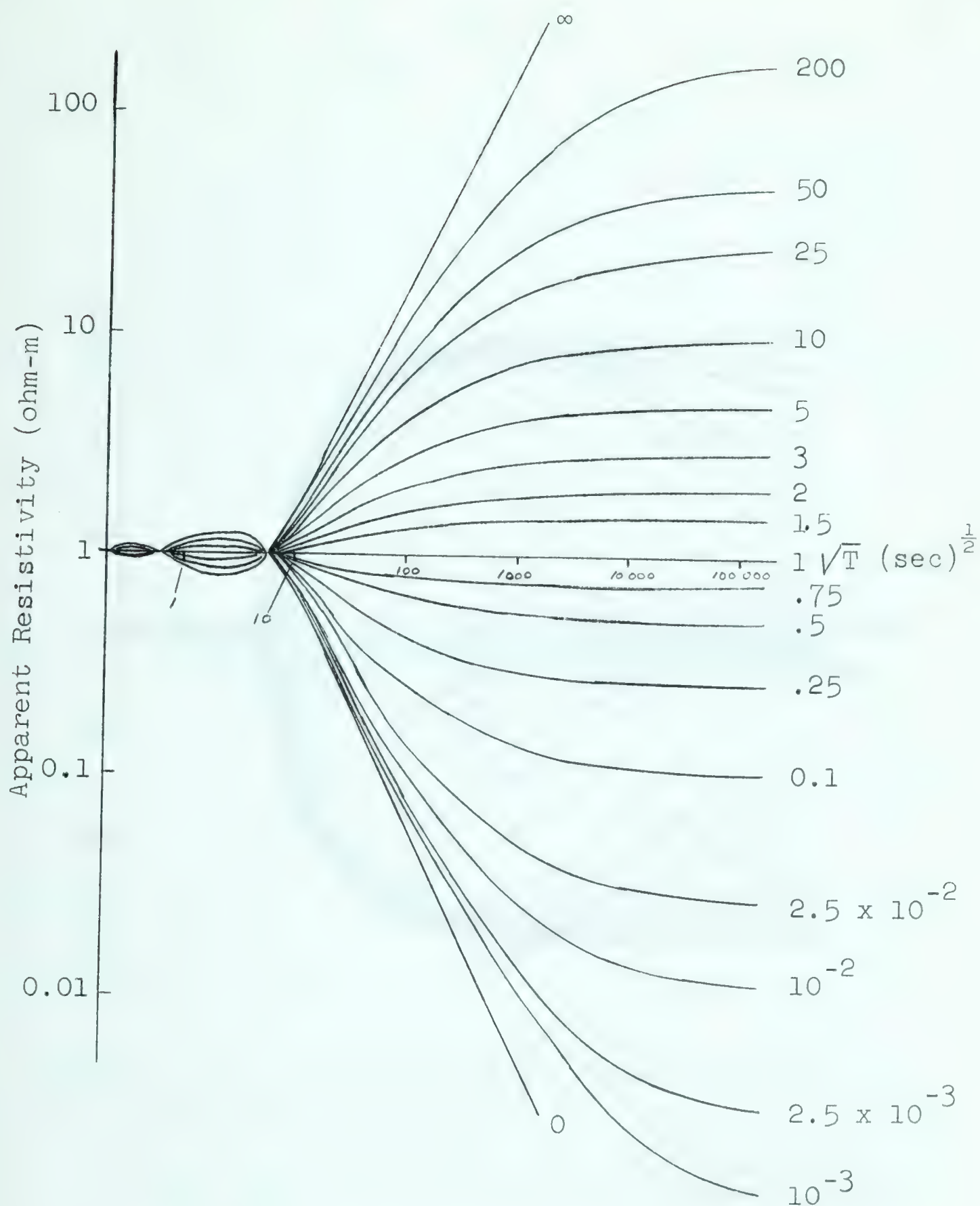


Figure A-1. Cagniard two-layer apparent resistivity curves. Numbers on the curves show the resistivity of the lower medium in ohm-m. The upper medium always has a resistivity of one ohm-m and is one km in thickness (from Cagniard, 1953).

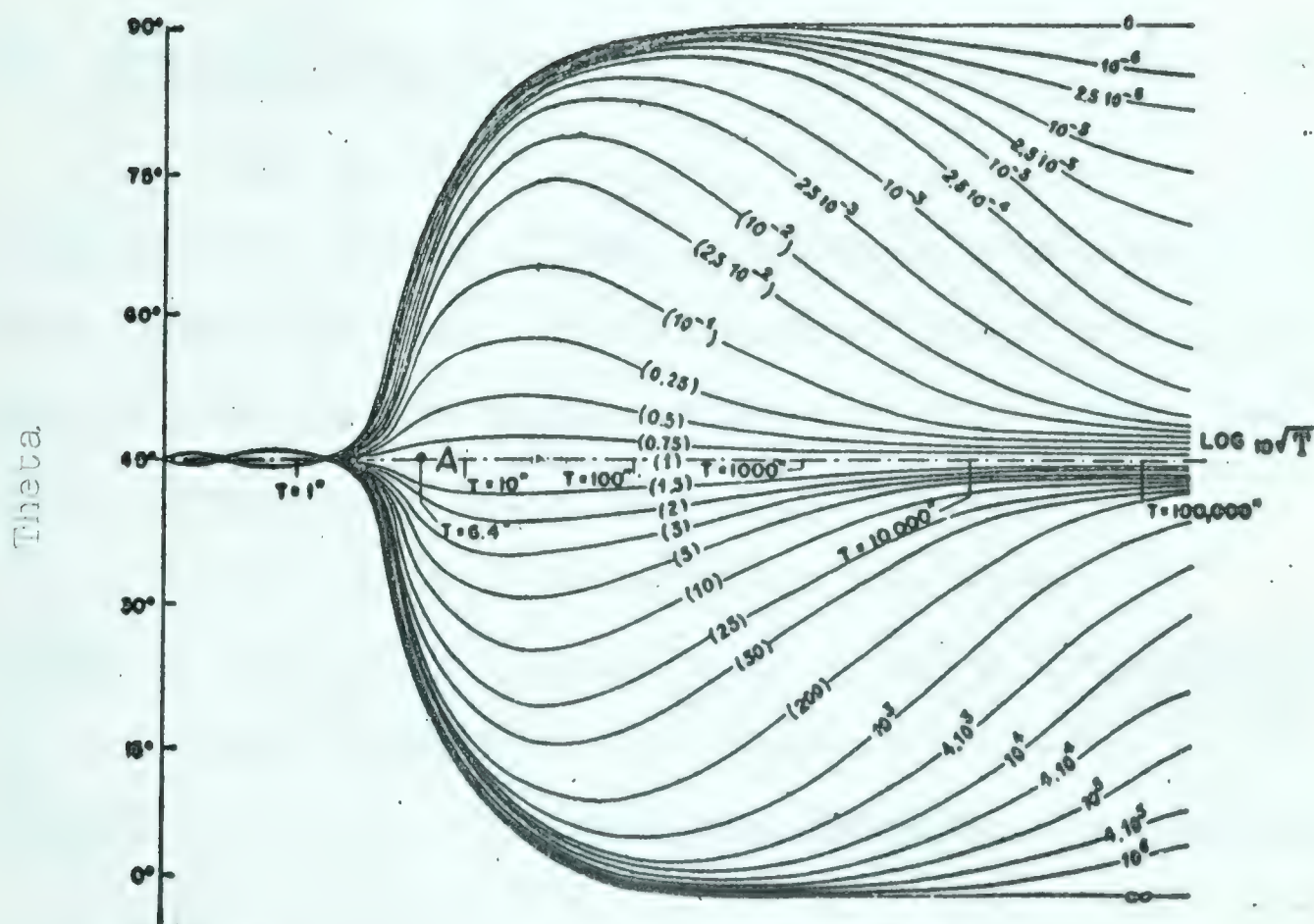


Figure A-2. Master curves of phase differences Θ (E-II) versus period for various resistivity contrasts in a two-layer earth. Numbers on the curves show the resistivity of the lower medium. The upper medium always has a resistivity of one ohm-m and is one m in thickness (from Cagniard, 1953)

Appendix B

Spectral Analysis

The purpose of this section is to present the general formulas of spectral analysis, the properties of the spectral windows used, and the fundamentals of prewhitening.

(a) Computational Formulas

Let $x_1, x_2 \dots x_n$ and $y_1, y_2 \dots y_n$ represent two series of data sampled at time intervals Δt whose means are zero. The spectra of these series are then only defined to the Nyquist frequency, $f_N = 1/2\Delta t$, the higher frequencies being aliased into frequencies $f \leq f_N$. Let L be a correlation lag index, $L = 0, \pm 1, \pm 2 \dots \pm(n-1)$, and J be a frequency index for the $(m+1)$ equally spaced spectral estimates in the range $0 \leq f \leq f_N$. The following quantities are computed.

1. Autocorrelations $L = 0, 1, \dots (n-1)$

$$A(L) = \frac{1}{n-L} \sum_{i=1}^{n-L} x_i x_{i+L} \quad , \quad A(-L) = A(L)$$
$$B(L) = \frac{1}{n-L} \sum_{i=1}^{n-L} y_i y_{i+L} \quad , \quad B(-L) = B(L)$$

2. Cross-correlations $L = -(n-1), \dots, (n-1)$

$$C(L) = \frac{1}{n - |L|} \sum_{i=1}^{n-L} x_i y_i + L \quad L \geq 0$$

$$= \frac{1}{n - |L|} \sum_{i=1}^{n - |L|} x_i + |L| y_i \quad L < 0$$

3. Autopower density spectra $J = 0, 1, \dots, m$

$$X(J) = \Delta t \sum_{L=-(n-1)}^{n-1} D_i(L) A(L) \cos \left(\frac{LJ\pi}{m} \right)$$

$$Y(J) = \Delta t \sum_{L=-(n-1)}^{n-1} D_i(L) B(L) \cos \left(\frac{LJ\pi}{m} \right)$$

where $D_i(L)$ is a weighting function - the lag window
(See part (b)) .

4. Cross-power spectrum $J = 0, 1, \dots, m$

Real part

$$Z(J) = \Delta t \sum_{L=-(n-1)}^{n-1} D_i(L) C(L) \cos \left(\frac{LJ\pi}{m} \right)$$

Imaginary part

$$W(J) = \Delta t \sum_{L=-(n-1)}^{n-1} D_i(L) C(L) \sin \left(\frac{LJ\pi}{m} \right)$$

5. Phase lead of the y series over the x series

$$J = 0, 1, \dots, m$$

$$\theta(J) = \text{Arc tan } \left(\frac{W(J)}{Z(J)} \right)$$

with θ taken between 0° and 180° if W is positive, and between 180° and 360° if W is negative.

6. Coefficient of linear coherency

$$R(J) = \frac{\sqrt{Z^2(J) + W^2(J)}}{\sqrt{X(J)Y(J)}}$$

The autocorrelation function contains the amplitude information of the spectrum but discards all phase information. In contrast, the cross-correlation retains the phase differences between the two time series. If the x_i 's are considered to be voltages across a pure resistance of one ohm, then $X(J) \Delta f$ is an estimate of the power dissipated in the frequency interval

$$\left(J - \frac{1}{2}\right) \Delta f < f < \left(J + \frac{1}{2}\right) \Delta f.$$

If the x_i 's are considered to be voltage and the y_i 's to be current, then $\sqrt{Z^2(J) + W^2(J)} \Delta f$ is an estimate of the power dissipated in the frequency interval. The coherency is a measure of how rapidly the cross power phase is changing.

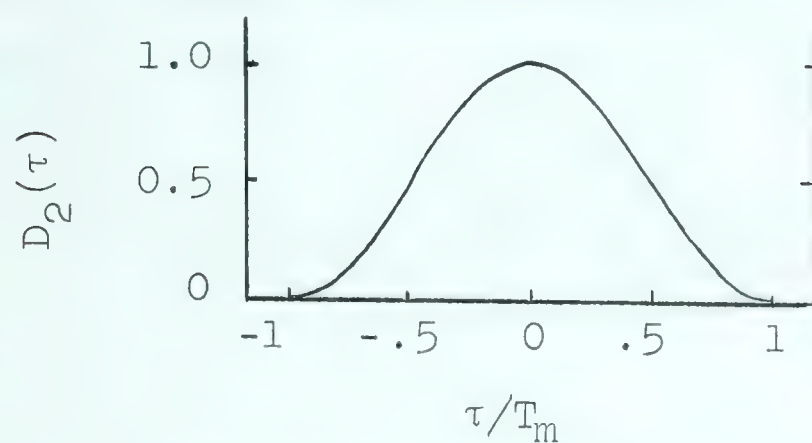
(b) The Hanning Window

In the above spectral estimates the autocorrelation functions are modified by a weighting function $D_1(L)$ called the lag window (Blackman and Tukey, 1958). This has the effect of convolving the Fourier transform of $D_1(\tau)$ ($Q_1(f)$ - the spectral window) with the raw spectra. A simple and widely used lag window (whose use is called "hanning") is given in continuous form by

$$\begin{aligned} D_2(\tau) &= \frac{1}{2} \left(1 + \cos \frac{\pi\tau}{T_m} \right) & |\tau| < T_m \\ &= 0 & |\tau| > T_m \end{aligned}$$

where T_m = maximum lag calculated. $D_2(\tau)$ and the corresponding $Q_2(f-f_0)$ are shown in Figure B-1. This window has the desirable properties of concentrating the main lobe of $Q_1(f-f_0)$ near f_0 and side lobes that fall off rapidly. For digital calculations $T_m = m\Delta t$. Since $D_2(\tau) = 0$ for $|\tau| > m\Delta t$, only m autocorrelations are required and the window is computationally inexpensive.

Hanning lag window



Hanning spectral window

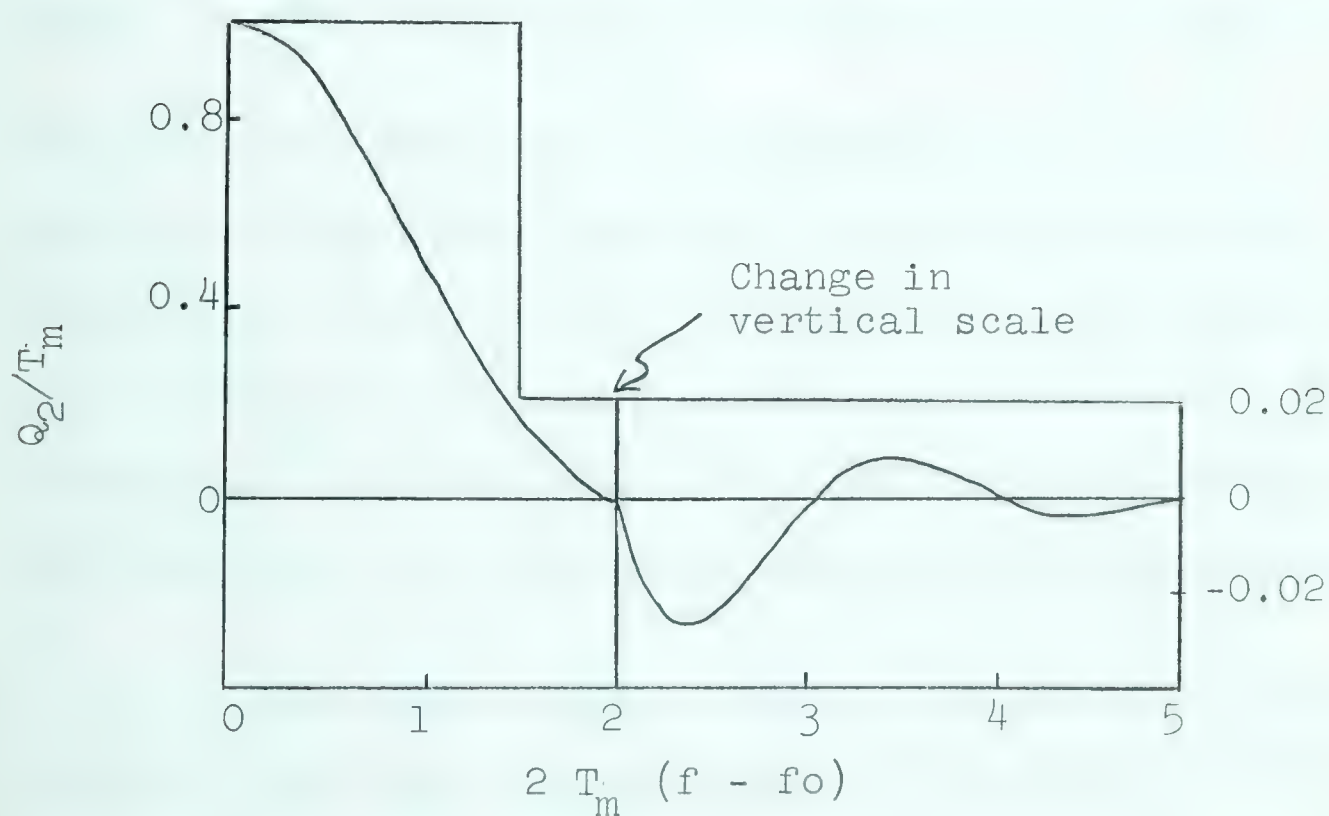


Figure B-1. The lag and spectral window for the hanning estimate (after Blackman and Tukey, 1958).

(c) The Daniell Window

The Daniell window (Hannan, 1960; Simpson et al, 1961) exhibits behaviour which can approach that of the ideal rectangular window. This method uses the complete transient (Wiener) autocorrelation of the time function $x_i, i=1, \dots, N$

$$A(L) = \frac{1}{N} \sum_{i=1}^{N-|L|} x_i x_{i+L} \quad L = 0, \pm 1, \dots, \pm(N-1)$$

The Daniell estimate is then

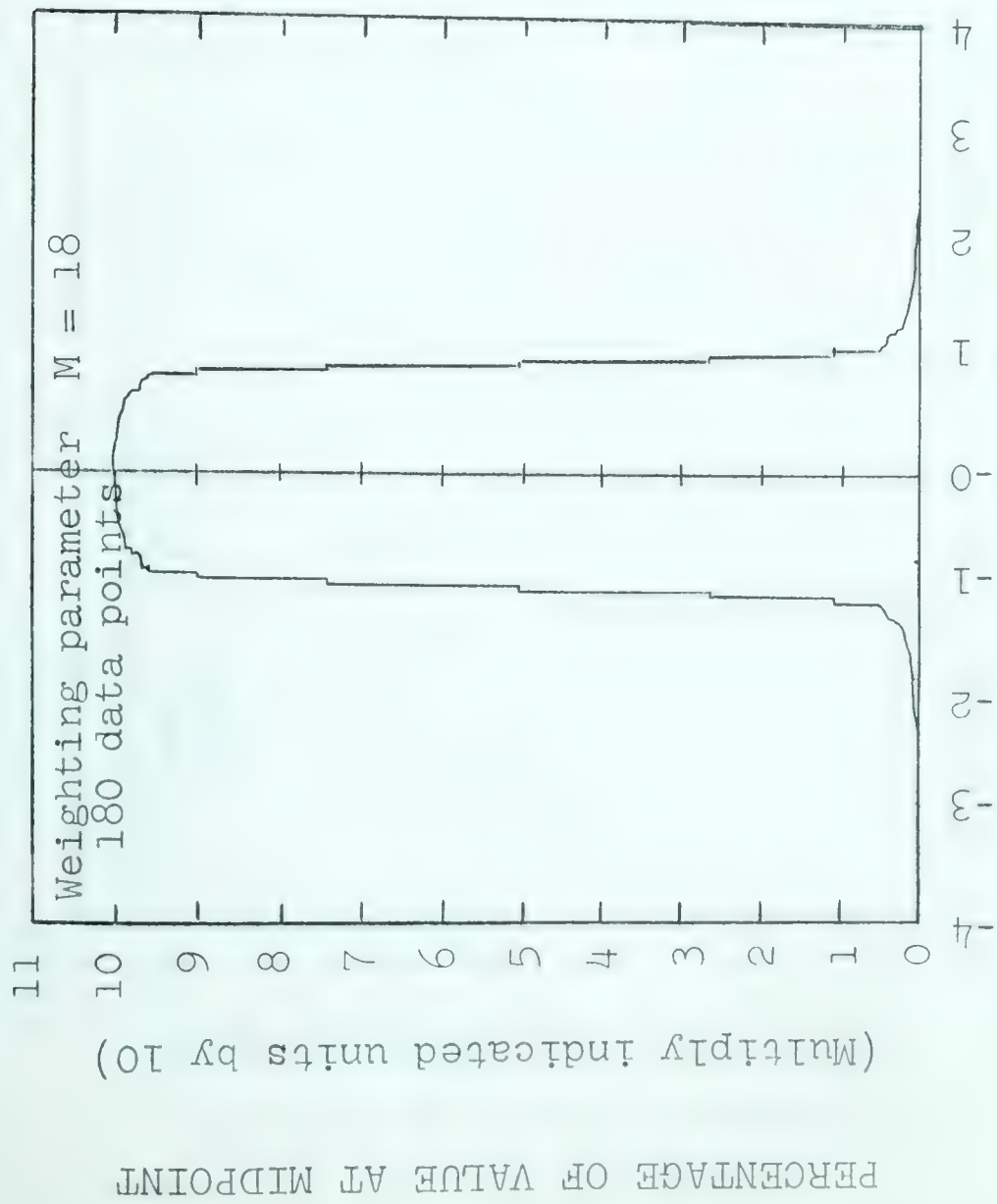
$$X(J) = \Delta t \sum_{L=-(N-1)}^{N-1} A(L) \frac{\sin \frac{L\pi}{m}}{L\pi/m} \cos\left(\frac{LJ\pi}{m}\right) \quad J=0, 1, \dots$$

where $\frac{\sin \frac{\pi L}{m}}{\frac{\pi L}{m}}$ is the Daniell lag window. It can be seen

that this estimate has the parameters m and n . In practice it is found that the window shape is rather well defined by the ratio n/m . Examples of these windows for $n/m = 10$ and 40 are shown in Figures B-2 and B-3. The windows are non-negative; they tend to become rectangular as n/m increases; and they are essentially non-oscillatory.

The basic disadvantage of the Daniell estimate is that all lags must be calculated. The window is therefore computationally expensive.

Overall spectral window of Daniell method



Exploded view of spectral window tail

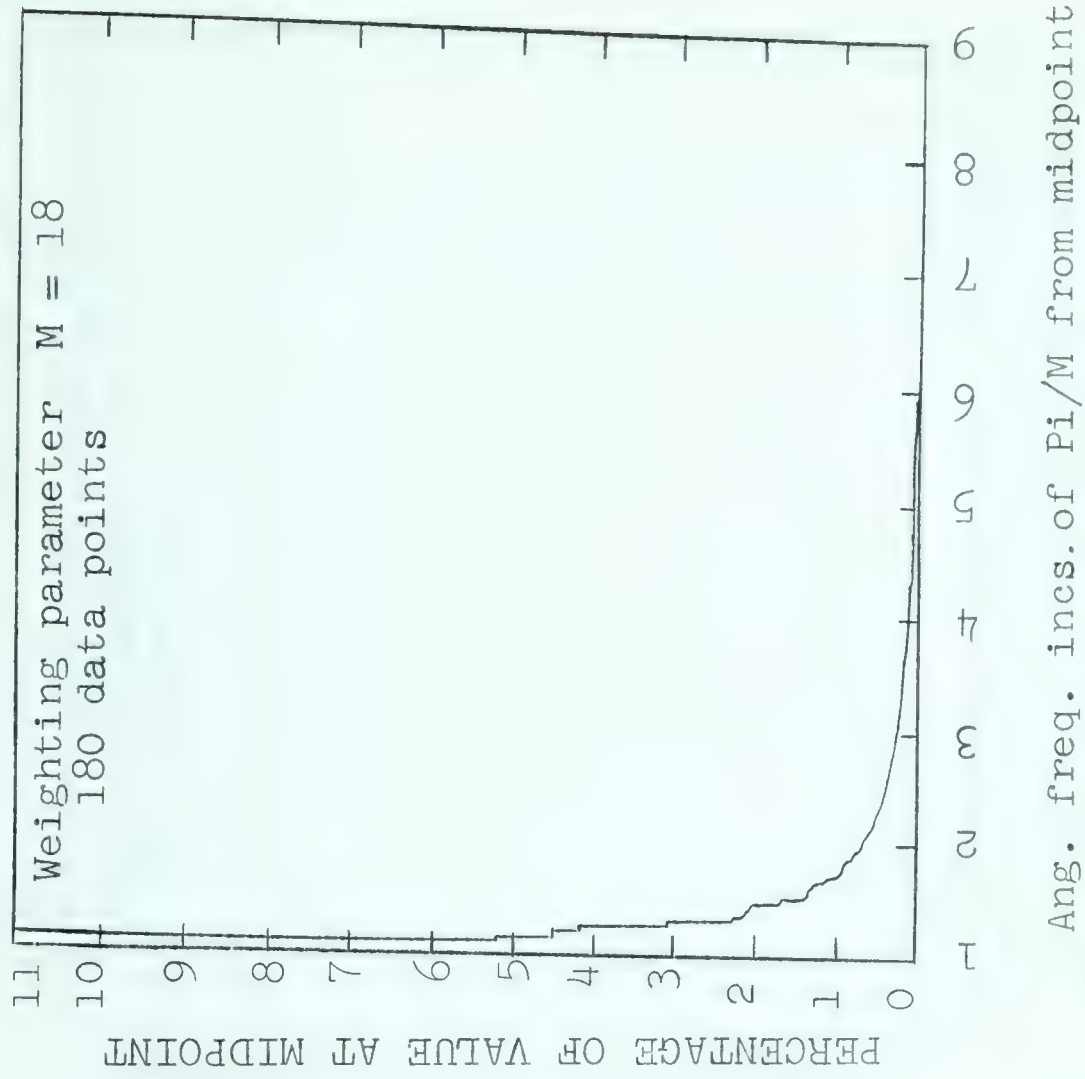
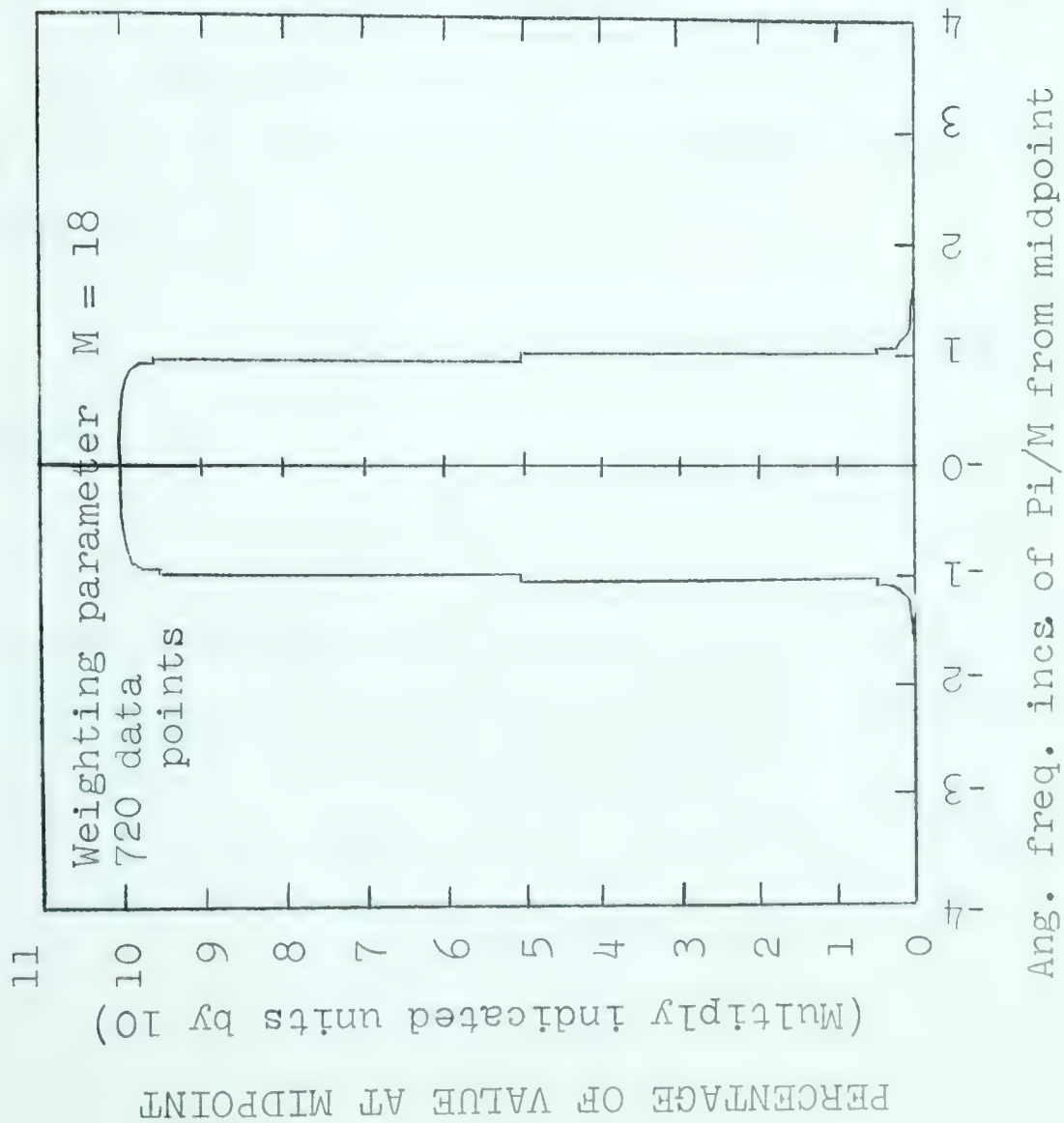


Figure B-2. Daniell window for $n/m = 10$
(from Simpson et al, 1961).

Overall spectral window of Daniell Method



Exploded view of spectral window tail

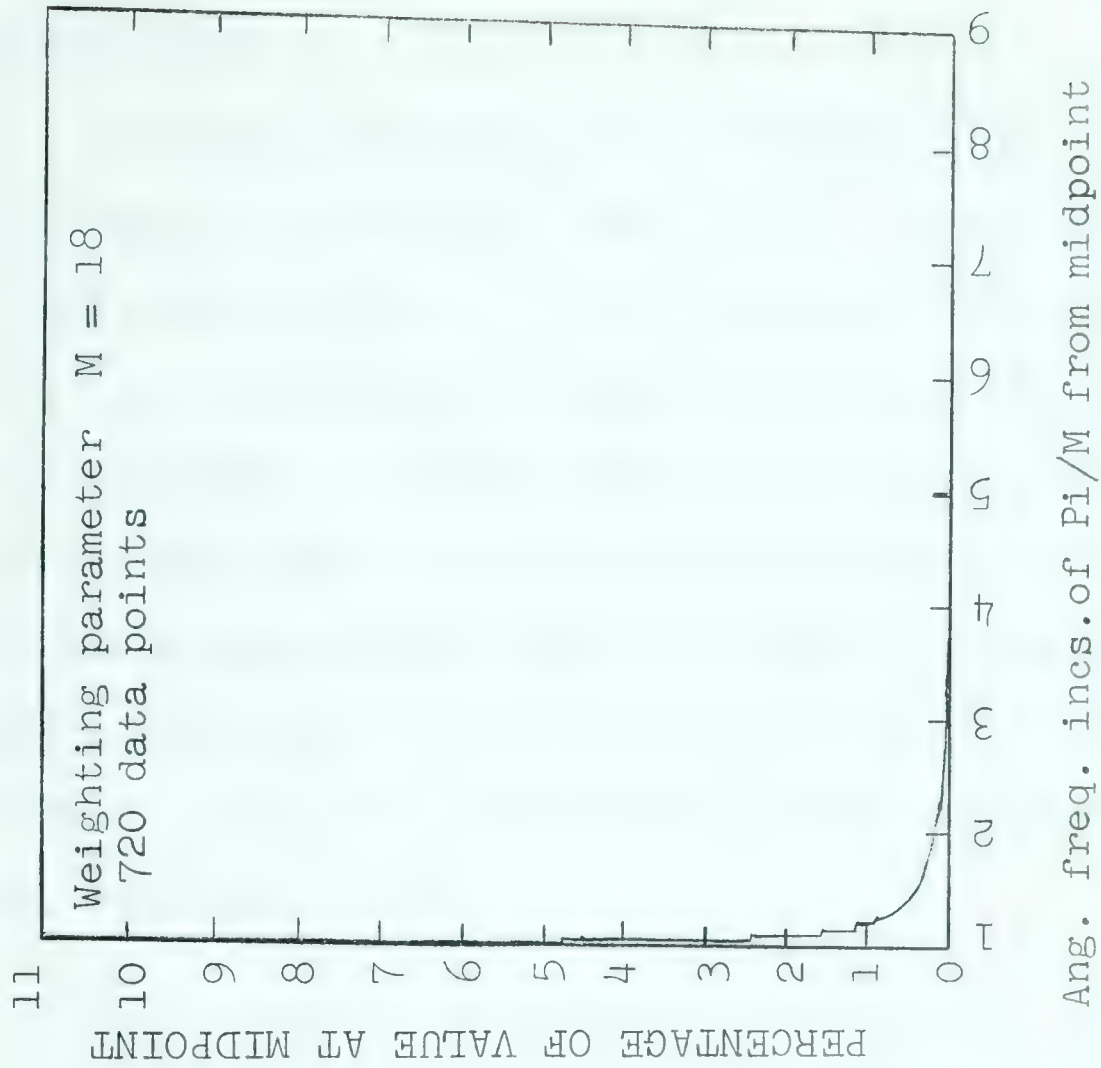


Figure B-3. Daniell window for $n/m = 40$.
(from Simpson et al, 1961).

(d) Prewhitening

If energy estimates at a frequency f_0 are to be useful, only frequencies close to f_0 should have a substantial contribution. If the spectrum rises steeply as f leaves f_0 , an extremely rapid fall-off in the spectral window is required. A simple way to avoid this problem is to filter the signal before analysis so that the spectrum to be analyzed is fairly constant or slowly varying. Since the ideal would be to bring the spectrum close to that of white noise, the process is called prewhitening (Blackman and Tukey, 1958).

The procedure is simple in principle. Given values of x_t , a linear operator is applied to obtain new values z_t . The relationship between the spectra can then be found by calculating the transfer function of the operator.

A simple moving linear combination which is often useful is

$$z_i = x_i + \lambda x_{i-1} \quad .$$

The transfer function (Y) is given by the inverse Fourier transform of the weighting coefficients. Therefore

$$Y(f) = 1 + \lambda \cos 2\pi f \Delta t + i \lambda \sin 2\pi f \Delta t \quad .$$

Hence

$$P_z(f) = P_x(f) (1 + \lambda^2 + 2\lambda \cos 2\pi f \Delta t).$$

The power transfer function is shown for various λ in Figure B-4.

Therefore to obtain improved estimates, the series is first prewhitened; the spectrum is calculated; and finally, the calculated spectrum is divided by the power transfer function of the prewhitening process.

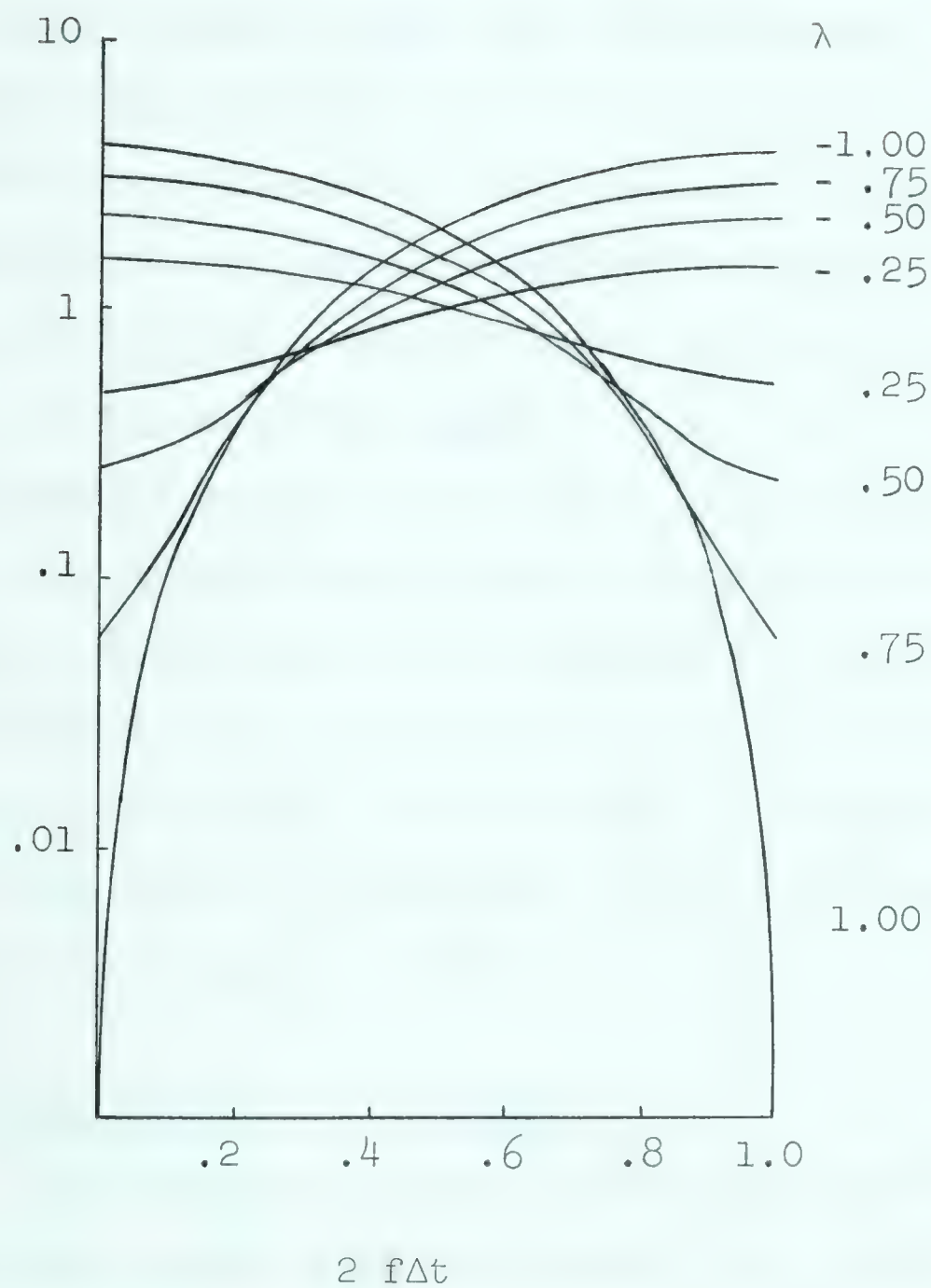


Figure B-4. Power transfer function of $z_i = x_i + \lambda x_{i-1}$ for various values of the parameter λ (after Munk et al, 1959).

APPENDIX C

Computational Experiments

The purpose of this section is to examine the effects on the spectral ratios of simultaneity of conversion, trend removal, prewhitening, and different spectral windows. Since under the Cagniard theory, the orthogonal components of the electric and magnetic field at any frequency are linearly related, the usual criterion of quality in comparing signals is coherency. As this relationship is independent of time, and the electric-magnetic field ratio is a smooth and continuous function of frequency, the smoothness of the ratio (or its square) may be used to examine the reliability of coherency as an indicator. Although the Cagniard theory does not apply at the Montreal Lake station, the interpreted results indicate that the measuring and geologic axes nearly coincide and hence the orthogonal components are linearly related.

Effect of Simultaneous Conversion

The analog-to-digital conversion system used for the 1961 data handled only one channel at a time. After selecting a record section of interest from the analog playback, start and end markers were fixed to the magnetic tape. The beginning and end of conversion were triggered manually by observing when the markers crossed the playback head of the tape recorder. At high playback speeds this is

difficult to do accurately and as a consequence we invariably ended up with an electric and magnetic time series of different lengths having an unknown relative time shift. For 3.2 conversions per sec, the normal difference was zero to two points. However differences of 18 points have occurred. For a tape speeded up by a factor of 16 during playback, this difference in length is 90 sec. Manual alignment of digital data is slow and unreliable. This leads to a loss of confidence in computational results. This section considers the effect of these shifts on spectral results by comparing independent conversions of given analog records. Bogert (1962) compares manual and electronic conversions of the same analog records. In a sense, this section is a continuation of his work.

Various parameters can be used to compare two records including their variance, auto- and cross-spectra, coherency and phase. The simplest of these is variance. Although it contains no indication of the way the energy is distributed in either frequency or time, it will show gross differences between independent conversions. Auto-spectra are more sensitive, but a pair of records can have identical spectra yet be incoherent. Either point-by-point equality in time, or identical autospectra and unity coherency serve as sufficient criteria for identity of a record pair.

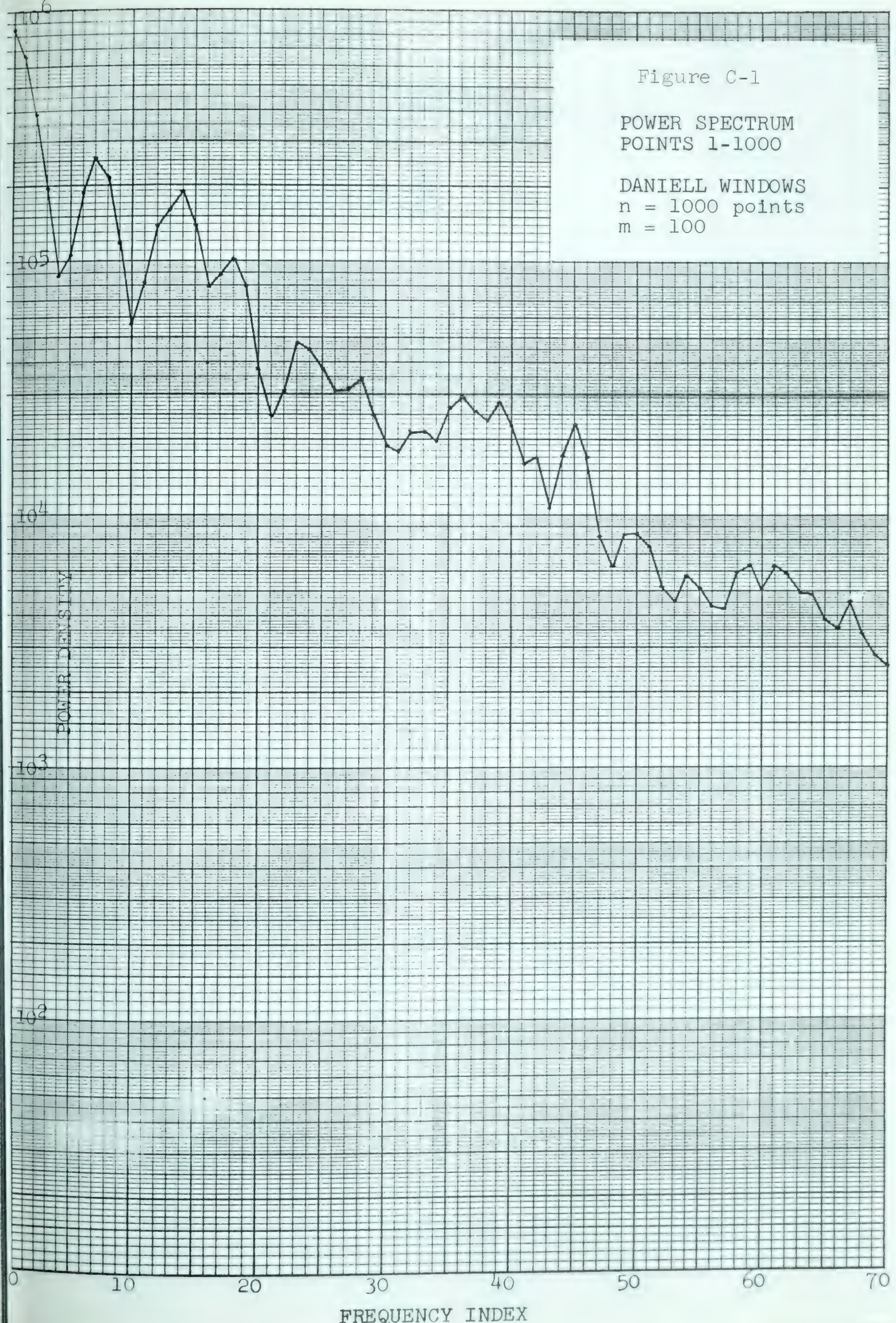
The first experiment consisted of analyzing slightly shifted segments of one digital record. The cross-spectra of points 1 to 1000 with points 11 to 1010, 21 to 1020, and 31 to 1030 were calculated. The results will of course depend on the differences between the non-overlapping segments. Figure C-1 shows the spectrum of points 1 to 1000; Figure C-2 shows the effect of shift on spectral ratio; and Figure C-3 shows the coherencies. The percentage differences in variance were 3.5, 6, and 10 percent. It is apparent that small shifts in real signals can lead to substantial differences in the ratios. This indicates that a particular spectral bump can often be associated with a discrete event on the analog record. This observation is borne out by many other examples.

Both coherency-squared and the percentage differences deteriorate with increasing record shift, as expected. There is a correlation of large positive percentage difference with low coherency and spectrum troughs in each case. However the outstanding percentage differences (ignoring sign) occur between frequencies of 10 and 20, where coherencies are only slightly lower than elsewhere. This example points out the typical behaviour of coherency as an indicator of ratio smoothness. Large coherency is necessary, but in itself is not sufficient to ensure a smooth spectral ratio.

Figure C-1

POWER SPECTRUM
POINTS 1-1000

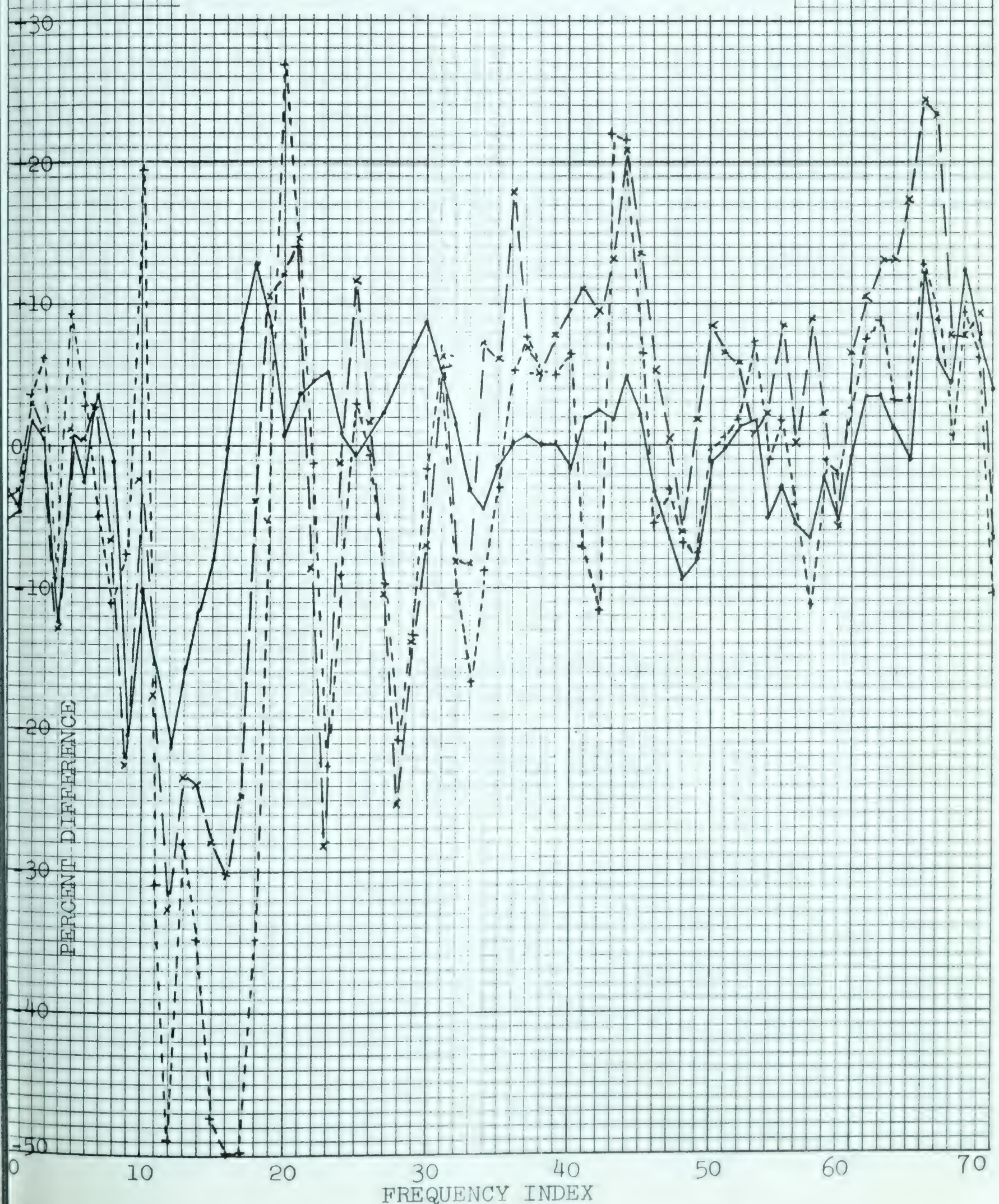
DANIELL WINDOWS
n = 1000 points
m = 100



THE
LIBRARY
OF THE
MUSEUM OF
COMPARATIVE ZOOLOGY
AT
HARVARD UNIVERSITY
CAMBRIDGE, MASS.

Figure C-2
PERCENTAGE DIFFERENCES
FROM THE SPECTRUM OF POINTS 1-1000

. POINTS 11-1010
x POINTS 21-1020
+ POINTS 31-1030





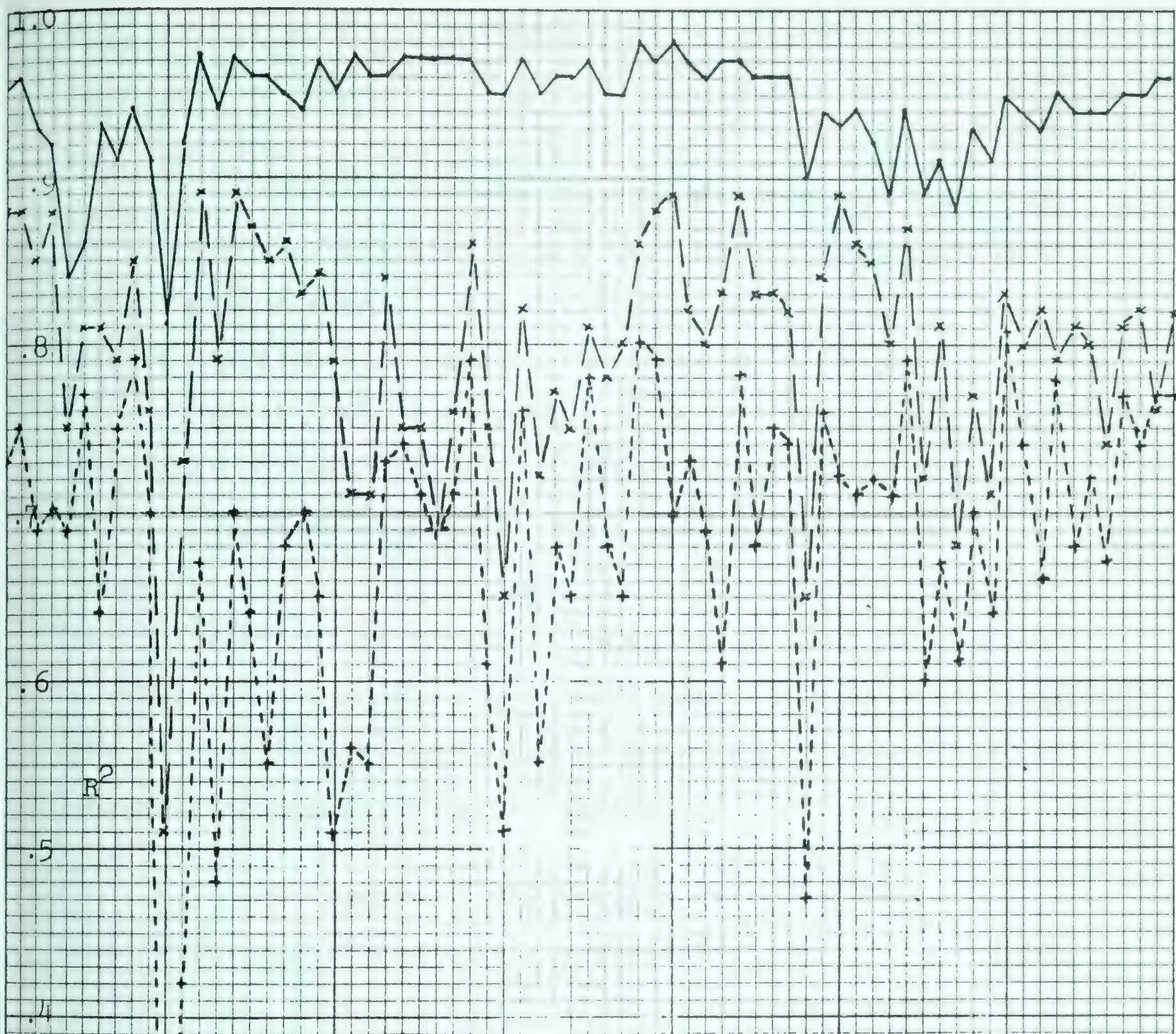
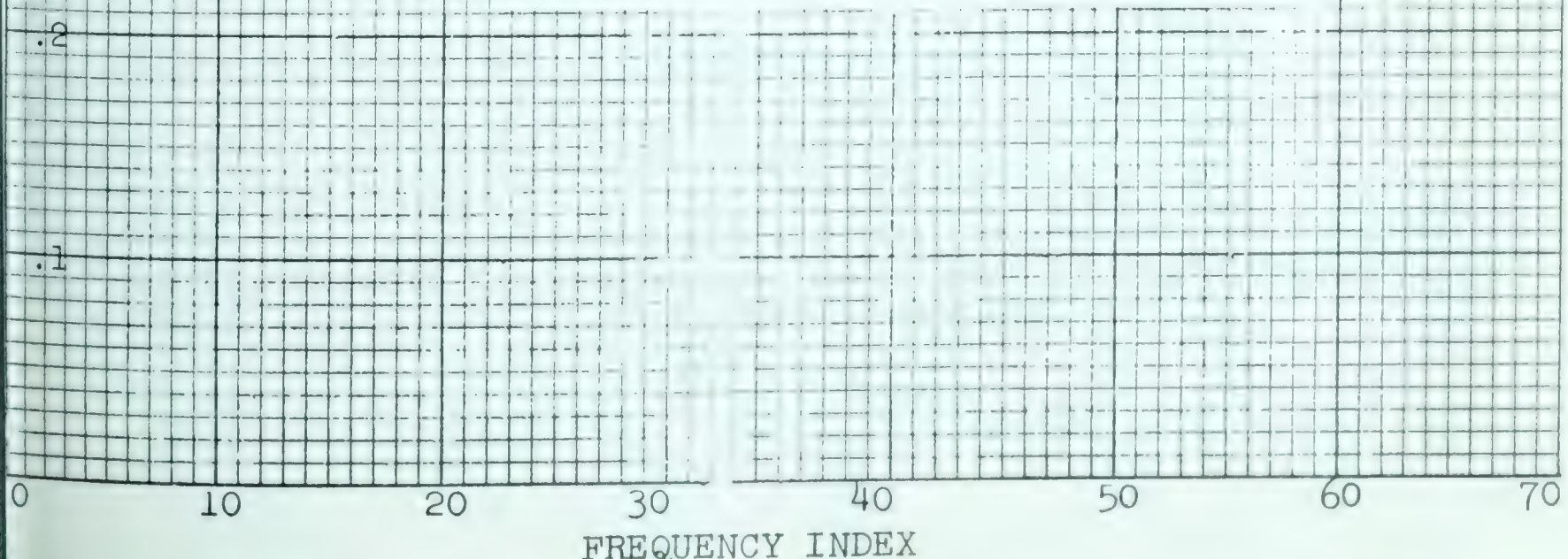


Figure C-3

(COHERENCY)² OF POINTS 1-1000
WITH SHIFTED RECORDS

- . 1-1000 WITH 11-1010
- x 1-1000 WITH 21-1020
- + 1-1000 WITH 31-1030



In the section on spectral programs is an example of the spectra resulting from a two-channel conversion of a single analog signal. Any differences must be due to the slight difference in sampling instant, and to minor differences in the response and noise of the playback filters. Although the vast majority of values of coherency-squared exceed .95, a few spectral ratios greater than 1.5:1 do emerge. As is to be expected, the major differences occur for low spectral amplitudes. Other examples of two-channel conversion of a single signal have led to the same conclusion. The process is very effective in improving coherency but not quite as successful in ratio smoothing.

One example of differences resulting from independent conversions is illustrated by Figure C-4. This shows a pair of spectra derived from separate conversions of, ¹ostensibly, the same segment of analog record. The difference in variance is 6 percent. Table C-1 summarizes variance differences found in independent conversions of 27 different analog records. The number of points were between 4000 and 5000 in all cases.

¹ It is unlikely that any appreciable part of the difference can be attributed to conversion round off.

Figure C-4

SPECTRA FROM TWO INDEPENDENT
CONVERSIONS OF THE SAME RECORD

$\frac{\text{VARIANCE of B}}{\text{VARIANCE of A}} = 1.06$

DANIELL WINDOWS

$n = 4000$ points

$m = 500$

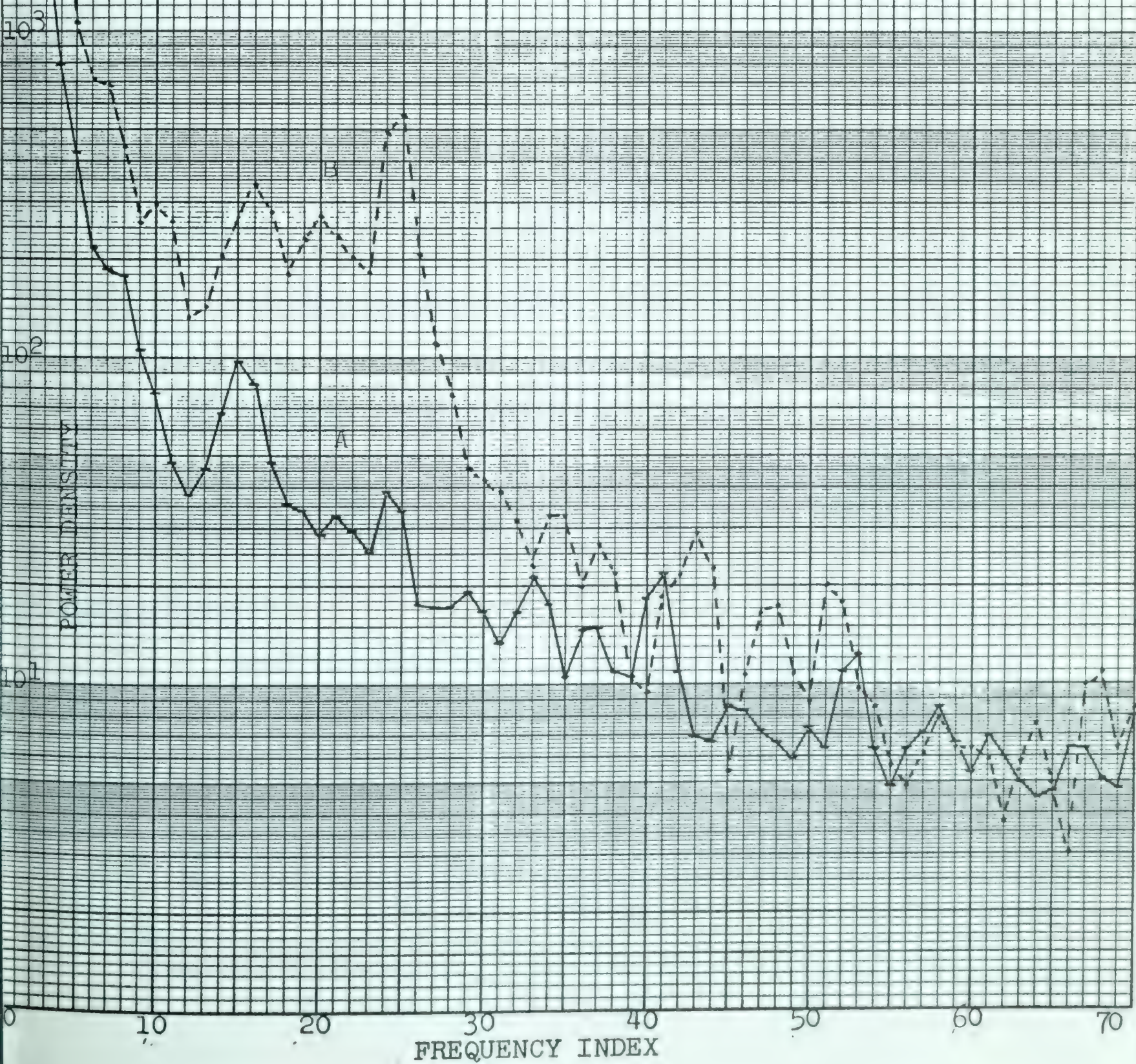


Table C-1

<u>Difference in Variance</u> %	<u>Number of Cases</u>
0 - 1	12
1.1 - 2	6
2.1 - 3	4
6	1
24	2
38	1
87	1

It should be emphasized that near-equality of variance does not guarantee near-identity of spectra.

The problem of ensuring conversion of corresponding sections with a single channel analog-to-digital conversion system can probably best be solved by post-recording pulses on a direct record channel of the tape. These pulses can then be used to trigger the converter.

Trend Removal

With the data acquisition and processing equipment used, and the spectra of the signals recorded, our raw digital data must be expected to contain finite power at zero frequency as well as finite power in the lowest energy band. Both of the spectral programs used for the 1962 data,

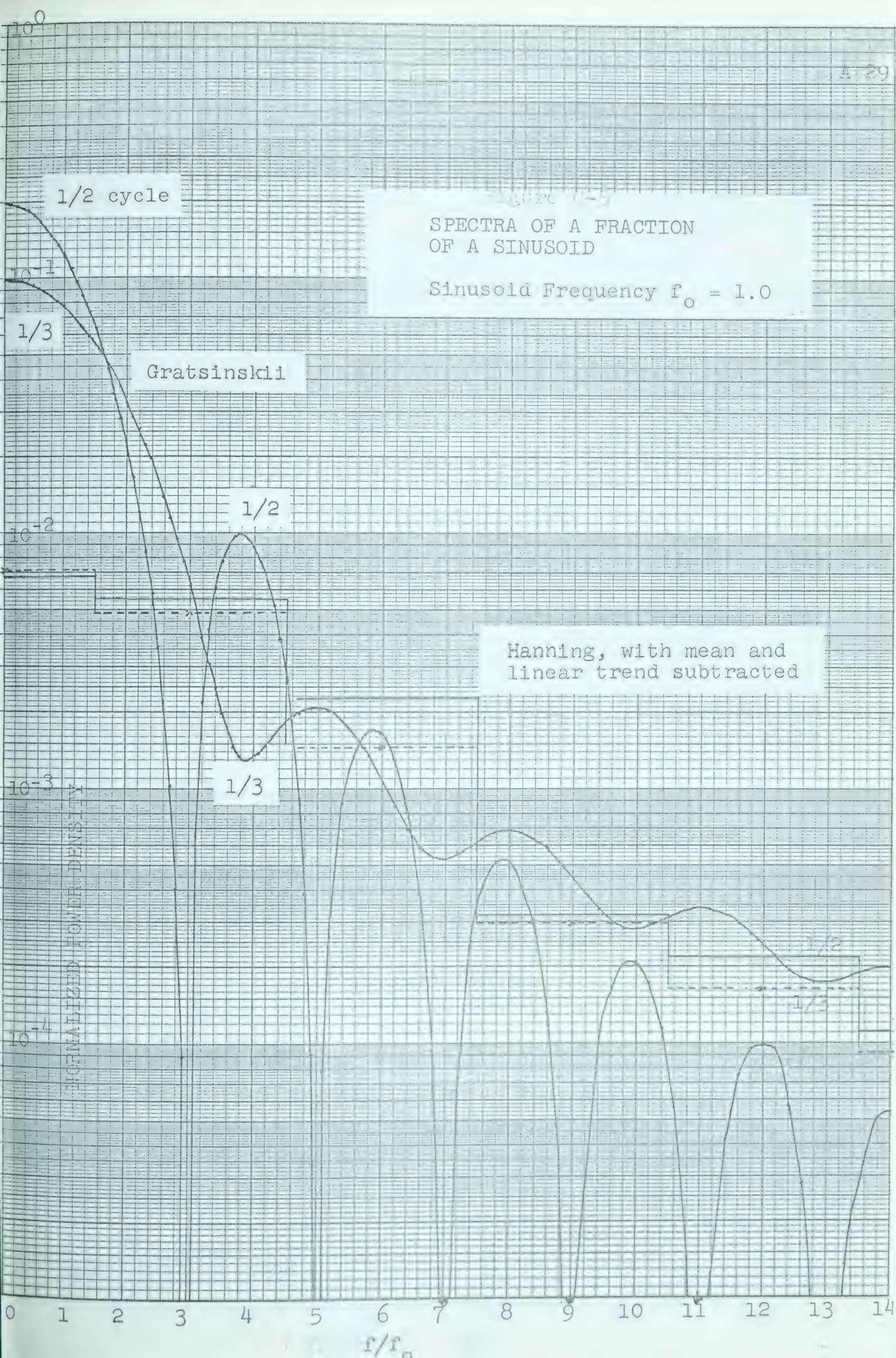
CROSP2 and CS TUKS, remove the mean but neither removes the slow trends. The program written here for the IBM 1620 and used in processing the 1961 data removes a linear trend based on the means of the first and last thirds of the record. Almost invariably the lowest frequency band contains a large percentage of the total record energy. If it were pure signal the spectra would probably be useable although the time series would first require prewhitening to prevent energy from leaking through the side lobes. More often than not, however, a large contribution is due to the baseline shift of the amplifiers used in the field due to ambient temperatures. The importance and techniques of trend removal are discussed by Blackman and Tukey (1958).

The experiments were of two kinds. One consisted of computing a number of spectra of real data, both with and without linear trends removed to determine the change in ratio and coherency. The other was the computation of the spectra of segments of sinusoids, for which the power spectra are known analytically.

Gratsinskiĭ (1962) shows that the spectrum of a fraction of a sinusoid (starting from a zero-crossing) undergoes a number of systematic changes as this fraction increases from 0.5 to 2 or more. For 0.7 of a cycle or less the spectral peak is shifted toward zero frequency and the energy is spread fairly uniformly over the spectrum up to

twice the frequency of a pure sinusoid. Some of his examples have been reprogrammed and are shown in Figure C-5. The results using the IBM 1620 program with mean and linear trend removal are shown in the same figure for two records, one consisting of the first 198 points of a 600 point cycle, the second consisting of the first 300 points of the same record. In both cases $m = 100$. All the data were normalized to have the proper variance. The results illustrate that mean and trend removal significantly decreases this long period energy and add energy to the higher frequency regions of the spectrum.

Inasmuch as the drifts actually observed are often nearly linear, it should be hoped that the subtraction of linear trend would eliminate a majority of the drift and improve the spectral estimates. The effect will of course also depend on the distribution of true energy in the lowest frequency band and the overall spectral shape. In Figure C-6 are shown two spectra calculated from the same digital record, with and without trend removal. In both cases the mean has been subtracted from the record. Figure C-7 shows the coherencies in the two cases, and Figure C-8 the resultant spectral ratios. Included in this last figure is the ratio computed after prewhitening the two series, as an indication of what this ratio "should" be. It is evident that the trend removal has decreased slightly the power in the first two bands but has added power to all others beyond the





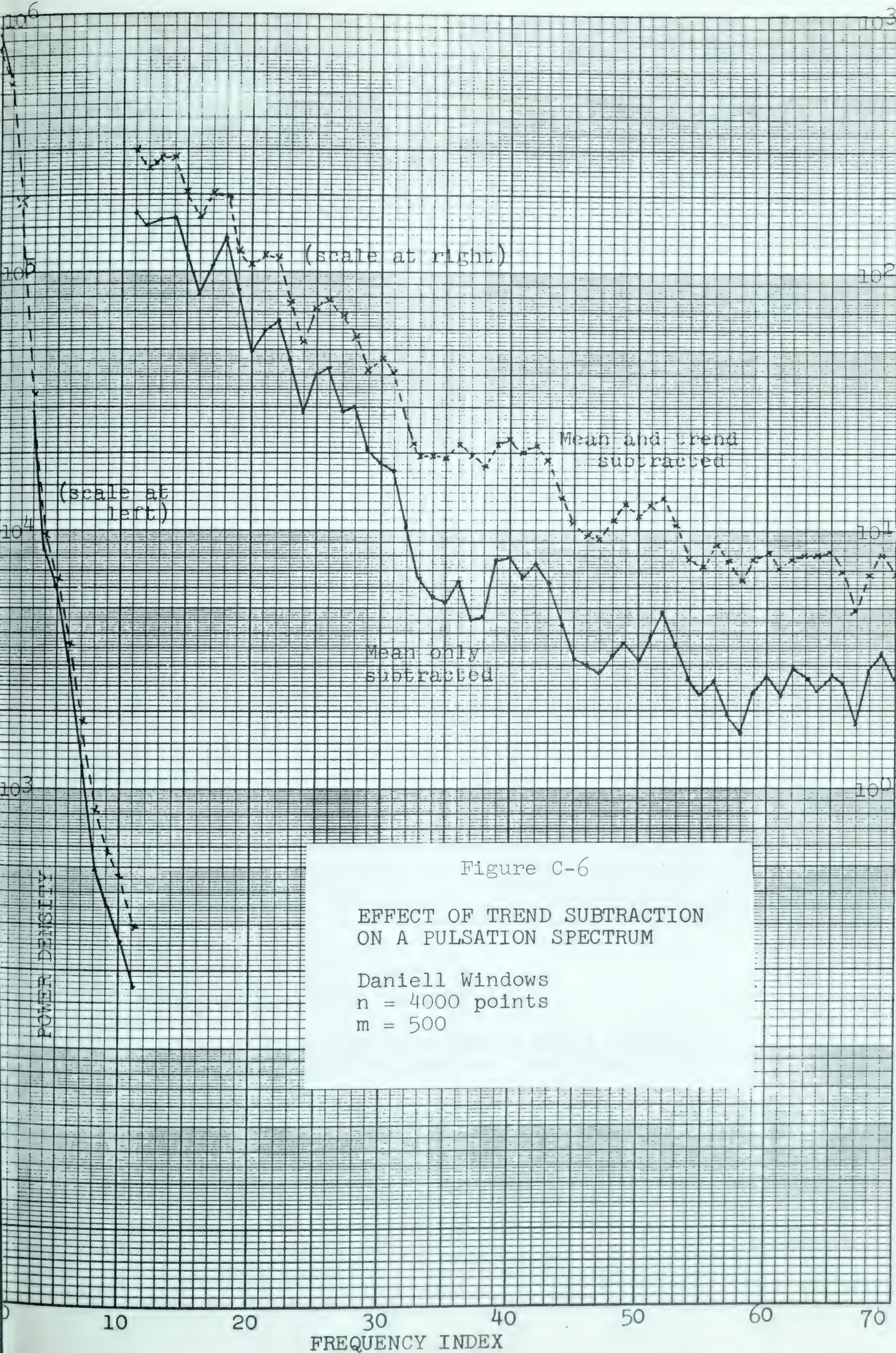


Figure C-6

EFFECT OF TREND SUBTRACTION
ON A PULSATION SPECTRUM

Daniell Windows
 $n = 4000$ points
 $m = 500$



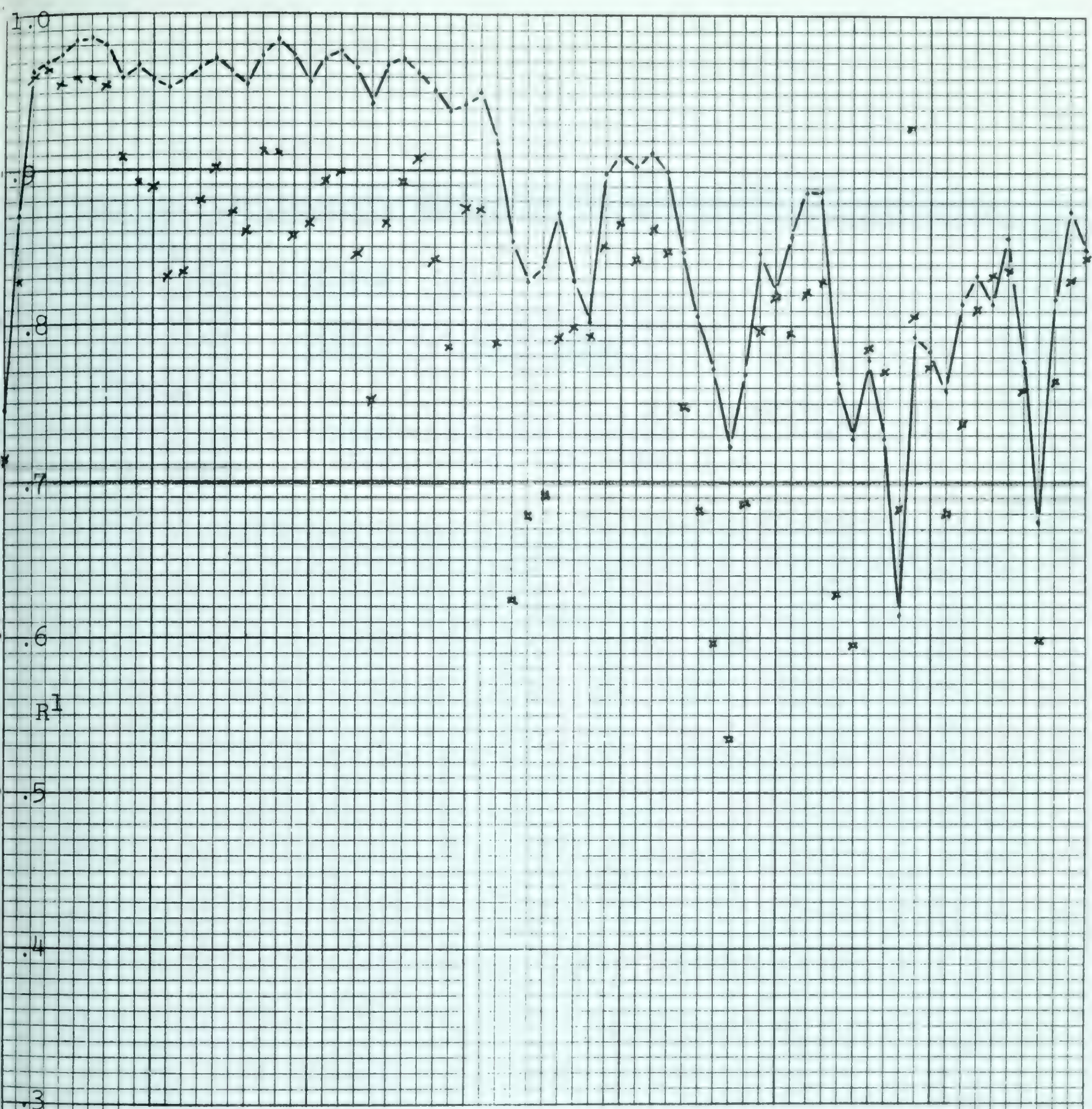


Figure C-7
EFFECT ON E-H COHERENCY OF
TREND SUBTRACTION FROM BOTH

. Mean only subtracted from E and H records
x Mean and trend subtracted from E and H records

0 10 20 30 40 50 60 70
FREQUENCY INDEX



third. It is also evident that the amounts added to the two spectra (electric and magnetic) were not the same, since the ratios are consistently larger in the trend corrected E-H pair.

In this example, removing the trend has reduced the coherency and the accuracy of the ratio in almost every frequency band including the lowest few. This example may be anomalous, as in other cases, trend removal has led to higher coherency and smoother ratios. However it does seem that trend removal must be used with considerable caution. This procedure will be discussed further in the next section.

Prewhitening

If the spectrum changes rapidly then prewhitening of the data before computing the spectrum is recommended. Since the raw high frequency spectra fall off approximately as $1/f^2$, a filter which strongly rejects the low frequencies is required. Because of the difficulties of using a computer at large distances, the only prewhitening filter used was $z_i = x_i - x_{i-1}$. The power transfer function of this filter is shown in Figure B-4 ($\lambda = -1$). This procedure invariably gave much improved ratios and coherencies. The low frequency (LF) data were not treated, since, with two exceptions, their spectra were already relatively flat and their coherencies high. (The low frequency data were subjected

to trend removal. In view of the results of the previous section, it appears likely that a form of prewhitening similar to that used for the HF data, but less drastic, would have given better results than the removal of linear trends.)

Figures C-9 and C-10 show HF spectra and coherencies without and with prewhitening, respectively. Figure C-11 shows the resultant ratios in the two cases. These ratios are computed from the raw spectra and are tilted by the difference in response curves of the electric and magnetic detection systems. Other examples of the effectiveness of prewhitening in smoothing spectral ratios can be seen in Figure C-8 and by comparing Figures C-19 and C-20.

Several sets of HF data were analyzed both with and without trend removal prior to prewhitening. It was found that the maximum spectral differences were of the order of 1-2 %. Thus, if one is going to use prewhitening filters which incorporate drastic long period rejection, trend removal is normally not required. This is, of course, expected.

Spectral Programs

Our early analyses included two types of data which are very demanding of spectral computations: sinusoidal

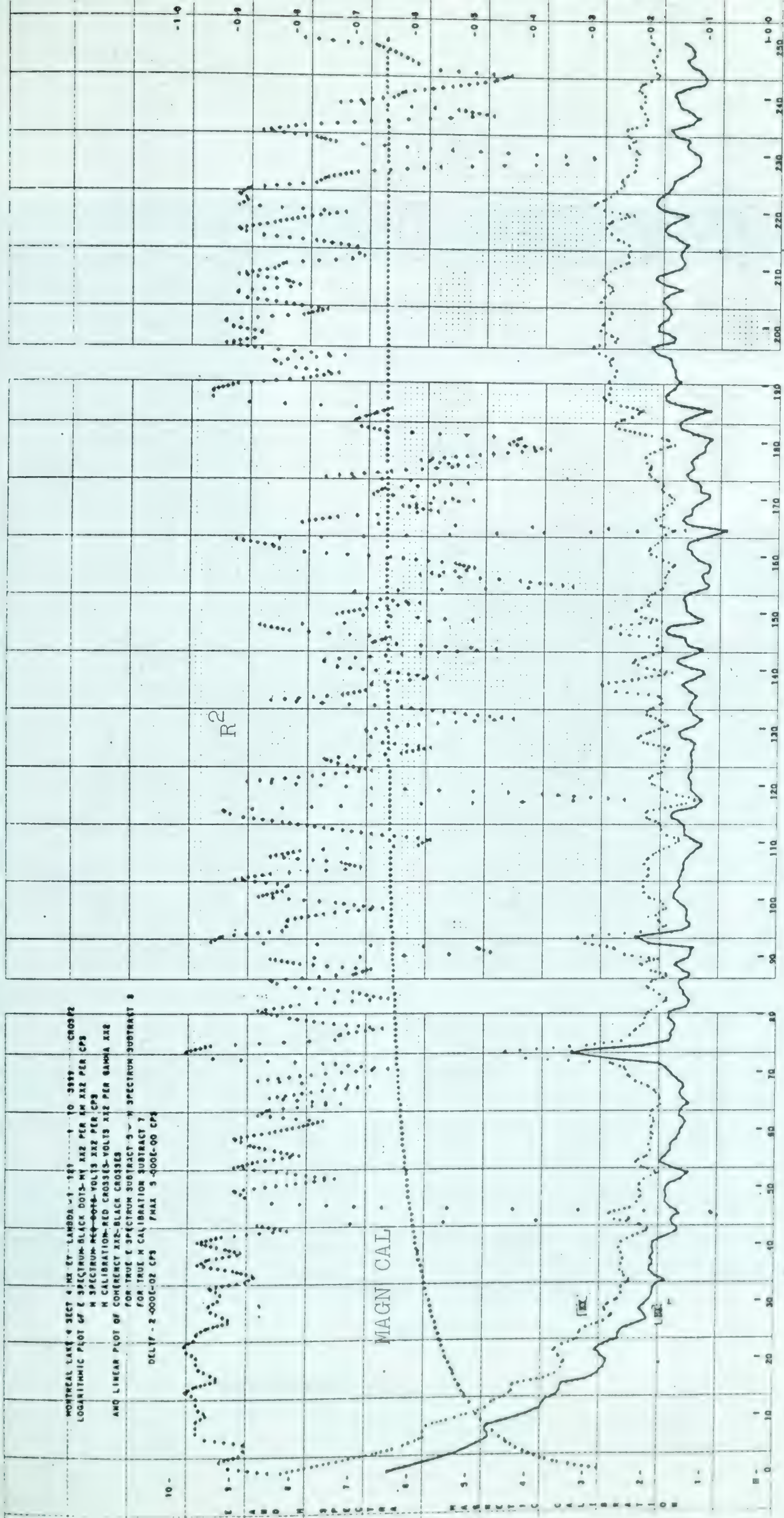
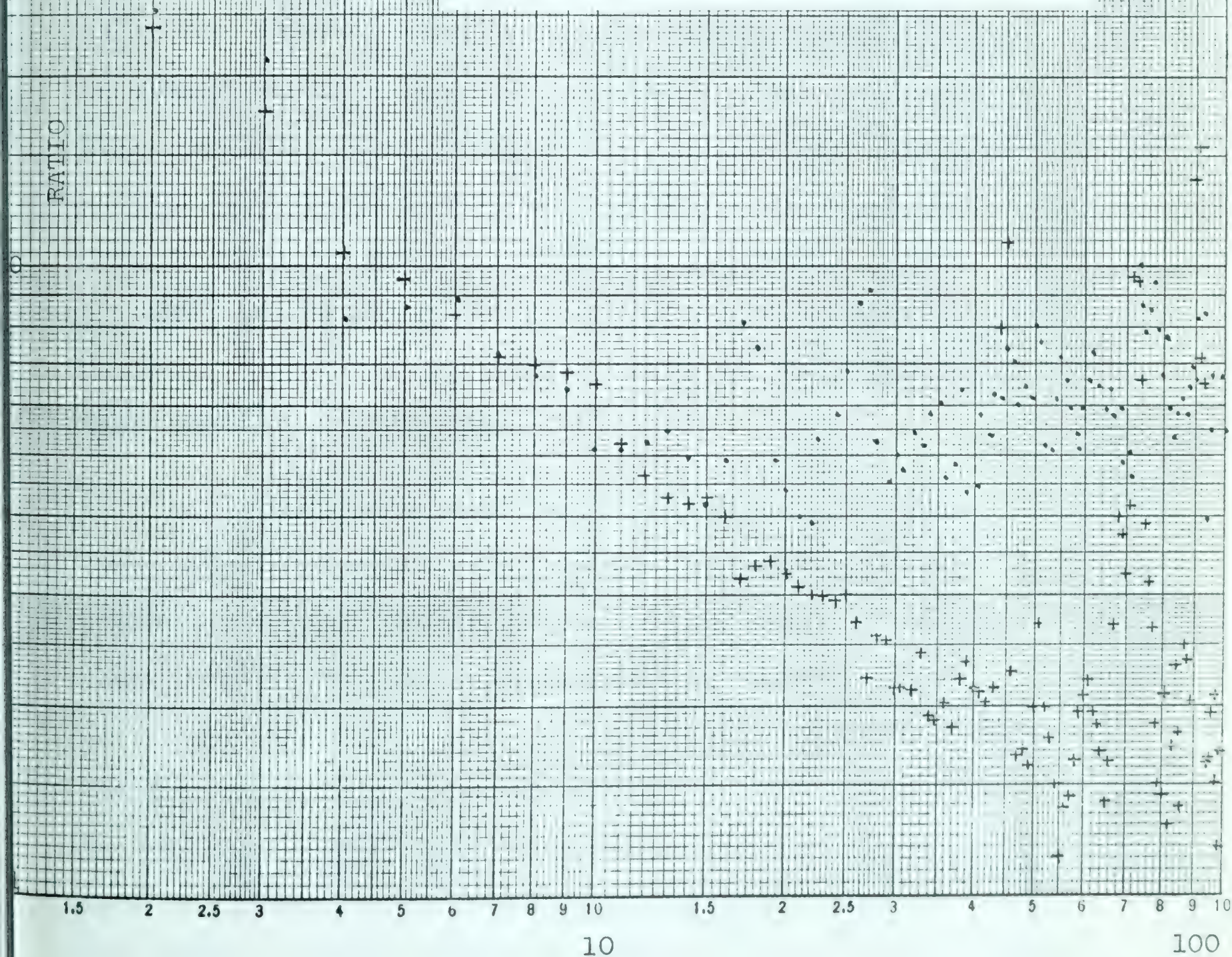


Diagram 79

Figure C-10. Illustration of HF spectra with prewhitening.

FIGURE C-11

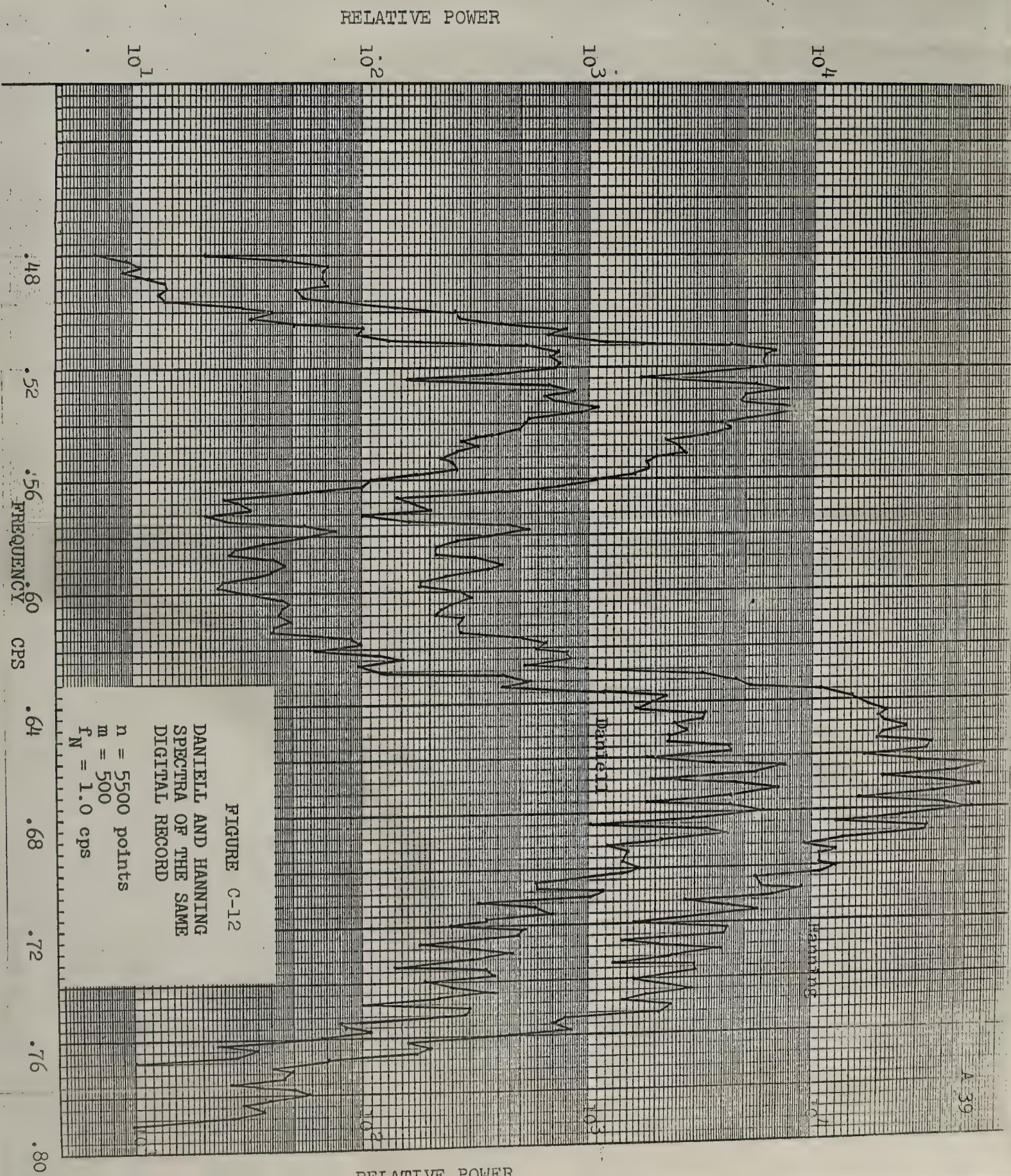
SPECTRAL RATIOS, ILLUSTRATING
EFFECT OF PREWHITENING○ Raw
+ Prewhitened

FREQUENCY INDEX

calibrations and untreated HF data. The digital data were obtained by a single channel conversion and the spectra calculated using CS TUKS which computes a hanning estimate. One source of difficulty arises from the negative side lobes of this window. These resulted in negative spectral estimates over as much as 90% of the spectrum when applied to the $1/f^2$ HF spectral functions. We also attempted to calculate the frequency response of the detection systems by comparing the computed magnitudes of spectral peaks of each component with those computed for an input calibration signal. The results were very erratic. This was probably due, in part, to slightly different conversion rates ($< .01\%$) and to not quite identical record segments. Another source of error was the contamination of small peaks by the side lobes of large peaks.

About this time the program CROSP2 (Simpson et al, 1961; 1962; Galbraith, 1963) became available. Since it computes a Daniell estimate and is very fast, it seemed ideal for our purposes. Micropulsation "pearl" data, previously analyzed using the hanning window, were kindly run for us by Prof. T. R. Madden using a Daniell estimate. A comparison showed that the Daniell window resolved the spectral fine structure of the pearls much more clearly on the sides of steep slopes, as shown by Figure C-12. Ratios





computed from these Daniell estimates in the same frequency range were also more consistent with the known electrical properties of the area. Coherency behaved much more reasonably in that values were always between zero and one. It is also found that they do not change drastically with m . As a consequence, for a majority of the 1962 analyses CROSP2 was used. A few data sets have since been found for which CS TUKS gives better results than CROSP2. (Other spectral programs are available, notably BOMM (Bullard et al, 1962) but CROSP2 would appear to be desirable for its speed.)

The two windows were compared by using the programs to analyze several kinds of signals: computer generated sinusoids of various amplitudes and frequencies, segments of calibration signal digitized from tapes recorded in the field, and natural data. It should be pointed out that CROSP2 rounds the records after removing the mean, but before computing correlations. The errors introduced will not exceed 1 part in 800 of the range of data values. CS TUKS uses the full data accuracy. This emphasizes that the results of computational experiments with CS TUKS and CROSP2 may reflect not only the different window properties but also the particular computational procedures involved in the program. Accuracy of the data itself is limited by the 3 digit plus sign fixed point form (1 part in 2000 of the maximum range). Thus at frequencies where the signal energy



is sufficiently low, the CROSP2 round off becomes evident in the spectra (Figure C-9) which are overly smooth, coherencies which are low, and ratios which are meaningless.

The two series

$$S_1(k) = 200 \sin(2k\pi/T)$$

and

$$S_2(k) = 900 \sin(2k\pi/T)$$

where $k = 1, 2, \dots, 4000$ (approximately)

$T = \text{period}$

were analyzed by each program to see whether the correct ratio was indicated on the peaks, and how this ratio changed with distance from the peaks. In both programs ratios computed at the peaks were correct to within one percent. In the CS TUKS output this same spectral ratio was maintained to within a few percent over the entire frequency range of the analysis. Ratios of the two CROSP2 spectra decrease monotonically to the order of unity at higher frequencies. The CS TUKS spectra alternated between positive and negative values beginning two points away from the peak whereas the CROSP2 spectra were all positive with the exception of a few points well down into noise.



Figure C-13 shows the spectra of $S_2(k)$ for a series of frequency $f_0 = .081 f_N$. As f increases beyond f_0 both spectra fall off 5 or 6 orders of magnitude with CS TUKS decreasing more rapidly with alternate values being negative. For f less than f_0 , CROSP2 only falls off 3 orders of magnitude to the program noise level while CS TUKS is down in excess of 5 orders of magnitude. The precise behaviour of the spectra depends on the place in the cycle where the series are terminated, and in the case of CROSP2, on input data format. The changes in relative energy dependent on these factors is negligible. This is expected since the series contained over 150 cycles.

These results indicate that the erratic calibration results using CS TUKS may not have been the fault of the program. It appears likely that the errors may have been caused by comparing slightly different sections of tape, using slightly different conversion rates, and if not enough cycles were used, different starting and termination points of the cycles. If errors are introduced by the side lobes, the problem could be resolved by analyzing one frequency at a time. Further experiments using multi-channel conversion are recommended.

1. The first part of the document discusses the importance of maintaining accurate records of all transactions and activities. It emphasizes the need for transparency and accountability in financial reporting.

2. The second part of the document outlines the various methods and techniques used to collect and analyze data. It includes a detailed description of the experimental procedures and the statistical analysis performed.

3. The third part of the document presents the results of the study. It includes a series of tables and graphs that illustrate the findings of the research. The data shows a clear trend of increasing activity over time.

4. The fourth part of the document discusses the implications of the findings. It suggests that the results have significant implications for the field of study and may lead to further research in this area.

5. The fifth part of the document provides a conclusion and a summary of the key findings. It reiterates the importance of the study and the need for continued research in this field.

6. The sixth part of the document includes a list of references and a bibliography. It cites the various sources used in the study and provides a comprehensive overview of the literature in this area.

7. The seventh part of the document includes a list of appendices and a glossary. It provides additional information and definitions for the terms used in the study.

8. The eighth part of the document includes a list of figures and a list of tables. It provides a detailed description of the visual elements used in the study.

9. The ninth part of the document includes a list of footnotes and a list of endnotes. It provides additional information and clarifications for the text.

10. The tenth part of the document includes a list of acknowledgments and a list of contributors. It expresses gratitude to the individuals and organizations that supported the study.

FIGURE C-13

SPECTRA OF A COMPUTER-GENERATED
SINUSOID, $f = .081 f_N$

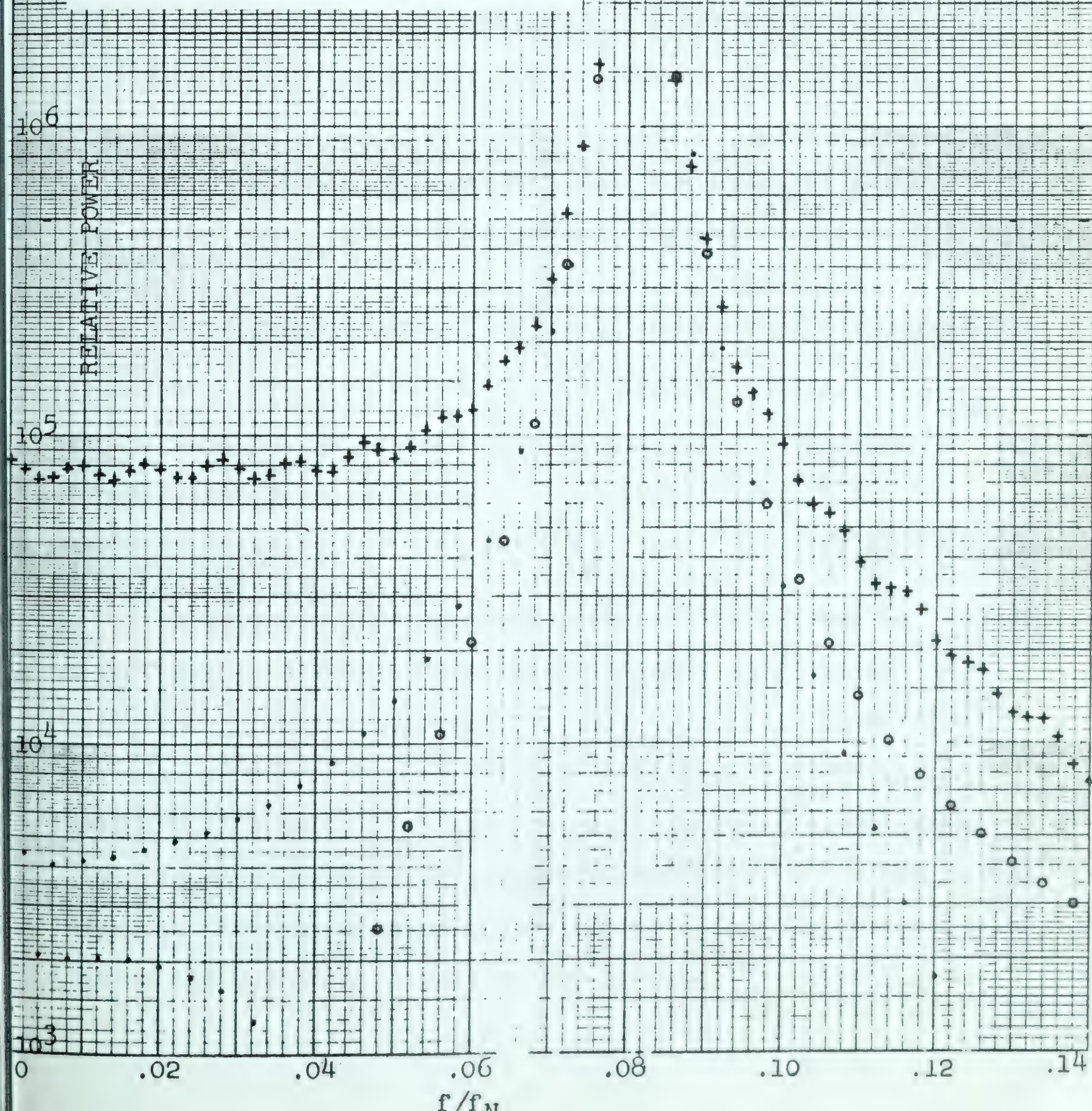
$n = 3927$

$m = 500$

+ CROSP2

• CS TUKS - Positive

○ CS TUKS - Negative



As applied to CROSP2, this problem has been treated by analyzing calibration signals converted by the 2-channel analog-to-digital conversion system. In the first example, a square wave of frequency .0961 cps was converted 13.6 times per second on two channels whose sampling instant differed by 12.4 ms. Auto- and cross-spectra were computed for the first 1000 points with $m = 250$. One of the spectra, coherency, and percentage difference between the two spectra are plotted in Figure C-14. The average difference of 2.3% is due to insertion loss differences between the two playback filter systems. The short dashed lines over the spectral peaks are the heights (relative to the first peak) predicted for an infinite number of input cycles. With increasing frequency the peaks computed for the odd harmonics diverge from their predicted values but the amount of energy in the even harmonics is seen to increase. At frequencies greater than 4 cps the playback filter reduces the signal at a nominal rate of 24 db per octave.

There are a number of interesting features in this figure. Ratios at odd harmonic peaks fall within 2-3% of the mean well beyond the 19th harmonic. There is an increase of the (smoothed average) ratios with increasing frequency, to about +10% near 5 cps, beyond which they again diminish. This suggests response differences in the two playback filters. Despite this, 50 percent of the power ratios lie within 6 percent of the mean.



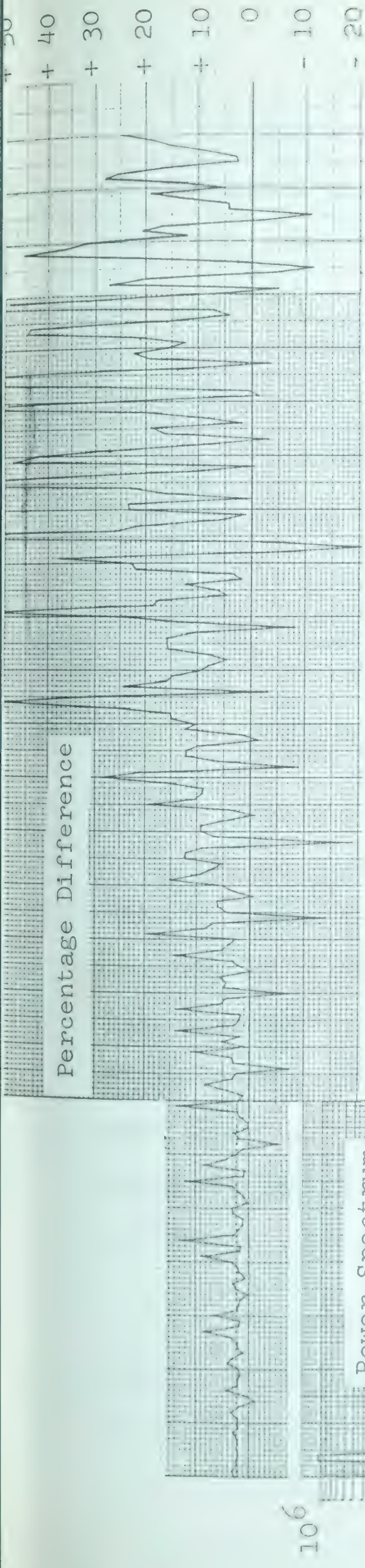


Figure . Spectrum of square wave of frequency .0961 cps with coherency and percentage difference between simultaneous conversions.



Another point of interest is that, if ratios are discarded on the basis of coherency the scatter becomes much less. There appears to be a limit (at $R \approx .95$) above which this is no longer very effective. More effective is the process of also discarding ratios adjacent to points where $R < .95$. Very few ratios near the mean, and all but one of the extreme values are eliminated in this manner. Since the two series used are derived from a single input signal converted at two slightly different instants, the results are also of interest to our earlier discussion of conversion techniques.

In the analysis of real calibration signals, spectral ratios versus frequency were computed. Their ratios agreed with predicted values to within two percent which is the accuracy of the predictions themselves. One advantage of digital processing of calibration data is that it serves as a check of the entire record and playback system. A second advantage lies in the fact that, in the magnetic systems there is always some natural signal superposed on the calibration. Digital processing permits calibrating even during periods of large natural signal.

An example is next shown in which CS TUES indicates larger coherencies than does CROSP2, although the ratios are of comparable smoothness. One pair of digital E-H

records had mean and trend removed. They were then analyzed by CS TUKS and CROSP2. The records were then prewhitened and reanalyzed. The spectral pairs and coherencies-squared are shown in Figures C-15, C-16, C-17, and C-18. The E/H ratios are shown in Figures C-19 (not prewhitened) and C-20 (prewhitened).

Finally, Figure C-21 illustrates the difficulties of using CS TUKS coherencies as a measure of spectral quality. Although the spectra appear to be unrelated, the coherency varies from near zero to much greater than one ($R^2 > 1$ is plotted at $R^2 = 1$). The Daniell window also encounters difficulty (Figure C-9). However the CROSP2 coherencies become very small indicating the unreliability of spectral values.

Conclusions

With several qualifications, it is concluded that digital power spectrum analysis can be used as a qualitative tool in the processing of magnetotelluric data. By operating on series whose spectra are relatively flat, the accuracy of estimates is significantly enhanced and the range of frequencies over which reliable estimates are obtained is increased. Prewhitening was the most effective process found for smoothing ratios and increasing coherency. Removal of a linear trend does not always improve the results.

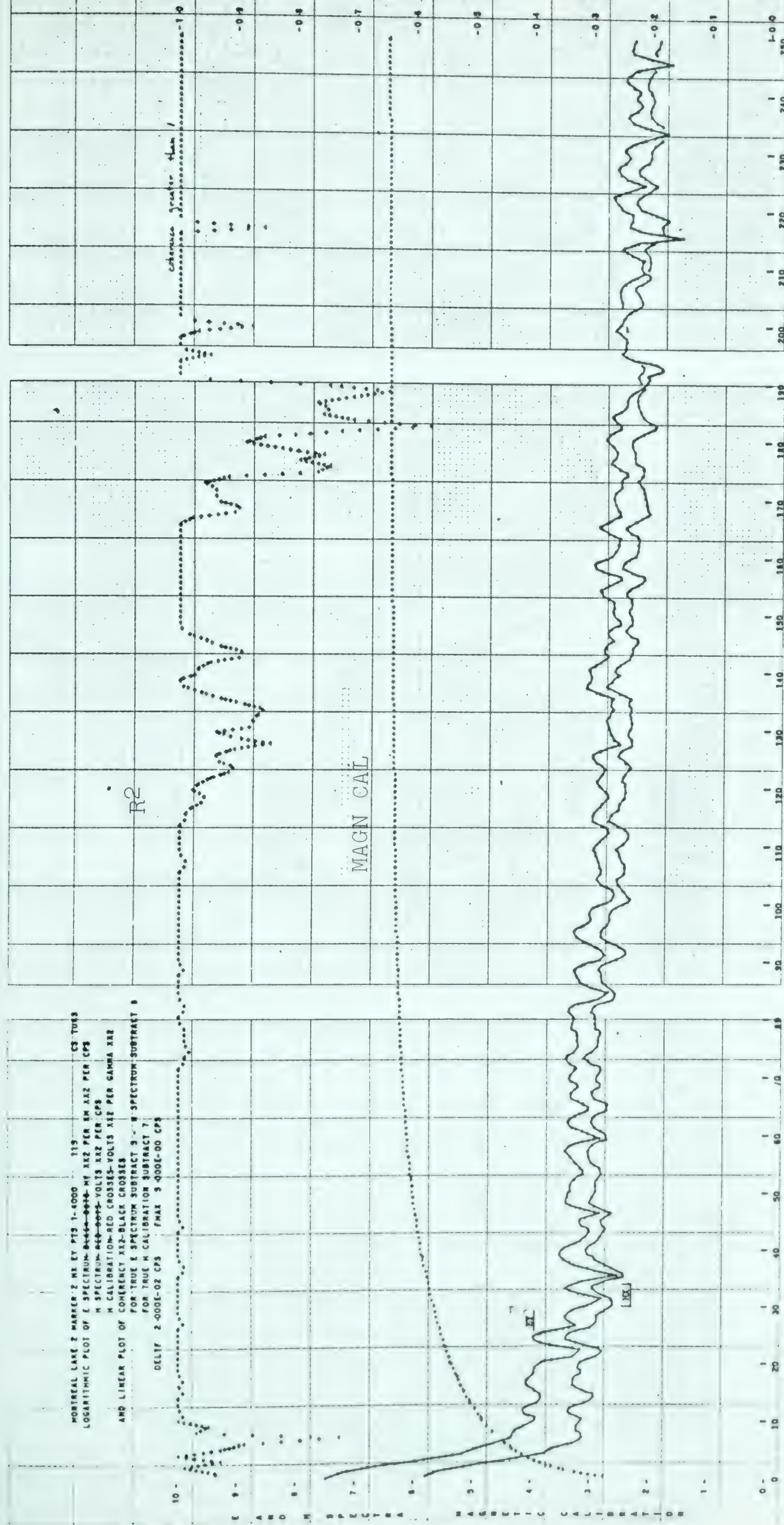
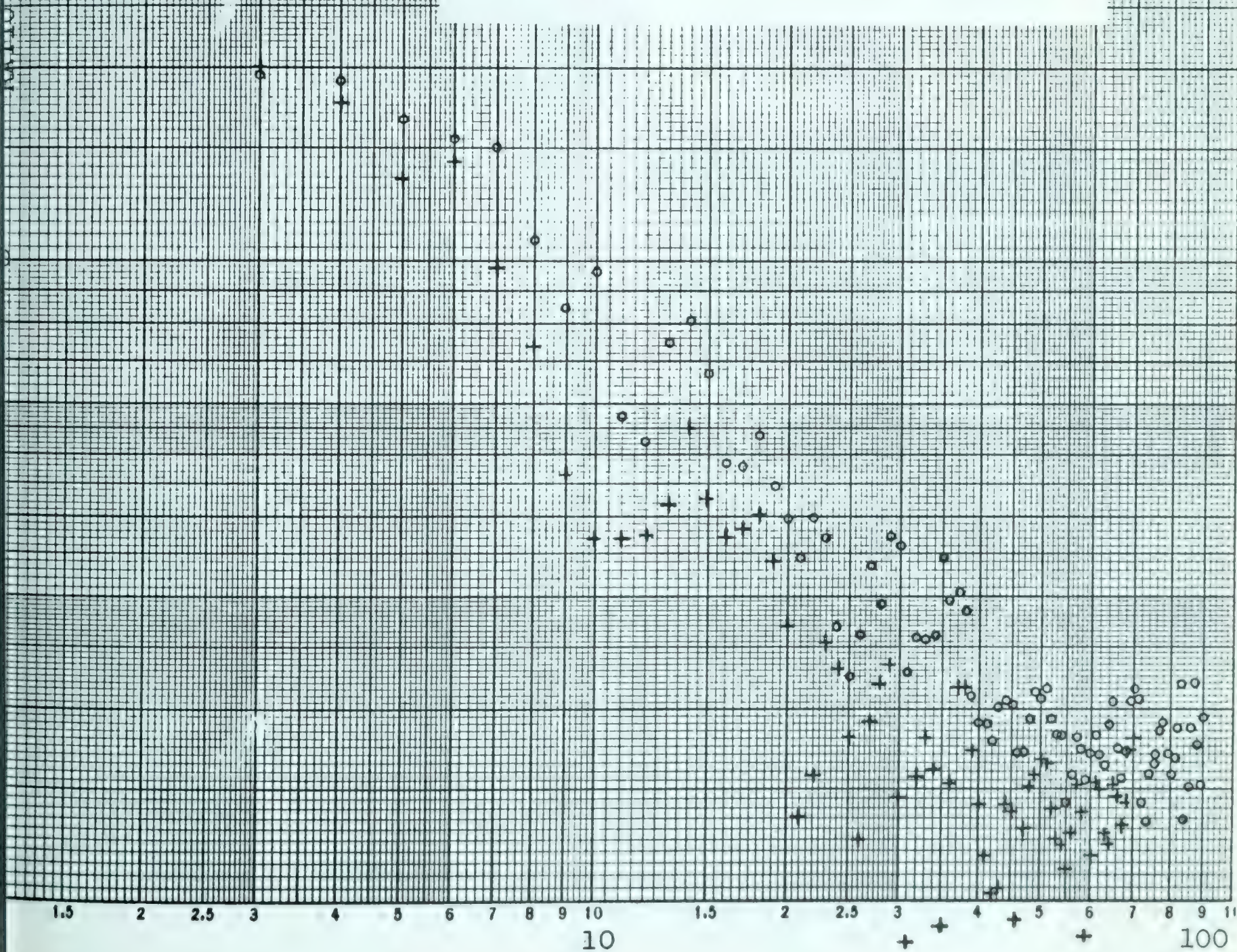


Figure C-15. Illustration of HF spectra without prewhitening (CS TUGS).

FIGURE C-19

SPECTRAL RATIOS, FOR COMPARING
CROSP2 WITH CS TUKS

Raw Data

○ CROSP2
+ CS TUKS

FREQUENCY INDEX

FIGURE C-20

SPECTRAL RATIOS, FOR
COMPARING CROSP2 WITH
CS TUKS

Prewhitened Data

○ CROSP2
+ CS TUKS

1.5 2 2.5 3 4 5 6 7 8 9 10 1.5 2 2.5 3 4 5 6 7 8 9 10
10 100

FREQUENCY INDEX

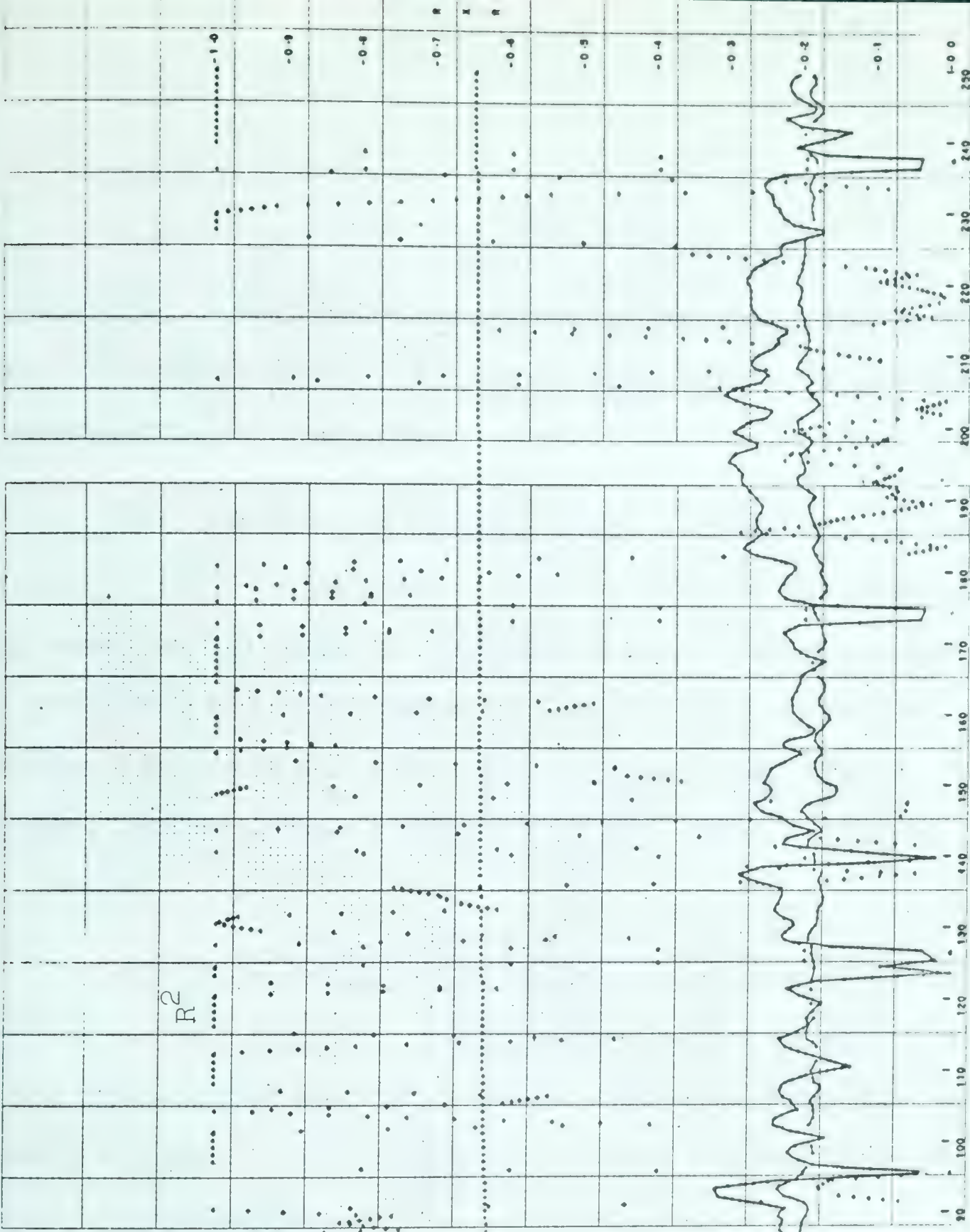
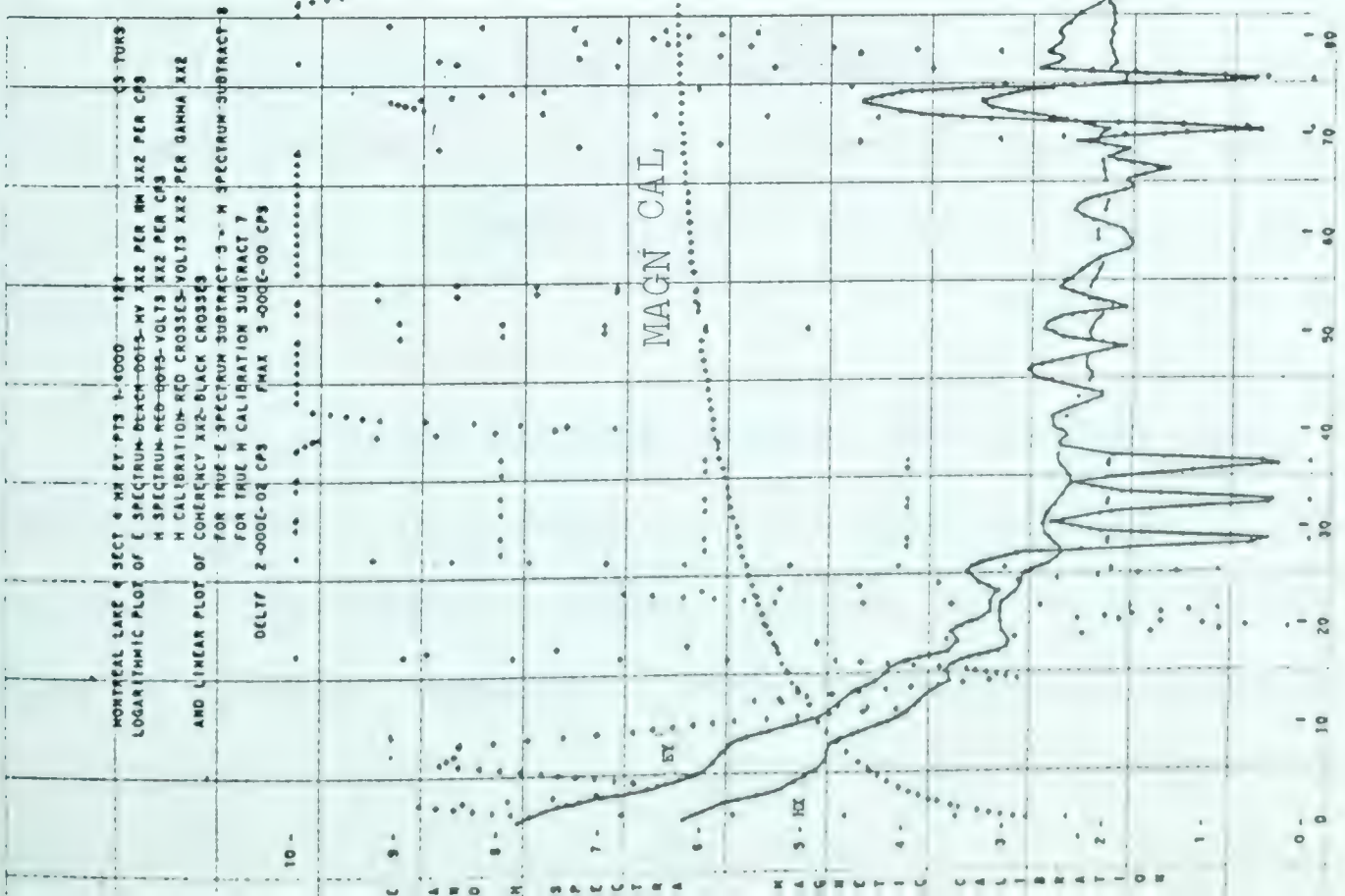


Diagram 83

Figure C-21. Illustration of the unreliability of CS TUKS coherency as measure of spectral quality.

If possible, undesirable energy should be removed from the lowest frequency band by a prewhitening filter rather than by subtraction of the trend.

In the case of spectra which contain one or more spikes, Daniell windows were found to be more satisfactory than were the hanning, in that the Daniell estimates are all positive, all coherencies are in the range zero to one (hanning estimates are often greater than one) and the spectral ratios are as predicted to the order of one or two percent.

It is necessary to synchronize digital records if they are to be compared. This is obvious for comparison in the time domain and our results show that they must be closely aligned if their spectral ratios and coherencies are to be meaningful.

Coherency is only a rough measure of the quality of data and spectra, as judged by spectral ratios. Even very large values of coherency ($> .99$) do not ensure smooth ratios.

For a given digital record, the spectra and consequently coherency depend on the computational techniques used in the particular program. Hence, values of coherency cannot be directly compared. Some experience is required with each program to enable one to judge the significance of its coherencies in a particular situation.

Appendix D

PLOTS OF SPECTRAL DATA

Notation and Conventions

As an aid in using the graphs, the abbreviated notation used on the plots is explained below.

<u>Notation</u>	<u>Meaning</u>
DELTF	- frequency increment at which parameters are calculated
FMAX	- maximum frequency calculated or plotted on graph
K	- frequency index (true frequency at K is K times DELTF)
LAMBDA - 1	- indicates data have been prewhitened using $z_i = x_i - x_{i-1}$
RHO	- apparent resistivity
R X R	- coherency squared
WEIGHTED COHERENCY	- $\frac{P_x(R_x \text{ X } R_x) + P_y(R_y \text{ X } R_y)}{P_x + P_y}$
	where P_x, P_y are H_x and H_y spectral densities; R_x, R_y are $H_x - H_z$ and $H_y - H_z$ coherencies-squared
XX	- indicates exponentiation

On some graphs the term "COHERENCY" is used while on others "COHERENCY XX 2" appears. In both cases these should be read as coherency-squared.



Diagram 25 will be used to explain the numbers on the record identification line. " 7 " indicates the analog-to-digital conversion run while "1 TO 1087" indicates the points from this conversion that were used in the analysis.

The \underline{E} and \underline{H} spectral plots have been corrected for amplifier settings, filtering during conversion, and prewhitening (if used). The electric spectra have also been corrected for the response of the detection system while for the magnetics it has been plotted on the same graph. Although the graphs indicate an absolute level for the spectra, there is an insertion loss of 41.5 percent in the analog-to-digital conversion system which has not been taken into account. Values of coherency-squared which are greater than one are plotted as equal to one. On graphs which are plotted as a function of K , the calculated values are plotted at integer values of K , with points between plotted using linear interpolation (except for apparent resistivity curves for which there is no interpolation). On graphs, which are plotted as a function of period, there is no interpolation. In this case, those points for which T is the same to two significant figures are averaged before plotting. All plots of field ratios are in terms of power.



Arrangement of Plots

This appendix contains the machine plots used in interpretation of the spectral data. For completeness of each set, those used in the text as examples are repeated in this section and are designated by the same diagram number.

The plots are arranged in two sets:

- (a) Plots of apparent resistivity and phase versus period.

The averaged Montreal Lake plots are followed by the plots from individual Montreal Lake tapes and the southern Alberta data in alphabetical order.

- (b) Plots of other parameters.

The plots from each tape are grouped together. The Montreal Lake data are first with the tape number used to determine sequence and the southern Alberta data following in alphabetical order. The data from each tape are arranged as follows:

Low Frequency (CROSP2 used for all spectral calculations)

- (1) H_x and E_y spectra, coherency-squared, H_x calibration
- (2) H_y and E_x spectra, coherency-squared, H_y calibration
- (3) H_z spectrum, vertical-horizontal power ratio, weighted coherency-squared, H_z calibration
- (4) H_x-H_z and H_y-H_z coherencies-squared



- (5) H_z/H_x and H_z/H_y power ratios
- (6) apparent resistivity versus frequency (southern Alberta data only)
- (7) any additional plots

High Frequency

- (8) H_x and E_y spectra, coherency squared, and H_x calibration (CROSP2 , prewhitened)
- (9) H_y and E_x spectra, coherency squared, and H_y calibration (CROSP2 , prewhitened)
- (10) any additional plots



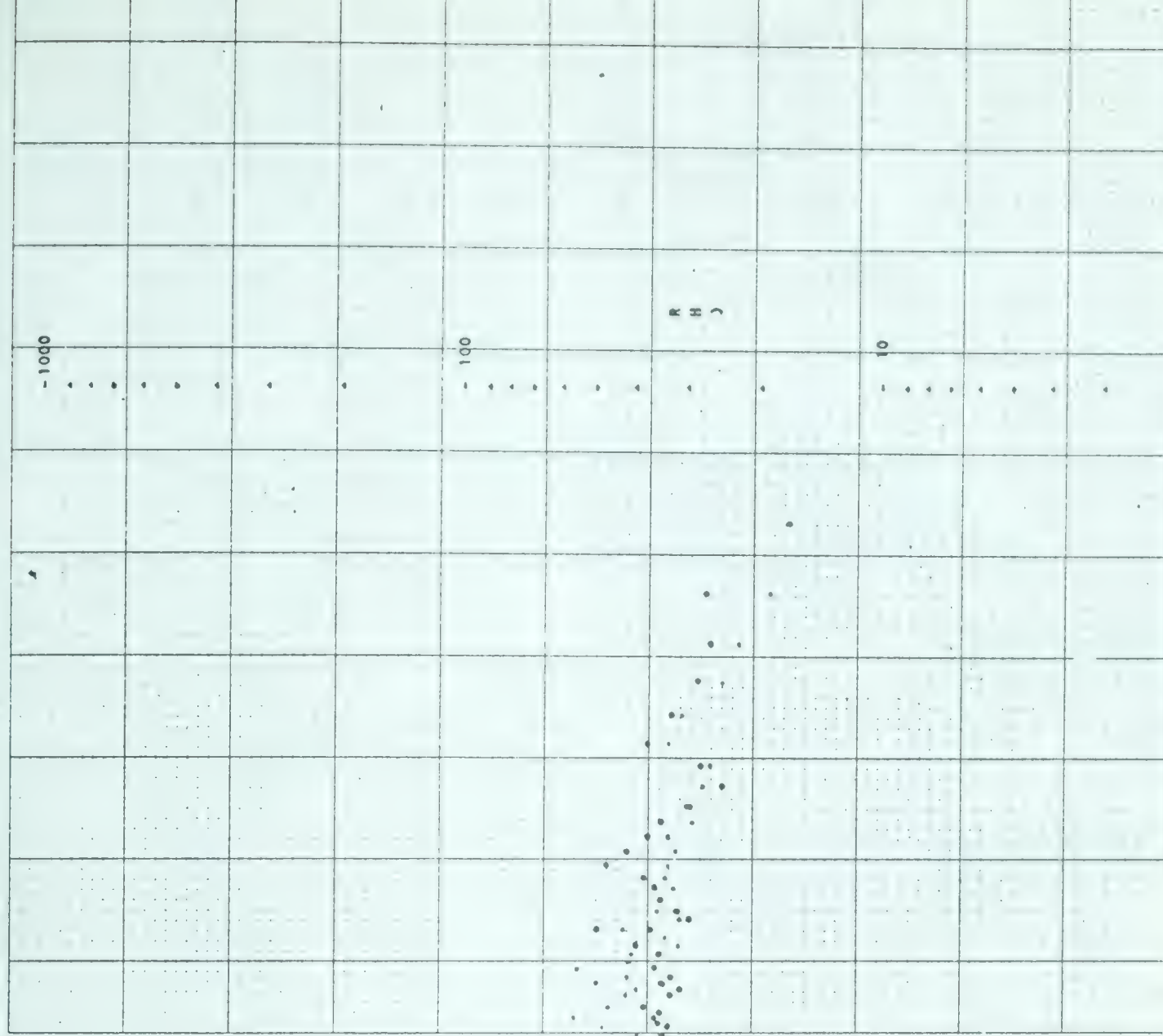
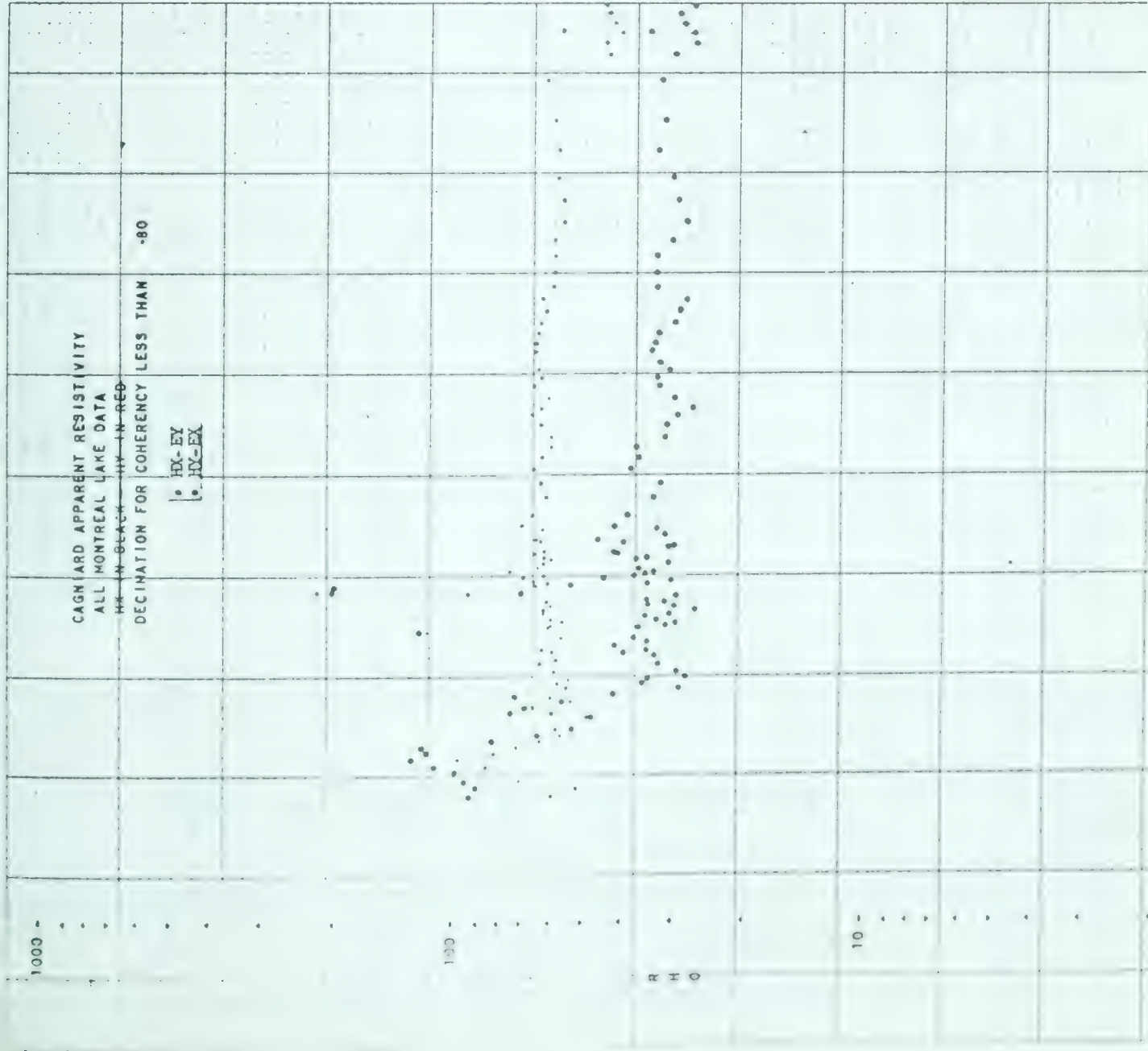
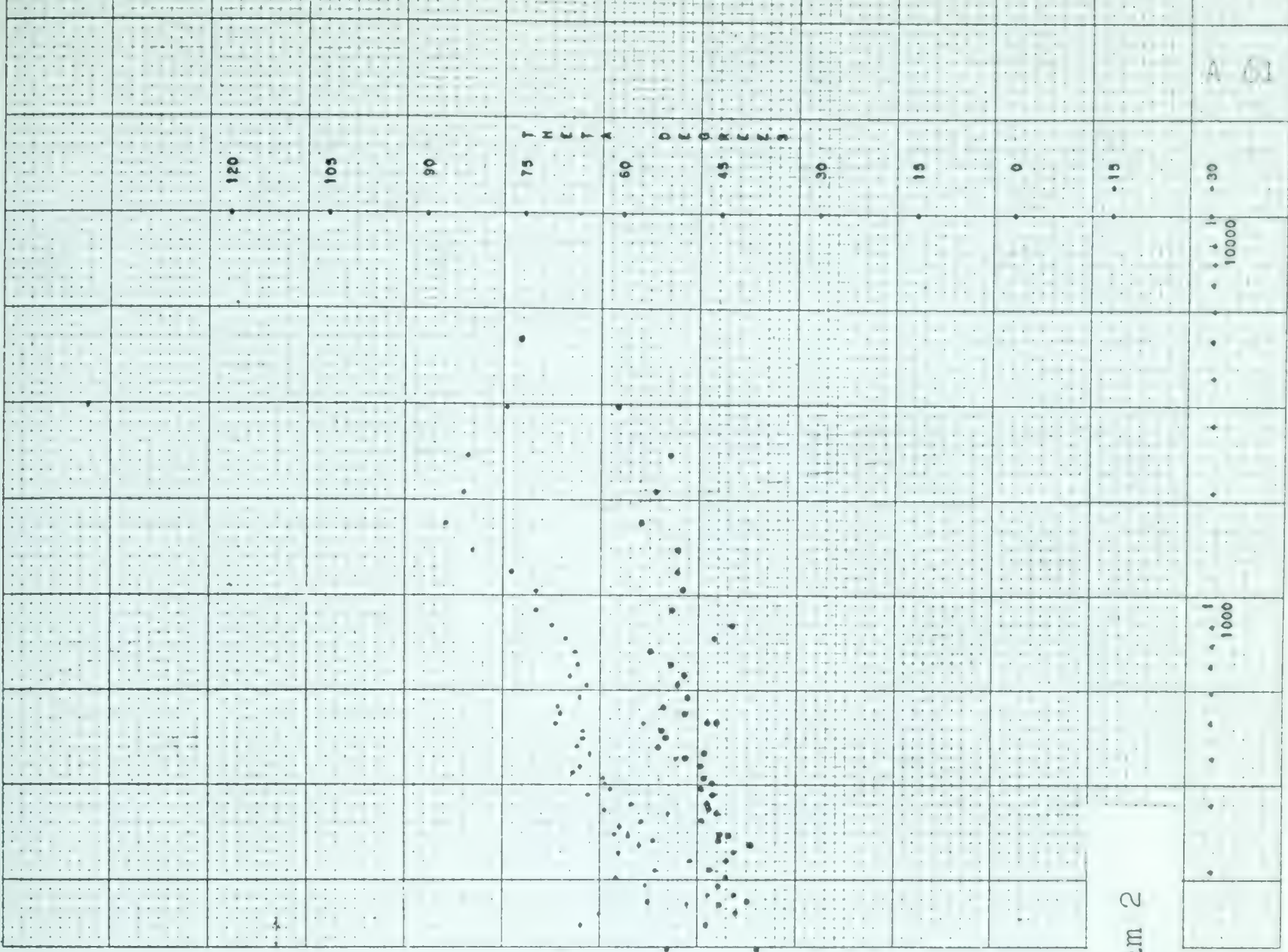
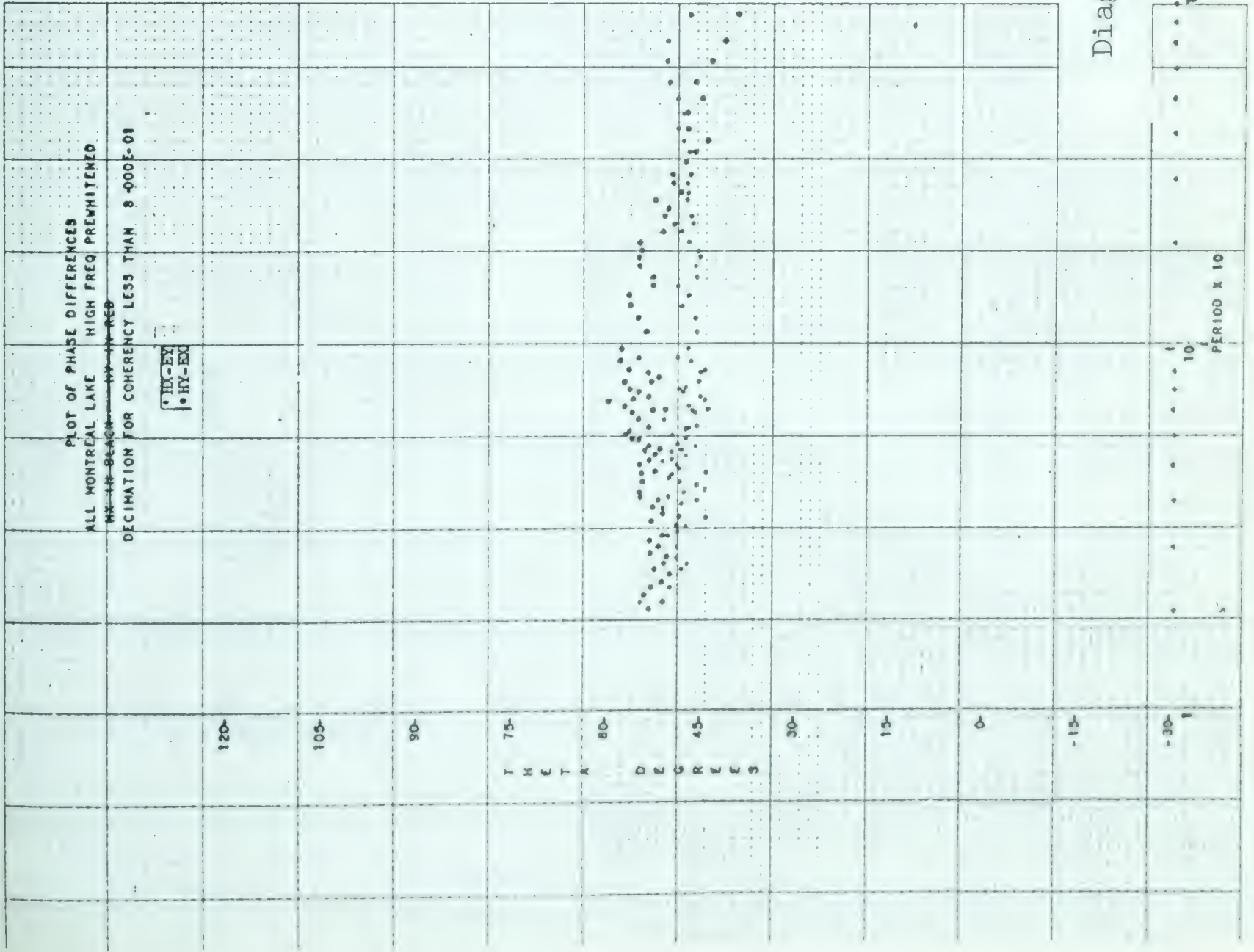


Diagram 1



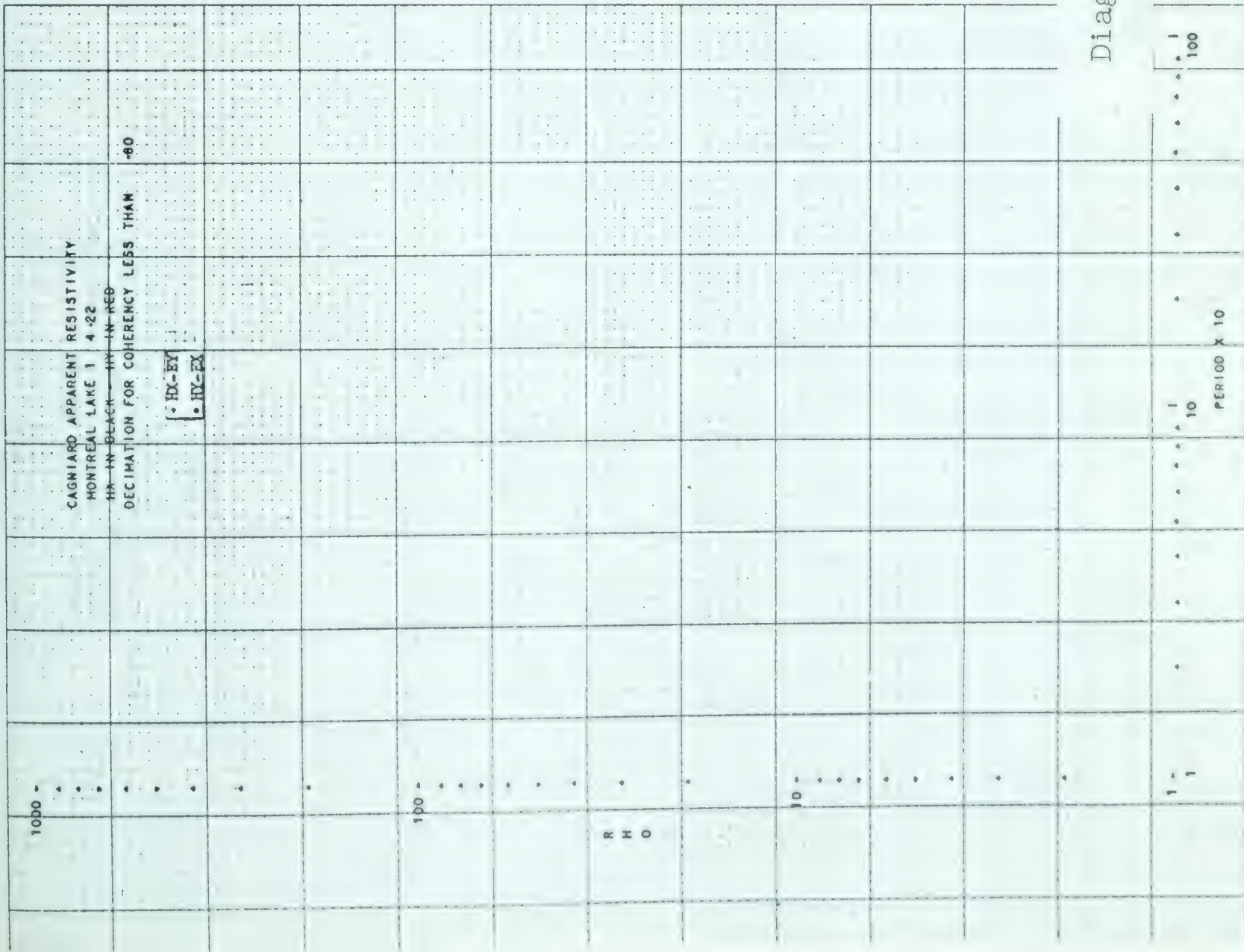
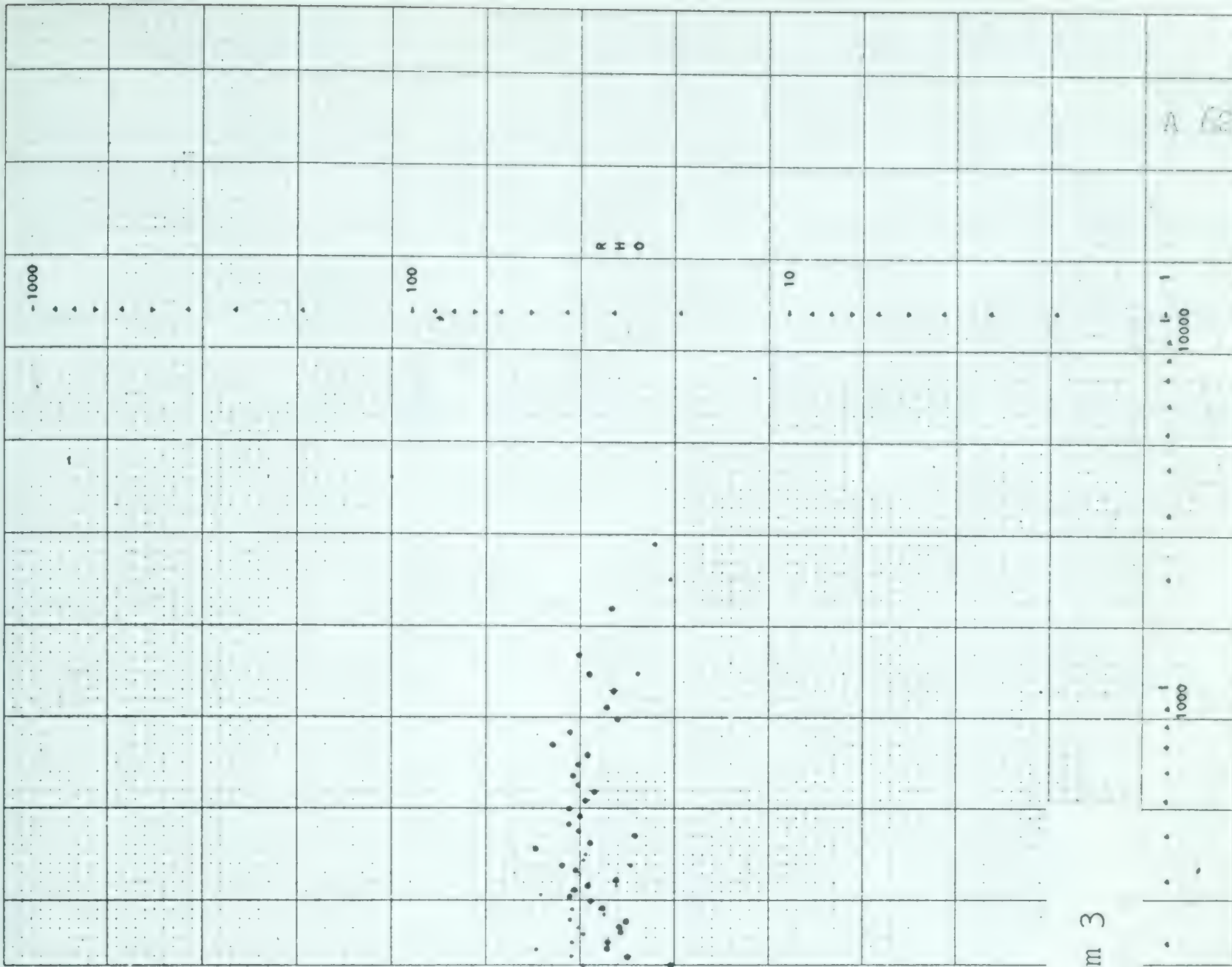
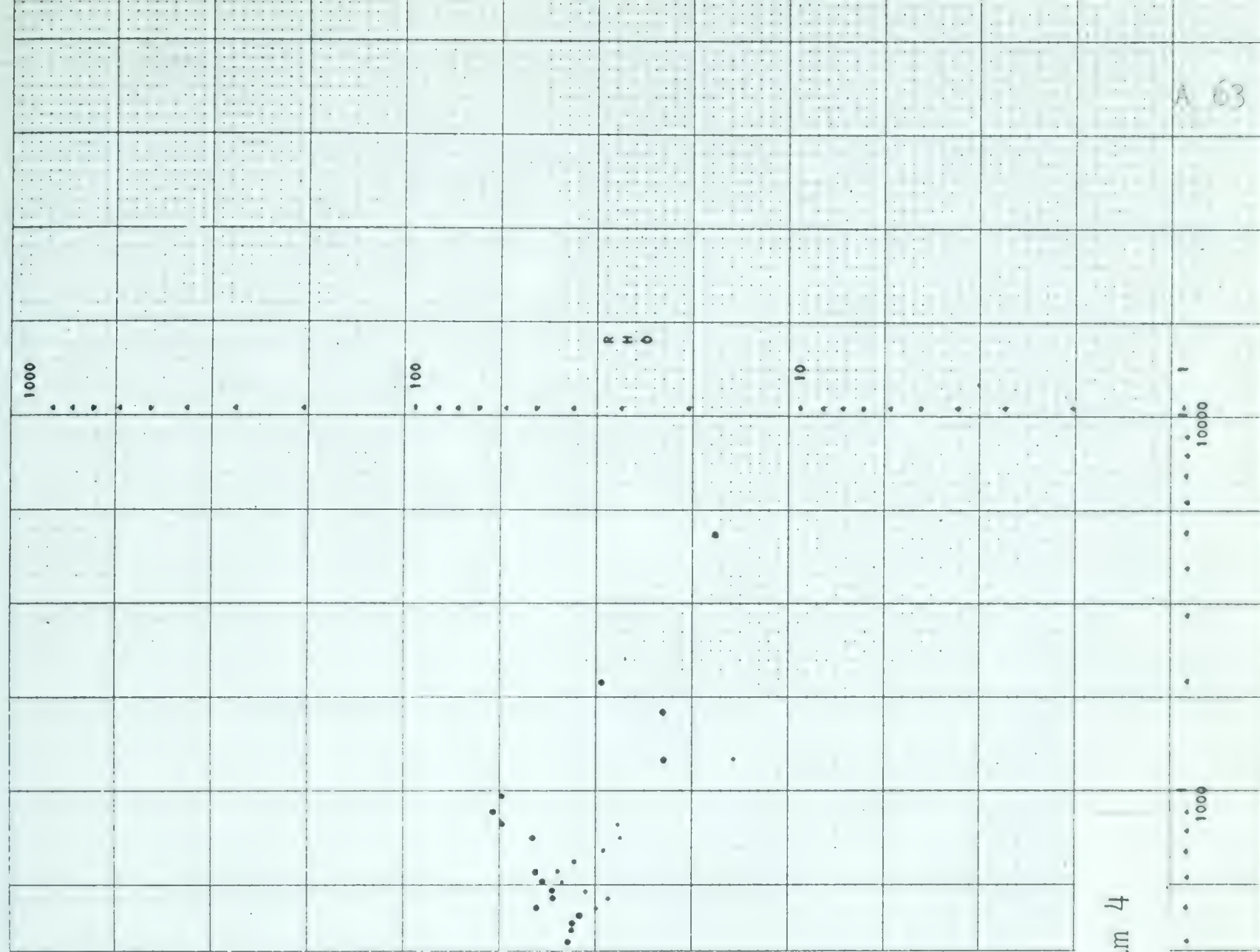
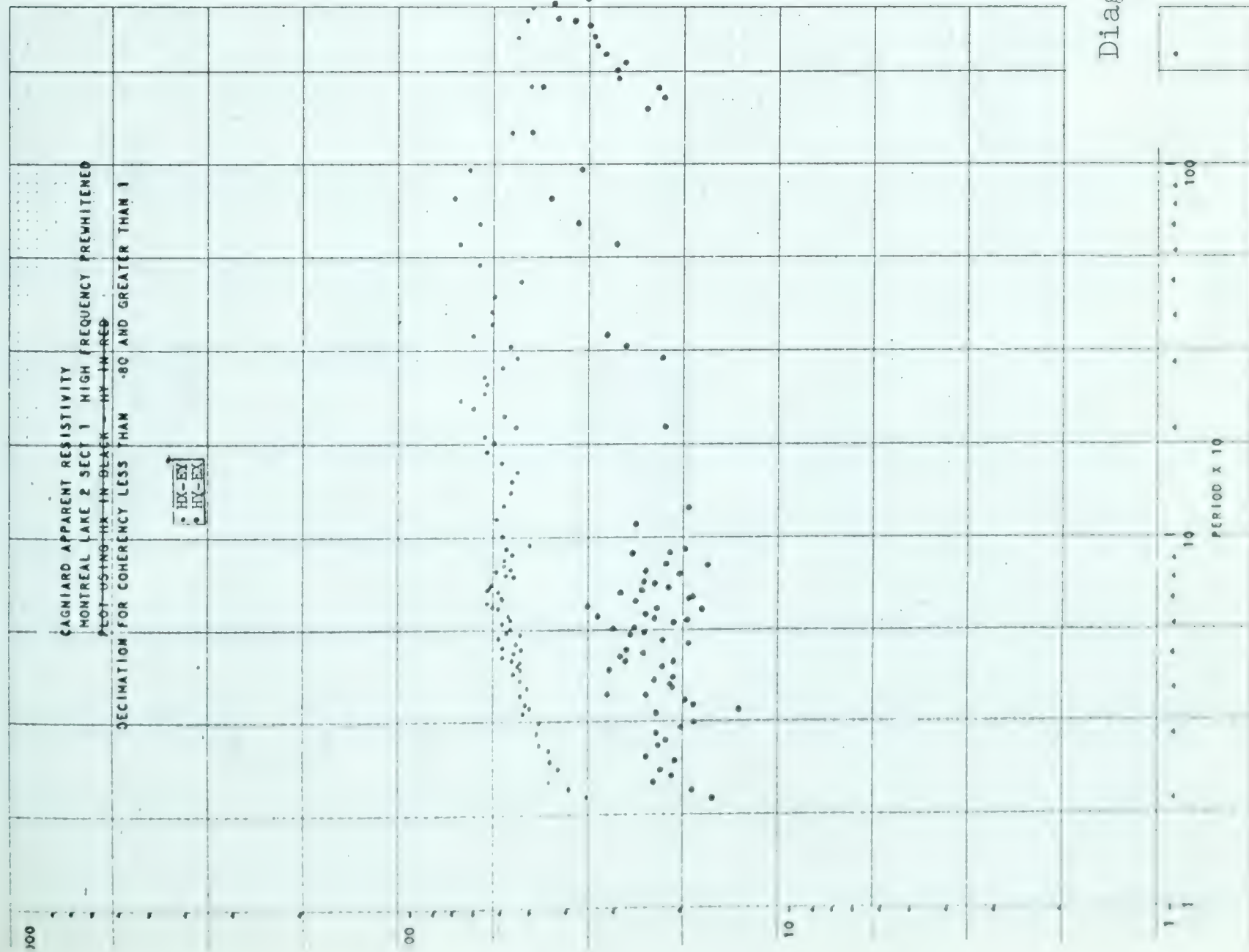


Diagram 3





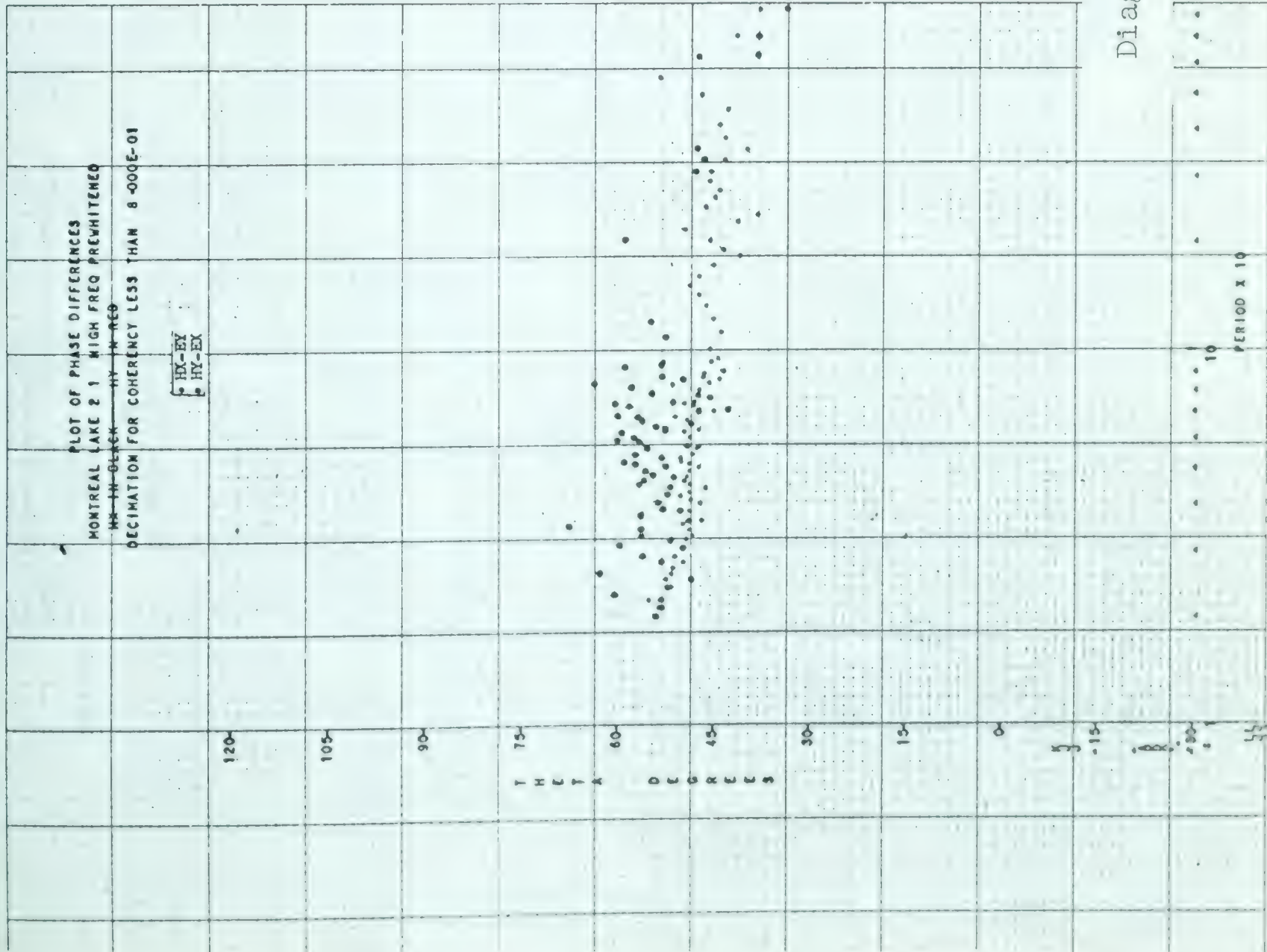
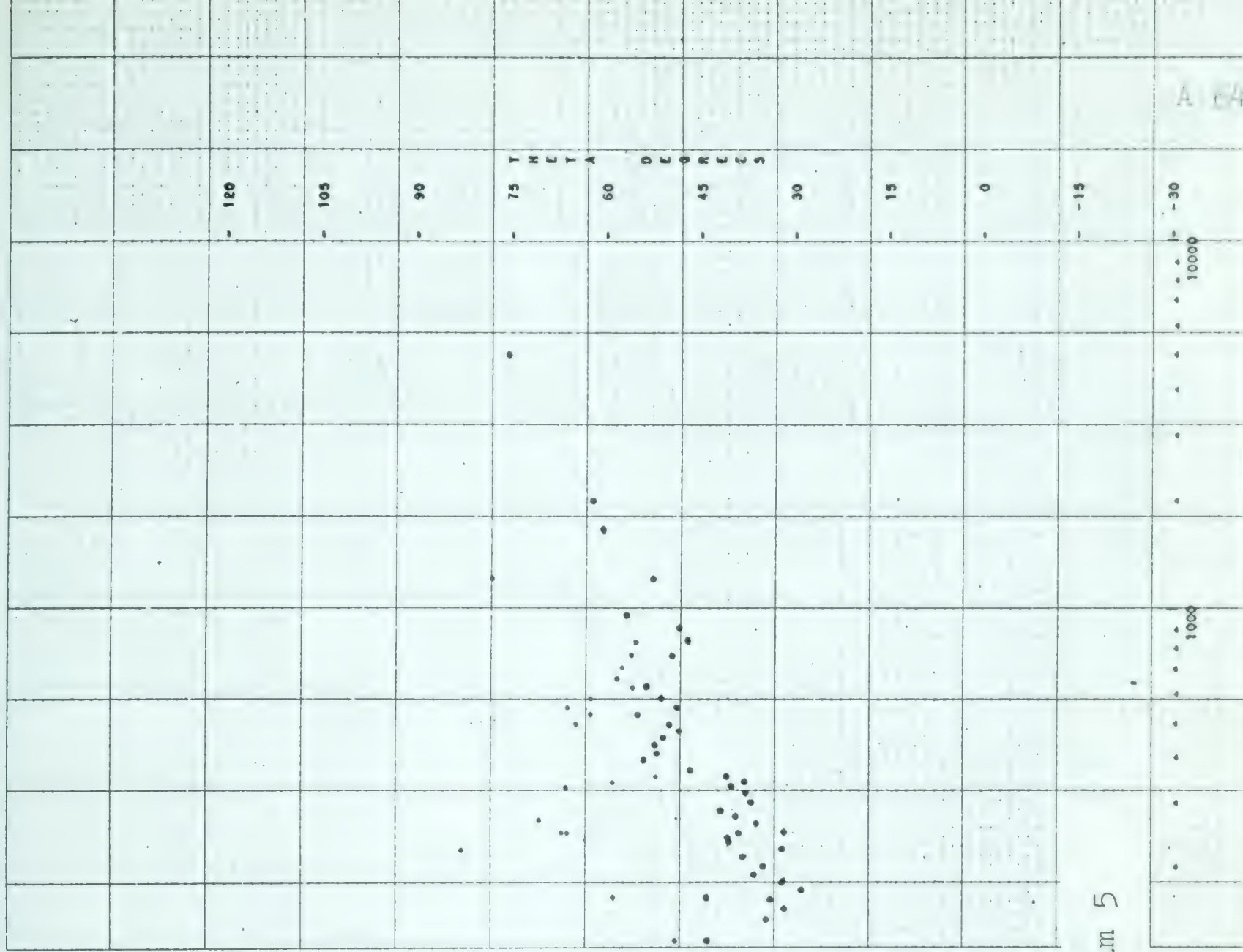
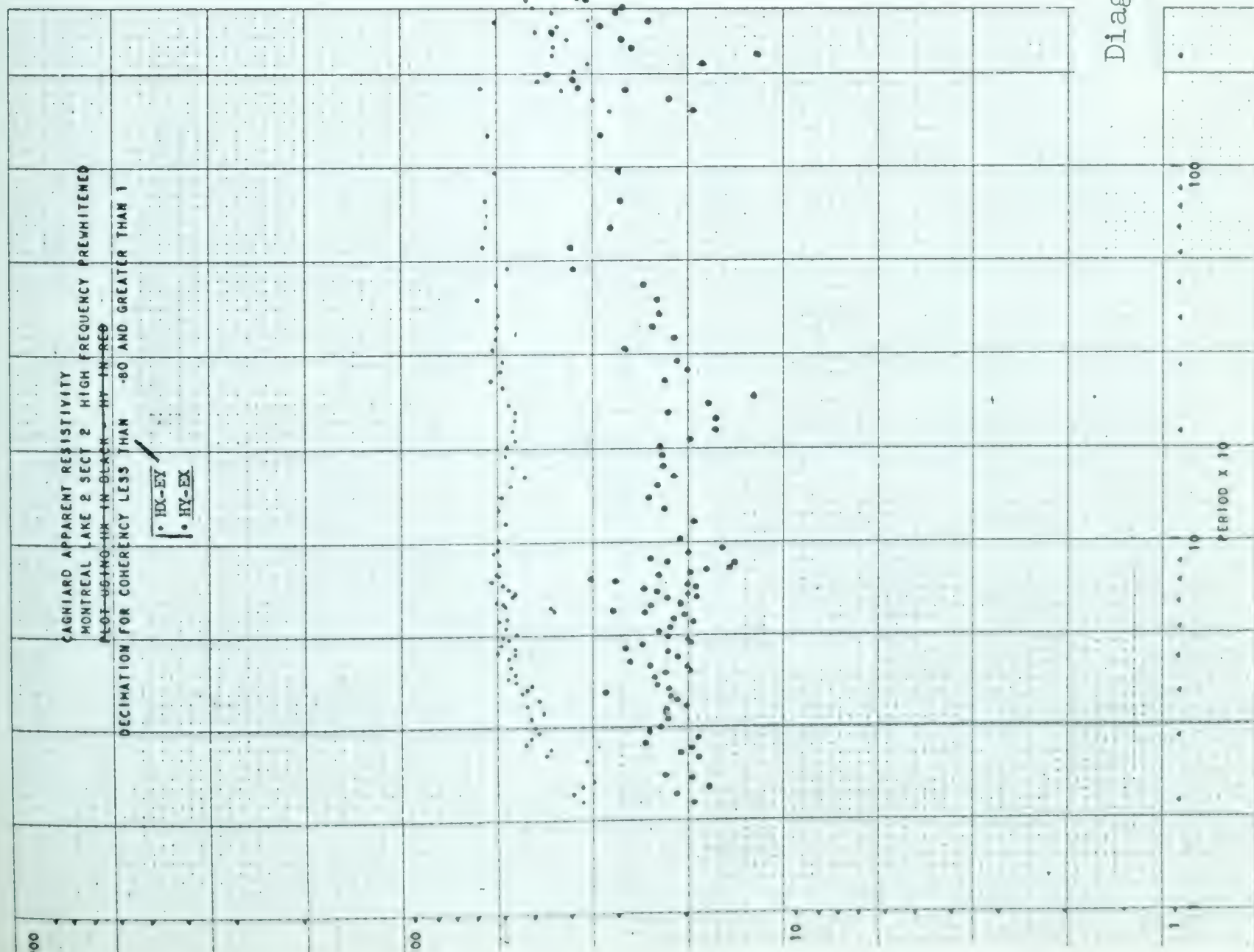
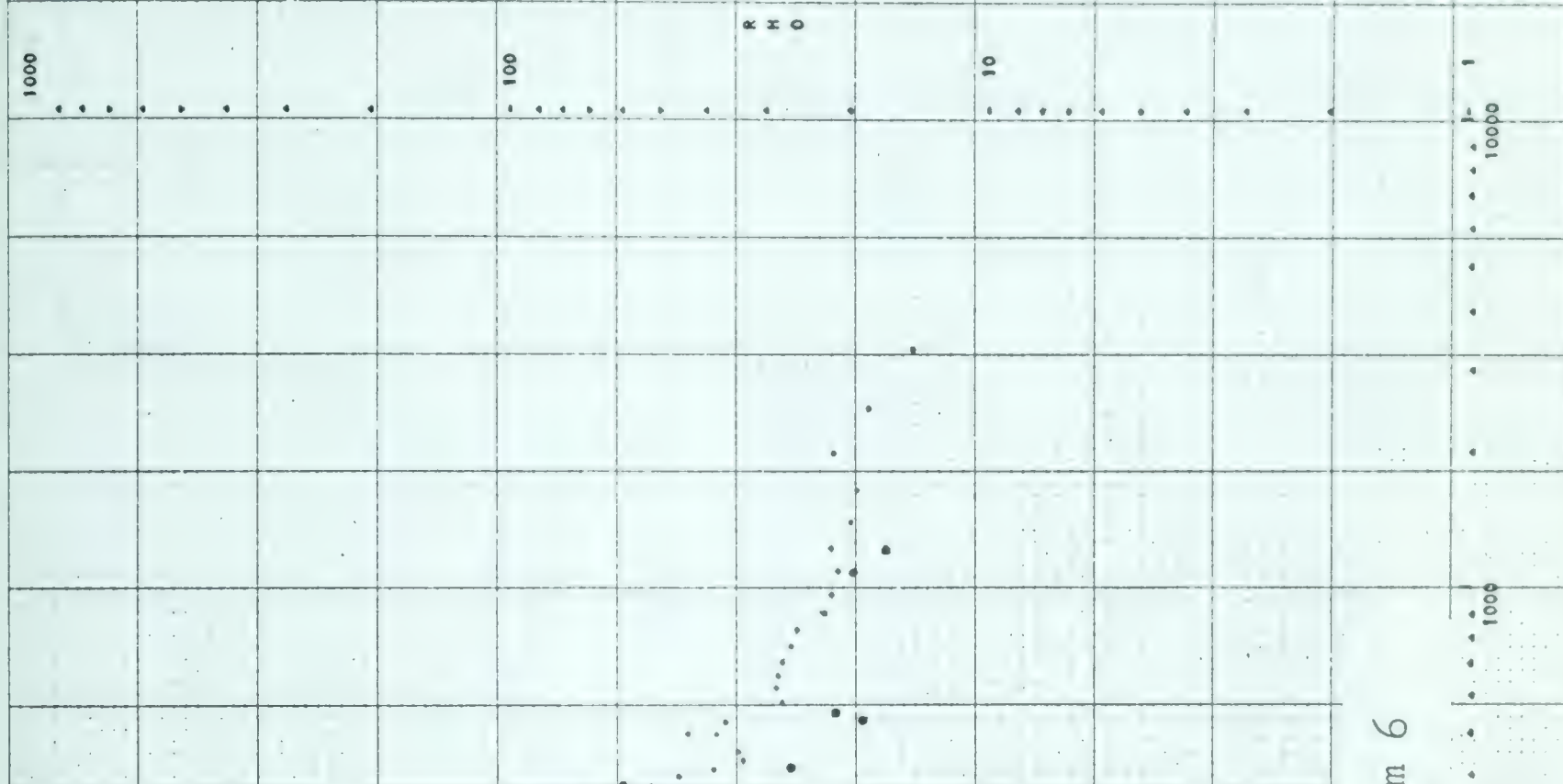


Diagram 5





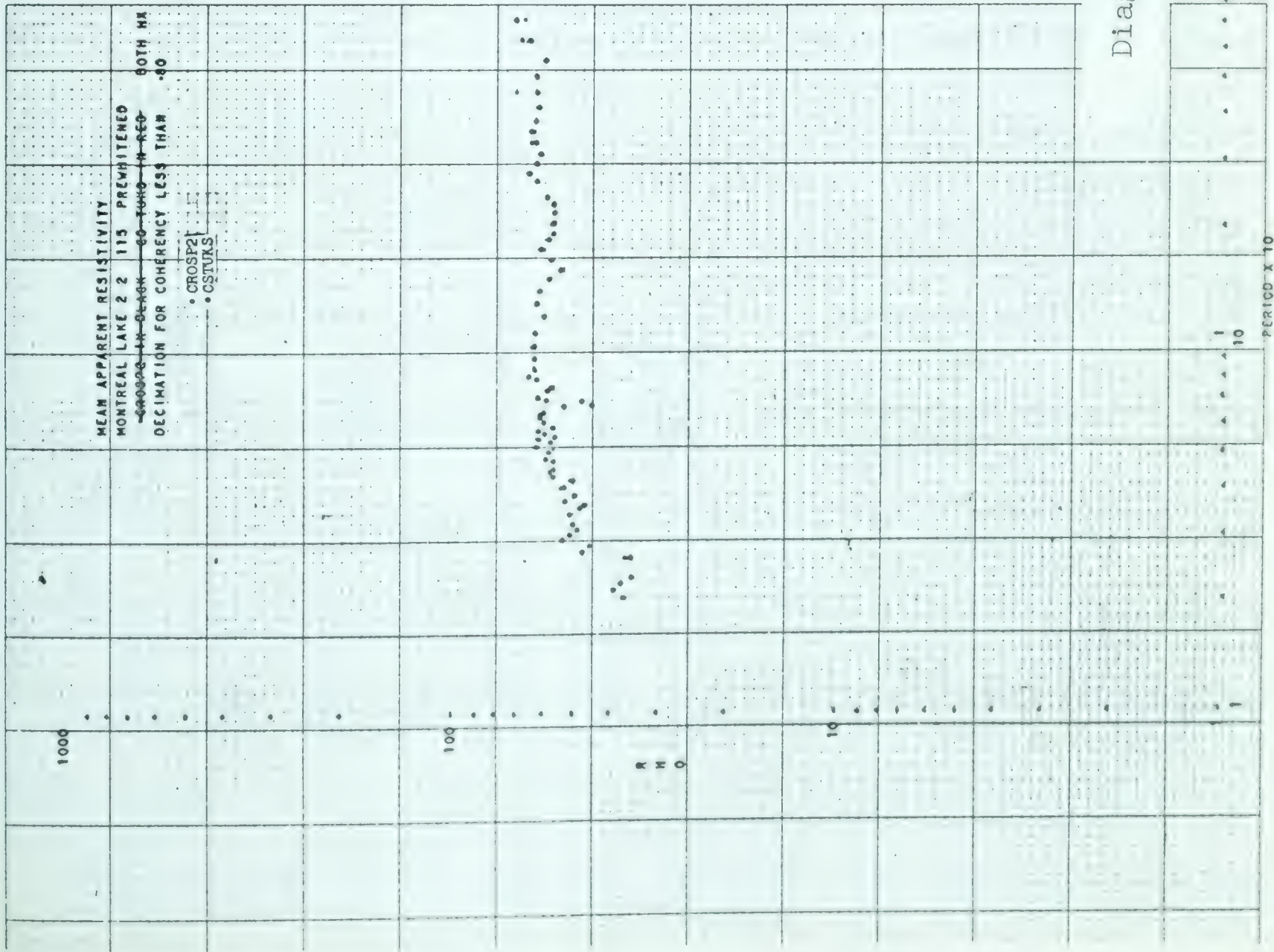
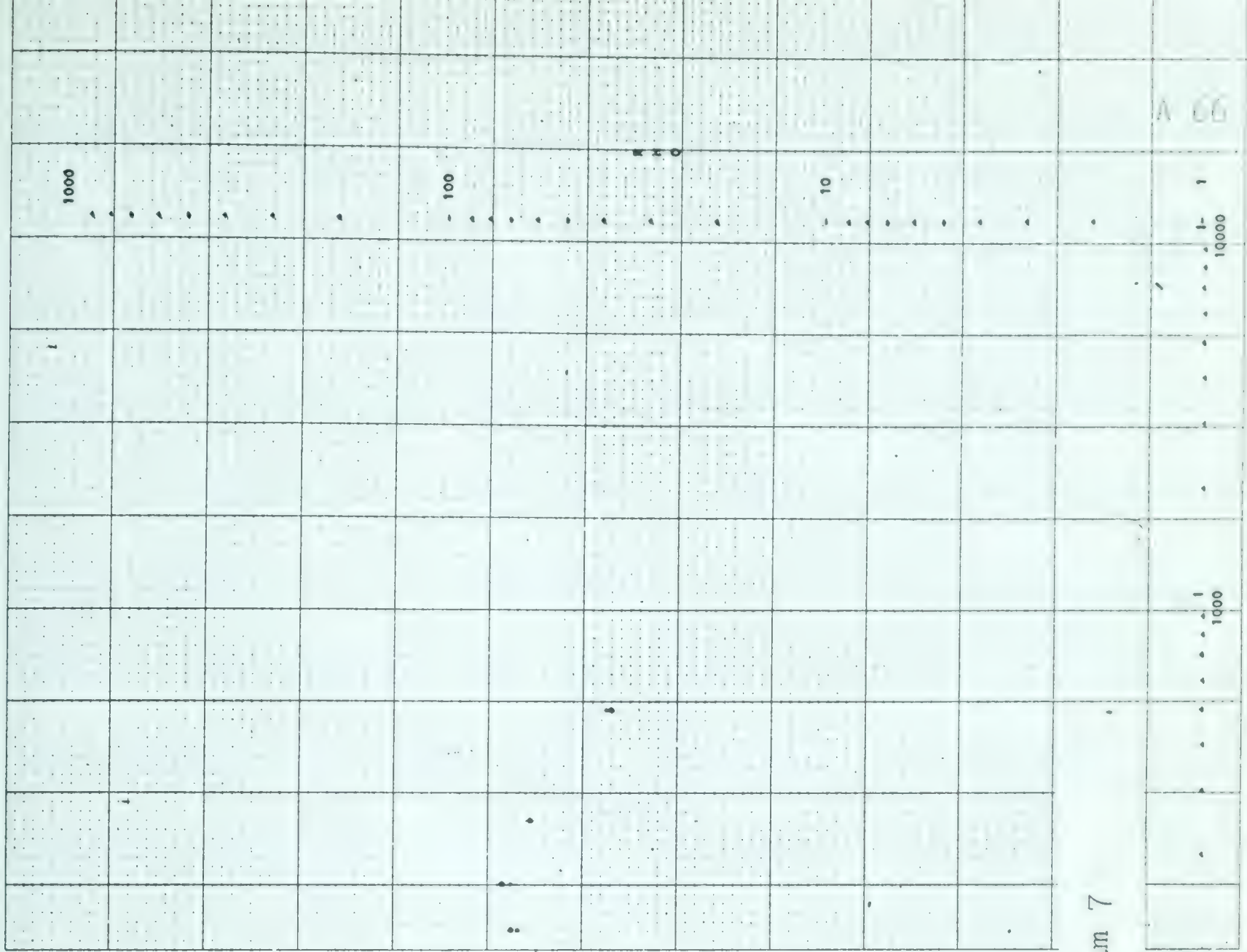


Diagram 7



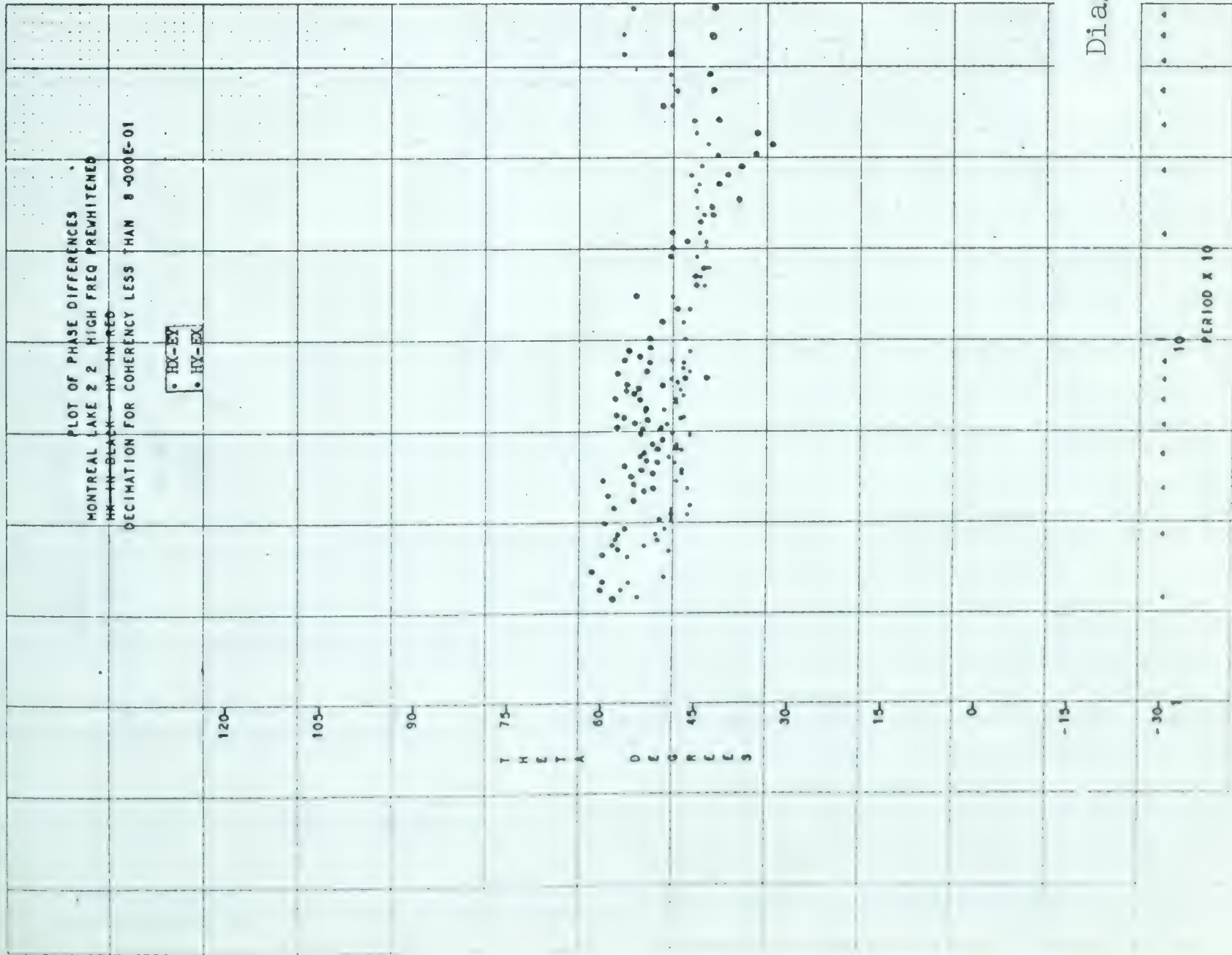
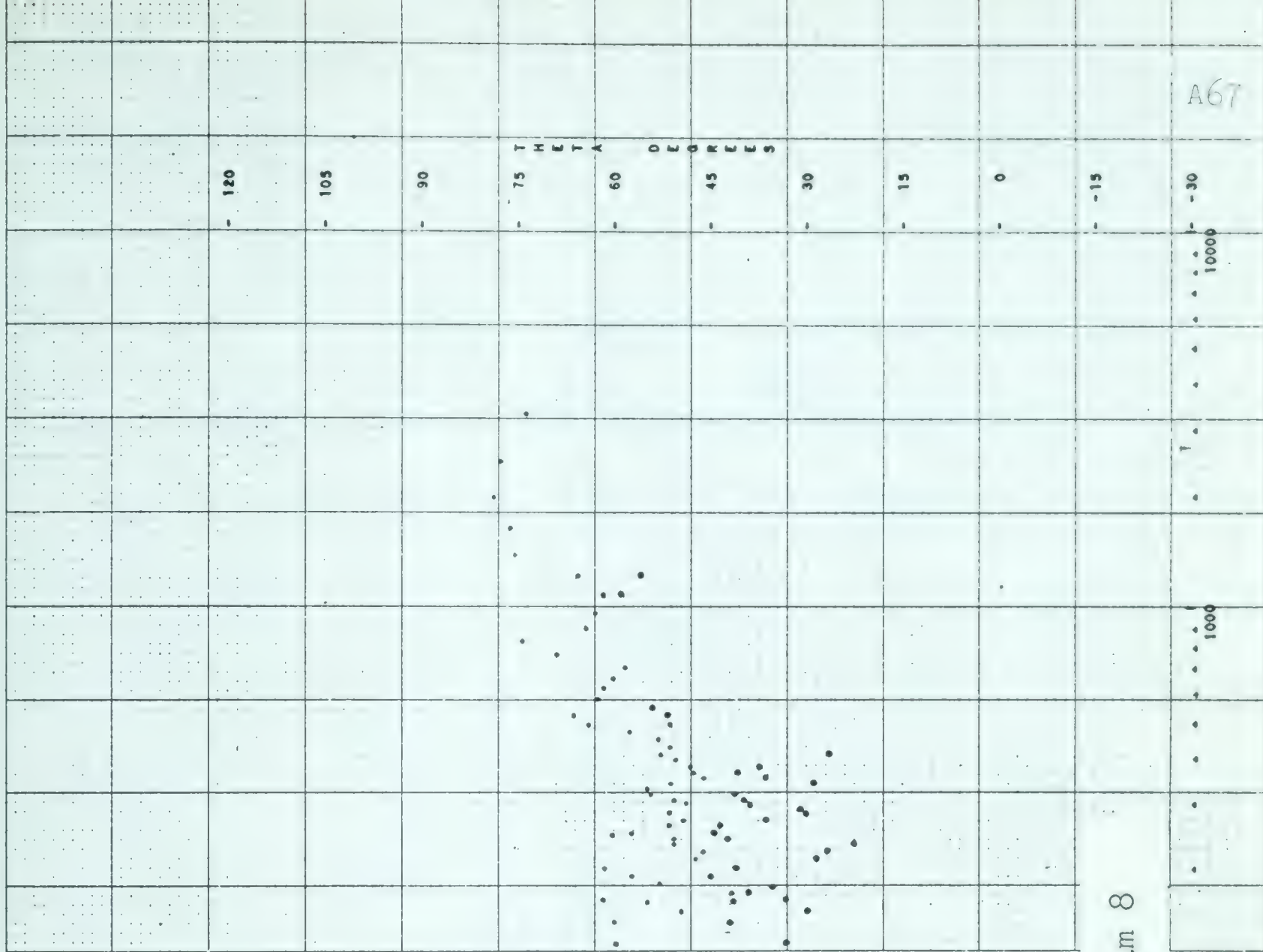


Diagram 8





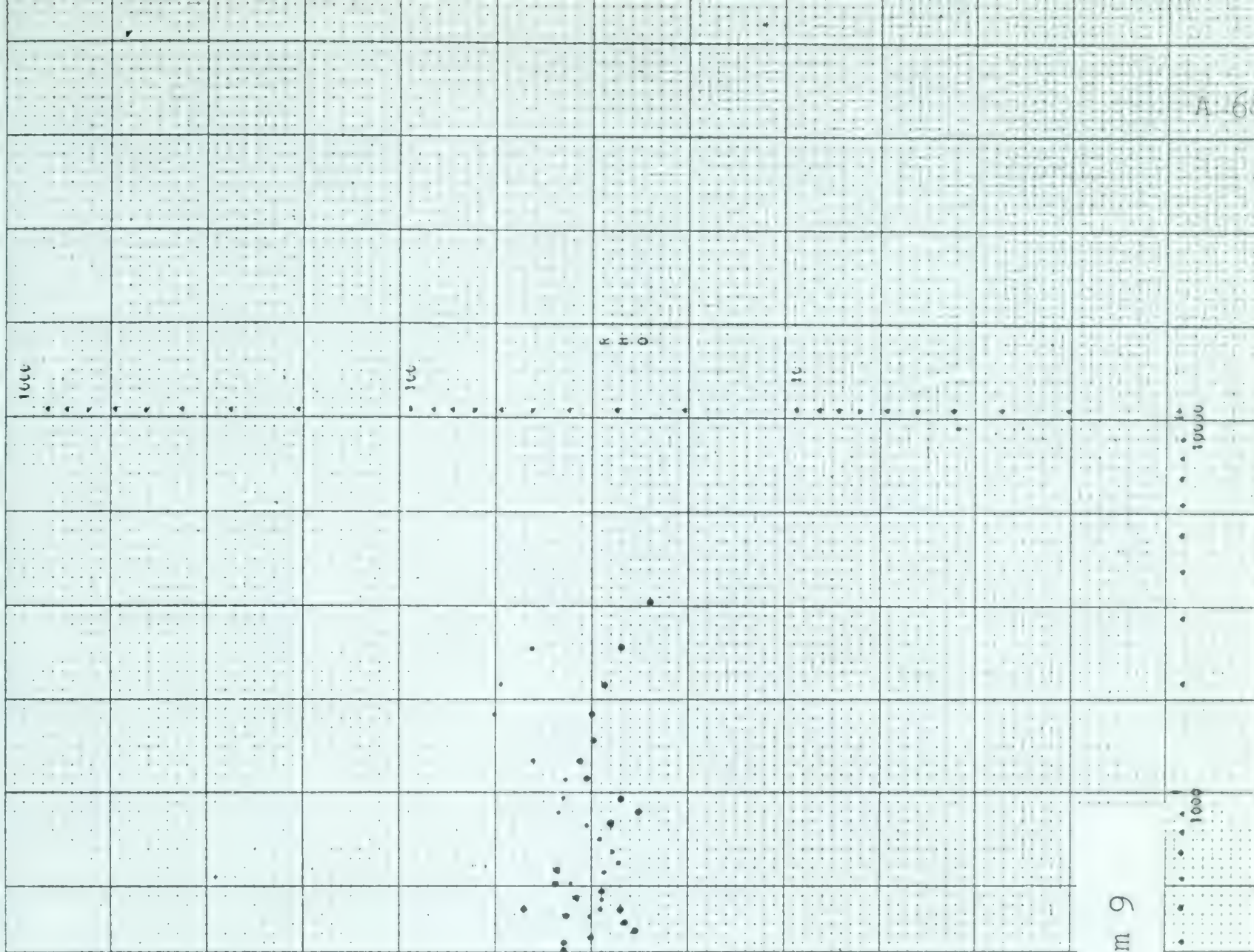
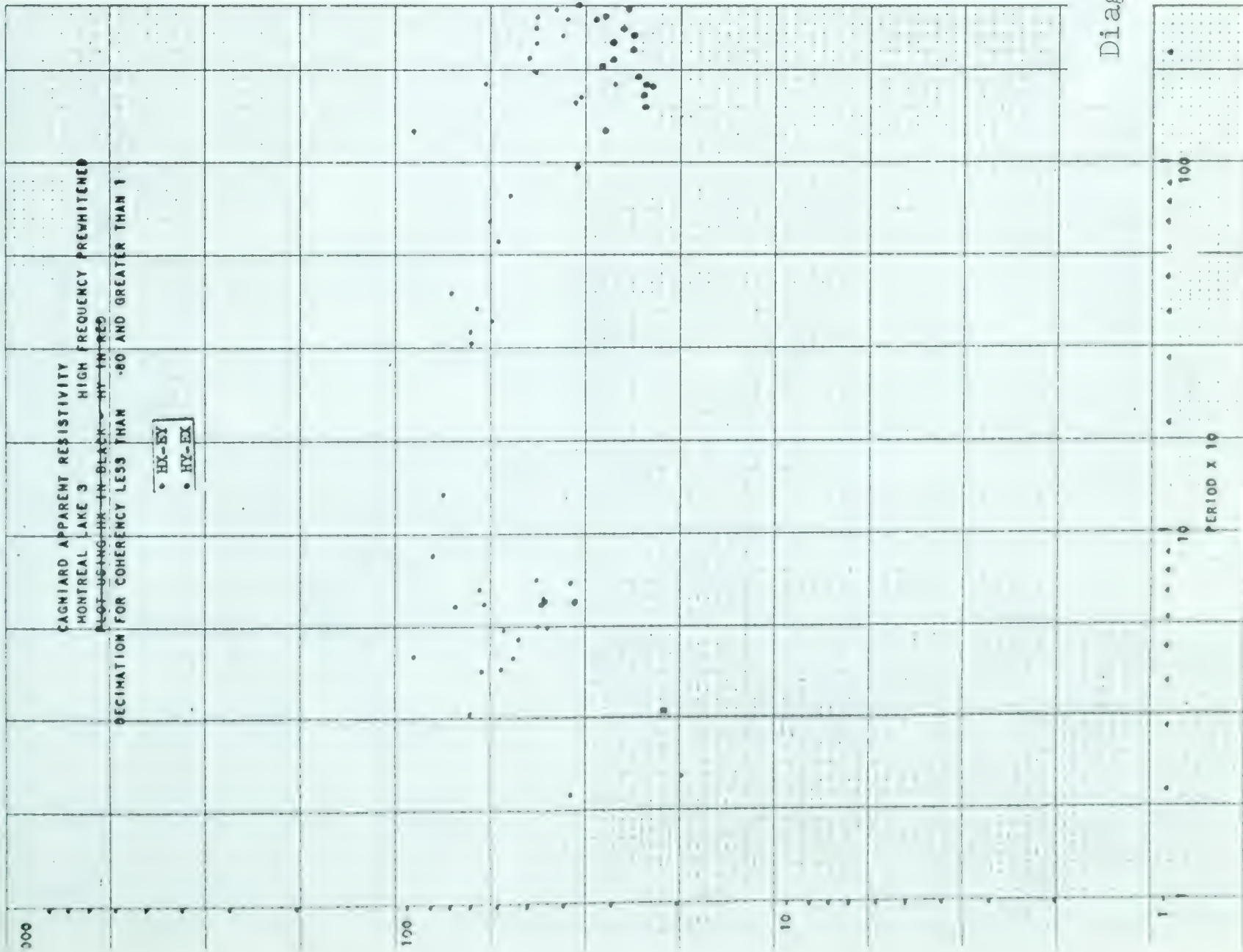


Diagram 9

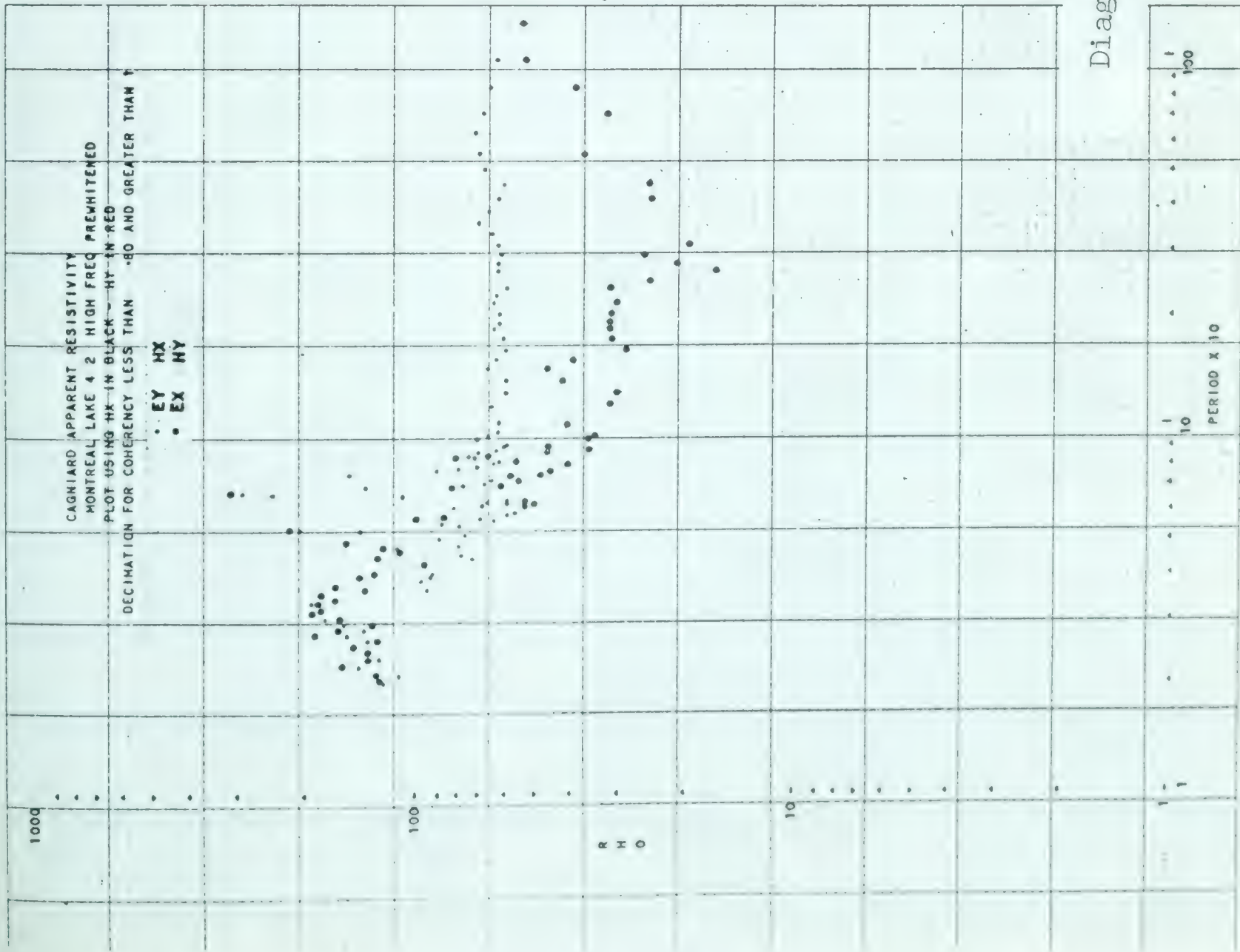
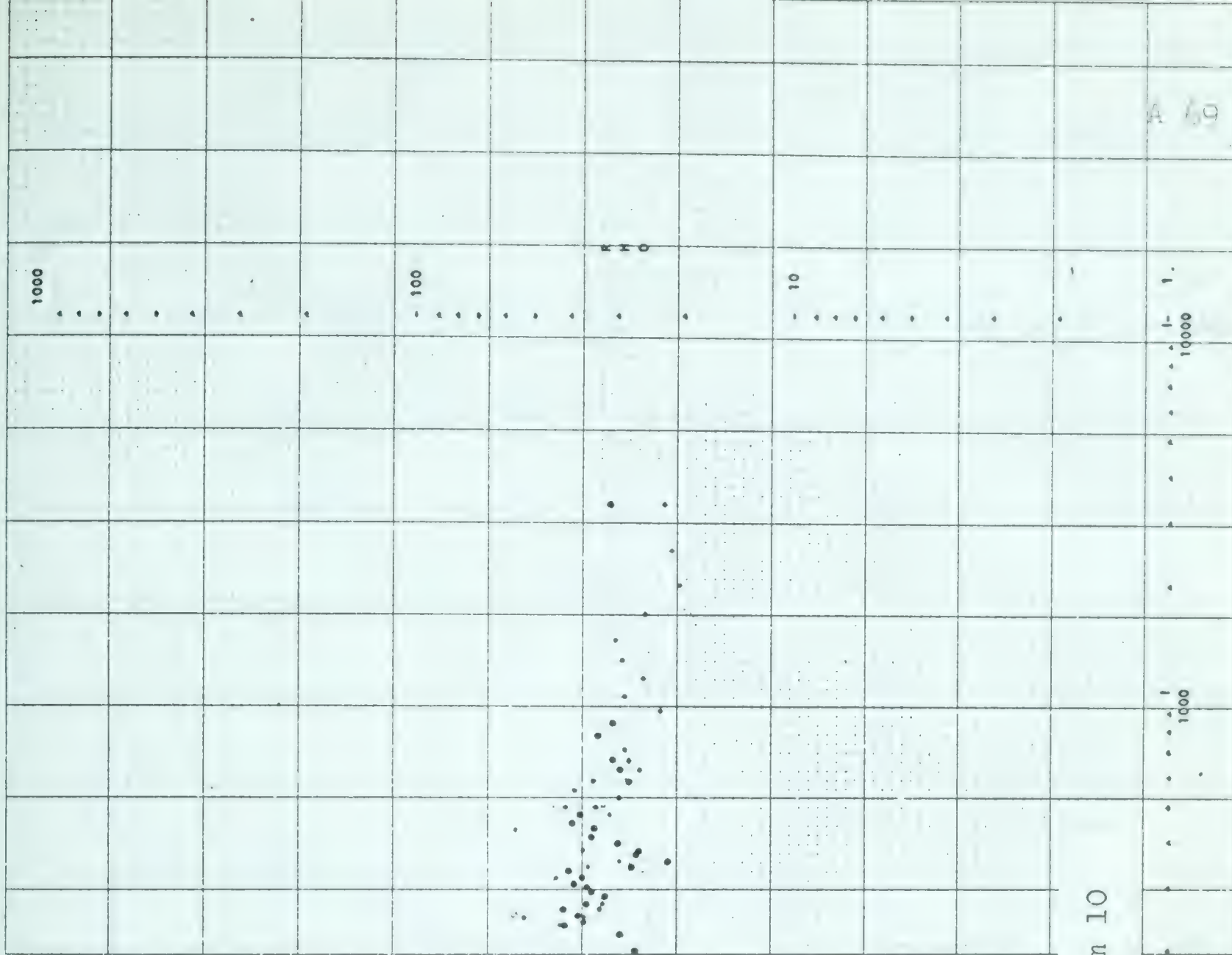


Diagram 10



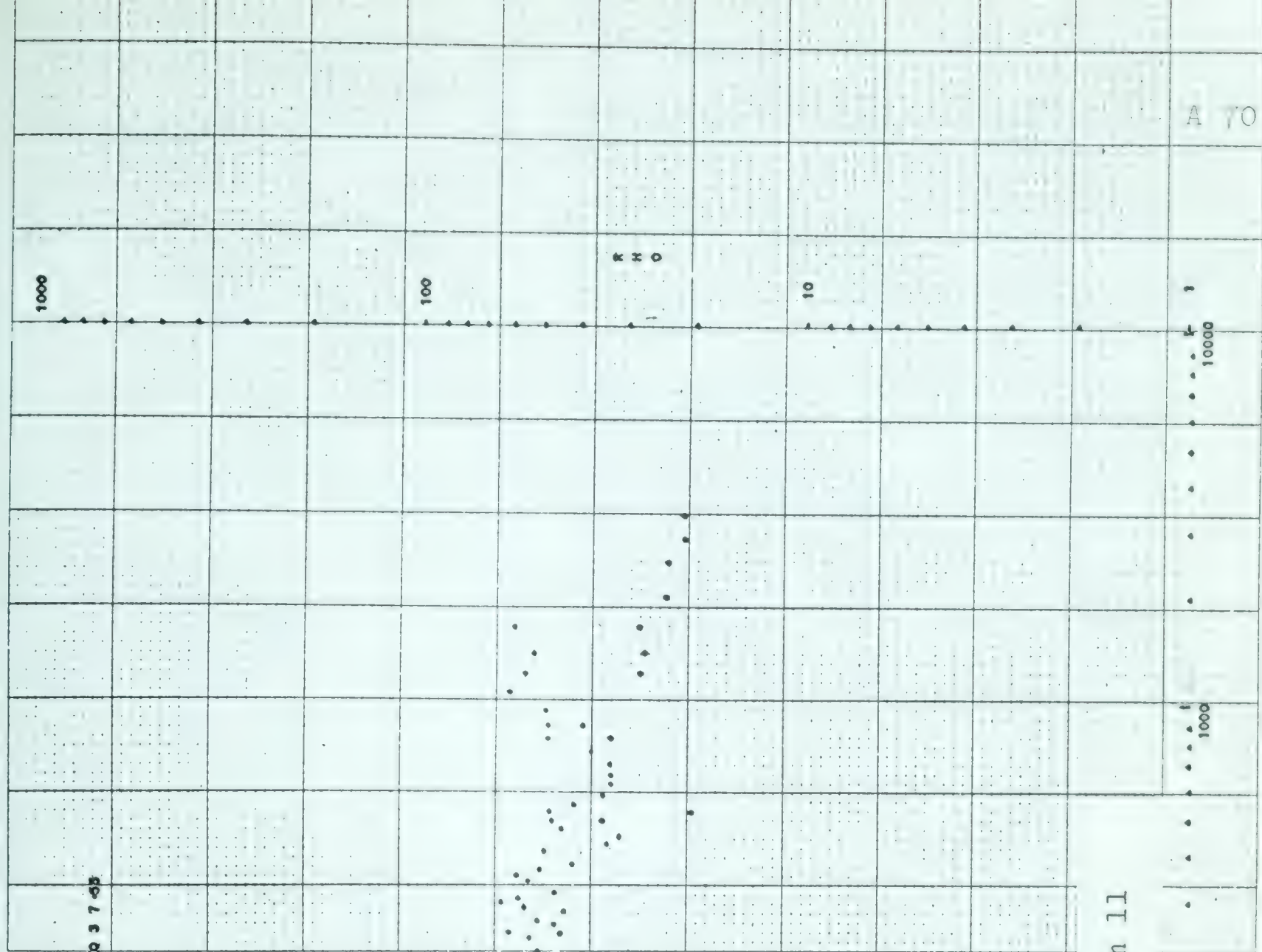
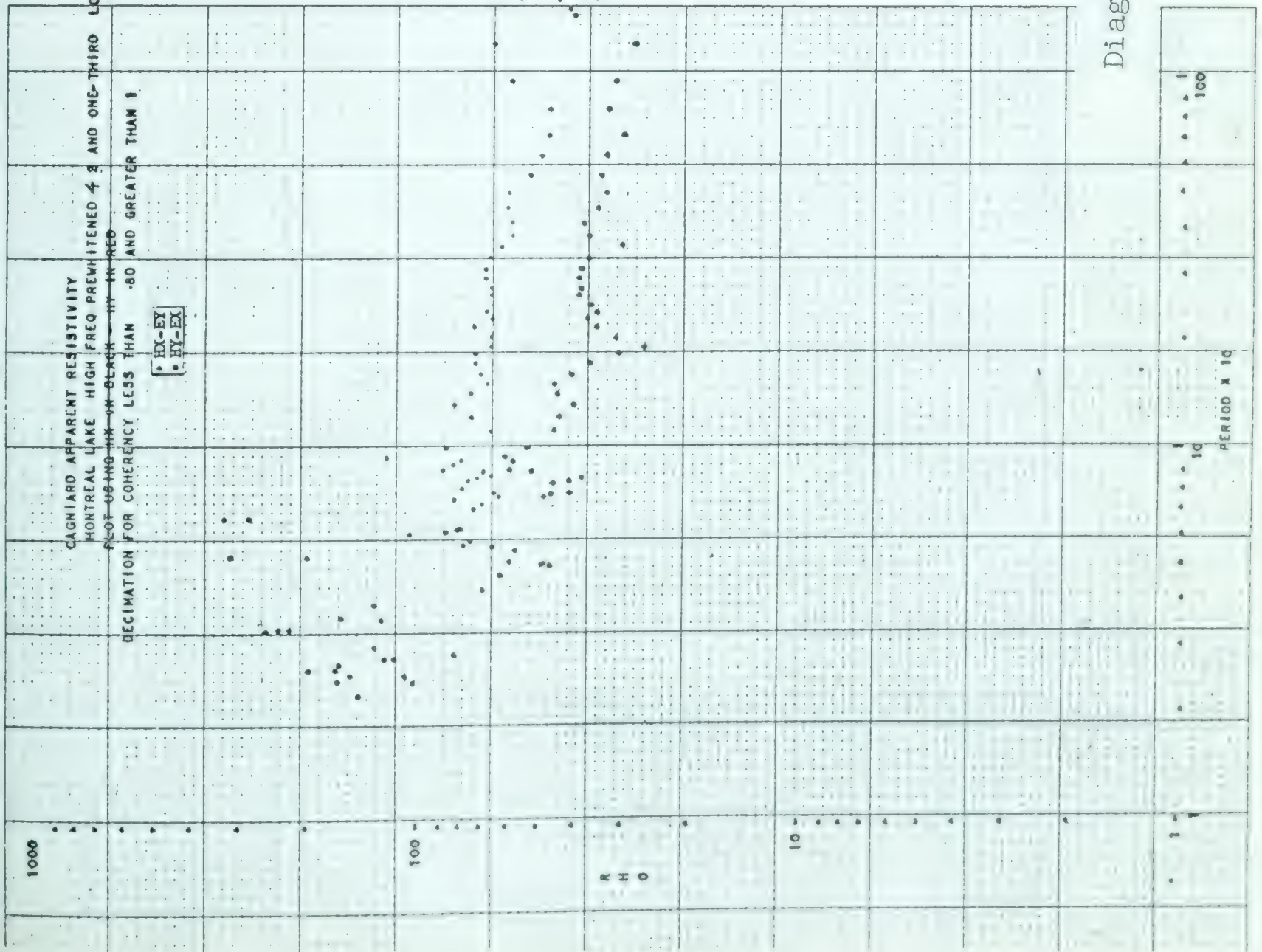


Diagram 11

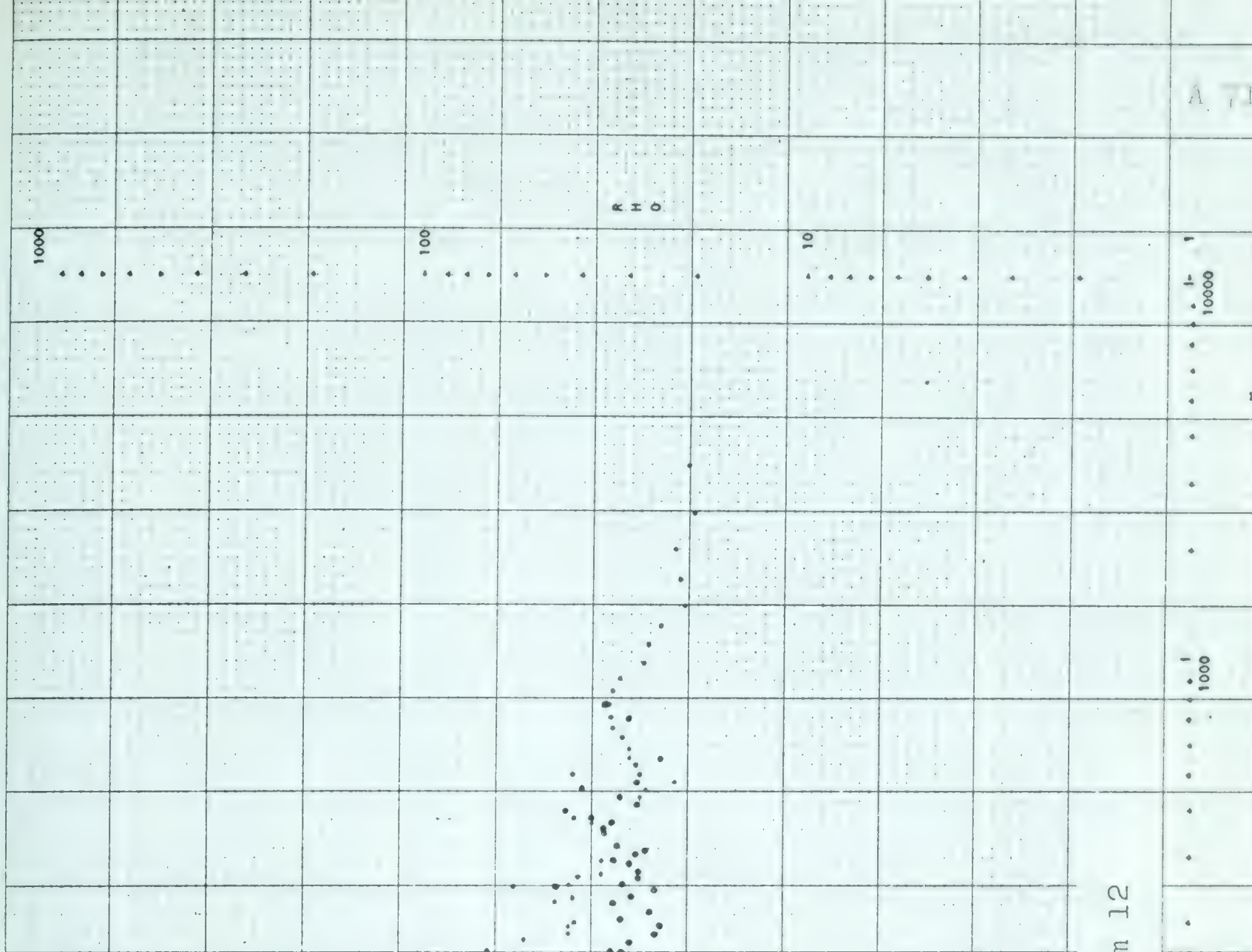
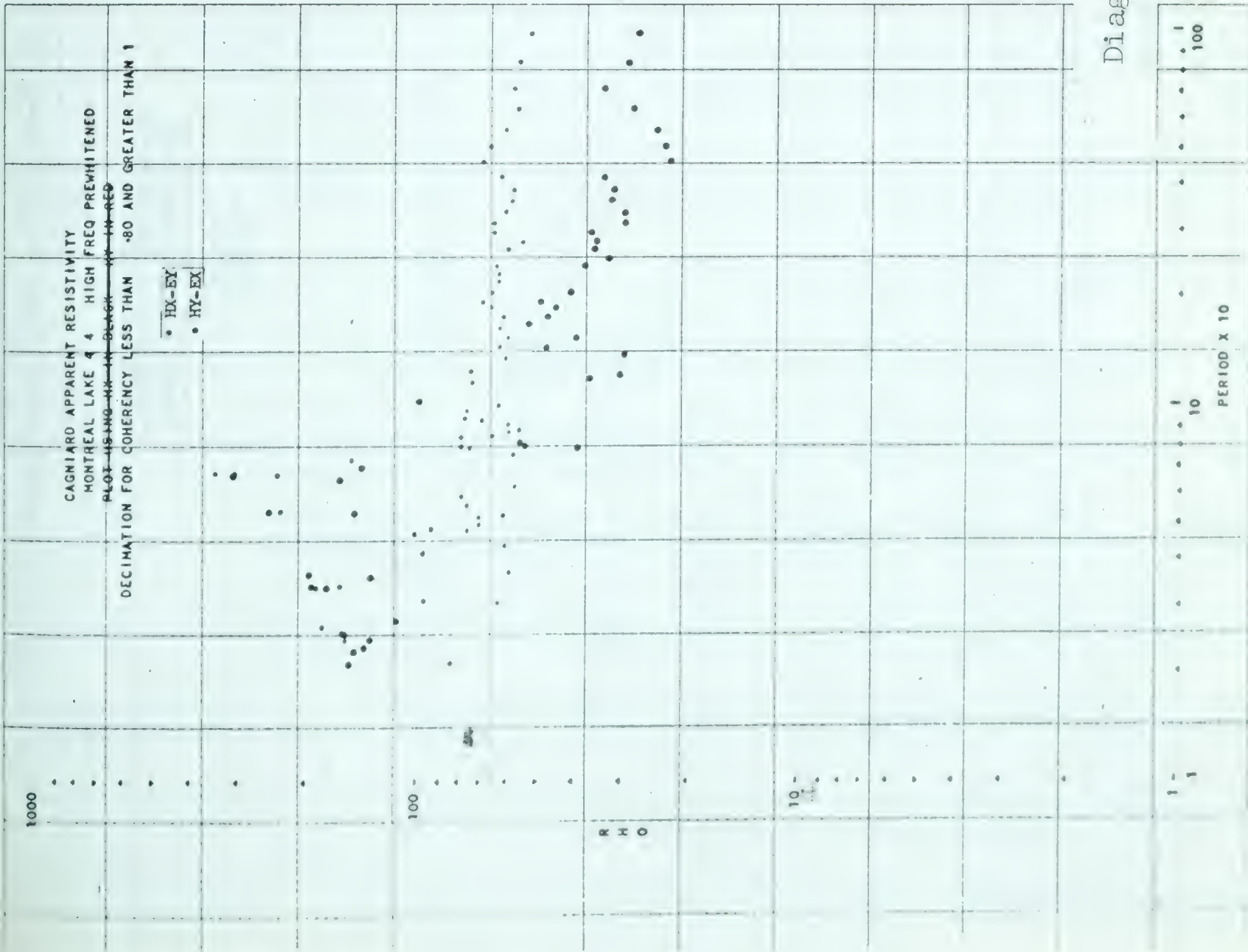


Diagram 12



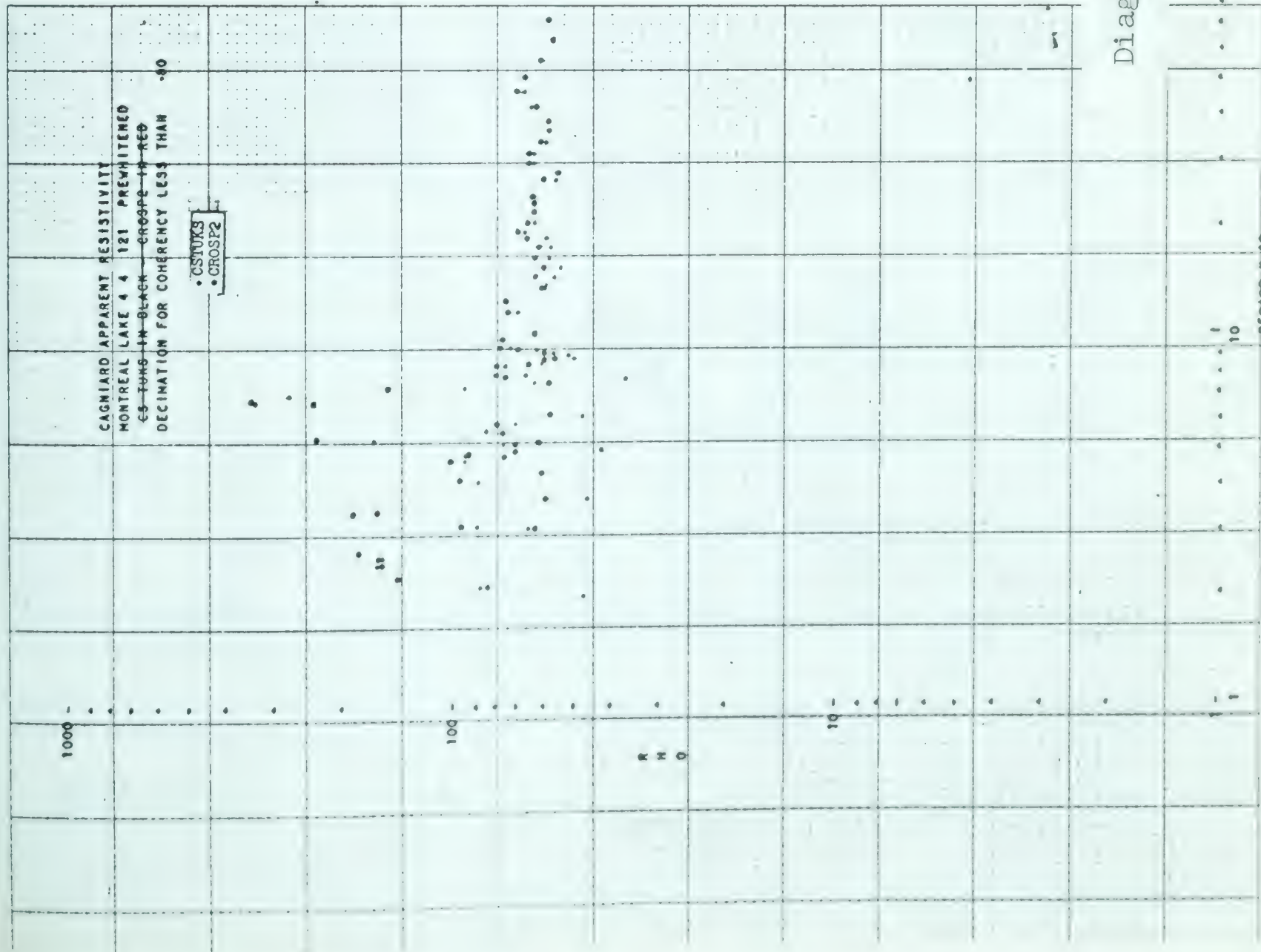
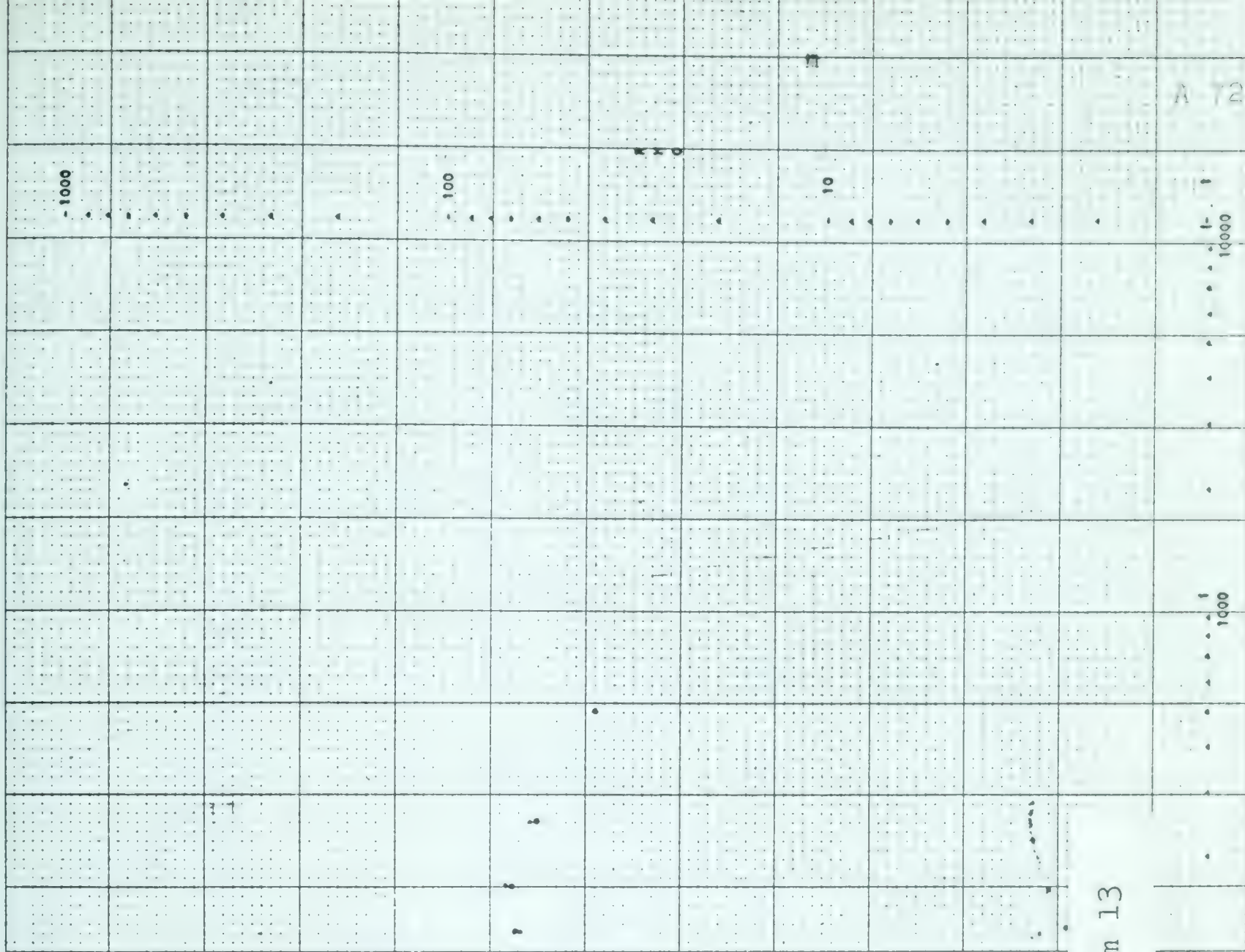


Diagram 13





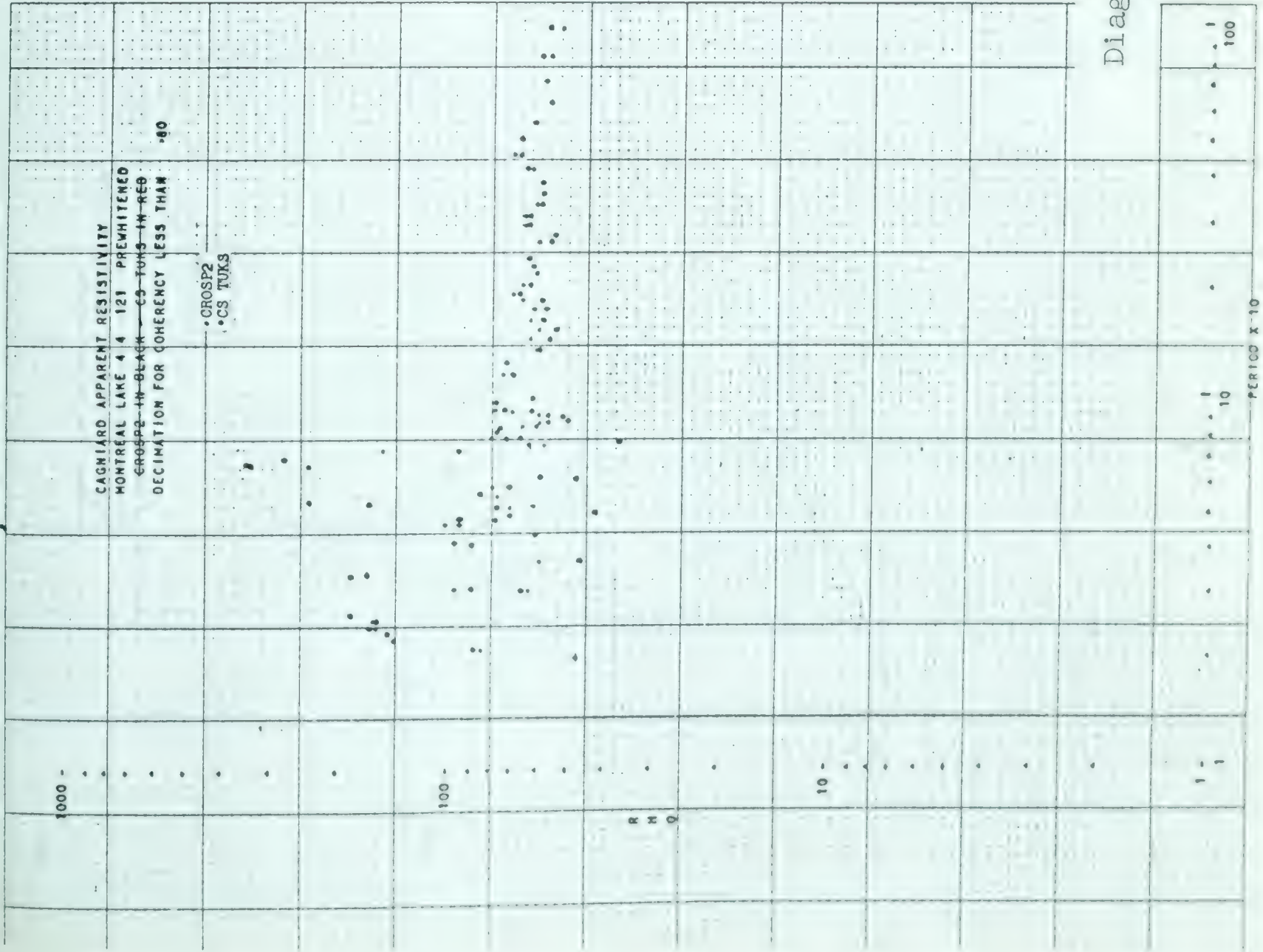
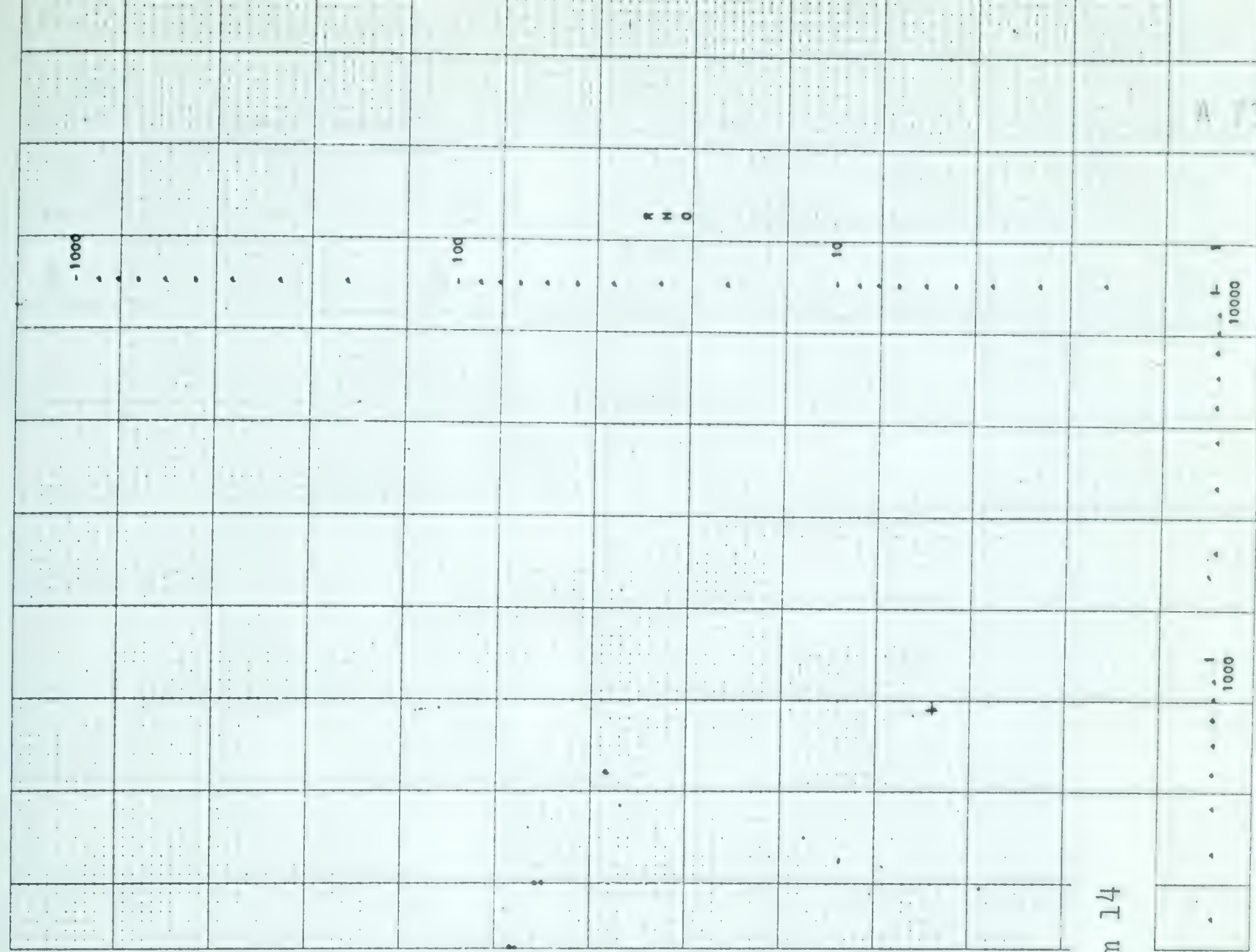


Diagram 14



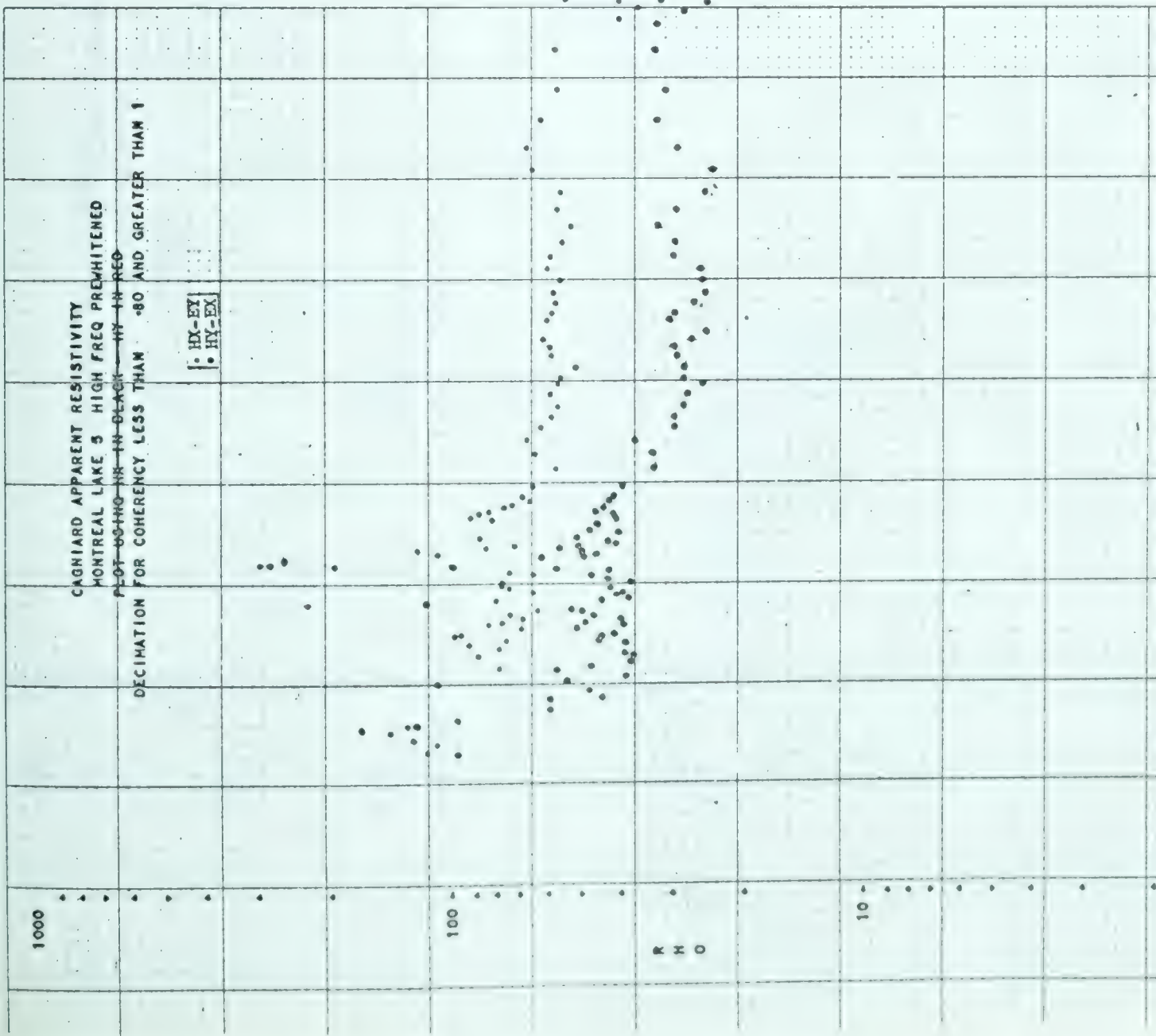
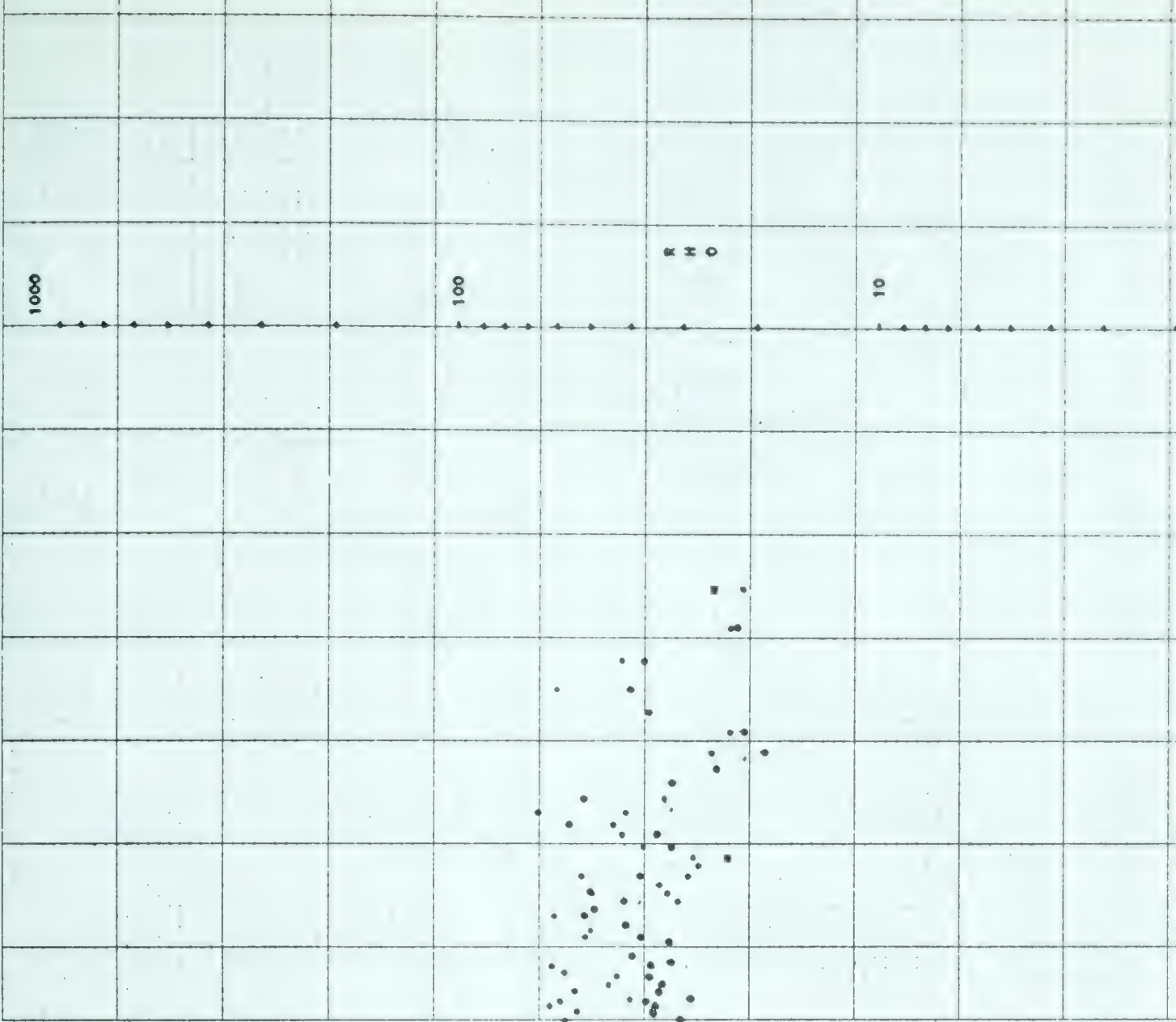
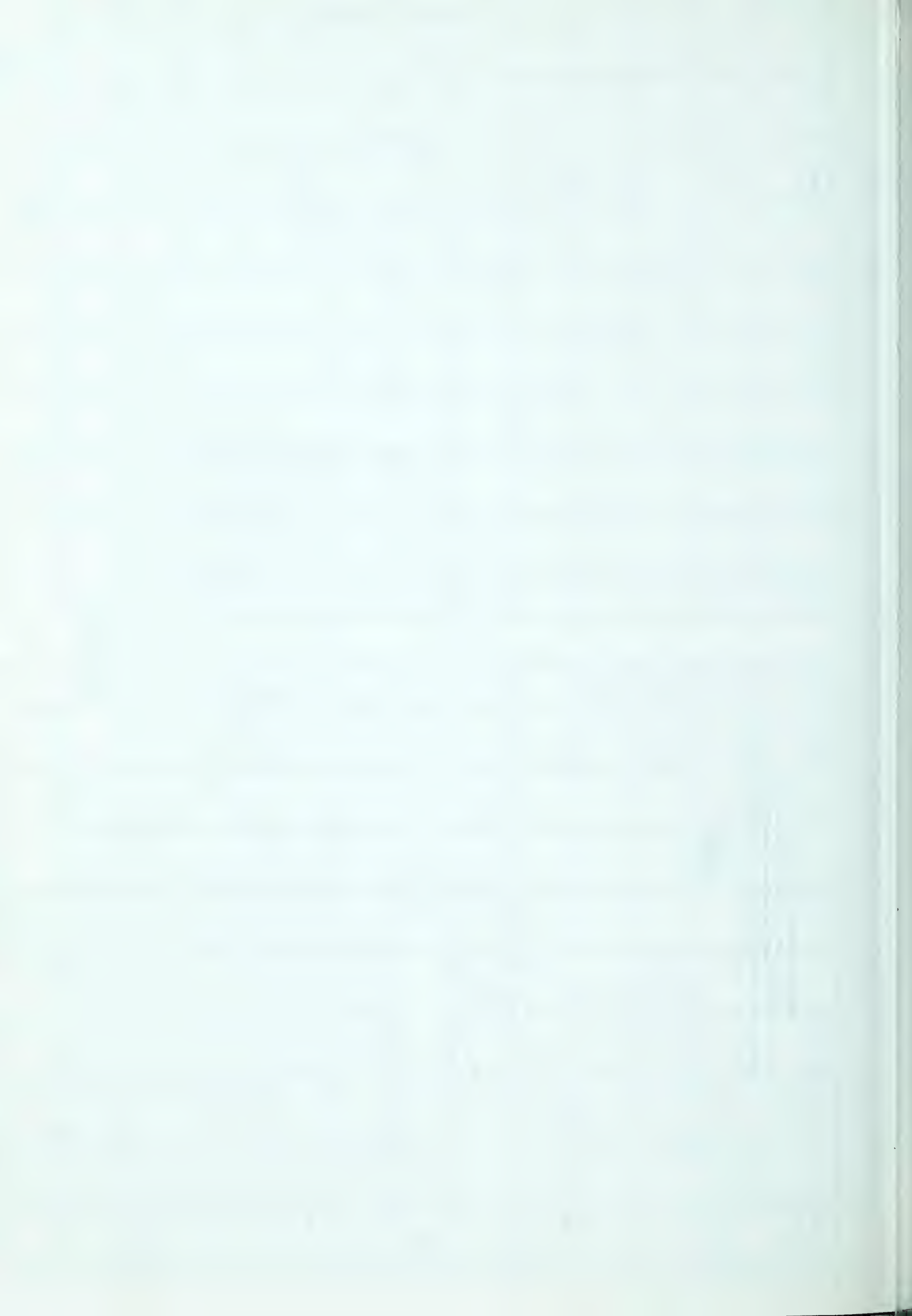


Diagram 15

CAGNIARD APPARENT RESISTIVITY
MONTREAL LAKE 5 HIGH FREQ PREWHITENED
PLOT US-HO-NR-IN-BLACK-HY-IN-RED
DECIMATION FOR COHERENCY LESS THAN -80 AND GREATER THAN 1

• HY-EX
• HY-EX



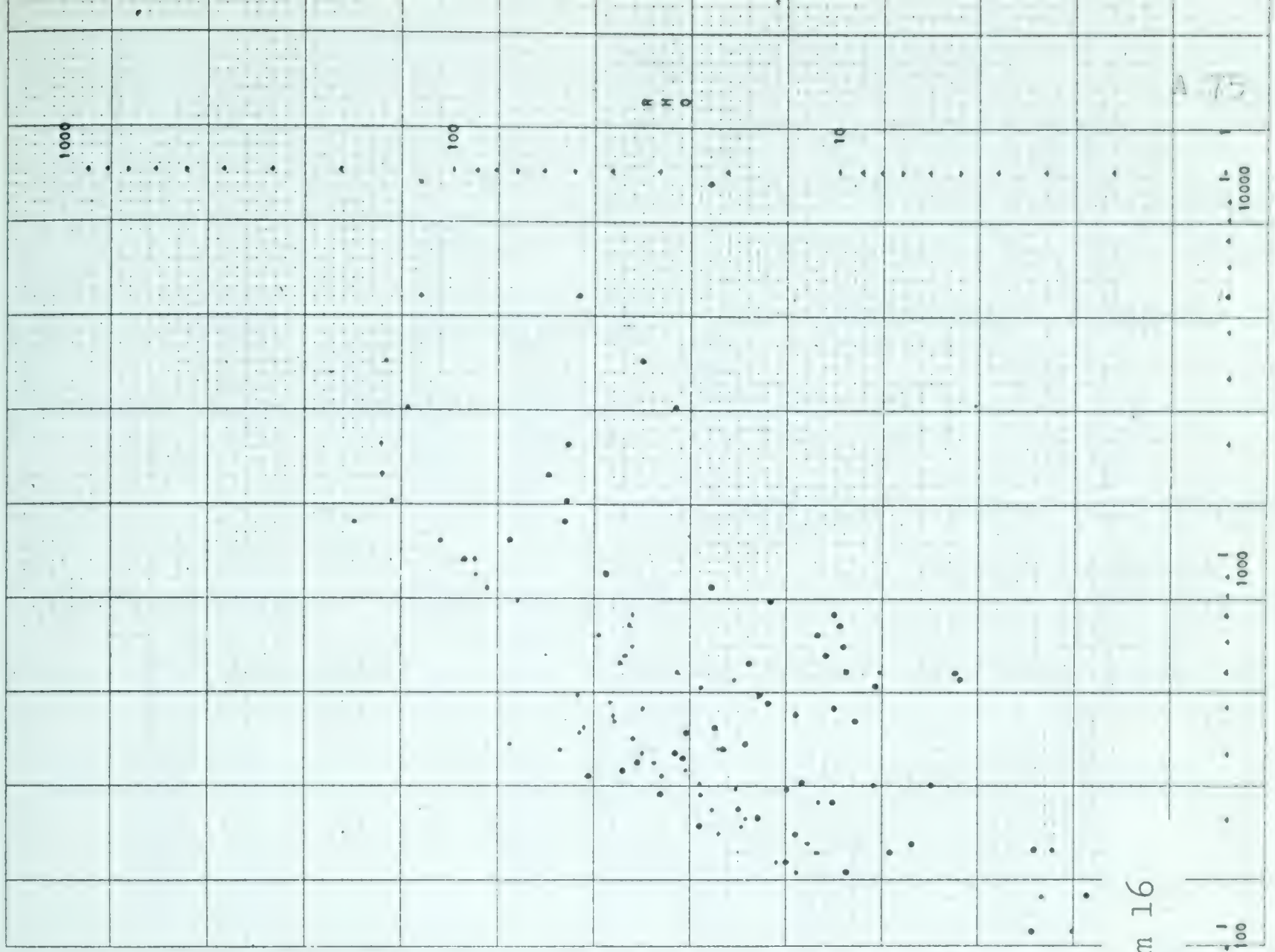
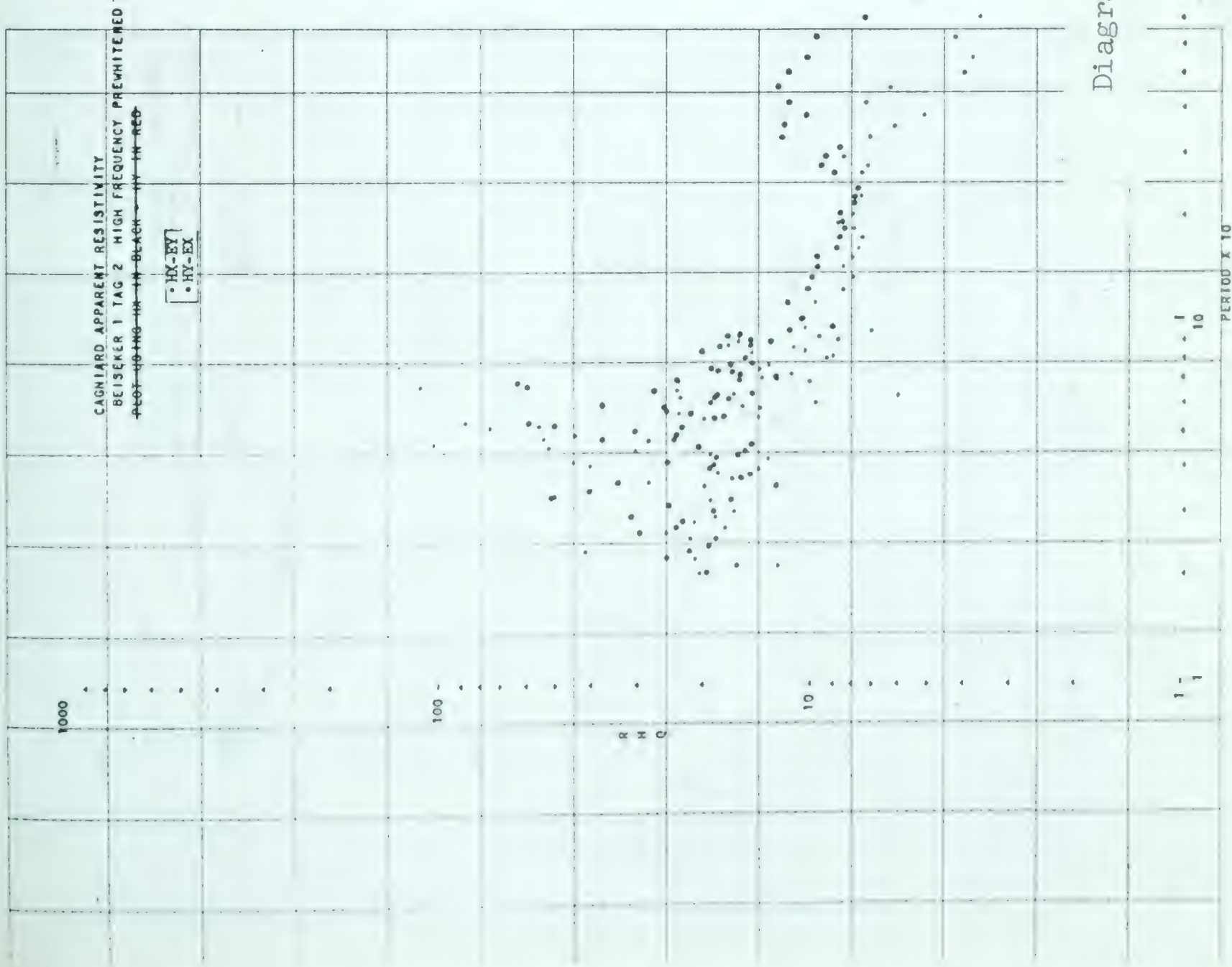


Diagram 16

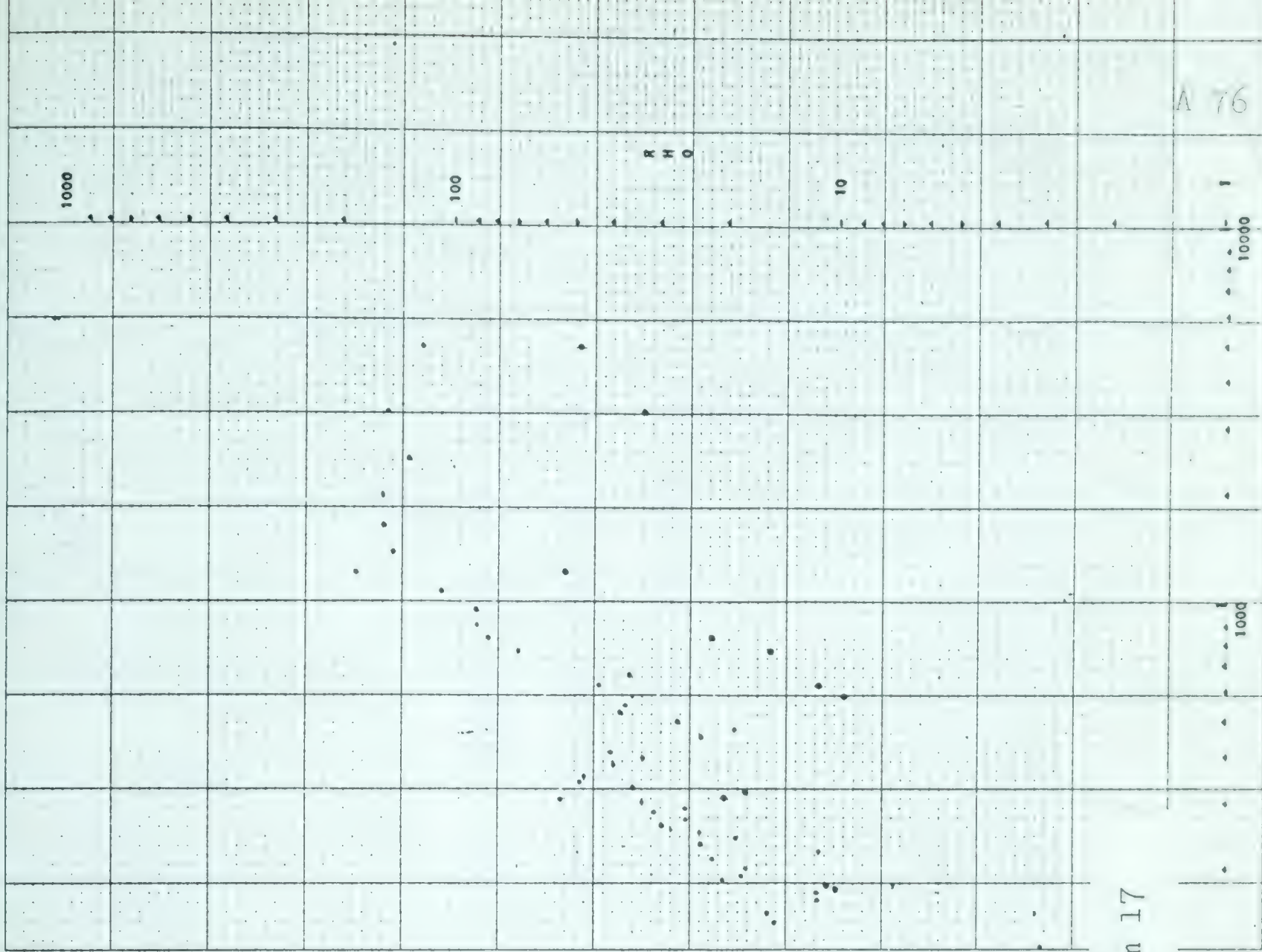
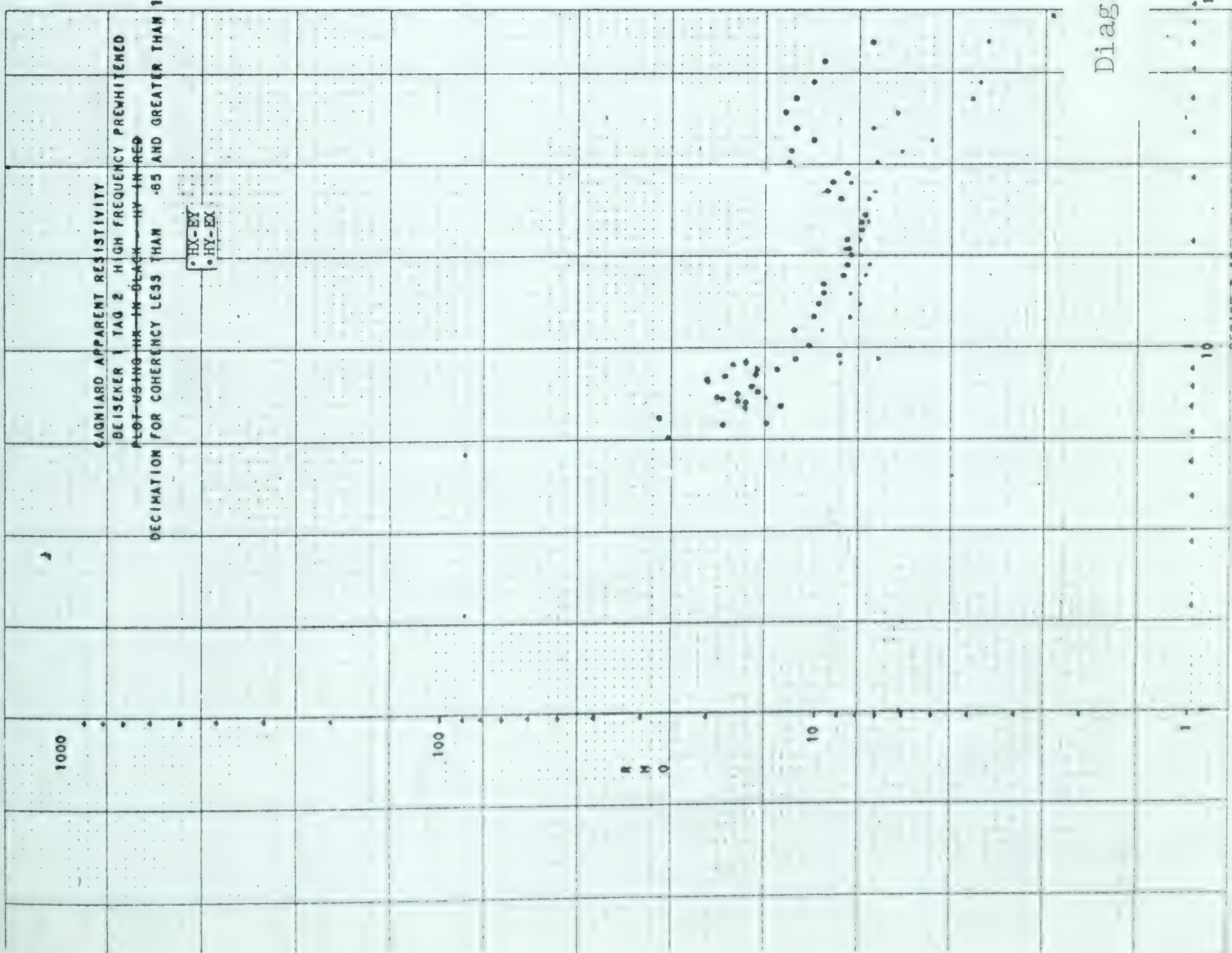


Diagram 17



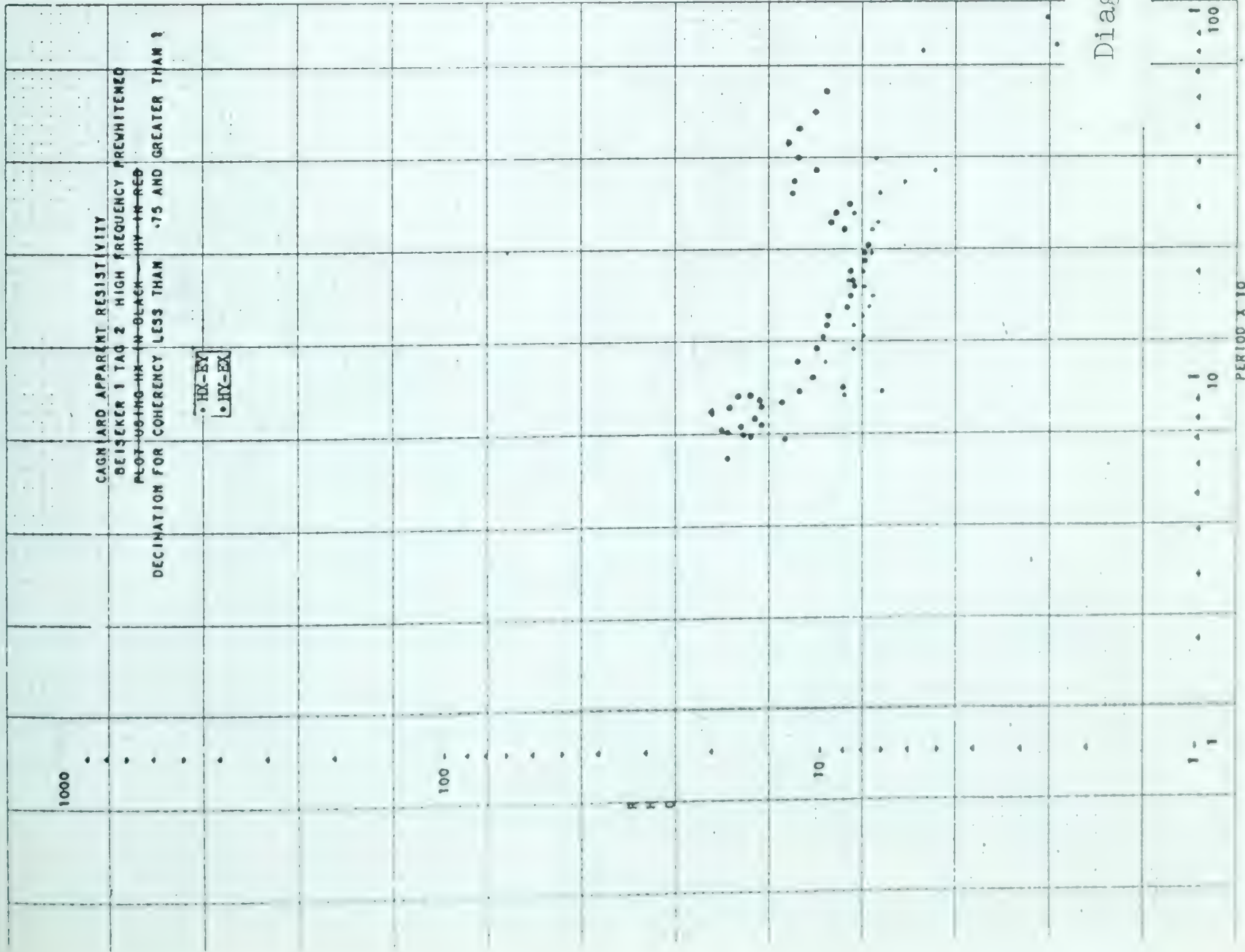
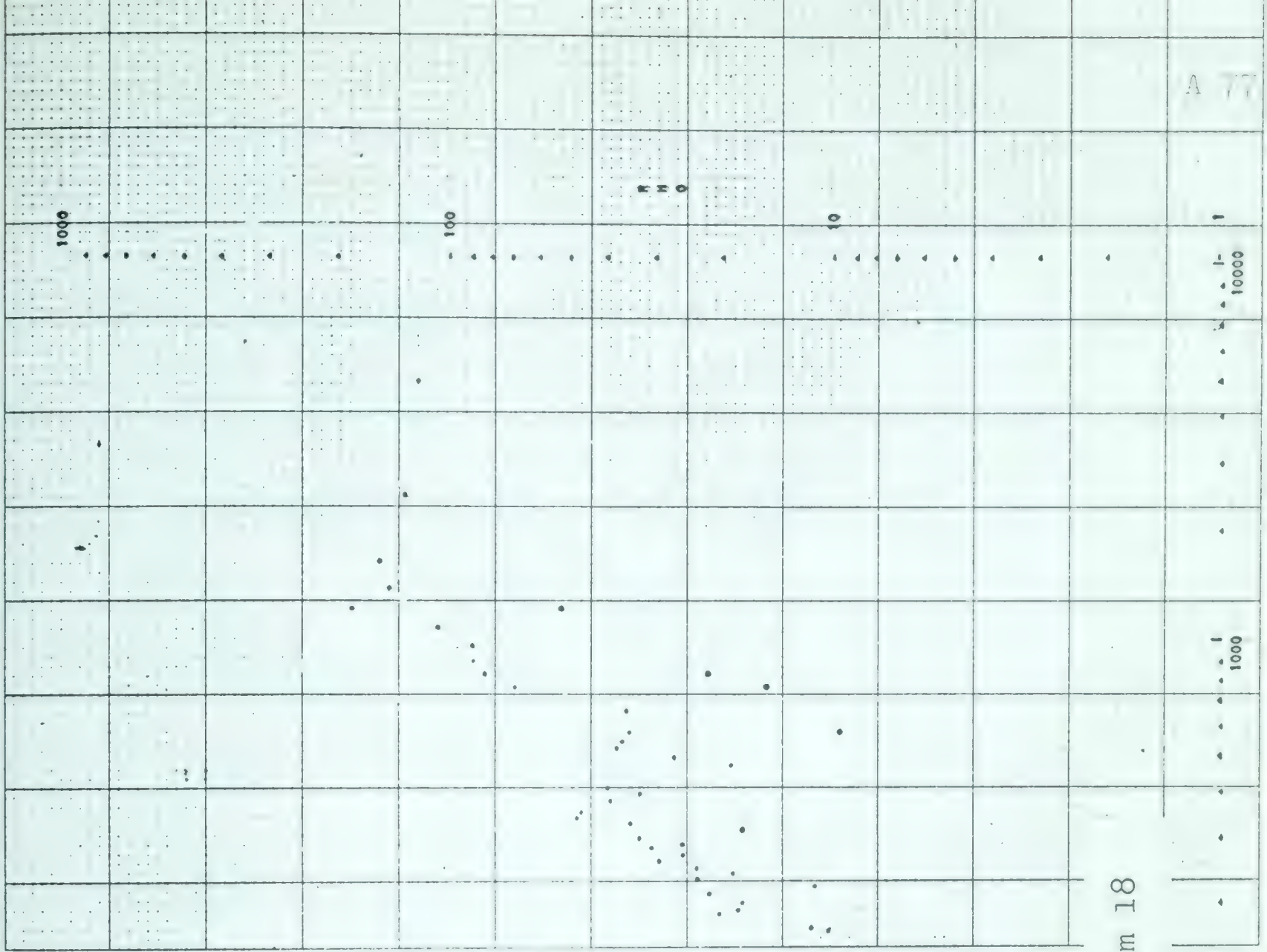


Diagram 18





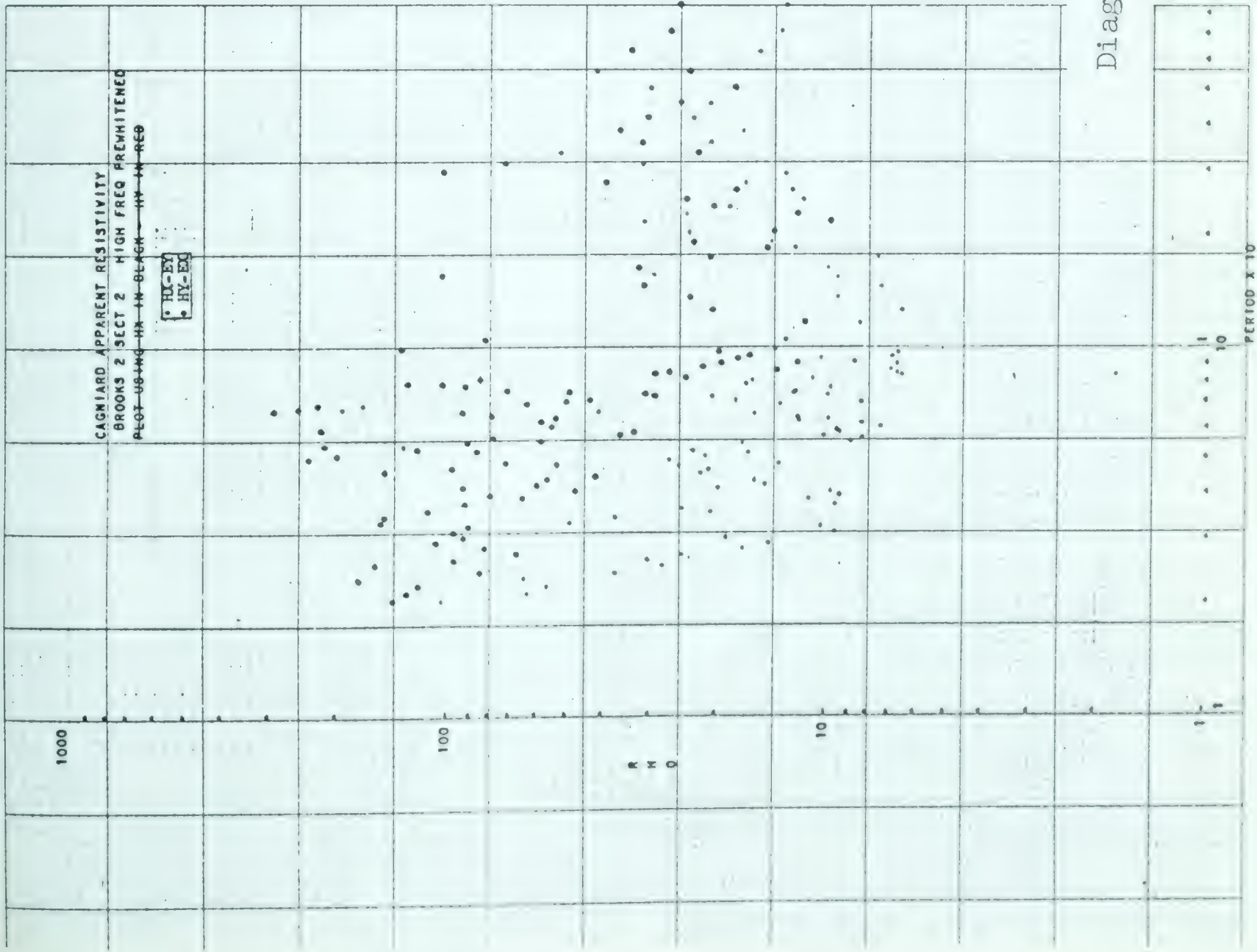
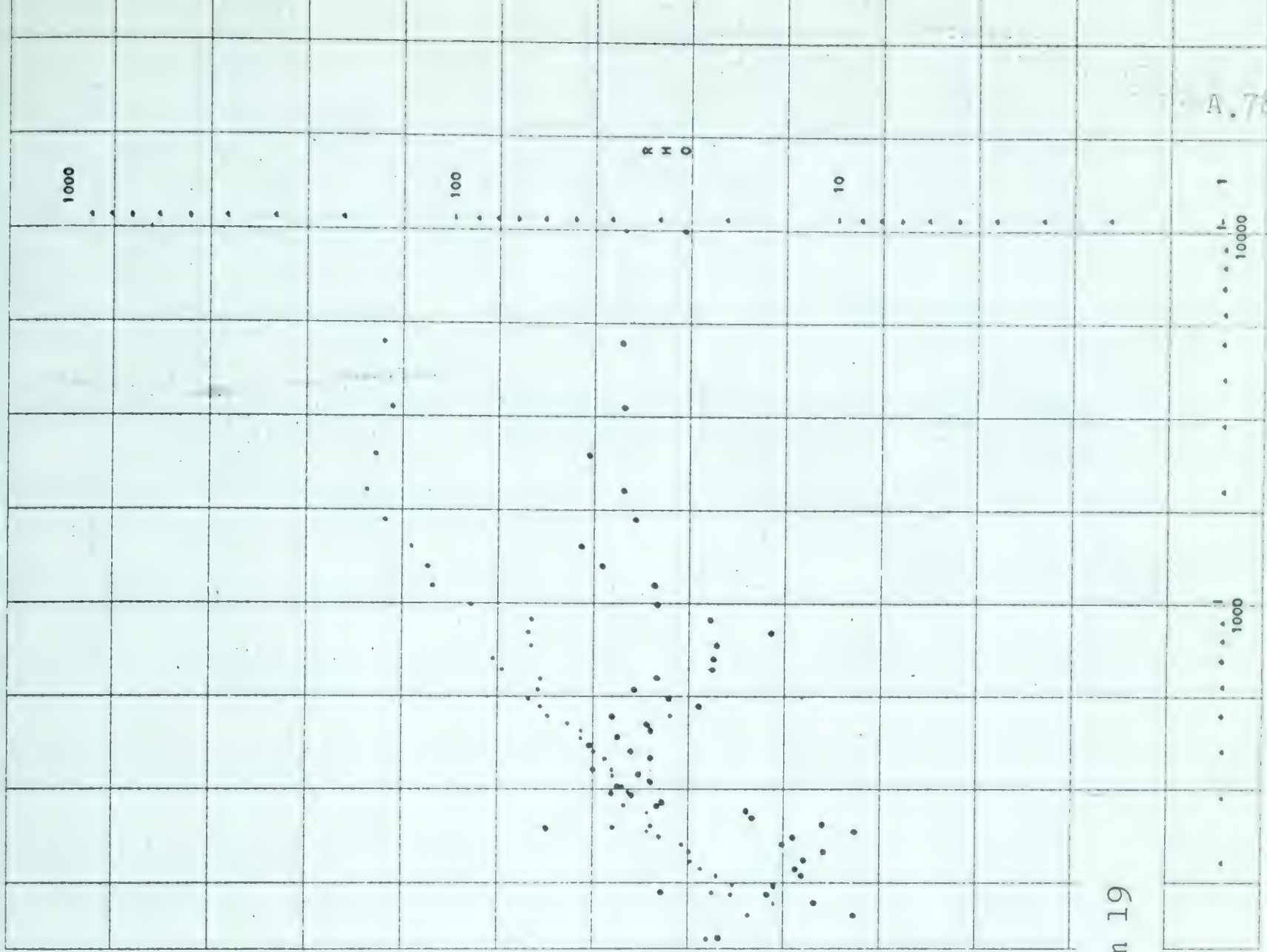


Diagram 19





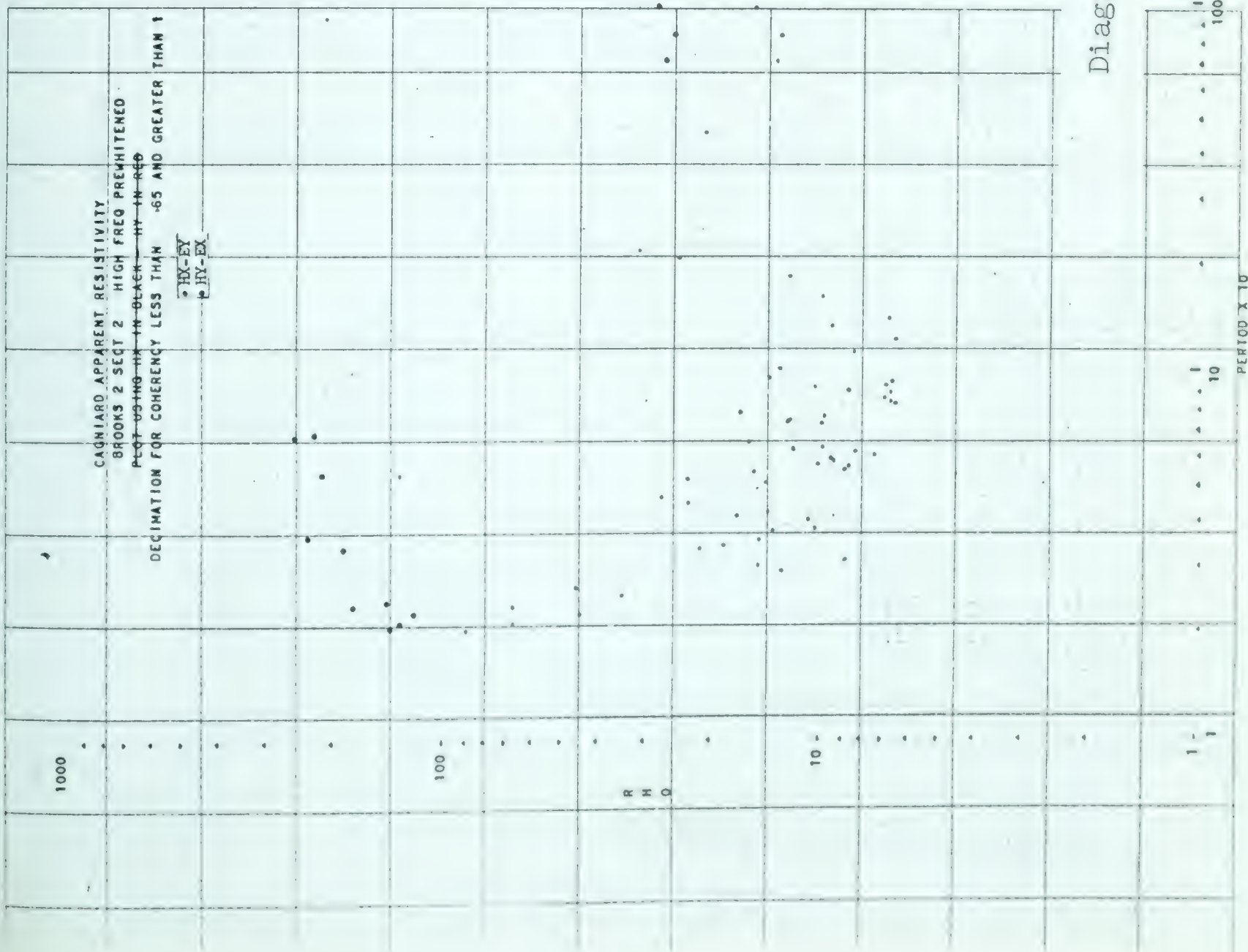
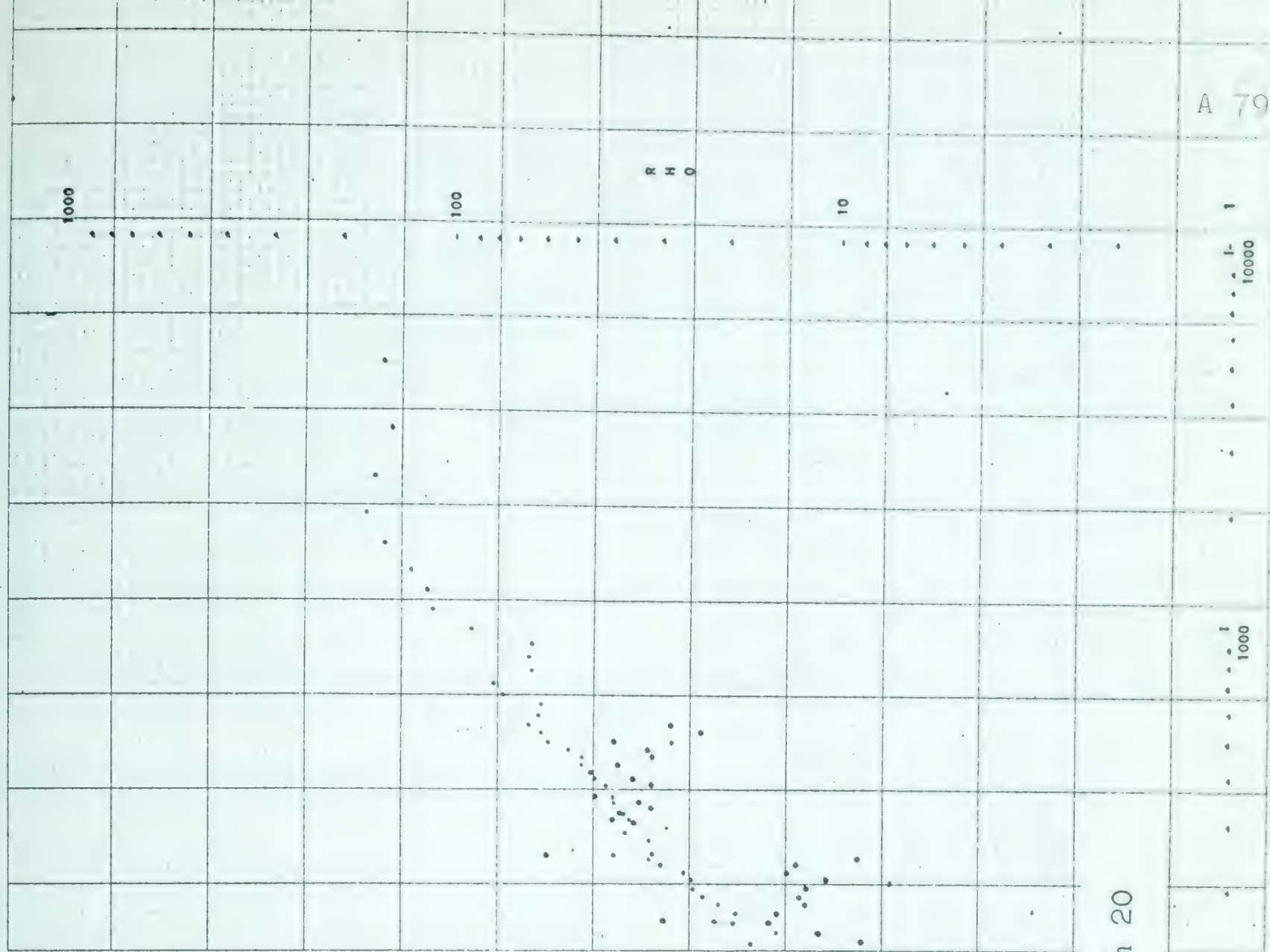


Diagram 20



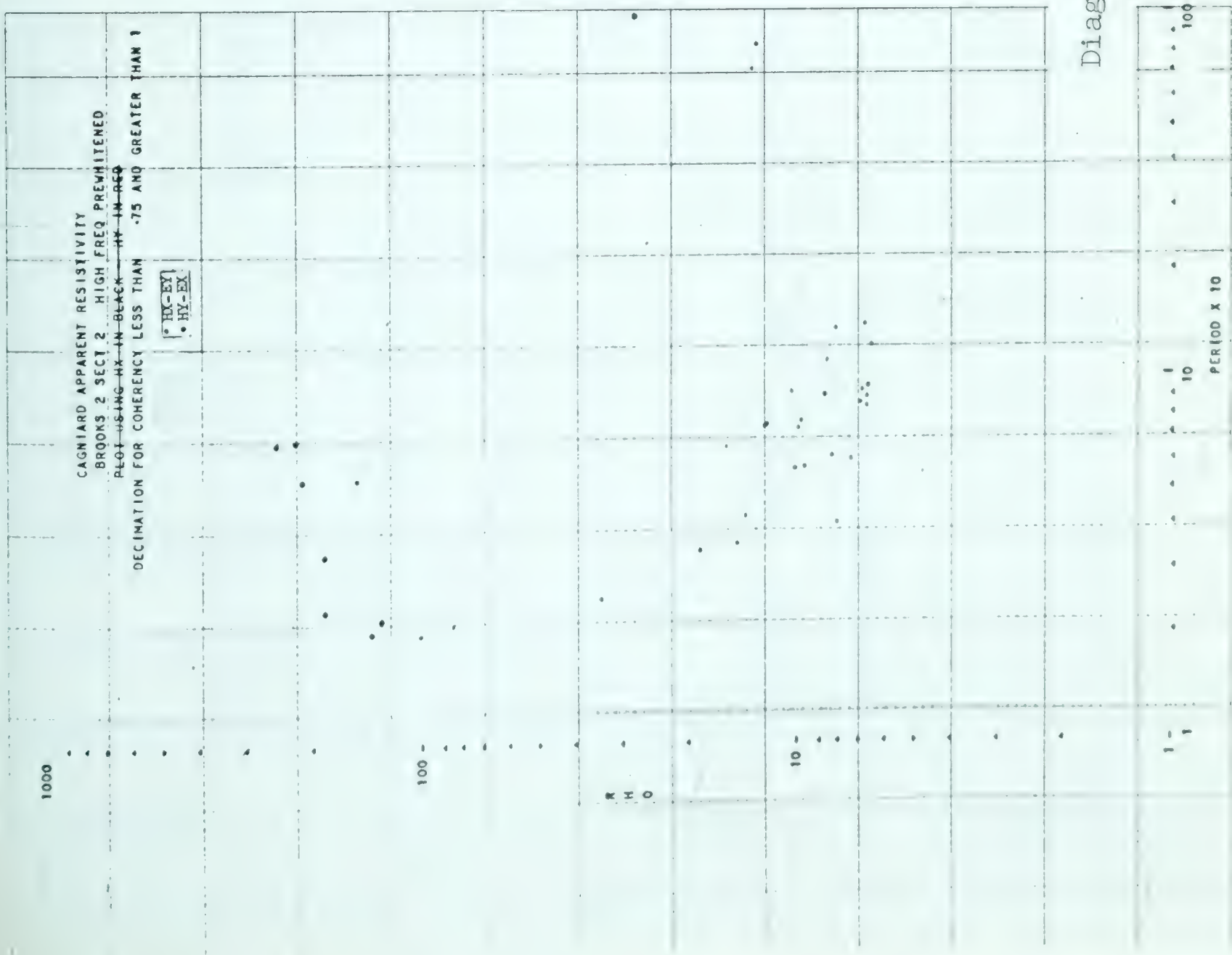
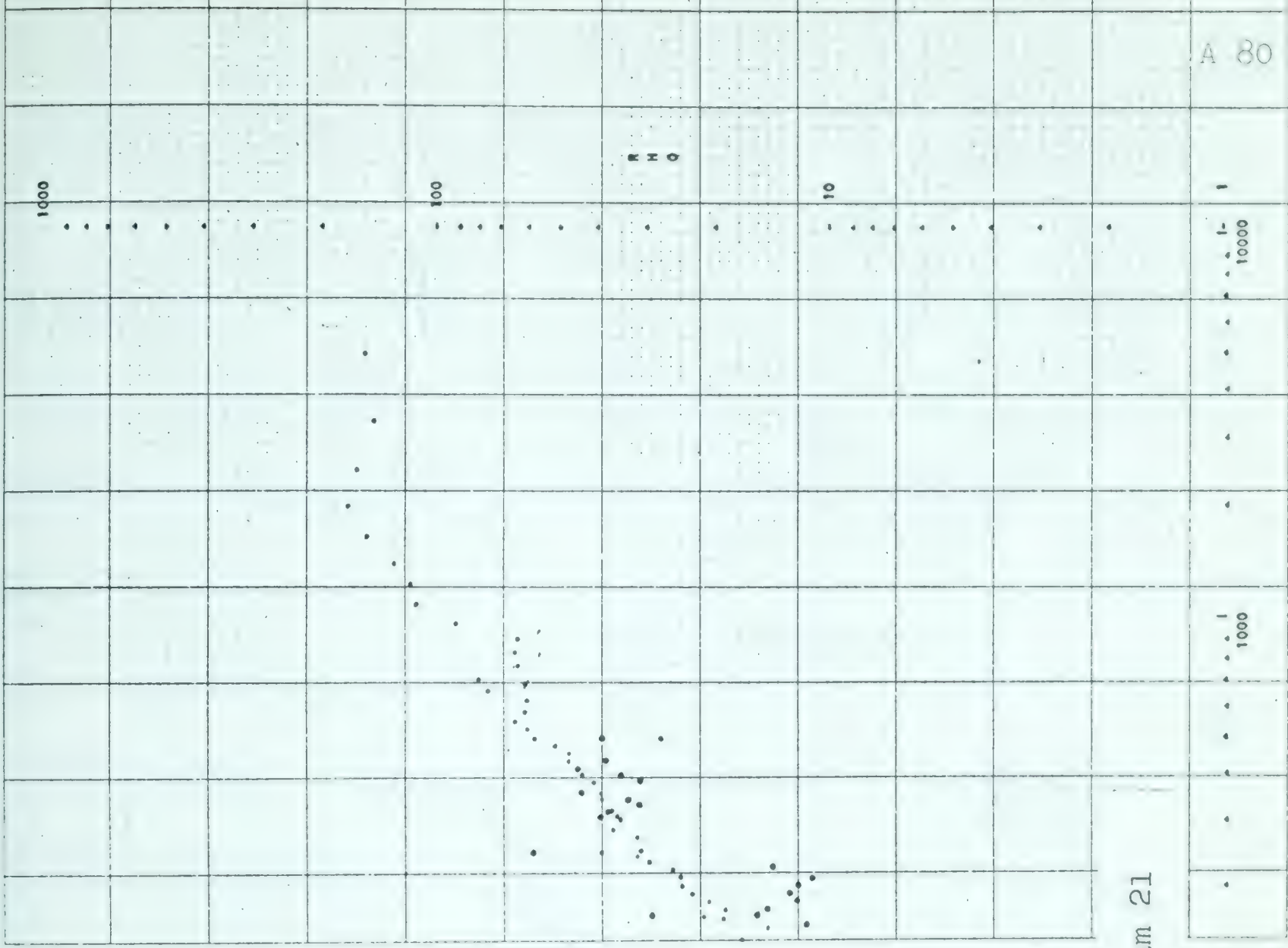


Diagram 21



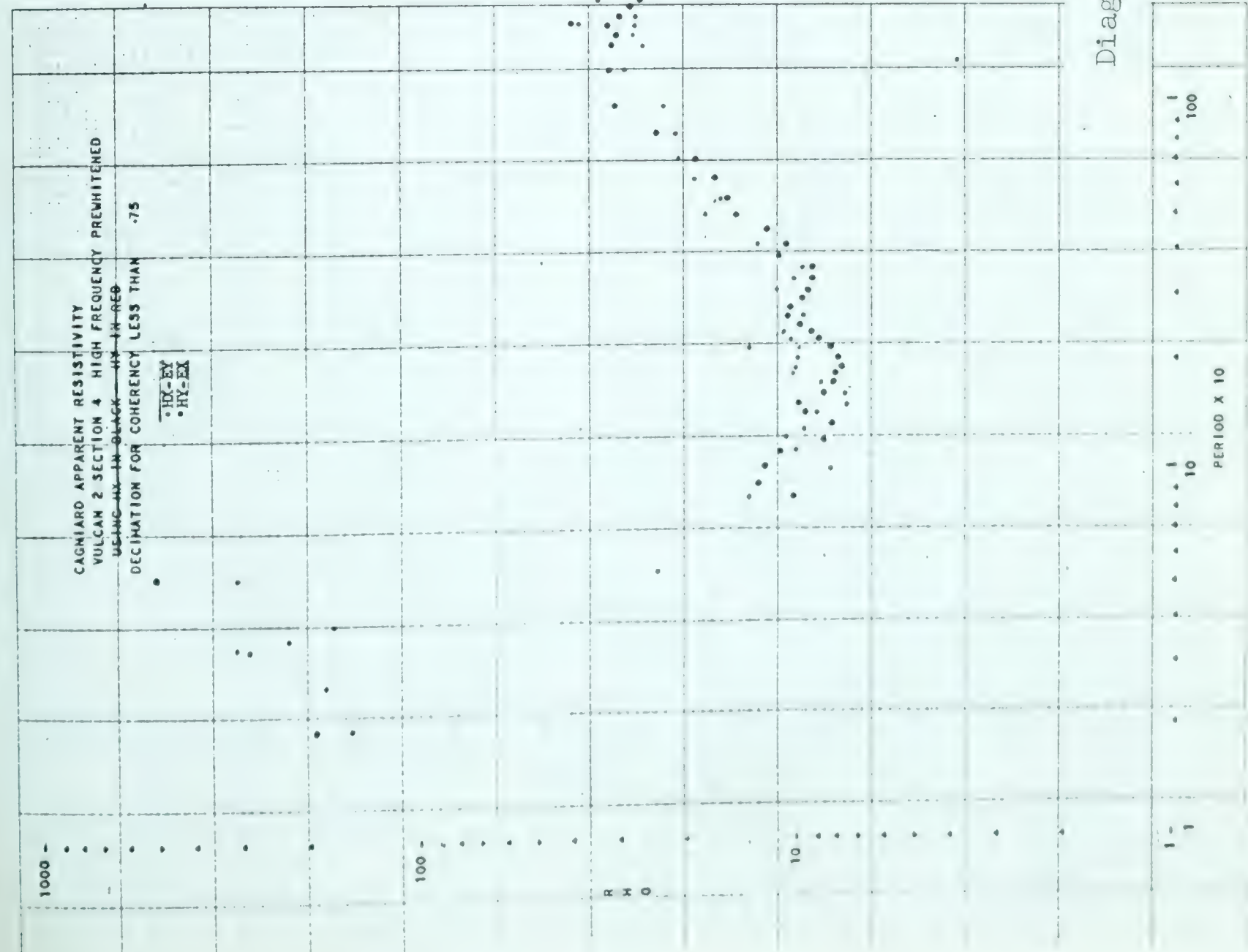
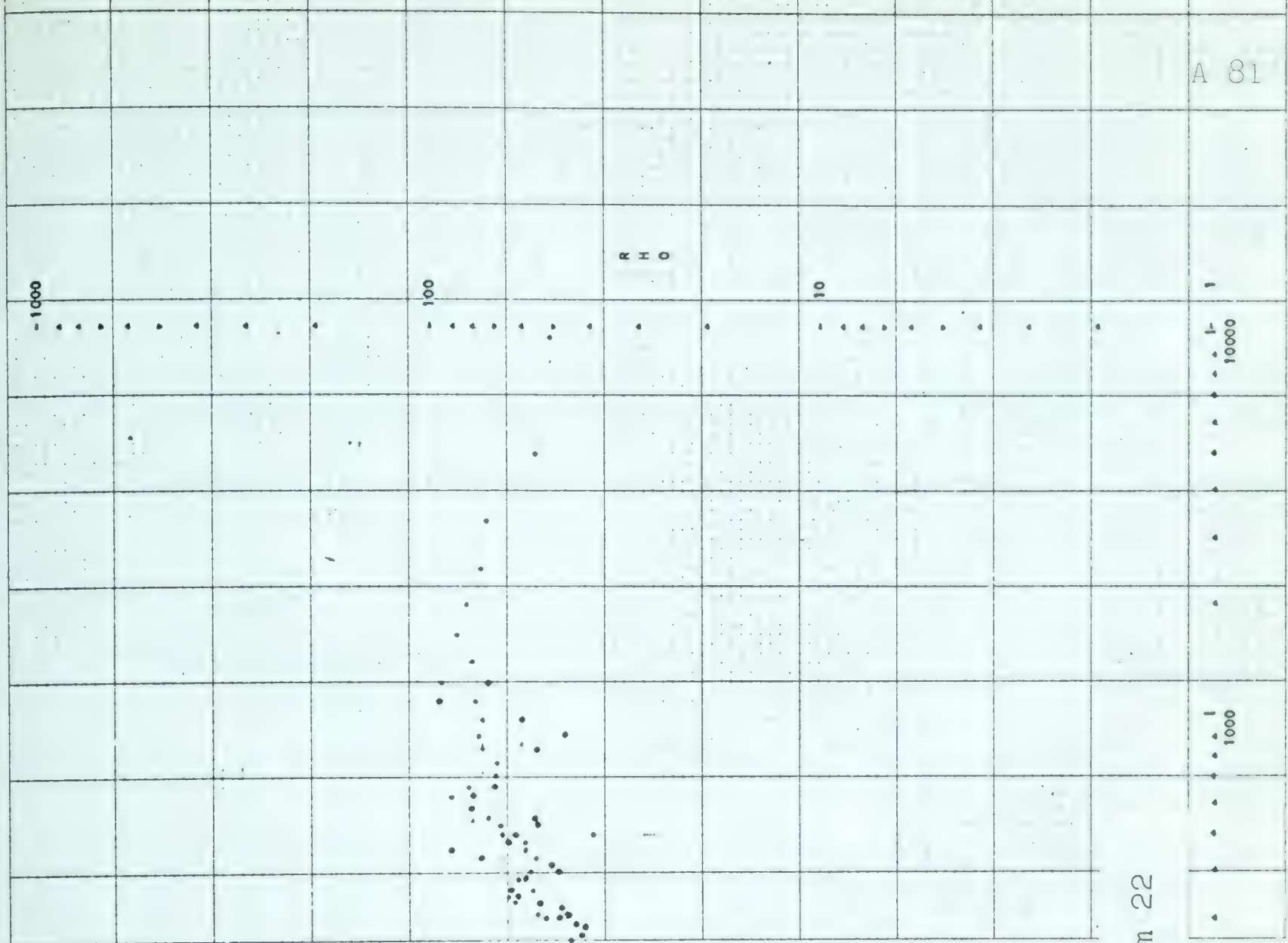


Diagram 22

PLOT OF PHASE DIFFERENCES
VULCAN 2 4 HIGH FREQ PREWHITENED

IN BLACK - HY IN RED

DECIMATION FOR COHERENCY LESS THAN 8-0000-01

• HY-EX
• HY-EX

120-

105-

90-

75-

60-

45-

30-

15-

0-

-15-

-30-

T H E T A D E Q R E E S

PERIOD X 10
1 10 100

Diagram 23

1000

10000

-30

-15

0

15

30

45

60

75

90

105

120

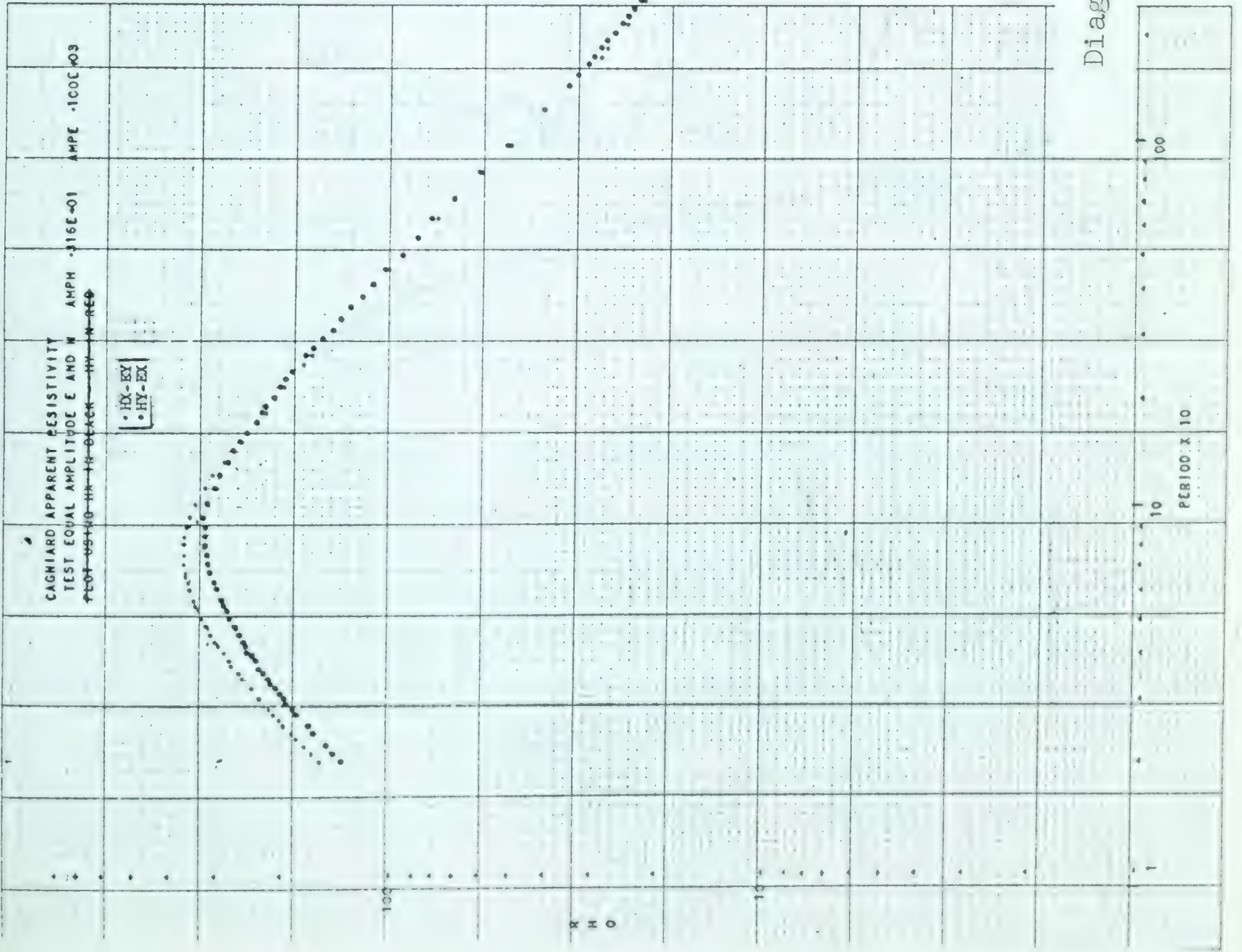
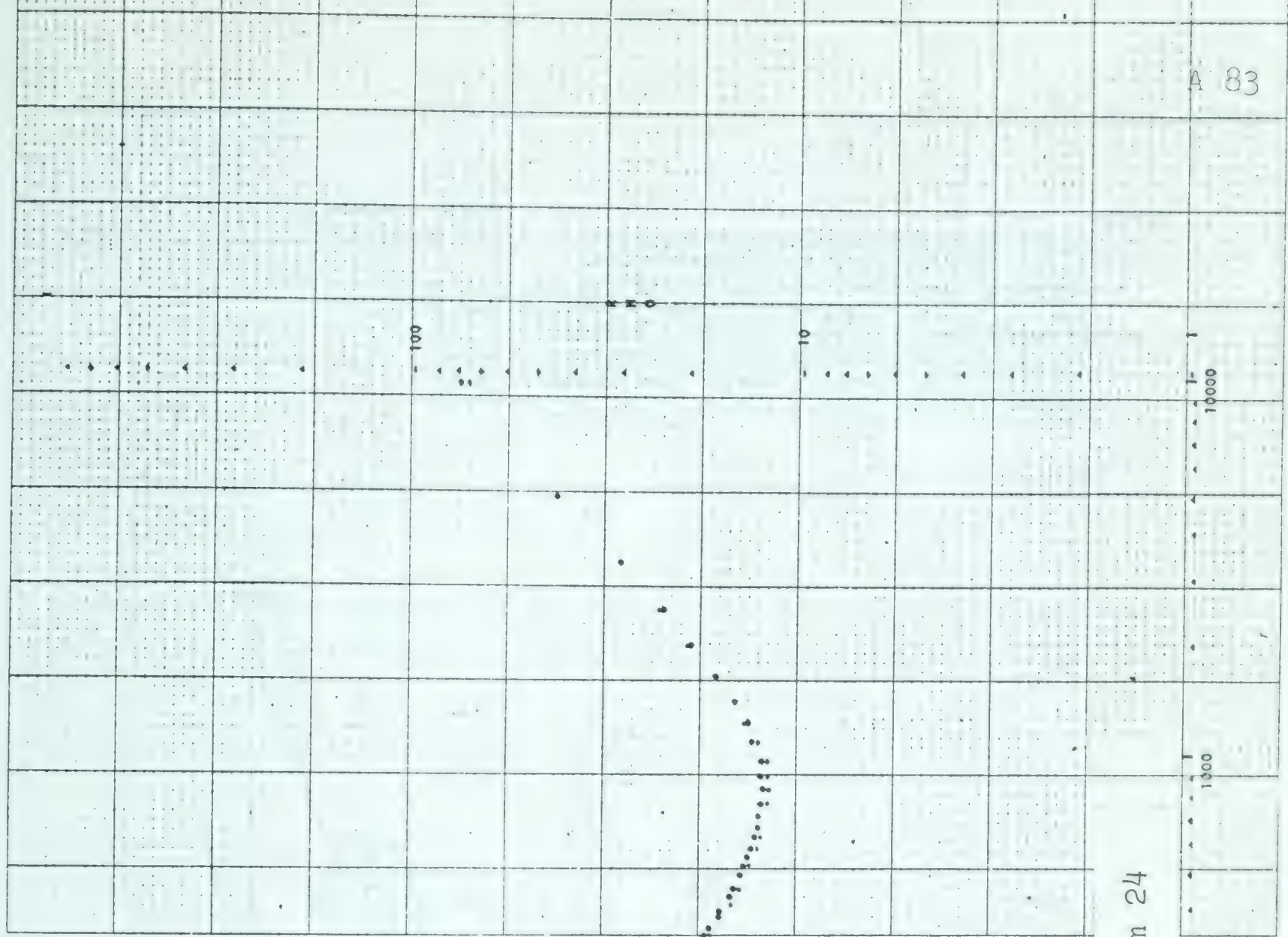


Diagram 24

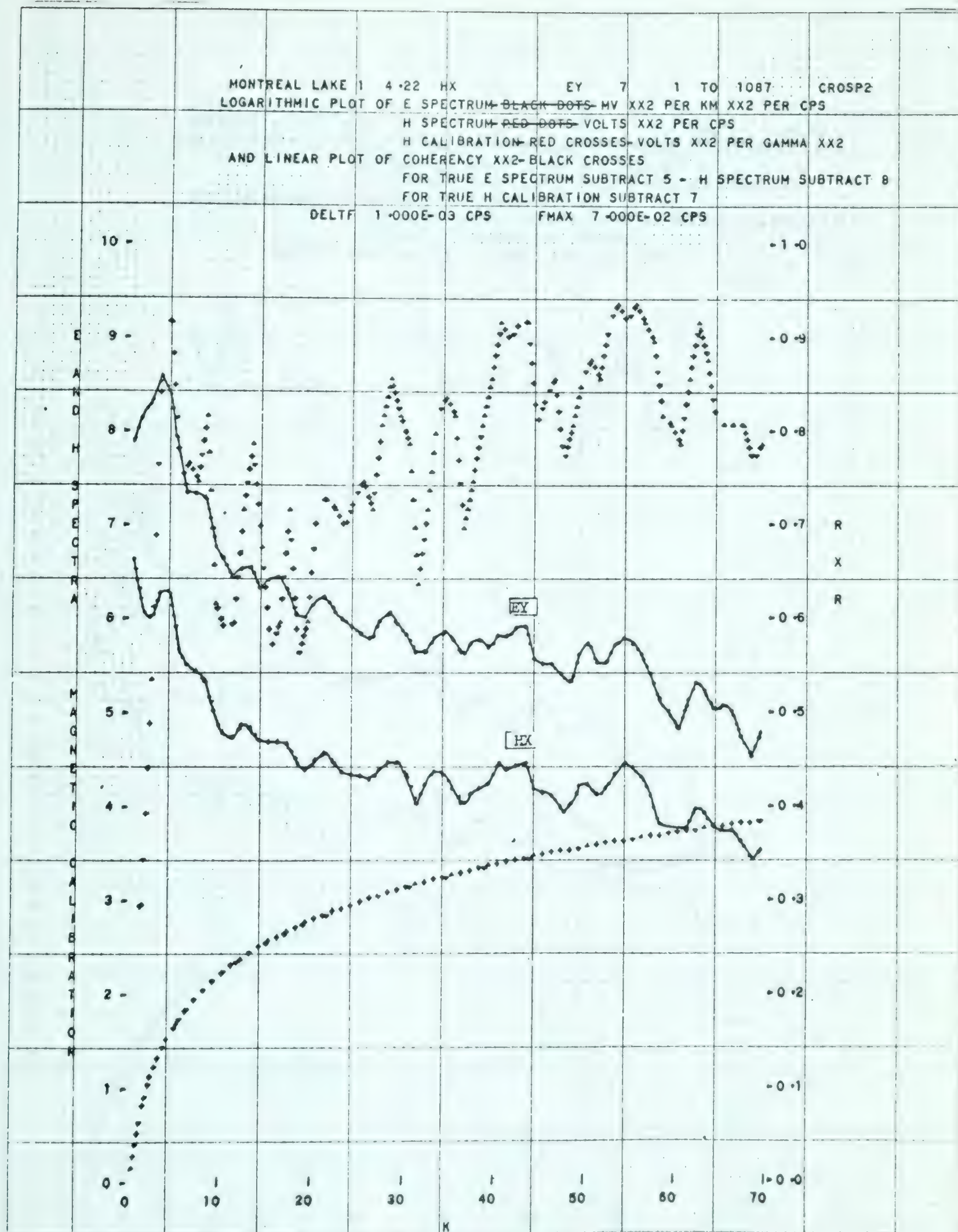


Diagram 25

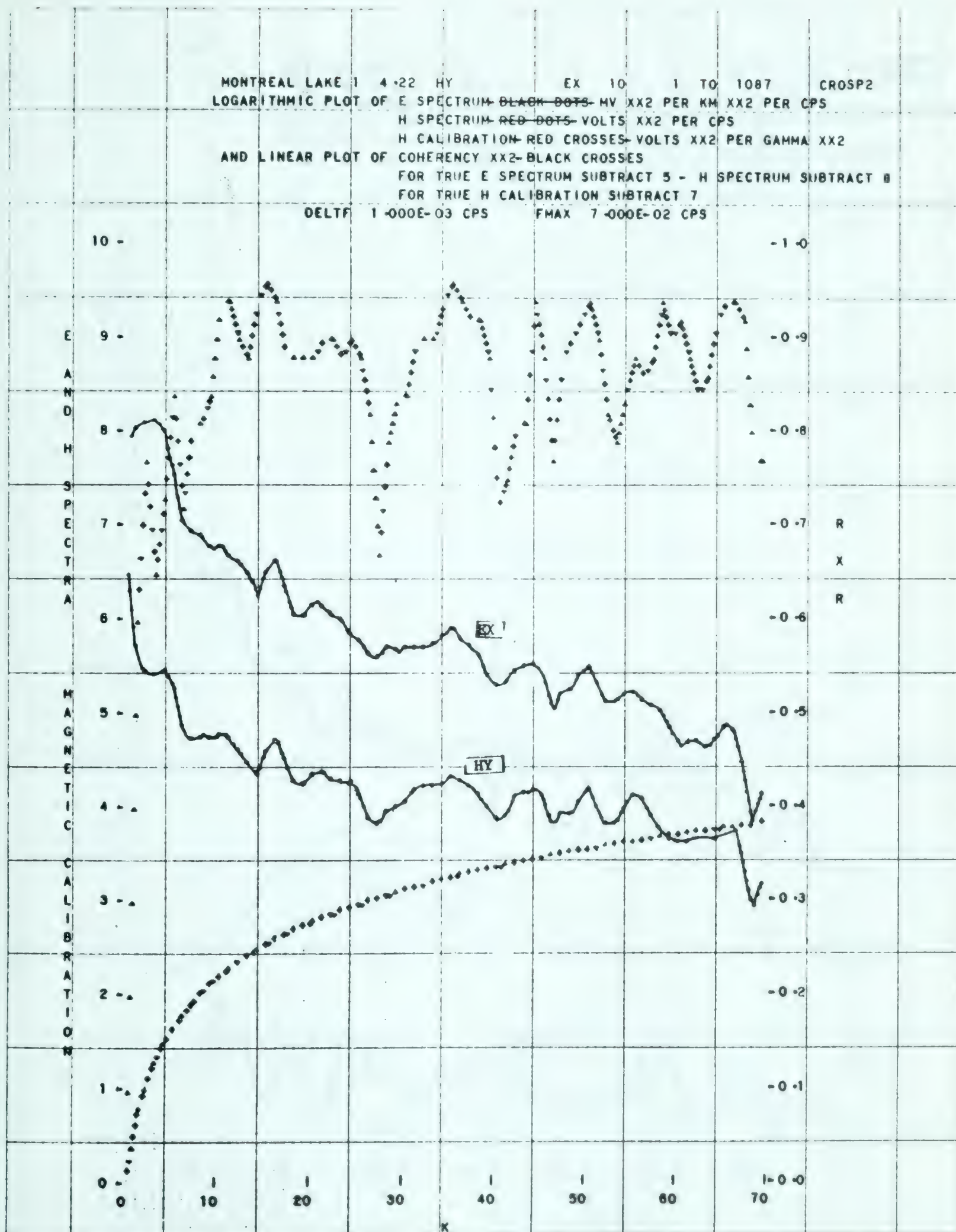


Diagram 26

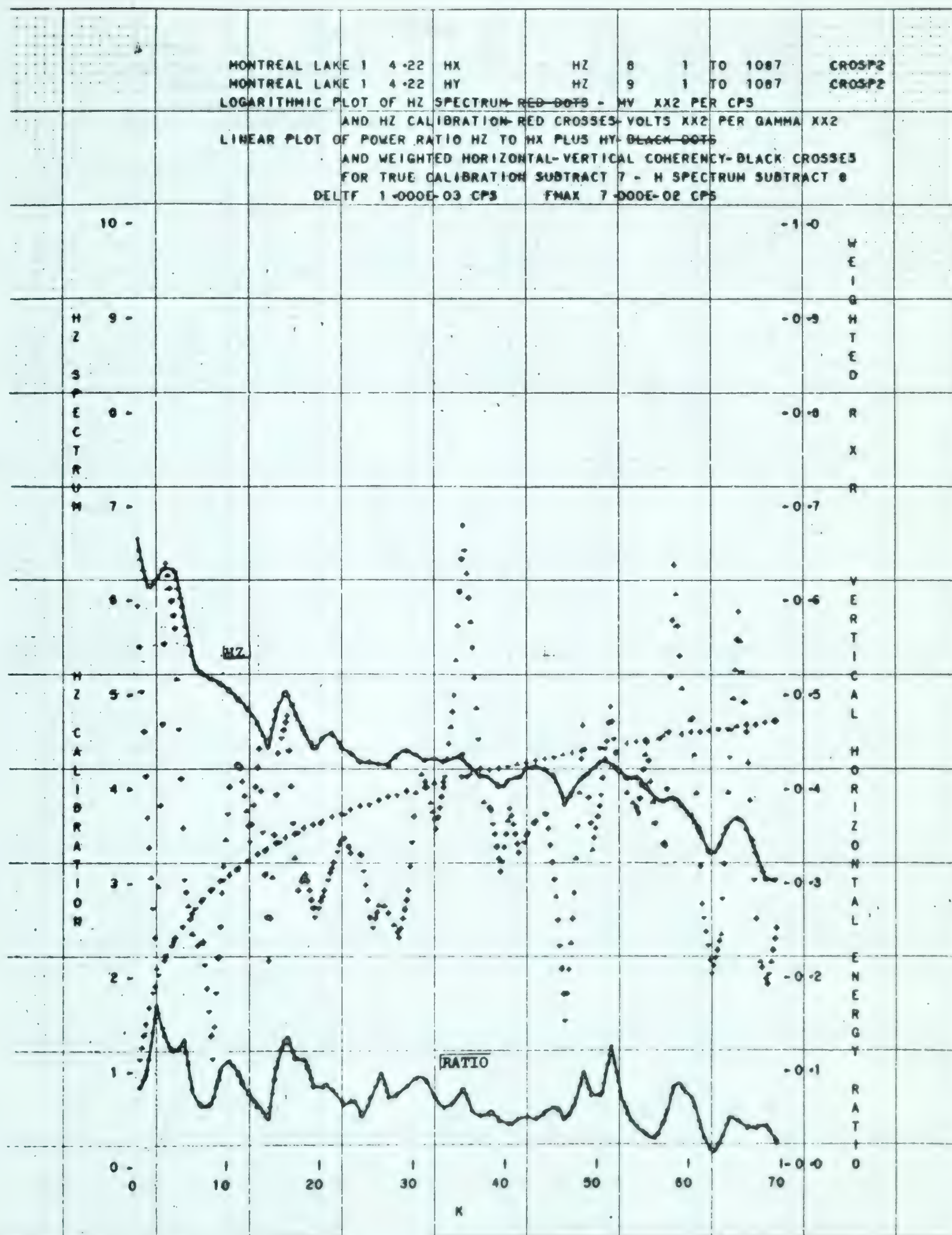


Diagram 27

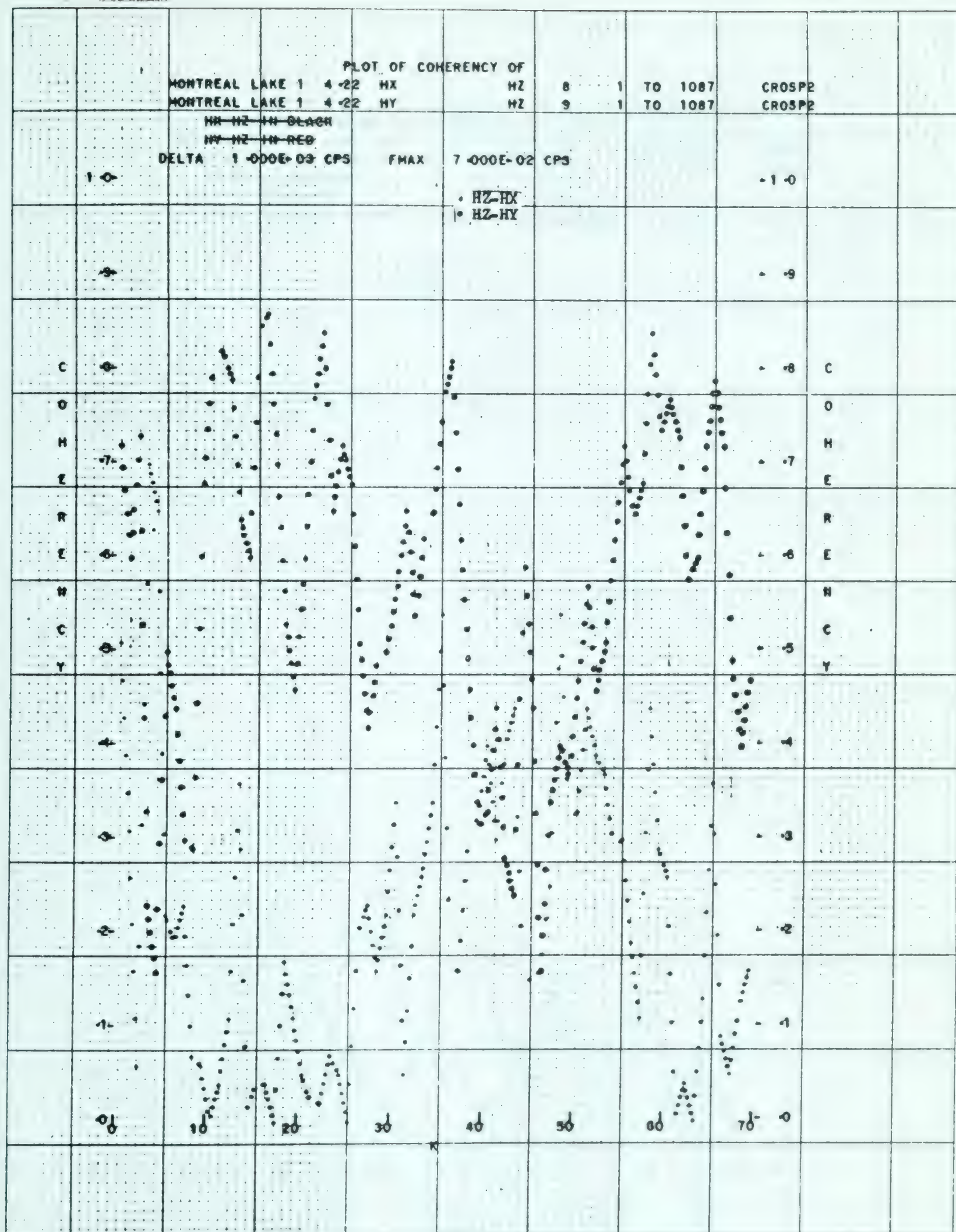


Diagram 28



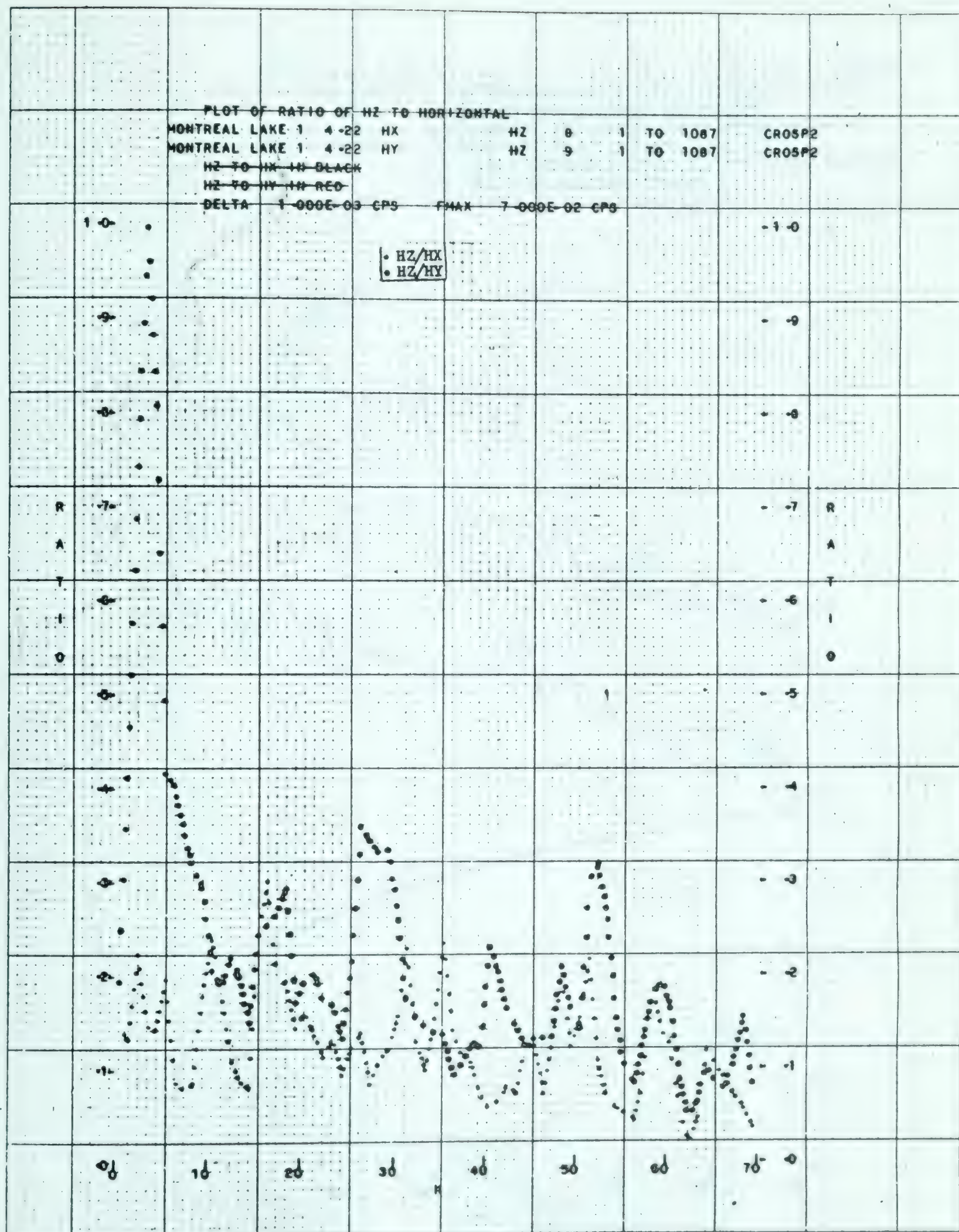


Diagram 29

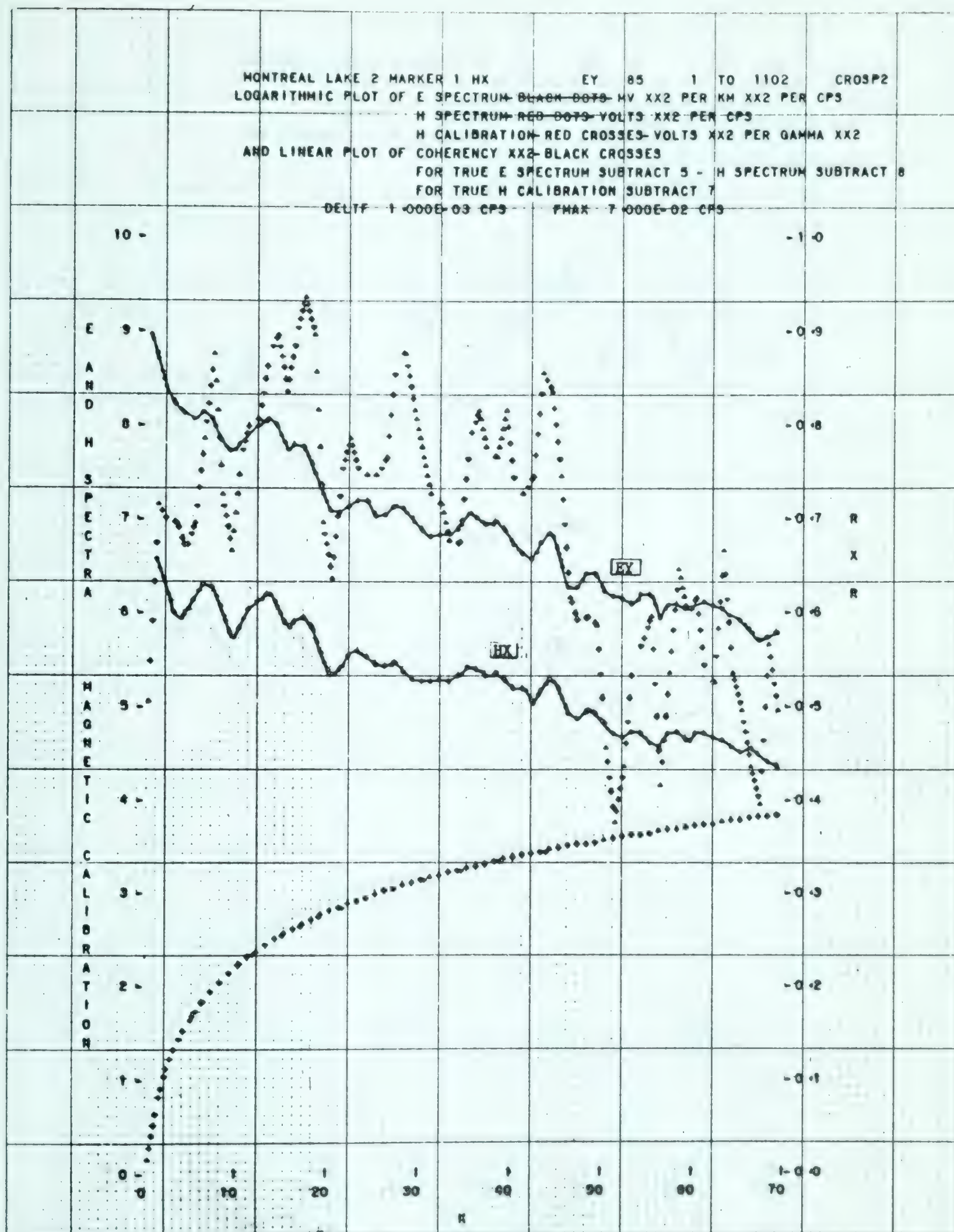


Diagram 30



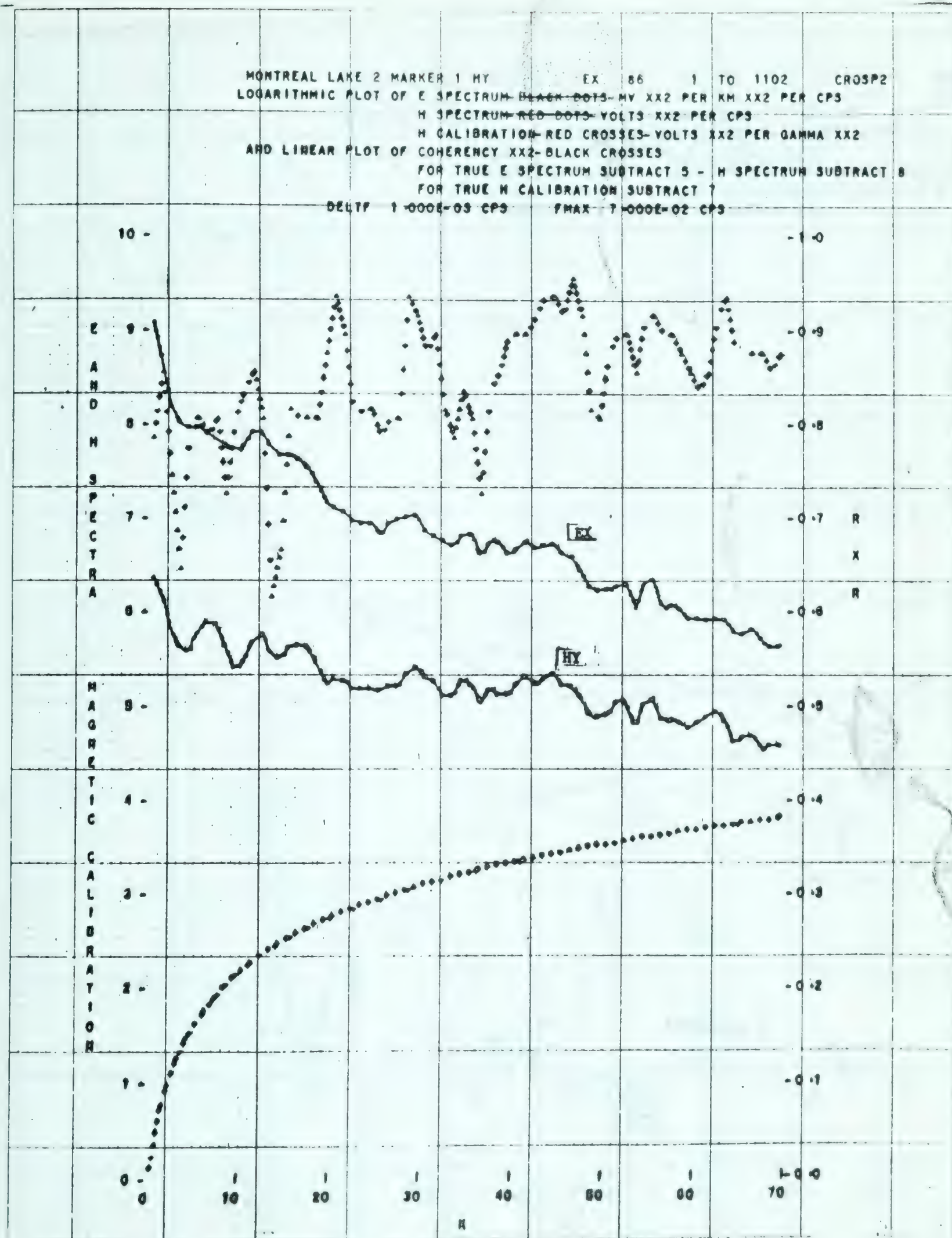


Diagram 31

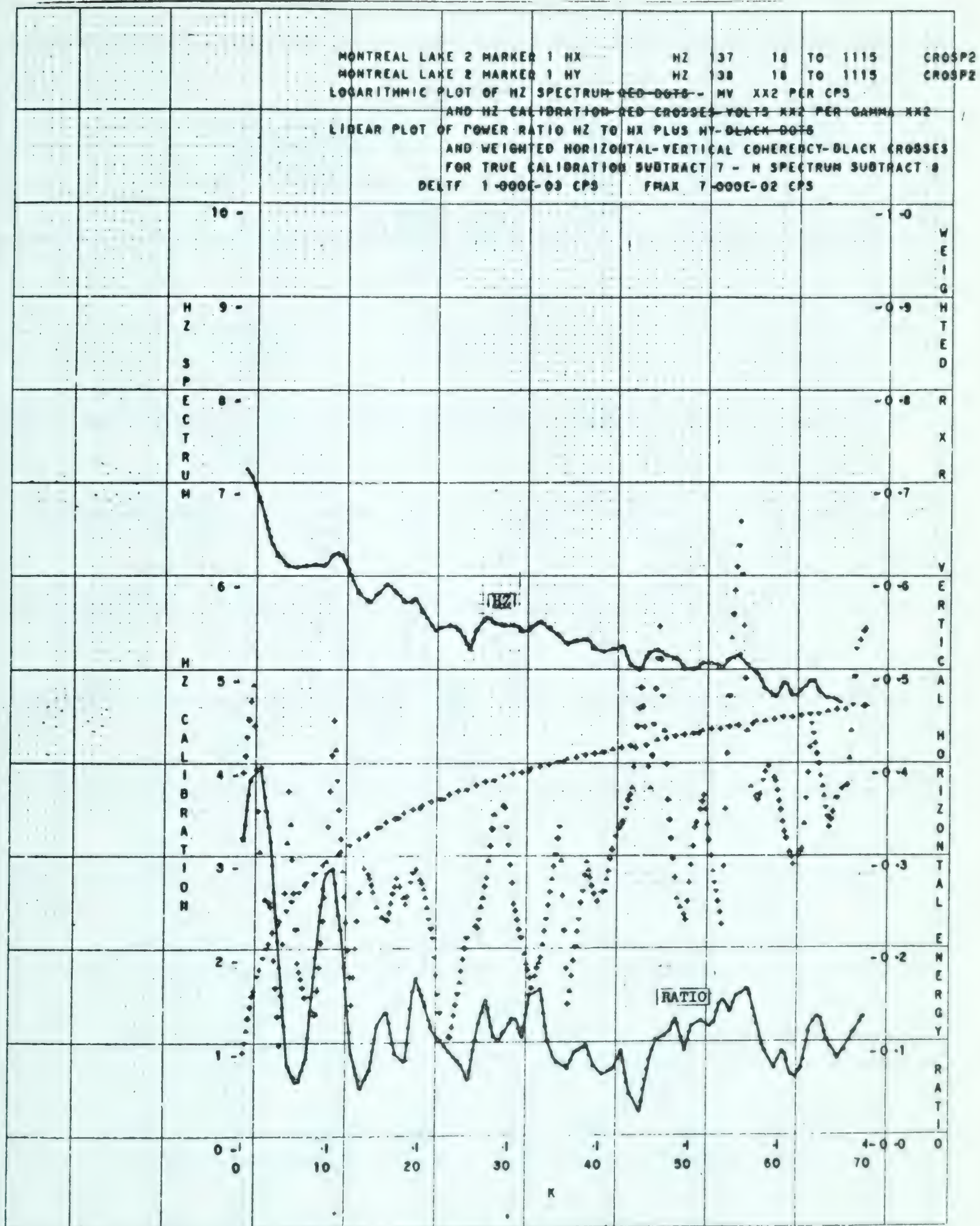


Diagram 32



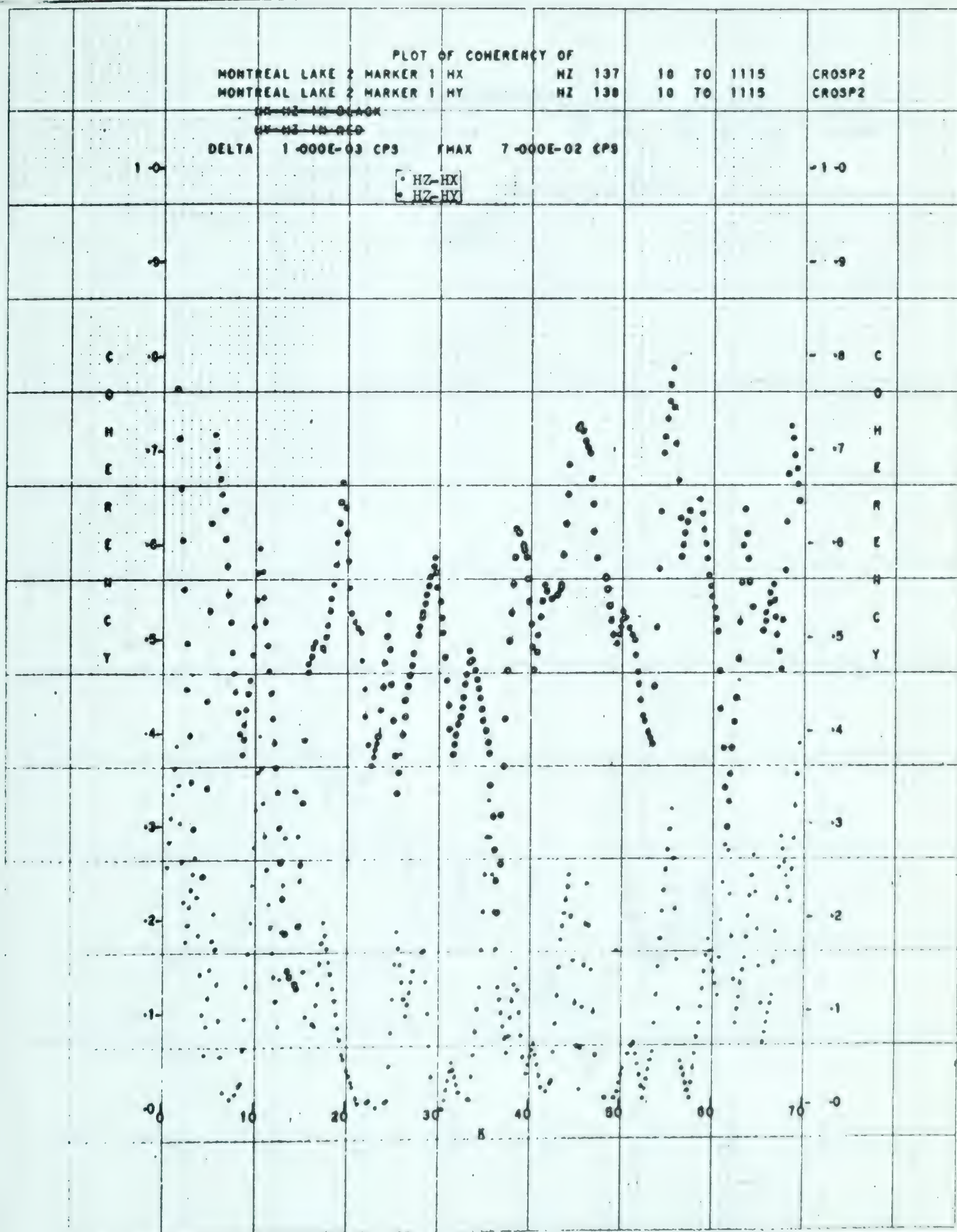


Diagram 33

1000

1000

1000

1000

1000

1000

1000

1000

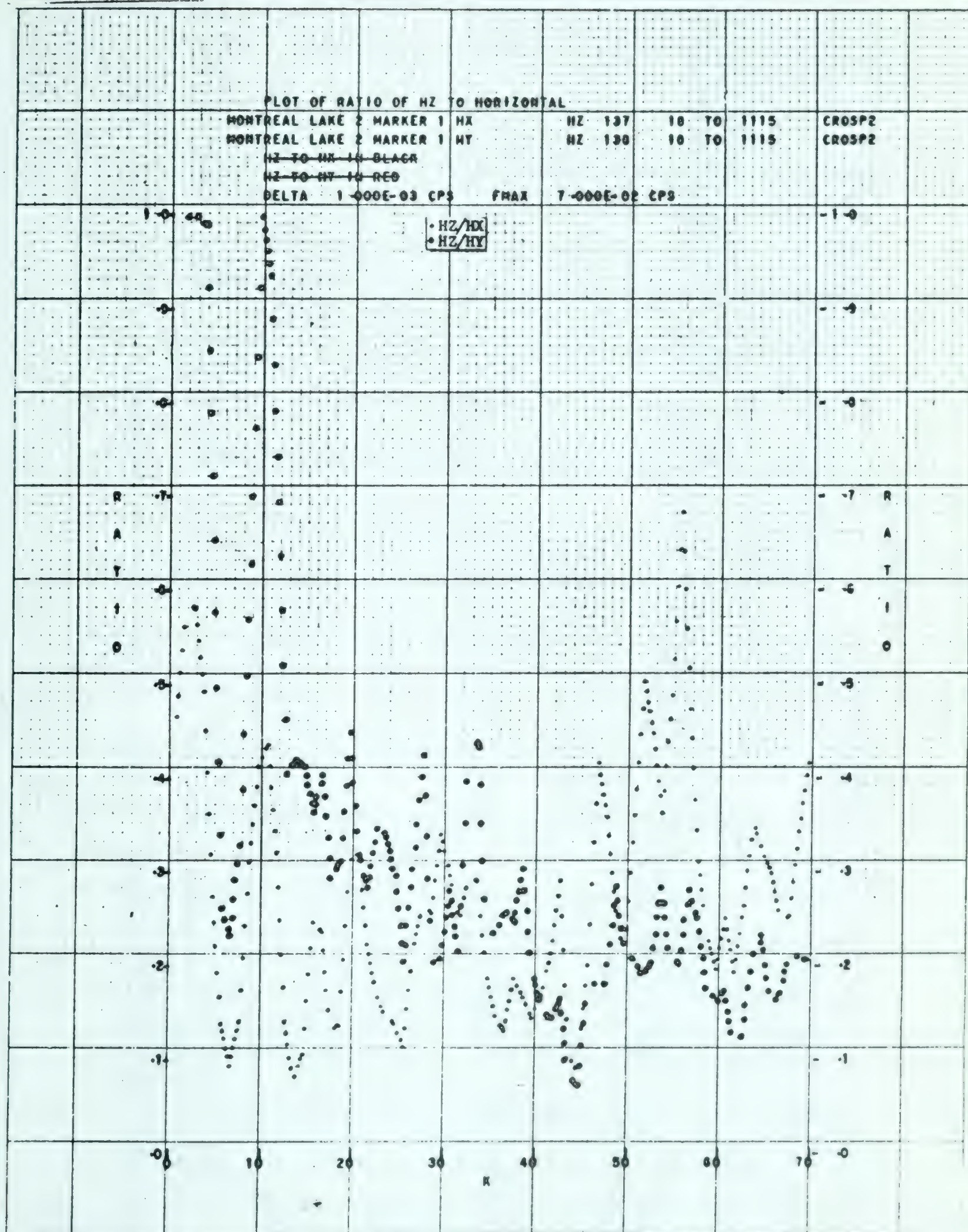


Diagram 34

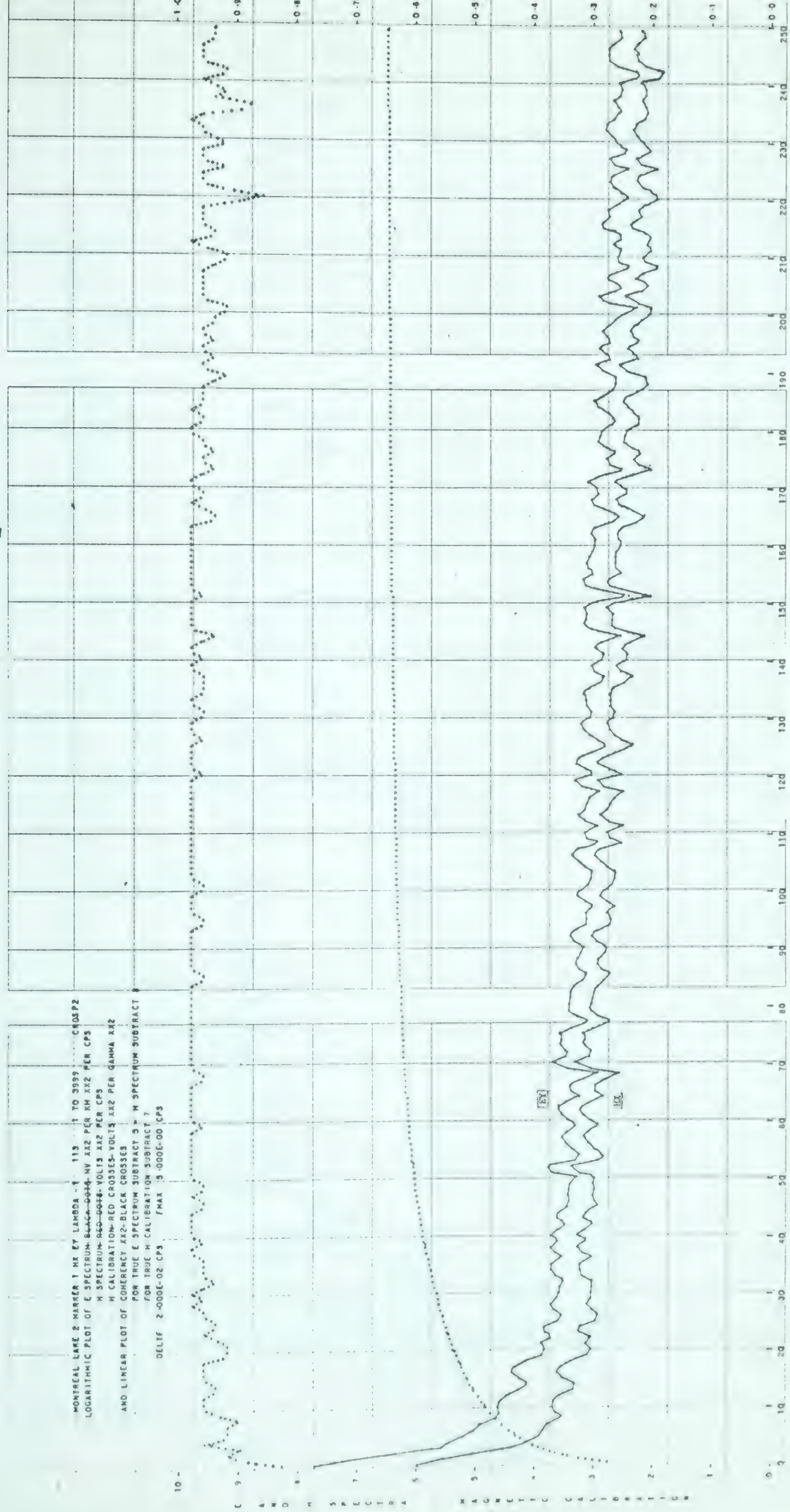


Diagram 35



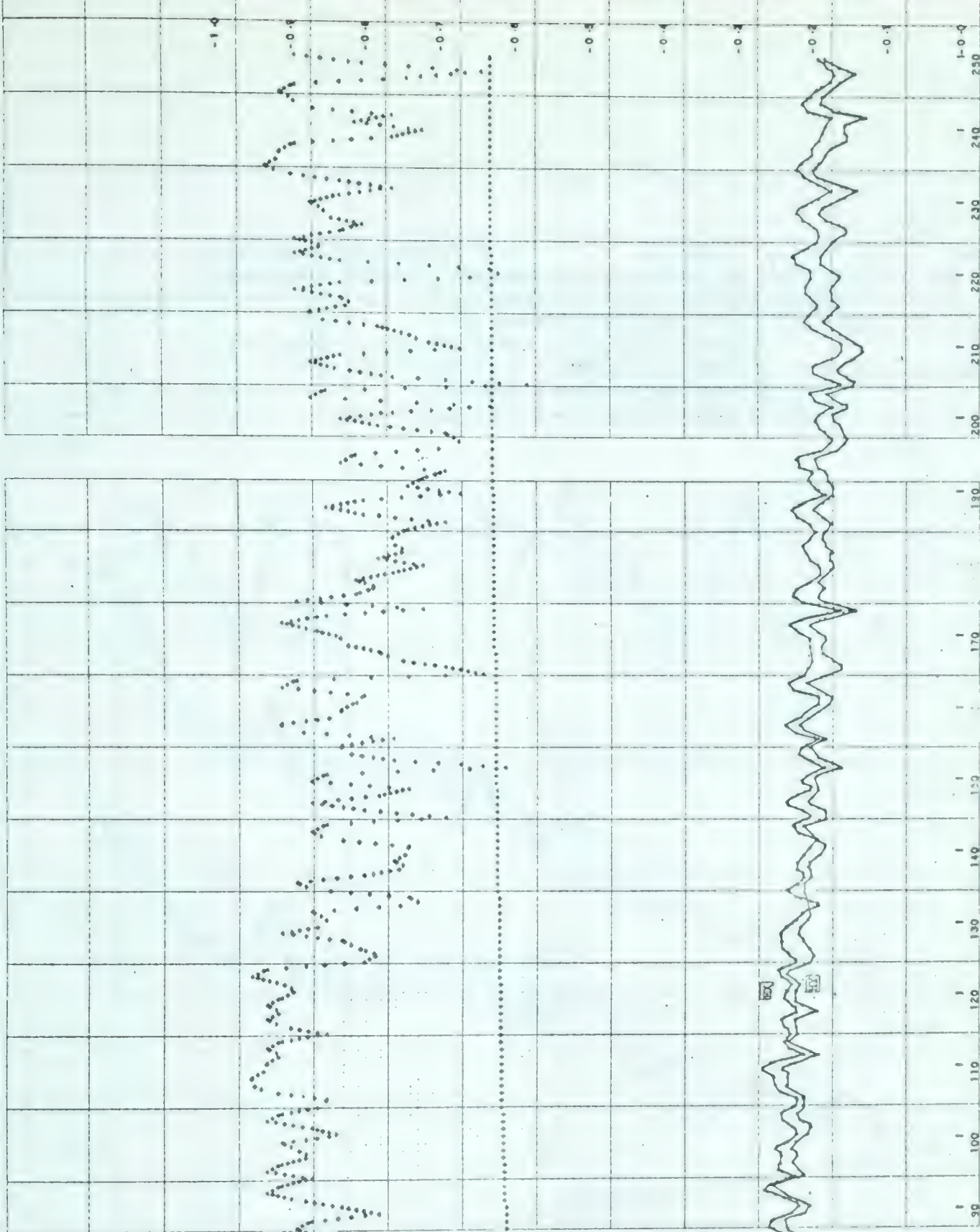
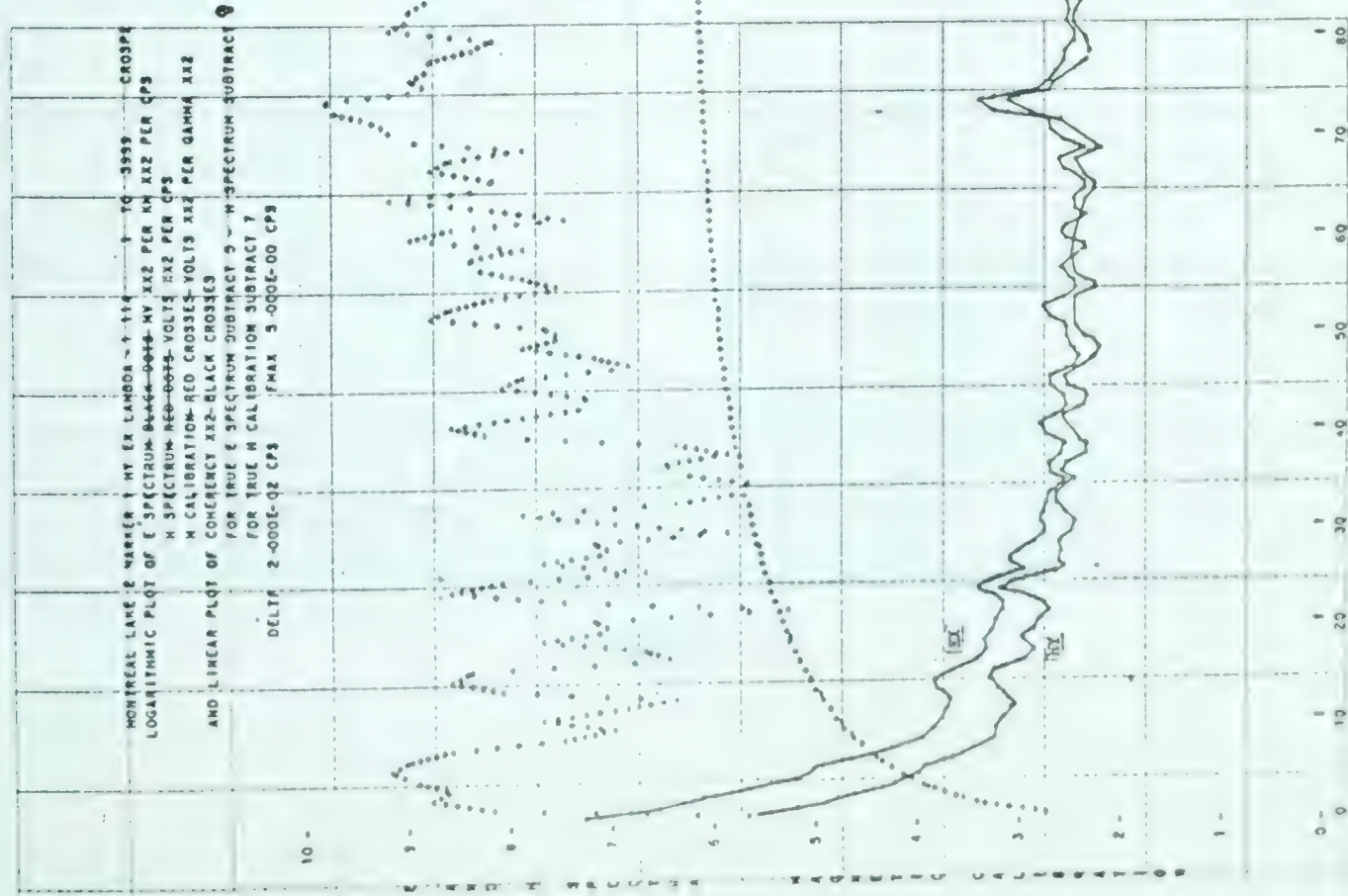


Diagram 36

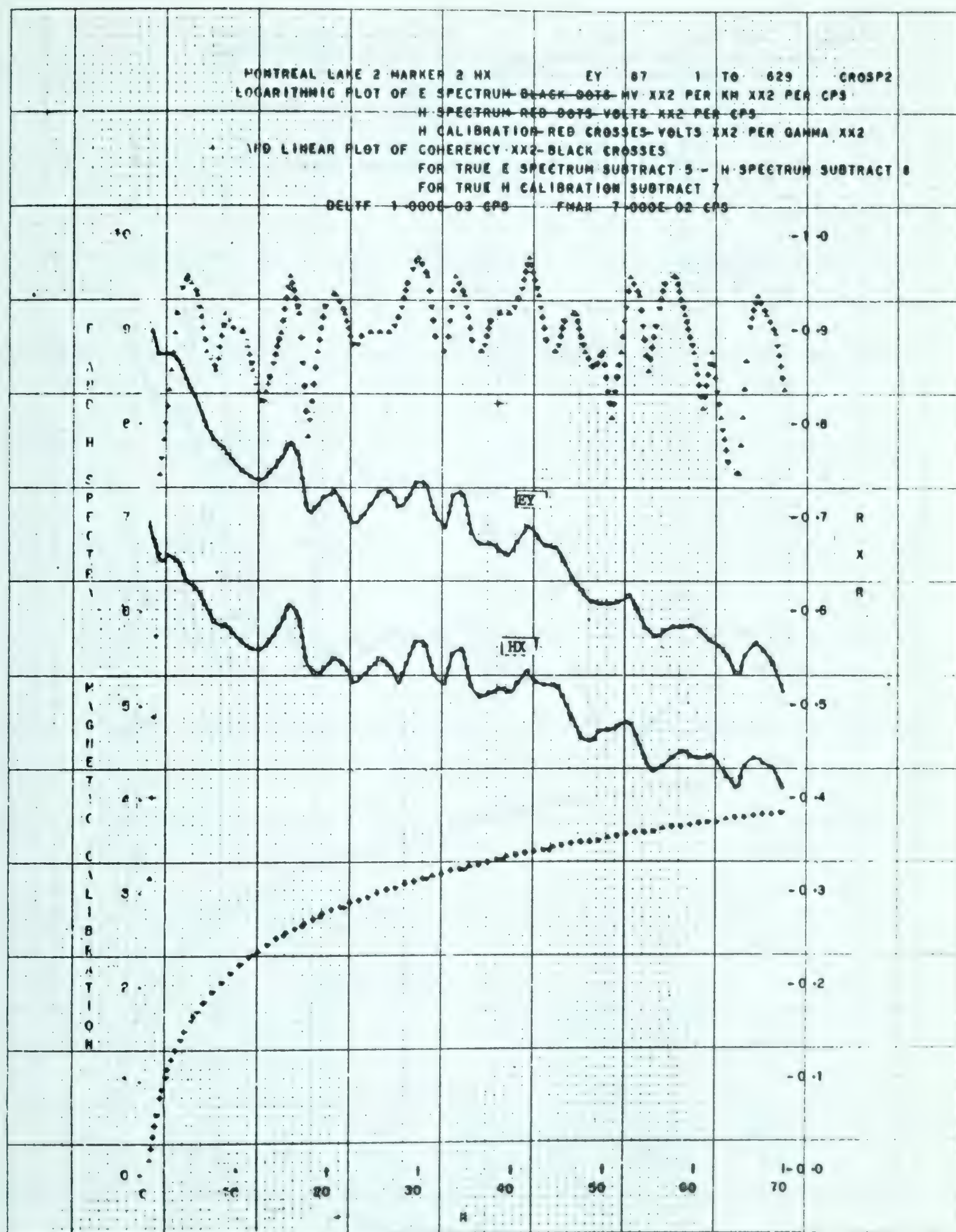


Diagram 37

Handwritten text at the top of the page, possibly a title or header.

Handwritten text in the second section, appearing as a list or series of notes.

Handwritten text in the third section, continuing the notes or list.

Handwritten text in the fourth section, possibly a paragraph or a detailed note.

Handwritten text in the fifth section, continuing the notes.

Handwritten text in the sixth section, possibly a paragraph or a detailed note.

Handwritten text in the seventh section, continuing the notes.

Handwritten text at the bottom of the page, possibly a footer or concluding note.

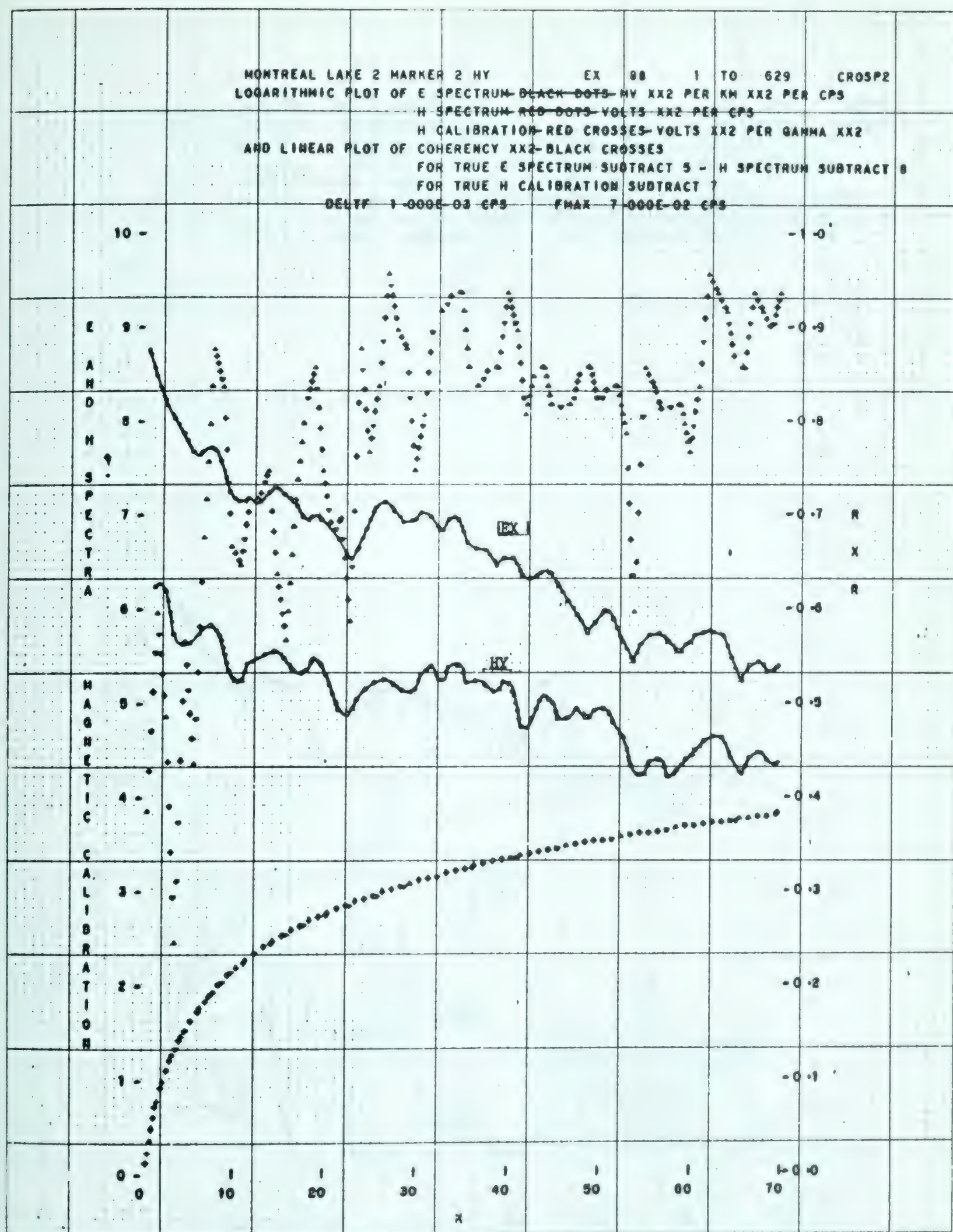


Diagram 38

Handwritten text at the top of the page, possibly a title or header, which is mostly illegible due to fading.



Handwritten text at the bottom center of the page, possibly a signature or a date.

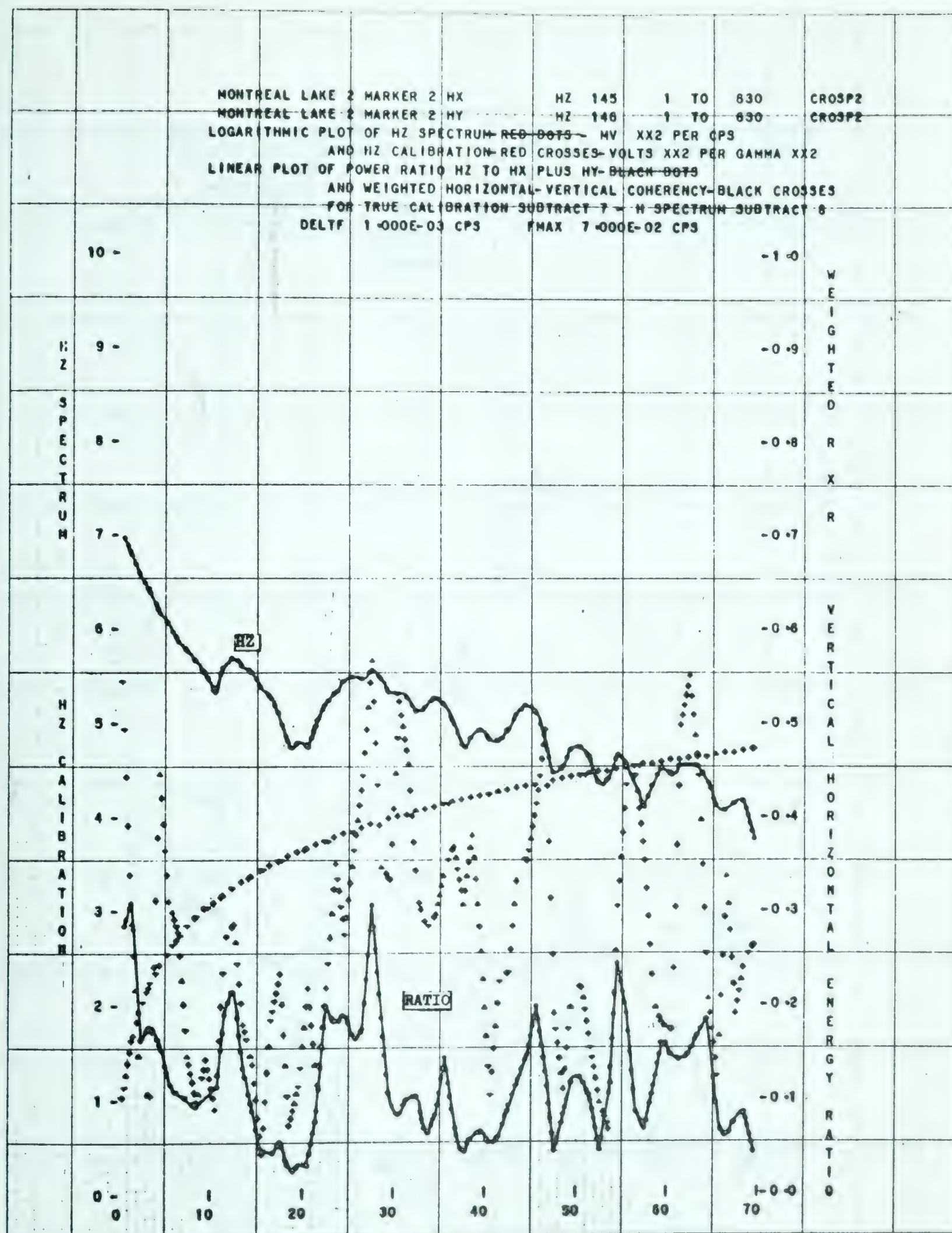


Diagram 39



100
 200
 300
 400
 500
 600
 700
 800
 900
 1000
 1100
 1200
 1300
 1400
 1500
 1600
 1700
 1800
 1900
 2000
 2100
 2200
 2300
 2400
 2500
 2600
 2700
 2800
 2900
 3000
 3100
 3200
 3300
 3400
 3500
 3600
 3700
 3800
 3900
 4000
 4100
 4200
 4300
 4400
 4500
 4600
 4700
 4800
 4900
 5000
 5100
 5200
 5300
 5400
 5500
 5600
 5700
 5800
 5900
 6000
 6100
 6200
 6300
 6400
 6500
 6600
 6700
 6800
 6900
 7000
 7100
 7200
 7300
 7400
 7500
 7600
 7700
 7800
 7900
 8000
 8100
 8200
 8300
 8400
 8500
 8600
 8700
 8800
 8900
 9000
 9100
 9200
 9300
 9400
 9500
 9600
 9700
 9800
 9900
 10000



100
 200
 300
 400
 500
 600
 700
 800
 900
 1000
 1100
 1200
 1300
 1400
 1500
 1600
 1700
 1800
 1900
 2000
 2100
 2200
 2300
 2400
 2500
 2600
 2700
 2800
 2900
 3000
 3100
 3200
 3300
 3400
 3500
 3600
 3700
 3800
 3900
 4000
 4100
 4200
 4300
 4400
 4500
 4600
 4700
 4800
 4900
 5000
 5100
 5200
 5300
 5400
 5500
 5600
 5700
 5800
 5900
 6000
 6100
 6200
 6300
 6400
 6500
 6600
 6700
 6800
 6900
 7000
 7100
 7200
 7300
 7400
 7500
 7600
 7700
 7800
 7900
 8000
 8100
 8200
 8300
 8400
 8500
 8600
 8700
 8800
 8900
 9000
 9100
 9200
 9300
 9400
 9500
 9600
 9700
 9800
 9900
 10000

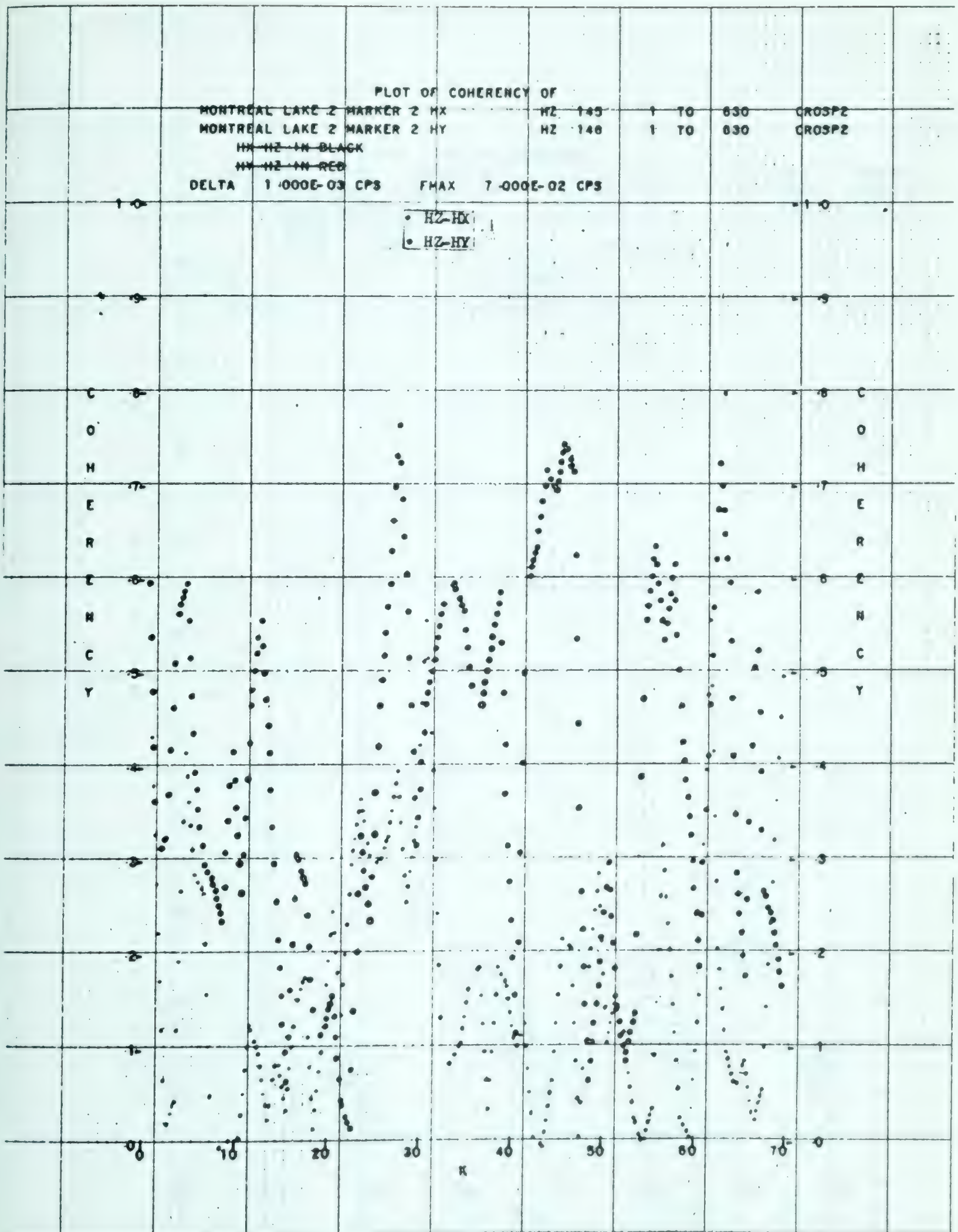


Diagram 40



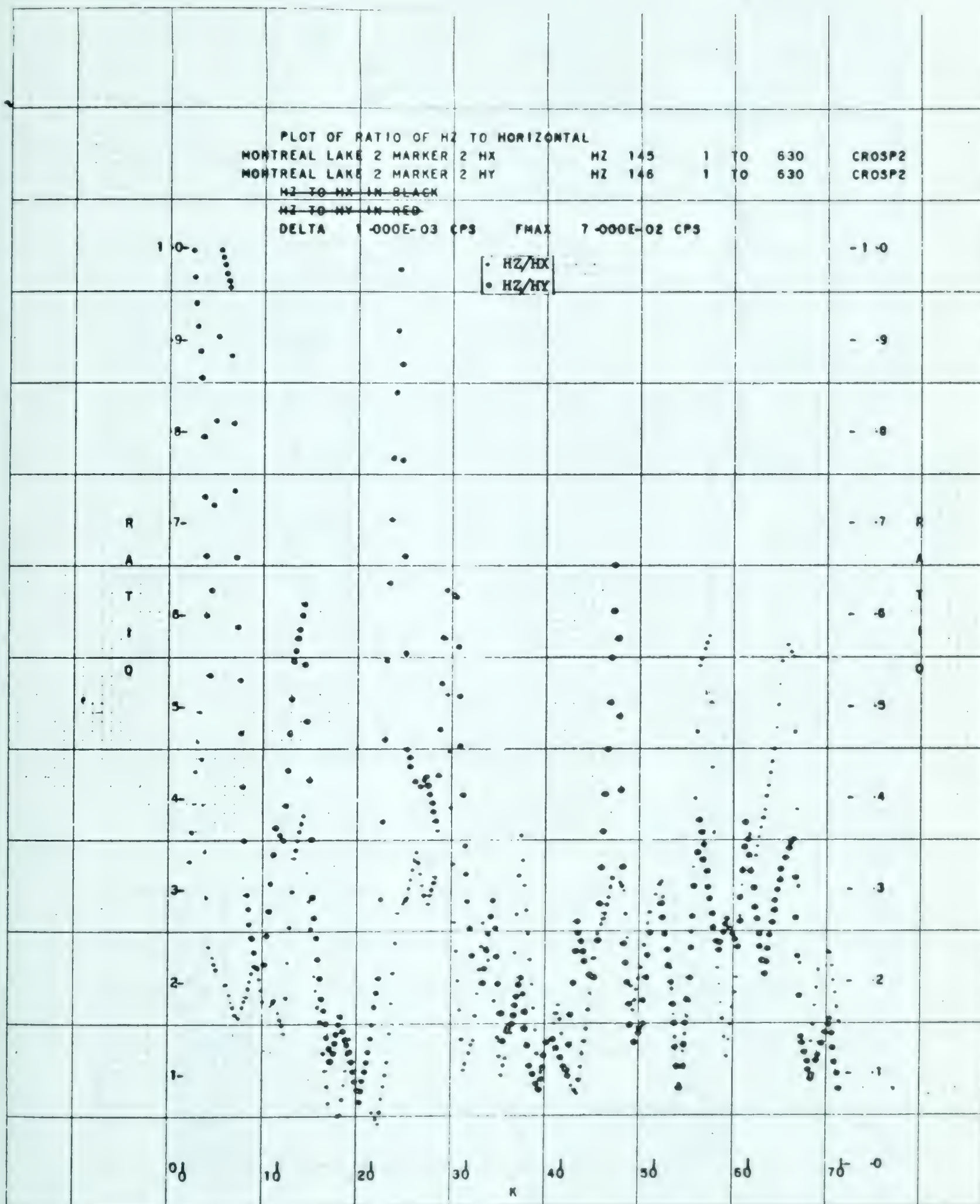


Diagram 41

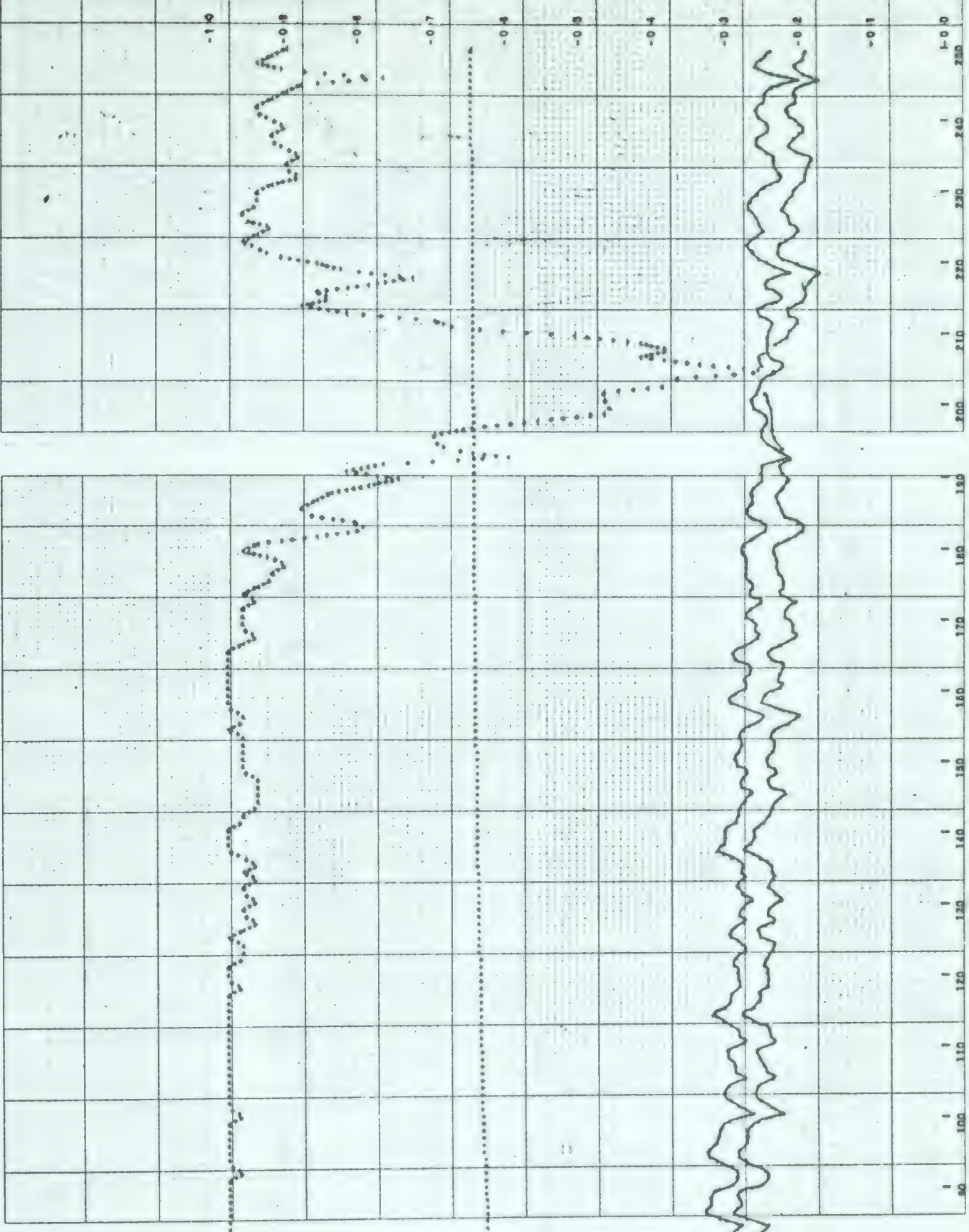
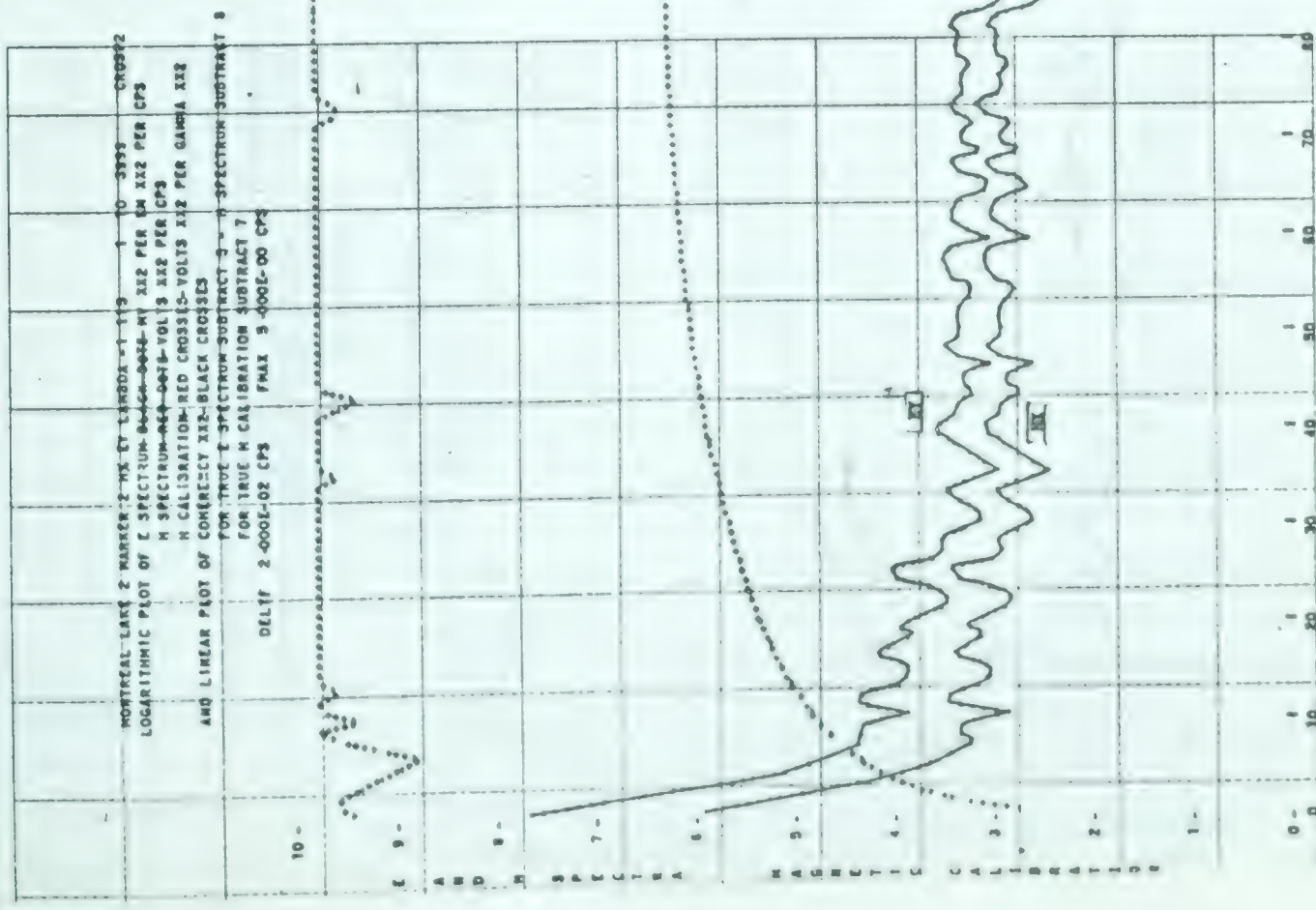


Diagram 42



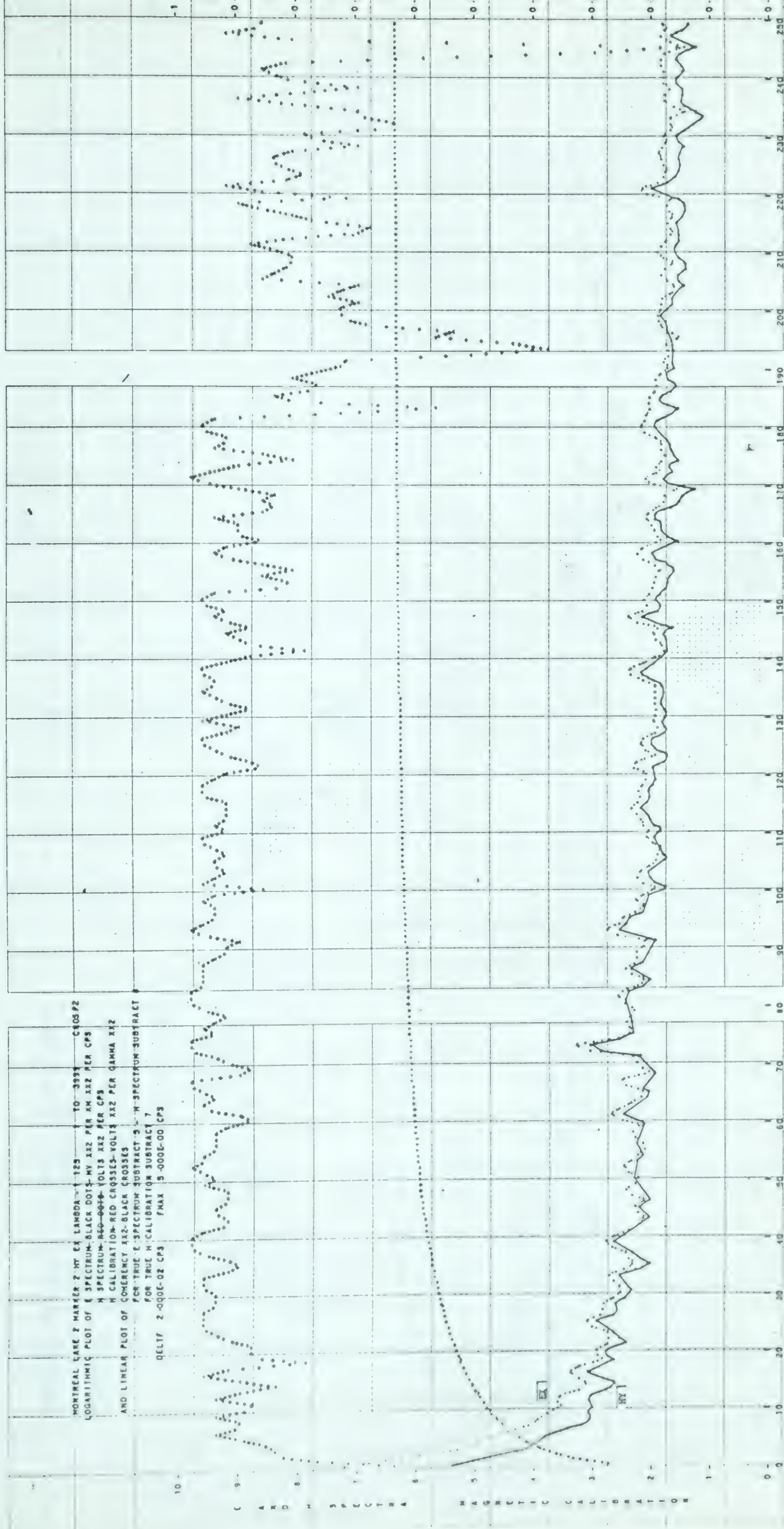


Diagram 43

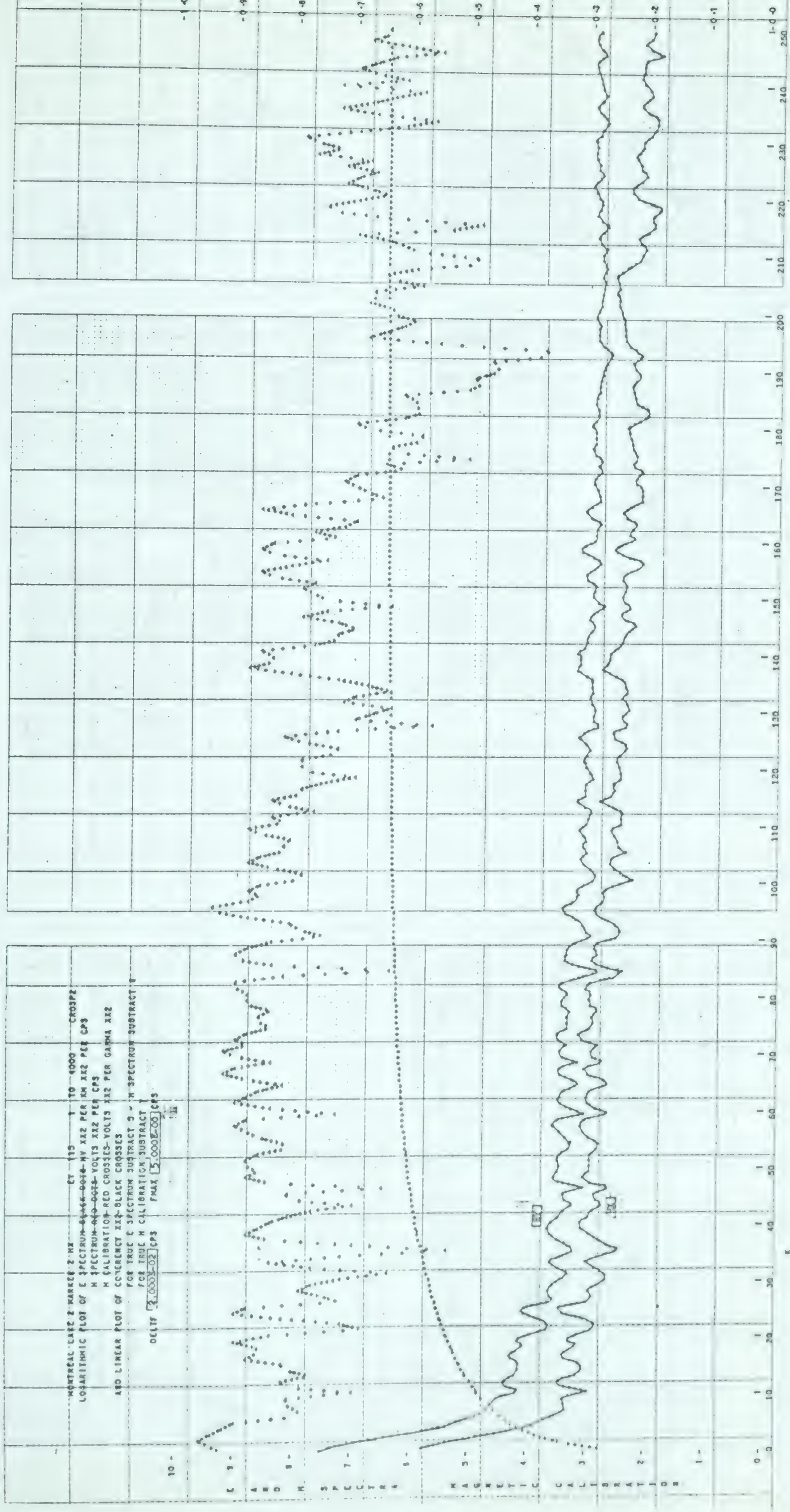
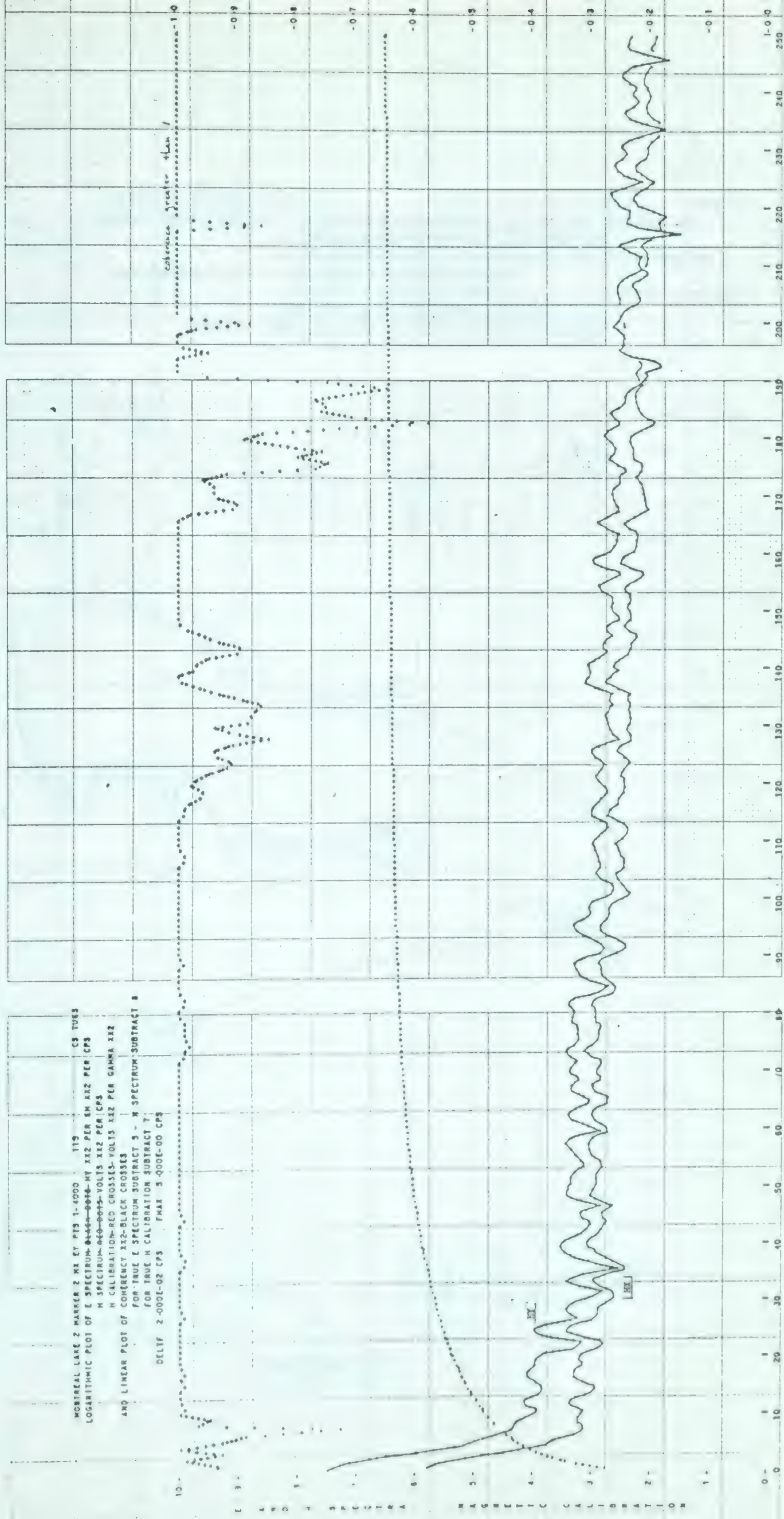


Diagram 44





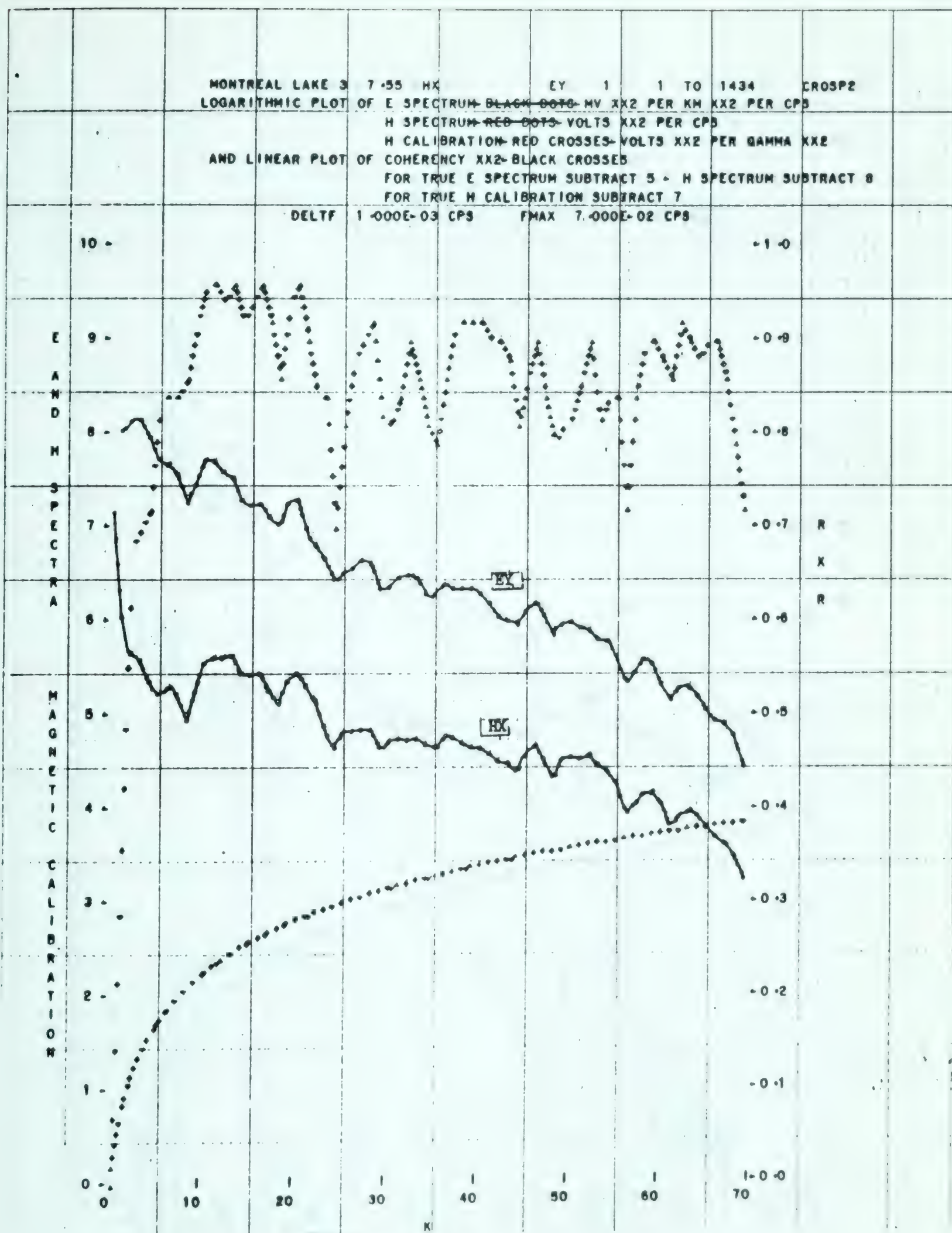


Diagram 47

Handwritten text at the top of the page, possibly a title or header.



Handwritten text at the bottom of the page, likely a legend or a concluding note.

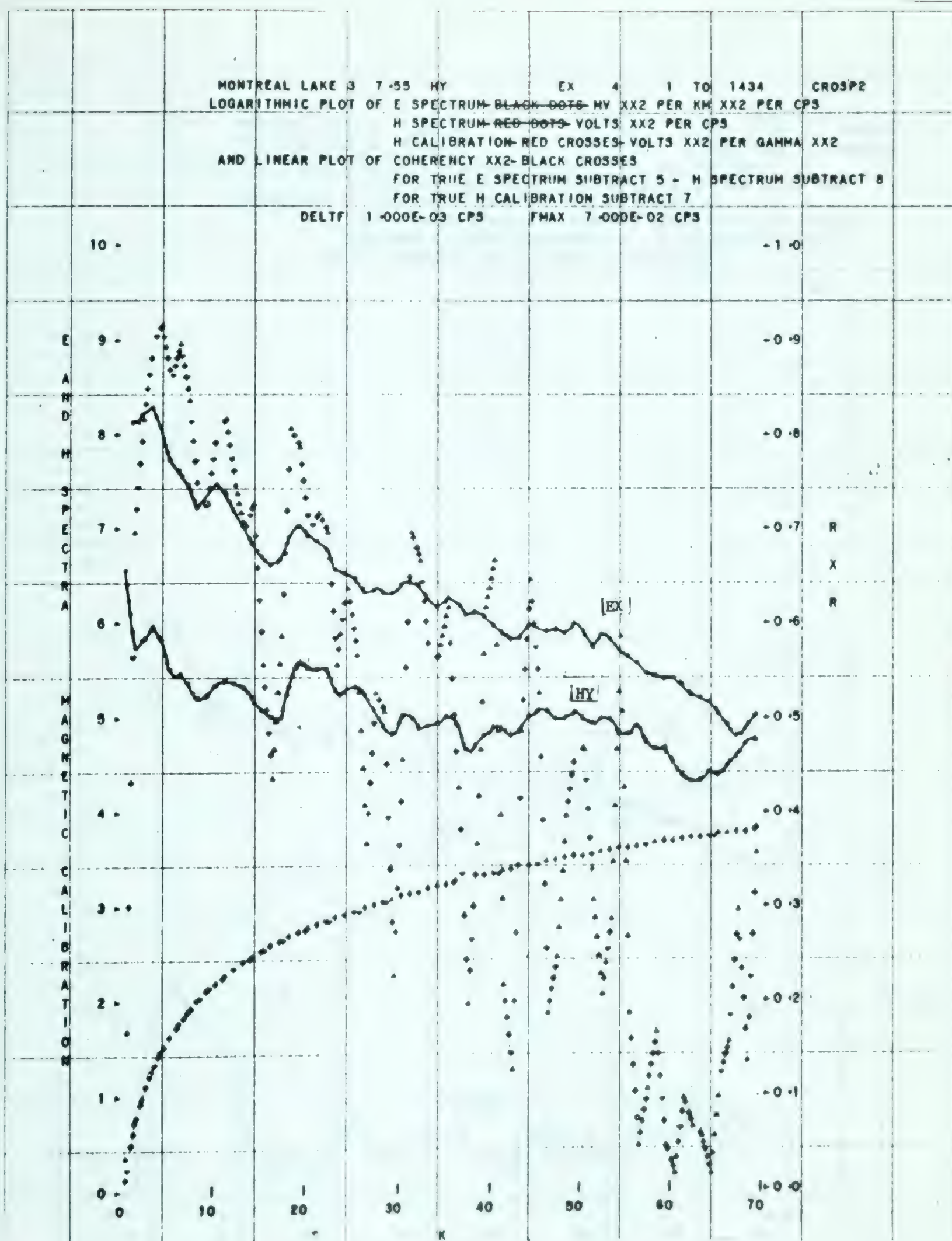


Diagram 48



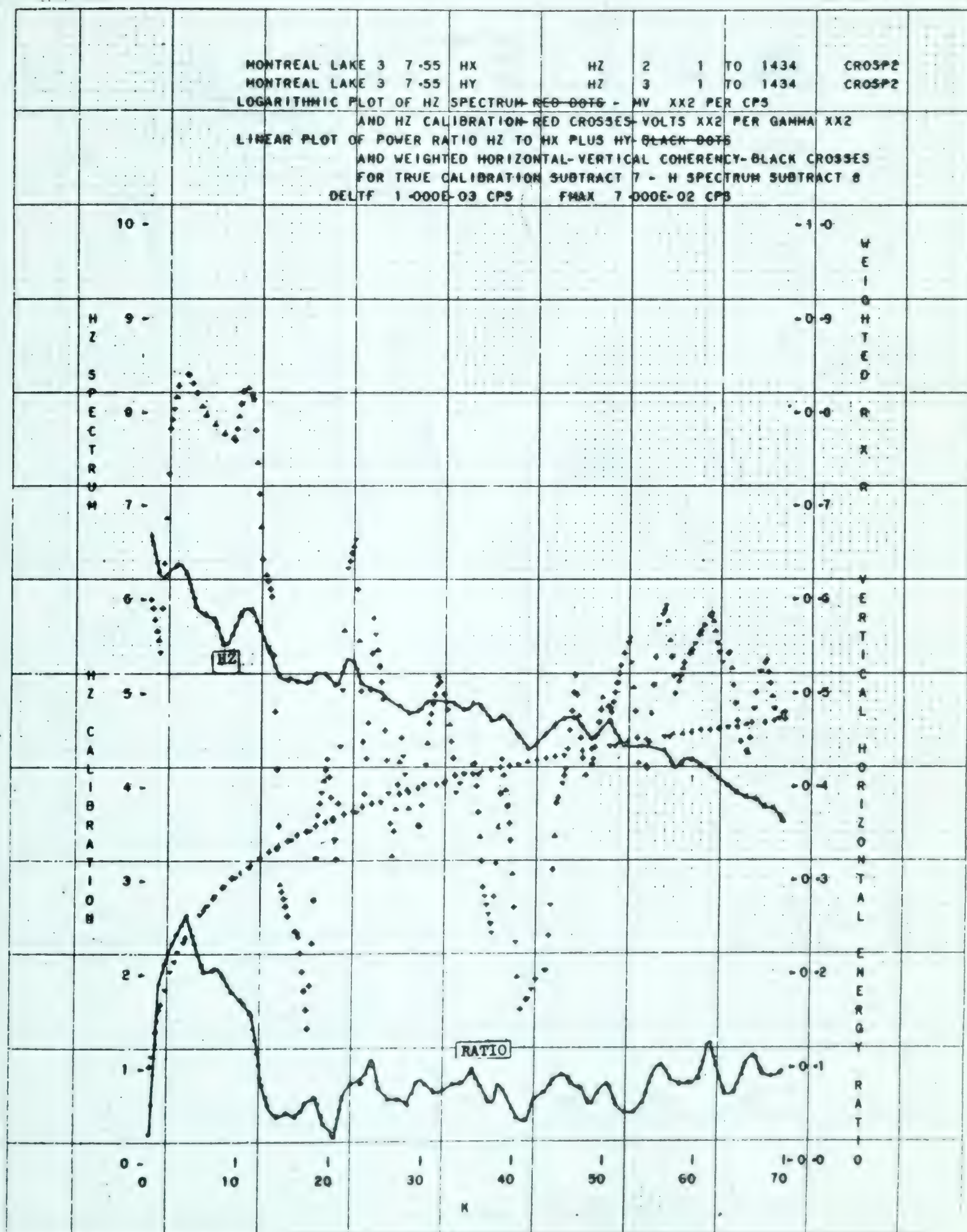


Diagram 49

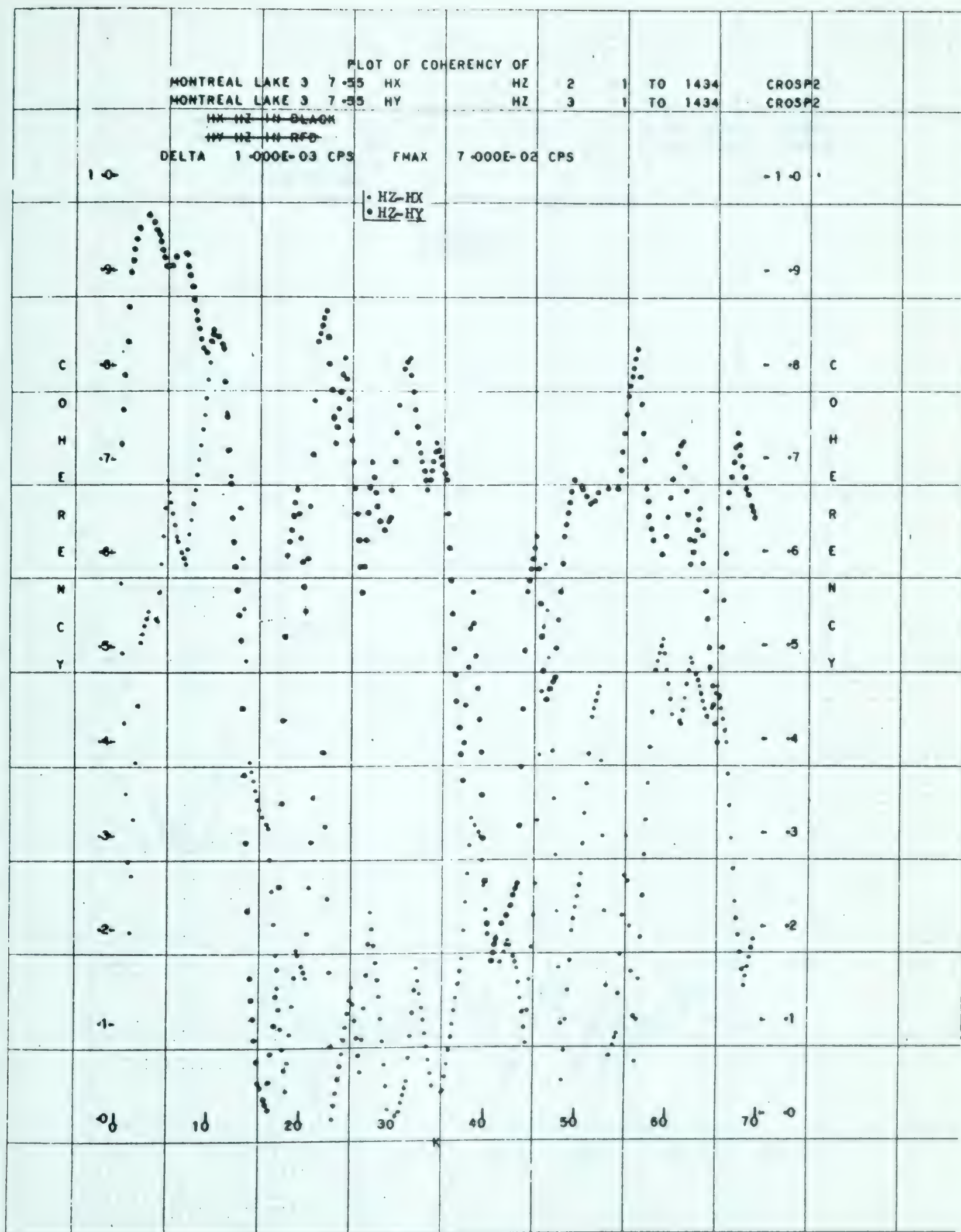


Diagram 50

THEORY OF THE EARTH

BY J. H. VAN DER KAM

1885

1885

The Earth is a sphere, and its surface is covered by water. The land is divided into continents and islands. The water is divided into oceans and seas. The air is divided into layers. The fire is divided into elements. The earth is divided into regions. The sky is divided into stars. The sun is a star. The moon is a satellite. The planets are celestial bodies. The comets are celestial bodies. The meteors are celestial bodies. The asteroids are celestial bodies. The galaxies are celestial bodies. The universe is a vast expanse of space and time.

The earth is a sphere, and its surface is covered by water. The land is divided into continents and islands. The water is divided into oceans and seas. The air is divided into layers. The fire is divided into elements. The earth is divided into regions. The sky is divided into stars. The sun is a star. The moon is a satellite. The planets are celestial bodies. The comets are celestial bodies. The meteors are celestial bodies. The asteroids are celestial bodies. The galaxies are celestial bodies. The universe is a vast expanse of space and time.

The earth is a sphere, and its surface is covered by water. The land is divided into continents and islands. The water is divided into oceans and seas. The air is divided into layers. The fire is divided into elements. The earth is divided into regions. The sky is divided into stars. The sun is a star. The moon is a satellite. The planets are celestial bodies. The comets are celestial bodies. The meteors are celestial bodies. The asteroids are celestial bodies. The galaxies are celestial bodies. The universe is a vast expanse of space and time.

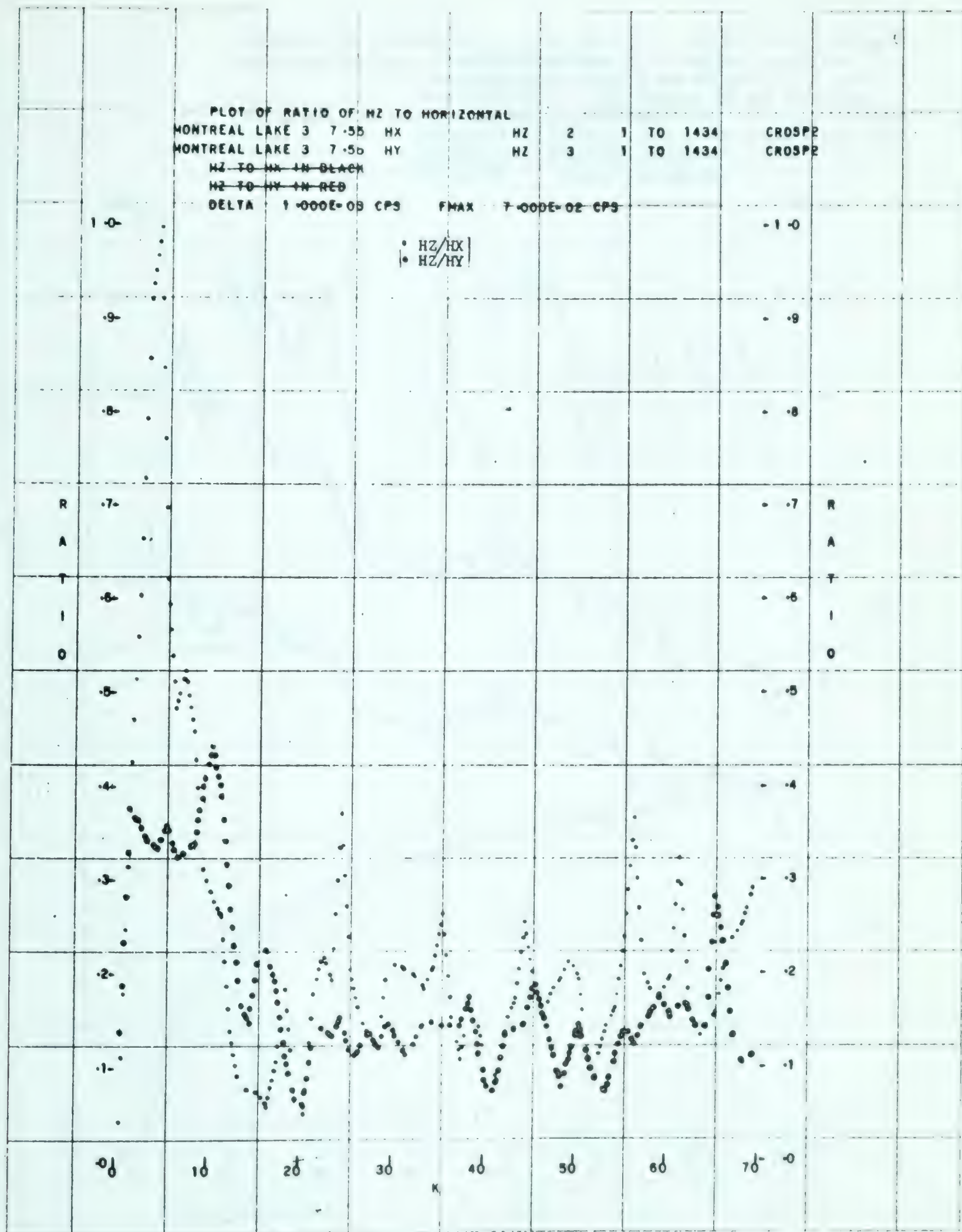


Diagram 51

==

1

1

1

1

1

MONTREAL LAKE 3 MARKER HX EY 29 1 TO 1175 CROSP
 LOGARITHMIC PLOT OF E SPECTRUM BLACK DOTS MV XX2 PER RM XX2 PER CPS
 H SPECTRUM RED DOTS VOLTS XX2 PER CPS
 H CALIBRATION RED CROSSES VOLTS XX2 PER GAMMA XX2
 AND LINEAR PLOT OF COHERENCY XX2 BLACK CROSSES
 FOR TRUE E SPECTRUM SUBTRACT 5 - H SPECTRUM SUBTRACT 6
 FOR TRUE H CALIBRATION SUBTRACT 7
 DELTA 1-000E-03 CPS PHAS 7-000E-02 CPS

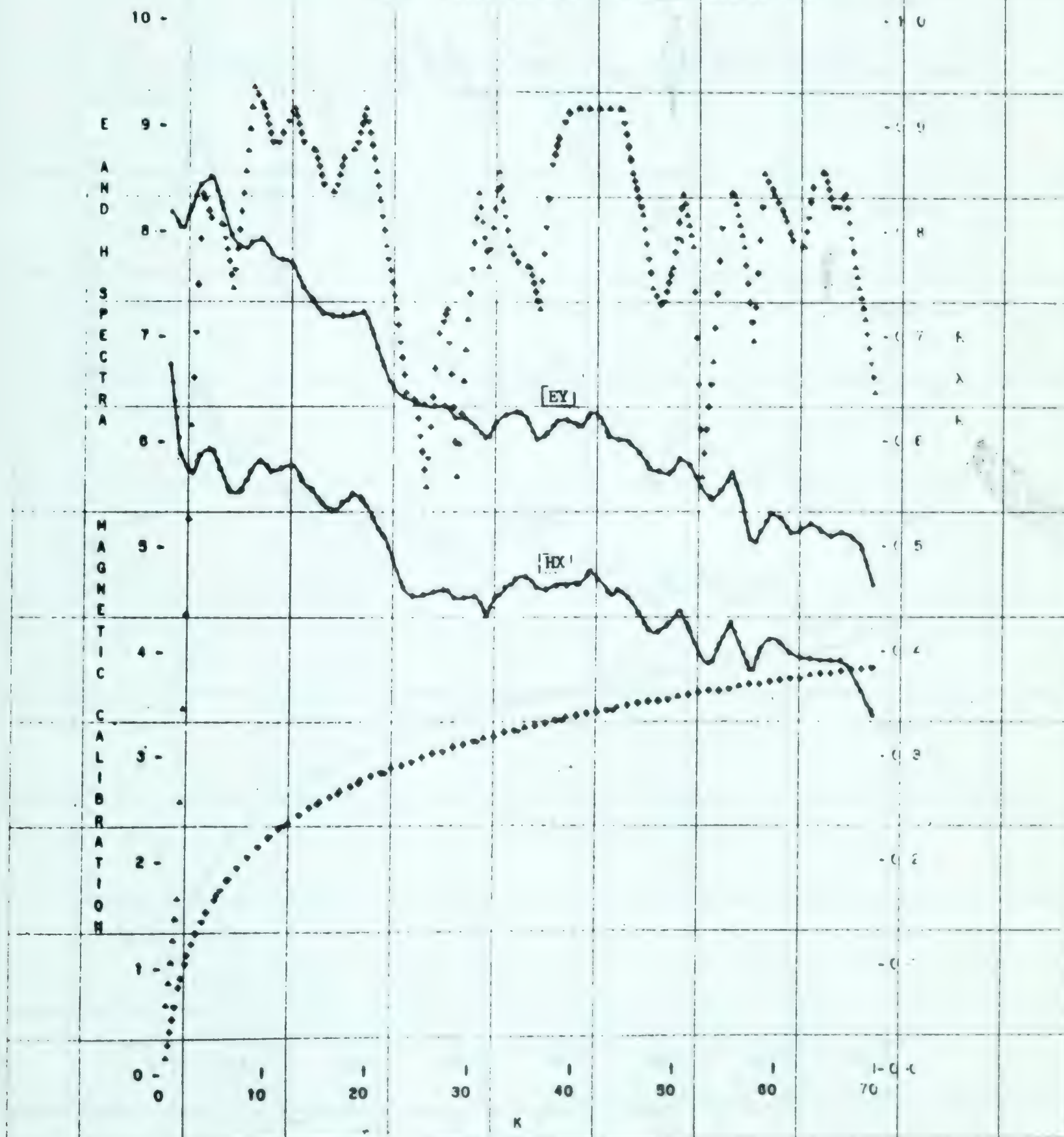


Diagram 52



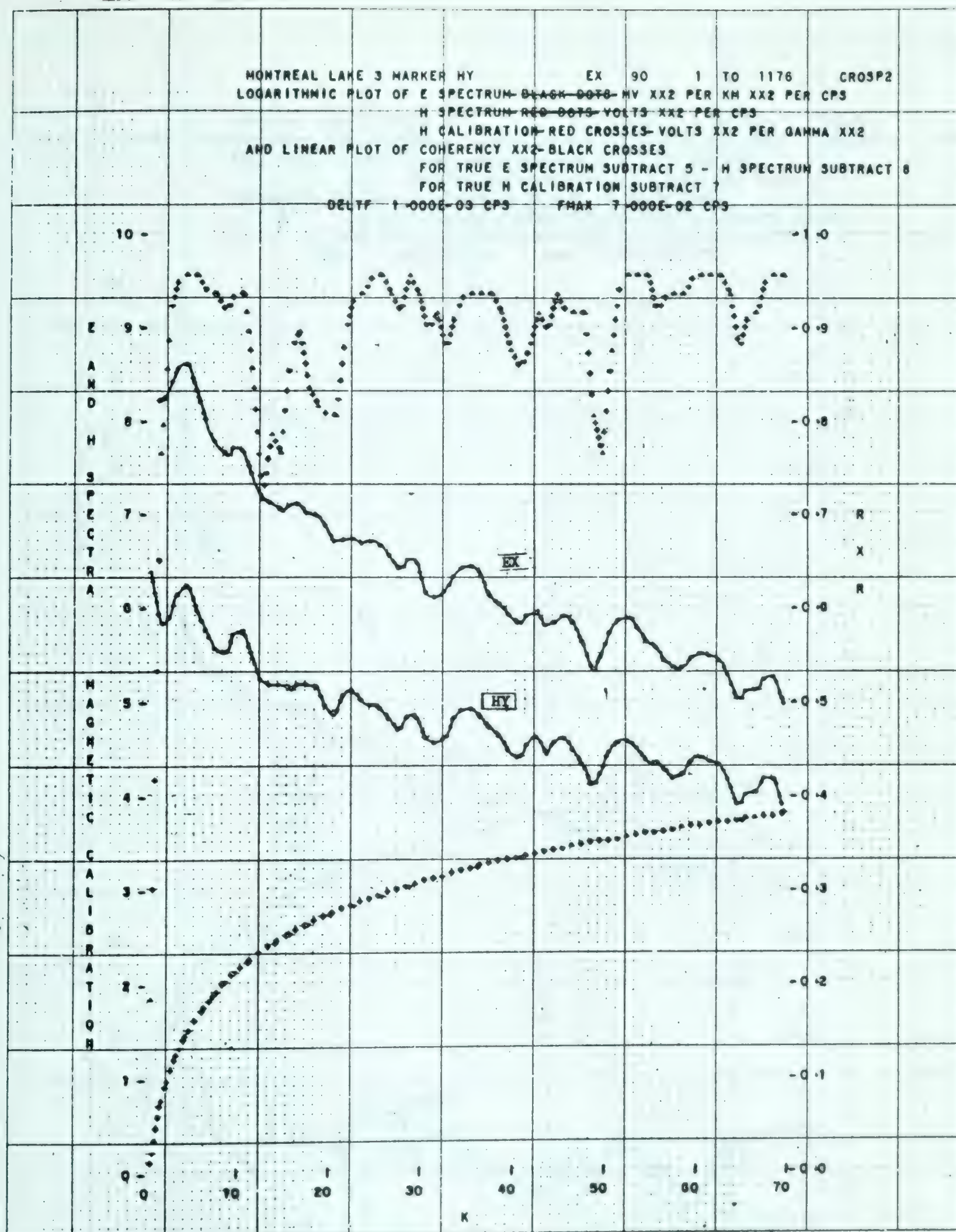


Diagram 53



Figure 1: A graph showing three data series plotted on a grid. The x-axis is labeled 1 to 10, and the y-axis is labeled 1 to 10. The series include a fluctuating line, a smooth curve, and a straight line.

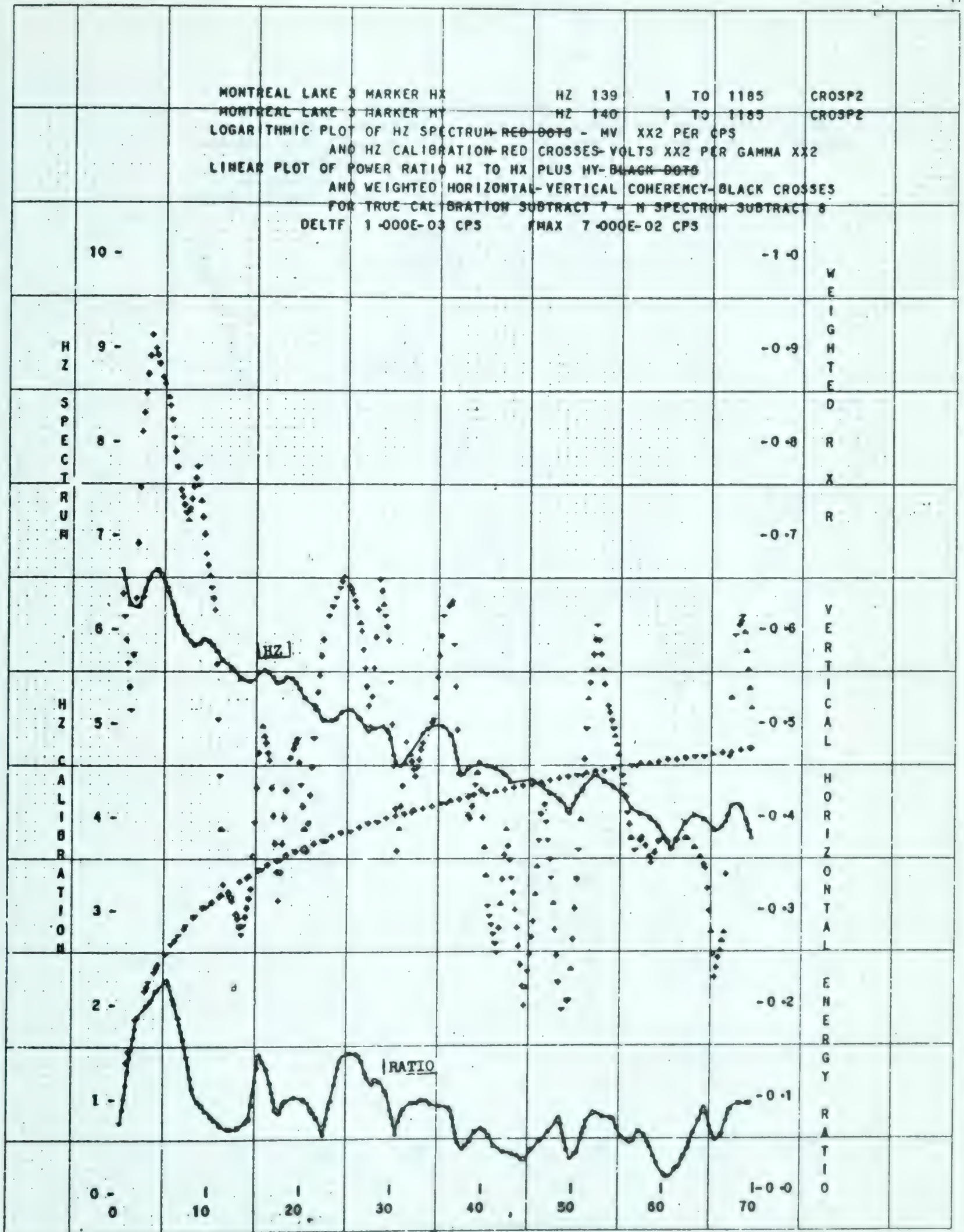


Diagram 54

Handwritten title and introductory text at the top of the page.



Handwritten caption or label for the graph.

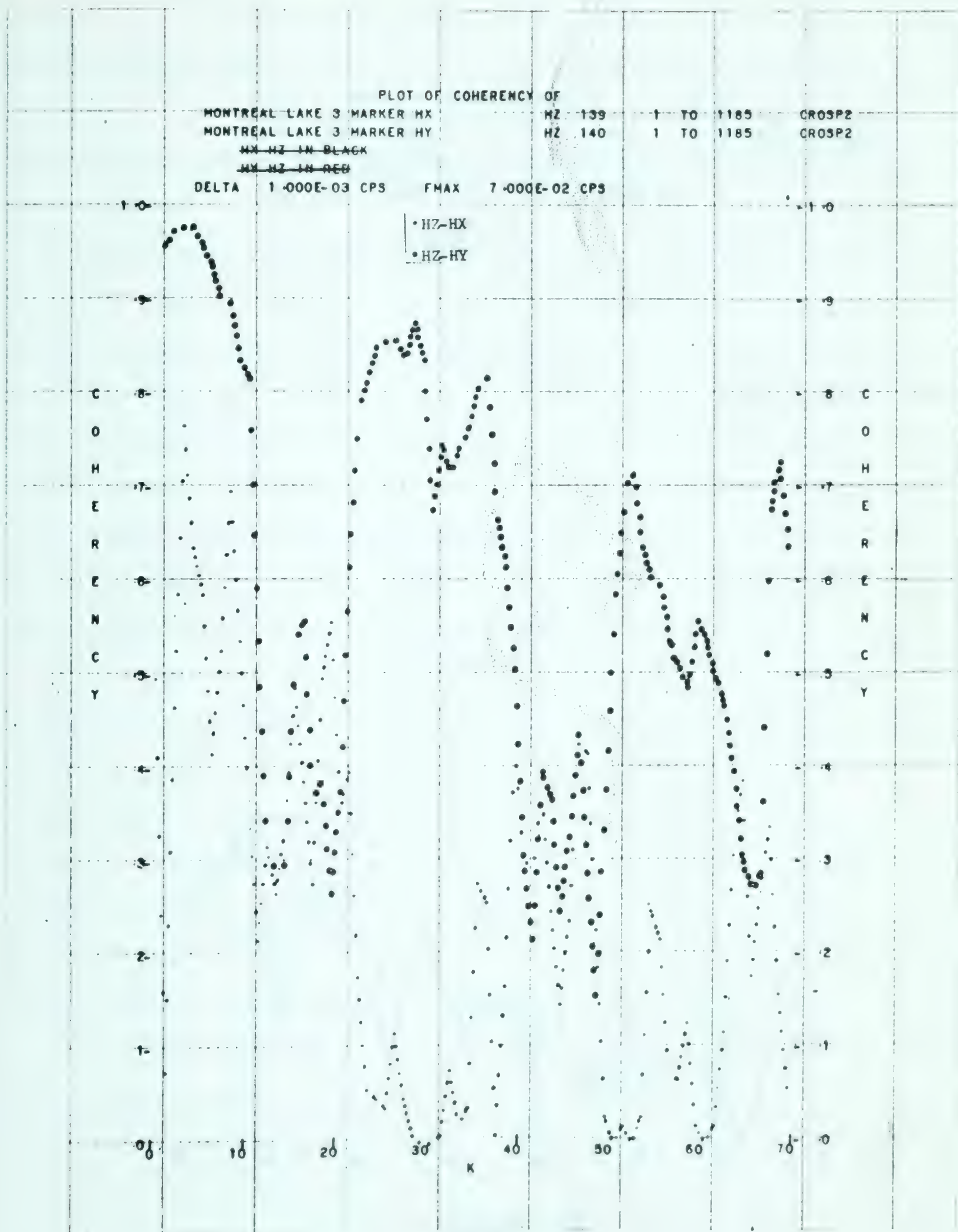


Diagram 55

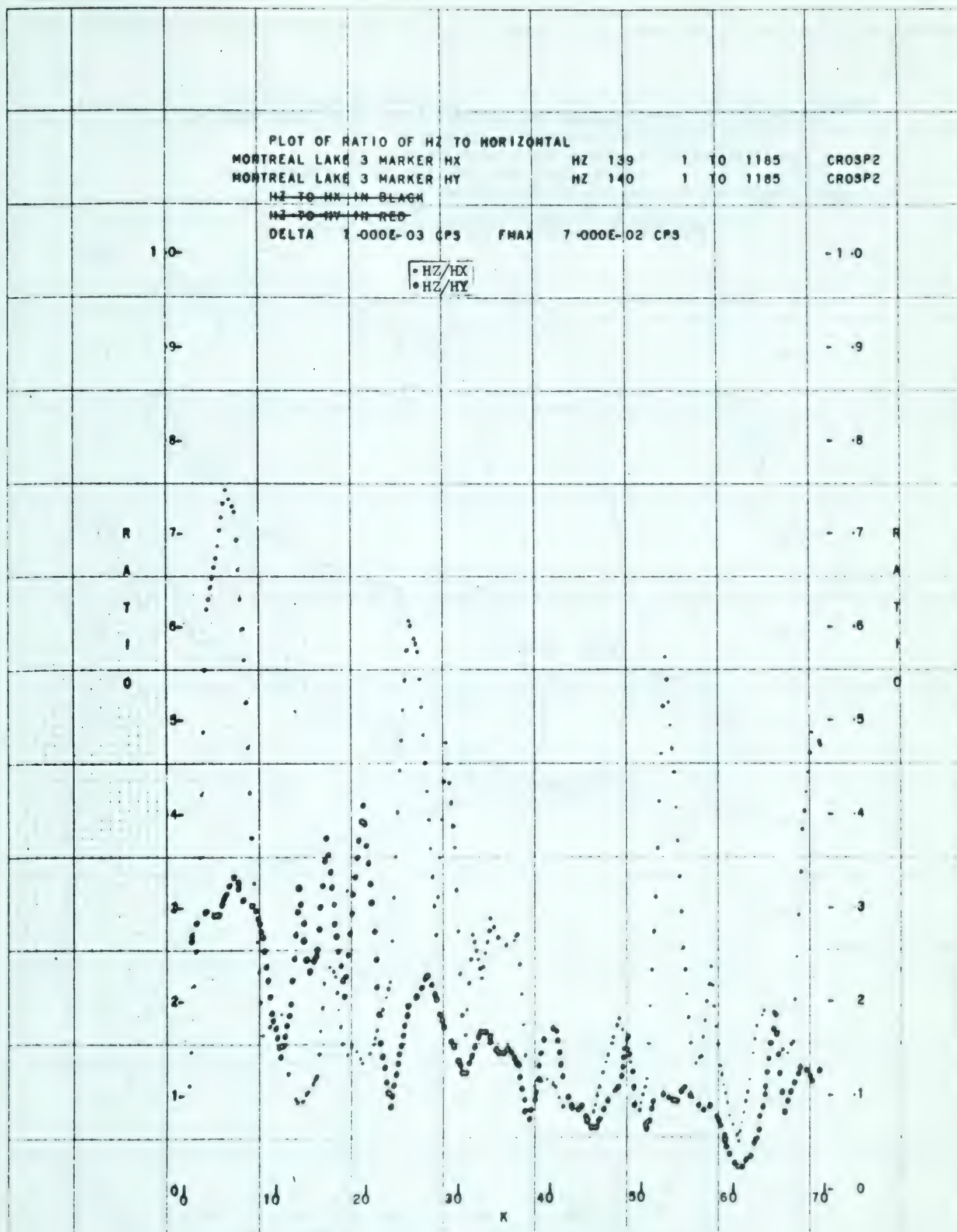


Diagram 56

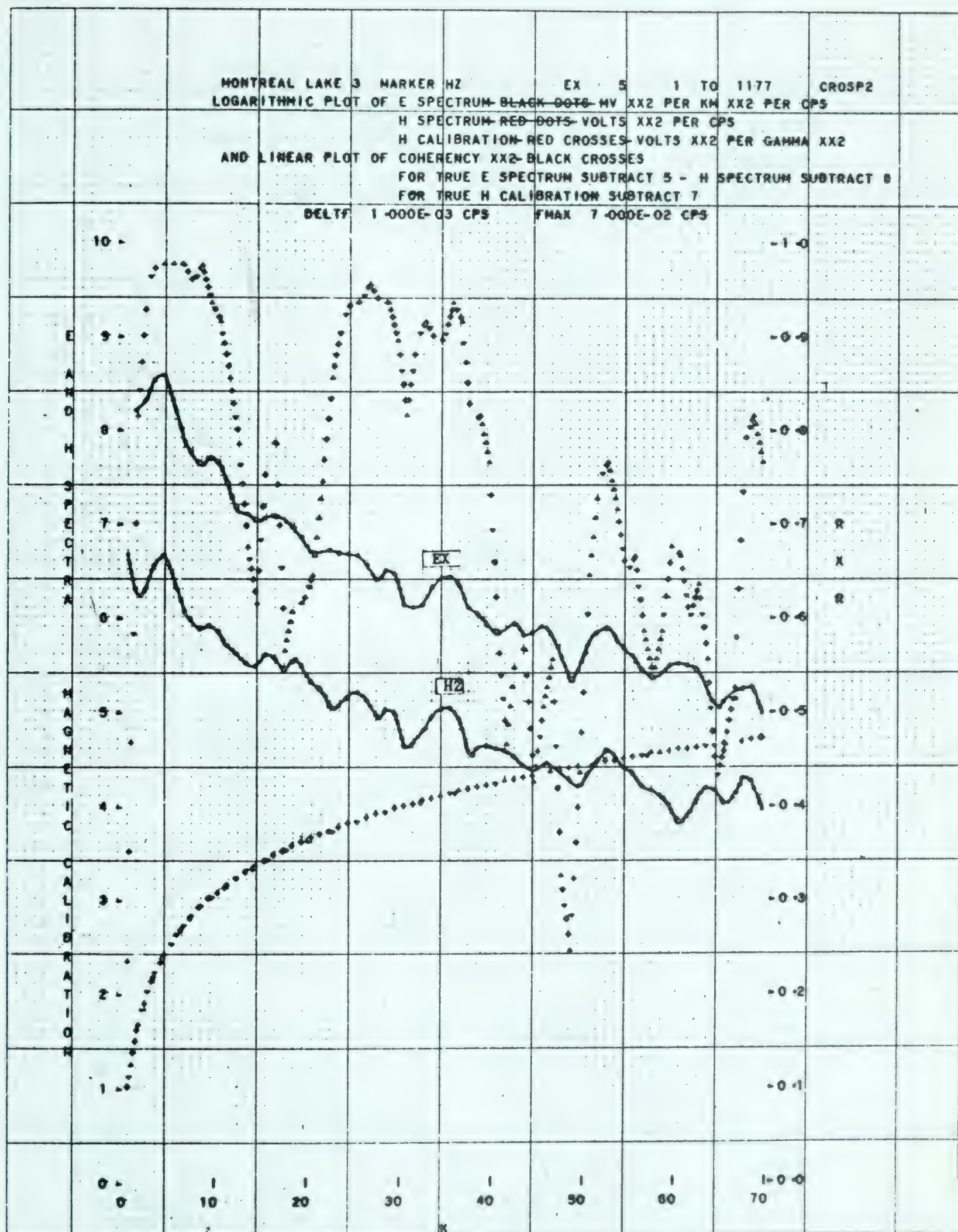


Diagram 57



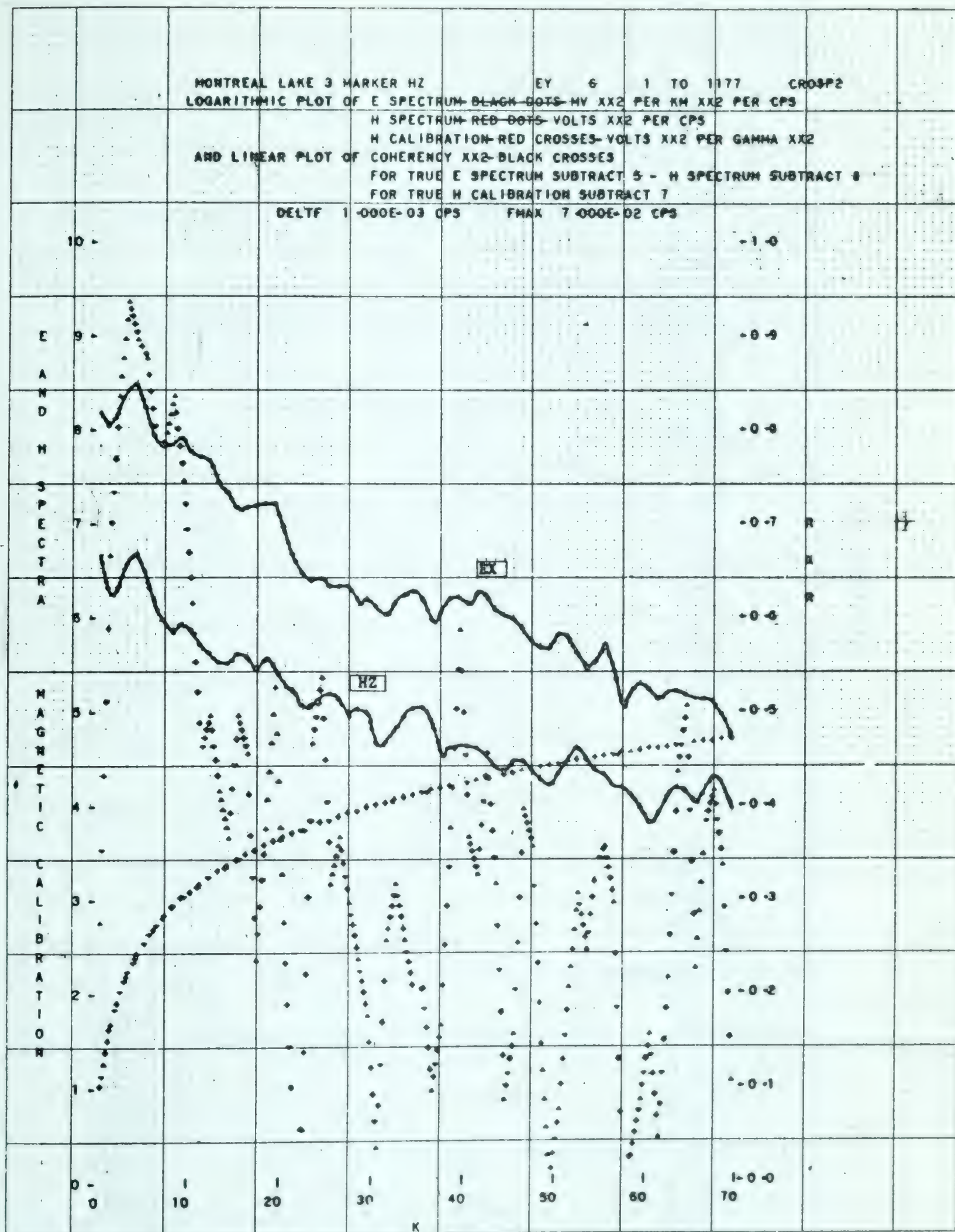


Diagram 58



Figure 1

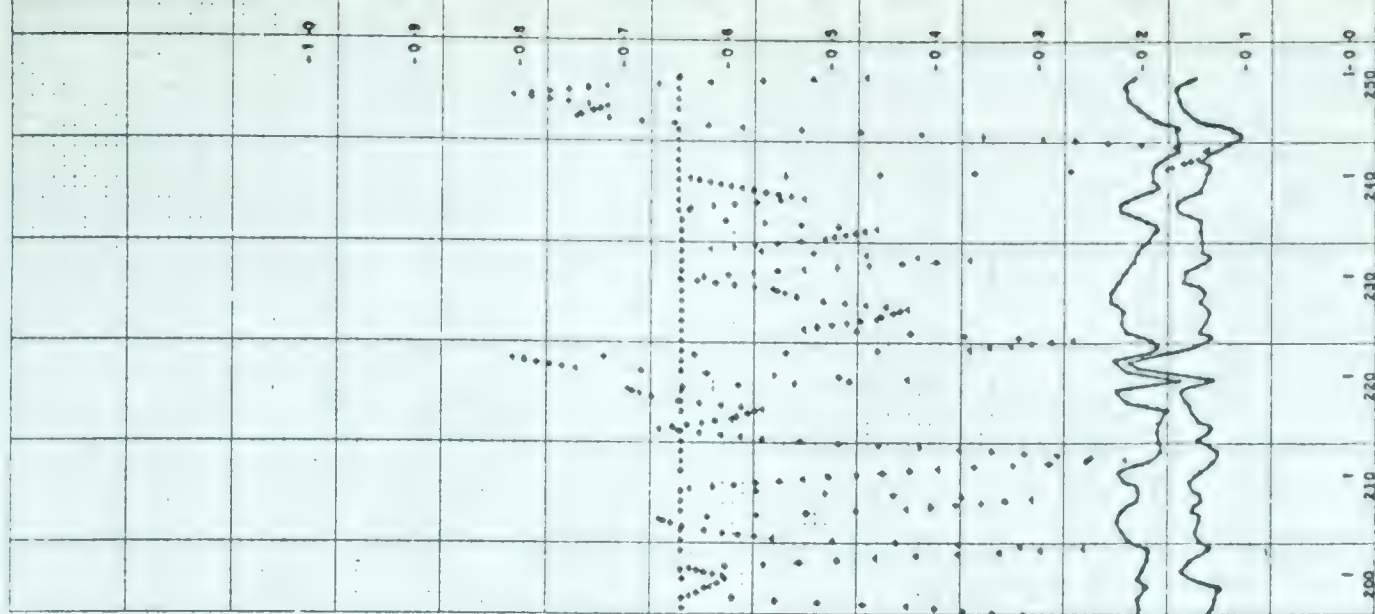
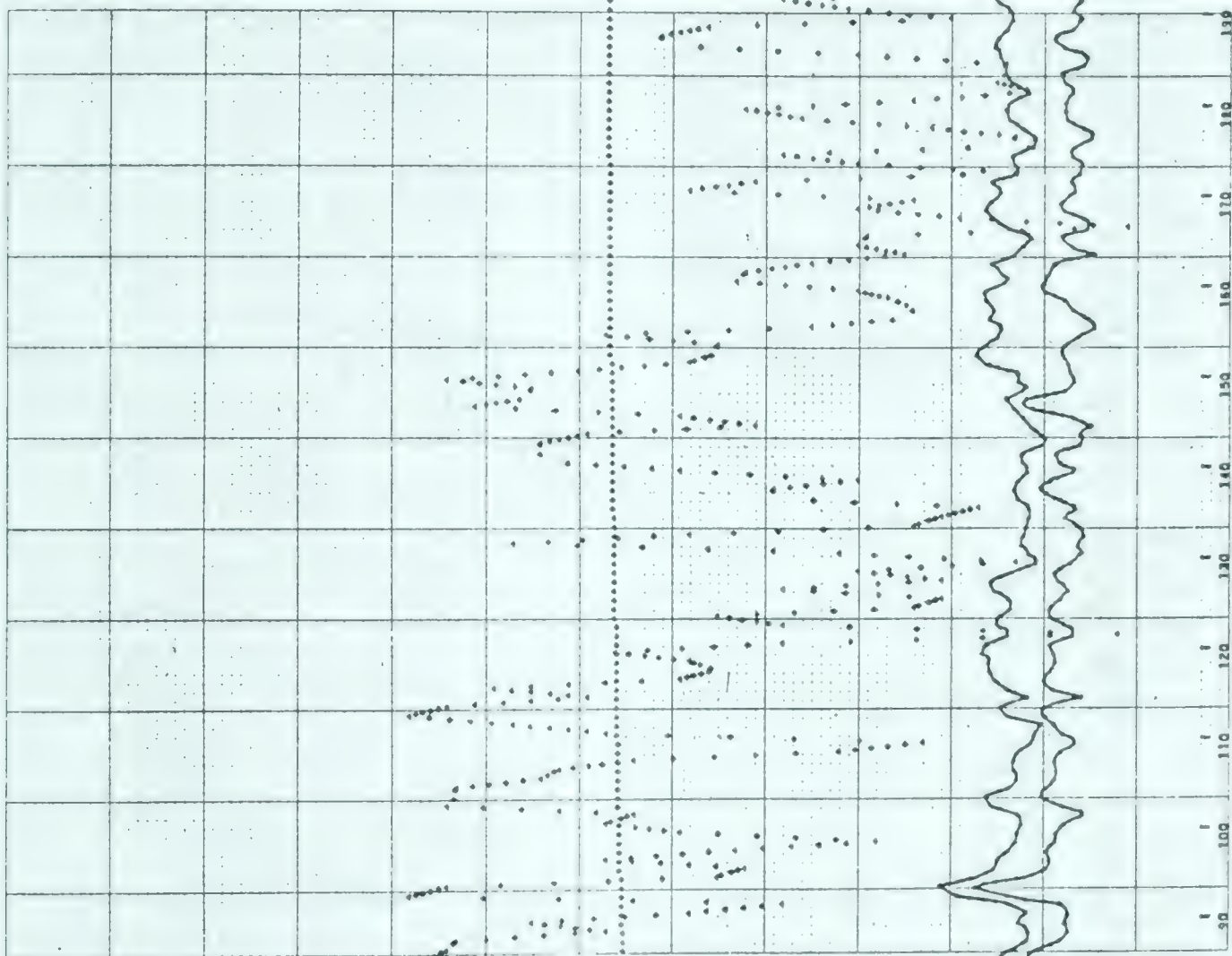
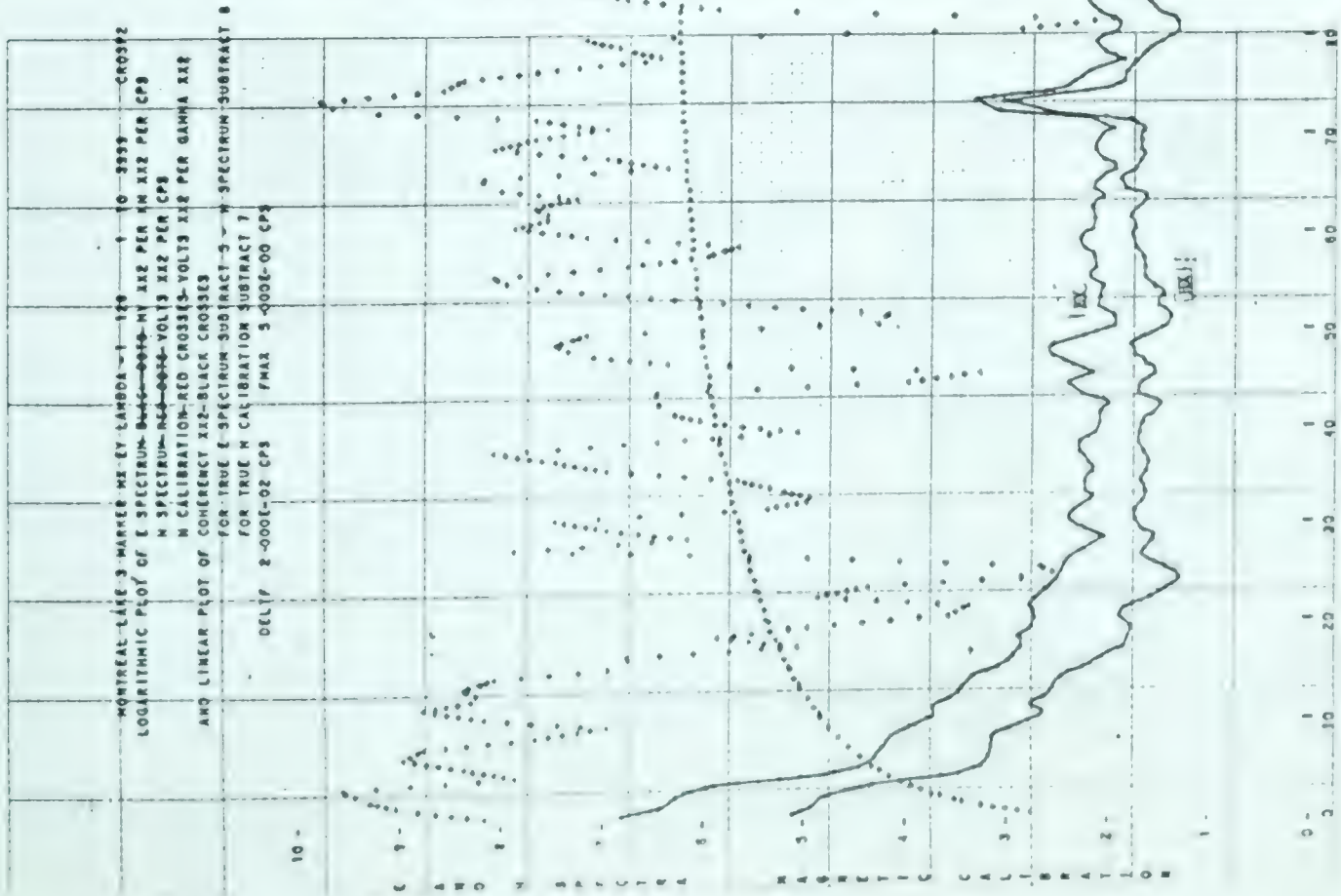


Diagram 59

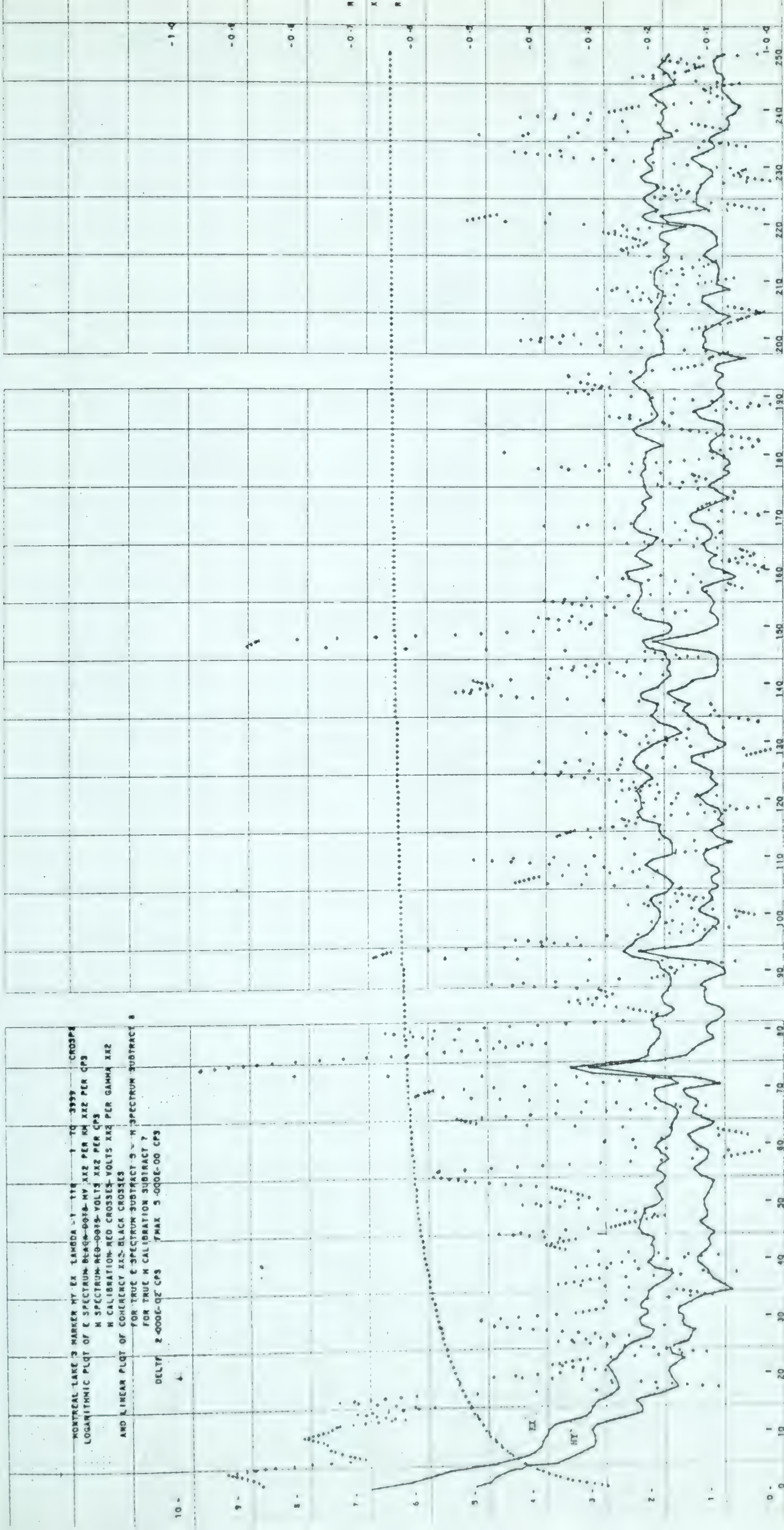


Diagram 60



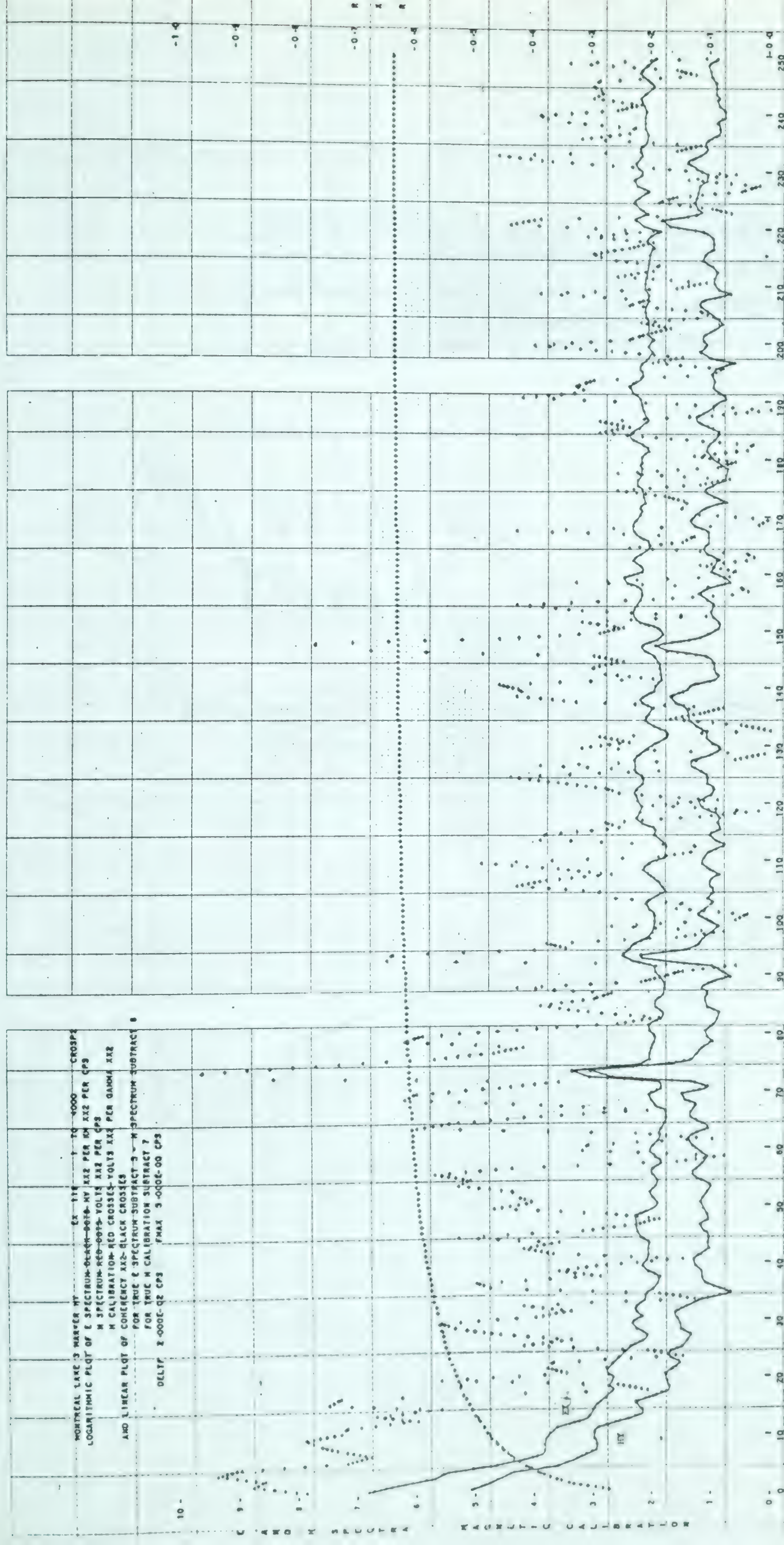


Diagram 61



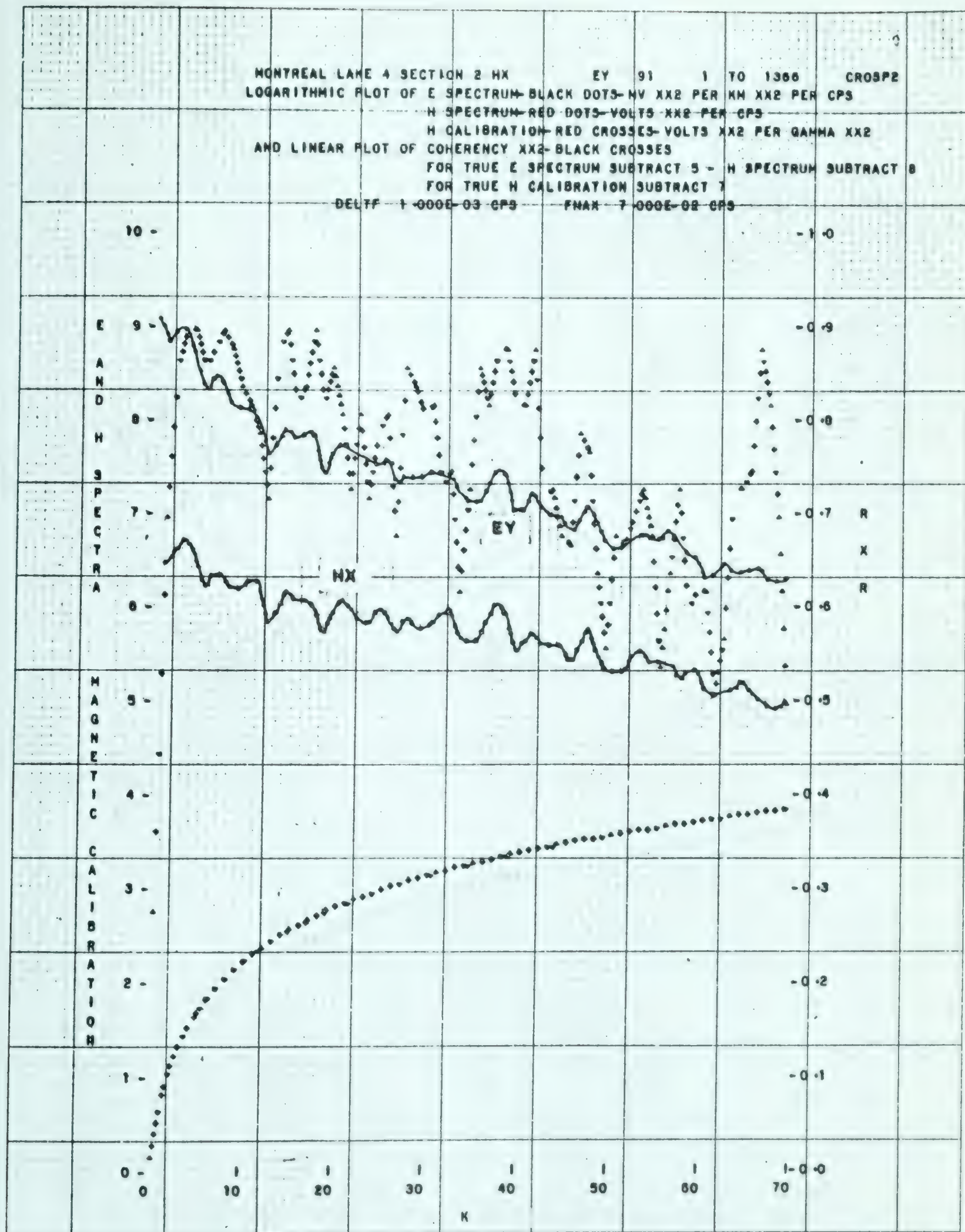


Diagram 62

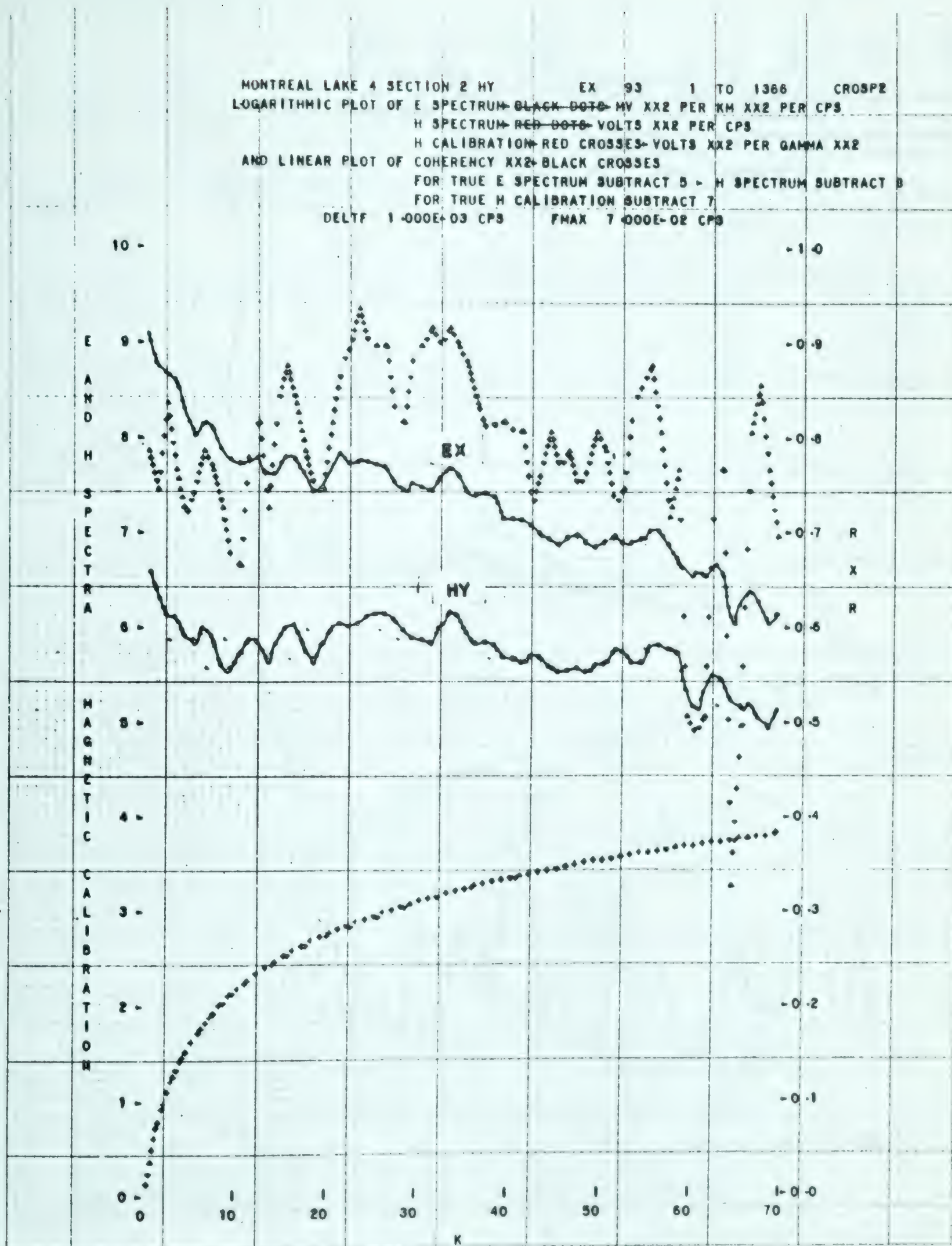


Diagram 63

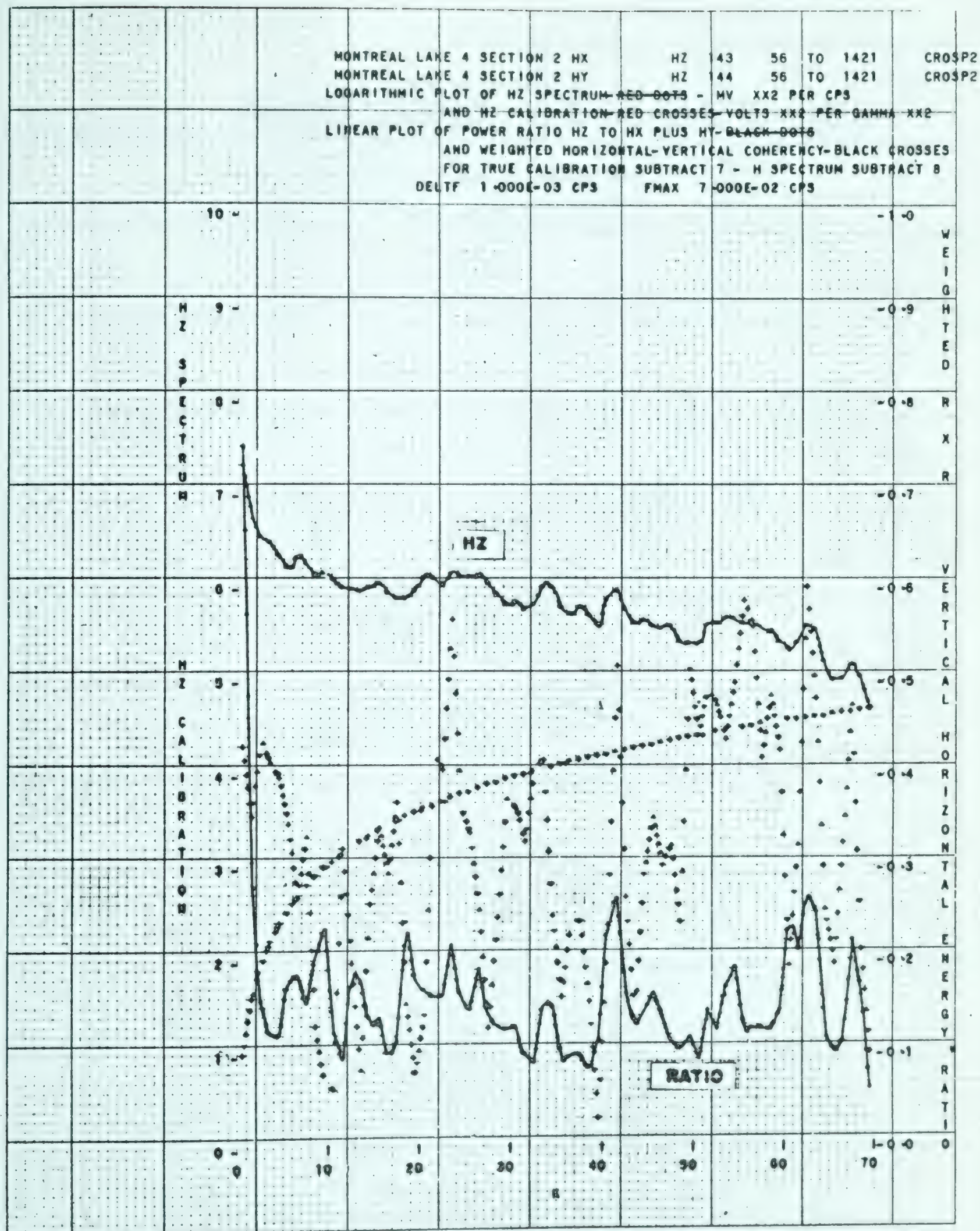


Diagram 64

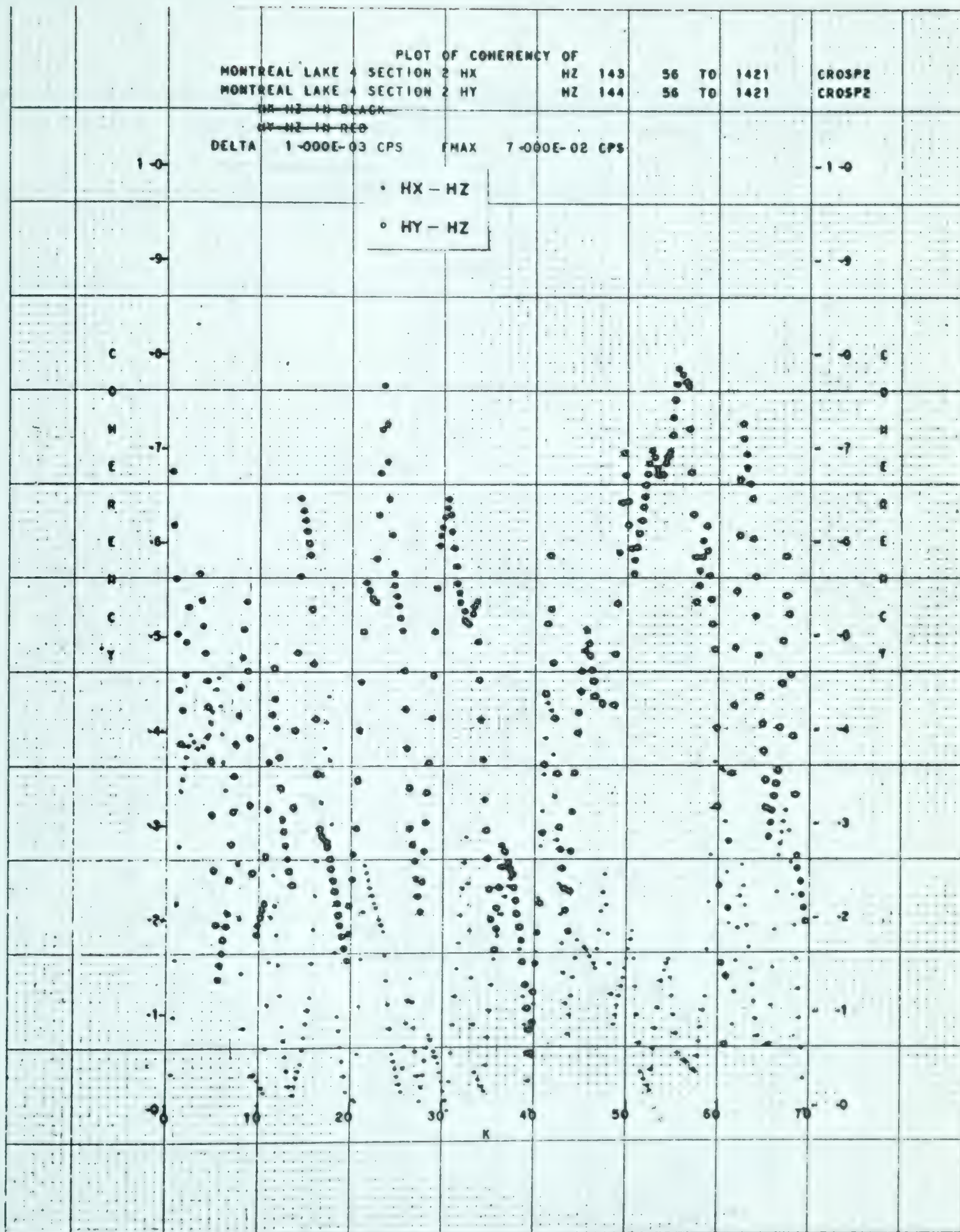


Diagram 65

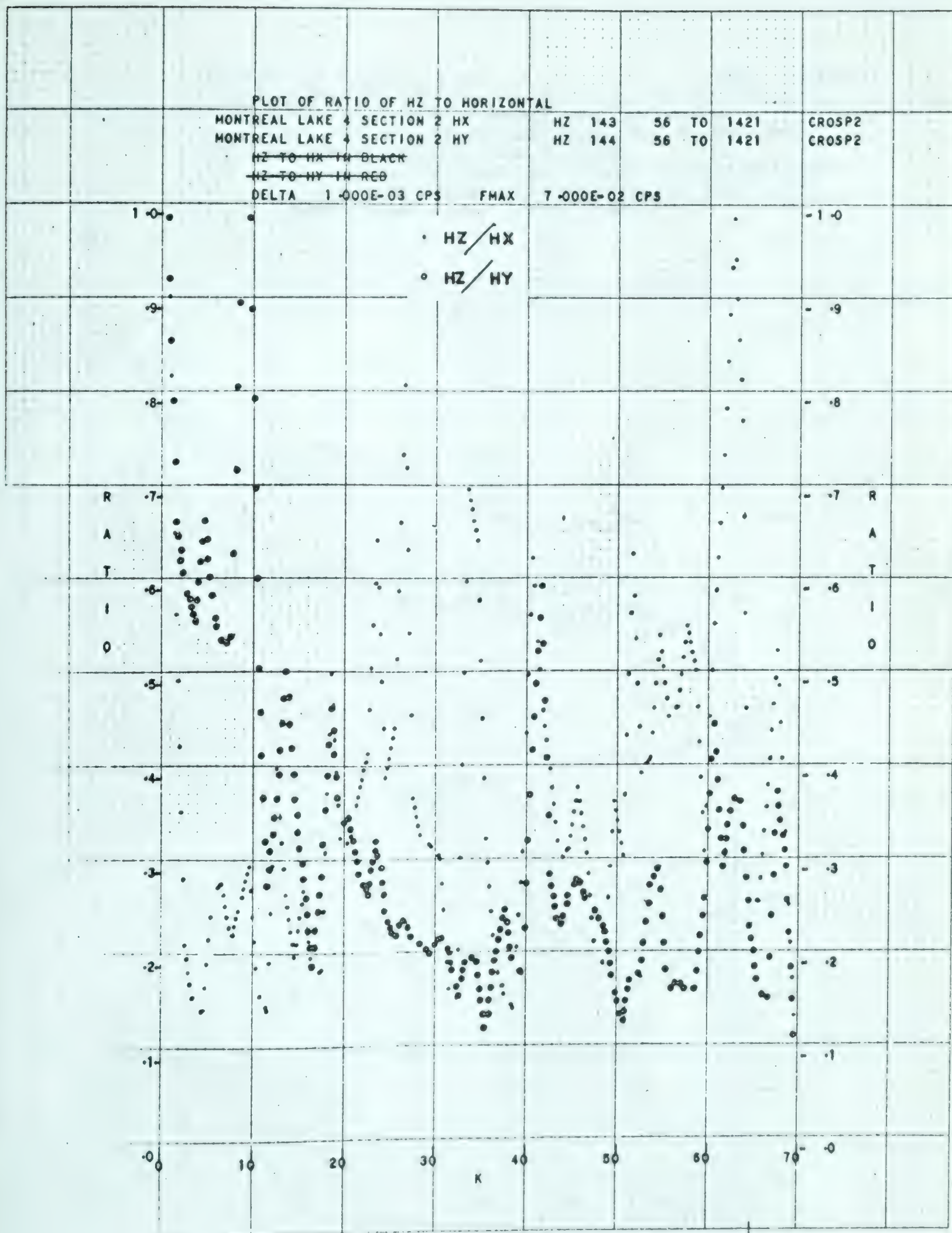


Diagram 66

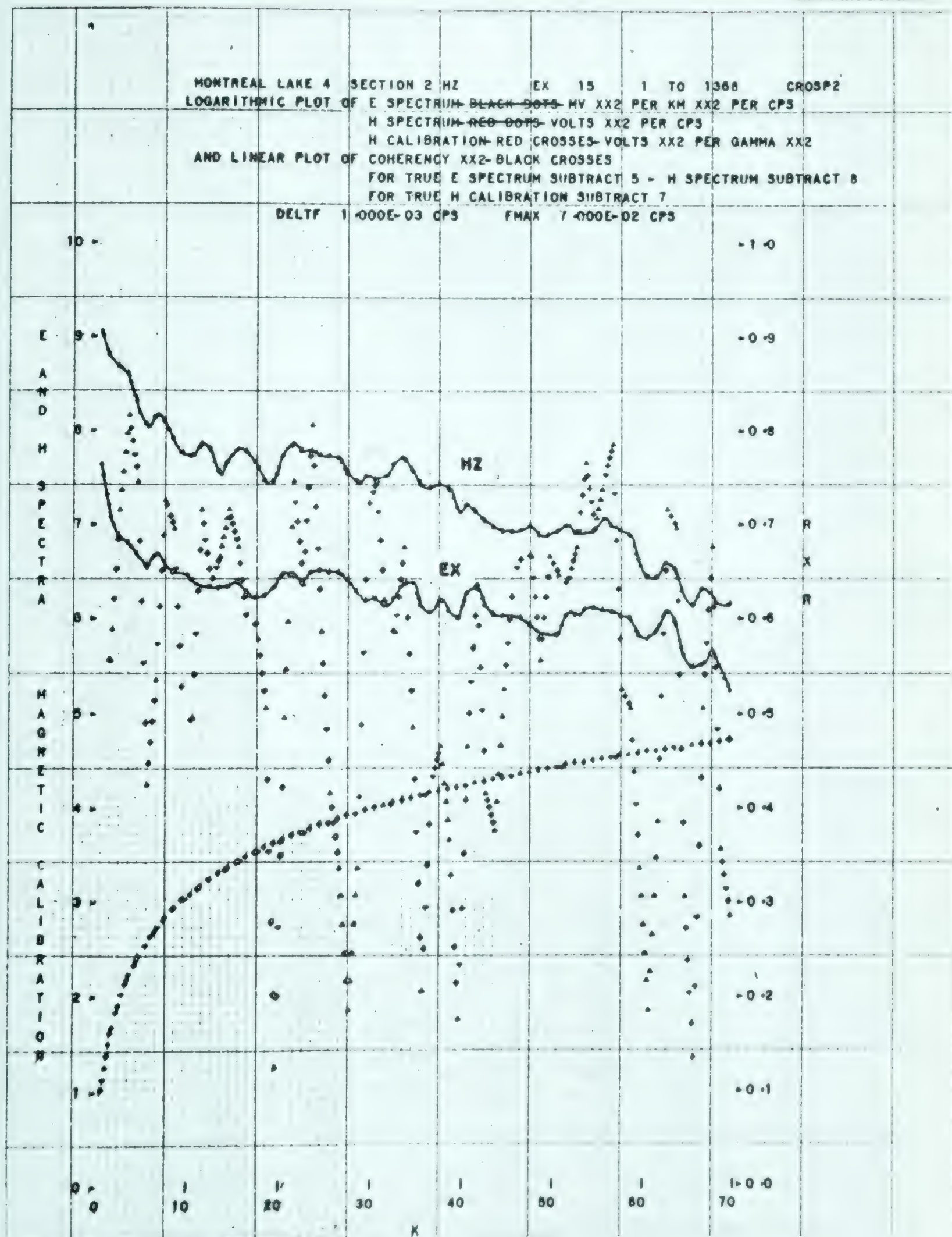


Diagram 67

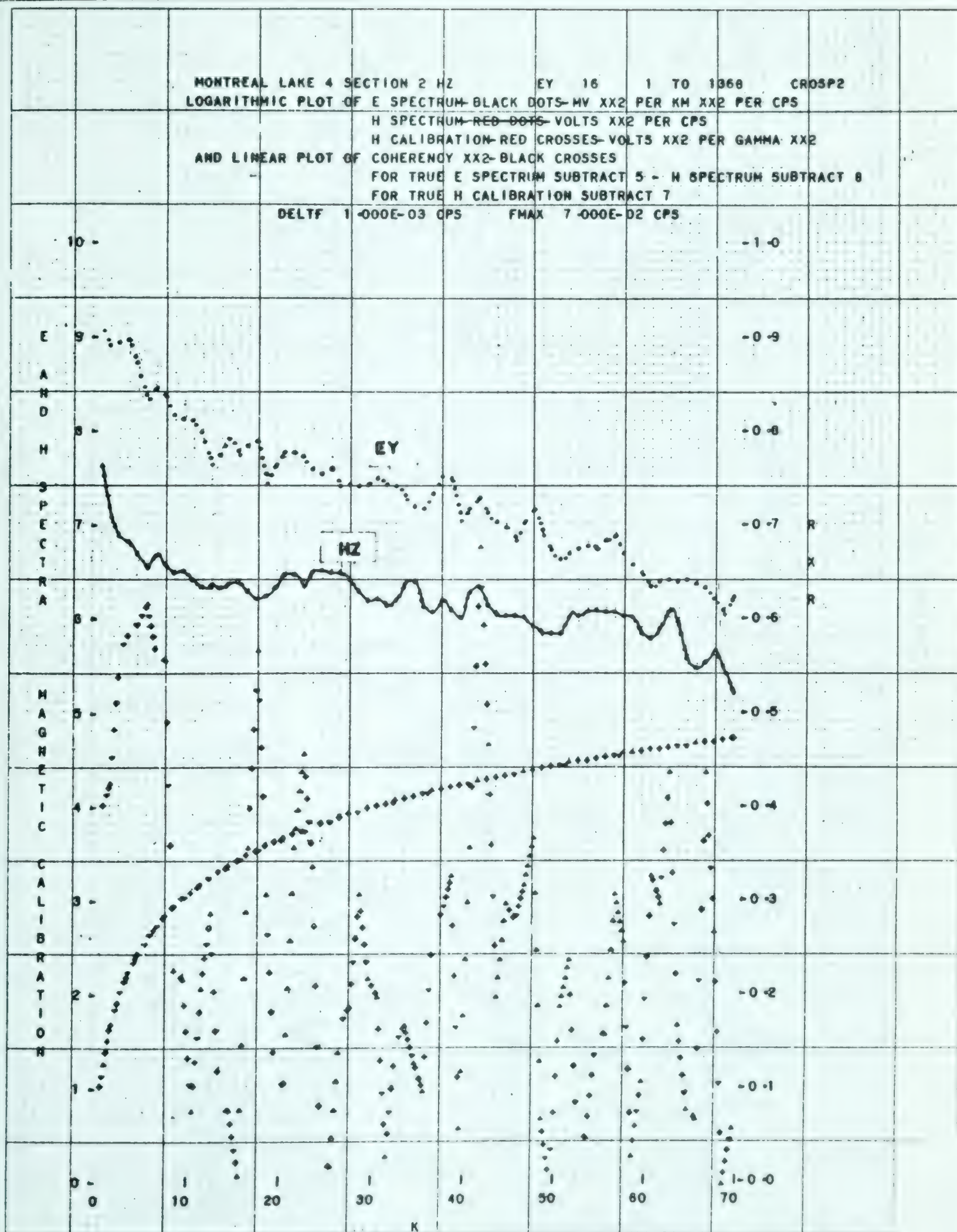


Diagram 68

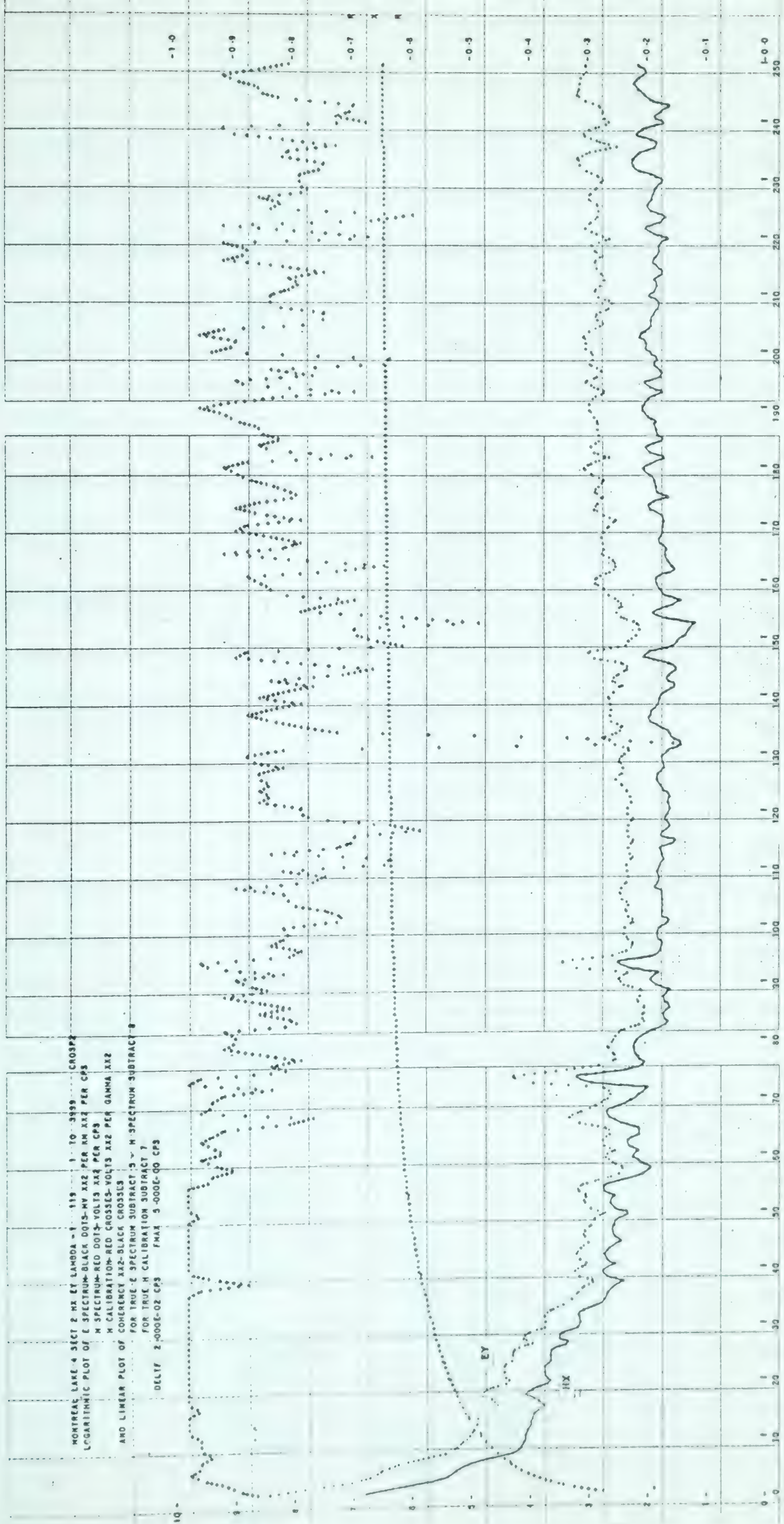


Diagram 69

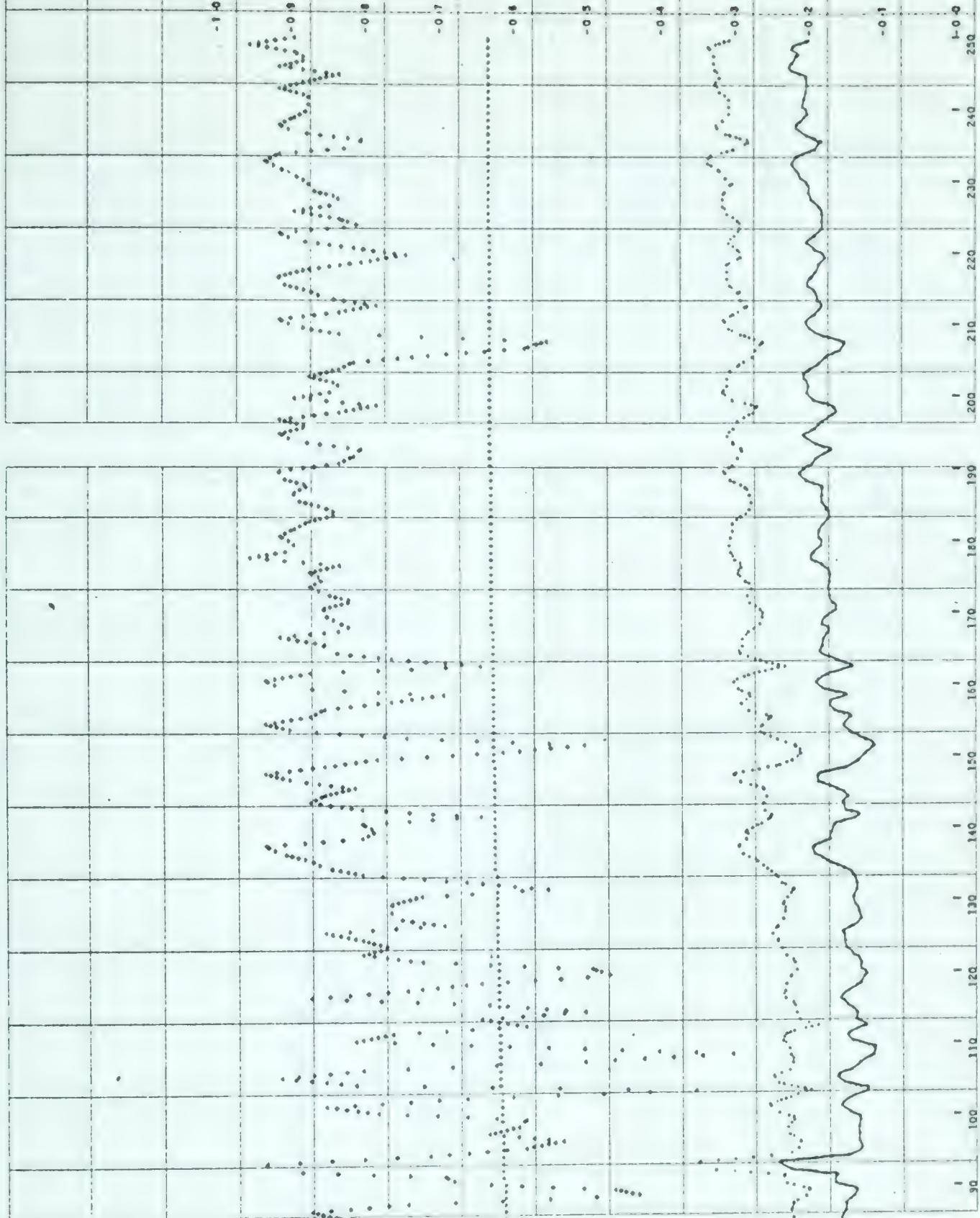
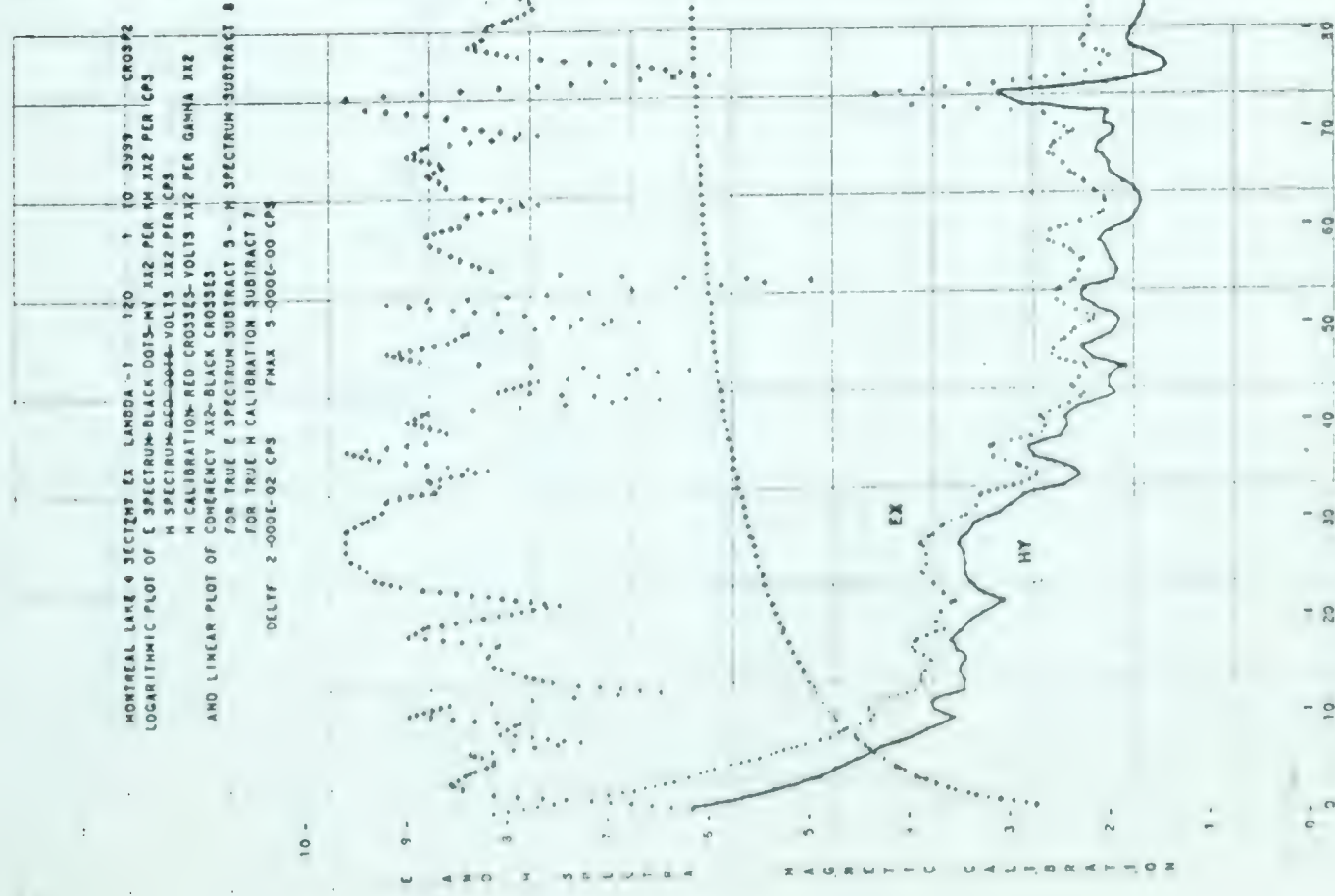


Diagram 70



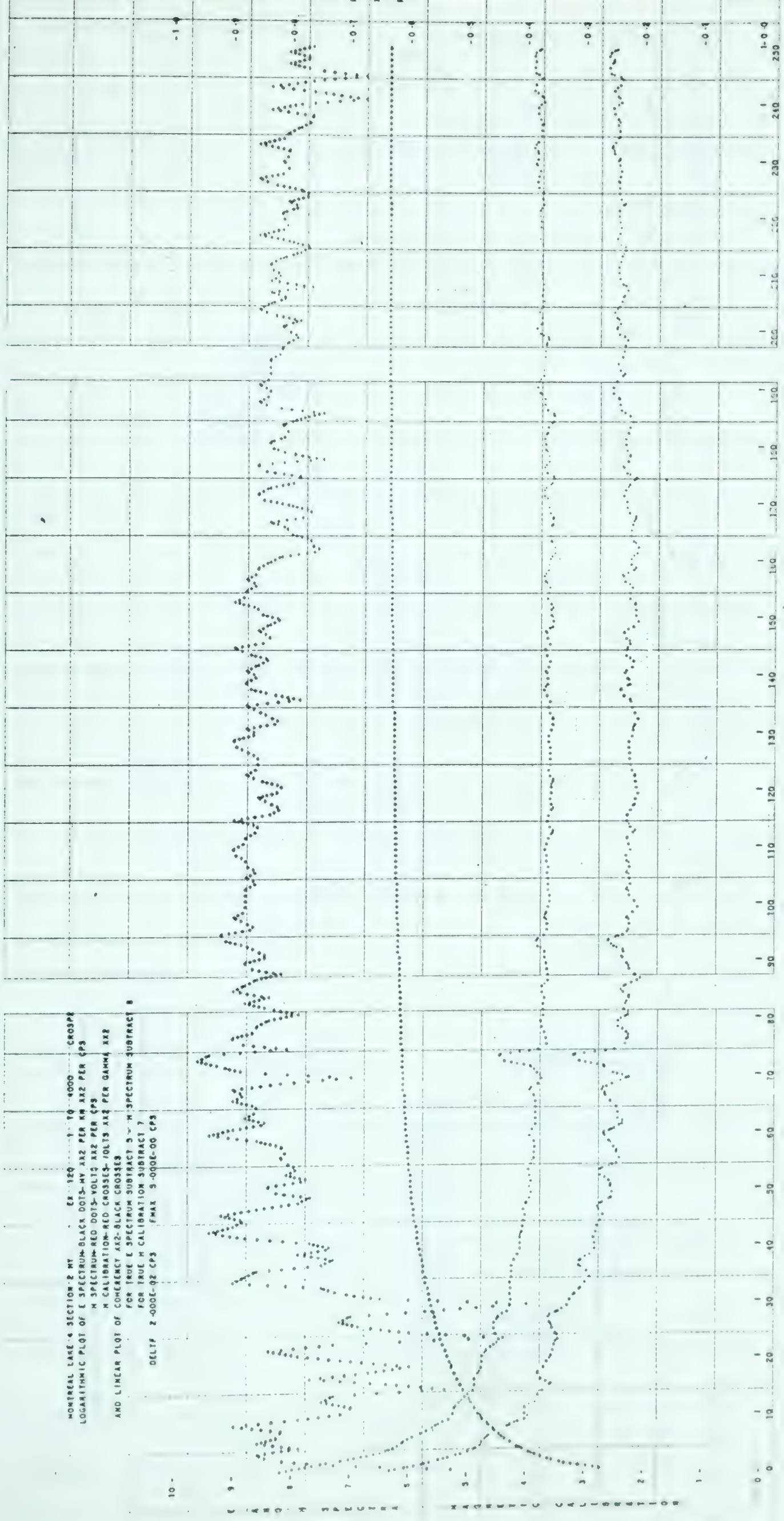


Diagram 71

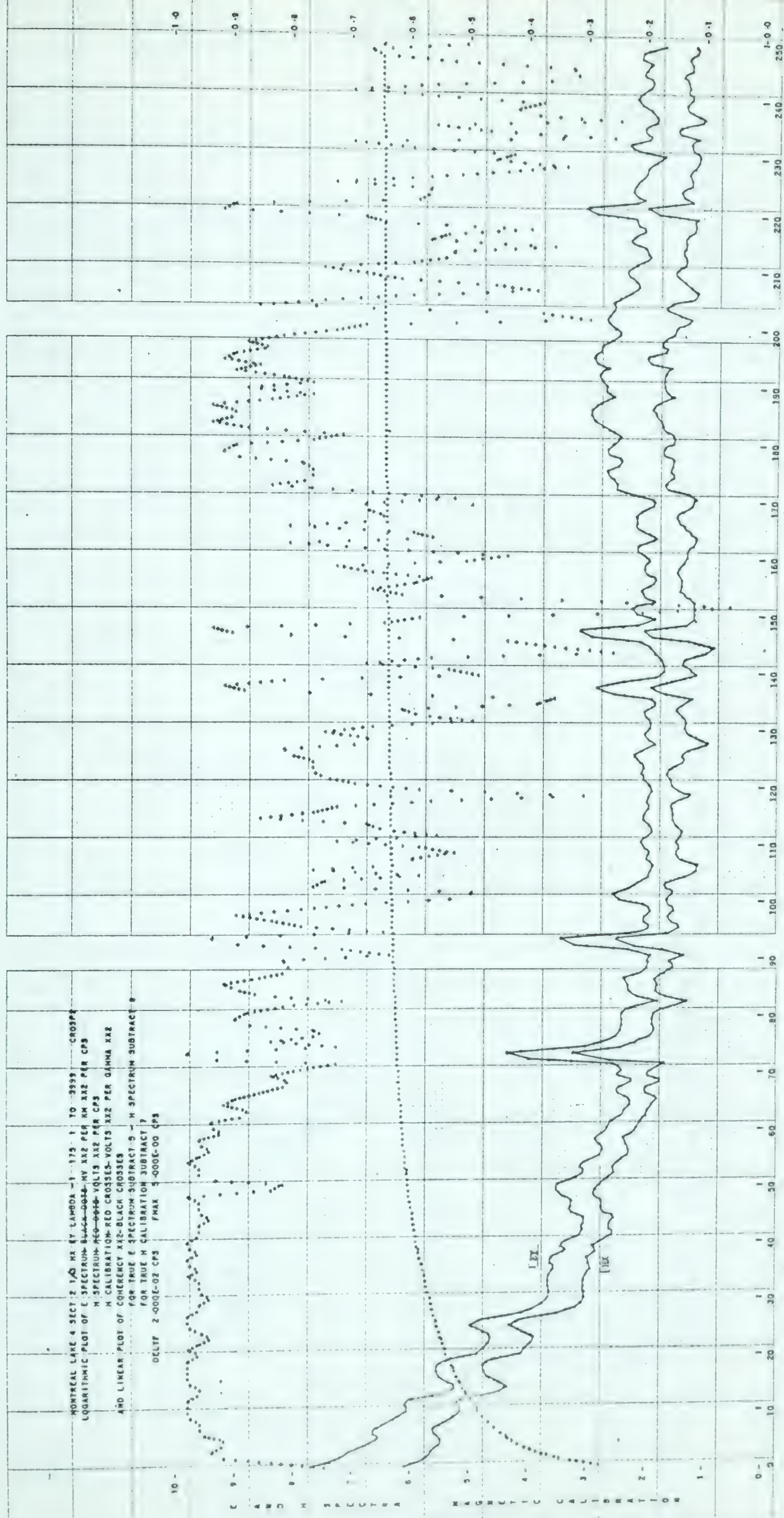
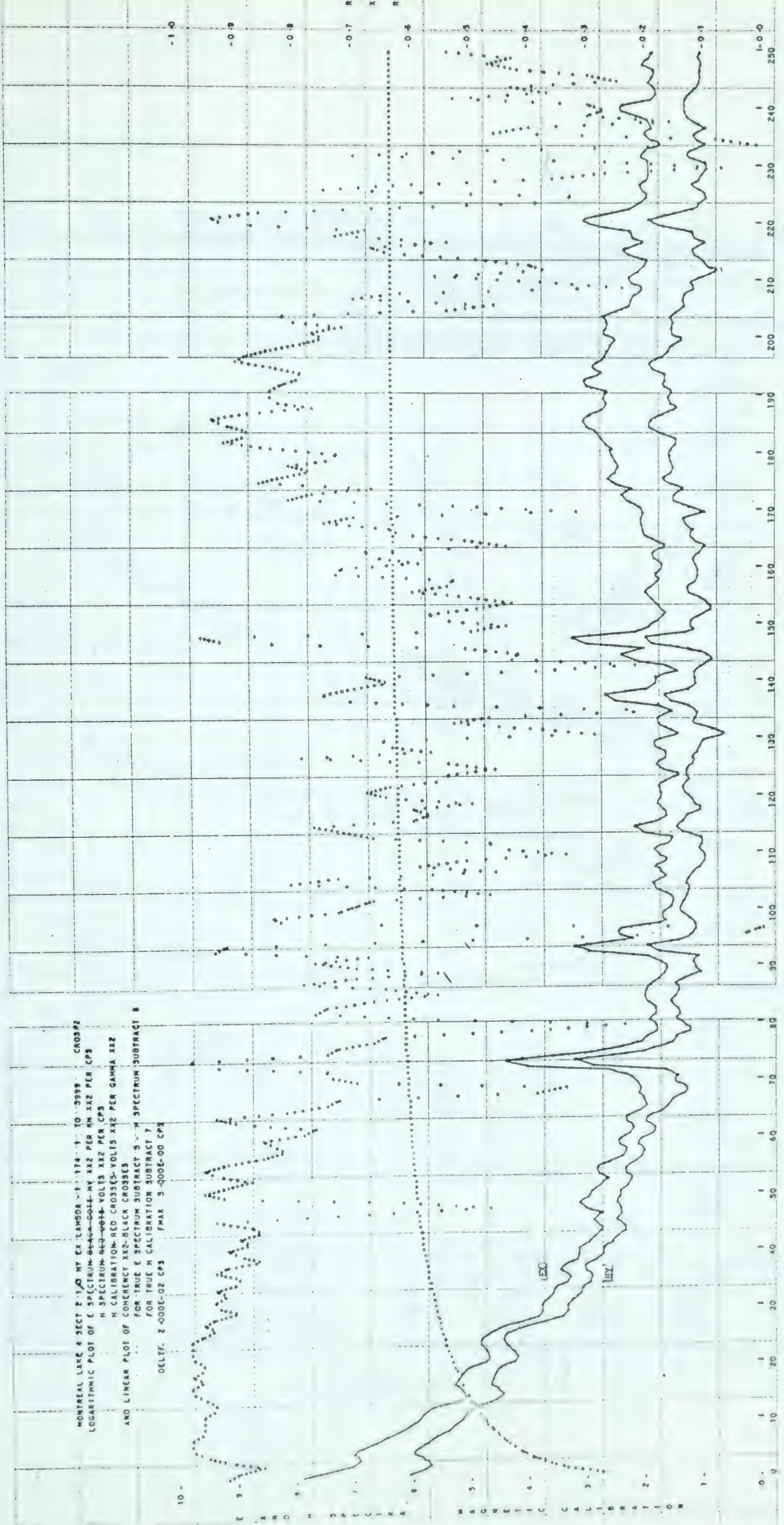


Diagram 72



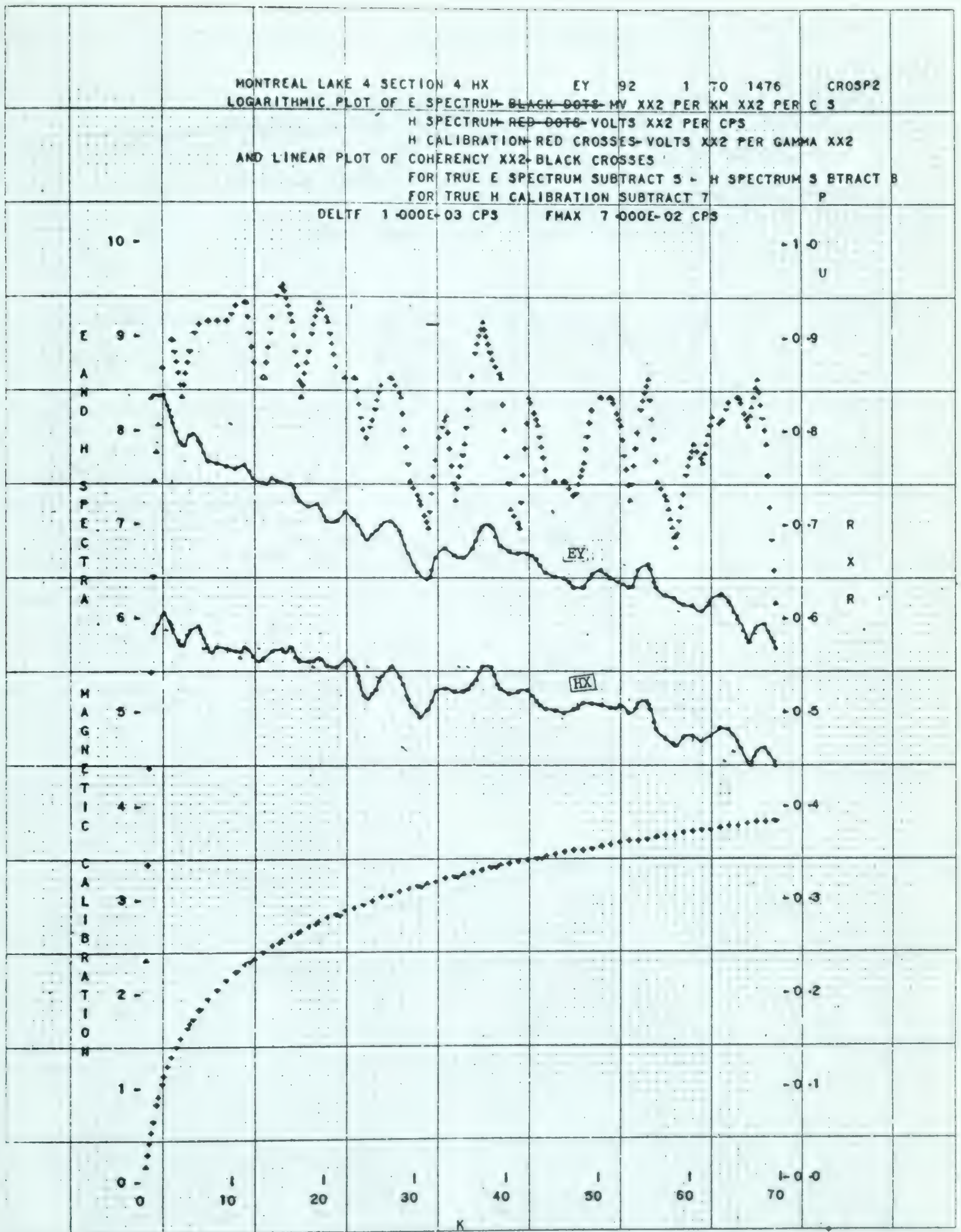


Diagram 74

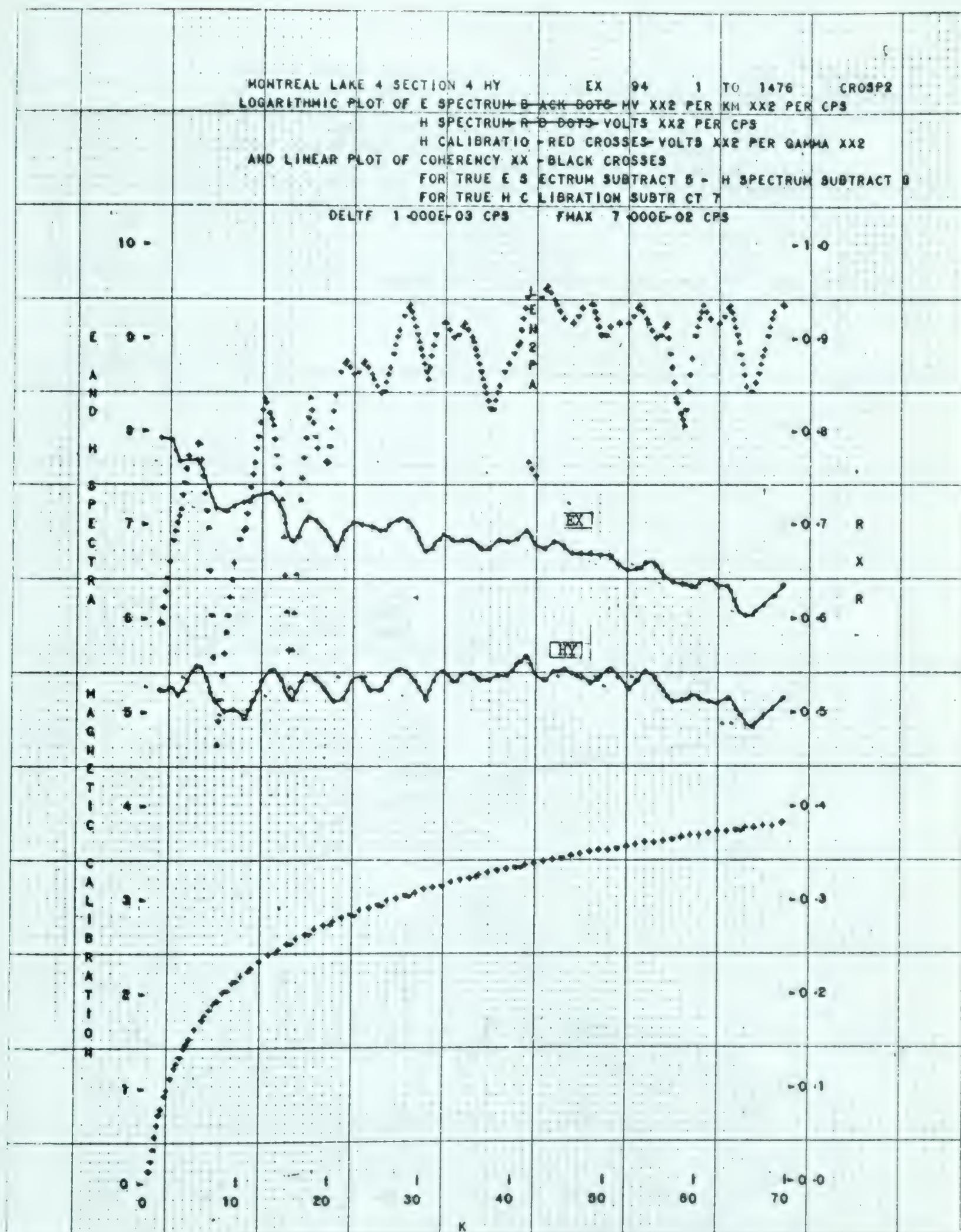


Diagram 75

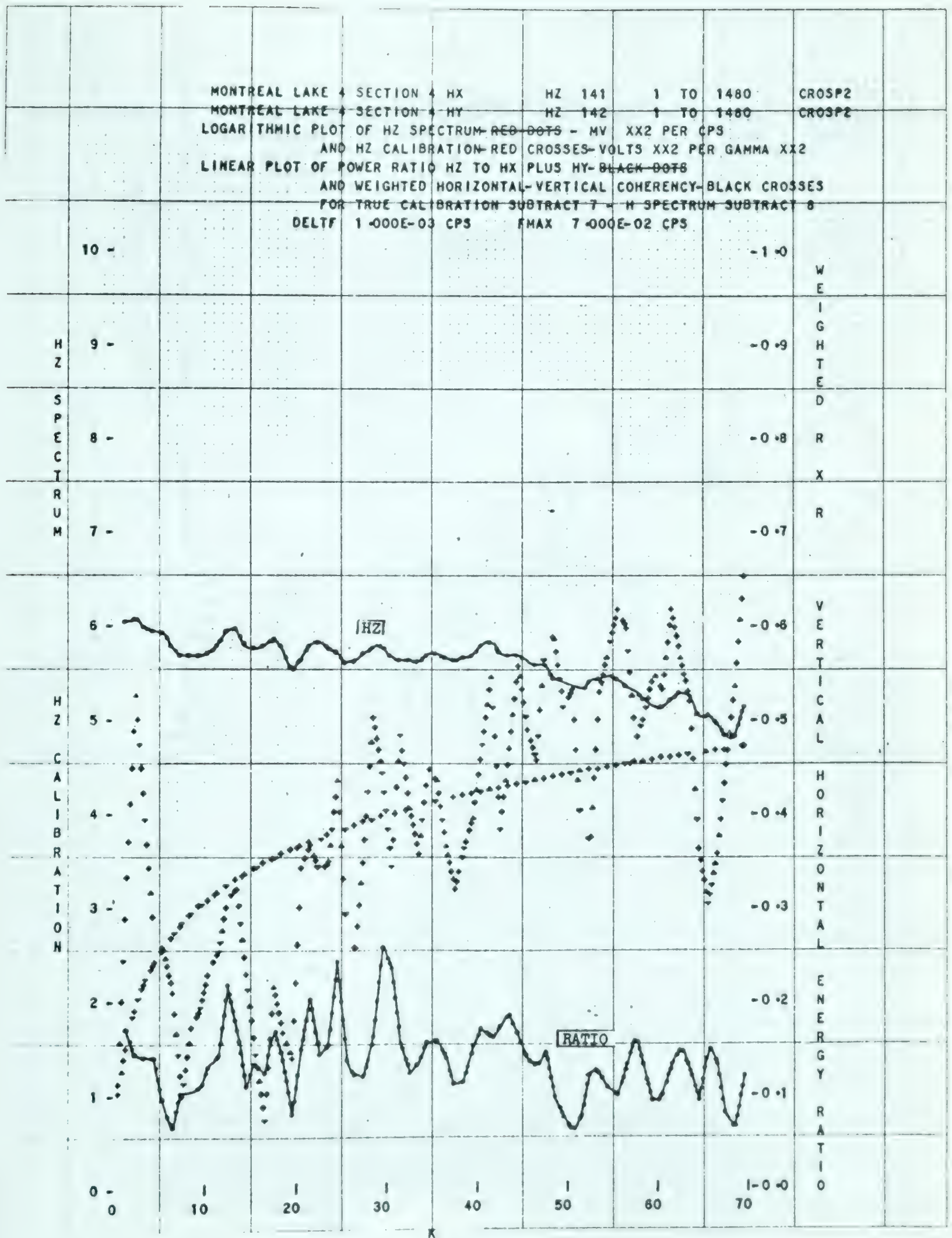


Diagram 76

1. The first part of the paper is devoted to a general discussion of the problem. It is shown that the problem is of great importance in the theory of differential equations.

2. In the second part, we consider the case of a linear differential equation. It is shown that the problem is solvable in this case.

3. In the third part, we consider the case of a nonlinear differential equation. It is shown that the problem is solvable in this case.

4. In the fourth part, we consider the case of a system of differential equations. It is shown that the problem is solvable in this case.

5. In the fifth part, we consider the case of a partial differential equation. It is shown that the problem is solvable in this case.

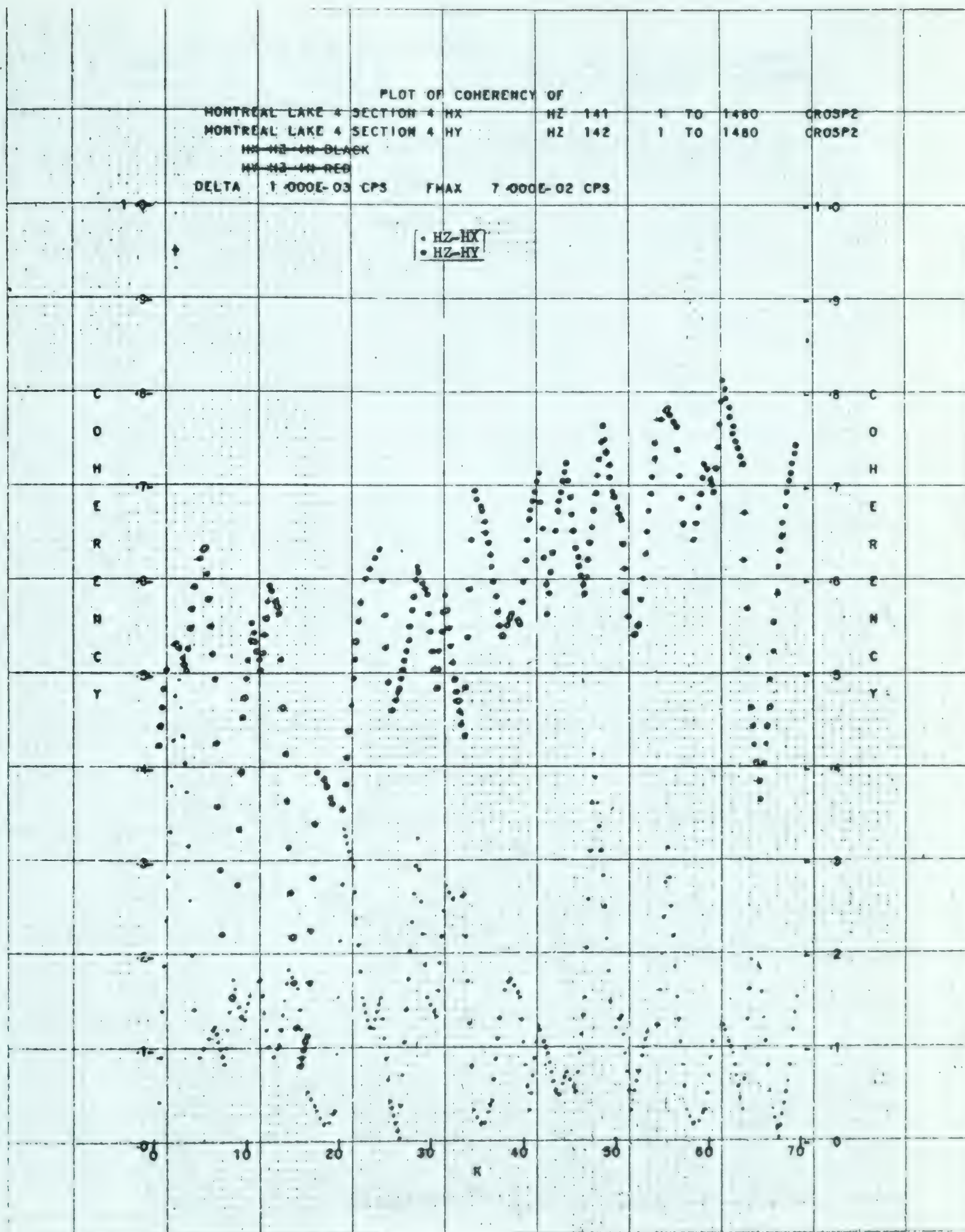
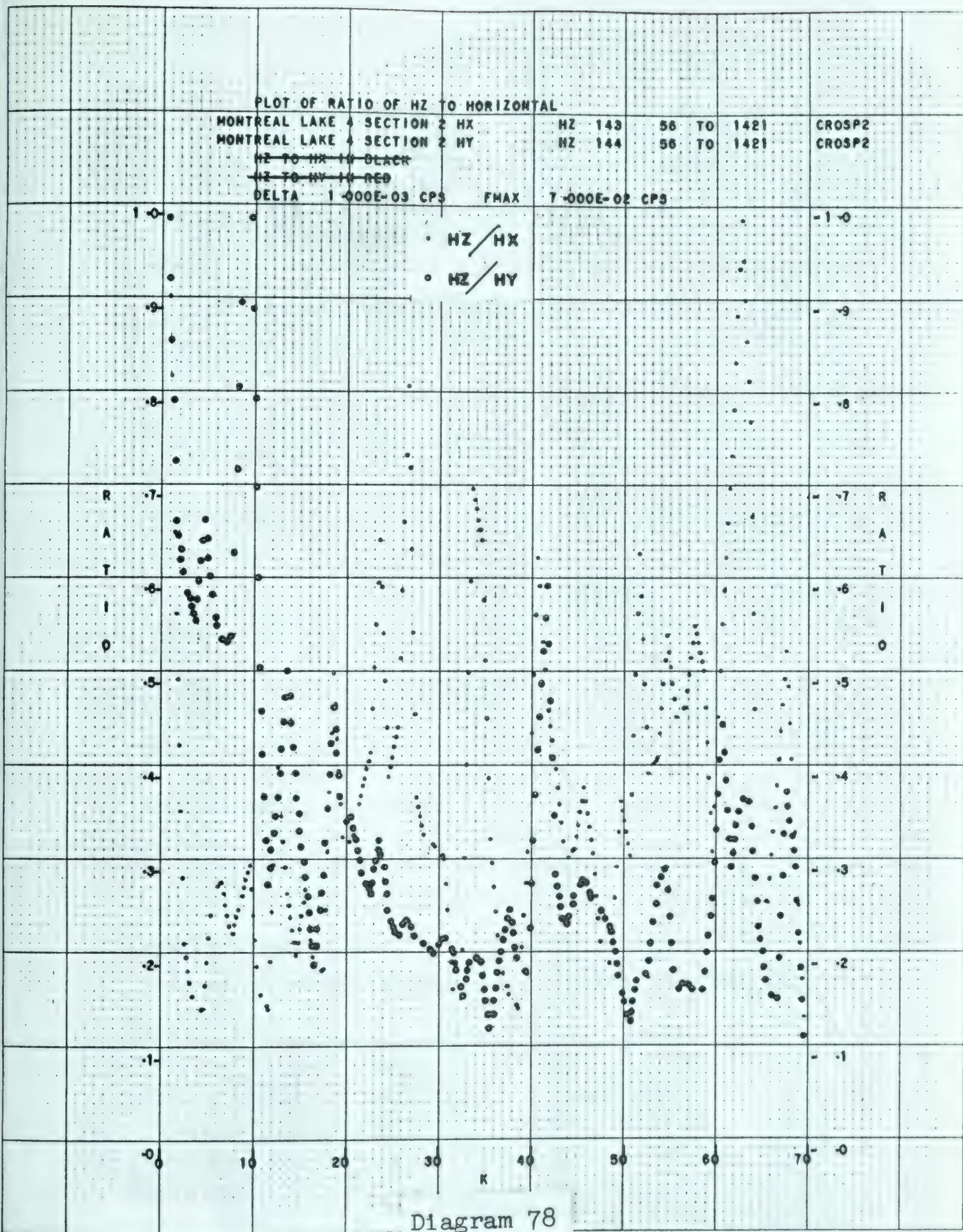
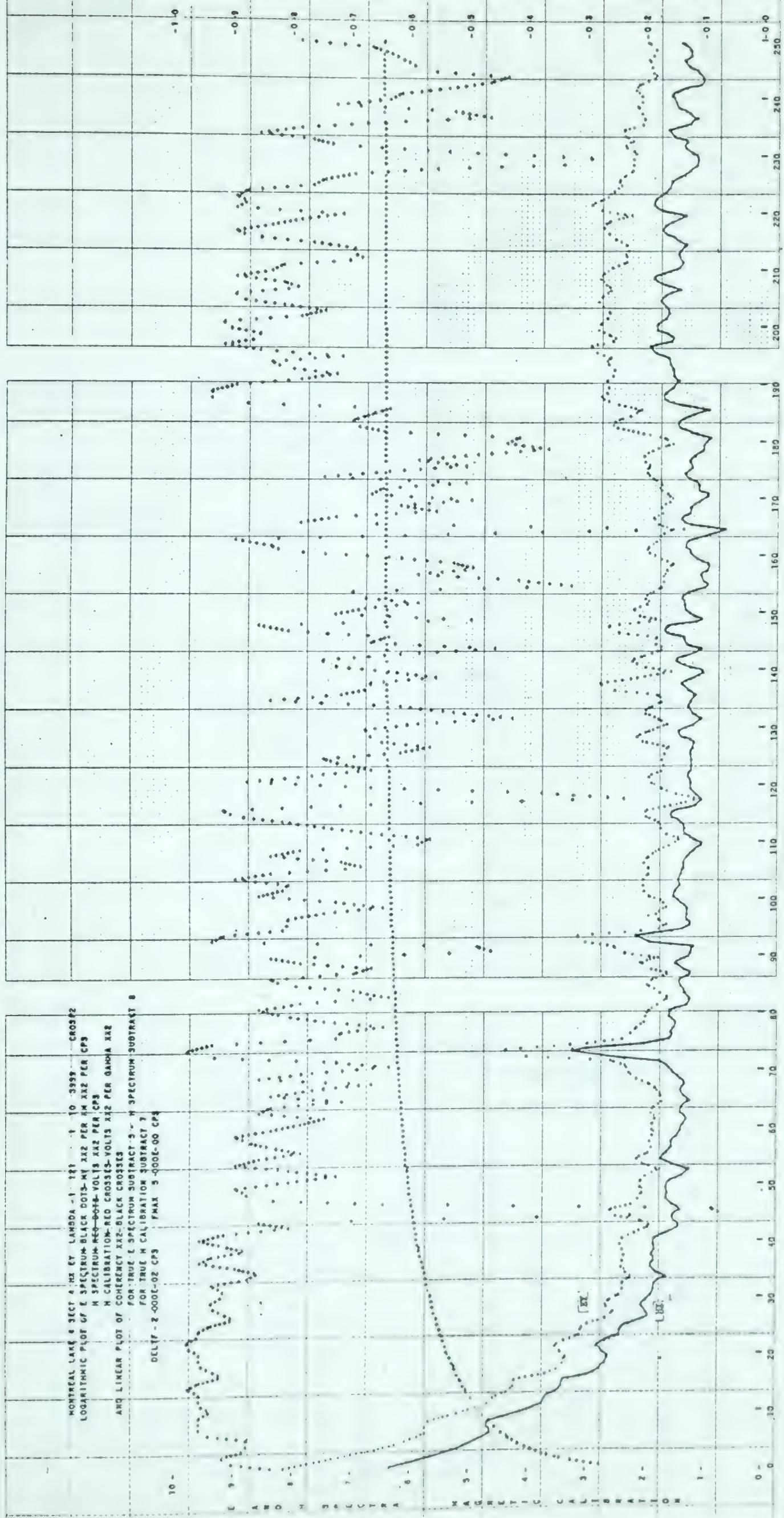


Diagram 77





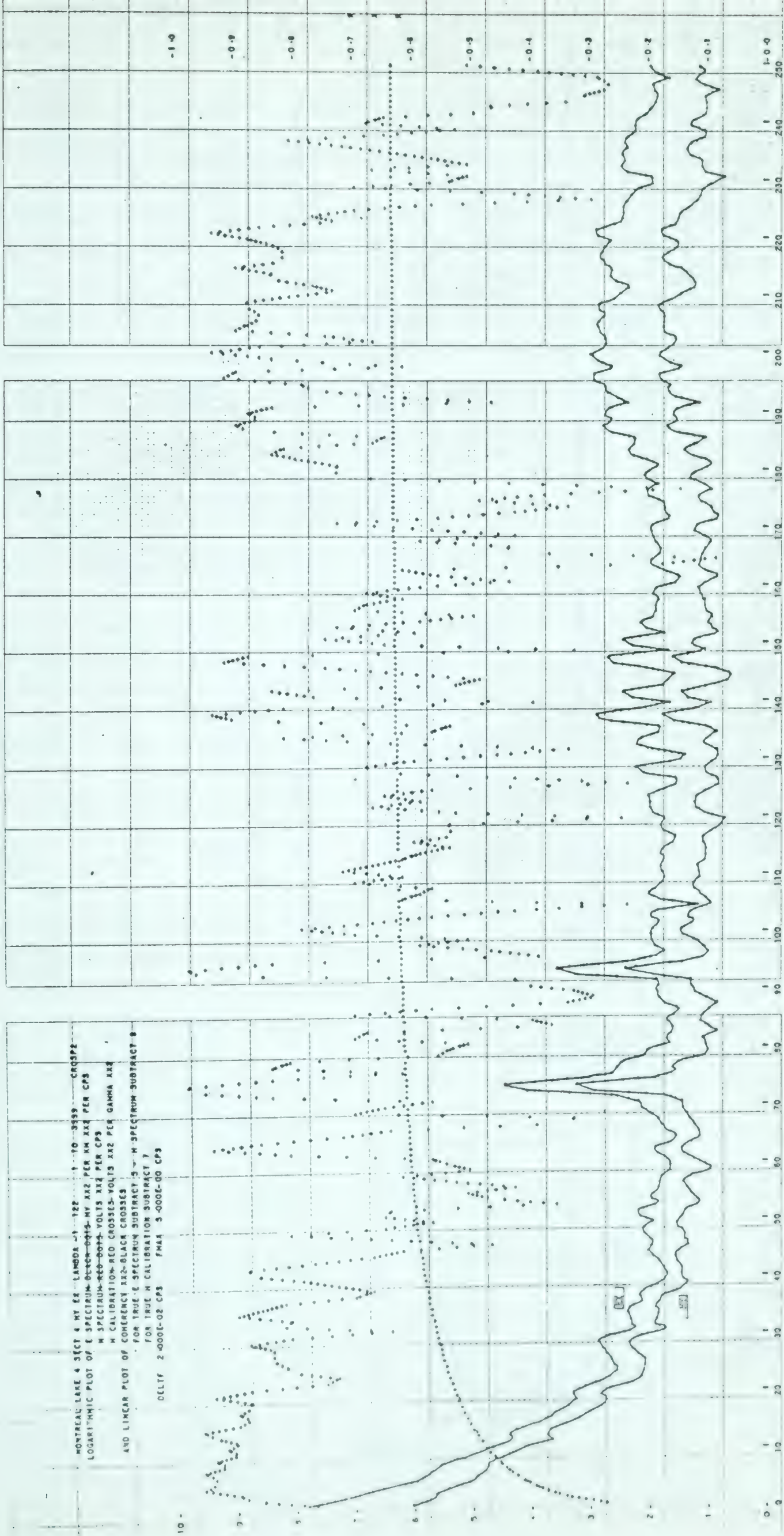


Diagram 80

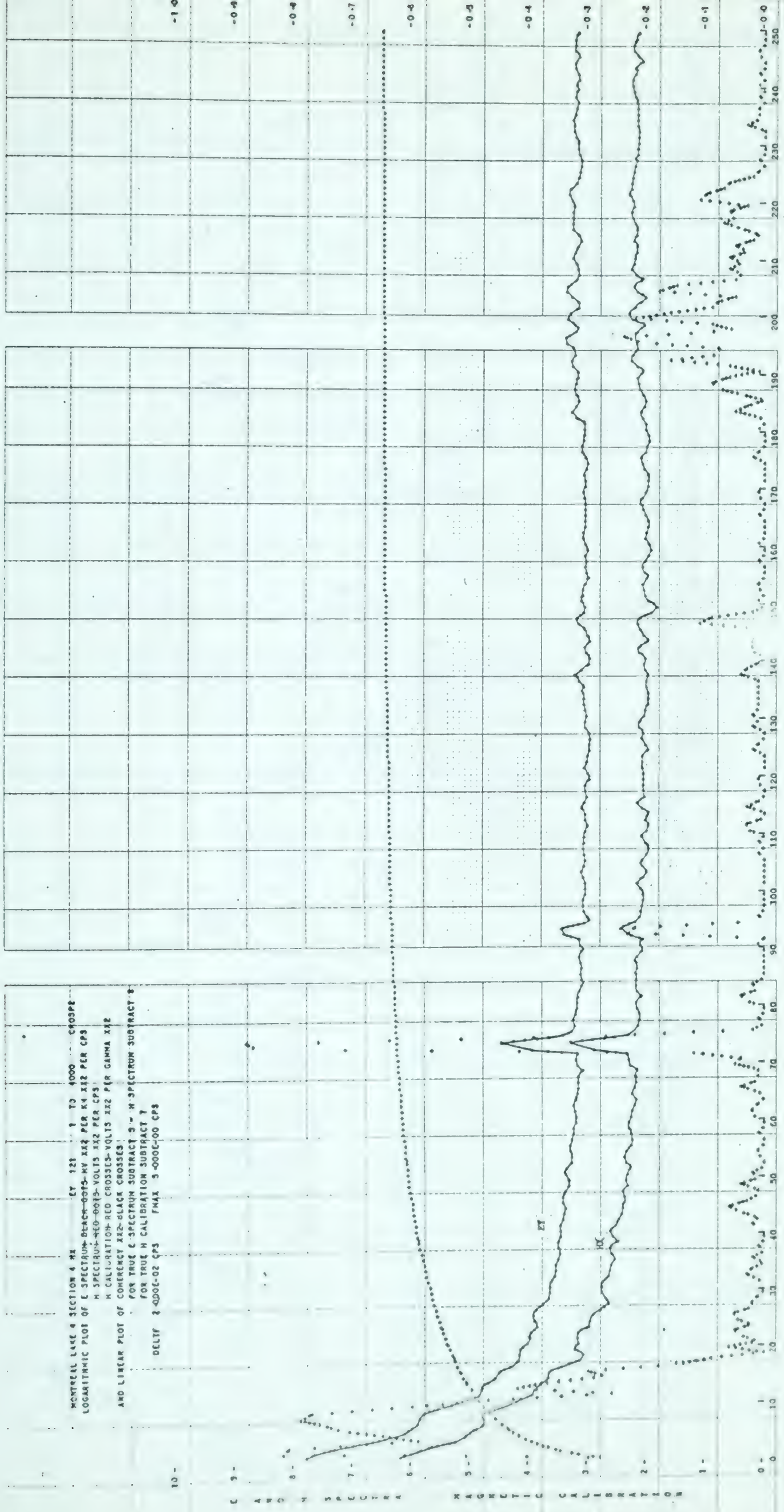
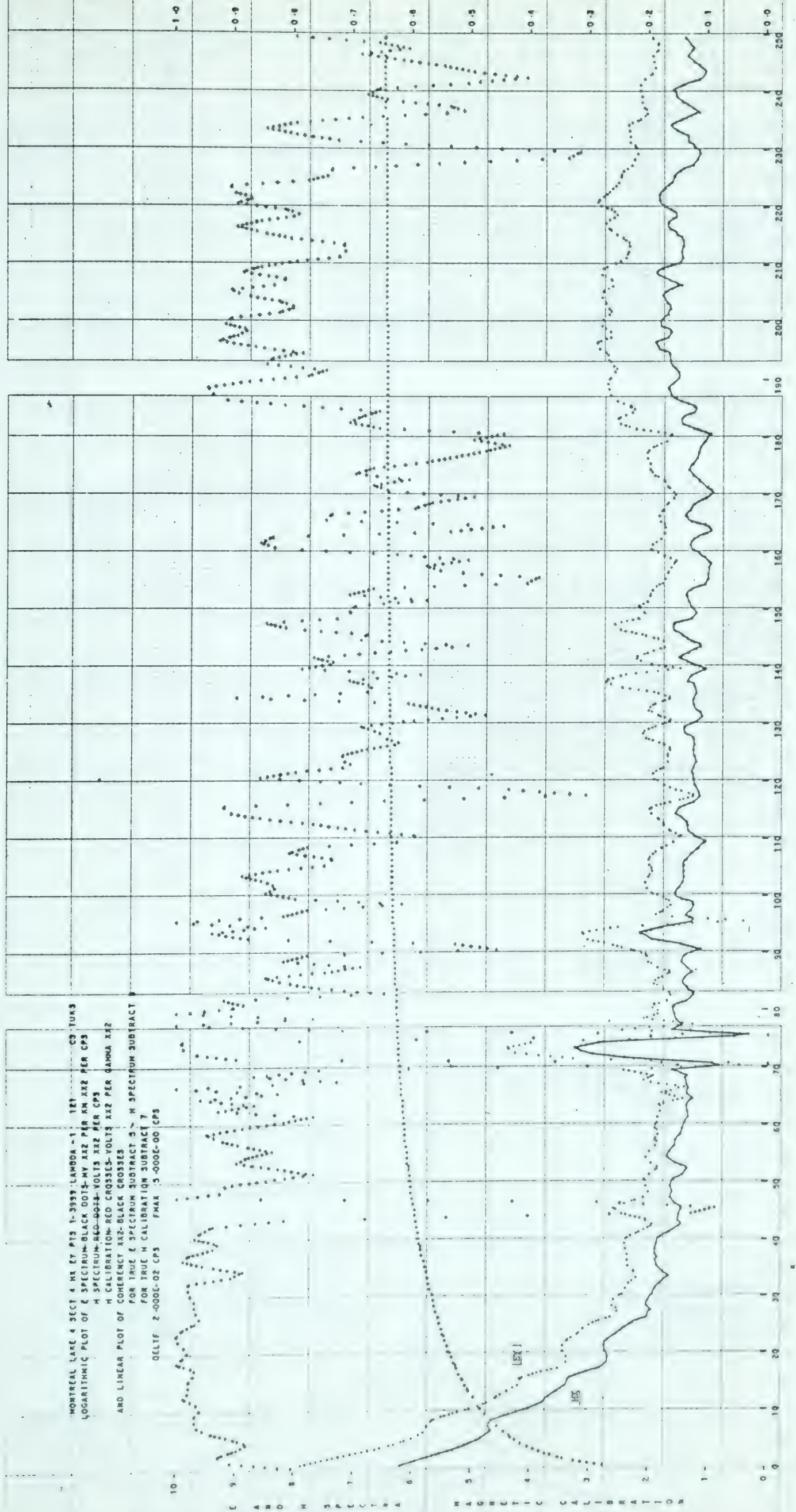


Diagram 81

MONTREAL LANE 4 SECT 4 MI 27 P13 1-3999 LAMDA - 1 121 --- CS TUKS
LOGARITHMIC PLOT OF SPECTRUM-BLACK DOTS-MY X12 PER KM X12 PER CPS
M SPECTRUM-RED CROSSES-VOLTS X12 PER KM X12 PER CPS
M CALIBRATION-RED CROSSES-VOLTS X12 PER LAMDA X12
AND LINEAR PLOT OF COHERENCY X12-BLACK CROSSES
FOR TRUE SPECTRUM SUBTRACT 3 ~ M SPECTRUM-SUBTRACT
FOR TRUE M CALIBRATION SUBTRACT 7
DELTF 2-000E-02 CPS PHAS 3-000E-00 CPS





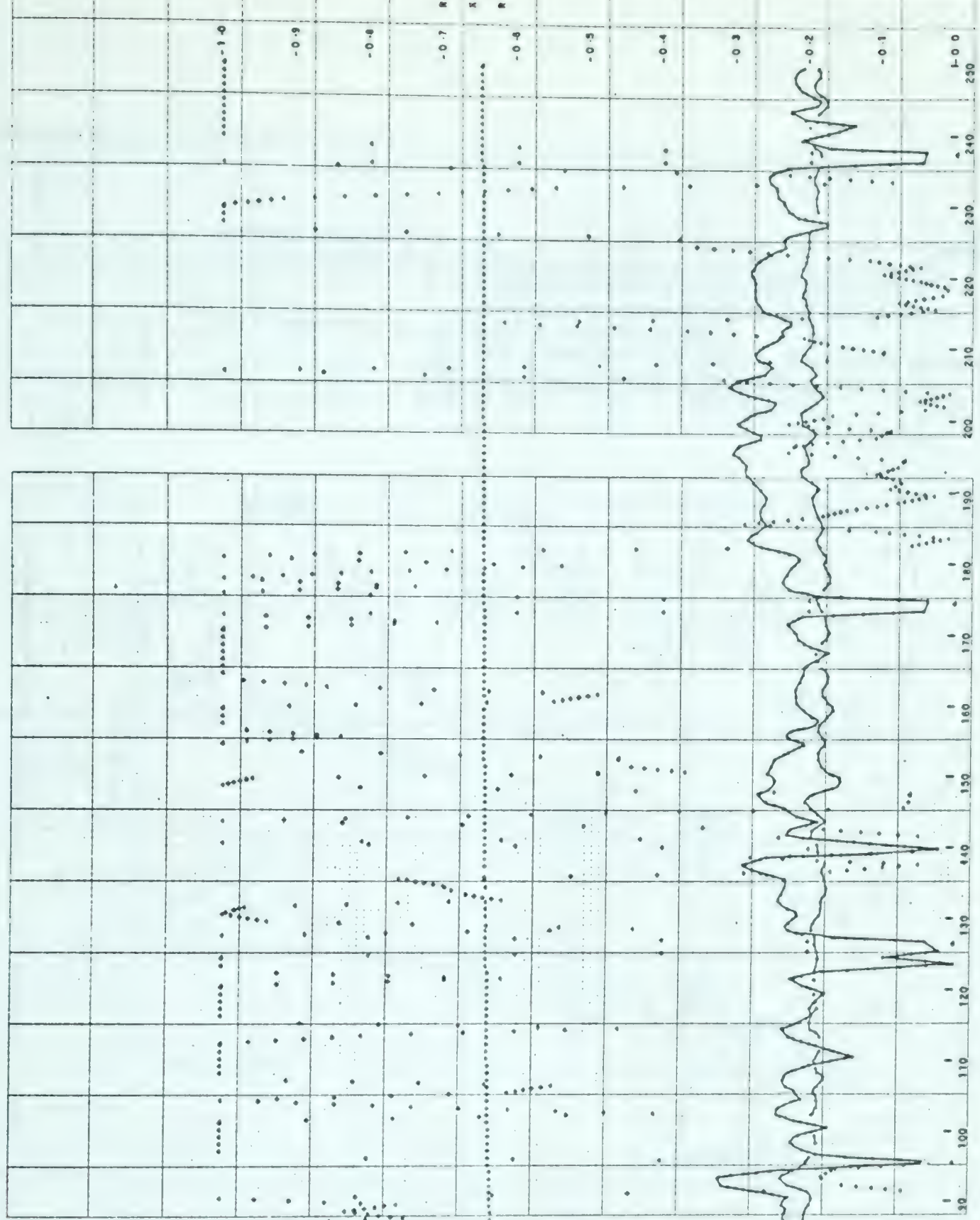
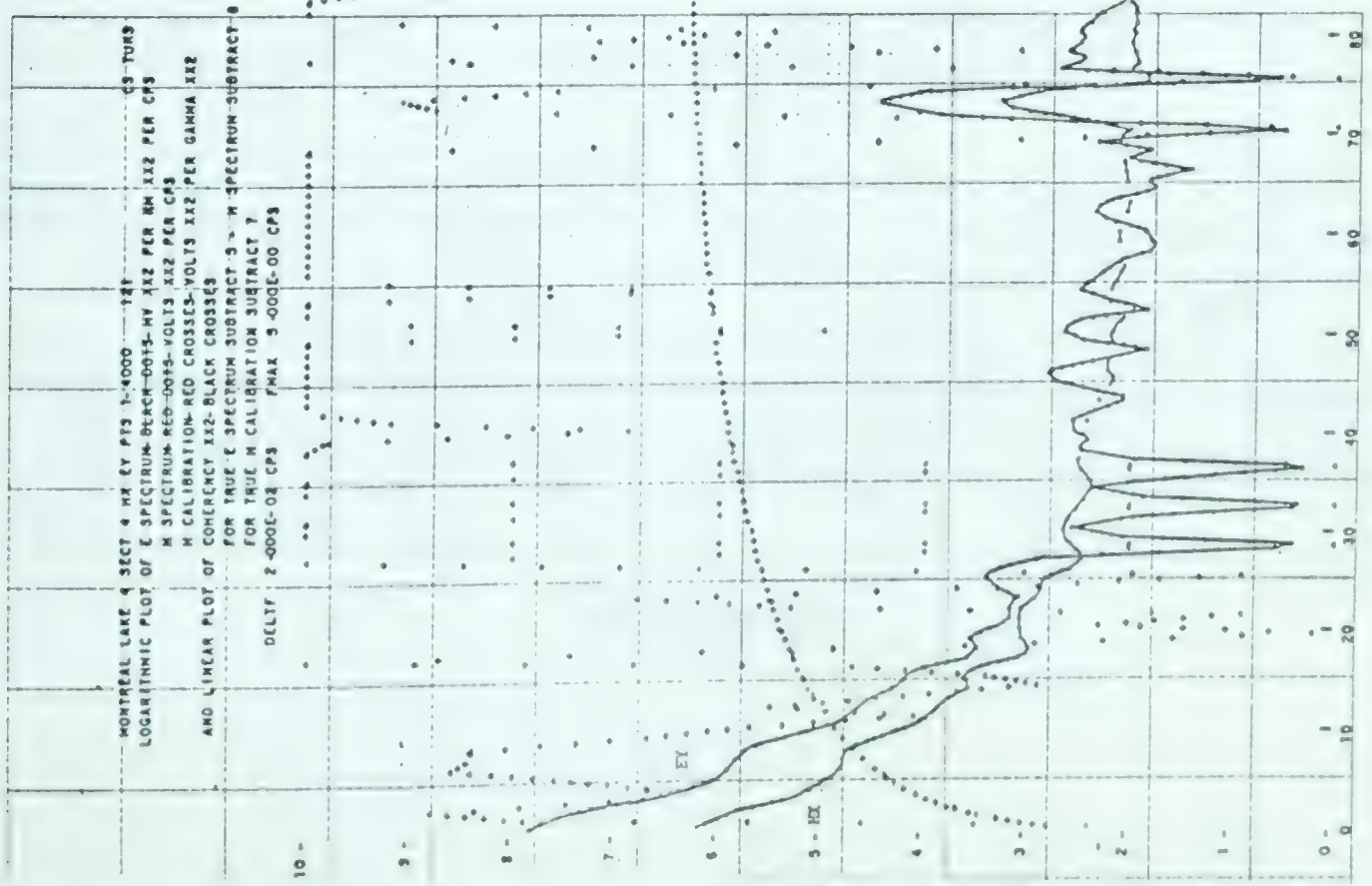


Diagram 83



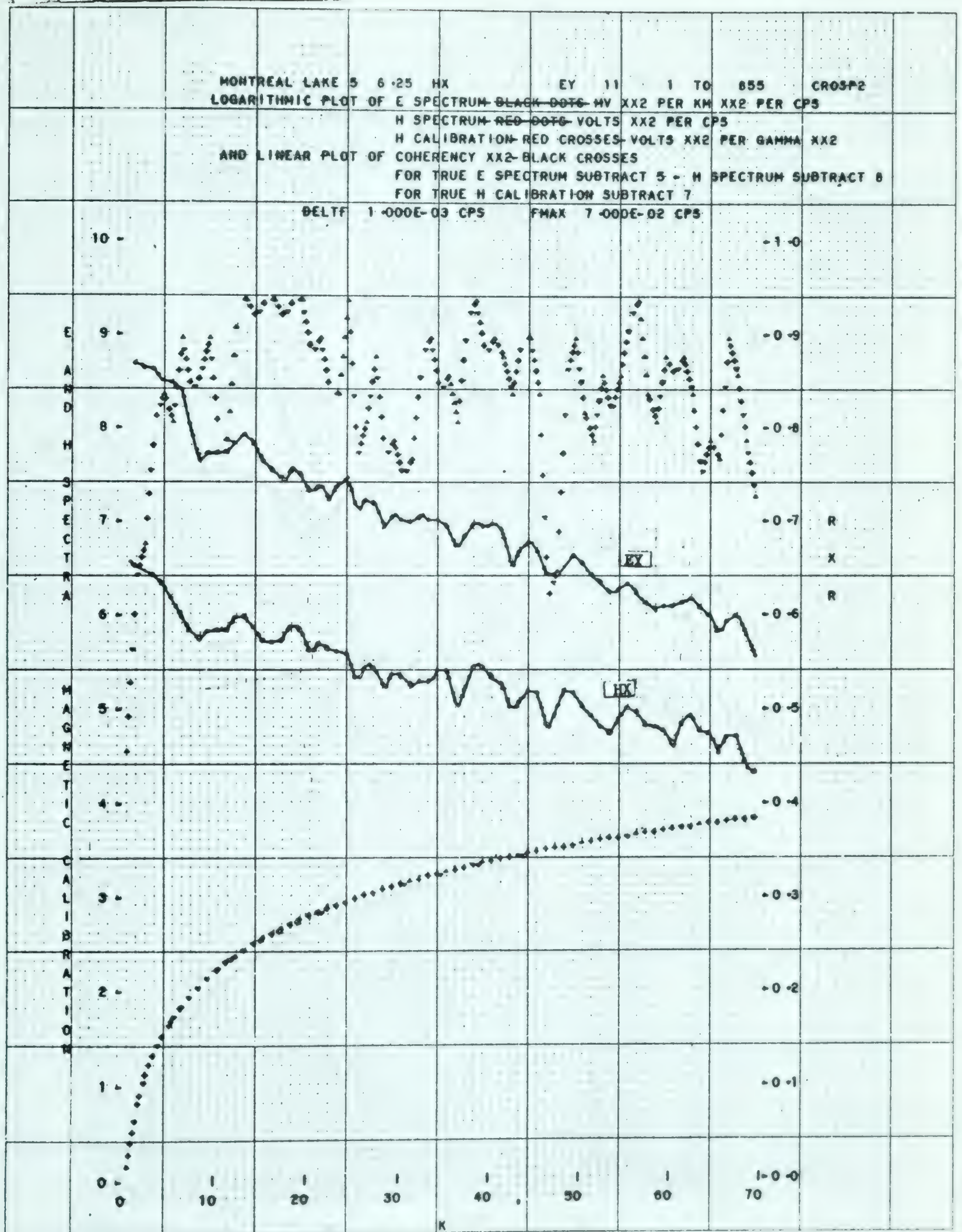


Diagram 84



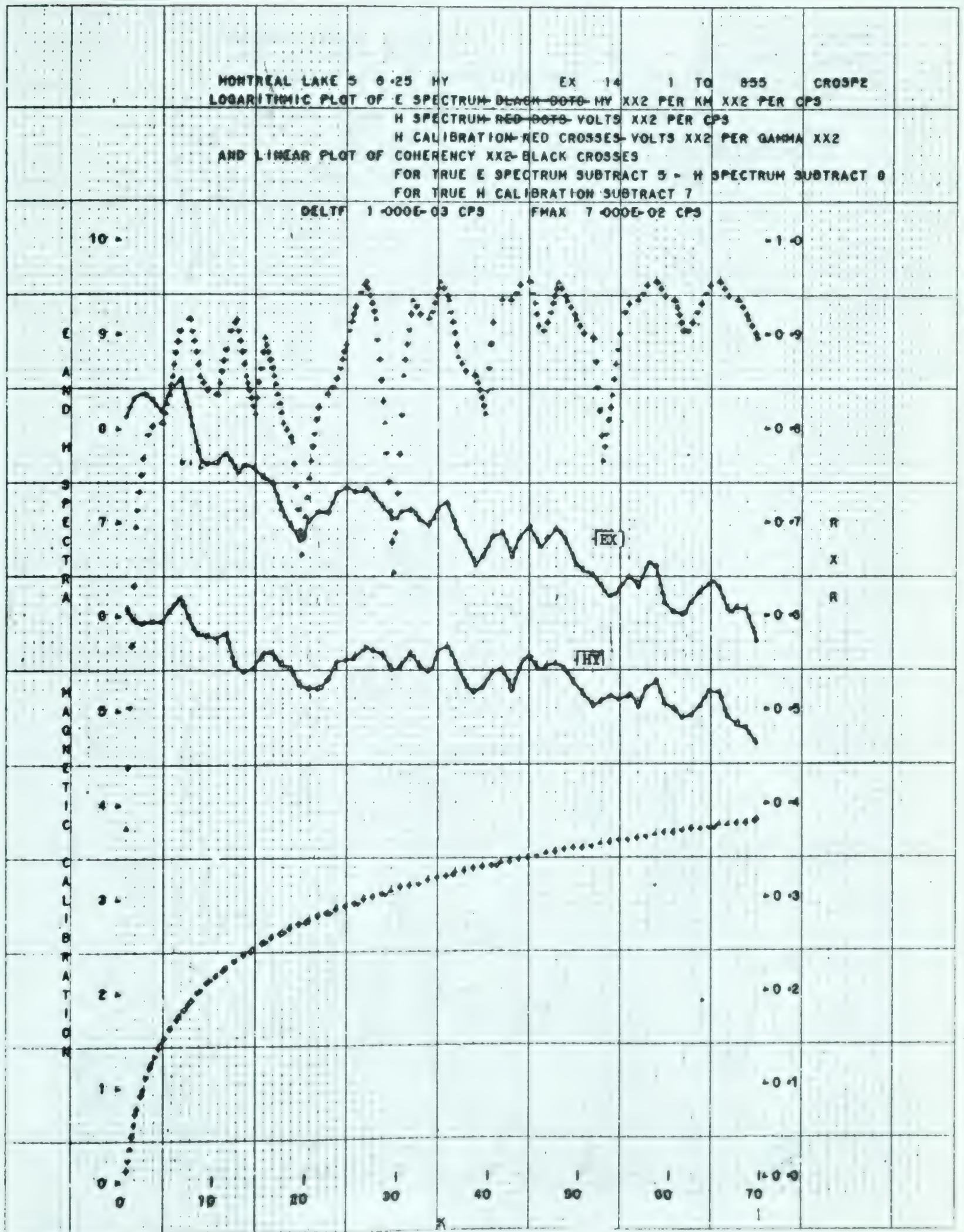


Diagram 85

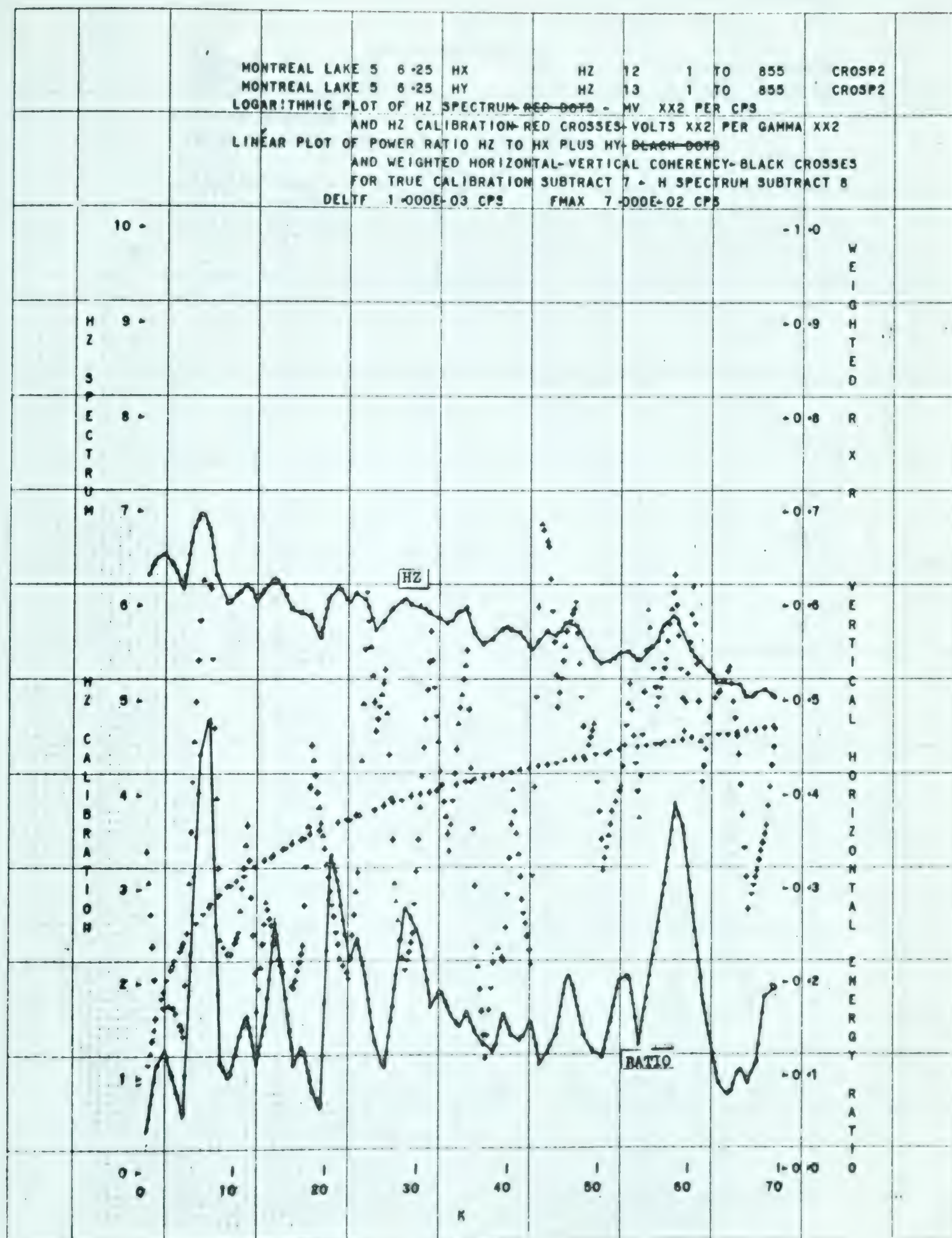


Diagram 86

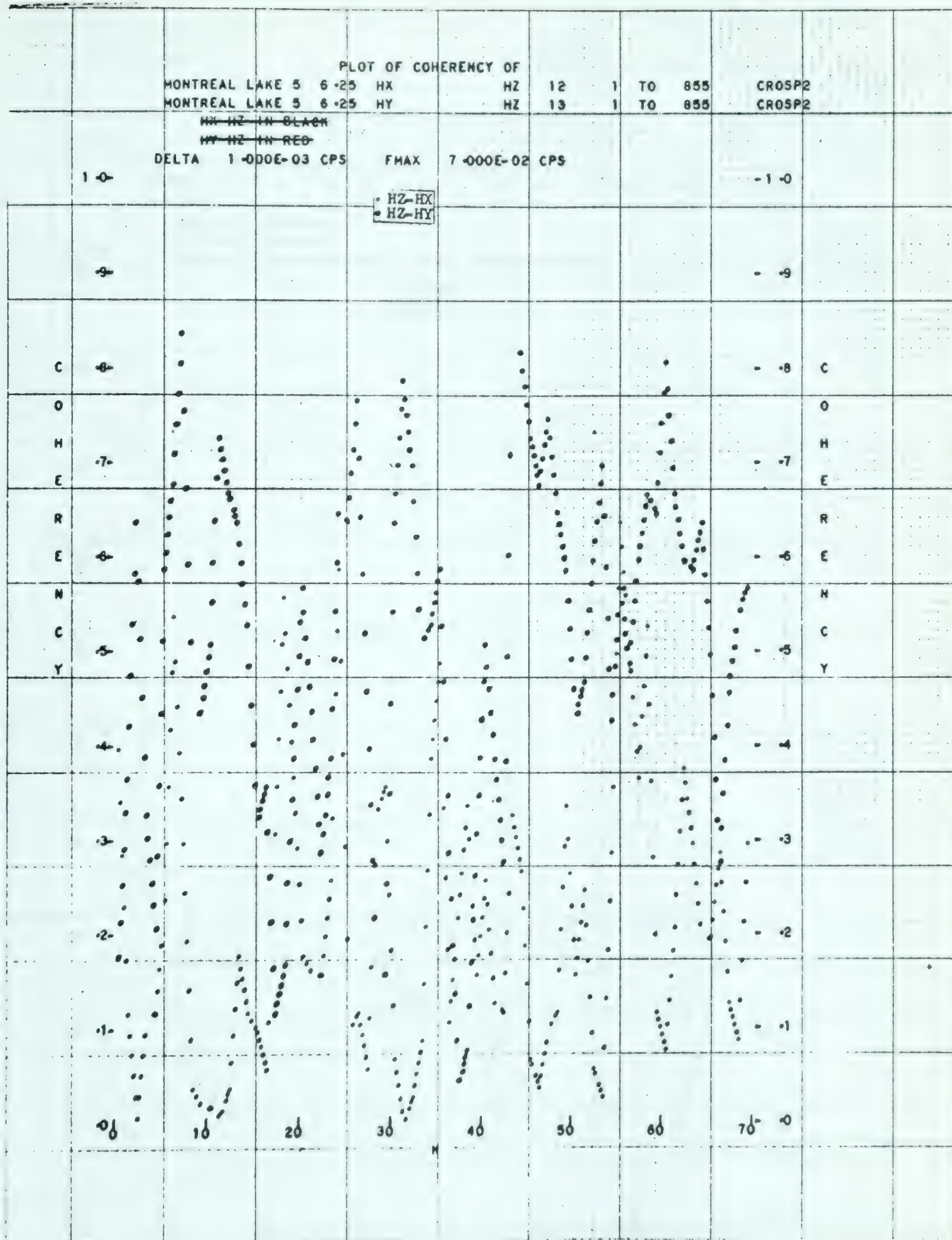


Diagram 87

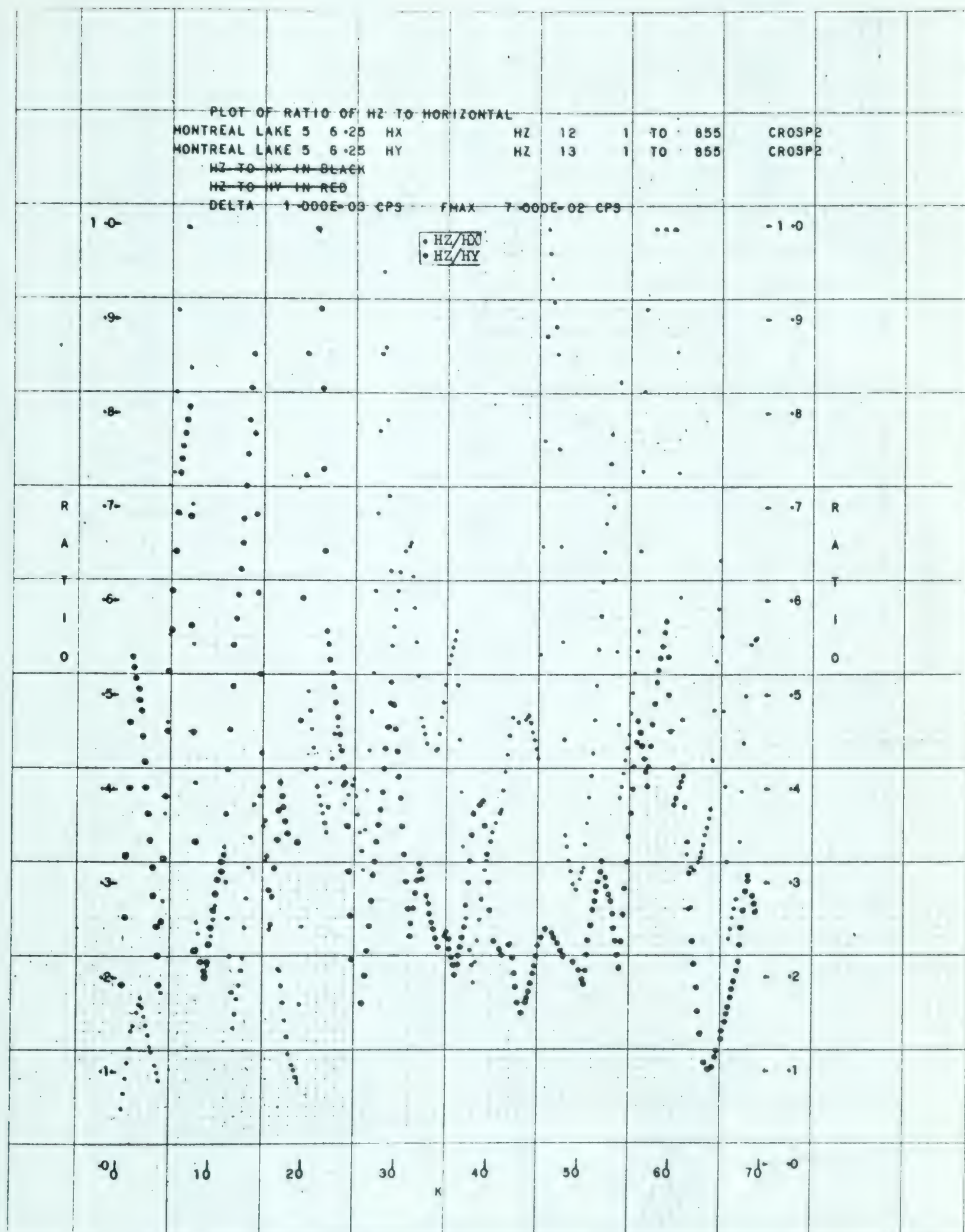


Diagram 88

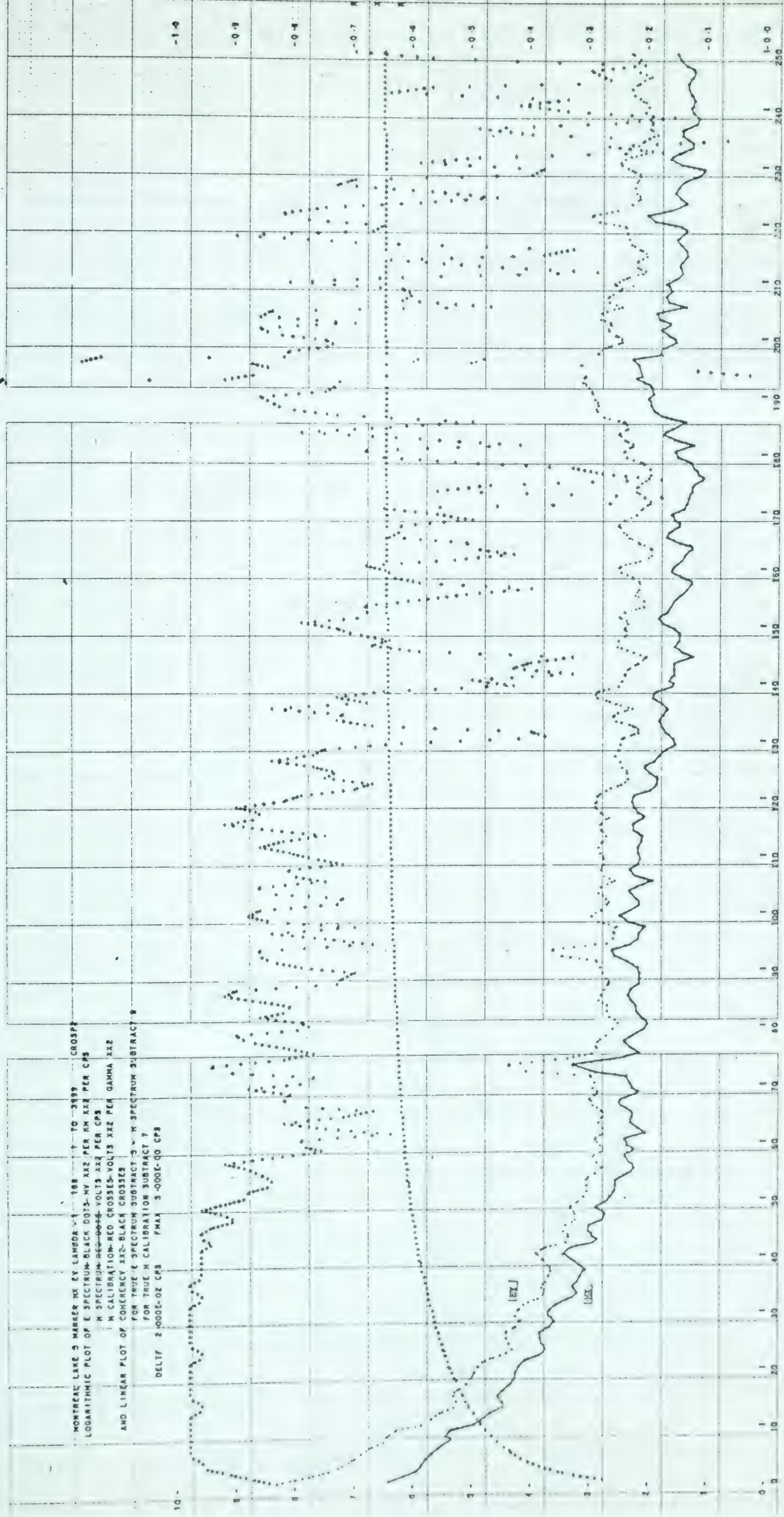


Diagram 89



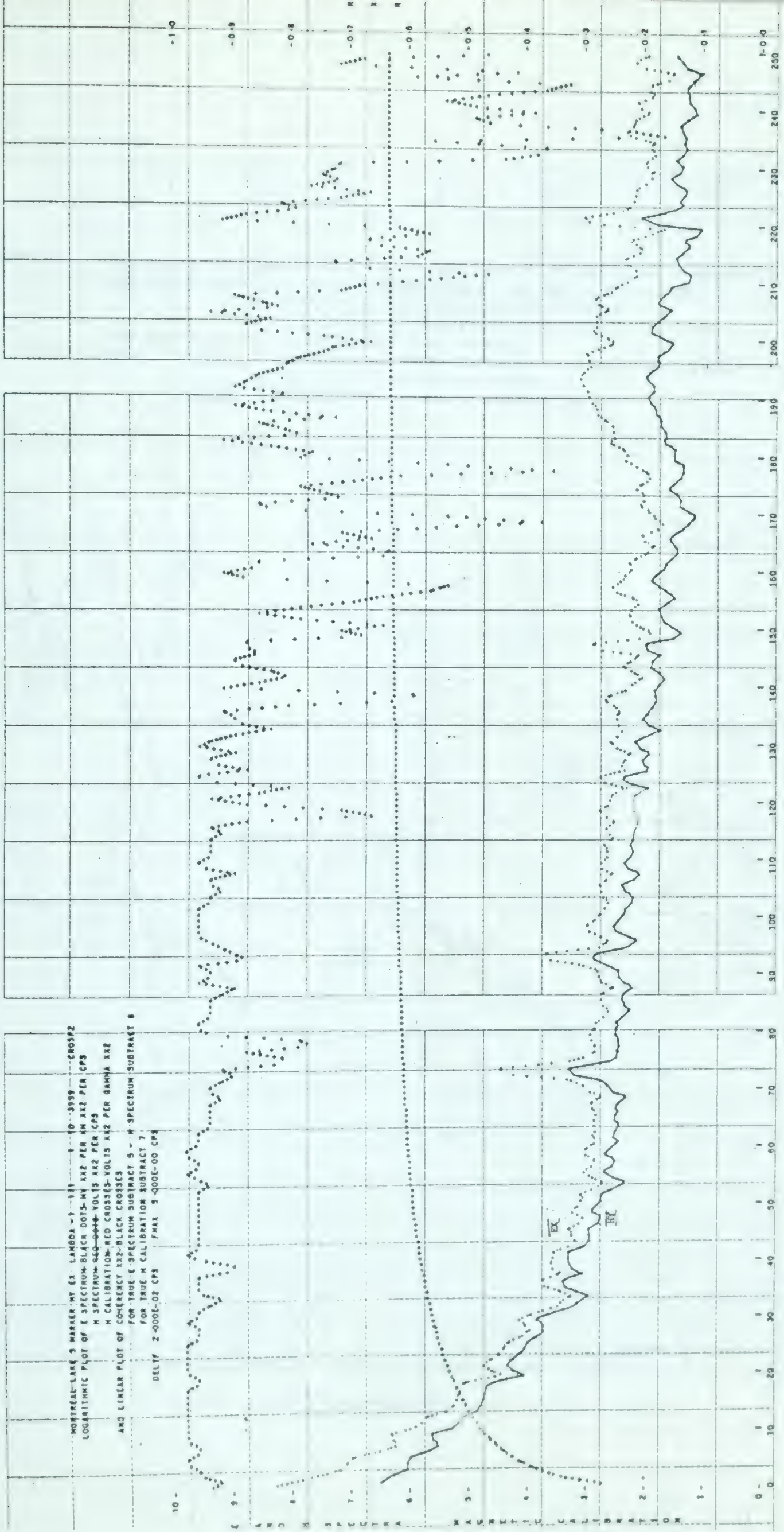


Diagram 90

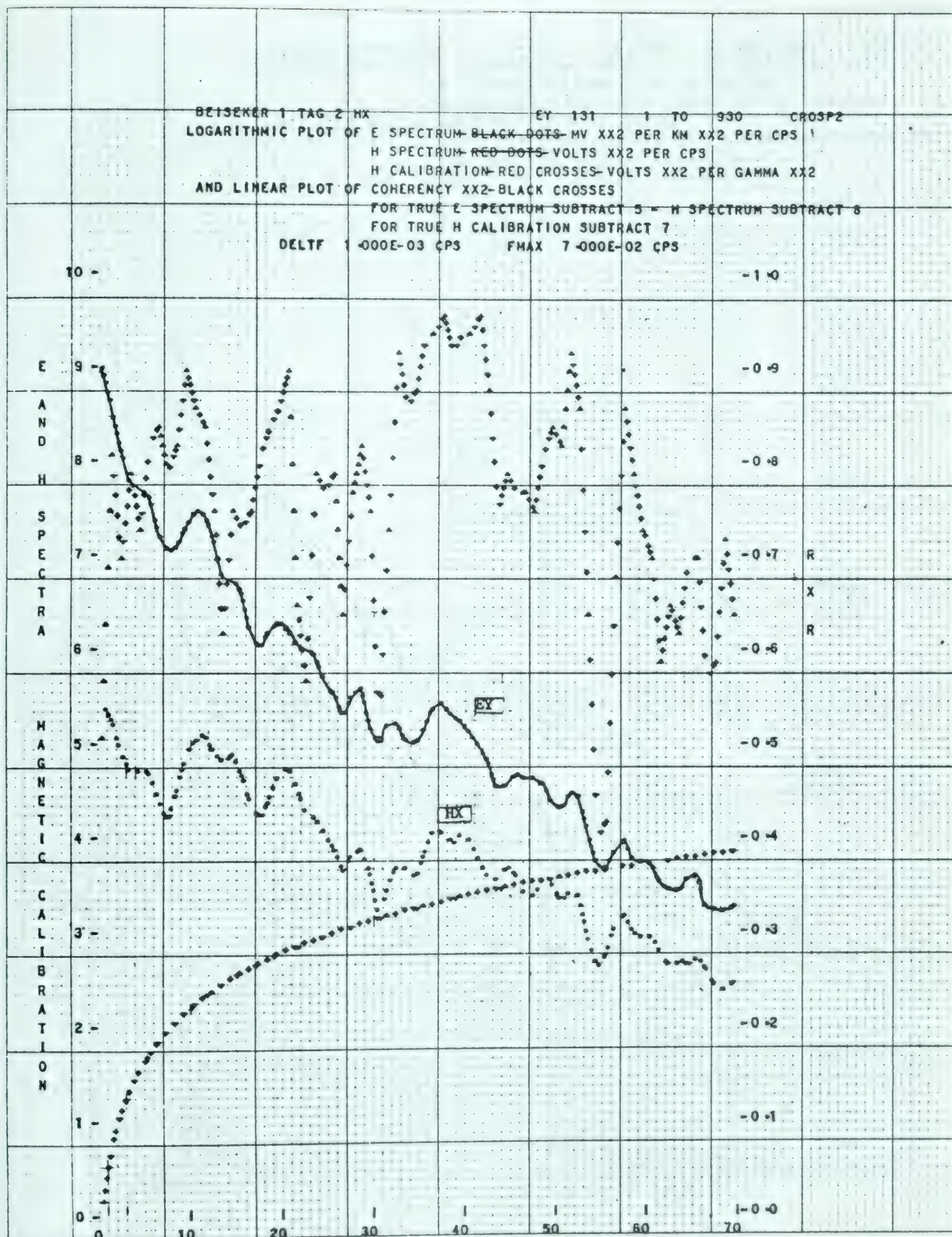


Diagram 91



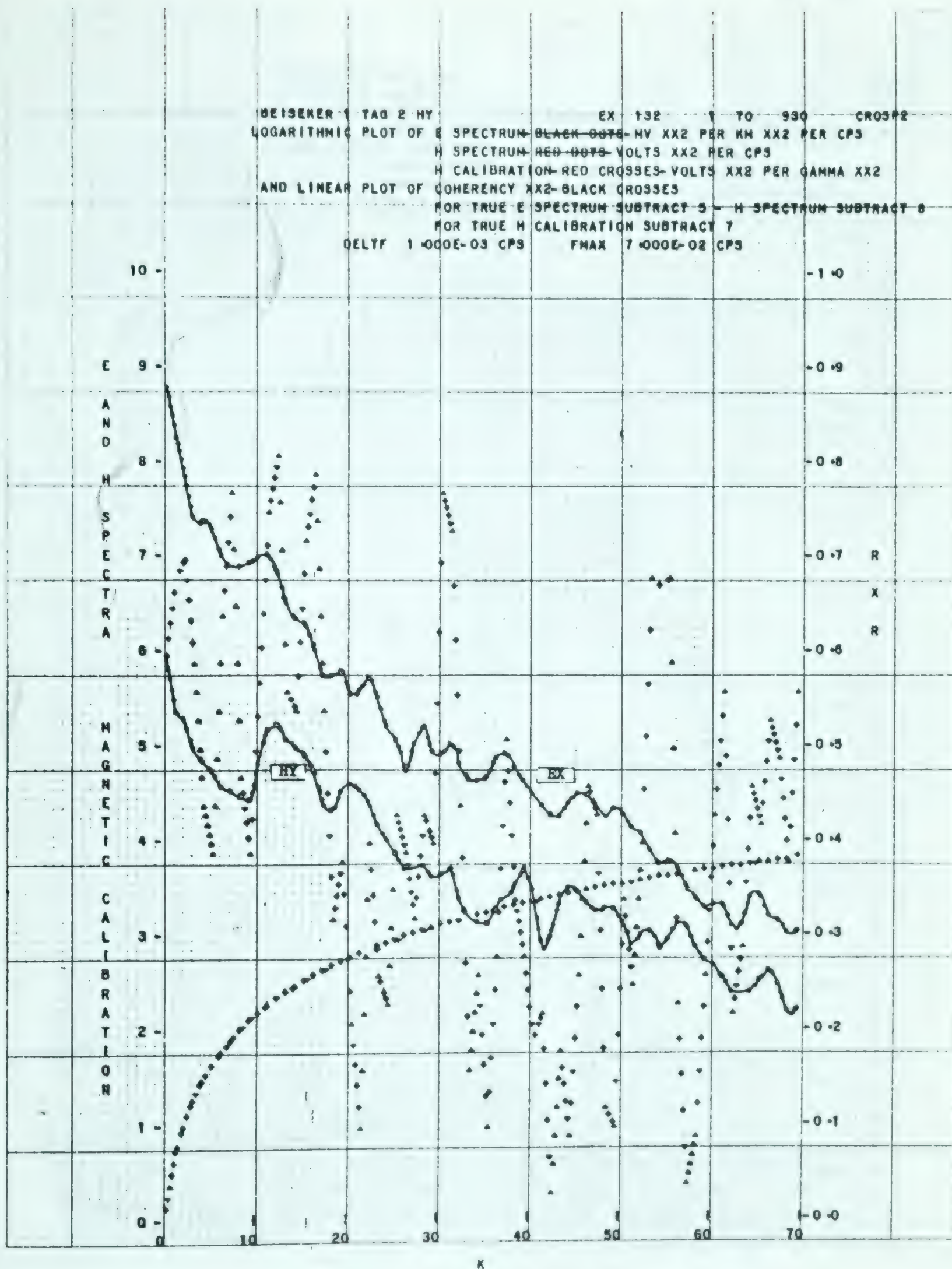


Diagram 92



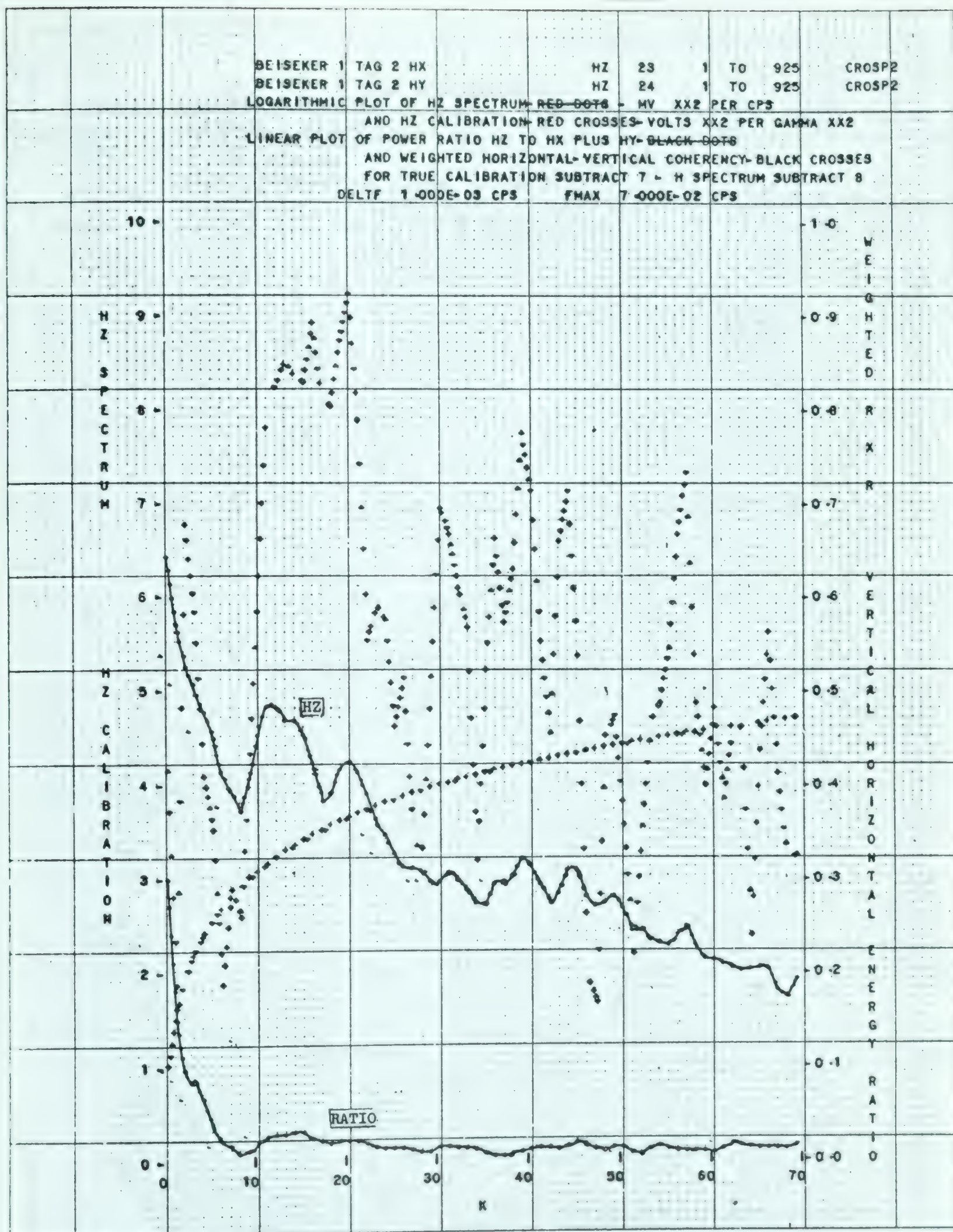


Diagram 93



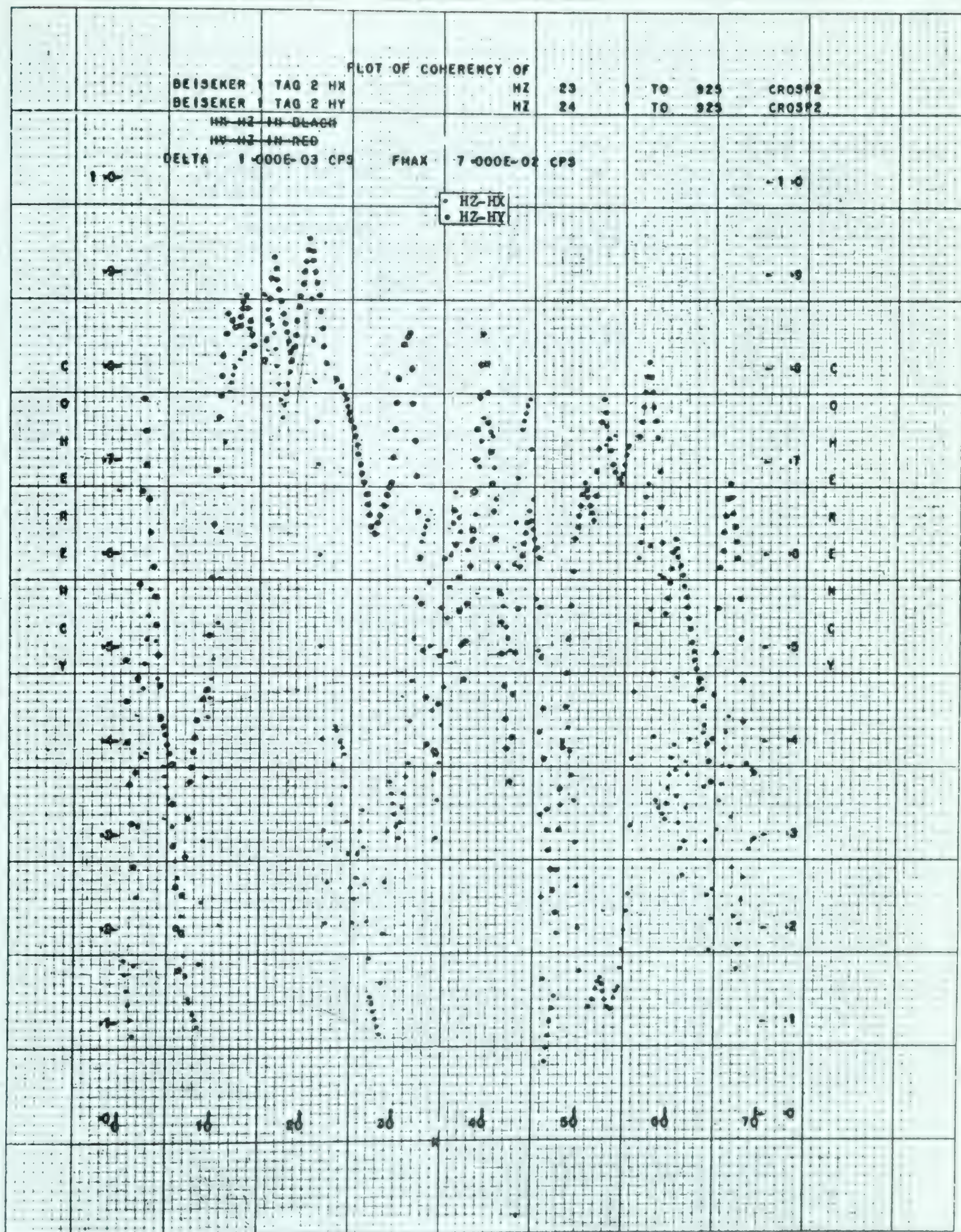


Diagram 94



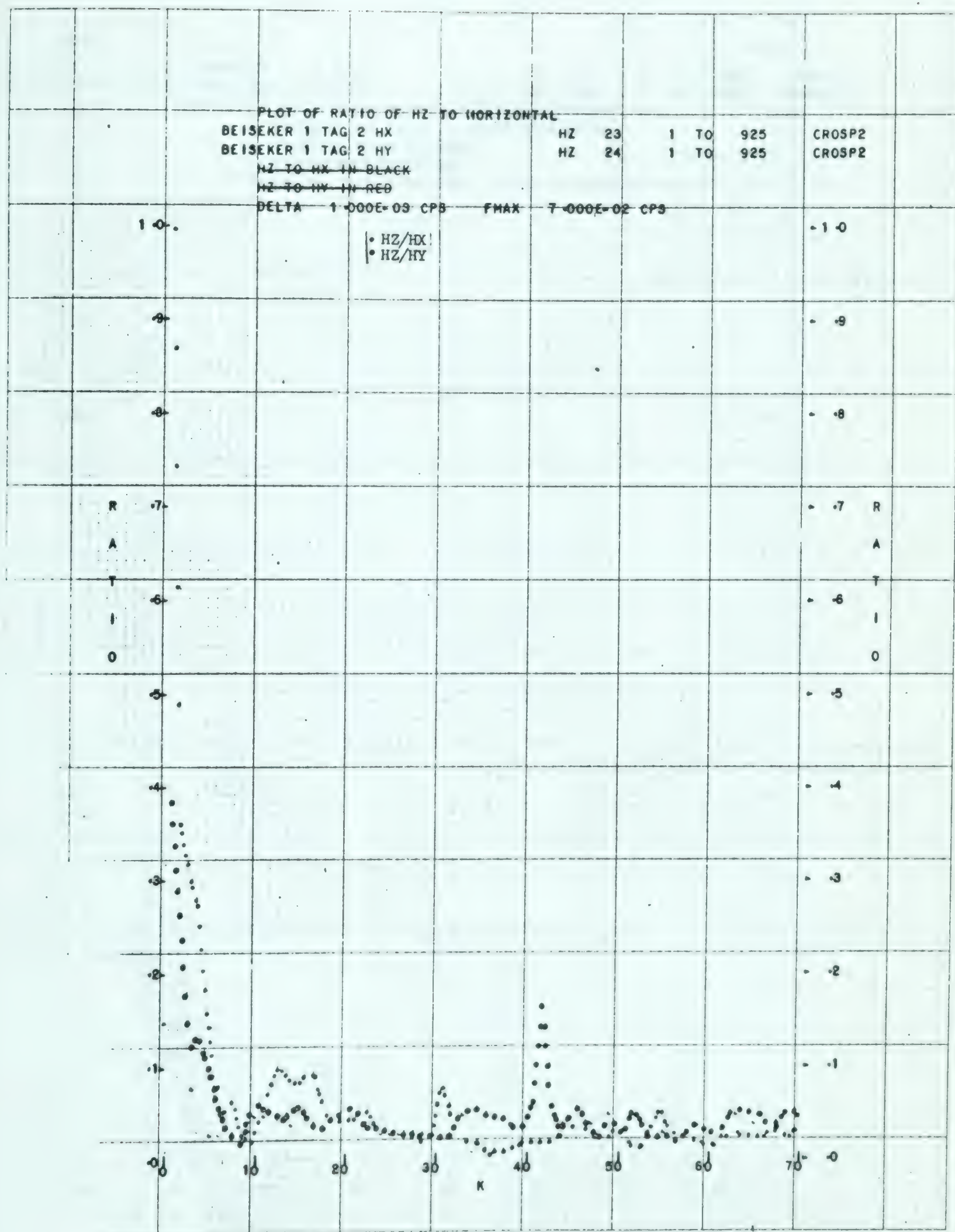


Diagram 95

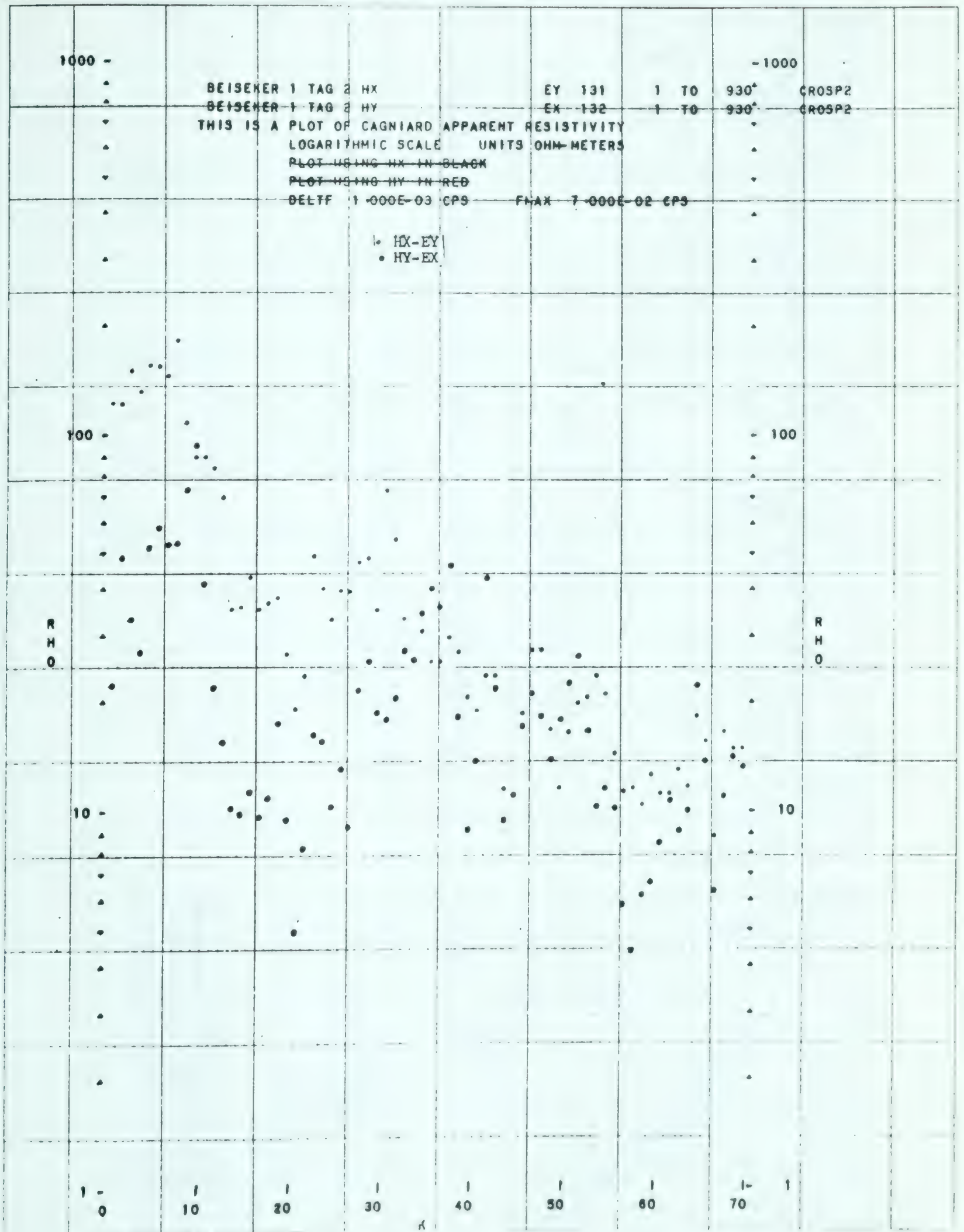


Diagram 96



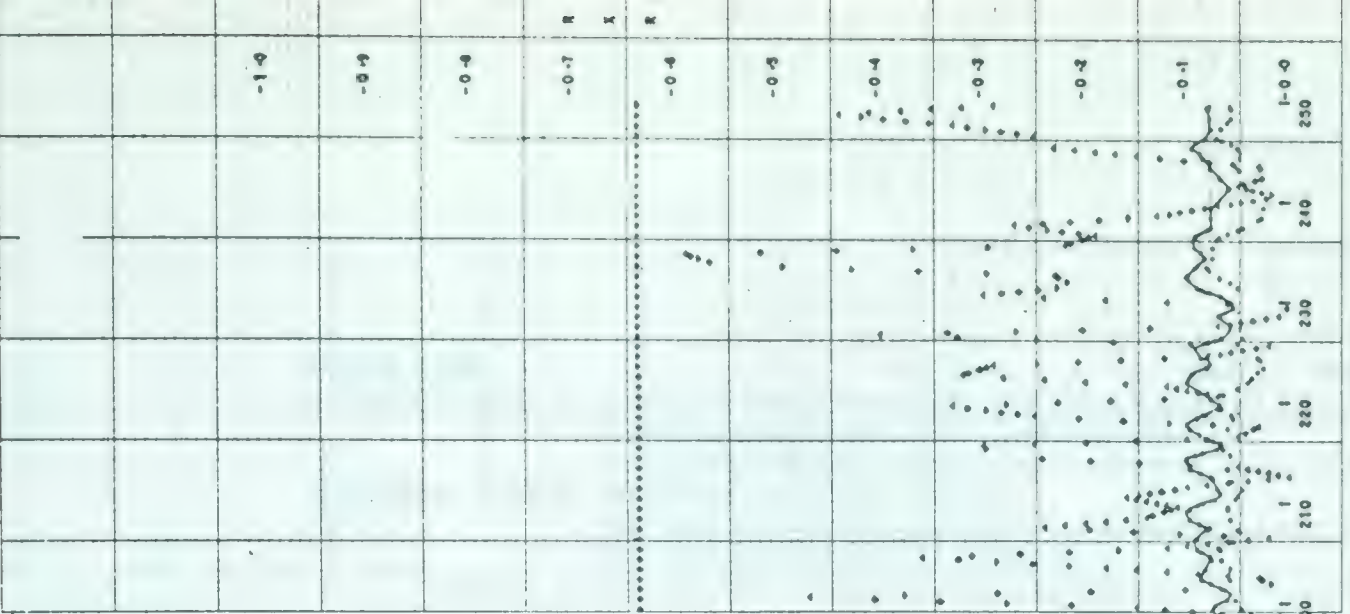
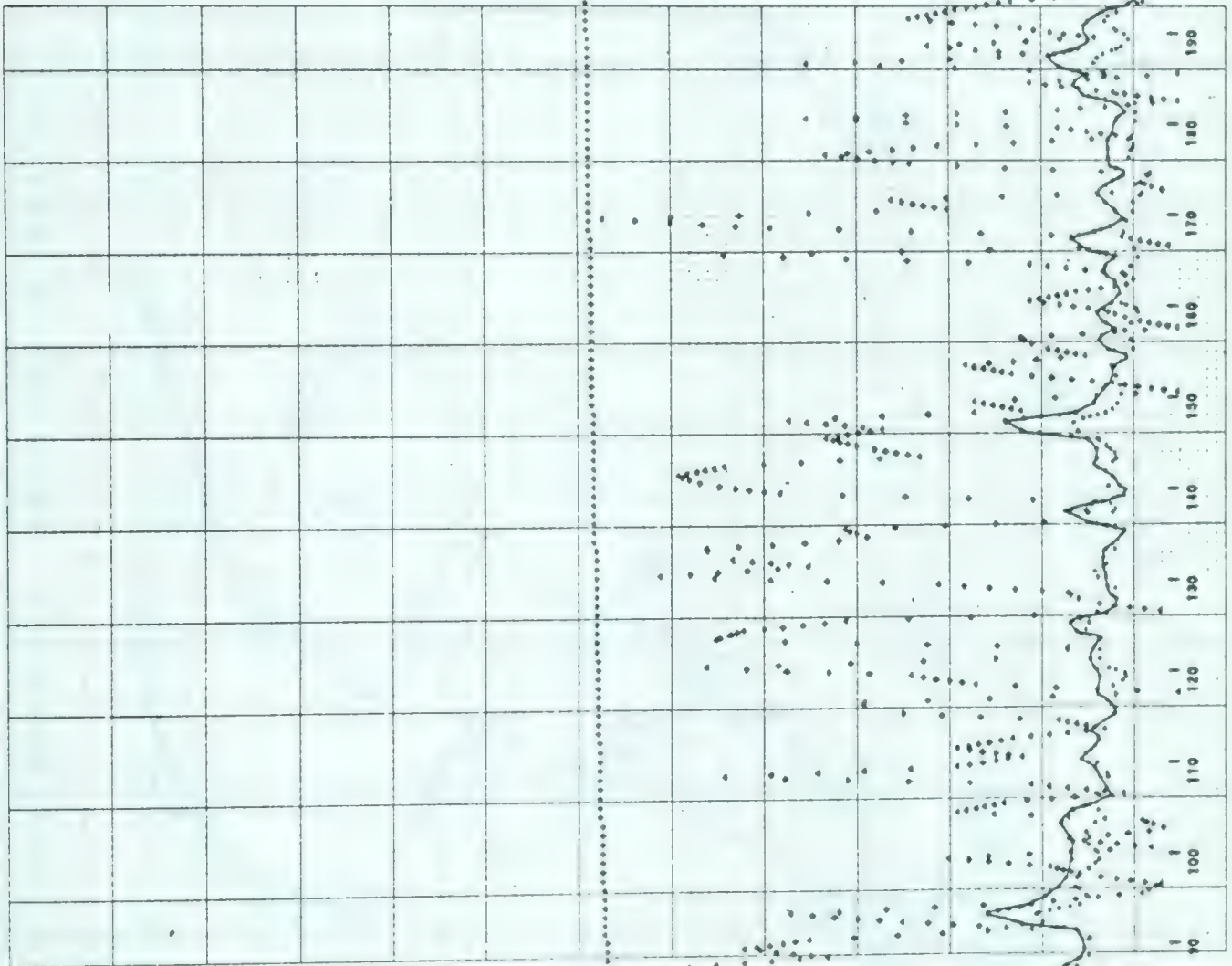
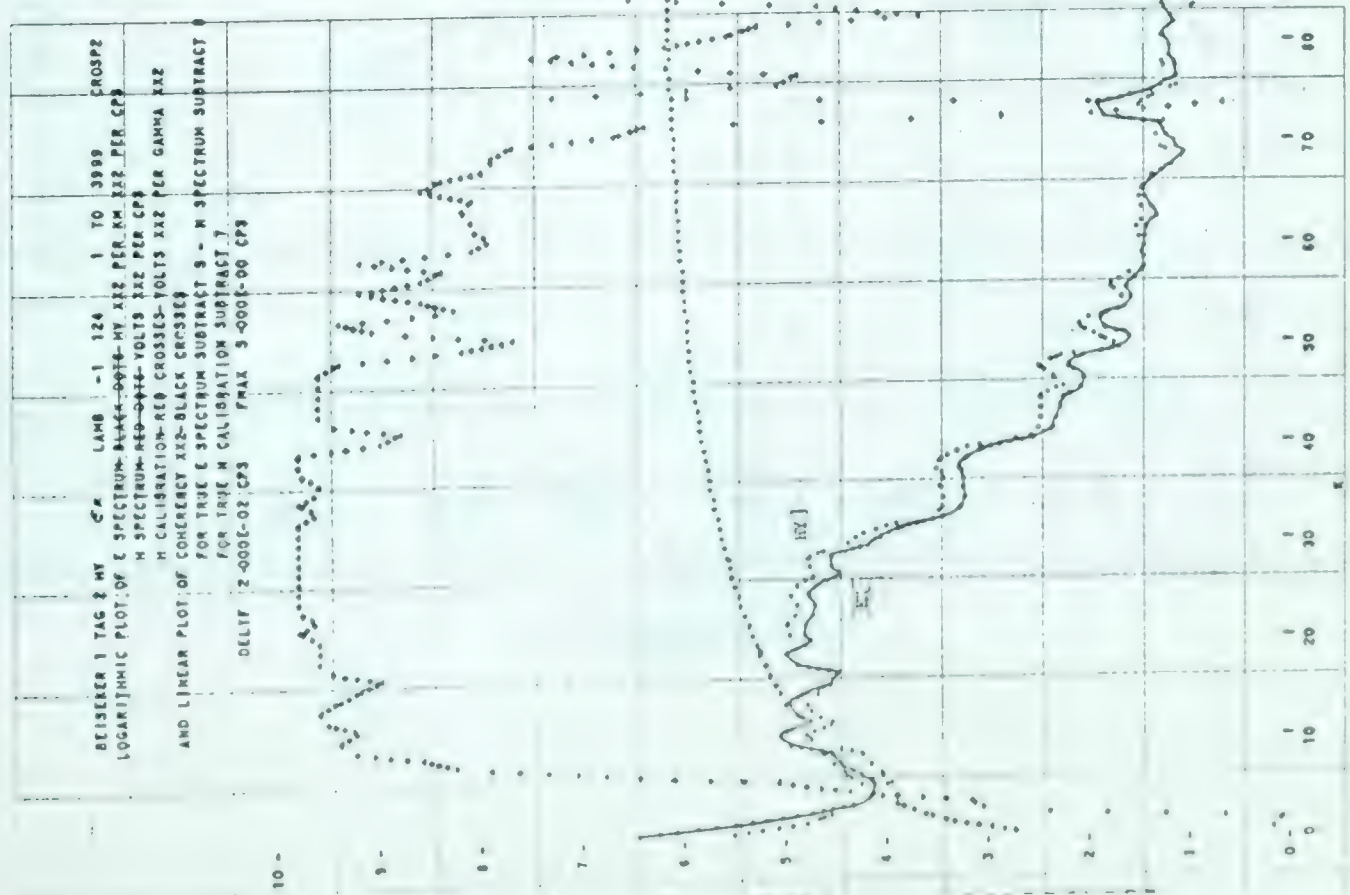


Diagram 98

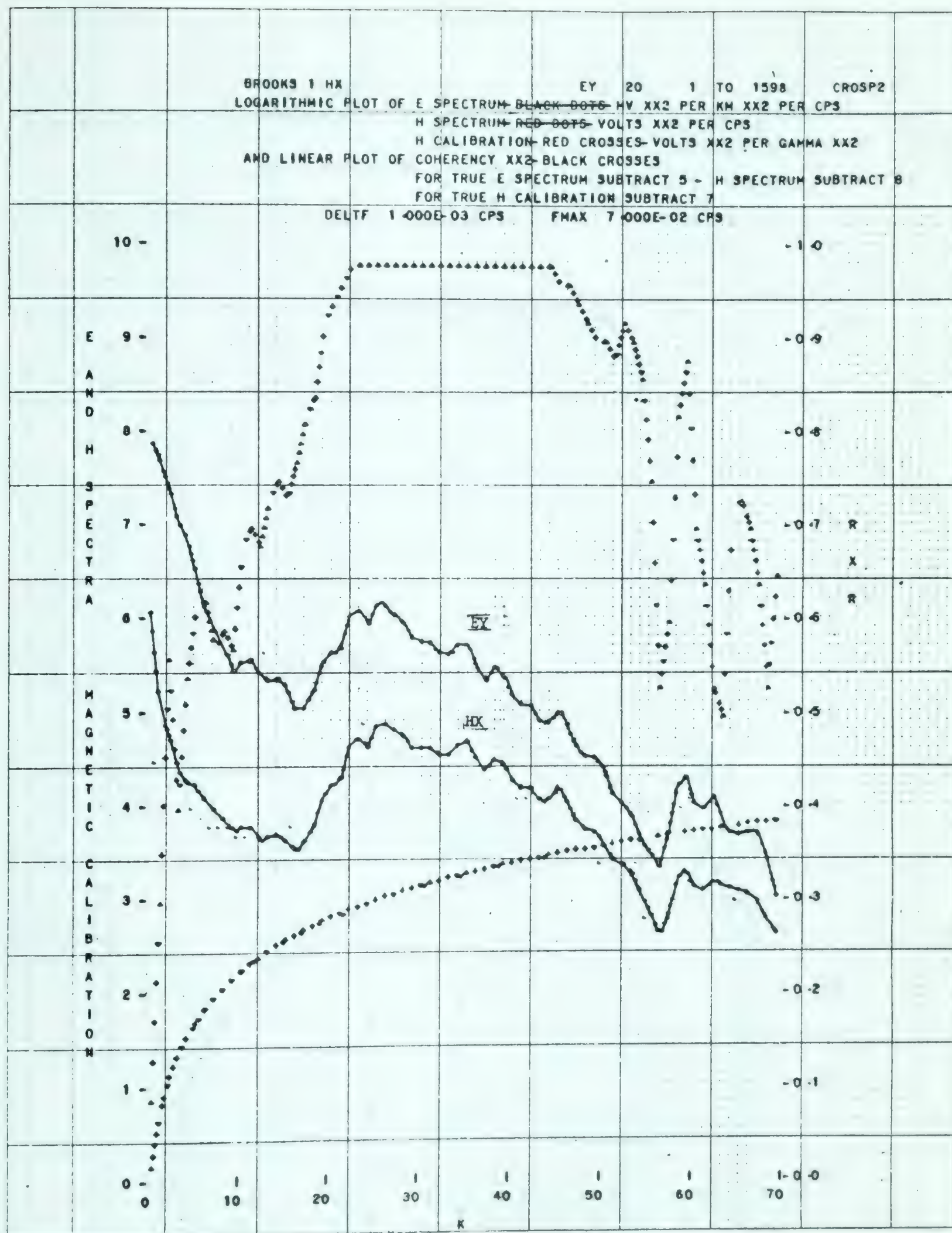


Diagram 99



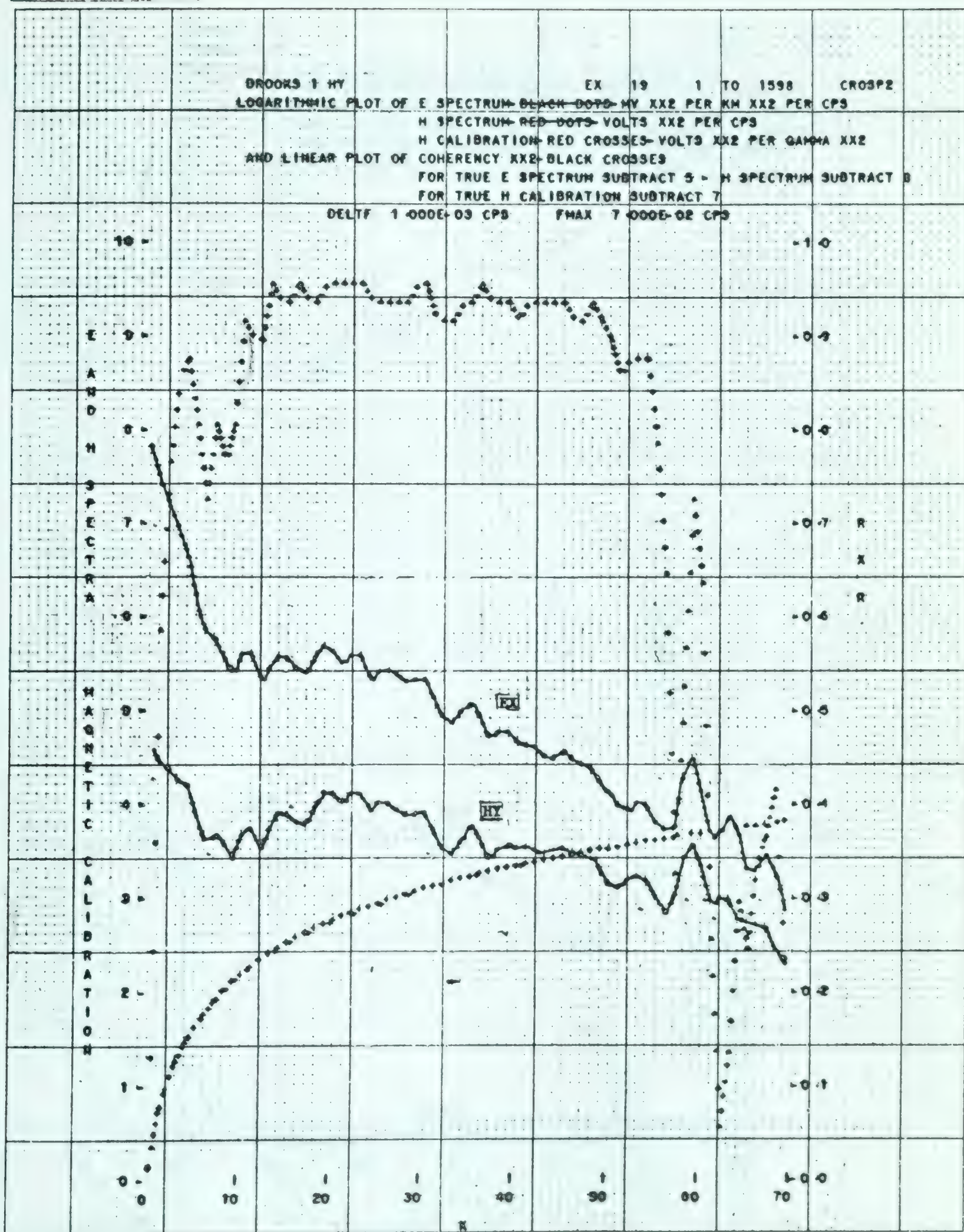


Diagram 100



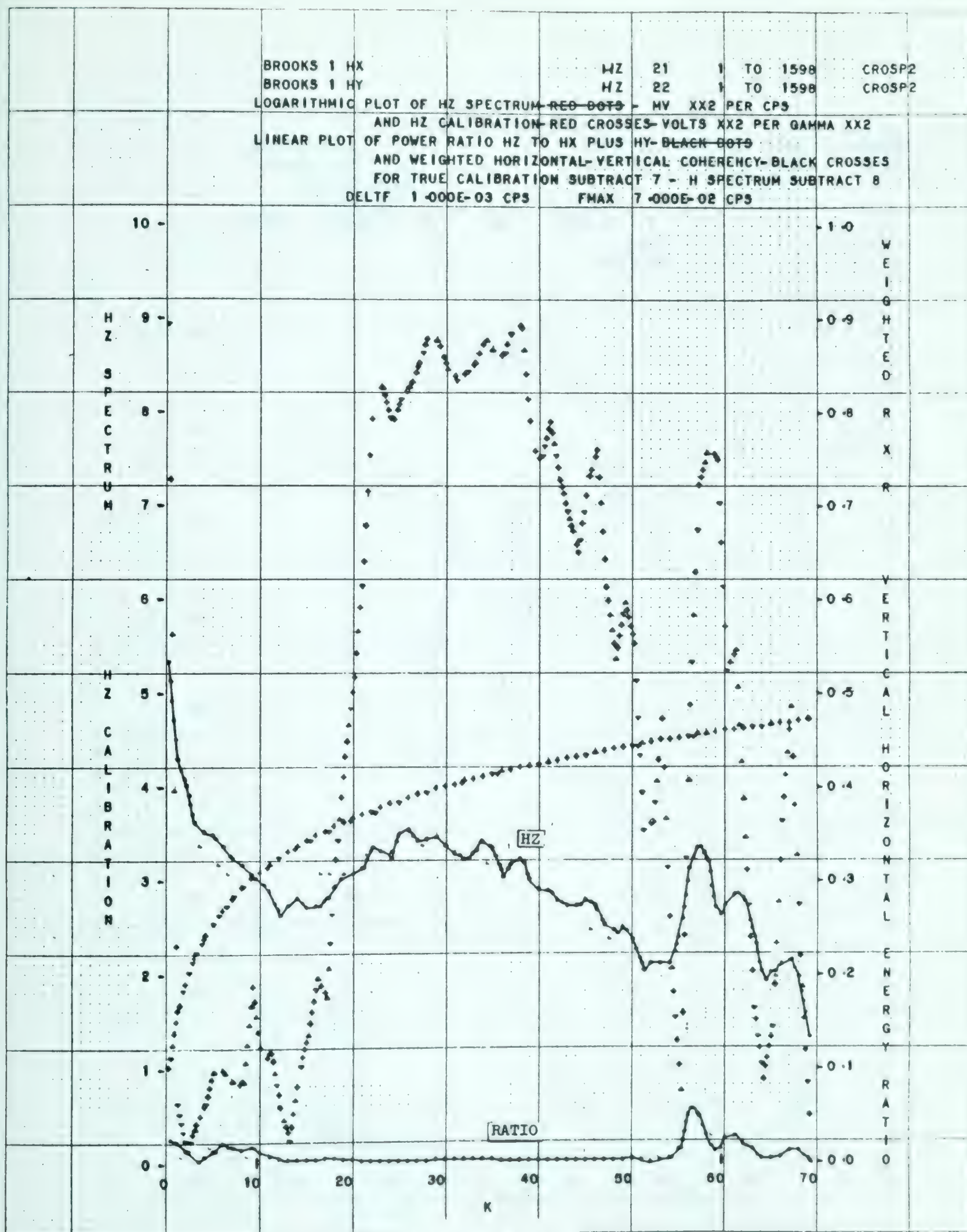


Diagram 101

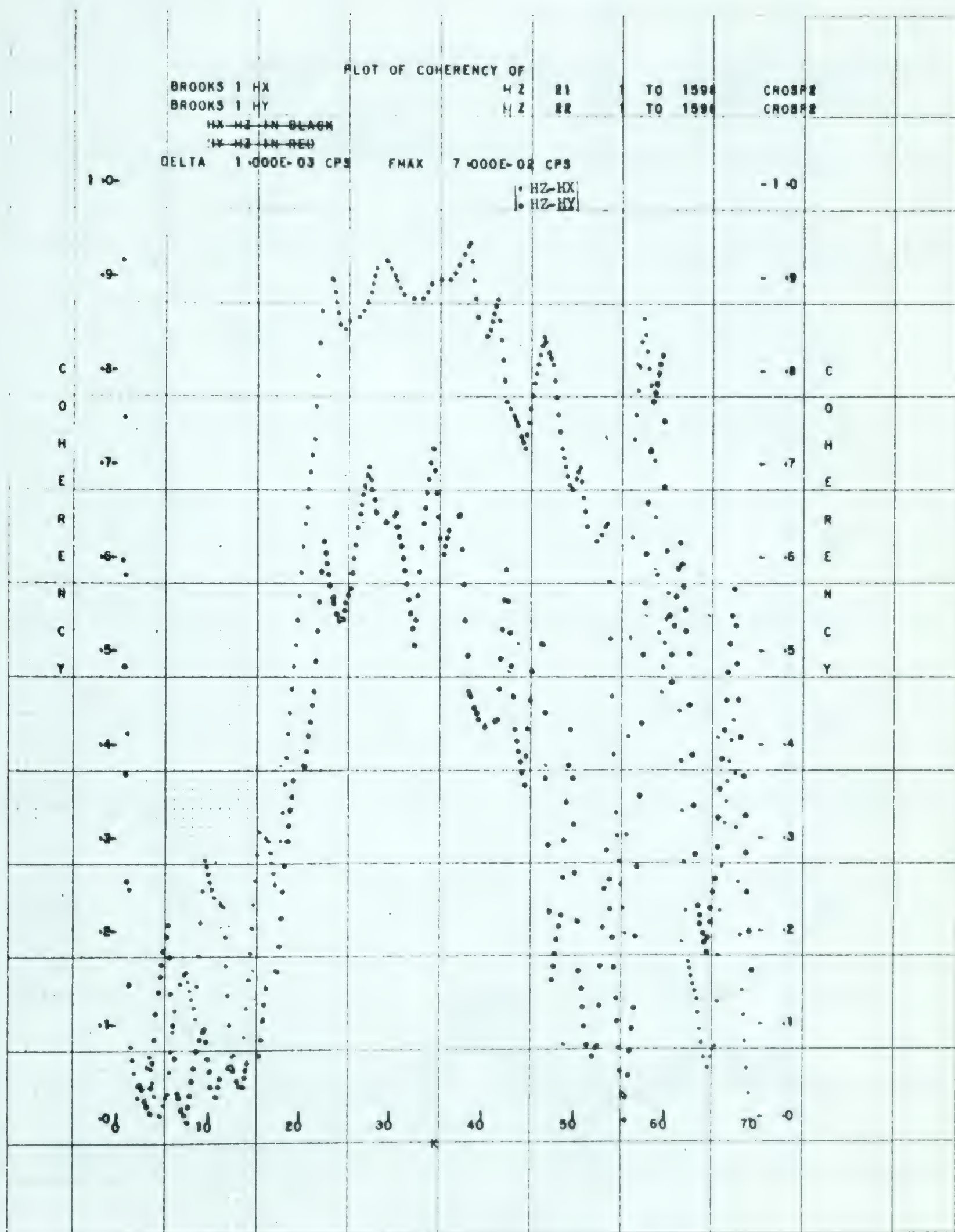


Diagram 102



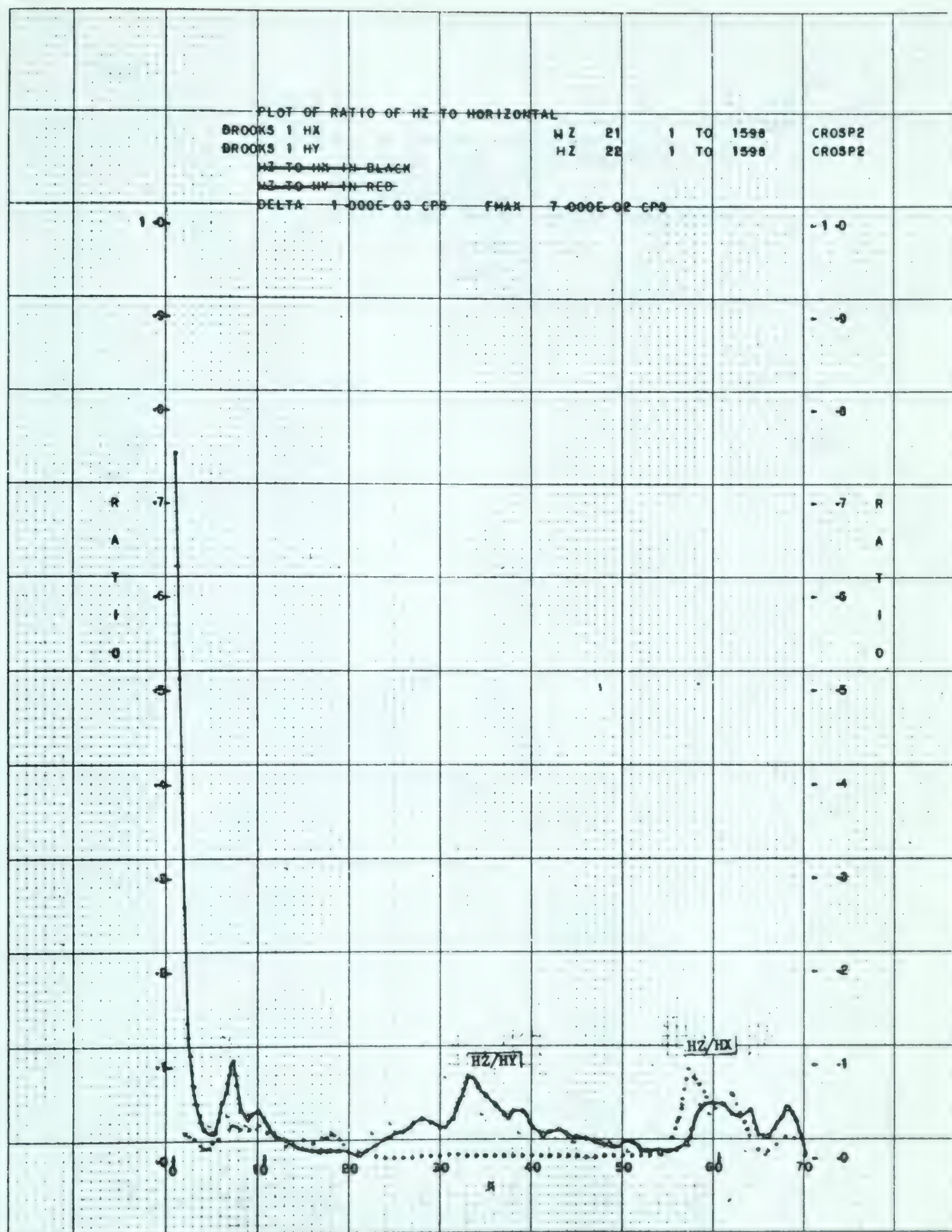


Diagram 103

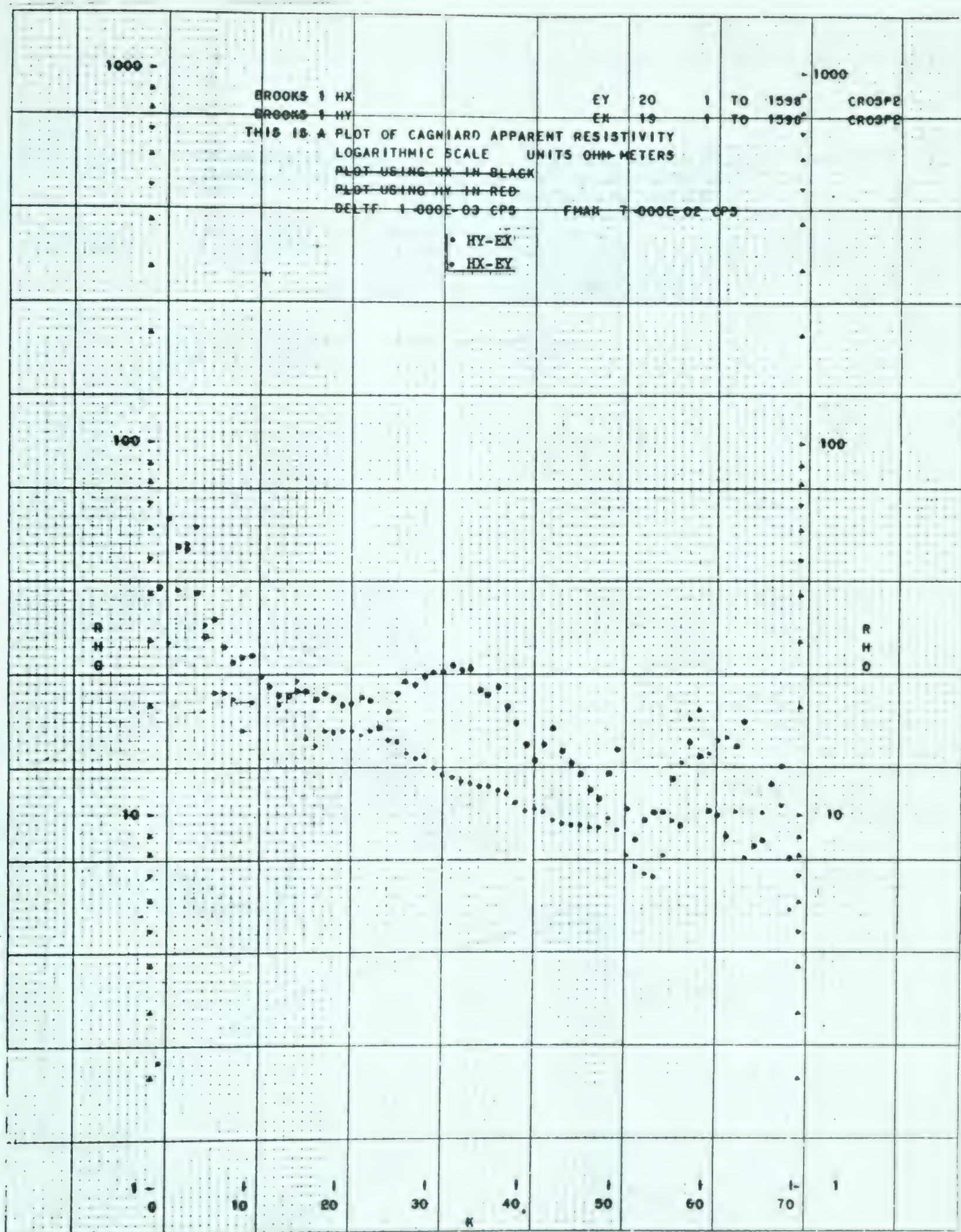


Diagram 104

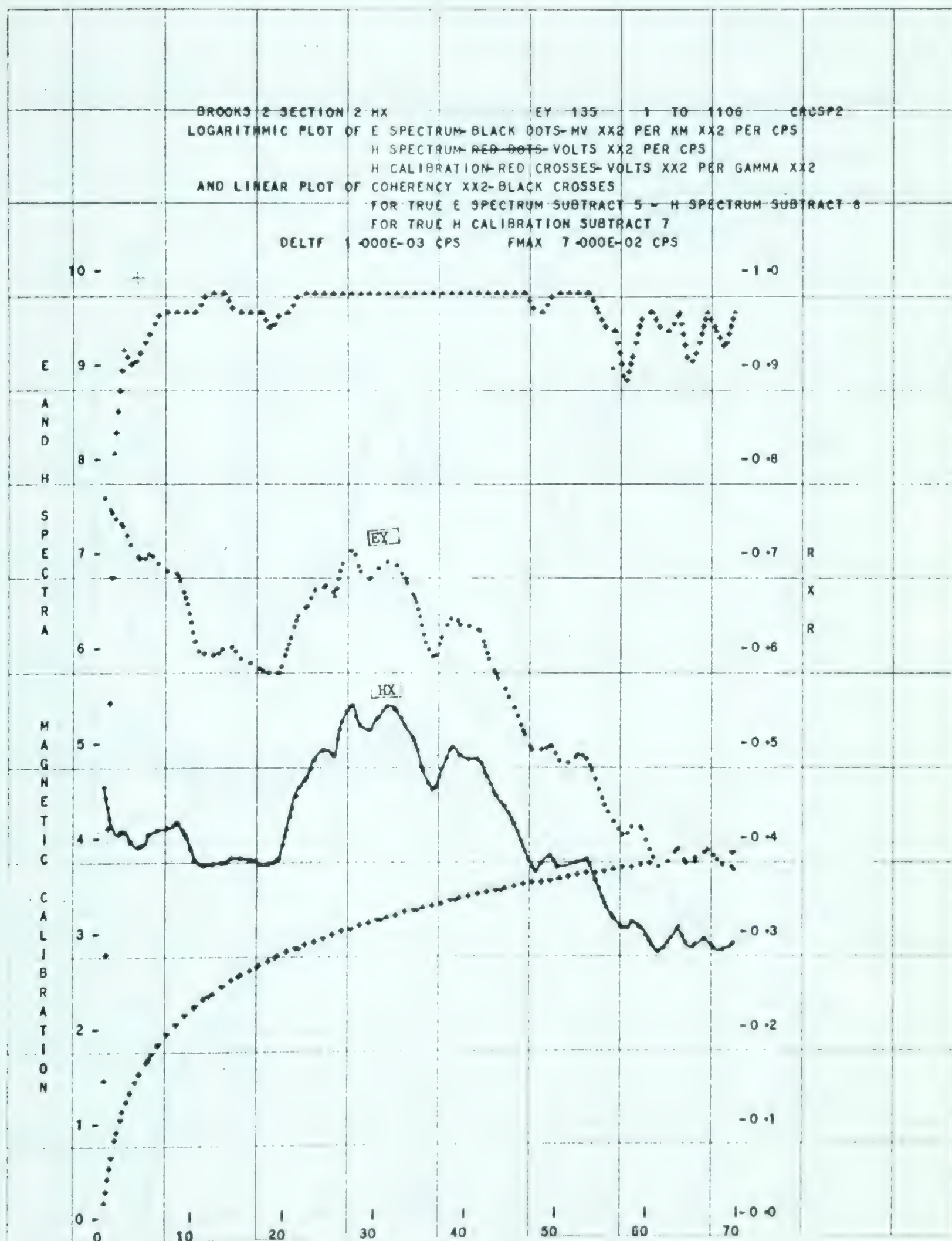


Diagram 105



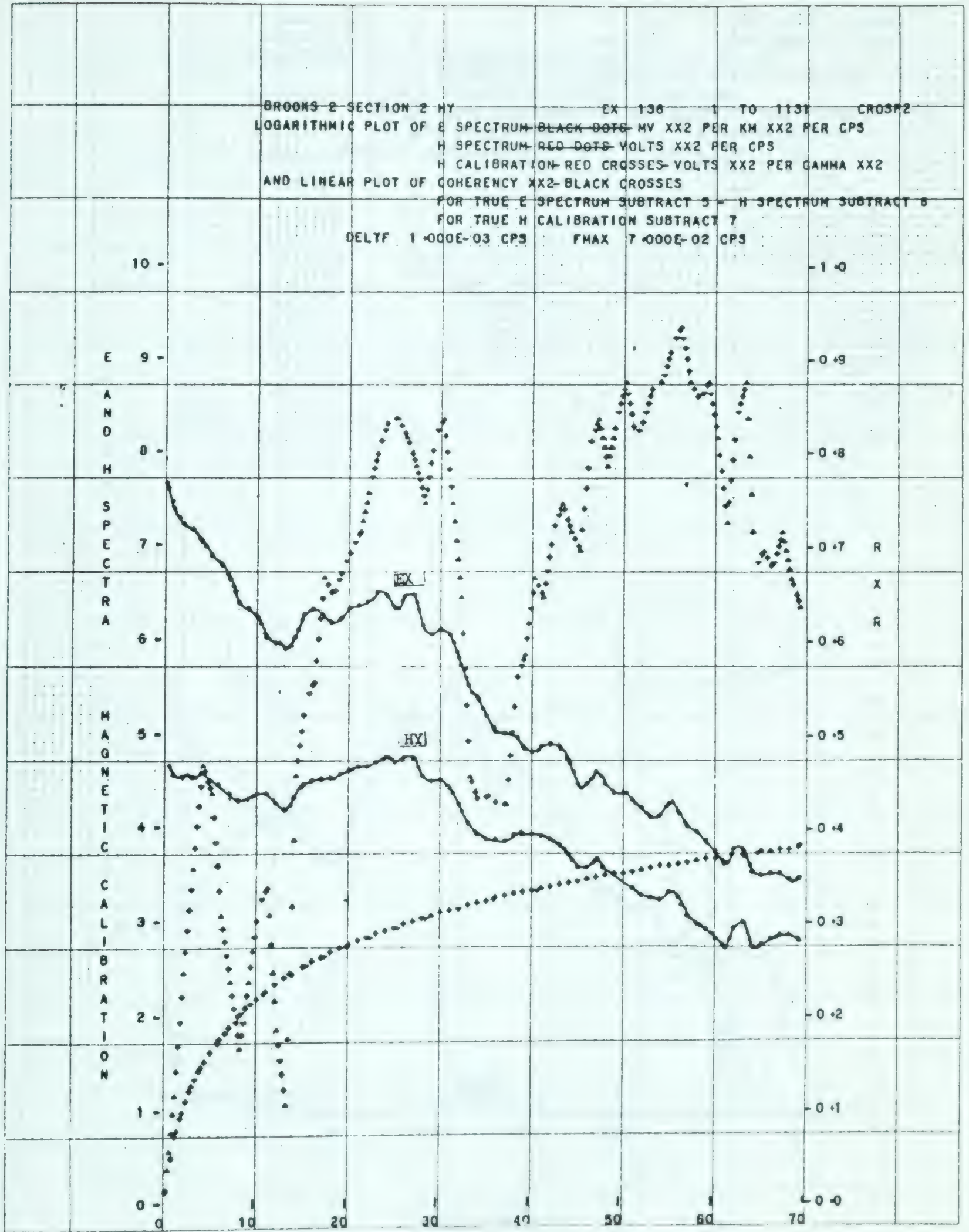


Diagram 106



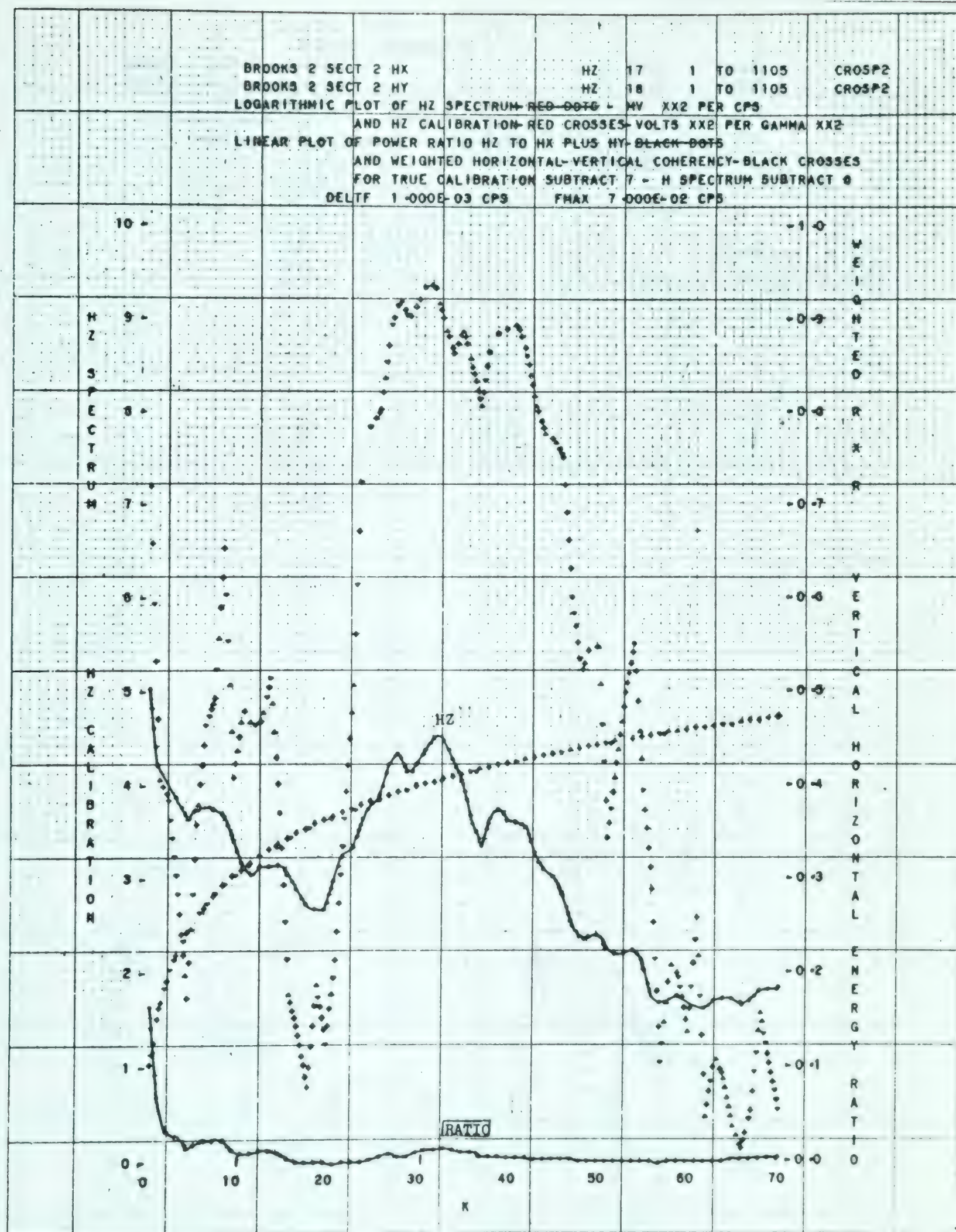


Diagram 107



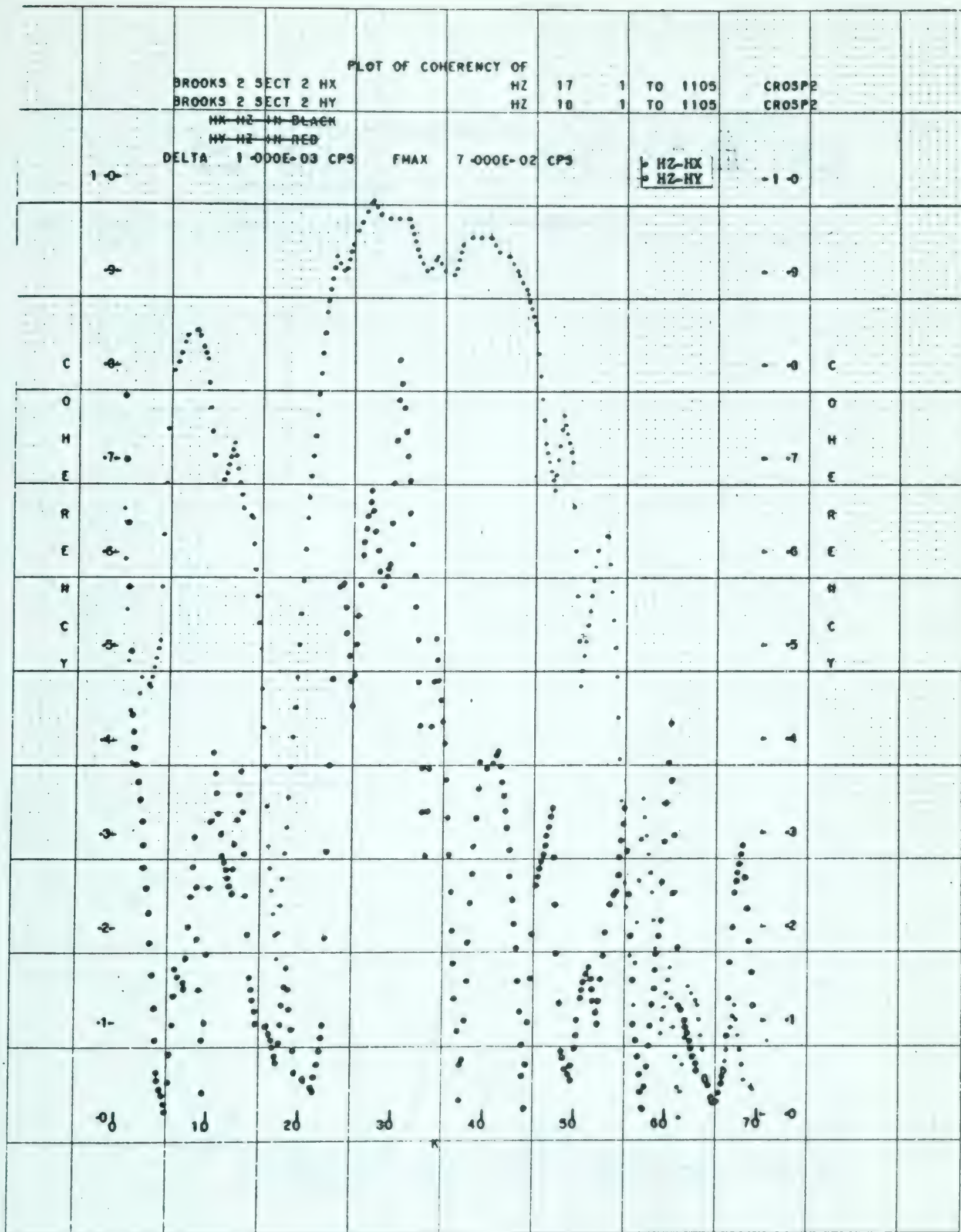


Diagram 108

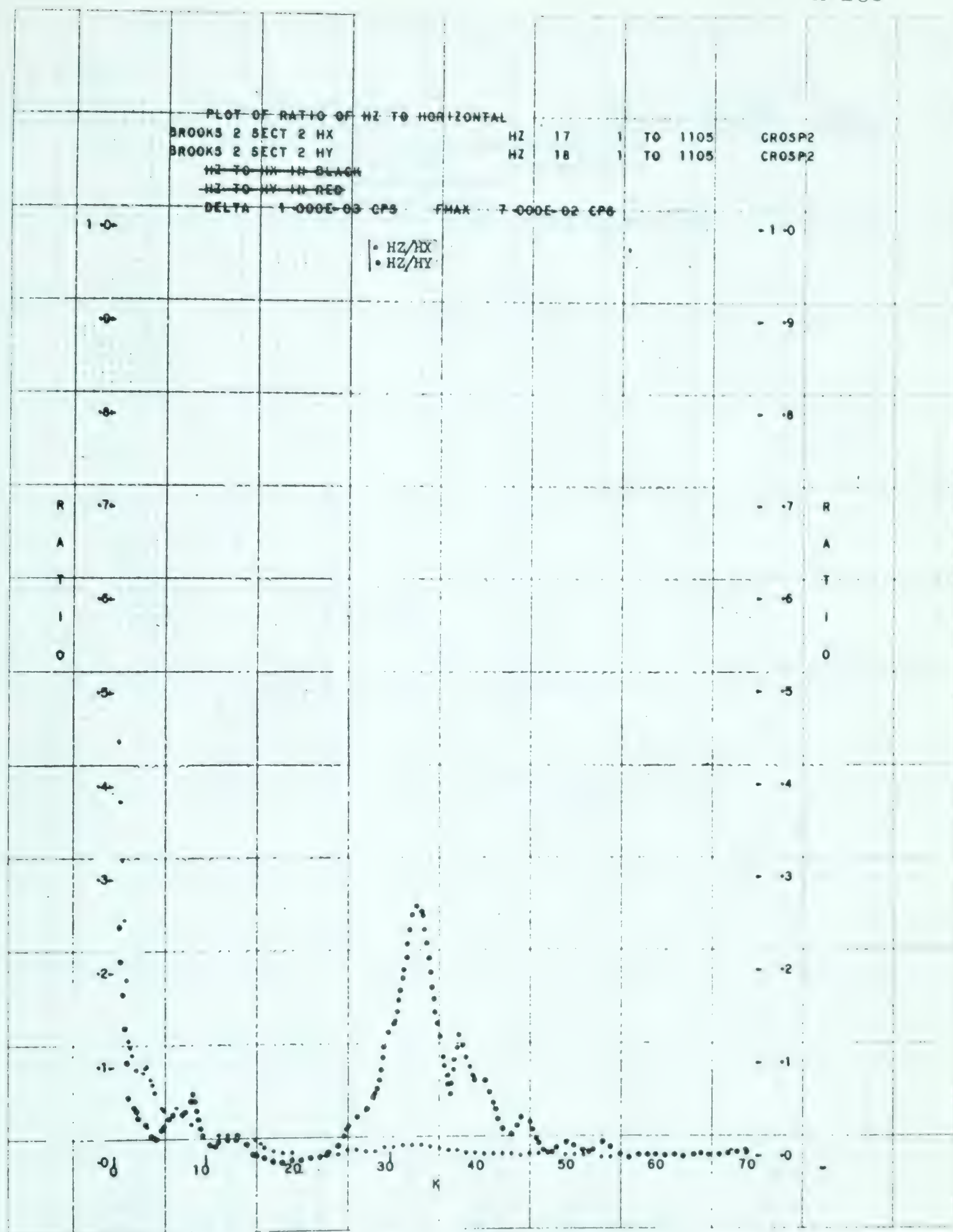
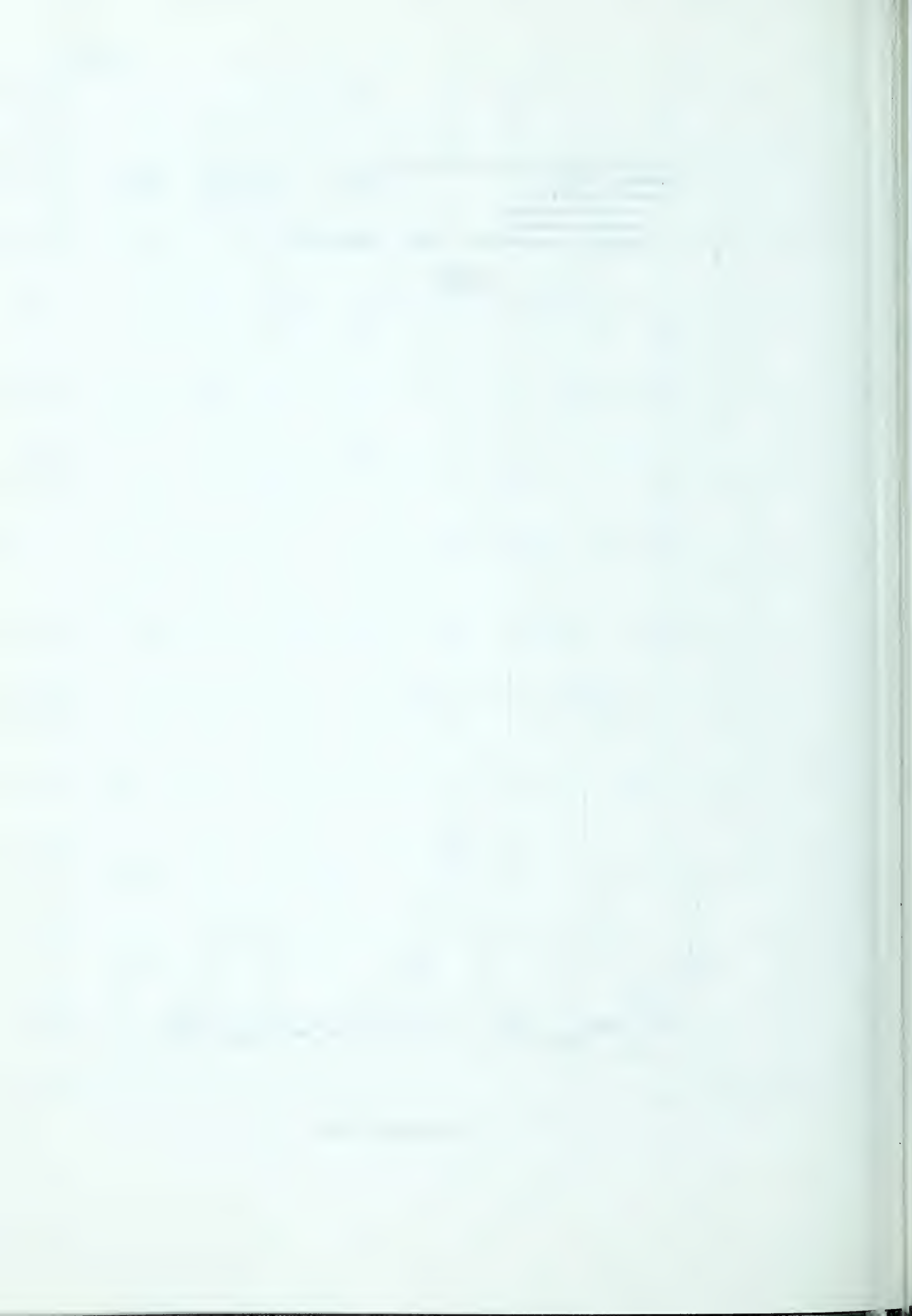


Diagram 109



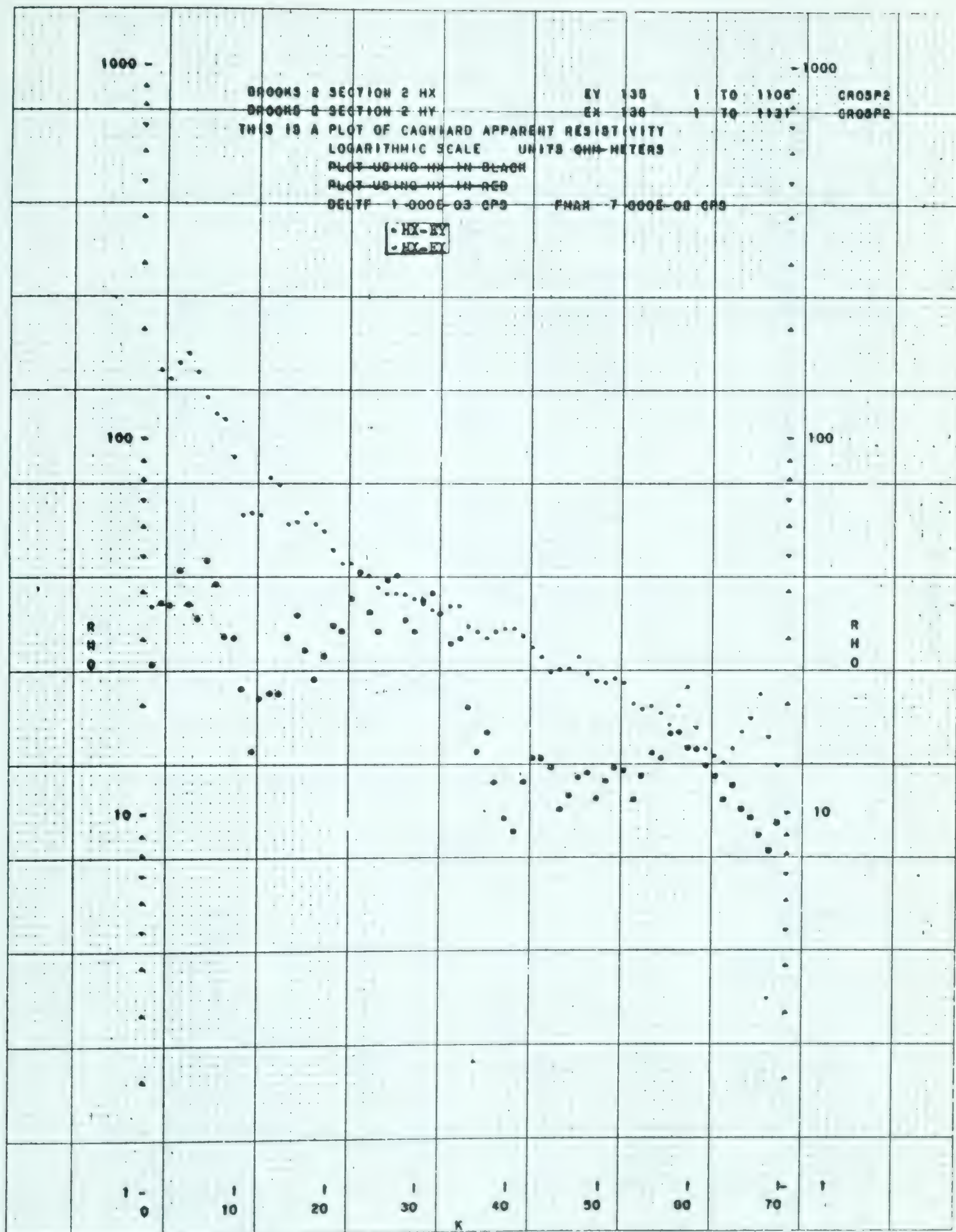


Diagram 110

Date		Description		Amount	
1890	Jan 1	Balance		100.00	
	Feb 1	Interest		5.00	
	Mar 1	Interest		5.00	
	Apr 1	Interest		5.00	
	May 1	Interest		5.00	
	Jun 1	Interest		5.00	
	Jul 1	Interest		5.00	
	Aug 1	Interest		5.00	
	Sep 1	Interest		5.00	
	Oct 1	Interest		5.00	
	Nov 1	Interest		5.00	
	Dec 1	Interest		5.00	
1891	Jan 1	Balance		100.00	
	Feb 1	Interest		5.00	
	Mar 1	Interest		5.00	
	Apr 1	Interest		5.00	
	May 1	Interest		5.00	
	Jun 1	Interest		5.00	
	Jul 1	Interest		5.00	
	Aug 1	Interest		5.00	
	Sep 1	Interest		5.00	
	Oct 1	Interest		5.00	
	Nov 1	Interest		5.00	
	Dec 1	Interest		5.00	
1892	Jan 1	Balance		100.00	
	Feb 1	Interest		5.00	
	Mar 1	Interest		5.00	
	Apr 1	Interest		5.00	
	May 1	Interest		5.00	
	Jun 1	Interest		5.00	
	Jul 1	Interest		5.00	
	Aug 1	Interest		5.00	
	Sep 1	Interest		5.00	
	Oct 1	Interest		5.00	
	Nov 1	Interest		5.00	
	Dec 1	Interest		5.00	
1893	Jan 1	Balance		100.00	
	Feb 1	Interest		5.00	
	Mar 1	Interest		5.00	
	Apr 1	Interest		5.00	
	May 1	Interest		5.00	
	Jun 1	Interest		5.00	
	Jul 1	Interest		5.00	
	Aug 1	Interest		5.00	
	Sep 1	Interest		5.00	
	Oct 1	Interest		5.00	
	Nov 1	Interest		5.00	
	Dec 1	Interest		5.00	
1894	Jan 1	Balance		100.00	
	Feb 1	Interest		5.00	
	Mar 1	Interest		5.00	
	Apr 1	Interest		5.00	
	May 1	Interest		5.00	
	Jun 1	Interest		5.00	
	Jul 1	Interest		5.00	
	Aug 1	Interest		5.00	
	Sep 1	Interest		5.00	
	Oct 1	Interest		5.00	
	Nov 1	Interest		5.00	
	Dec 1	Interest		5.00	
1895	Jan 1	Balance		100.00	
	Feb 1	Interest		5.00	
	Mar 1	Interest		5.00	
	Apr 1	Interest		5.00	
	May 1	Interest		5.00	
	Jun 1	Interest		5.00	
	Jul 1	Interest		5.00	
	Aug 1	Interest		5.00	
	Sep 1	Interest		5.00	
	Oct 1	Interest		5.00	
	Nov 1	Interest		5.00	
	Dec 1	Interest		5.00	

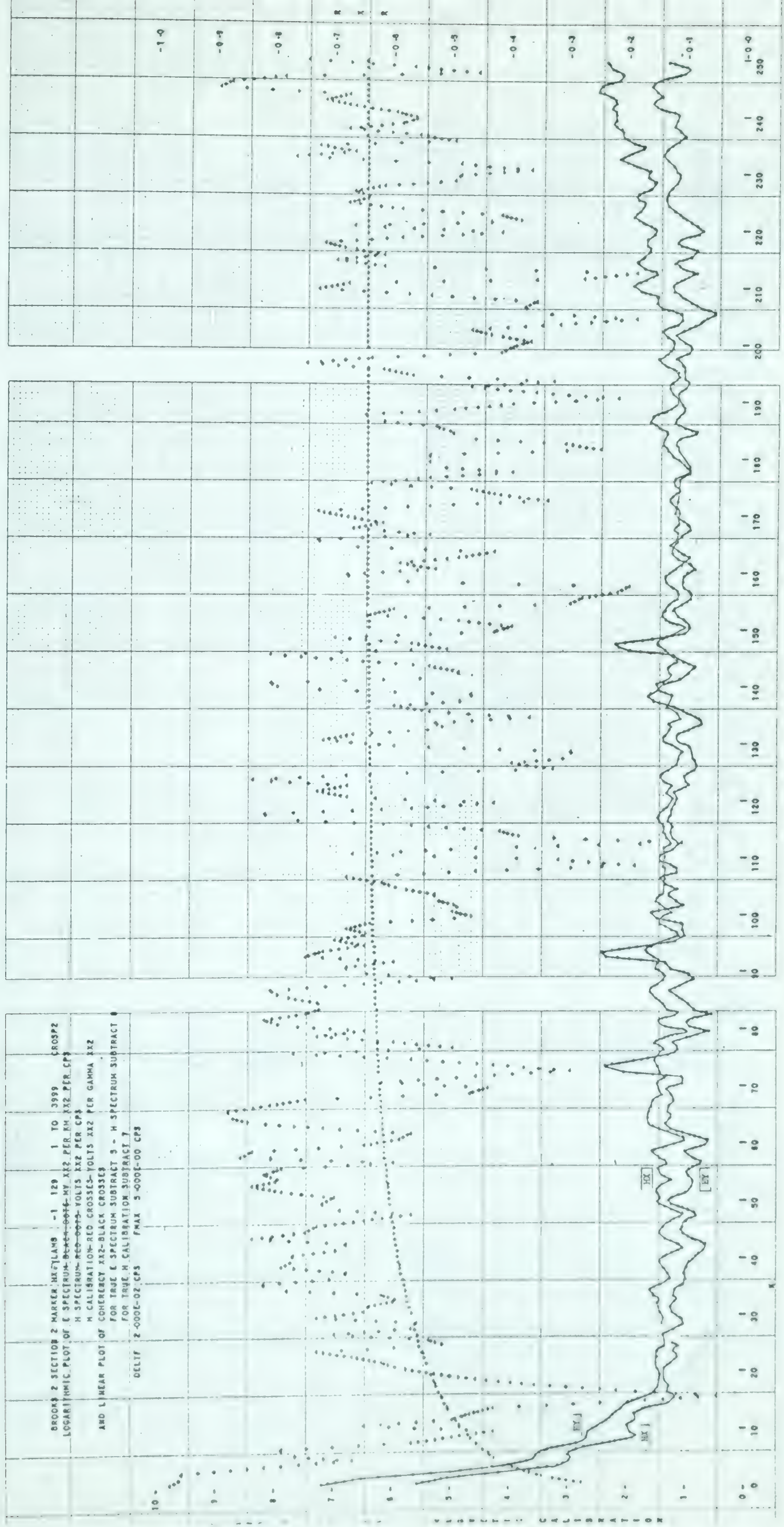


Diagram 111



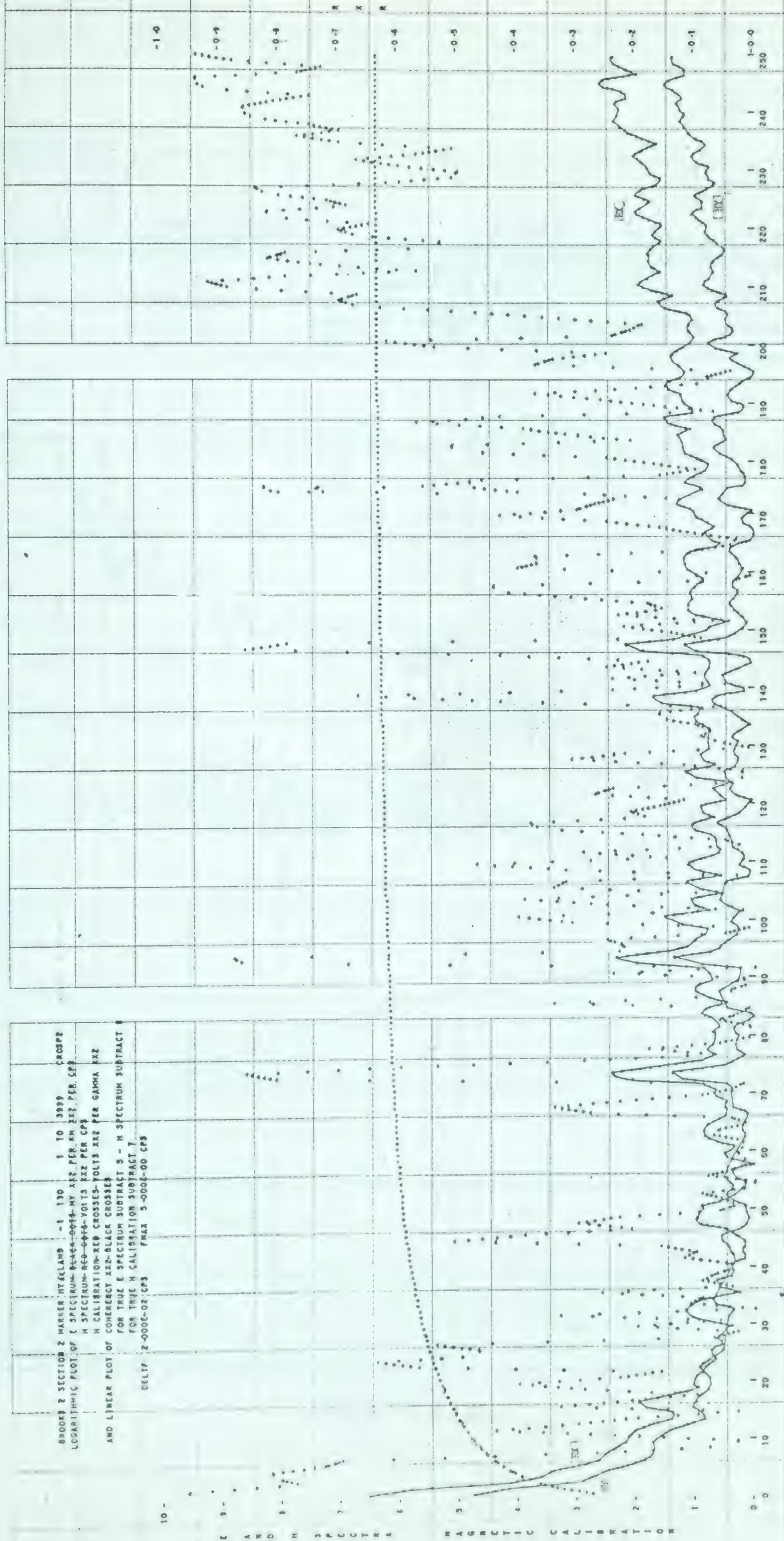


Diagram 112



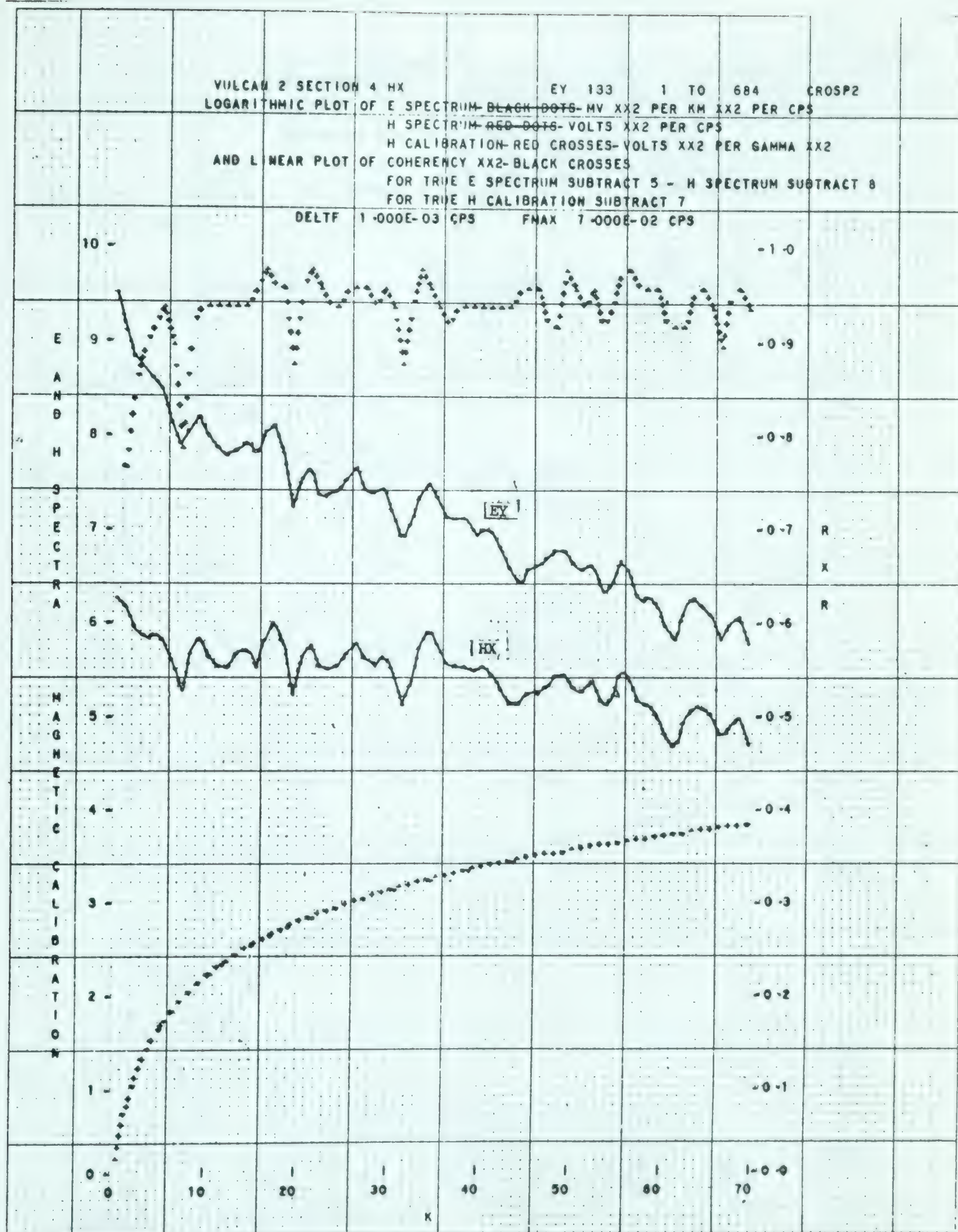


Diagram 113

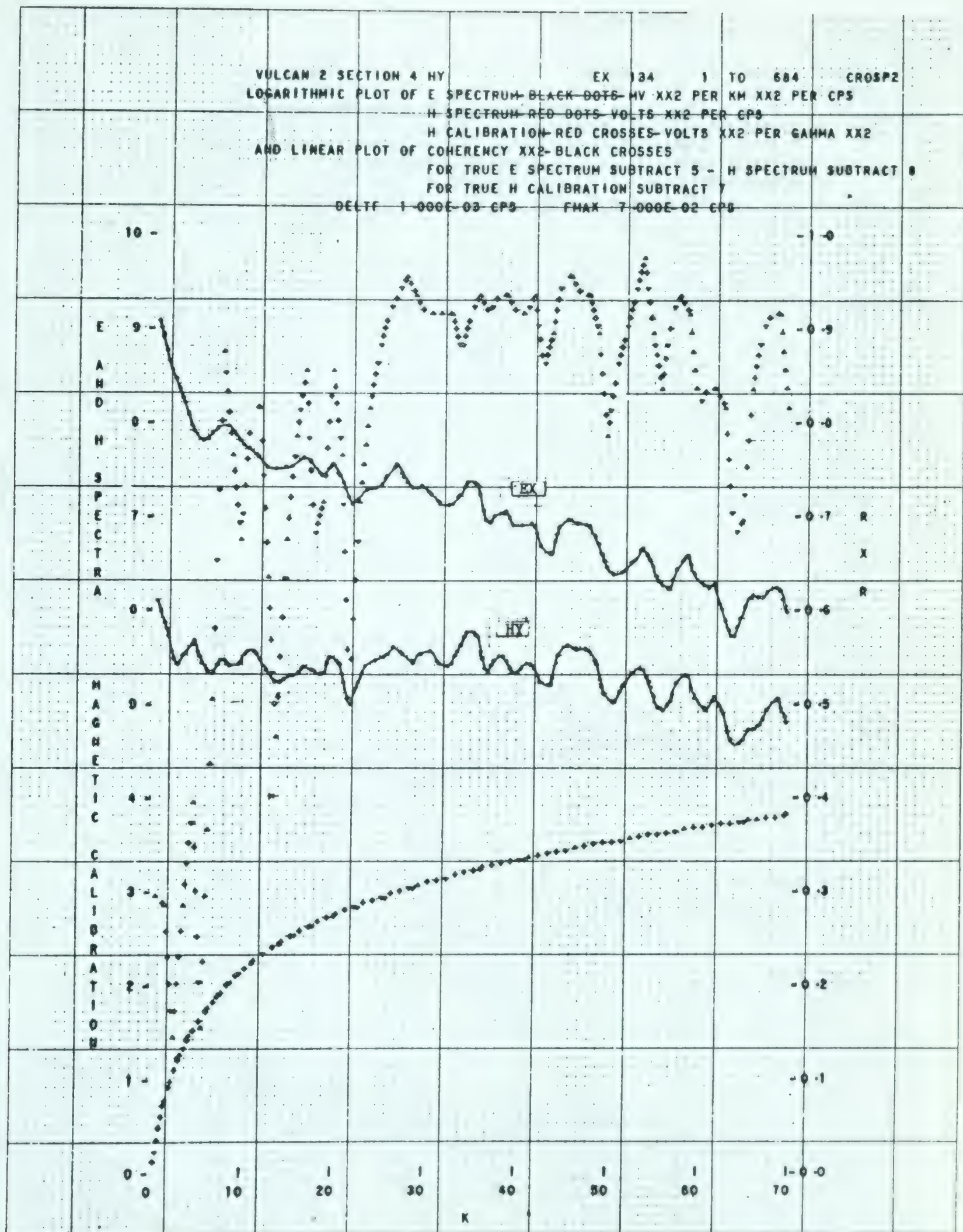


Diagram 114

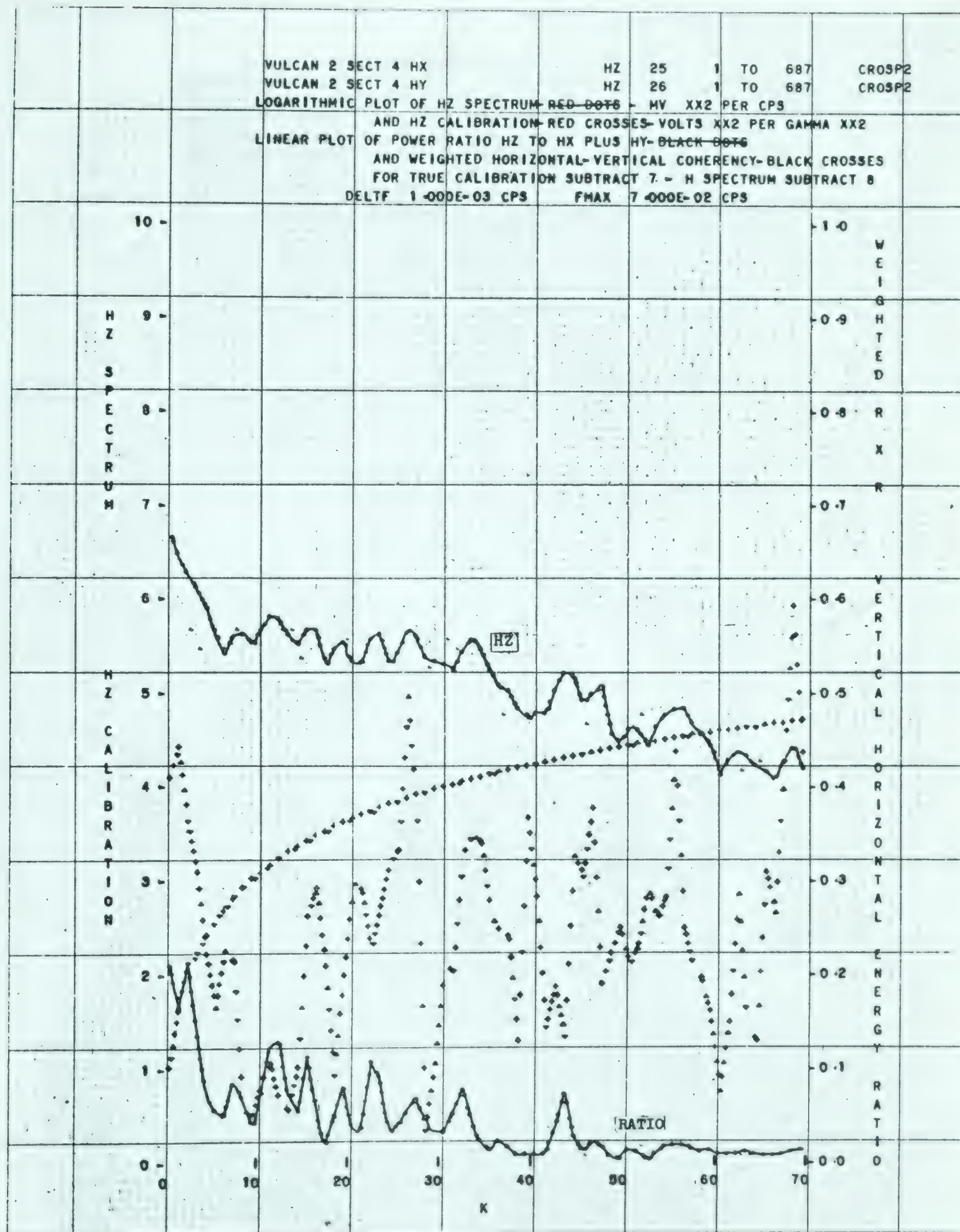


Diagram 115

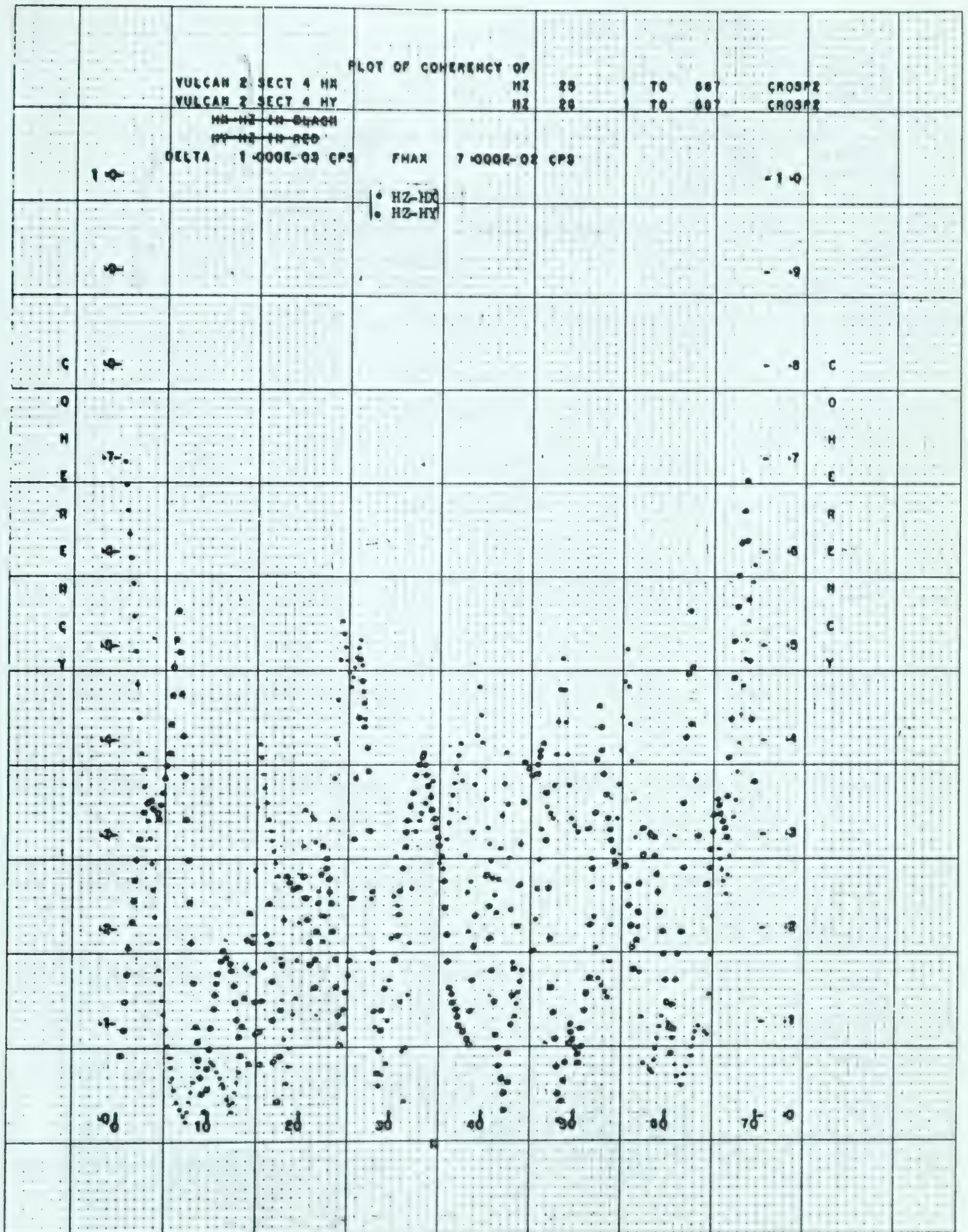


Diagram 116

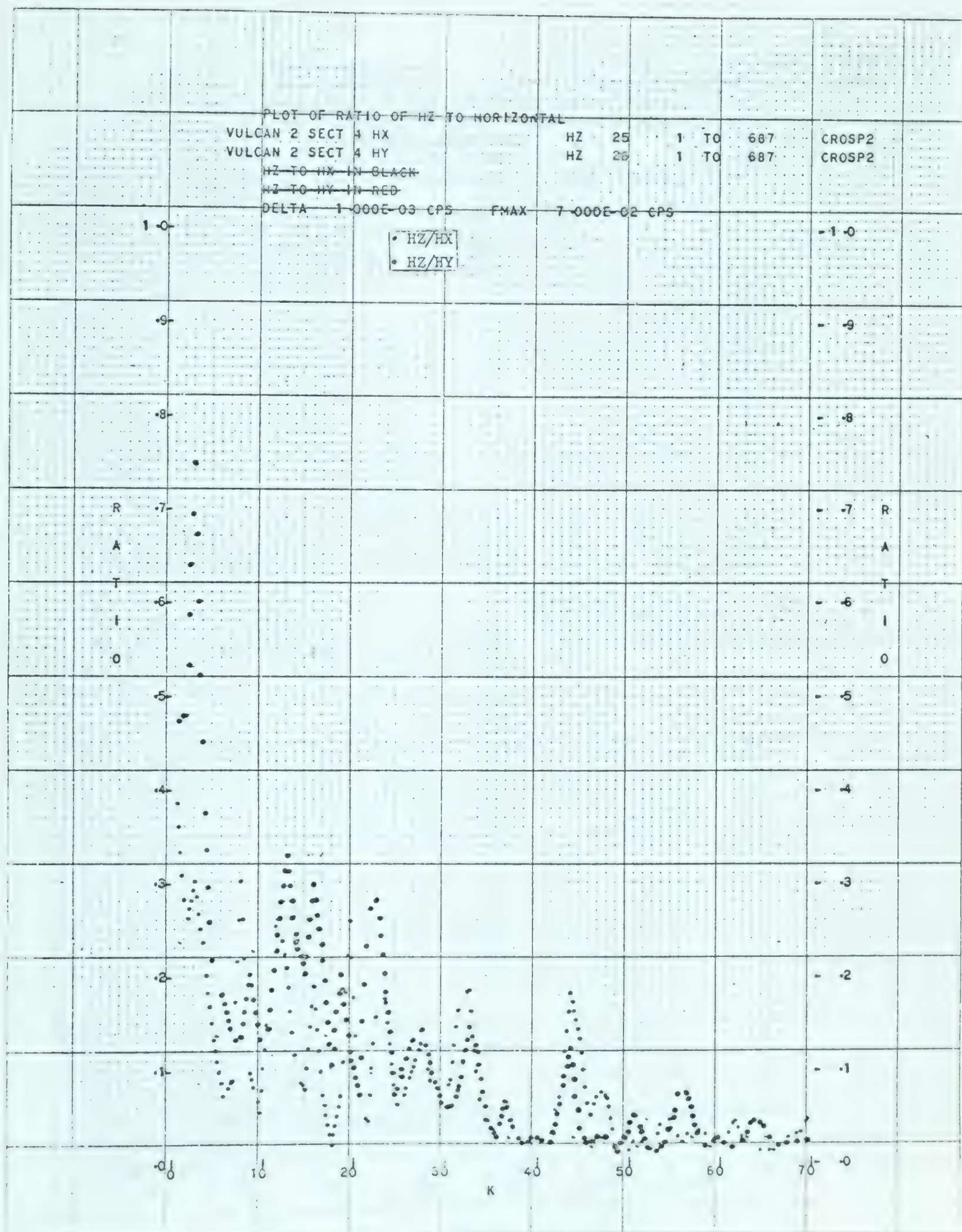


Diagram 117

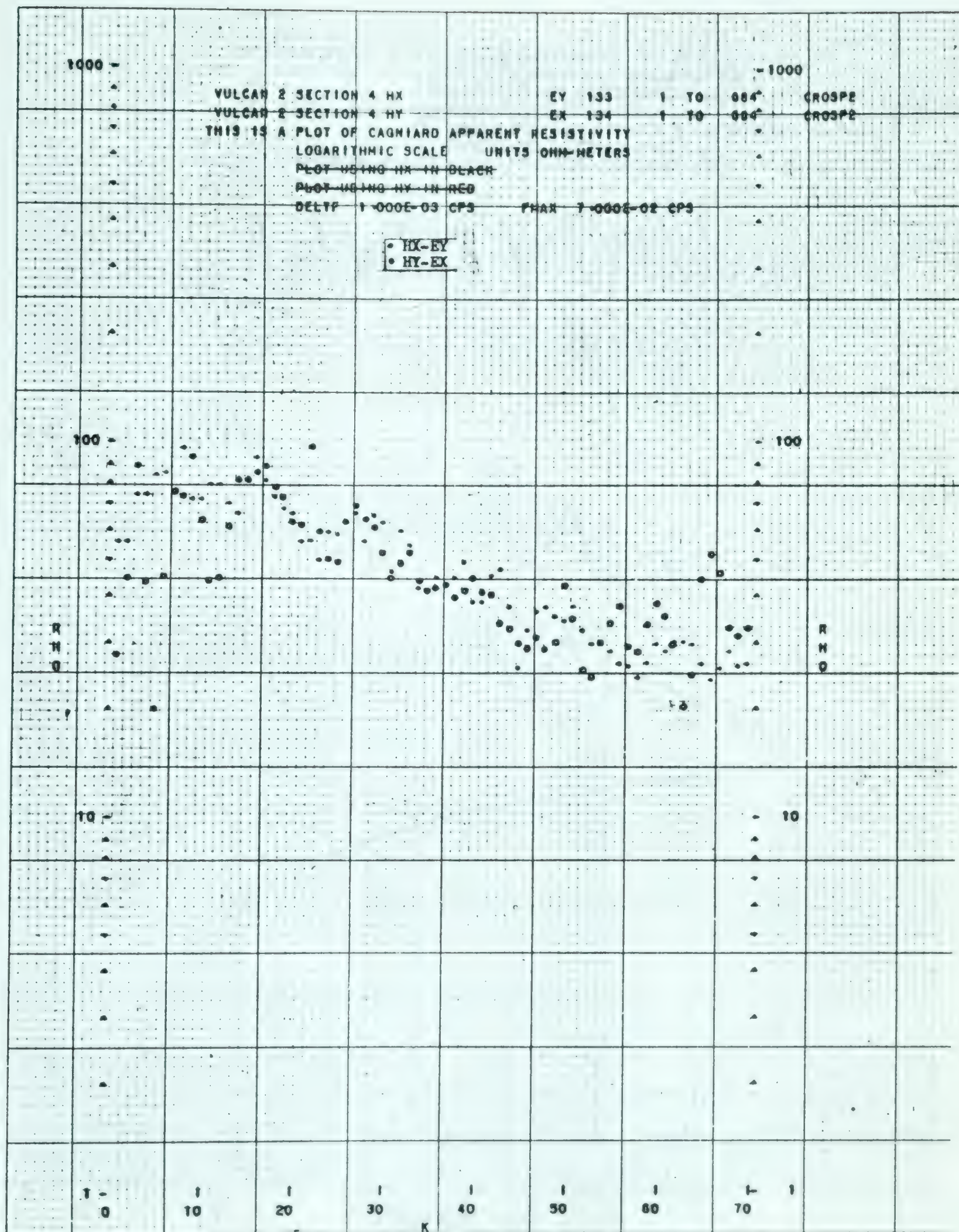


Diagram 118

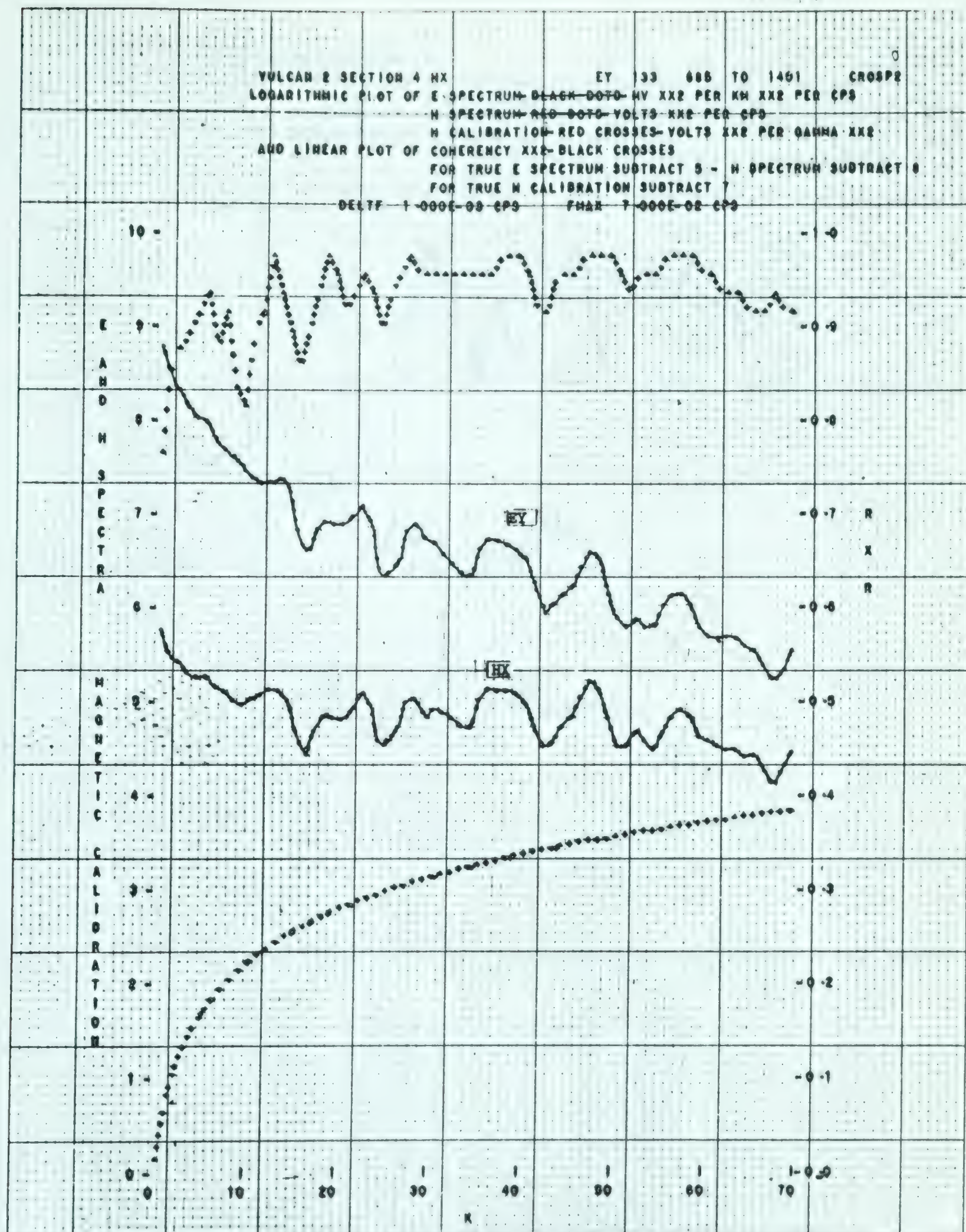


Diagram 119

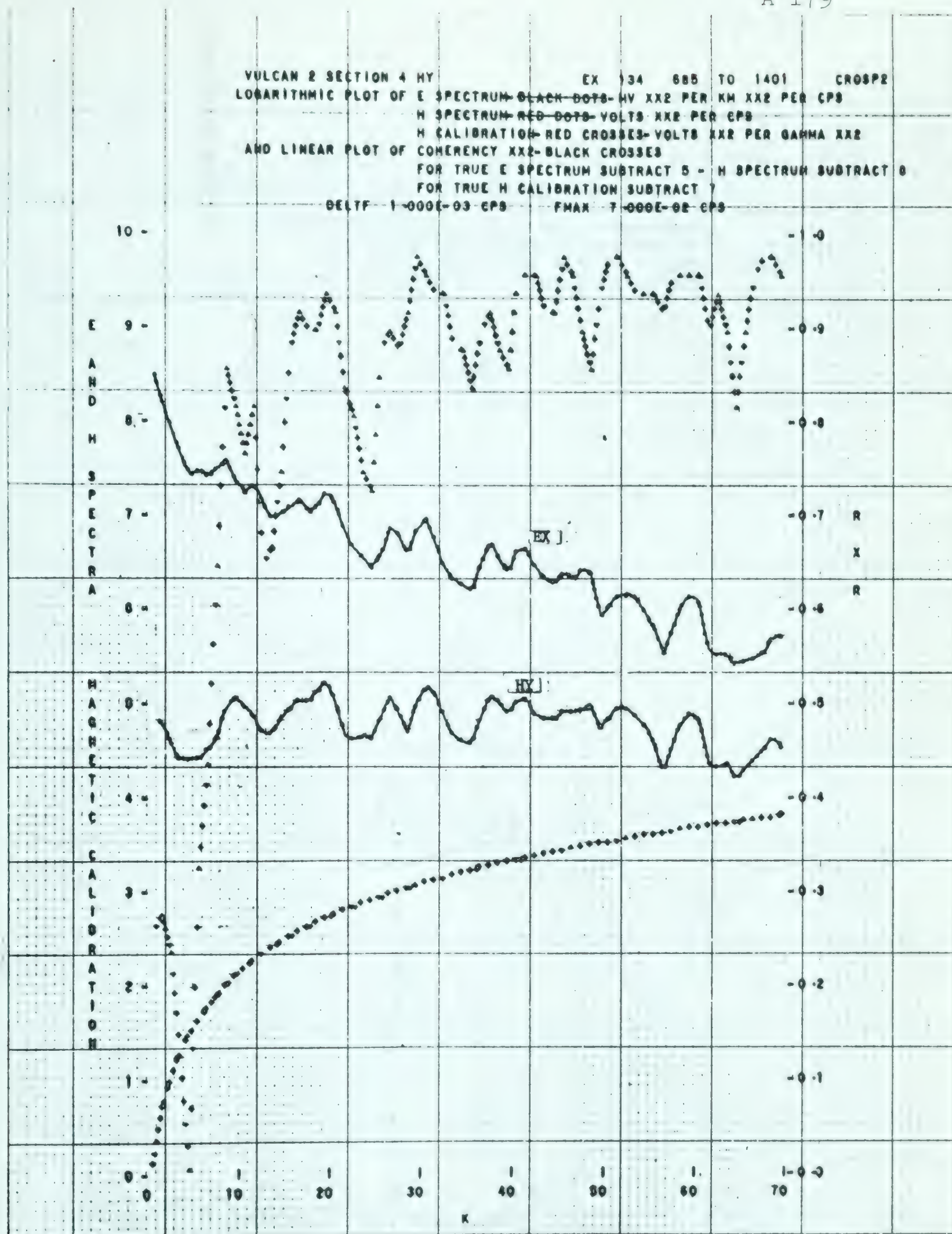


Diagram 120



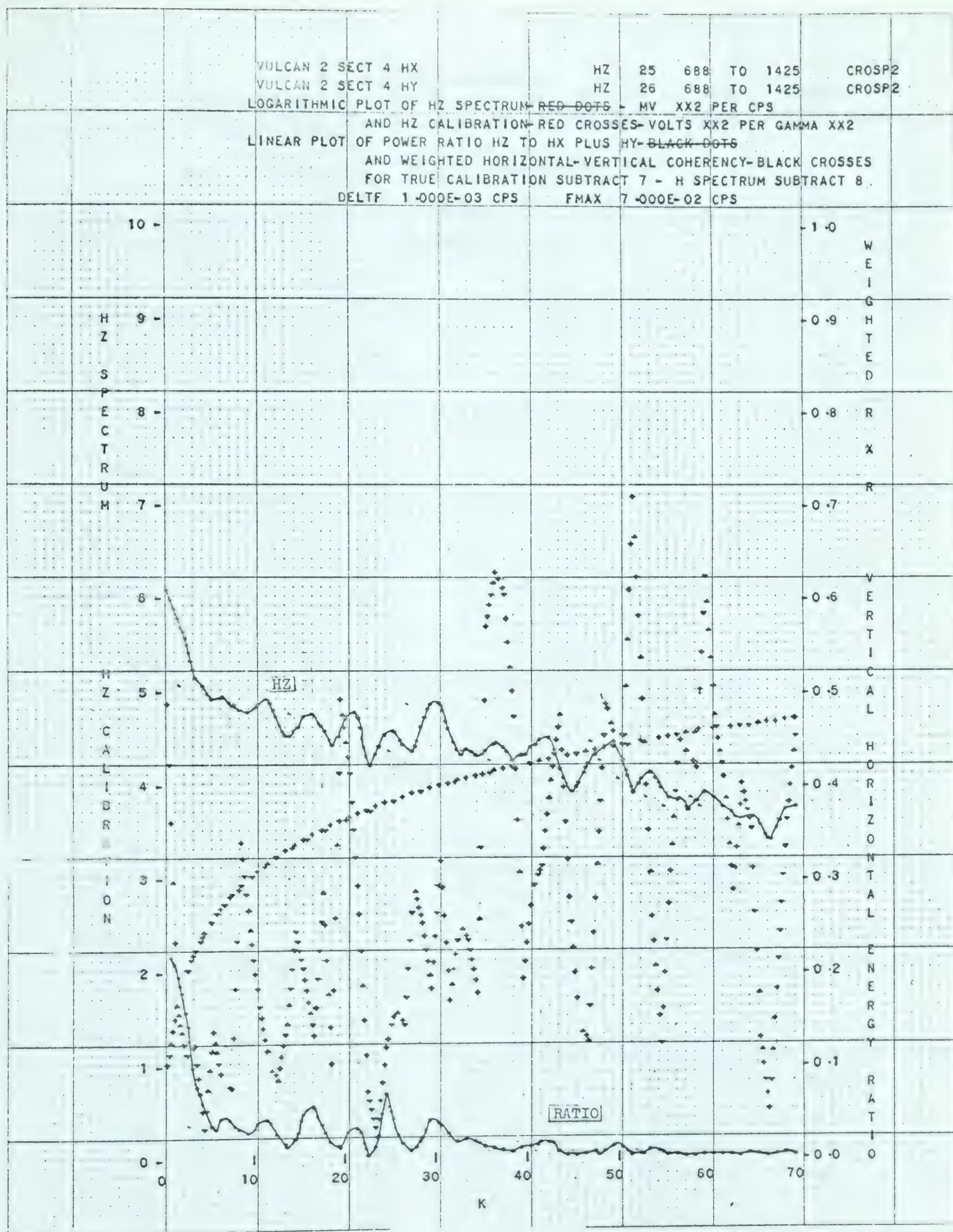


Diagram 121



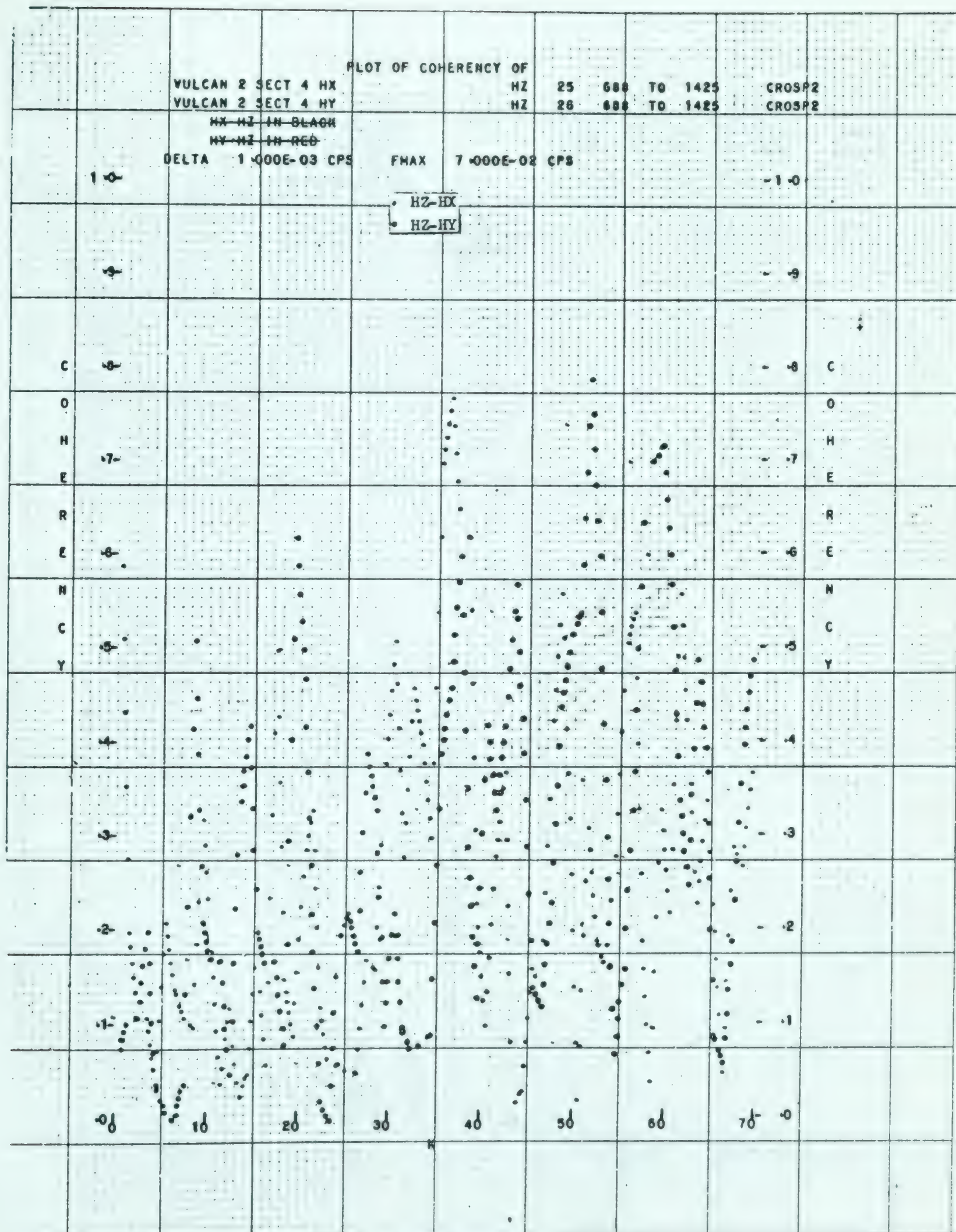


Diagram 122



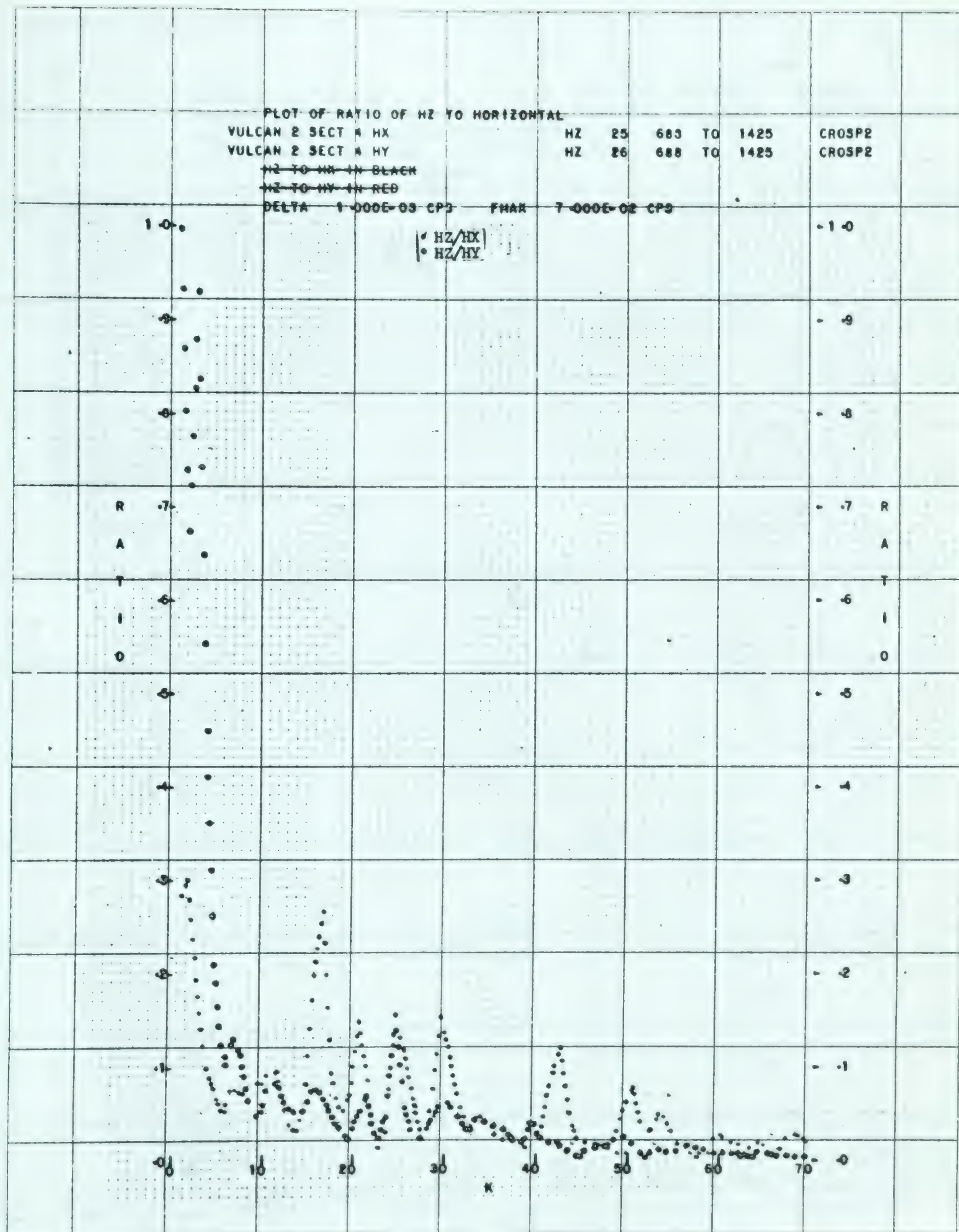


Diagram 123

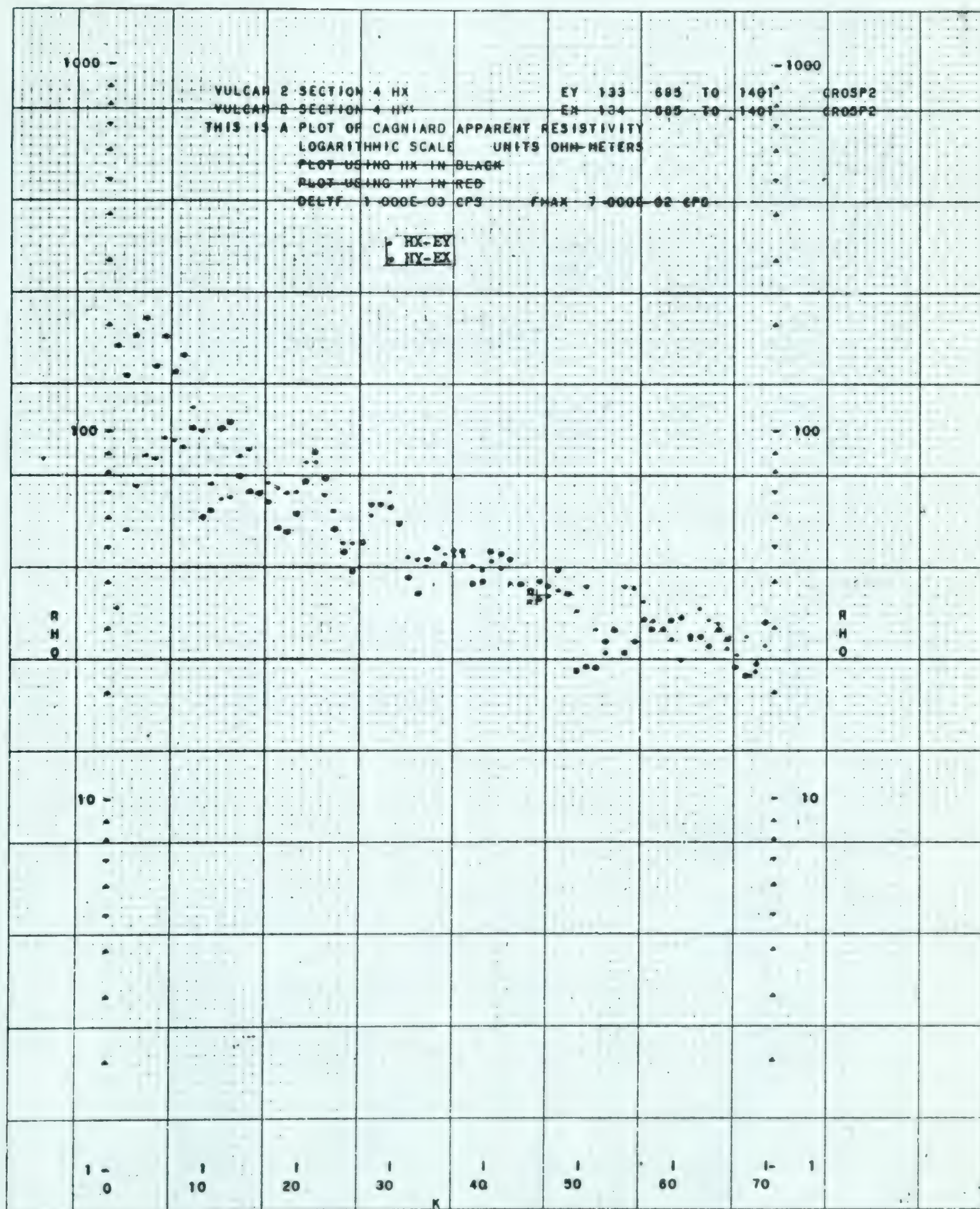


Diagram 124

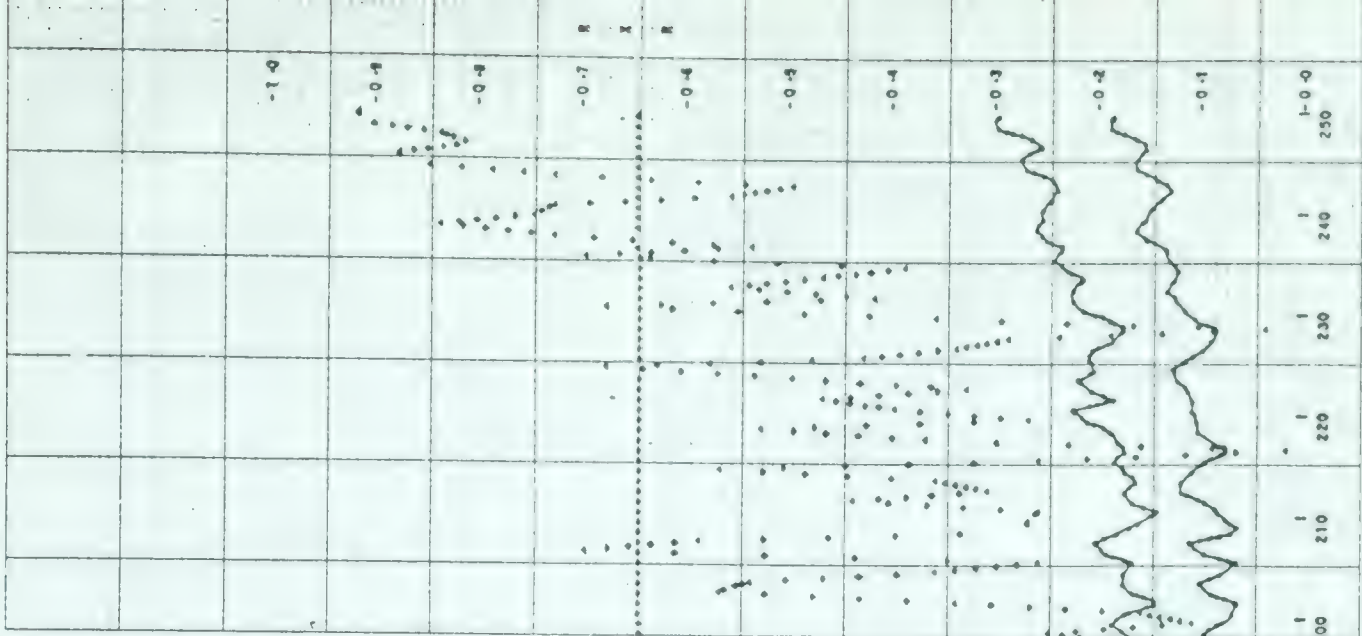
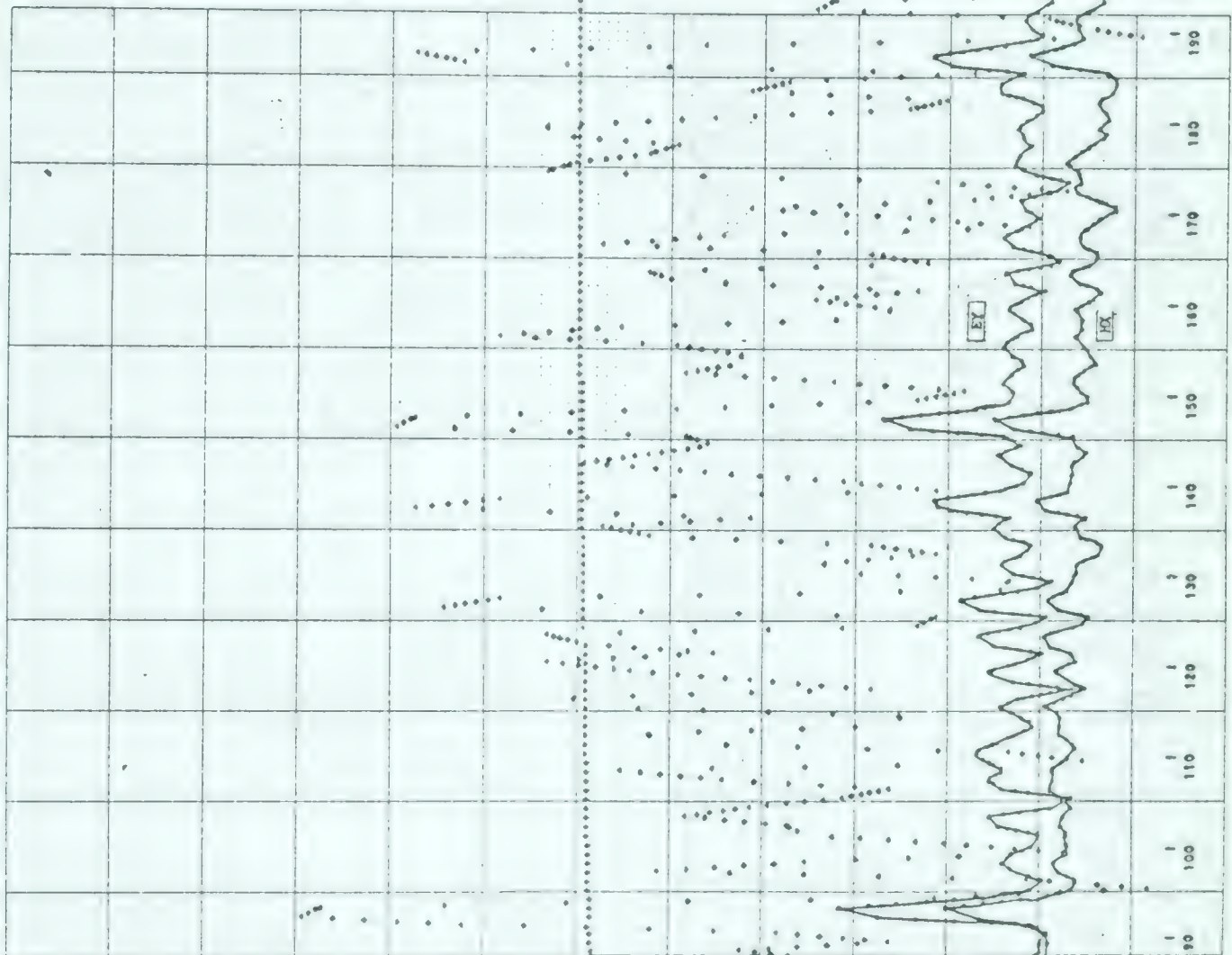
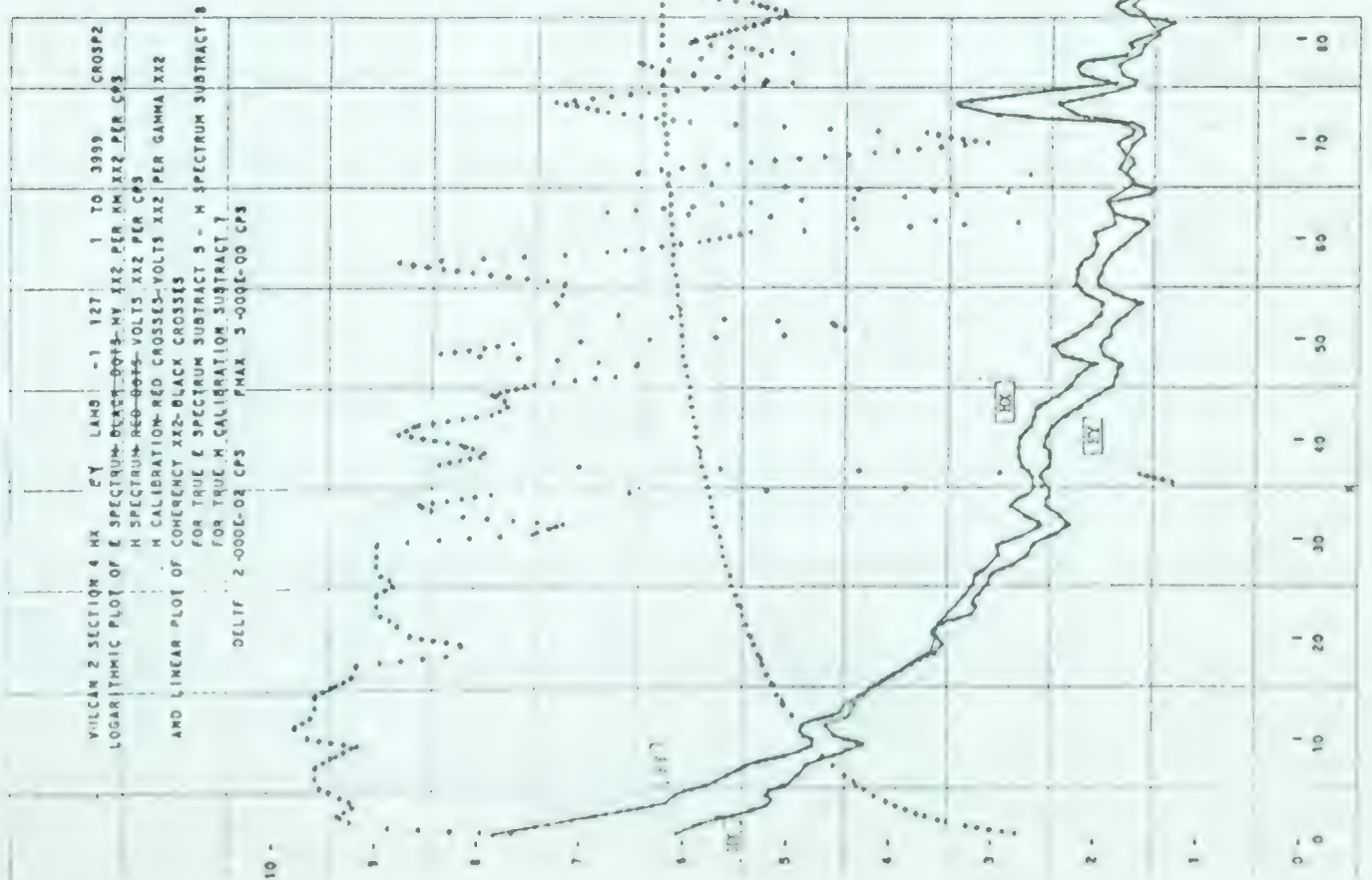


Diagram 125



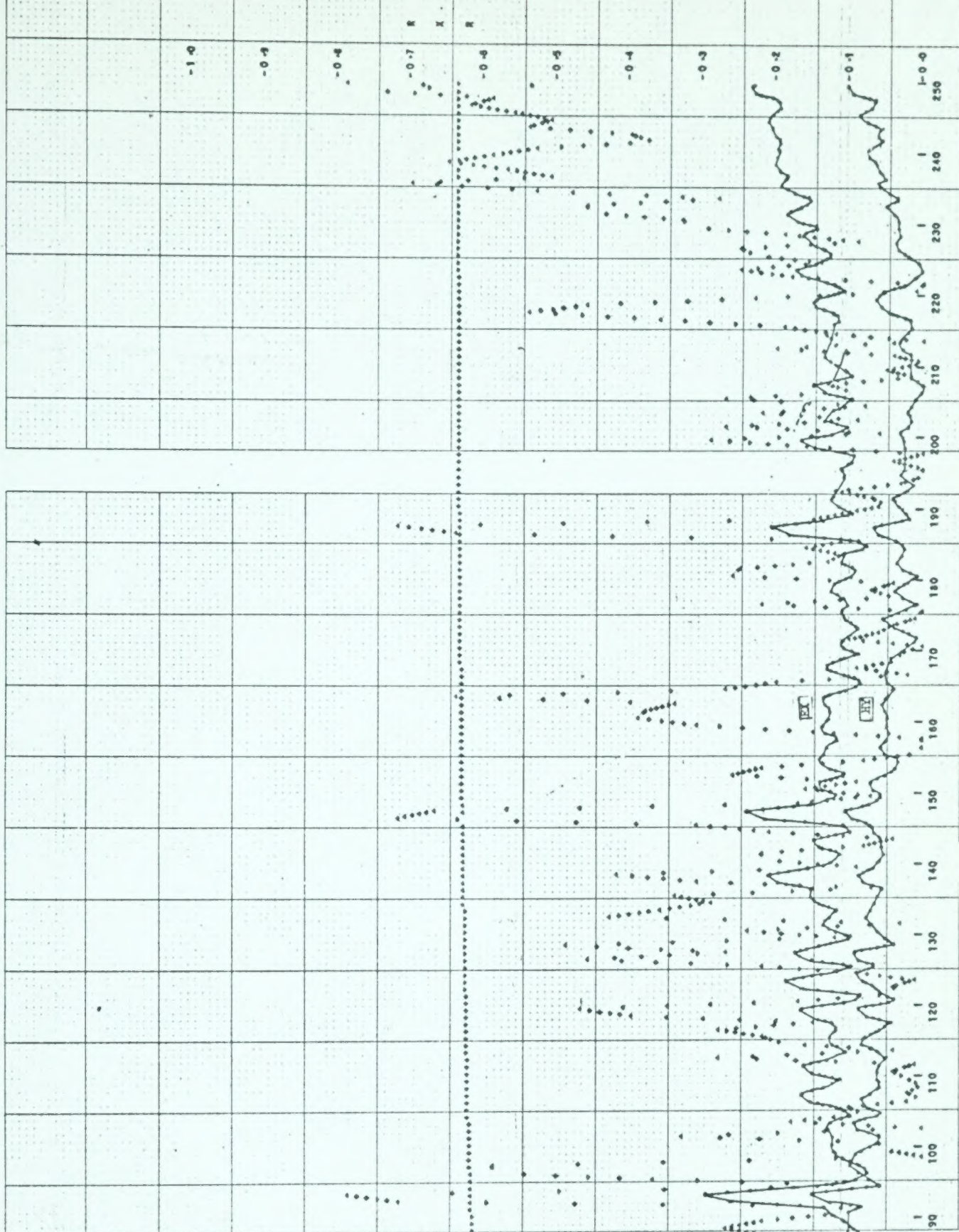
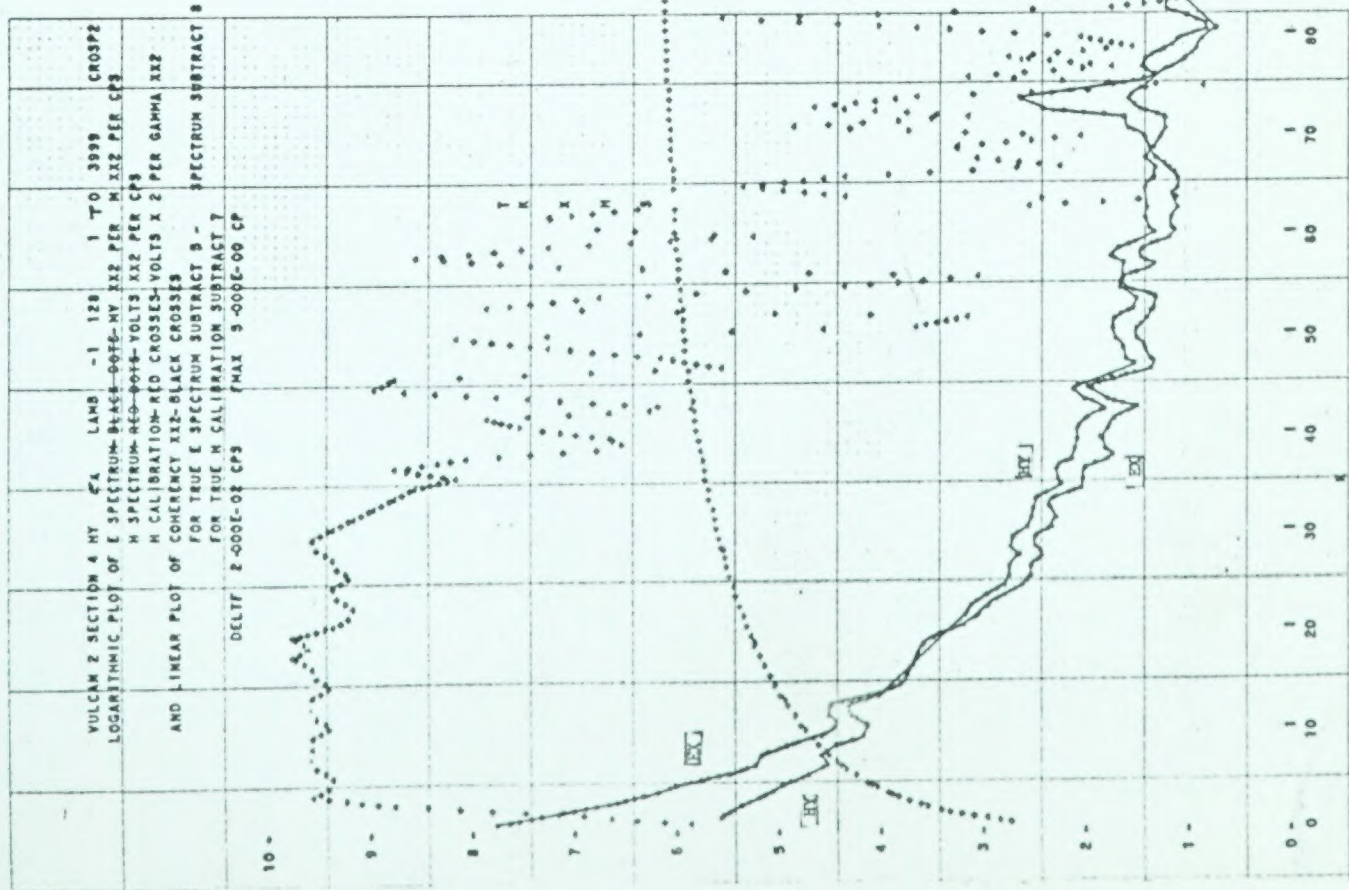


Diagram 126





B29826